IDENTIFICATION AND CHARACTERIZATION OF THE GENETIC AETIOLOGY OF A RARE DISEASE KNOWN AS ORAL-FACIAL-DIGITAL SYNDROME TYPE II OR MOHR SYNDROME

MOHAMMAD ABDULLAH SALEEM AL-SHBOUL

(B.Sc., Jordan University of Science and Technology, Jordan)

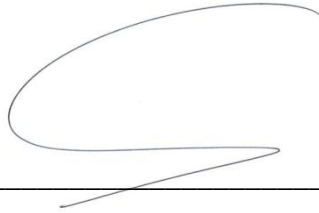## A THESIS SUBMITTED FOR THE DEGREE OF DOCTOR OF PHILOSOPHY

DEPARTMENT OF PAEDIATRICS
NATIONAL UNIVERSITY OF SINGAPORE

2014

DECLARATION

I hereby declare that this thesis is my original work and it has been written by me in its entirety. I have duly acknowledged all the sources of information which have been used in the thesis.

This thesis has also not been submitted for any degree in any university previously.

_____

Mohammad Abdullah Saleem Al-Shboul

28 October 2014

Acknowledgements

First, I would like to personally thank my supervisor Prof. Bruno Reversade for giving me the opportunity to work in the lab. I am deeply grateful for his help, guidance and trust in me as a PhD student. I am heartily thankful to him for supervising my PhD thesis in a patient and encouraging manner. He was not only my boss but also a good friend that I will never forget. This work could not be done without his help.

My sincerest thanks also go out to all members of the lab; the present and the others who left for their help and encouragement throughout my PhD. Special thanks to Dr. Srikanth and Dr. Gopianth for their help and invaluable advice during the course of this work. I will never forget all of you. Thank you SO MUCH!

I also thank our collaborators, Dr. Sudipto Roy, Dr. Semil Choksi, Dr. Laura Lee and Dr. Jeanne N. Jodoin for their invaluable work. Barry Marriman, Hane Lee are gracefully thanked for the mapping and sequencing analysis. Thanks also to the members of the Stem Cell Bank, Grace, Michelle and Eeswari for their help.

I would also like to extend my acknowledgments to Prof. Hanan Hamamy, who diagnosed the disease and Prof. Amira Almasri, Dr. Osama Ababneh and Dr. Baeth Al-Rawashdeh, the clinicians from the university of Jordan hospital for further investigations of the affected children and clarifications on the clinical manifestations. I would like to express my gratitude to Wesam and

Table of contents

Summary

Mohr syndrome is a rare autosomal recessive disorder belonging to a multisystemic and heterogeneous group of diseases called oral-facial-digital (OFD) syndromes. OFD comprises 14 clinical subtypes that are characterized by congenital defects in the oral cavity, facial structure, and digits. Until now, only 6 OFD genes responsible for types (I, IV, VI, XI, XIII and XIV), have been identified and the encoded proteins were found to play important roles in primary cilia formation and/or function. We ascertained two girls affected with Mohr syndrome (OFDII) in a consanguineous Jordanian family. Both presented with craniofacial dysmorphisms, clefts of the lip and palate, dental abnormalities and digital anomalies indicative of a ciliopathy.

Following homozygosity mapping and massive parallel sequencing we found a homozygous frameshift mutation in the *ASUN* gene that segregated with the disease. This mutation results in the production of a truncated protein in patients' cells. In *Drosophila* where *asun* is crucial for spermatogenesis, this human *ASUN* mutant allele failed to rescue *asun* null flies, suggesting that it behaves as a loss-of -function allele.

In mammalian cells, we found that ASUN displays ubiquitous localization in nucleus, cytoplasm and marks primary cilia. In patient's ciliated cells, we found that although the frameshift mutation had no effect on primary cilia formation *in vitro*, motile cilia formation was disrupted in patients' nasal epithelial cells. This suggests that the mutant allele is hypomorphic or specifically affects motile cilia formation.

In line with this hypothesis, loss of ASUN functions using either RNAi or morpholino (MO)-mediated knock-down in both cultured RPE cells and animal models lead to defective cilia formation and function. Both zebrafish and *Xenopus* morphant embryos showed developmental delay accompanied with motility defects and specific ciliary phenotypes.

Overall, I conclude that *ASUN* plays an essential role in cilia formation and function and that its biallelic disruption in humans causes Mohr Syndrome. The identification of *ASUN* as a causative gene for OFDII may provide insights into the identification of other OFD causative genes.

List of Tables

List of Figures

List of Appendices

List of Symbols

A

ADPKD	Autosomal Dominant Polycystic Kidney Diseases
ASUN	Asunder
AHI1	Abelson Helper Integration Site 1
ALMS	Alstrom Syndrome
ARPKD	Autosomal Recessive Polycystic Kidney Diseases
APC	Adenomatous Polyposis Coli

B

bp	Base Pairs
BB	Basal Body
BBS	Bardet-Biedl Syndrome
BMP	Bone Morphogenetic Protein
BSA	Bovine Serum Albumin

C

cDNA	Complementary DNA
CDK	Cyclin-Dependent protein Kinase
CE	Convergent Extension
CED	Cranioectodermal Dysplasia
CEP83	Centrosomal Protein 83 kDa
CEP164	Centrosomal Protein 164 kDa
CEP170	Centrosomal Protein 170 kDa
CEP290	Centrosomal Protein 290 kDa
CFNS	Craniofrontonasal Dysplasia
CHX	Cycloheximide
CK1	Casein Kinase I
CL	Cleft Lip
CLP	Cleft Lip/Palate
cM	CentiMorgan
CNCC	Cranial Neural Crest Cells
CNS	Central Nervous System
CNV	Copy number Variation
CORS	Cerebello-Oculo-Renal Syndrome
CP	Cleft Palate
CPO	Cleft Palate Only
CRPT1	Carpenter Syndrome Type 1

D

ddH2O	Double Distilled Water
DDX	DEAD-box-helicases
DHC	Dynein Heavy Chain
DHH	Desert HedgeHog
DMEM	Dulbecco Modified Eagle Medium
dNTPs	Deoxyribonucleotides

Dsh/Dvl	Dishevelled	
DTT	DiThioThreitol	
DYNC2-H1	Dynein Homodimeric Heavy Chain	
DYNC2LI1	Dynein Light Intermediate Chain	
DYNLL	Dynein Light Chain	

E

EB	End-Binding Proteins
ERK	Signal-Regulated Kinase
EBV-LYB	Epstein Barr Virus-transformed B-Lymphoblastoids
EVC	Ellis-Van Creveld Syndrome

F

FBF1	Transition Fiber Protein
FCS	Fetal Calf Serum
FGF	Fibroblast Growth Factor
FITC	Fluorescein Isothiocyanate
FND	Frontonasal Dysplasia
FZ	Frizzled

G

gDNA	Genomic DNA
Gli proteins	Effectors of Hedgehog Signaling
GPCR	G Protein-Coupled Receptors
GSK3β	Glycogen Synthase Kinase 3β

H

HEK293T	Human Embryonic Kidney 293T cell line
HH	HedgeHog Signaling
HLS1	Hydrolethalus Syndrome-Type 1
hpf	hours post fertilization

I

IBD	Identical-By-Descent
IDA	Inner Dynein Arms
IFT	Intraflagellar Transport
IGFIR	Insulin-Like Growth Factor Receptor
IHH	Indian HedgeHog
IMB	Institute of Medical Biology
INT	Integrator Complex
INTS	Integrator Complex Subunits
INV	Inversin
iPS	Induced Pluripotent Stem Cells
ISC	Ion-Secreting Cells

J

JATD	Jeune Asphyxiating Thoracic Dystrophy Syndrome
JBTS	Joubert Syndrome

K

KAP	Kinesin Associated Protein
kb	Kilo Base
KD	Knock-Down

	kDa	Kilo Dalton
	Kif24	Kinesin Family Member 24
	KS	Kartagener Syndrome
L		
	LCA	Leber Congenital Amaurosis
	LDL	Low Density Lipoprotein
	LEF	Lymphocyte Enhancer Factor
	LR	Left and Right
M		
	MAP	Mitogen-Activated Protein Kinase
	MCC	Multi-Ciliated Cells
	MCHR1	Melanin-Concentrating Hormone Receptor 1
	min	Minutes
	MKS	Meckel-Gruber Syndrome
	µl	Microliter
	mM	MilliMolar
	MO	Morpholino
	MRI	Magnetic Resonance Imaging
	mRNA	Messenger Ribonucleic Acid
	MSC	Mucus Secreting Cells
	MS	Mass Spectrometry
	MT	Microtubules
	MTOC	Microtubule Organizing Center
N		
	NIH3T3	Mouse Embryonic Fibroblast Cells
	NMD	Nonsense-Mediated mRNA Decay
	NPC	Neural Precursor Cells
	NPHP	Nephronophthisis
O		
	ODA	Outer Dynein Arms
	ODF2	Outer Dense Fiber 2
	OFD	Oral-Facial Digital Syndromes
	OSN	Olfactory Sensory Neurons
	ORF	Open Reading Frame
P		
	P2Y&P3Y	Purinergic (GPCRs)
	PBMC	Peripheral Blood Mononuclear Cells
	PBS	Phosphate Buffer Saline
	PCD	Primary Cilia Dyskinesis
	PCM	Pericentriolar Material
	PCP	Planar Cell Polarity
	PDGF	Platelet-Derived Growth Factor
	PDGFRα	Platelet-Derived growth Factor Receptor-α
	PHS	Pallister–Hall Syndrome
	PKC	Protein Kinase C
	PKD	Polycystic Kidney Disease

	PKHD1	Polycystic Kidney and Hepatic Disease-1
	PTC	Pretermination Codon
	PTCH1	Patched1
	PVDF	Polyvinylidene Fluoride
Q		
	qRT-PCR	Quantitative Real-Time PCR
R		
	RPE	Retinal Pigmented Epithelial Cells
	RPGRIP1L1	Retinitis Pigmentosa GTPase Regulator Interacting Protein 1-Like
	rpm	Rounds Per Minute
	RT	Room Temperature
S		
	SCTL1	A transition fiber/distal appendage protein
	SEM	Scanning Electron Microscopy
	SDS-PAGE	Sodium Dodecyl Sulfate Polyacrylamide Gels
	SGBS2	Simpson-Golabi-Behmel Syndrome Type 2
	SHH	Sonic HedgeHog Signaling
	siRNA	Small interference RNA
	SLOS	Smith-Lemli-Opitz Syndrome
	SLSN	Senior-Loken Syndrome
	SMO	Smoothened
	SNP	Single Nucleotide Polymorphism
	SRP	Short Rib Polydactyly Syndrome
	SSTR3	Somatostatin Receptor 3
	SUFU	Suppressor of Fused
T		
	TCF	Transcription of 'T' Cell Factor
	TCTN	Tectonic
	TEM	Transmission Electron Microscopy
	Tie	Angiopoietin Receptors
	TE	Tris-EDTA
	TZ	Transition Zone
	TRPV4	Transient Receptor Potential Vaniloid 4 Channel
U		
	UTR	Untranslated Region
V		
	V2R	Vasopressin Receptor
W		
	WDR34	Dynein Intermediate Chain
	WNT	A signal transduction pathway

Chapter 1: Introduction

1.1. Congenital defects

The failure to initiate or complete key developmental processes during embryogenesis can lead to congenital malformations also referred to as birth defects. It is estimated that over 3.3 million children under the age of 5 years die every year and around 270,000 newborns die during the first 28 days of their life every year (Disease Control Priorities Project (DCP2, 2008), Congenital Anomalies WHO, 2012) as a consequence of congenital anomalies. Whereas, congenital birth defects are frequent, the underlying causes for most of them are still unclear. Around 9 million children are born every year with serious congenital defects with estimated birth prevalence over 82 per 1,000 in middle- and low-income countries compared to 40 per 1,000 live births in high-income countries (DCP2, 2008). Congenital anomalies are defined as physical and developmental abnormalities affecting the body structure or functions that are present before birth, at birth and even after birth. These defects can affect one or several organs in the body and can also be associated with mental, visual and auditory abnormalities. These defects cause adverse effects on embryonic development, health, or functional abilities which may lead to a strong impact on the quality of life for infants and their parents or even be lethal leading to fetal death or stillbirth. Congenital defects can be inherited or can be found as isolated in particular pregnancies. Chromosomal abnormalities, single gene defects, environmental factors and multifactorial inheritance (genetic and environmental interaction) are the major causes of birth defects. It has been reported that around 6% and

7.5% of birth defects are caused by chromosomal and single gene defects, respectively; 5% to 10% are due to environmental factors (drug or chemical exposures during the pregnancy) and 20% to 30% are associated with a multifactorial inheritance (Turnpenny and Ellard, 2005). The causes of the majority of congenital anomalies (50% to 70%) remain unknown, while some of them could be due to *de novo* autosomal dominant mutations, uniparental disomy or submicroscopic chromosomal deletions (Turnpenny and Ellard, 2005). Thousands of genetic disorders have been identified so far, with multiple congenital malformations and most of them are inherited as autosomal recessive or dominant, or X-linked. The rate of autosomal recessive disorders is much higher in countries where consanguineous marriages are common; at least 20% of general population (DCP2, 2008). This social custom also increases the prevalence of unknown congenital disorders in these communities. The majority of these disorders are monogenic, caused by single gene mutations. Around two thirds of all disease-associated mutations are caused by base pair (bp) substitutions. Chromosomal abnormalities including deletions, insertions and duplications account for one third and mutations in regulatory regions that affect the level of expression of a gene account for only 1% of known mutations (Krawczak et al., 2000). It was reported that many single-gene disorders causing defects in multi-system organ result in a wide range of phenotypes with a variable severity that can be correlated to the type and the position of the mutation (Coene et al., 2009; Delous et al., 2007; Leitch et al., 2008; Valente et al., 2010). The overall birth prevalence of disorders due to morphogenesis defects is approximately estimated to 2% to 3 % of the population (Kalter and Warkany, 1983). Craniofacial anomalies,

skeletal dysplasia, congenital heart disease and neural tube defects are among the most common congenital anomalies of the fetus or newborn and comprise approximately one third of all congenital abnormalities.

1.1.1. Craniofacial anomalies

Craniofacial anomalies are a group of deformities affecting facial bones and the head (WHO - Craniofacial abnormalities). Orofacial clefts of lip and palate are the most common craniofacial malformation. Orofacial clefts have been categorized into two groups: (i) Cleft palate only (CPO) and (ii) Cleft lip with or without cleft palate (CL/P) and they can be found as unilateral, bilateral, median, complete, or incomplete. These anomalies can be found as isolated (non-syndromic) anomalies with an estimated incidence of approximately 1:600 and affecting around 70% of infants with CL/P and approximately 50% of CPO (Dixon et al., 2011; Jugessur and Murray, 2005; Mangold et al., 2011). The remaining percentage, cleft palate and lip can be associated with other congenital anomalies including other facial dysmorphisms, oral anomalies (tongue, teeth), liver and kidney cysts, heart defects and neurological features (central nervous system, mental retardation). The causes of orofacial clefts are complex or unknown; some of them are caused by multifactorial inheritance or could be only environmental, for example, due to a maternal exposure to teratogens or folic acid deficiency during pregnancy.

1.1.2. Skeletal defects

Skeletal defects are a group of anomalies affecting the formation and the development of the skeleton resulting in abnormalities in the development,

growth of bones and cartilage tissues of a baby (Alman, 2008; Ikegawa, 2006).

The classification of these conditions is based on clinical and radiological criteria. The defect in skeleton results in malformation of skull and limbs along with various abnormalities in the shape and structure of other skeletal structures. Limb defects are characterized by missing, extra, or abnormalities in the digits (fingers or toes), malformation of the entire leg, arm, hand, or foot, spine, pelvis and thorax. Skeletal anomalies are also frequent among birth defects with an estimated prevalence around 2.4/10,000 pregnancy in the neonatal period and accounts for 1% to 2% of perinatal deaths, mainly stillbirths (Pradhan et al., 2007). Skull abnormalities usually results from neural tube defects that may cause abnormalities in the brain, which in turn leads to skull developmental defect such as microcephaly.

Skeletal abnormalities as well as craniofacial anomalies can be found separately or as a combination, and potentially associated with other organ system defects. These conditions collectively can cause a group of rare syndromes known as ciliopathies. The aetiology of these congenital syndromes has been shown to be associated with ciliary function and/or formation defects resulting in disruption of developmental signaling pathways that play an essential role during embryonic development (Adams et al., 2008; Baker and Beales, 2009; Brugmann et al., 2010b; Ferkol and Leigh, 2012; Fliegauf et al., 2007; Toriello and Parisi, 2009; Waters and Beales, 2011). More than 50 ciliary related disorders have been identified so far; however, hundreds of diseases are potentially linked to ciliary function are still uncharacterized. Examples of ciliopathies include the following syndromes: Bardet-Biedl syndrome (BBS, MIM 209900), Meckel syndrome (MKS, MIM

249000), Joubert syndrome (JBTS, MIM 213300), Oral-facial digital syndrome type I (OFDI, MIM) and IV (OFDIV, MIM), Ellis van Creveld (MIM 225500), Jeune asphyxiating thoracic dystrophy syndrome (JATD, MIM 208500) Kartagener syndrome (KS, MIM 244400), Alstrom syndrome (ALMS, MIM 203800), Polycystic kidney diseases (ADPKD, MIM 173900, 613095; ARPKD, MIM 263200), Primary cilia dyskinesis (PCD, MIM 242650), Leber Congenital Amaurosis 1 (LCA1, MIM 204000), Short rib polydactyly syndrome, type II (SRPII / Majewski syndrome, MIM 263520), and others.

The discovery of the genetic causes of many congenital disorders and the knowledge gained about these birth defects played an essential role in decreasing the prevalence of these defects and maximizing the number of healthy children. A growing number of countries are putting in place policies in order to reduce the burden of many common and serious birth defects. These policies include education programs, genetic counseling, premarital, prenatal and postnatal screening for common recessive disorders, control of women's diets and regular follow up of pregnant women. These strategies have contributed significantly to the decrease of birth defects (March of Dimes Global Report, 2006; DCP2, 2008).

In line with this approach, I undertook to elucidate the genetic aetiology of a rare recessive syndrome that was first reported by Otto L. Mohr in 1941 (Martinot et al., 1994; Toriello, 2009). This disorder, called Mohr syndrome belongs to the class of Oral-facial digital syndromes (OFD) causing congenital anomalies in craniofacial structures, digits and other organs. Till date, the

genetic aetiology of Mohr syndrome has not been determined. This syndrome was diagnosed in two patients born to consanguineous parents in Jordan. The two affected girls, display similar phenotypes consisting of a constellation of craniofacial dysmorphisms (hypertelorism, microcephaly, wild nasal bridge, low-set ears, cleft lip and micrognathia); abnormalities in the oral cavity (cleft palate, epiglottis anomalies and teeth defects) and digits anomalies (polydactyly and clinodactyly). Other marked features include heart defects, ear discharge associated with deafness and recurrent respiratory tract infections accompanied by chronic cough and other manifestations. The observed phenotypes in the two affected girls bear cardinal features of ciliopathies, suggesting that the causative gene could be associated to cilia biogenesis and or ciliary functions.

After this brief introduction, I will provide in the next chapter a detailed description of cilia structure, biogenesis, function and the most common developmental signaling pathways associated with these organelles. At the end of this chapter, I will also provide a general overview about ciliopathies including OFD and finally give a thorough clinical description of symptoms specifically encountered in Mohr syndrome patients.

1.2.   Cilia: a general introduction

Cilia (or cilium in singular meaning *eyelash* in Latin) were first observed in protozoans by Anthony van Leeuwenhoek in 1679 using light microscope. He defined them as little legs or thin feet, which were moving very nimbly (Satir, 1995). Early research on these organelles were started in 1786 and focused on their motility (Satir, 1995). Cilia are ancient structures and highly conserved

throughout evolution found in all vertebrates such as mouse, zebrafish, chicken or *Xenopus*. The ciliated *Paramecium* and *Tetrahymena*, the nematode *Caenorhabditis elegans*, *Chlamydomonas*, *Trypanosoma* and the green algae also are also recognized as ciliary organisms, and have provided great insights in cilium biology, with the exception of many fungi, yeast, red algae and higher plants, and invertebrates such as *Drosophila* are not ciliated (Ginger et al., 2008; Vincensini et al., 2011a). Since then a lot of research using advanced technologies and different model organisms have propelled the study of cilium structure and function and confirmed the crucial role of these organelles for human biology and developmental disorders.

1.3. Cilium structure

Cilia are tiny microtubule-based organelles that extend from the surface of almost all cells. Although cilia are found across a wide range of organisms, they are ubiquitous only in vertebrates (Fliegauf et al., 2007). Cilia can be found in two categories depending on the cell type as either a single (non-motile) or clusters of multi-cilia (motile) (Figure 1). The structure of cilia is conserved and can be subdivided into different compartments that include the basal body (BB) (a specialized centriole), the transition zone (TZ), the axoneme, the ciliary membrane and the tip. A schematic representation of the cilium structure is presented in figure 1.
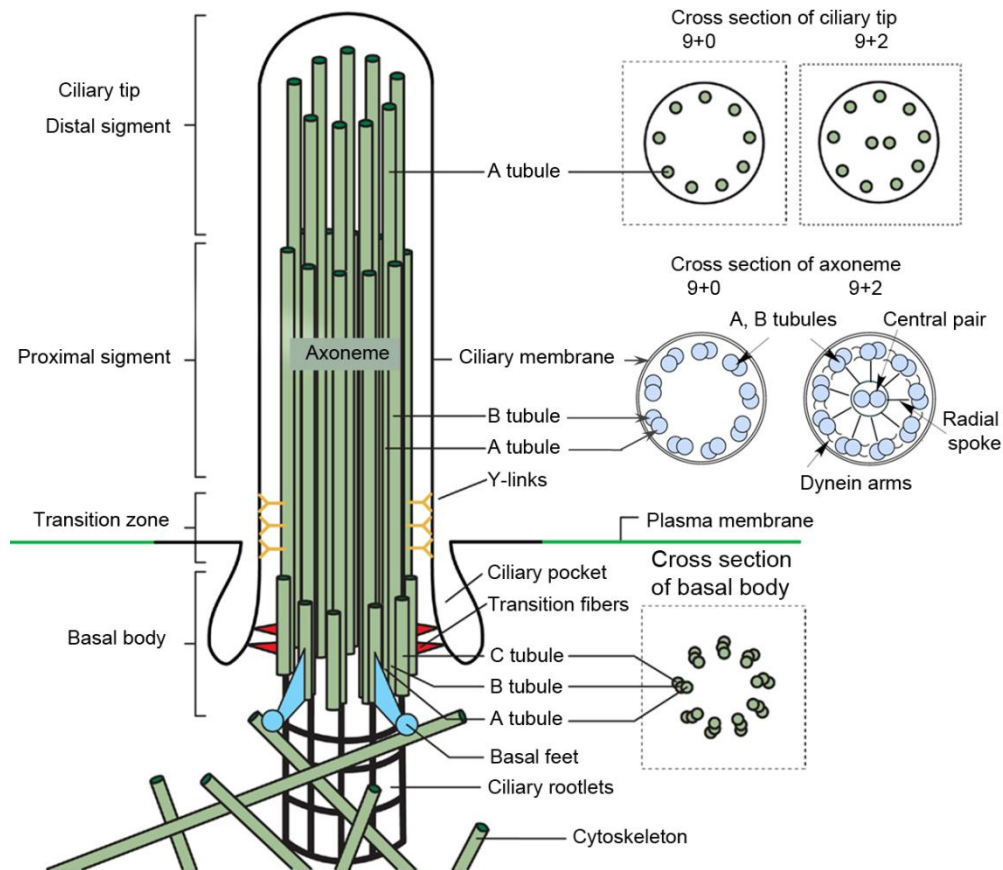
Figure 1: Schematic representation of a basic cilium structure. A typical cilium consists of the basal body (BB), the transition zone (TZ), the axoneme, the ciliary membrane and the tip. Both motile and non-motile cilia share common ciliary architectures. Motile cilia axonemal cross section (9+2) is composed of nine MT doublets (A and B tubules) surrounding two single central MT. Inner and outer dynein arms are attached to A-tubules joining to the B-tubules of the next doublet. The doublets are connected to each other by nexin links. This cilium also contains radial spokes that are projected towards the central pair of MT. However, the central MT, the radial spokes as well as the inner and outer dynein arms are absent in the non-motile (9+0) axonemal cilia. The BB composed of 9 triplets MT and is docked at the cytosolic MT through the basal feet, and it is anchored to the ciliary membrane by the transition fibers. The ciliary rootlets extend from the BB into the cytoplasm. The TZ is characterized by the presence of Y-links. The cilium is shielded by the ciliary membrane, and at the ciliary base a plasma membrane invagination, called the ciliary pocket. Adapted from Broekhuis (2013), cross section of axoneme adapted from Dawe HR (2007).

The BB is located at the base of cilia, normally originates from the mother centriole and anchors the cilium on the cell surface. Other than the anchoring of cilia, BB is required for the correct positioning and orientation of cilia in response to fluid flow. Moreover, BB regulates the entry of ciliary proteins that are required for cilia biogenesis through the intraflagellar transport (IFT) machinery (Stephan et al., 2007). The internal structure of BB is identical to a centriole. Therefore it is also known as a specialized centriole. Centrioles are cylindrical hollow structures typically consisted of a set of nine triplet microtubules (MT) designated as A, B, and C and arranged in a circular manner (Figure 1). Pair of centrioles are located perpendicular to each other and embedded in an electron-dense pretentious mass called the pericentriolar material (PCM) that forms the core of the centrosome and harbors a large number of proteins required for MT maintenance, anchoring and nucleation (Moser et al., 2010) (Figure 2a). These include PCM-1 and the mother centriole subdistal appendages proteins (ninein, centrosomal protein 83 kDa (CEP170), end-binding protein 1 (EB1), or EB3 that are involved in MT anchoring, whereas γ-tubulin and other associated proteins such as pericentrin, polo and aurora kinases are required for MT nucleation. Other proteins such as katanin are accountable for releasing MT from the centrosome into the cytoplasm (Badano et al., 2005; Blagden and Glover, 2003; Bornens, 2002). Cells usually exhibit single centrosome (two centrioles) or two centrosomes (two pairs of centrioles) depending on whether they are in G1 or G2 phases of the cell cycle, respectively. The centrosome is relatively small (1 μm in diameter) and was first described by Theodor Boveri at the end of 19th century as a special compartment of cell cycle. The vertebrate centrosome/centrioles

are highly organized structure and serve as the cell MT organizing center (MTOC) that regulates MT of cytoskeleton and spindle of mitotic cells which are required for cell division (Nigg and Raff, 2009). The centrosome plays a pivotal role in several cellular processes, including cell motility, polarity, adhesion, maintenance the cell shape, vesicles transportation and harbor many signaling proteins (Bettencourt-Dias and Glover, 2007; Debec et al., 2010; Moser et al., 2010)

At the BB, the A and B tubules extend to form the axoneme and the C tubules terminate before the axoneme at a region is annotated as the transition zone (TZ) (Figure 1). The TZ is located distal to the mother centriole, above the BB linking it to the upper part of cilia, the ciliary axoneme, where the triplet MT of the BB become more characteristic and convert into doublet microtubular structure of the axoneme. The TZ is also characterized by distinct structures called transition fibers or alar sheets which are enriched with proteins implicated in cilia biogenesis and required for entry of ciliary proteins to the cilium. Transition fibers are electron dense fibers that typically originate from the distal appendages of mother centriole, and contain several proteins such as OFDI (oral-facial-digital syndrome type 1), ODF2 (outer dense fiber 2), CEP164 (centrosomal protein 164 kDa), CEP83, SCTL1 and transition fiber protein (FBF1) required for the BB docking and anchoring to the cell membrane (Ishikawa et al., 2005; Kim and Dynlacht, 2013; Pedersen et al., 2012; Schmidt et al., 2012). On the other hand centrosomal proteins such as, CEP97, CP110 and kinesin family member 24 (Kif24) suppress ciliogenesis (Kobayashi et al., 2011; Spektor et al., 2007). TZ is also composed of Y-shaped linker fibers that anchor the MT in their position to the most proximal

region of the ciliary membrane, a protein-rich membrane region called ciliary necklace (ciliary pores). This region is likely function as a membrane diffusion barrier, regulating the entry of ciliary proteins from the cytoplasm to the cilia and *vice versa* (Garcia-Gonzalo et al., 2011; Omran, 2010). The TZ and BB comprise a growing number of proteins which constitute the ciliary gate and function as gatekeepers that regulate the ciliary trafficking (Benzing and Schermer, 2011; Williams et al., 2011).

The extracellular part of cilia called the axoneme, which extends from the BB and is surrounded by a ciliary membrane. The axoneme structure represents the core of cilia and consists of nine doublets MT, A and B MT arrange in a circle (Ringo, 1967) (Figure 1). These MT are composed of polymers of α- and β- tubulin that undergo posttranslational modifications and rapidly growing at one end (plus-end). The other end of MT (minus-end) usually anchors at the BB and assemble more slowly, resulting in a directional growing of MT toward the ciliary tip. The ciliary tip is the most distal part of the cilium that harbors the MT plus-end. The ciliary tip is a highly specialized structure, at which the IFT cargo proteins are switched between anterograde and retrograde transport. The ciliary tip is enriched with end-binding proteins that maintain the axoneme structure by regulating the MT dynamics (Pedersen et al., 2012; Sloboda, 2005).

The extracellular part of cilia is surrounded by a bilayer lipid membrane called the ciliary membrane which extends from the plasma membrane of the cell and is enriched with many receptors, ion channels and signaling molecules,

suggesting that cilia and flagella function as cellular signaling centers (Berbari et al., 2009; Rohatgi and Snell, 2010; Singla and Reiter, 2006).

1.4.   Types of cilia

1.4.1.   Motile cilia

Motile cilia length is ~10-15 μm and normally found as clusters of multi-cilia on the epithelial cells of many organs in the body (Figure 2a). The axoneme of motile cilia contains, in addition to the A and B tubules, a central pair of MT which is found predominantly in these types of cilia; therefore, they are defined as (9+2) axonemal cilia. This central pair is important to generate force required to induce motility. The doublets MT of motile cilia are attached to each other by nexin links and they are fixed in their place along the axoneme structure by radial spokes that extend into the central MT pair. The outer doublets are also decorated with several protein complexes called inner dynein (IDA) and outer dynein (ODA) arms. These motor arms are rigidly attached to A tubules that cause sliding of MT over each other by ATP-dependent reactions, thus regulating their dynamics and they are responsible for the circular movement of cilia (Colantonio et al., 2009; Ibanez-Tallon et al., 2003; Lindemann and Lesich, 2010; Marshall and Nonaka, 2006).

1.4.2.   Primary cilia

Primary cilia are highly conserved organelles, found in a single entity on the surface of most vertebrate cells (Figure 2b,c). The length of primary cilia ranges from 3 to 10 μm. The axoneme of primary cilia is devoid of several structural components present in motile cilia such as, the motor structures and the central MT pair; therefore they are non-motile and designated as (9+0) axonemal cilia.

1.4.3. Other types of cilia

Based on whether the axoneme of cilium has the central MT pair, cilia are categorized into motile (9+2) and non-motile (primary) (9+0) cilia. Many studies showed an exception to this classification in few cell types. For example, motile cilia with axoneme architecture (9+0) which incorporate radial spokes and dynein arms can be found in the embryonic node (nodal cilia), that generate leftward fluid flow required for left-right asymmetry of developed embryo (Hirokawa et al., 2006; Ibanez-Tallon et al., 2003; Nonaka et al., 1998; Praetorius and Spring, 2005). However, their motility is different from that of motile cilia (McGrath et al., 2003). The photoreceptor connecting cilia in the retinal epithelia have a (9+0) axoneme (Figure 2d). The vertebrate hair cells in the inner ear are required for hearing and balance. Each of these cells consists of a hair bundle comprises of specialized actin-based microvilli, known as stereocilia (Figure 2e). The stereocilia are arranged in a staircase-like pattern and the kinocilium is located adjacent to each bundle. Mature kinocilia possesses a (9+2) ultrastructure, while immature cilia have the (9+0) but they are not motile (Dabdoub and Kelley, 2005; Muller, 2008; Nayak et al., 2007). These cilia play a role in the development and polarity of the stereocilia bundle (Montcouquiol et al., 2003). In our olfactory tissues, the site of odorants sensation, also have non-motile (9+2) cilia on the olfactory sensory neurons (ONS) (McEwen et al., 2008; Moran et al., 1982; Satir and Christensen, 2007) (Figure 2f). Interestingly, in many vertebrates, such as zebrafish and frogs, they display both '9+0' and '9+2' cilia (Malicki et al., 2011; McEwen et al., 2008).

14

Rare structure of motile cilia with '9+4' axoneme has been identified in rabbit embryos notochordal plate (Feistel and Blum, 2006). Cilia with variable axoneme structures can be seen in other organisms such as *Caenorhabditis elegans* and protists expressing non-motile and motile cilia, respectively (Evans et al., 2006; Gluenz et al., 2010).
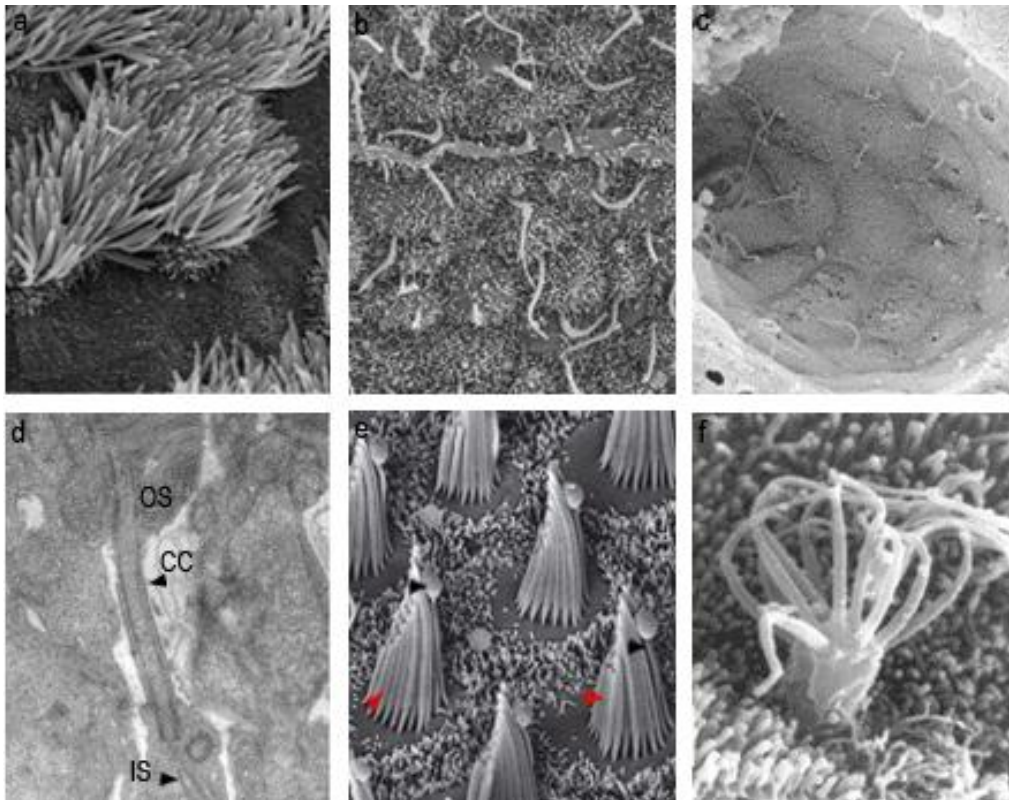
Figure 2: Ultrastructure of different types of cilia. (a-c,e,f) Scanning electron microscopy (SEM) and (d) Transmission electron microscopy (TEM). (a) Motile cilia in the epithelial cells of trachea. (b) Nodal cilia. (c) Renal primary cilia. (d) Longitudinal section of the connecting cilium of a mouse rod photoreceptor cell. CC, connecting cilium; IS, inner segment; OS, outer segment. (e) Stereociliary bundle (red arrows) with kinocilium (black arrows) and cuticular plate. (f) Olfactory cilia. Pictures (a and b) are adapted from http://biodidac.bio.uottawa.ca/search.htm; (c-f) are adapted from (Eley et al., 2005); (e) is a cover image of journal of physiology.

1.5.　　Formation of a cilium

Cilia are synthesized *de novo* in cells before emanating to the cell surface and in most cells, this occurs more than once during the lifetime of single cell. The formation of cilia is known as ciliogenesis, and it is strongly coordinated with the cell cycle (Quarmby and Parker, 2005). Cilia normally nucleate and grow to the cell surface during G1/G0 phase of the cell cycle. Once mitosis is completed, each new cell contains only one centrosome that harbors a single pair of centrioles, located perpendicular to each other and in close proximity to the surface of the nuclear envelop (Figure 3a). One of these centrioles is called the mature (mother) centriole; at which the cilium is extended and the other is less mature known as the (daughter) centriole. Cells then enter quiescent state (G0) or proceed to G1 phase of cell cycle; during which the centrosome migrates to cell surface and cilia are formed. Prior to mitotic cell cycle entry, the cilium is gradually resorbed and BB and centrioles are freed. Centrioles are then duplicated during S phase and progressively elongated throughout the G2 phase. At G2 phase, cells have a pair of centrosomes attached to each other, each of them comprising two mature (mother and daughter) centrioles surrounding by PCM (Pan and Snell, 2007; Rohatgi and Snell, 2010; Tanos et al., 2013) (Figure 3b). Centrosomes are then separate from each other and move to the poles of cells during mitosis, to allow for the formation of spindle MT. Spindles are required for correct chromosomal segregation and downstream mitotic events. When cells complete cell cycle, the mother centriole docks to the plasma membrane and form the BB, from which cilia are assembled.
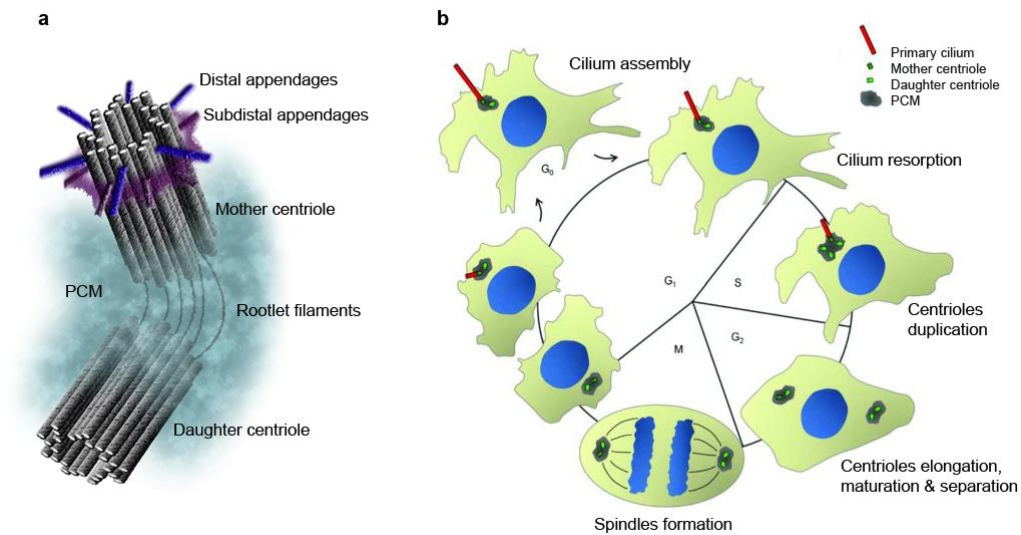
Figure 3: Assembly and disassembly of primary cilia. (a) Scheme of a centrosome/centrioles structures. The mammalian centrosome is composed of two (mother and daughter) centrioles which are cylindrical in structures each one is composed of 9 triplets of MT and connected to each other by rootlet filaments at their proximal regions. The mother centriole represents the site of the basal body nucleation. It has distal (blue) and subdistal (purple) appendages where MT nucleation takes place. The two centrioles are embedded in the pericentriolar matrix (PCM). Adapted from (Anderhub et al., 2012). (b) Primary cilia and cell cycle. Formation of the primary cilium is coordinated by cell cycle and is assembled and completely formed cells in the G0/G1 phase of the cell cycle. As cells prepare for cell cycle, the cilium starts to resorb and then duplicates in the S phase of the cycle. The old centrioles become mother centrioles associated with newly daughter centrioles followed by elongation and maturation of centrioles occurs during the G2/M phase of the cycle. During mitosis the mature centrosomes are separated and migrate to the poles of the nucleus, an essential step for mitotic spindles assembly. At the end of mitosis, two cells are produced each with single centrosome (mother and daughter) centrioles. Adapted from (Pedersen et al., 2012).

1.6.   Constructing a functional cilium

The cilium is a compartmentalized structure which is devoid of ribosome. Thus, there is no protein synthesis within the ciliary matrix. Proteins that contribute to the formation, function and maintenance of cilia are transported from the cell body along the ciliary axoneme toward the tip (anterograde) and then back down to the cell body (retrograde), a process mediated by a conserved machinery of transport called IFT (Figure 4). IFT was first observed by Kozminski in 1993 in the green alga Chlamydomonas. It is composed of two MT-associated motor protein complexes called kinesins and dyneins (Cole et al., 1998). IFT machinery is well conserved in eukaryotes and is indispensable for assembly, disassembly, function and maintenance of cilia and flagella, as well its vital role in these organelles for generating signaling (Scholey and Anderson, 2006). In the anterograde transport, the cargo of proteins derived from Golgi-derived vesicles are loaded onto IFT and then attached to a heterotrimeric complex kinesin-II. A kinesin-II complex consists of two motor subunits (KIF3A and KIF3B) and a non-motor subunit kinesin-associated protein (KAP) (Cardenas-Rodriguez and Badano, 2009; Pedersen and Rosenbaum, 2008). The IFT particles composed of 2 distinct sub-complexes IFT-B (involved in anterograde transport) and IFT-A (involved in retrograde transport); and each sub-complexes comprises of 14 and 6 protein subunits, respectively (Ishikawa and Marshall, 2011; Scholey, 2008) (Figure 4). Once the kinesin-II motors reach the ciliary tip, the IFT is remodeled, thus the proteins cargo is released. The kinesin-II motors become inactive and cytoplasmic dynein 2 motors hence are activated, and initiating the retrograde transport back to the cilium base, (Lucker et al., 2005; Scholey and Anderson,

2006). Cytoplasmic dynein 2 is composed of a homodimeric heavy chain; DYNC2-H1, a light intermediate chain; DYNC2LI1, an intermediate chain, WDR34, and a light chain, DYNLL (Broekhuis et al., 2013). Many proteins that are associated with BBS form a large protein complex called a BBSome, that have been shown to be involved in proteins trafficking to the cilium (Jin et al., 2010; Nachury et al., 2007). BBSome also corporates with multiple small GTPases, such as rab8 and other GTPases to regulate protein passage from Golgi vesicles to the cilium and vice versa (Drummond, 2012; Nachury et al., 2007; Westlake et al., 2011).

The length of cilia is not fixed and can be modified. After cilia are assembled, they undergo continuous growing and turnover at their tips. This dynamic process depends on the balance between the anterograde and retrograde transport, modification of mictrobular axoneme and other structural proteins such as TCTN1, TCTN3 and MKS proteins that reside at the TZ (Broekhuis et al., 2013). Impairment of their function may cause Meckel and Joubert syndromes which are associated with shortened cilia. Mutations in many nephronophthisis (NPHP) proteins result in elongation of primary cilia (Patzke et al., 2010). Conversely, components of IFT-A complex, a centrosomal protein Nde1 and many proteins involved in deacetylation of ciliary axoneme, depolymerization of MT and polymerization of actin filaments, all negatively regulate cilia length (Kim and Dynlacht, 2013). In addition, several regulatory proteins (e.g. mitogen-activated protein (MAP) kinases, NIMA-related kinases, cyclin-dependent protein kinase (CDK)-related kinase, aurora-like kinases, and GSK3) (Malicki et al., 2011) have been identified to affect cilia length by an unknown mechanism.
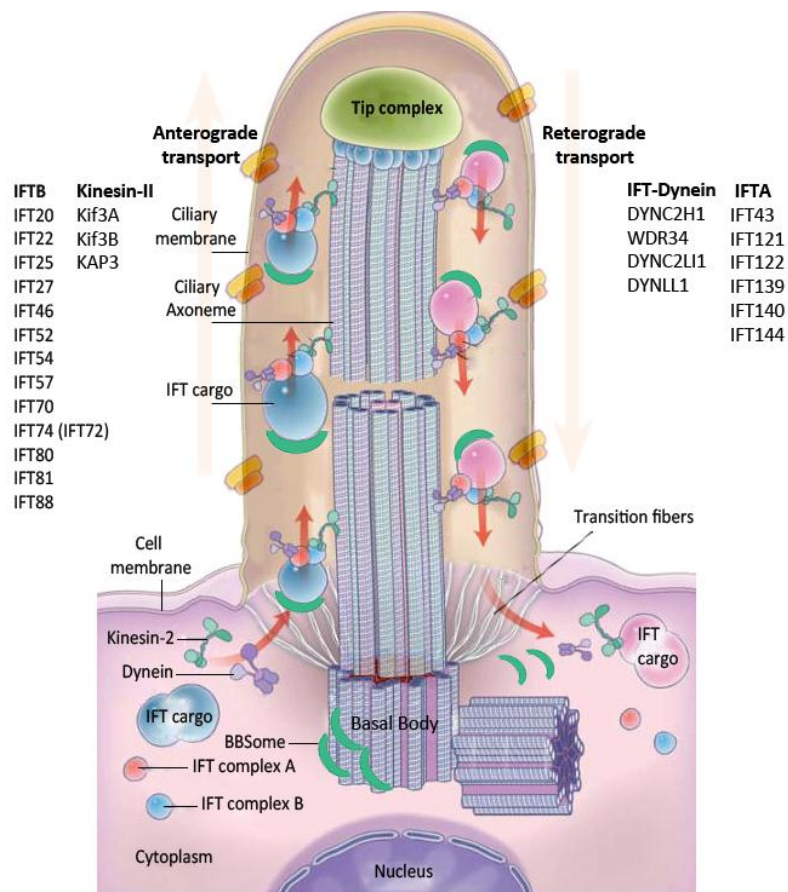
Figure 4: Cilia structure and the intraflagellar transport (IFT). A typical cilium consists of an axoneme of nine doublets MT extend from the basal body MT triplets. The axoneme is surrounded by a ciliary membrane that is separated from the cell membrane by a zone of transition fibers. Ciliary assembly and maintenance is achieved by IFT, which consists of IFT particles (protein sub-complexes: IFT-A and IFT-B and are possibly associated with the BBSome which coat the IFT particles). BBSome regulates vesicle trafficking from post-Golgi vesicles through the interaction with Rab8. The MT motor proteins kinesin 2 and cytoplasmic dynein-2 move the IFT particles and their associated cargo up and down the length of the cilium. Adapted from (Hildebrandt et al., 2011).

1.7.   Function of cilia

The major function of cilia is motility, which is predominantly attributed by motile cilia. Motile cilia are found in clusters with large numbers on the surface of many cells in the body, and they beat in a coordinated fashion resulting in cellular movement and fluid flow generation. They line the upper and lower respiratory system (trachea and bronchial tubules) where they are required for mucus clearance. They are also found to be enriched on the ependymal surface of the brain and responsible for cerebrospinal fluid movement. Furthermore, motile cilia are located on the epithelial cells lining the fallopian tube of the female reproductive system; carrying the ova along the female reproductive tracts (Johnson et al., 2008). Likewise, they are expressed on the epididymis of male reproductive system, which serve as absorptive function (Davenport and Yoder, 2005). The sperm is also considered a specialized cilium with (9+2) architecture that confers motility (Satir and Christensen, 2007).

In contrast to motile cilia, primary cilia are found virtually on most cells in our body as a single cilium. Currently, a primary Cilia Resource Site (http://www.primary-cilium.co.uk/) has developed, listing the cell types known to possess primary cilia. They are found on epithelial cells such as the liver cholangiocytes that line the bile duct (Masyuk et al., 2008), the kidney tubules (Praetorius and Spring, 2005), the endocrine cells of the Langerhans islets and ductal epithelia, the pancreas (Cano et al., 2004), mammary gland (McDermott et al., 2010) and the thyroid. Non-motile cilia are also present on non-epithelial cells such as fibroblasts, neurons, endothelial cells of the

22

cardiovascular system(Geerts et al., 2011), Schwann cells (Satir and Christensen, 2007), osteocytes and chondrocytes (Jensen et al., 2004; Whitfield, 2003). primary cilia were proposed to be vestigial structures in these cells and tissues; however, this thought has changed in the beginning of this century (Veland et al., 2009).

Non-motile cilia are sensory organelles which have also been shown to play a role in mechanosensation. For example, polycystic kidney disease proteins complex (PKD1 and PKD2) in renal tubular primary cilia regulates the intracellular calcium (Ca^{+2}) level which in turn modulates the downstream signaling pathways in response to fluid flow (Basten and Giles, 2013). In addition, non-motile cilia function as chemosensing organelles. For example, sensing of light through the specialized cilia in photoreceptor cells (retinal-connecting cilium) (Insinna and Besharse, 2008). In pancreatic cells, they potentially play a significant role in chemosensing (Cano et al., 2004). In addition, sounds vibrations by kinocilia and stereocilia as well as smell sensation by olfactory sensory neurons (Snell et al., 2004). The sensory function of cilia has also been established in motile cilia (Shah et al., 2009). For example, the angiopoietin receptors (Tie-1 and Tie-2), progesterone receptor, PKD1 and PKD2 as well as a transient receptor potential vaniloid 4 channel (TRPV4) localize to motile cilia of mammalian oviduct (Pedersen et al., 2012; Teilmann and Christensen, 2005; Teilmann et al., 2006).

1.8.   Cilia and left-right determination

In vertebrates including human, the external body plan show bilaterally symmetry of many of structures, such as eye, ear and limb and clear left-right asymmetry in the position of internal organs. They are normally placed between the left and right (LR) side of the body including heart, spleen and pancreas lie to left side and the liver always located to the right. This normal pattern of sidedness called situs solitus which is evolutionary conserved throughout vertebrates and controlled by the activity of motile and non-motile primary cilia in the embryonic node (McGrath et al., 2003). Disruption of symmetry during embryonic development leads to complete randomization of body axis referred to situs inversus or partial defect of organs positioning denoted heterotaxy. Interestingly, the link between cilia and asymmetries in LR was first described in 1976 in patients with KS, presented with situs inversus in about half of patients and respiratory dysfunction as a result of defective cilia in their airway (Afzelius, 1976). In mice embryos with mutations in ciliary proteins Pkd-1 (polycystin-1) and Pkd-2 cause LR defects (Nauli et al., 2003). Likewise, lacking of ciliary kinesins (Kif3a and Kif3b), and OfdI caused absent of nodal cilia and failure of LR asymmetries specification (Ferrante et al., 2006; Hirokawa et al., 2006; Nonaka et al., 1998; Takeda et al., 1999).

The LR asymmetry in vertebrates occurs very early during embryonic development and depends on the leftward fluid flow in the node. In humans and chick, as well as mouse embryos, the node represents the site of the organizer located at the anterior end (the tip) of the primitive streak during gastrulation. The primitive streak defines the dorso-ventral axis. The ventral

part of the node is covered with cilia rotating clockwise and generating leftward fluid flow called (nodal flow) (Essner et al., 2002; Hirokawa et al., 2006; McGrath and Brueckner, 2003). Similarly, in *Xenopus* the gastrocoel roof plate (GRP) (Schweickert et al., 2007) and zebrafish Kupffer's vesicle (KV) (Essner et al., 2005) embryos are equivalent to the mammalian node. These structures express motile primary cilia that are required for the establishment of LR patterning. This nodal flow results in activation of Nodal signaling pathway at the left side of the node. TGFβ family proteins (Nodal and Lefty) and the transcription factor Pitx2 play significant roles in the initiation of LR asymmetry. The mechanism of transmission is still unclear, but it is known that the fibroblast growth factor (FGF), Wnt, Hedgehog (HH), Bone morphogenetic protein (BMP) and Notch pathways regulate the activity of Nodal (Hirokawa et al., 2006; Okada et al., 2005; Raya and Izpisua Belmonte, 2006; Shiratori and Hamada, 2006).

1.9.   Cilia as developmental signaling centers

The ubiquity of primary cilia on the surface of a wide variety of organs and tissues including those derived from the three germ layers, argues that they may have a central role in the development of organs and tissues. Cilia serve as hubs for a variety of developmental signaling pathways implicated in organogenesis, skeleton and craniofacial structure development as well as tissue homeostasis (Berbari et al., 2009). For example, sonic hedgehog signaling (Shh) (Haycraft et al., 2005; Rohatgi et al., 2007; Siggins et al., 2009); Wnt signaling (Corbit et al., 2008; Rohatgi et al., 2007; Siggins et al., 2009); platelet-derived growth factor (PDGF) signaling (Schneider et al.,

2005); FGF (Hong and Dawid, 2009; Tanaka et al., 2005), notch (Ezratty et al., 2011; Marcet et al., 2011) and others (Figure 7).

1.9.1. Sonic hedgehog signaling (Shh)

The Hh pathway was first identified in *Drosophila* (Nusslein-Volhard and Wieschaus, 1980). The vertebrate hedgehog family comprises 3 members: Sonic hedgehog (Shh), Indian hedgehog (Ihh), and Desert hedgehog (Dhh). Shh signaling pathway is the most widely studied Hh pathway and it plays a critical role during embryonic development and it is importance extends into adulthood. Shh signaling components Smoothened (Smo), Patched1 (Ptch1), Suppressor of fused (Sufu) and the Gli transcription factors (Gli1, Gli2, and Gli3), localize to the primary cilium and play a critical role in patterning of several organs such as lung, gut, teeth, hair follicle and limb bud where it is essential for specifying the number and identity of digits. Shh signaling is also essential for patterning craniofacial structures, the neural tube and brain (Drummond, 2012; Eggenschwiler and Anderson, 2007; Goetz and Anderson, 2010; Michaud and Yoder, 2006; Nozawa et al., 2013). Mutations in any of these components lead to a plethora of congenital abnormalities such as polydactyly, hypertelorism, cyclopia (fused brain structure) and clefts of lip and palate (Lipinski et al., 2010). Moreover, mutations in many of ciliary genes such as *Ift122, Kif3a*, *Ift88,Ift172, Ofd1* and many others cause patterning defects in the limb, neural tube, and hair follicle that are characteristic of aberrant Shh signaling (Eggenschwiler and Anderson, 2007; Goetz and Anderson, 2010; Huangfu and Anderson, 2005; Huangfu et al., 2003; Sharma et al., 2008).

Shh is also implicated in the development of different kinds of cancers (Al-Halabi et al., 2011; Chari and McDonnell, 2007; Pasca di Magliano and Hebrok, 2003; Song et al., 2011). Shh signaling pathway is conserved from flies to mammals. In brief, Hh signaling pathway is initiated by binding of Hh ligands to the transmembrane receptor, Ptch1 that is localized at the cilia base and axoneme (Rohatgi et al., 2007) and works as negative regulator of the pathway by inhibiting the activation of another transmembrane protein Smoothened (Smo) in the absence of Hh ligand. Once Hh ligand bound to Ptch, the Smo becomes active and accumulates at the ciliary membrane. Consecutively, active Smo will activate the Gli transcription factors (GliA) that is normally inhibited by the Sufu protein. GliA then transfers to the nucleus and initiates transcription of downstream Hh genes. In the absence of Hh ligand, Ptchs inhibit Smo to transduce the signal, consequently, the Gli transcription factors are proteolytically processed to a repressor forms (GliRs) that keep the Hh pathway switched off (Corbit et al., 2005; Rohatgi et al., 2007; Wilson and Stainier, 2010). Figure 5 outlines the mechanism of the Shh transduction pathway.

Dhh is expressed in neuronal compartments and testes, where it is essential for the development of testis, spermatogenesis and external genitalia (Bitgood et al., 1996; Zou et al., 2012). Ihh has been found in the mesenchymal cells around the eye (Wallace and Raff, 1999), in the osteocytes and the chondrocytes where it is needed for cartilage and bone growth including the axial, appendicular and facial skeleton (Hilton et al., 2005; Pan et al., 2013). All Hh members bind to the same receptor (Ptch1) and they have similar downstream components.
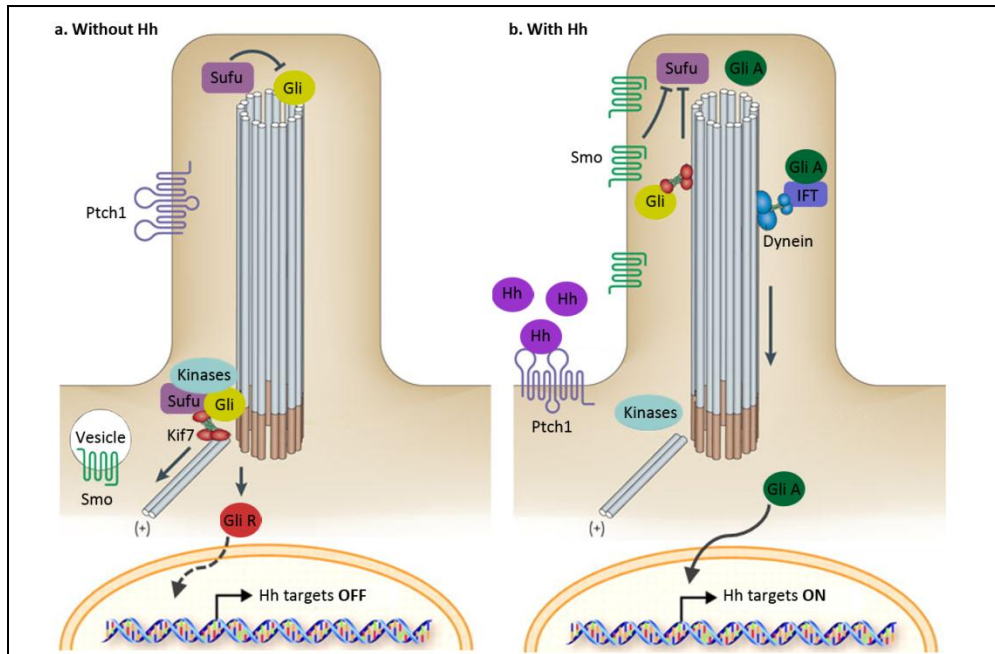
Figure 5: The mechanism of the Shh transduction pathway. (a) In the absence of Shh ligand, Ptch1 enriched in primary cilium and prevents Smo from entering the cilium. Sufu is localized to the tip of the cilium and Kif7 is localized to the base of cilium, both contribute to the inhibition of the pathway. The repressor forms of the Gli proteins (GliR) inhibit transcription of downstream Hh target genes. (b) In the presence of Shh ligand, Ptch1 moves out of the cilium and targeting of Smo into the cilium. Smo and Kif7 inhibit the Sufu resulting in proteasomally processing of Gli proteins into their activator (GliA) isoforms, activating transcription of Hh targets. Adapted from (Goetz and Anderson, 2010).

1.9.2. Wnt signaling

The Wnt signaling pathway like the Shh pathway is a primordial pathway during development that regulates embryonic cell migration, stem cell renewal, cell polarity, cell patterning, cell fate determination, cell survival and apoptosis (Hari et al., 2002; Li et al., 2006; Pecina-Slaus, 2010). Wnt pathway is also essential for the patterning of body axis and the development of cardiovascular and central nervous system and other organogenesis including ear, craniofacial structures, limb bud, and kidney (Li et al., 2006; Patapoutian and Reichardt, 2000; Wang et al., 2011).

Traditionally, Wnt pathway is divided into 2 evolutionarily conserved branches; a canonical (Wnt/β-catenin dependent) pathway and a non-canonical (β-catenin independent) pathway which can be further divided into a Planar Cell Polarity pathway (PCP) and the intracellular Ca^{+2} (Wnt/Ca^{+2}) signaling pathways. These pathways are usually induced through the activation of a cytoplasmic phospho-protein Dishevelled (Dsh/Dvl) by binding of Wnt proteins to Frizzled (Fz) receptors and the Low Density Lipoprotein (LDL) receptor-related proteins (Lrp5/6), both are localized to the ciliary membrane. In the canonical pathway, Dvl controls the activity of β-catenin by destabilizing the destruction complex, that consists of β-catenin, casein kinase I (CKI), adenomatous polyposis coli (APC), axin 1 and glycogen synthase kinase 3β (GSK3β). The β-catenin then released from the complex and translocates to the nucleus which serves as a transcriptional co-regulator interacting with transcription of T cell factor (TCF)/lymphocyte enhancer factor (LEF) to activate downstream target genes (Gerdes and Katsanis, 2008; Komiya and Habas, 2008; Reya and Clevers, 2005; Veland et al., 2009; Vlad

et al., 2008; Widelitz, 2005). In contrast, in the absence of Wnt ligand, the inhibition of destruction complex by Dv1 no longer exists, the cytoplasmic β-catenin then is captured in the destruction complex and becomes phosphorylated by GSK3β, which in turn is targeted for degradation by the proteasome (Saito-Diaz et al., 2013). The canonical pathway was shown to be negatively regulated by the Wnt/PCP and Wnt/Ca^{+2} in ciliated cells (Basten and Giles, 2013).

In non-canonical pathway (PCP), binding of Wnt with FZ receptors, recruits Dvl to the plasma membrane resulting in activation of small GTPases such as Rho, Rac, and Cdc42 which have a direct role on the cytoskeleton organization and docking of basal bodies for cilia formation (Matthews et al., 2008; Pan et al., 2007). Additionally, PCP controls cell polarity that is responsible for the correct orientation of cells within a tissue such as convergent extension (CE) (movement of cells during gastrulation, necessary for establishing the germ layers and body axis) through the activation of JNK pathway (Kim and Han, 2005; May-Simera and Kelley, 2012; Yamanaka et al., 2002; Ybot-Gonzalez et al., 2007). Figure 6, describes the mechanism of the Wnt signaling pathways.

PCP proteins have been shown to localize at primary cilia and play a role in ciliogenesis (Jones and Chen, 2007). PCP is also implicated in organization and orientation of the mitotic spindle, stereocilia in the inner ear (Gong et al., 2004; Kelly and Chen, 2007), cilia on the reproductive, respiratory tracts, kidney tubular epithelial cells, neural crest migration as well as controlling the patterns of hair follicles on the skin of mammals.

Disruption of PCP in mouse causes shortened body axis and failure to close the neural tube as a result of a defective of CE, craniofacial dysmorphisms, open eye lid and disturbance of the stereociliary hair bundles in cochlea (Badano et al., 2006; Jones et al., 2008; Ross et al., 2005; Simons et al., 2005). Mutation in PCP genes such as *Inversin* (*Inv*) causes inversion of LR asymmetry and severe renal cysts formation (Simons et al., 2005). A recent study showed that disruption of PCP signaling in mouse causes limb morphogenesis and skeletal defects (Wang et al., 2011). Similar PCP-related defects were observed in zebrafish and *Xenopus* ciliary mutants (Ferrante et al., 2009; Gerdes et al., 2007; Ross et al., 2005).
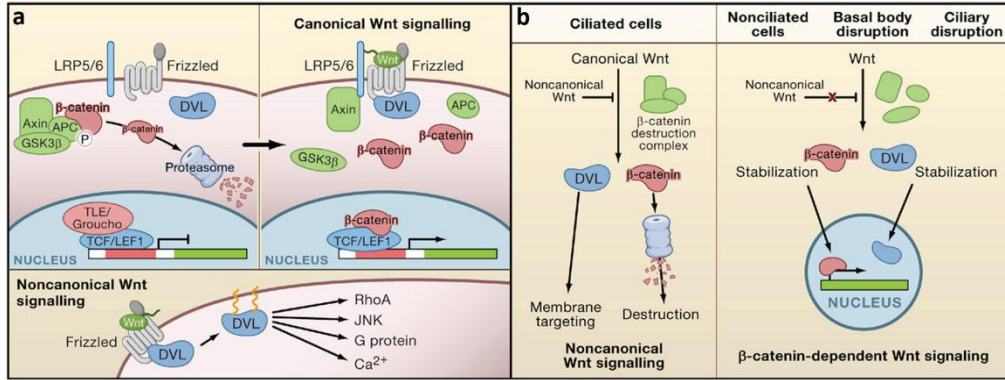
Figure 6: Overview of canonical and non-canonical Wnt signaling pathways. (a) The absence of the Wnt ligand, the destruction complex (Axin, APC, and GSK3β) promotes the β-catenin phosphorylation and targeting it for degradation. The Wnt targeted genes are then repressed by TCF/LEF. In the canonical pathway, binding of Wnt to Frizzled (Fz) receptor and Lrp5/6, activates cytoplasmic Dvl. Dvl then recruits Axin to the plasma membrane, inhibiting the β-catenin degradation by destruction complex resulting in β-catenin stabilization. The β-catenin then translocates to nucleus and interacts with TCF/LEF to activate transcriptional of target genes. In non-canonical signaling, Dvl recruits to the plasma membrane and activates downstream targets. (b) Effects of ciliary and basal body disruption on Wnt signaling. The canonical pathway is also activated and suppressed by the primary cilia. In ciliated cells, this pathway is repressed by the noncanonical pathway resulting in β-catenin degradation and membrane targeting of Dvl. In non-ciliated cells or ddisruption of ciliary or basal body components, canonical Wnt signaling stabilizes cytoplasmic β-catenin and Dvl, leading to increased nuclear levels of both Dvl and β-catenin, initiating transcription of TCF/LEF1-responsive genes. Adapted from (Gerdes et al., 2009).

1.9.3. Other signaling pathways coordinated by cilia

In addition to HH and Wnt signaling pathways, primary cilia coordinate different branches of receptor tyrosine kinase (RTK) signaling transduction pathways such as platelet-derived growth factor receptor-α (PDGFRα) signaling cascade (Figure 7). This pathway is linked to primary cilia in fibroblast at G0 phase to promote cell cycle entry and progression, fibroblast migration, proliferation and apoptosis and its role in wound healing regeneration (Christensen et al., 2012; Schneider et al., 2010). Binding of PDGFRα ligand with receptors results in activation of the Akt and the MEK1/2-ERK1/2 (mitogen-activated protein kinase kinase-extracellular signal regulated kinase) pathways (Schneider et al., 2005). PDGFRα signaling plays a vital role in gastrulation and in the development of variety of organs and tissues such as neural crest cells formation, lung, intestine, teeth, gonads, skin, central nervous system (CNS), and skeleton (Andrae et al., 2008). Moreover, it provides a link between cilia and different types of tumors (Mans et al., 2008). FGF is another pathway with links to cilia through binding of a family of RTKs called fibroblast growth factor receptors (FGFR 1-4) (Christensen et al., 2012; Eswarakumar et al., 2005) (Figure 7). This signaling pathway plays multiple pivotal roles in both vertebrates and invertebrates development; regulating cell proliferation, differentiation and migration. FGFs comprise a large group of genes that are expressed during early embryonic development and play dynamic roles in patterning of the nervous system, limb outgrowth and craniofacial development, development of eye, ear, heart, palate, teeth and salivary glands (Marques et al., 2008; Nakayama et al., 2008; Nie et al., 2006; Pirvola et al., 2000). FGF also works as a morphogen in the embryonic node

that is involved in the establishment of LR asymmetry in mice and zebrafish embryos (Tanaka et al., 2005; Yamauchi et al., 2009). In addition, FGF pathway activates several downstream signaling pathways such as p38 mitogen-activated kinases, extracellular signal-regulated kinase (ERK), phospholipase C gamma, protein kinase C (PKC) and phosphatidylinositol 3-kinase (PI3K) (Maffucci et al., 2009; Mason, 2007).

Furthermore, FGF is involved in the regulation of cilia biogenesis, function and length in zebrafish and *Xenopus* through the regulation of many ciliary genes (Neugebauer et al., 2009). Knock-down of FGFR2, FGF8 and FGF24 causes shortened cilia and perturbation of nodal fluid flow (Neugebauer et al., 2009). Likewise, disruption of FGF signaling is associated with CLP, skeletal and neurological defects in a variety of human diseases such as craniosynostosis (Kimonis et al., 2007) and skeletal dysplasia syndromes, Kallmann syndrome (KS) (Dode et al., 2003; Kim et al., 2005; Riley et al., 2007) and Apert syndrome (Riley et al., 2007; Slaney et al., 1996). Other RTKs have also been linked to cilia and play essential events in cell cycle, migration and differentiation including epidermal growth factor receptor (EGFR), insulin-like growth factor receptor (IGFIR) and the angiopoietin receptor (Tie-2) (Christensen et al., 2012).

Notch signaling is another signaling pathway involved to control cilia function (Figure 7). Notch signaling is well studied in vertebrates and invertebrates, is essential for embryonic development, where mutations in this pathway lead to defects in several organs and tissues such as the heart, kidney, limb, rib, and the craniofacial structures (Iso et al., 2003). Recent studies have demonstrated

the link between Notch and cilia in vertebrates. Notch signaling is important for cell fate determination and differentiation of many cell types such as the multi-ciliated cells in skin and respiratory and tubular epithelial cells (Ezratty et al., 2011; Liu et al., 2007; Marcet et al., 2011). Notch regulates the cilia length which is essential for establishment of LR asymmetry, as the up-regulation of Notch leads to longer cilia, whereas the down-regulation of the pathway leads to shorter cilia in the embryonic node (Lopes et al., 2010).

Other biochemical signaling transduction pathways have also been shown to be modulated by primary cilia such as the Hippo signaling (Habbig et al., 2011), phosphatidylinositol signaling (Conduit et al., 2012), mTOR (Bell et al., 2011; Boehlke et al., 2010), neuronal signaling receptors include G protein-coupled receptors (GPCRs) such as somatostatin receptor 3 (SSTR3), 5-HT_6 serotonin receptor, Jouberin (AHI1) and melanin-concentrating hormone receptor 1 (MCHR1) and their downstream signaling cascades (Berbari et al., 2008a; Berbari et al., 2008b; Pedersen et al., 2012).

Primary cilia also harbor other chemosensory signaling receptors in renal epithelial cells to regulate ion channels function include vasopressin receptor (V2R), GPCRs e.g. purinergic (P2Y and P2Y) receptors, Tie-1 and Tie-2 receptors and a variety of other signaling receptors e.g. Transient receptor potential vaniloid 4 channel (TRPV4) that have osmo-, thermo-, chemo-, and mechano-sensory functions in many tissues (Figure 7). The defects of these receptors cause e.g. cystic and fibrotic liver diseases (Christensen et al., 2007; Masyuk et al., 2008; Oh and Katsanis, 2012; Pochynyuk et al., 2013).
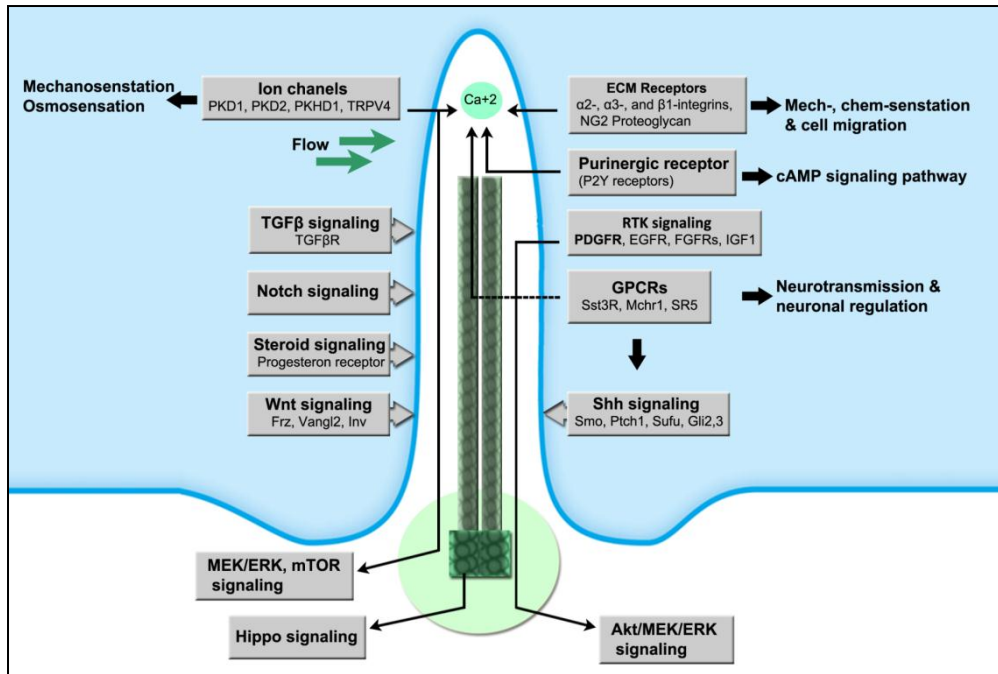
Figure 7: **Brief overview of different signaling pathways through cilia.** The polycystin multiprotein (PKD2)/PKD1/PKHD1) complex serves as a regulator of mechanosensation of cilia, regulates the intracellular Ca^{2+} levels and other specific signal transduction pathways (MEK/ERK and mTOR). Cilia also possess other ion channels such as TRPV4 and purinergic receptors P2X and P2Y that plays role in osmo-, thermo-, chemo-, and mechano-sensation. Additional signaling cascades implicated at the cilium include, the extra-cellular matrix (ECM) receptors which play role in mechanosensation and GPCRs (Sstr3, Mchr1, 5-HT6) signaling that mediates neurotransmission and neuronal regulation. Other signaling at least partly regulated through the cilium including TGFβ and Notch and Hippo-signaling. PDGFRα signaling through their receptors in cilium leads to the activation of two pathways: the Akt and the MEK1/2-ERK1/2 pathways. In addition to PDGFRα other receptors including IGF-1, EGFR and FGFR also regulate the RTK signaling. This figure was created by me according to all published ciliary signaling pathways. I collected these written data and assembled in one figure.

36

1.10.   The ciliary proteome

A paradigm shift has occurred during the last decade in the field of cilia biology with the initiation of repertoires of ciliary proteins derived from different species thus defining the ciliary proteome (http://v3.ciliaproteome.org/cgi-bin/) or ciliome (www.sfu.ca). These databases contain more than 2700 different ciliary proteins (Fliegauf and Omran, 2006; Gherman et al., 2006; Inglis et al., 2006). Recently, new databases have been further developed such as a centrosomal proteomic database: centrosome:db (www.centrosome.dacya.ucm.es) and more extensive database: Cildb (www.cildb.cgm.cnrs-gif.fr), that contains the proteomes of 33 different species, each relevant protein is linked to human diseases information OMIM database and to the reported high throughput ciliary studies (Arnaiz et al., 2009; Nogales-Cadenas et al., 2009). These databases are available as a freely accessible online resource. New proteomic information has also been generated from the proteomic analysis of cilia of specific organisms and tissues for example, the *Chlamydomonas reinhardtii* flagellar phosphoproteome and the rat olfactory sensory neurons cilia proteome (Boesger et al., 2009; Mayer et al., 2009). These resources will provide valuable information that may help to further understanding of the molecular composition of cilia and their role in the development of disorders.

The same ciliary protein has been found to be mutated in more than one type of ciliopathy. This may explain the phenotypic overlap, variability and severity within ciliary diseases which have been explained by genetic and physical interactions between ciliary proteins that share a ciliary localization. Using proteomic techniques such as mass spectrometry, comparative genomic

or transcriptional profiling and bioinformatics resulted in identification of several protein complexes (Boldt et al., 2009) such as BBSome complex (Nachury et al., 2007), Usher network (Richardson et al., 2011), NPHP-MKS-JS proteins (Sang et al., 2011), central spindle/midbody complex (Smith et al., 2011), LisH/CTLH protein complex and polycystin complex (Wang et al., 2007), that interact separately with each other. Other unique protein-protein interactions have been also reported including Nek4/ RPGRIP1 and RPGRIP1L (Coene et al., 2011), CC2D2A/CEP290 (Gorden et al., 2008), Lebercilin-OFDI interactions (Coene et al., 2009) and many others. These distinct protein-protein interactions have provided valuable insights in the function of ciliopathy proteins and facilitate the delineation of disease mechanisms. Together, the available databases and the reported protein-protein interaction networks would help researchers to identify novel ciliopathies causative genes. Additionally, using a combination of genetic, *in silico* proteomics and biochemistry tools could therefore help to identify a possible interaction between the novel proteins and those implicated in similar ciliary diseases phenotypes. Figure 8 outlines the ciliopathy network.
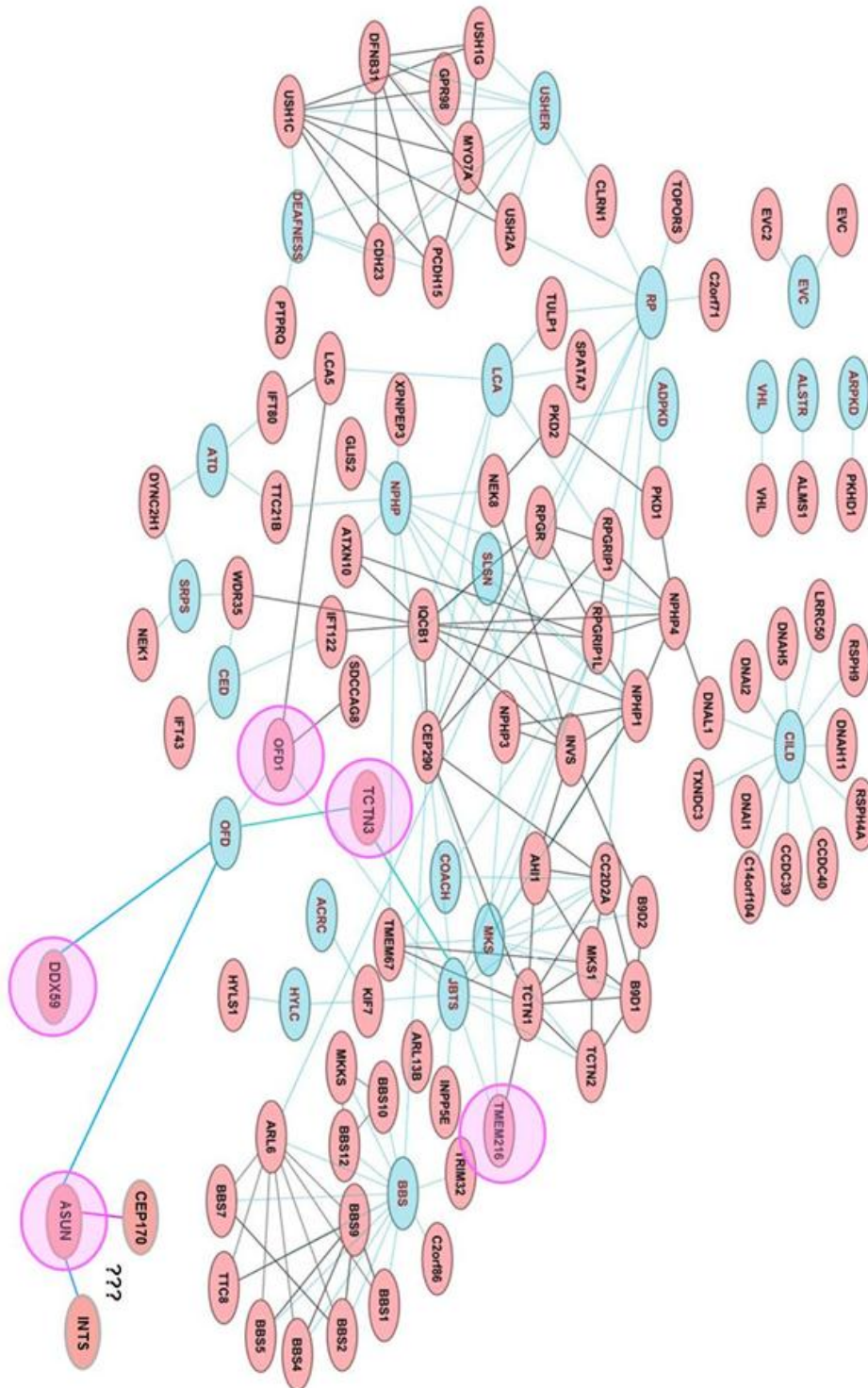
Figure 8: The ciliopathy protein interaction network. This network shows the interaction of proteins (red spheres) known to be associated with phenotypically overlapping human ciliopathies (cyan spheres). In this network, the BBSome, the Usher network and NPHP-JS-MKS modules and other reported Protein–protein interactions can be distinguished. Protein–protein interactions, direct and complex, (grey lines) were derived from the literature. Blue lines indicate that a specific protein is associated with the ciliopathy it connects to. Adapted from (van Reeuwijk et al., 2011).

1.11.   Ciliopathies

Because of the fundamental role of cilia in the normal physiology and development of many tissues and organs in our body, mutations of ciliary genes, which encode for proteins localized to the cilium, BB or centrosome (Baker and Beales, 2009) give rise to devastating genetic disorders collectively classified as ciliopathies. Both motile and non-motile cilia are associated with ciliary disorders but the majority of ciliopathies results from perturbation of primary cilia; and are termed non-motile ciliopathies. Ciliopathies are rare and heterogeneous disorders that lead to a wide range of clinical phenotypes that include craniofacial dysmorphisms, polydactyly, organ asymmetry, retinal degeneration, cognitive defects and anosmia, although other manifestations can be seen in organs including ear, brain, heart, kidney, liver, biliary duct, pancreas and skeletal tissues (Badano et al., 2006; Baker and Beales, 2009; Ferkol and Leigh, 2012; Waters and Beales, 2011) (Figure 9). Impairment of respiratory tract functions, infertility and obesity have also been observed in several ciliopathies. Phenotypic manifestations of ciliopathies can affect a single organ such as polycystic kidney disease (PKD) as well as multiple organs, resulting in a low quality of life and often lethality (Figure 9). Many syndromes such as BBS, MKS, EVC, JATD, Sensenbrenner syndrome (MIM 218330) JBTS, OFD, KS, ALMS, PKD, PCD, LCA and SRPII, are also categorized as ciliopathies (Figure 9). In addition, several studies have confirmed the association of ciliopathies with many types of cancers (Han and Alvarez-Buylla, 2010; Michaud and Yoder, 2006; Yuan et al., 2010).

The first ciliary gene was described by Ansley's group in 2003 (Ansley et al., 2003). Since then, hundreds of ciliary related genes have been identified. Since the list of ciliopathies is growing, scientists have categorized these diseases into two main groups according to the clinical features: ciliopathies with skeletal defects such as JATD, OFD and recently SRPII, and those without skeletal anomalies including BBS, NPHP, MKS, JBTS, ALMS and LCA (Hildebrandt et al., 2011; Tobin and Beales, 2009; Waters and Beales, 2011). The increasing number of ciliopathies with craniofacial anomalies has led to them to be further classified as craniofacial ciliopathies (Brugmann et al., 2010b). These craniofacial ciliopathies can be further categorized into renal and retinal ciliopathies when renal or retinal manifestations are present, respectively. (Arts and Knoers, 2013; Otto et al., 2010). The overlap of phenotypes within these disorders has raised the possibility that other uncharacterized craniofacial syndromes could in fact be ciliopathies.
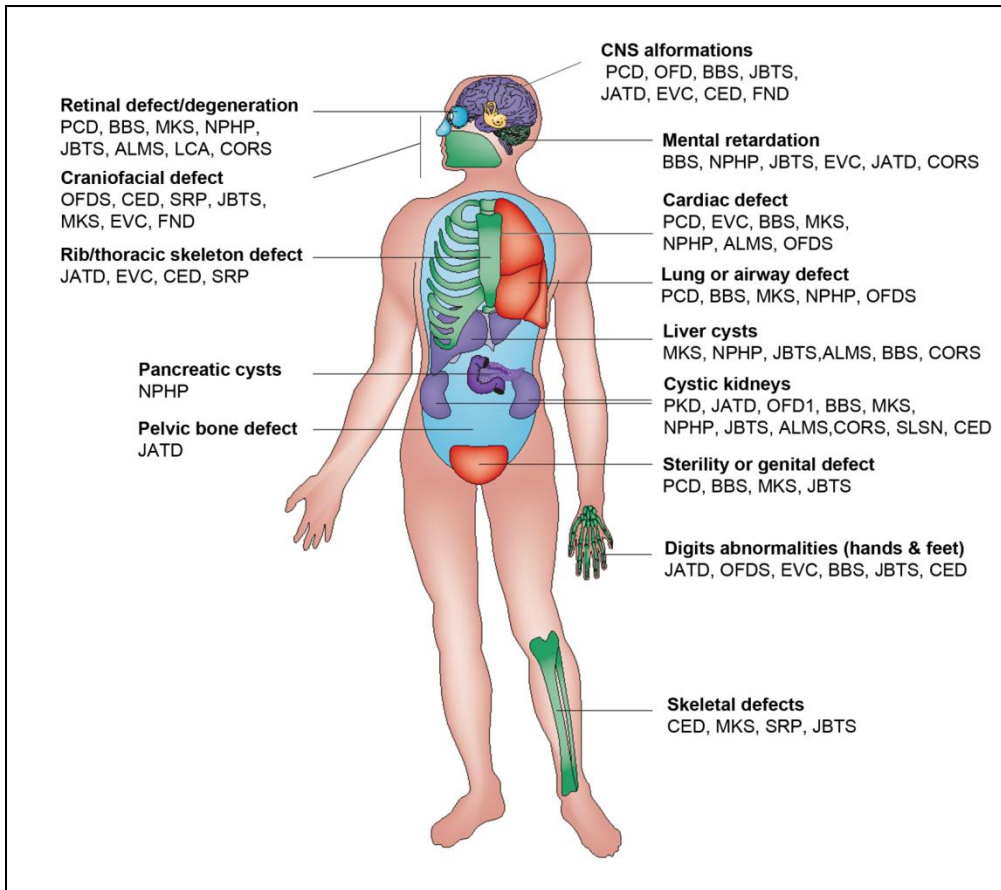
Figure 9: Cilia related disorders. Ciliopathies show prominent and overlapping features in several organs including the brain, craniofacial structures, digits, kidney, liver, eye, heart, genitalia and skeleton. Adapted from (Goetz and Anderson, 2010; Lee and Gleeson, 2011).

1.12. Oral-facial-digital syndromes (OFD)

1.12.1. Clinical manifestation of patients with OFD

All OFD patients have oral anomalies, facial dysmorphisms, and digital malformation; which together constitute the cardinal features of OFD. The oral features include cleft palate or high arched palate, multiple oral frenula, tongue anomalies, alveolar ridge clefting, hypoplastic zygomatic arches and teeth abnormalities. The common facial features include ocular hypertelorism, cleft lip and malformed nose. The digital findings in hands and feet include polydactyly, syndactyly, brachydactyly and camptodactyly or a combination of these. Various additional malformations have also been described in skin, brain, kidney, genitalia and limb. Detailed clinical manifestations are illustrated in table 1.

General features of OFD	
Oral features	Hypertrophic or duplicated frenula, lobulated or nodular tongue (lingula hamartoma), bifid or trifid tongue, absent or supernumerary teeth, especially incisors (primary and secondary), widely spaced teeth, cleft palate (primary or secondary), High arched palate, cleft alveolar ridge, vomer, ethmoid, and crista galli hypoplastic zygomatic arches, cleft uvula, odontogenic keratocys
Facial features	Frontal bossing, ocular hypertelorism / telecanthus, nasal changes: Broad, flat nasal bridge, Broad nasal tip, alar anomalies Notched or hypoplastic alae, short columella, thin nares, hoanal atresia, low set or posteriorly rotated ears, hypoplastic maxilla, cleft lip (median, pseudocleft), micrognathia
Digital features (hands and feet)	Polydactyly (meso-, pre- or postaxial), syndactyly, brachydactyly, clinodactyly, duplicated hallux (generally involving great toe, meta-carpal malformation
Other anatomical changes	
Central nervous system	Agenesis of the corpus callosum, intracerebral, single or multiple epithelial or arachnoid cysts and porencephaly, heterotopia of gray matter, cerebellar, malformations, abnormal gyrations, and microcephaly, vermis hypoplasia/aplasia, Dandy–Walker anomaly, myelomeningocele, stenosis of the acqueduct of sylvius
Kidney	Polycystic or ectopic kidney, hydronephrosis
Heart	Cardiac malformation (endocardial cushion defect, tetralogy of Fallot, aortic stenosis, heart malformations, such as atrioventricular canal and endocardial cushion defects
Limbs	Skeletal dysplasia, especially mesomelic, short, variably bowed tibiae, joint, dislocations, shortened arms, narrow thorax; short sternum; abnormal ribs, wide metaphyses, talipes deformities
Reproductive system	Genital defects (agenesis or hypoplasia of penis, hypospadias, shawl scrotum, cryptorchidism, testicular hypoplasia, ambiguous female genitalia)
Respiratory system	Defects of upper airway (paresis of hypopharynx; hypoplasia of epiglottis, larynx, or trachea; tracheomalacia)
Cutaneous findings	Milia, alopecia
Miscellaneous	Hearing impairment, eye abnormalities, perforated anus, adrenal hyperplasia, absent of pituitary

Table 1: Summary of general features in the OFD types. Source from Guerrier (2007), Siebert (2008), Sukarova-Angelovska E (2012).

1.12.2. Classification of OFD

OFD are very rare disorders that occur 1:50000 to 1:250000 live births. The incidence is higher in females than in males, approximating 2:1 and much higher in patients with cleft lip or palate (Sakai et al., 2002; Siebert, 2008). The most common types are OFDII and OFDI (Toriello, 2009). OFDI is an X-linked dominant disorder that occurs in 1:50,000 births and causes prenatal lethality in affected males.

The first case reported as OFD was in 1941 by Mohr, followed by another case reported by Papillon-Le´age and Psaume in 1954. These two cases were latter termed the autosomal recessive OFDII (Mohr syndrome) and OFDI (Papillon-Leage-Psaume syndromes), respectively (Pedersen and Rosenbaum, 2008). Since then, hundreds of cases have been reported as OFD with additional, variable and overlapping phenotypes, resulting into the delineation of new types (Baraitser, 1986). Besides the well-defined conditions of OFDI and OFDII, 7 subtypes have been classified based on the presence of one or more unusual clinical manifestations (Toriello, 1988). This classification has changed over time. For instance, a case of OFD diagnosed with Mohr syndrome by Edwards is now classified as OFDVIII (Edwards Syndrome) (Edwards et al., 1988). Later on, OFDIX (OFD syndrome with retinal degeneration or Guerrier syndrome) (Gurrieri et al., 1992; Jamieson and Collins, 1993; Nagai et al., 1998) was added to the group. In 1993, an affected girl with a new combination of manifestations was included as a new OFD subtype (Figuera et al., 1993) which is known as OFDX (OFD with fibular aplasia or Figuera syndrome). A year later, an affected fetus showed a

transitional phenotype between OFDII and OFDVI syndromes (Camera et al., 1994), which is called OFDXI (Gabrielli syndrome). In 1997, the first 7 OFD subtypes were re-classified according to the limb anomalies in the affected patients (al-Qattan and Hassanain, 1997). In 1998, an additional type of OFD with myelomeningocele and heart defects was named Moran-Barroso syndrome or OFDXII (Moran-Barroso et al., 1998). A year later, OFDXIII (Degner syndrome) characterized by additional brain abnormalities were described (Degner et al., 1999; Gurrieri et al., 2007).

To conclude, 13 subtypes have been reported and characterized based on specific and distinctive clinical features (Gurrieri et al., 2007; Toriello, 2009) (Table 2). This classification is based on the extent and the severity of characteristic clinical manifestations and mode of inheritance.

However, this classification is not always straightforward since most of the reported cases were single cases or patients within a same family displayed phenotypic variability that hinders the diagnosis. Moreover, many cases are difficult to classify due to the phenotypic similarity between OFD (Digilio et al., 1996; Gabrielli et al., 1994; Martin et al., 1971; Moran-Barroso et al., 1998). For instance, Chung reported a case of OFD with overlapping manifestations between OFDV and OFDVI, suggesting a possible new OFD variant (Chung and Chung, 1999). Recently, another patient has been reported with similar features between Mohr syndrome and OFDVI indicating a new OFD subtype (Panigrahi et al., 2013). On the other hand, OFDIV shares a combination of manifestations between OFDII and SRPII (Baraitser et al., 1983; Silengo et al., 1987). This syndrome was thought to be allelic of Mohr

syndrome until recently, when it was re-diagnosed as a distinct syndrome (Thomas et al., 2012).

Besides phenotypic similarity between OFD subclasses, OFD often occurs in conjunction with other congenital diseases. For instance, two OFD cases reported in 1997 and 1999 showed high phenotypic resemblance with EVC (Phadke et al., 1999; Toriello et al., 1997). Many patients with Short rib polydactyly syndrome type IV (SRPIV; MIM 269860), SRPII, Acrocallosal syndrome (ACLS, MIM 200990), Carpenter syndrome (CRPT1, MIM 201000), Pallister-Hall syndrome (PHS, MIM 146510), Acro-fronto-facio-nasal syndrome (MIM 239710, 201180), Craniofrontonasal dysplasia (CFNS, MIM 304110), Hydrolethalus syndromes (HLS1, MIM 236680), Joubert syndrome, and Smith-Lemli-Opitz syndrome (SLOS, MIM 270400), have similar and indistinguishable clinical features with that of OFD variants (Siebert, 2008).

As a conclusion, the classification of these disorders is very complex and mainly due to the clinical overlaps between each other and with other known congenital diseases, as well as, the wide spectrum of symptoms. New manifestations are often added to the known OFD (Ghossaini et al., 2002; Liu et al., 2012). Many cases are still unclassified and wait to be added to the official list of OFD as new subtypes (Siebert, 2008). Although diagnosis may be sometimes challenging, it is highly recommended to perform a detailed clinical synopsis of each patient and family members before classification and identification of the genetic aetiology. Several isolated OFD phenotypes are commonly found within the general population, such as cleft lip and palate,

digits abnormalities, polycystic kidney and heart dysfunction. Unraveling the genetic cause for these disorders and their link to cilia may shed light on the molecular mechanisms behind these disorders and other human diseases (Tobin and Beales, 2009). Moreover, study of known OFD could be very important for the correct diagnosis of other hitherto uncharacterized OFD.

Type/Name	MIM #	Inheritance	Distinctive (distinguishing) features
OFDI **Papillon-Léage-Psaume syndrome**	311200	XR	Hyperplastic frenula, lobulated tongue, hypoplasia of nasal cartilage, alar hypoplasia, cutaneous milia, polycystic kidney disease, porencephaly, absence of lateral incisors, agenesis of corpus callosum
OFDII **Mohr syndrome**	252100	AR	Bilateral bifidity of big toe, bifid tip nose, absence of medial incisors, short humerus
OFDIII **Sugarman syndrome**	258850	AR	Abnormal ocular movement (See-saw winking), myoclonic jerks
OFDIV **Mohr-Majewsky syndrome**	258860	AR	Tabial dysplasia, short stature
OFDV **Thurston syndrome**	174300	AR	Cleft lip only, postaxial polydactyly, early dental loss
OFDVI **Varadi syndrome**	277170	AR	Tongue hamartoma, mesoaxial polydactyly, lingual, sublingual swellings, hypothalamic hamartoma, Y shaped metacarpals
OFDVII **Whelan syndrome**	608518	XD/XR	Facial asymmetry, tongue split, hydronephrosis
OFDVIII **Edwards syndrome**	300484	AR	Short tibiae or radii, preaxial and postaxial polydactyly, epiglottis anomaly
OFDIX **Guerrier syndrome**	258865	AR	Retinal abnormalities, non-median cleft lip, Dandy-Walker anomaly, retrobulbar cysts, short stature
OFDX **Figuera syndrome**	165590	AR	Fibular aplasia
OFDXI **Gabrielli syndrome**	612913	AR	Postaxial polydactyly, ventriculomegaly, alar hypoplasia, Duplicated vomer, Cleft ethmoid and vertebral bodies
OFDXII **Moran-Barroso syndrome**	NA	AR	Myelomeningocele, stenosis of aqueduct of sylvius, atrioventricular valves dysplasia
OFDXIII **Degner syndrome**	NA	AR	Brachyclinosyndactyly; leukoaraiosis

Table 2: The pathognomonic features of OFD types. AR; autosomal recessive, AD; autosomal dominant, XR; X-linked recessive, XD; X-linked dominant. Source from (Gurrieri et al., 2007; Lopez et al., 2013; Siebert, 2008; Toriello, 2009)**.**

1.12.3. The genetic aetiology of OFD

OFD are genetically heterogeneous disorders and cause variable phenotypes among OFD patients and between patients within the same family. Subsequently, the mode of inheritance also should be different in these syndromes. Transmission of the majority of OFD is autosomal recessive, although many reported cases also display X-linked or autosomal dominant modes of inheritance. Only four genes have been identified so far; the causative genes for the rest of OFD are yet to be unraveled. The first gene is *CXORF5*. It is located on chromosome X and mutations in this gene causes OFDI (MIM 311200) (Ferrante et al., 2001). By linkage analysis for 7 cases present with OFDI followed by direct sequencing of the candidate region, Ferrante and coworkers found different causative mutations. *CXORF5* codes for a protein localized at the basal body of primary cilia which plays a pivotal role in the ciliary formation and function (Ferrante et al., 2009; Ferrante et al., 2006; Singla et al., 2010). The second OFD gene is *TCTN3* (*Tectonic 3*) which when mutated causes OFDIV (MIM 258860) (Thomas et al., 2012). Several pathogenic mutations within *TCTN3* gene were found in 8 unrelated patients diagnosed with OFD anomalies and dysgenesis of tabia without short ribs. Biochemical analysis revealed that TCTN3 is essential for ciliary function and is necessary for transduction of Shh signaling (Thomas et al., 2012). Few months ago, a new gene *DDX59* was identified in two Arab families affected with OFDV. This gene is located in chromosome 1and encodes a member of DEAD-box-helicases family (DDX) which comprises more than 40 proteins (Shamseldin et al., 2013). The function of many of these proteins including the DDX59 remains unclear but most of them are involved in RNA processing

and ribosomal biogenesis. However, an interesting finding was observed in the affected patients; the ciliogenesis in patient's fibroblast cells was found to be unaffected. This suggests that DDX59 is not implicated in ciliary formation which is consistent with the absence of this protein in the available ciliome databases. Interestingly, the Shh signaling was markedly perturbed in the patients' cells (Shamseldin et al., 2013).

The fourth gene named *C5ORF42* has been recently identified and causes the Varadi-Papp syndrome (OFDVI; MIM 277170) (Lopez et al., 2013). This syndrome is autosomal recessive and differs from other OFD by tongue hamartoma, hypothalamic hamartoma and mesoaxial polydactyly (Lopez et al., 2013). Even though, mutations in the *TMEM216* gene (MIM 613277) have been associated with known ciliopathies such as MKS2 (MIM 603194) and JBTS2 (MIM 608091) syndromes, were also identified in two patients diagnosed with OFDVI syndrome (Valente et al., 2010). The new study showed that *C5ORF42* seems to be the major gene for this syndrome (Lopez et al., 2013). Moreover, C5ORF42 mutations have been reported in many patients with MKS and JBTS syndromes and causes atypical phenotypes of the disease (Alazami et al., 2012; Shaheen et al., 2013; Srour et al., 2012a; Srour et al., 2012b), providing evidence for allelic heterogeneity of OFDVI, MKS2 and JBTS2 syndromes. In support of this, *TCTN3* mutations were also observed in subset of patients with MKS, JBTS and cystic kidney. (Thomas 2012). Likewise, the spectrum of OFDI phenotypes have lately been extended and mutations in *CXORF5* were found in patients with X-linked JBTS10 (MIM 300804) (Bisschoff et al., 2013; Coene et al., 2009; Field et al., 2012), X-linked Retinitis pigmentosa (RP; MIM 268000) (Webb et al., 2012) and

Simpson-Golabi-Behmel syndrome Type 2 (SGBS2; MIM 300209) (Budny et al., 2006). *OFDI* mutations have also been established in a few patients with OFDVII and OFDVIII, a further indication of variable expressivity of *OFD* genes (Budny et al., 2006; Nowaczyk et al., 2003).

Late last year, the two genes *C6ORF170* (*TBC1D32*; MIM *not available*) and *SCLT1* (MIM 611399) have been separately identified in two patients diagnosed with OFDIX (Adly et al., 2014). The two genes have been described as ciliary protein, found to play roles in ciliogenesis and centrosomal biology (Ishikawa et al., 2012; Ko et al., 2010; Tanos et al., 2013).

Finally, a very recent study has uncovered a new subtype of OFD (OFDXIV; MIM 615948) with severe microcephaly and cerebral malformations caused by mutations in *C2CD3* gene (MIM 615944) (Thauvin-Robinet et al., 2014). This gene is localized to primary cilia and required for cilia biogenesis and centriole elongation (Hoover et al., 2008; Thauvin-Robinet et al., 2014; Ye et al., 2014).

Taken together, the phenotypic overlaps between many known ciliopathies and OFD suggesting that OFD could have ciliary involvement (Toriello, 2009). In addition, the involvement of *CXORF5, TMEM216* and *TCTN3* in cilia biogenesis and function (Brugmann et al., 2010b; Singla et al., 2010; Thomas et al., 2012) and the recent identification of *TBC1D32*, *SCLT1* and *C2CD3* as ciliary players, support the hypothesis that the rest of uncharacterized OFD could be ciliopathies as well. We can therefore anticipate that the genes responsible for the other OFD including Mohr syndrome could have ciliary involvement. Since the genetic cause for most of

these conditions with the exception of OFDI, OFDIV, OFDV, OFDVI and OFDXIV are still unknown, and chromosomal analysis have generally been reported to be normal, the explanation for the other forms of OFD is yet to be determined. It is possible that the different phenotypes observed in the Mohr syndrome and the other OFD are caused by different mutations in the same gene (Toriello, 2009).

Homozygosity mapping and next generation sequencing will be helpful to identify the causative gene responsible for Mohr syndrome. Furthermore, by means of downstream functional analysis using biochemical tools, patients' cells and animal models, we will be able to get a better understanding of the biological pathways and underlying mechanisms to explain the pathogenesis of this disorder.

1.12.4. Clinical spectrum of Mohr syndrome

Mohr syndrome is a very rare autosomal recessive disorder; with an estimated incidence rate of 1 to 300 000 live births. Like other OFD, Mohr syndrome is defined by malformations of the face, oral cavity as well as hand and foot digits. Craniofacial dysmorphisms include hypertelorism, microcephaly, micrognathia, broad nasal ridge and cleft upper lip. Defects of the oral cavity development including clefts of the palate and tongue together with oral frenula and dental abnormalities have been also reported in most cases. Digital anomalies are also common including brachydactyly, syndactyly, clinodactyly, and preaxial or postaxial polydactyly. Other minor features were reported in single families, such as tongue lipoma and a sacral dermal pit (Ghossaini et al., 2002), muscular hypotonia and respiratory infections (Gustavson et al., 1971;

53

Haumont and Pelc, 1983; Prpic et al., 1995; Reardon et al., 1989); absence of the pituitary, epiglottis abnormalities, micropenis and adrenal hypoplasia (Shashi et al., 1995); choroid coloboma, jerky eye movement, hydrocephaly and zygomatic hypoplasia (Anneren et al., 1984; Kalyan et al., 2012). Additionally, absence of olfactory nerve, natal teeth, lung malformation, Dandy-Walker malformation, corpus callosum agenesis and tachypnea have also been observed in many cases (Balci et al., 1999; Gustavson et al., 1971; Haumont and Pelc, 1983).

To date, tens of cases have been reported in the literature presenting with variable phenotypic manifestations in face, oral cavity, digits and other organs.

1.13. Animal modeling for Mohr syndrome

To understand the function of the disease causative gene, animal models have been helpful. Human ciliopathies have been well studied in different animal models including mouse, rat and zebrafish. Several mouse and zebrafish models have been used to study the role of primary cilia in various developmental and physiological disorders including ciliopathies (Hildebrandt et al., 2011; Leightner et al., 2013; Menezes and Germino, 2009; Perrault et al., 2012). Both mouse and zebrafish animals were also used to understand the function *OFDI* in the development of disease phenotypes (Ferrante et al., 2009; Ferrante et al., 2006; Hunkapiller et al., 2011). These animal models gave interesting insights of the invaluable role of cilia in the development and function in human organ systems. For instance, skeletal system, craniofacial structures, eye, kidney, teeth, ear and other internal organs (Brugmann et al., 2010a; Tasouri and Tucker, 2011; Tayeh et al., 2008; Tobin et al., 2008). In

addition to zebrafish, *Xenopus*, which is a common animal model in our lab, was used to study the aetiology of Mohr syndrome. There are two species of *Xenopus* that are widely used by researchers, *Xenopus leaves (X. leaves)* and *Xenopus tropicalis (X. tropicalis)*. However, the African clawed frog, *X. leaves* has been well described and widely used as a vertebrate model system to study events during embryonic development. Moreover, *X. leaves* embryos are particularly applicable to address the function of many genes during vertebrate embryonic development (Bonnard et al., 2012). The female *Xenopus* can be stimulated to lay eggs by exogenous injection of Human gonadotropin hormone (HCG); each female can release more than 1000 eggs per day. Eggs are quite large (around 1.3 mm in diameter), easy to handle, allows for detailed visualization of developmental progress, and ease for microinjection and surgical manipulation. Frog embryos are relatively large compared to zebrafish embryos, and can be obtained by *in vitro* fertilization, therefore it is easy to manipulate the embryos as they grow. They undergo rapid embryonic development; taking 48 hours from fertilization to a swimming tadpole stage. For these reasons, *X. leaves* has emerged as another excellent organism to model human disease. For examples, *Xenopus* model helped to uncover the molecular mechanisms and the pathophysiology of many diseases, including, ciliopathies, and other developmental disorders (Bonnard et al., 2012; Pratt and Khakhalin, 2013). The process of craniofacial development is conserved between *Xenopus* and mammals, therefore *Xenopus* is a suitable animal model to study these events during embryonic development (DeSimone et al., 2005). Moreover, the "*ex utero*" development of frog embryos facilitates manipulation such as loss-of-function assays and

classical surgical experiments. Besides using zebrafish and frog embryos, an experiment in *Drosophila* will be performed to investigate the pathogenicity of the defective disease mutation I isolated.

1.14.   Animal modeling for Mohr syndrome

In a period of time during early development of *Xenopus*, the epidermis normally processes three main cell types; mucus-secreting goblet cells (MSC), multi-ciliated cells (MCC) and ion-secreting cells, (ISC) (Figure 10b-e). MSC are the largest cells that occupy the majority of *Xenopus* skin, the ultrastructure of these cells revealed the presence of exocytic vesicles reside on their apical surface are responsible for the secretion of mucus (Billett and Gould, 1971; Hayes et al., 2007). The MCC bear multiple beating cilia that generate directional fluid flow from anterior to posterior throughout the *Xenopus* skin and decorate the epidermis with regular puncta patterns (Mitchell et al., 2007; Park et al., 2008; Wallingford, 2010). The ISC reside a long side MCC and MSC, and express large numbers of ion channels and display irregular scattered patterns throughout the embryonic epidermis (Dubaissi and Papalopulu, 2011; Hayes et al., 2007; Quigley et al., 2011).

The frog epidermis has been well used as powerful model system for epithelial development, biogenesis of cilia and studying planar cell polarity (PCP) signaling (Dubaissi and Papalopulu, 2011; Mitchell et al., 2009; Wallingford, 2010).

The mature MCC of *Xenopus* originate from their ciliated cell precursors residing in the inner layer of the epidermis that undergo several changes

during embryonic development. Between stage 15-19, MCC as well as ISC are specified by Notch/Delta signaling. Activation of Notch-signaling prevents the formation of MCC and ISC, while inhibition of the pathway promotes the specification of these cells (Deblandre et al., 1999; Hayes et al., 2007; Stubbs et al., 2006; Tsao et al., 2009). After specification of these cells, they translocate from the deep layer and undergo intercalation into the outer layer (Quigley et al., 2011). By the end of stage 19, the ciliated cells become totally differentiated and spatially distributed in an even pattern, while, the ISC distributed in a scattered patterns (Stubbs et al., 2006) (Figure 10).

The human respiratory epithelium comprises three cell types; the mucus-secreting cells, the ciliated cells, and the serous acinar cells (ion-transporting cells). This cellular composition of human airway epithelium showed remarkable similarities with the cells of *Xenopus* epidermis (Hayes et al., 2007; Werner and Mitchell, 2012). Because both patients we studied suffer from recurrent respiratory tract infection and cough, which also could be related to ciliary defects, therefore the *Xenopus* larval epidermis will be a good model for studying ciliogenesis and ciliary function. The possible defect in the Asun morphants epidermal cell types could potentially phenocopy the defects in the patients' respiratory epithelial cells.
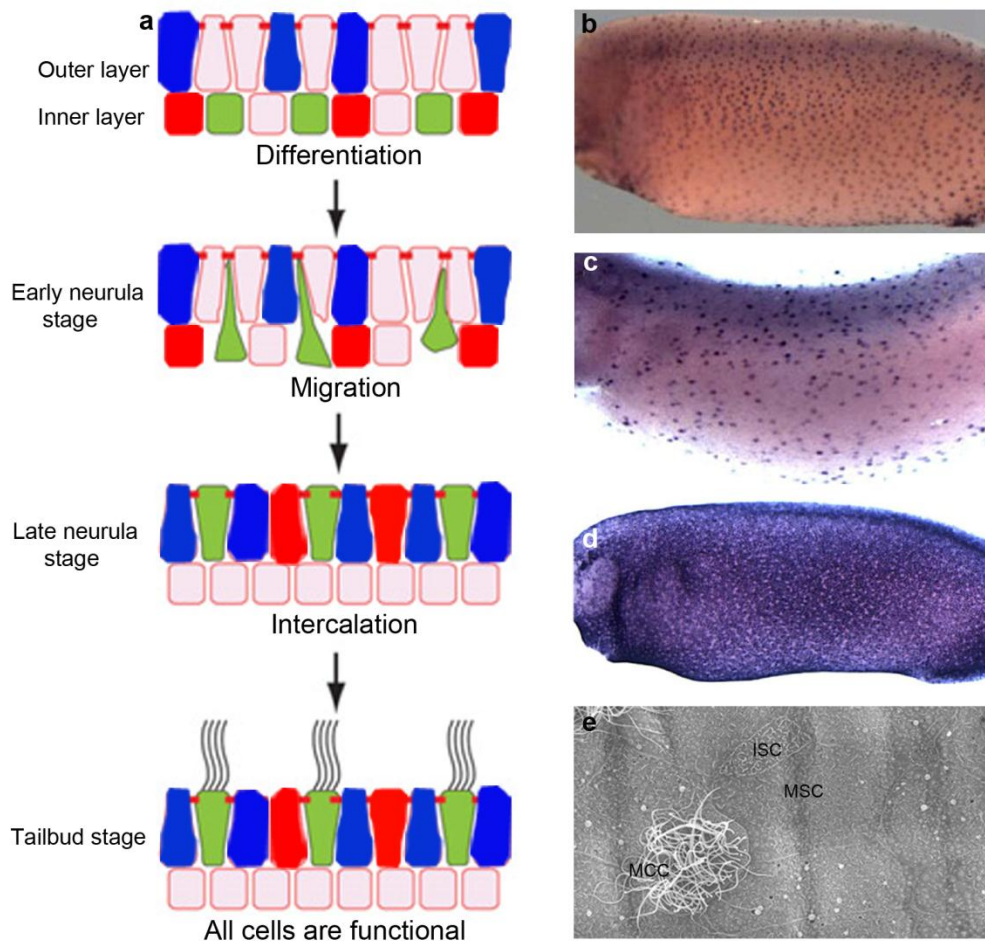
Figure 10: A diagram of *Xenopus* epidermal cells development. (a) During the embryo develops from gastrula stage to adult epidermal cells undergo rounds of differentiation and remodeling; MSC (blue), ISC (red), MCC (green). At neurula stage, MCC precursor cells and INC reside in the inner layer. From gastrula stage onward, cells start to migrate to the outer layer. At tailbud stage, cells become totally differentiated, MCC start to be ciliated; MSC and ISC become functional. (b-d) *In situ* hybridization for genes expressed in epidermal cells: (a) MCC marked with ccdc19, display regular spaced punctate pattern, (b) ISC marked with *xema* shows randomly scattered punctate pattern, (c) MSC labeled with *xeel* covers the whole epidermis. (e) SEM for the *Xenopus* epidermal cells. (a) Modified from (Werner and Mitchell, 2012, 2013). (b-d) Adapted from (Hayes et al., 2007). (e) Our own work on wild-type *Xenopus* embryo.

1.15. Objectives and significance of this study

As outlined in the above introduction, OFD are rare genetically heterogeneous disorders with different modes of inheritance. Most of OFD reported cases exhibit inter- and intra-familial phenotypic variability with variable degree of severity. These syndromes are supposed to be ciliary related disorders due to the ciliary related causative genes for OFD types I, IV, V, VI and XIV and their phenotype overlapping with other known ciliopathies. The molecular background for the rest of OFD is still unknown.

Mohr syndrome is a well-defined disorder with phenotypes typical of OFDII. The gene(s) responsible for Mohr syndrome have yet to be found. Identifying the first gene responsible for this human disease was my prime objective for my thesis project.

In one consanguineous family two girls were diagnosed with a likely autosomal recessive Mohr syndrome-like disorder. Therefore, the main aim of this study was to delineate the genetic aetiology of Mohr syndrome and to confirm or reject the hypothesis that Mohr syndrome is a ciliopathy.

To identify the candidate locus or loci, I first used high density single nucleotide polymorphism (SNP)-array-based homozygosity mapping followed by high throughput sequencing to find the causative gene. The second step was to investigate the effect of the mutation on the encoded protein synthesis and function using patients and wild type cells and specific antibodies. The specific objectives of this study were to:

Investigate whether any ciliogenesis defects are detected in patient's cells. This was achieved using different biochemical approaches such as immunofluorescence staining, scanning electron microscopy (SEM) and small interference RNA (siRNA) techniques.

I order to explore the role of the causative gene during embryogenesis; its expression patterns in animal models such as *Xenopus* and zebrafish were examined using whole mount *in situ* hybridization (WISH) and antibody staining at different stages of development. In order to recapitulate the human disease, the expression of the causative gene was knocked-down in the above mentioned animal models using morpholino antisense oligonucleotides.

The variability of clinical features between the two patients and other reported cases, suggests a possible contribution of genetic modifiers that could modulate the severity of disease phenotypes. Therefore, I will attempt to uncover the possible interaction between the causative protein and other ciliopathy proteins using a combination of genetic and biochemical tools.

Overall, studying of ciliopathies has exponentially increased since the discovery of cilia and their related disorders. Hundreds of genes have been reported so far that are linked to cilia biogenesis and function. However, the functions of many of ciliary proteins are well understood; the majority of them are poorly understood or generally unknown. Most ciliary proteins are linked directly or indirectly to each other and supposed to function collectively in complexes according to their genetic and structural properties and other unknown reasons. For these reasons, the identification of the causative gene of Mohr syndrome may shed light towards the identification of the other OFD

genes. Furthermore, the disease protein could be indispensable for cilia and it could also be linked with other ciliary proteins that are required for cilia function and/or formation. As such, many diseases could be unraveled as a result of this study.

Chapter 2: Materials and Methods

2.1. Patients and samples

The two affected (IV.6 and IV.7) sisters were initially evaluated at the age 5 and 3.5 years, respectively at the National center for Diabetes, Endocrinology and Genetics by Prof. Hanan Hamamy. Between the age of 1.5 and 3 years the two patients underwent many surgical operations to correct the cleft lip/palate (CLP). The youngest affected girl had cardiac surgery to correct the pulmonary stenosis. During the last four years, patients have been carefully examined by ultrasound scanning, ear, nose and tracheal examination, ophthalmic evaluation, dental assessment, magnetic resonance imaging (MRI) and computer tomography in order to find out new phenotypes or congenital defects associated to this syndrome. Informed written consent was obtained from the parents of the family who gave their consent for the publication of photographs and to use their sample for diagnosis and research purposes. The study was approved by the respective local ethical commission in Jordan and Singapore. Saliva and blood samples were collected from the whole family in addition to 34 saliva samples collected from uncles, aunts and cousins (Supplementary Figure 1). Skin biopsies were also obtained from one of the affected, the unaffected mother. Blood and skin biopsy were also collected from age-matched healthy individual as a control.

2.2. Sample collection and genomic DNA extraction

Genomic DNAs (gDNAs) were extracted from saliva samples collected in Oragen™ DNA self-collection kit (DNA Genotek, Ontario, Canada, Cat. No.

OG-500) using the manufacturer protocol. After incubation of Oragene kits containing saliva at 50°C overnight or at least 1 hour, 0.5-1 ml of mixed saliva was transferred in a 2 ml microcentrifuge tube. 40 µl of Oragene Purifier (DNA Genotek, Ontario, Canada, Cat. No. OGL2P-5) per 1ml of saliva was added in each tube and mixed by vortexing for few seconds. After that, tubes are incubated on ice for 10 minutes (min). Then, tubes are centrifuged at room temperature for 5 min at 13,000 rounds per min (rpm). The clear supernatant was carefully transferred into new 2 ml microcentrifuge tubes. Then, equal volume around 1ml of 95% to 100% ethanol was added to each sample and mixed gently by inversion 6-10 times. Samples were left on bench for 10 min for efficient precipitation of DNA. Samples were centrifuged at 13000 rpm, 2 min, and the clear supernatants were carefully removed and discarded avoiding the disturbance of the light pellet. 500 µl of 70% ethanol was added to tube and centrifuged at 13000 rpm, 1 min. Finally, after removing the supernatant, DNA pellets were resuspended into 50 to 100 µl of Tris-EDTA (TE) buffer or H_2O. Additional vigorous pipetting and vortexing, samples were incubated at 50°C for 1 hour with frequent vortexing or overnight at room temperature for better reconstitution. The purity and concentration of the extracted gDNAs were evaluated by measuring the absorbance at 260/280 nm ratio using Nanodrop 8000 spectrophotometer (Thermo Scientific, Wilmington, USA). The quality of DNA was further assessed on a 1% agarose gel. The double stranded DNA was also quantified using Quant-iT™ PicoGreen® dsDNA (Invitrogen, USA, Cat. No. P11496) for single nucleotide polymorphism (SNP) genotyping (Singer et al., 1997) and kept at -20°C or (-80°C) until used. In this study we collected also saliva from both parents and

the healthy parent's siblings in addition to the affected patients. Skin biopsies were collected from the affected patients and the healthy mother.

2.3.   Genotyping and homozygosity mapping

To identify the candidate loci for Mohr syndrome, homozygosity mapping was performed in this family.

Saliva samples from parents (1, 2), unaffected (3, 4, 5) and affected (6, 7) children were collected after informed consent (Figure 12a) using Oragene DNA self-collection kits. After DNA extraction, the purity and quality of each gDNA were determined and confirmed to be appropriate for genotyping.

For linkage analysis, we first genotyped all samples using SNPs array-based genotyping by Illumina 610k SNP (Illumina 610-Quad) Genotyping BeadChip (Illumina, CA, USA), with 500,000 SNP markers, according to the manufacturer's guidelines at the Genome Institute of Singapore (GIS). Genotype results were normalized using the Illumina BeadStudio software with a final call rate >99% for each sample.

To test for possible deletion or supernumerary copies of a gene that may contribute to the etiology of this syndrome, the density of Mendelian genotype errors throughout the genome was examined and the signal intensity of each SNP probe presents in the Illumina Infinium array was analyzed. No deletion bigger than 10 SNPs or 30 kb was detected and no Copy Number Variation (CNV) was found to segregate with the disease. All genotyping analyses were done by Dr. Barry Merriman (Geffen School of Medicine, University of California, Los Angeles).

The principle of homozygosity mapping is to find the shared regions that are homozygous and identical-by-descent (IBD) in the 2 affected patients using custom programs written in the Mathematica (Wofram Research) data analysis software. The larger the regions of homozygosity were considered as candidate IBD homozygous blocks that are likely to harbor recessive disease gene. IBD blocks of 2 centiMorgan (cM) or above were taken to be significant and further investigated. The HapMap Phase II recombination rate map was used to determine the cM distances between SNPs. The homozygous or the identical but not homozygous regions shared by affected and unaffected siblings were excluded. Visual Genome Studio (VIGENOS) program (Hemosoft Inc, Ankara) allowed genome-wide haplotyping of SNP data (Kayserili et al., 2009).

2.4. Genomic loci capture assay

This technique is usually composed of 5 main steps (Figure 11). All experiments and analysis were performed at the University of California, Los Angeles (UCLA) following manufacturer's instructions.

2.4.1. Genomic DNA sample and capture array preparation

Samples were processed following the Illumina Library Generation Protocol version 2.3 (Figure 11). Around five µg of genomic DNA from each sample were diluted with water to a final volume of 150 µl. The DNA was sheared using a sonicator (Bioruptor, Diagenode) to generate short fragments between 150 bp to 400 bp. After PCR purification using QIAquick PCR Purification

Kit (Qiagen, Germany, Cat. No. 28106), samples were concentrated in 30 µl of elution buffer. T4 and Klenow DNA polymerases, T4 PNK, dNTPs and T4 DNA ligase buffer with 10 mM ATP were added to repair 3' and 5' overhangs and generate blunt ends for all the double stranded DNA fragments. The DNA solution was then purified and eluted in 32 µl of elution buffer. After elution, single 'A' base was added to the fragments using Klenow exo- (3' to 5' exo minus) and incubated at 37°C for 30 min. After purification with MinElute PCR purification kit (Qiagen, Germany, Cat. No. 28004), and elution in 10 µl of elution buffer, the adaptors, supplied by Solexa, were ligated to the genomic fragments using T4 DNA ligase, adapter oligo mix and T4 DNA ligase buffer. The samples were incubated for 15 min at room temperature (RT) and then purified using QIAquick PCR Purification Kit. After that, templates were run on a 2% agarose gel and fragments with a size-range of 150-200 bp were excised and gel extracted using Gel Extraction Kit (Qiagen, Germany, Cat. No. 28704) and eluted in 30 µl of elution buffer. Fragments with the right adaptors pairs ligated were amplified by PCR using Phusion DNA Polymerase (Finnzymes Oy, Espoo, Finland, Cat. No. F-530S) and primers complementary to the adaptors. To generate sufficient DNA to hybridize on the capture array, four replicates of PCR reactions were run to generate a yield ~4 µg of amplicon. Samples were purified, eluted in in 50 µl of elution buffer and quantified with Nanodrop spectrophotometer.

2.4.2. Hybridization

The experiment was performed according to Agilent CGH 244 K array protocol. Around 4 µg of amplified products were mixed with 50 µg of

Human Cot-1 DNA (Invitrogen, Carlsbad, USA, Cat. No. 15279-11), 52 µl of Agilent 10X Blocking Agent, 260 µl of Agilent 2X Hybridization Buffer and 8 µl of each of the Illumina primer stock (100 µM each). The hybridization mix was then incubated at 95°C for 3 min and 37°C for 30 min. 490 µl of the hybridization mix was added to the array and hybridized in the Agilent Hybridization oven at 65°C for 65 hours, 20 rpm.

2.4.3. Washing and stripping

After hybridization, the arrays were washed to remove unbound DNA fragments following CGH wash procedure. To increase stringency the second wash was further extended to 5 min. After washing, the arrays were stored in a glass dish with Agilent Oligo aCGH wash buffer 1 until the next step was ready. The array was stripped by incubation with 1.09X Titanium Taq PCR Buffer in the 95°C rotating oven at 20 rpm for 10 min. The solution was collected and aliquoted into 4, 1.5 mL microcentrifuge tubes. 1 µl Illumina primer pair (final concentration 0.1 µM), 1 µl of Titanium Taq (final concentration 0.5X), and 1 µl of dNTPs (10 mM each) were added to a final volume 100 µl. The stripped DNA was amplified by 15 cycles of PCR and purified using QIAquick PCR Purification Kit and eluted in 50 µl of elution buffer. To confirm that the size of fragments matched the size extracted from the gel, the concentration of DNA was measured and the size was checked on a 2% agarose gel. After purification, the samples were diluted to 10 nM, the working concentration for cluster generation (Lee et al., 2009).
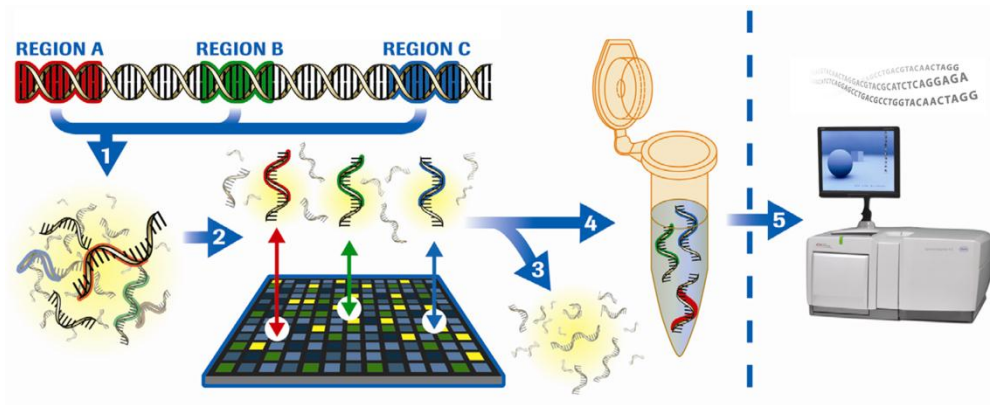
Figure 11: Sequence capture array re-sequencing in 5 steps:

1. The genomic DNA sample is fragmented, followed by linker ligation
2. The fragment pool is denatured and hybridized to a custom sequence capture array
3. Array washing to remove unbound fragments
4. The target-enriched fragment pool is eluted and amplified by ligation-mediated PCR
5. High-throughput sequencing of the enriched sample

2.4.4. High-throughput re-sequencing and analysis

Samples were loaded on the Solexa Flowcell and sequenced by Illumina Genome Analyzer (GAII) according to the manufacturer's standard protocol. The image data was processed through the Firecrest version 1.3.4 and Bustard version 1.3.4 algorithms. A Blat-like Fast Accurate Search Tool (BFAST, https://secure.genome.ucla.edu/index.php/BFAST/) was used to align all sequence reads to the human reference genome (University of California, Santa Cruz, build 18, http://genome.ucsc.edu/). Variants were called using SAMtools pileup tool (SAMtools, http://samtools.sourceforge.net/) and submitted to an internal database for further filtration and annotation. Mismatches were further mapped to the dbSNP129 database to identify variants homozygous and to filter out known SNPs from *de novo* variants. An additional SeqWare tools and the "knownGene" gene model from the UCSC hg18 were used to identify the non-synonymous mutations. The open source SeqWare project which provides a LIMS tool for tracking samples (SeqWare LIMS) and a pipeline for sequence analysis (SeqWare Pipeline, http://seqware.sourceforge.net/) was used throughout this work (O'Connor et al., 2010).

The sequence coverage at each position along the chromosome and the positional candidate genes were obtained from the GenBank (http://www.ncbi.nlm.nih.gov/mapview/) and Ensembl (http://www.ensembl.org/) databases. Flanking primers for each exon were manually designed and direct Sanger re-sequencing was performed with the

BigDye Terminator cycle sequencing kit (Applied Biosystems, UK, Cat. No. 4337455).

2.5.   Culture and maintenance of human cell lines

Skin biopsies were cut into pieces of 2 mm and washed with phosphate buffer saline (PBS). Skin pieces were then fixed in 10 cm Petri dish on scratches made by a sterile blade. After that, Dulbecco modified Eagle medium (DMEM) (HyClone, Thermo Scientific, USA, Cat. No. SH30022.01) supplemented with 10% fetal bovine serum (FBS) (HyClone, Thermo Scientific, USA, Cat. No. SH30070.03) and 10% 100 units/ml penicillin G and 100 µg/ml streptomycin (Gibco, USA, Cat. No. 15140-122) was carefully added. Primary fibroblast cells usually take from 3-5 days to start growing out of the skin biopsies. The hTERT-RPE1 cells were cultivated in DMEM/Ham's F12 (1:1) (Gibco, USA, Cat. No. 11330-032), supplemented with 0.348% sodium bicarbonate solution; mouse primary fibroblast (NIH3T3) and human embryonic kidney (HEK293), cells in DMEM, all were supplemented with 10% FBS, 100 units/ml penicillin, and 100 µg/ml streptomycin. Cells were maintained in a humidified 5% CO_2 atmosphere at 37ºC till confluency. After that, cells were washed with PBS and harvested. Cells were either re-plated into a new flask at a dilution of 1:10 for further passages (culture starts at P0) or supplemented with 1:10 DMSO-FBS and transferred to 2 ml cryotubes for freezing in -80ºC overnight and then in liquid nitrogen tank for long storage.

2.6.   Analysis of non-sense mediated decay (NMD)

To examine the effect of NMD on mutant mRNA stability, cultured cells were treated with cycloheximide (CHX) (Sigma-Aldrich, USA, Cat. No. C4859) at 100 mg/ml for 4 hours before RNA extraction.

2.7.   Transient transfection of mammalian cells

To induce expression of appropriate proteins, transient transfection of cultured cells was performed using lipofectamine 2000 (Invitrogen, USA, Cat. No. 11668-019) according to the manufacturer's protocol. Briefly, Cells were seeded 24 hours prior to transfection until they reach 70% to 80% confluency. Lipofectamine and plasmid DNA were mixed with the appropriate volume of Opti-MEM (Invitrogen, USA, Cat. No. 31985-070) in a 1:3 ratio and added drop wise to cells. After 4 hours of incubation in (5% CO_2, 37ºC) condition, the growth media was then replaced using medium supplemented with penicillin/streptomycin and incubated for 48-72 hours to allow for expression before being processed.

2.8.   Small interference RNA (siRNA) knock-down

To silence the expression of the putative gene, primary fibroblast and hTERT-RPE1 cells were seeded the day before transfection so as to reach a confluency of ~70%. Cells were transiently transfected using RNAi MAX (Invitrogen, USA, Cat. No. 13778-075) using two different siRNA duplex oligonucleotides designed to specifically knock-down *ASUN* gene (see Appendix 1) following the manufacturer's instructions. 20 µM of siRNA oligos (Integrated DNA technology (IDT), Singapore) were mixed in separate microcentrifuge tubes

with 100 µl of serum free OPTI-MEM and incubated at room temperature (RT) for 5 min. The targeting sequences for siRNAs are listed in Appendix. The RNAi MAX-Opti-MEM mix was then added to each oligo mix in a final volume of 200µl and incubated for 20-30 min at RT. The mix was then added drop wise to the 6-well plate and incubated overnight (5% CO_2, 37ºC). The media was then removed and replaced with 0.5% serum media for 48-72 hours. After that, cells were harvested and investigated for ciliogenesis using immunofluorescence staining with the desired antibodies. Cells were also transfected with control siRNA. To confirm the transfection efficiency, cells were also co-transfected with siGLO Red (Dharmacon, USA, Cat. No. D-001630-02).

2.9. RNA isolation and cDNA synthesis

Total RNA was extracted from cultured cells using the TRIzol (Invitrogen, USA, Cat. No. 15596-026) together with RNeasy mini kit (Qiagen, Germany, Cat. No. 74106) according to manufacturer's protocol. Cells were washed with PBS and then lysed directly in the culture Petri dish by adding 500 µl of TRIzol reagent, mixed up and down by pipette and transferred to 1.5 ml micro-centrifuge tubes. Samples in Trizol were incubated at RT for 5 min. After incubation, 200 µl of chloroform was added to the samples, vortexed for 1 min at high speed and centrifuged at 4°C, max speed for 15 min. After centrifugation, the upper aqueous RNA-containing phase was transferred to a new 1.5 ml micro-centrifuge containing equal volume of isopropanol. The samples were mixed by gently inverting many times and centrifuged at 4°C, max speed for 15 min. The supernatant was then removed and the pellet

washed with 75% ethanol and re-suspended in 34 µl of sterile RNase free double distilled water (ddH2O). RNA cleanup was then performed using the RNeasy mini column clean up protocol. RNA was brought up to 100 µl total volume with RNase free ddH2O, to which 350 µl of buffer RLT was added and mixed thoroughly. 250 µl of absolute ethanol was then added to the lysate, mixed and passed through RNeasy spin column, centrifuged at 10000 rpm for 15 sec. The column was then washed once with 350 µl of RW1 buffer. To remove any traces of genomic DNA contamination, DNase I (Qiagen, Germany, Cat. No. 79254) digestion was performed by adding 70µl of DNase I reaction buffer (RDD) and 10 µl of DNase I (2 units) to the column and incubating at RT for 15 min. After that, column was washed once with 350 µl of RW1 buffer and twice with 500 µl of RPE buffer, centrifuged at 10000 rpm for 2 min. The RNA was then eluted from the column in 30 µl of ddH2O. The amount and purity of the RNA was determined by measuring absorbance at 260 nm (A260) and 280 nm (A280) with a Nanodrop spectrophotometer. An A260/A280 ratio of 1.8-2.0, indicating RNA free of contaminants, was obtained for all samples. RNA was stored at -80°C until use.

Around 1 µg of isolated RNA was used for complementary DNA (cDNA) synthesis. cDNA was synthesized using iScript reverse transcriptase (Bio-Rad, USA, Cat. No. 170-8841). Firstly, RNA was added in PCR tubes containing 4 µl of iScript reverse transcription master mix and adjusted to a total volume of 20 µl with ddH2O. After incubation the mix for 5 min at room temperature was transferred to PCR machine and incubated at 42°C for 30 min and then at 85°C for 5 min, samples were then cooled to 4°C. cDNA was stored at -80°C

until required and then either used neat or diluted 1/10 depending on abundance of the transcript.

2.10.   Quantitative real-time PCR

Real-time qRT-PCR was performed using SYBR Green (Fast Start Universal SYBR Green Master, Roche diagnostic, USA, Cat. No. 04913850001), the sequence of primers were used are detailed in Appendix 1, primers were designed using Primer 3 software. The housekeeping gene *β-ACTIN* was used for normalization. All primers were used at a concentration of 10 μM. qRT-PCRs were performed in a total volume of 10 μl, 4 μl of 1:10 diluted cDNA mixed with 5 μl of SYBR Green and 1 μl of forward and reverse primers mix. QRT-PCR reactions were performed in Optical 234-Well Thermal Cycling plate (Applied Biosystems, USA, Cat. No. 4309849), sealed with optical adhesion film (Thermo Scientific, UK, Cat. No. AB-0558) and run on an ABI Prism 7900HT Fast Real-Time PCR System (Applied Biosystems, US). Reactions were run in biological triplicate under the following conditions: 50°C for 2 min, 95°C for 10 min to activate the DNA polymerase, followed by 40 cycles of 95°C for 20 sec and 60°C for 30 sec and 72°C for 1 min. A melt curve from 95°C to 60°C was used at the end of the run to ensure PCR product purity. Each amplicon was run in triplicate with the average values of Ct used in calculation. Relative transcripts expression of the gene was quantified using the comparative Ct method.

2.11.   Rapid amplification of cDNA ends (RACE)

In order to identify the missing sequence of the *Xenopus pkhd1l1* gene, 5'RACE-PCR was carried out using a SMARTer RACE cDNA Amplification Kit (Clontech, USA, Cat. No. 634923) according to the manufacturer's instructions. The first strand DNA was synthesized from the RNA obtained from stage 38 embryos. PCR primers were designed from the closely related *X. tropicalis* sequence. Nested PCR was used to amplify the part of 5'UTR and the beginning of 5' coding regions.

2.12.   Plasmid construction

A full length ASUN cDNA was generated by specific primers with restriction sites. ASUN was tagged with PC tag at 5' end and cloned to pCS2+ expression vector. pCS2+-PC-ASUN construct was prepared from transformed bacterial cultures using Qiagen maxiprep kits (Macherey-Nagel, Düren, Germany, Cat. No. 740416.50) according to manufacturer's instructions. This construct was used for further experiments such as siRNA co-transfection, preparation of capped mRNA, synthesis of anti-sense RNA probe and co-immunoprecipitation. A mutated construct was also prepared using site specific mutagenesis kit (Stratagene, USA, Cat. No. 200522), following manufacturer's protocol. The sequence of primers were used are detailed in Appendix 1.

2.13.   Western blot analysis

Protein was extracted from cells using protease inhibitor and phosphatase inhibitor cocktails-complete EDTA-free (Roche Diagnostics, Germany, Cat.

No. 12245300). Cells were grown until they become 70% to 80% confluent, around $2x10^6$ cells, and then incubated with 0.5% serum media for 72 hours. After washing with PBS, 500-1000 µl of lysis buffer was added to each 10 cm Petri dish and incubated on ice for 10 min. Lysed cells were retrieved by scraping with a cell scraper and transfer to 1.5 ml microcentrifuge tubes, mixed by pipetting and centrifuged for 1 min at maximum speed at 4°C to pellet cellular debris. Supernatant was removed and protein stored at -20°C until required. Protein concentration was measured using the Pierce BCA protein assay (Thermo Scientific, USA, Cat. No. 32225). The working reagent was freshly prepared by mixing of BCA reagent A and B (50:1). 5 µl of protein lysate and standards were loaded in triplicate to a 96-well plate. 200 µl of working reagent was then added into each well and incubated for 30 min at 37°C or 2 hours at Room temperature. After that, samples were cooled at Room temperature and the absorption was then measured at 595 nm with the FluroSkan Ascent (Thermo Fisher). To obtain the protein concentration of lysates, absorption of samples were compared with those of a standard curve. Extracted proteins were mixed with 2X reducing loading buffer (1X stacking gel buffer; 4% sodium dodecyl sulfate (SDS); 20% Glycerol; 10 mg bromophenol blue; 1.65 g dithiothreitol (DTT); ddH$_2$O to 50 ml) (Bio-Rad, USA, Cat. No. 161-0710), denatured by heating to 100°C for 10 min and allowed to cool, and separated by electrophoresis on sodium dodecyl sulfate polyacrylamide gels (SDS-PAGE) with reducing DTT, followed by transfer on polyvinylidene fluoride (PVDF) membrane (Bio-Rad, USA, Cat. No. 170-4157). All samples were made to the same volume with PBS. In addition, 10µl of protein molecular weight ladder (Bio-Rad, USA, Cat. No. 161-0374).

Protein was transferred onto mini and midi transfer packs containing the 0.2 μm PVDF membrane and the stacks immersed in the transfer buffer. The transfer conditions were (25 V, 1.3 A for 7 min and 25 V, 1.3 A for 7 min) for mini and midi gels, respectively using a Trans-Blot Turbo system (Bio-Rad, USA, Cat. No. 170-4155). Membranes were then blocked in 5% milk blocking solution for at least 1 hour at room temperature. After that, membranes were incubated with 1μg/ml of primary antibody diluted in blocking solution, overnight at 4°C with rotation or at room temperature for 1 hour. All primary and secondary antibodies used in this experiment are found in Appendix 1. On the next day, membranes were washed three times for 10 min with rocking in PBS-Tween (5% (w/v) milk, 0.05% (v/v) Tween20 (Sigma-Aldrich, USA, Cat. No. P1379) in PBS at room temperature and then incubated with the horseradish peroxidase (HRP) conjugated secondary antibody, diluted in a final dilution 1:4000 in blocking solution for 1 hour at room temperature. After that, membranes were washed 3 times for 15 min with at room temperature. Bound antibody was then visualized using SuperSignal enhanced chemiluminescent substrate (Thermo Scientific, USA, Cat. No. 34080, 34076, 34096) according to manufacturer's instructions.

2.14. Immunofluorescence assay

2.14.1. Immunofluorescence on cultured cells

Around 15x10^3 cells were seeded on 12 mm cover slips. Cells were grown to around 80% confluency and then incubated with 0.5% serum media for 72 hours to induce cilia formation. Cells were then washed with PBS and fixed

with 4% paraformaldehyde (Sigma-Aldrich, USA, Cat. No. P6148) at room temperature for 15 min. Cells were then washed 3 times with PBS for 5 min and permeabilized with 300 µl of (10% bovine serum albumin (BSA)-PBS-0.01% Triton-X100) (Sigma-Aldrich, USA, Cat. No. BSA, 05470; TritonX-100, 93443) incubated at room temperature for 10 min. To block the non-specific antibody binding, coverslips were maintained in permeablized solution / 1% BSA at room temperature for a minimum of 30 min. Cells were then washed 3 times with PBS and incubated with an appropriate volume 25 µl of 1:200 to 1:1000 primary antibody at room temperature for 1 hour. After primary antibody incubation, cells were washed 3 times for 5 min with PBS and then incubated in the dark to protect the flurochrome from bleaching for 1 hour at room temperature with the appropriate Fluorescein isothiocyanate (FITC)-conjugated secondary antibody; alexa Fluor 594 goat anti-rabbit immunoglobulin (IgG) (Invitrogen, USA, Cat. No. A-11012) and 488 goat anti-mouse IgG (Invitrogen, USA, Cat. No. A-11001) were used to detect the primary antibodies. Prior to mounting, cells were washed 3x with PBS, one drop of ProLong® Gold antifade reagent with 4',6-diamidino-2-phenylindole (DAPI) (Molecular Probes, Eugene, USA, Cat. No. P36934) was added onto each slide, the cover-slips were then mounted on slides. Visualization was performed using a Zeiss Apotome Axiovert Z1 microscope or Olympus Fluoview 1000. Images were assembled in Adobe Photoshop. All primary antibodies and secondary used in this study are found in Appendix 1.

2.14.2. Immunofluorescence on nasal epithelial cells

Human nasal epithelial cells were obtained by nasal-brush biopsy (Cytobrush Plus, Medscand, Sweden) and suspended in cell culture medium (RPMI) (Invitrogen, USA, Cat. No. 21870-076) without supplements to avoid artifacts caused by serum. The cytobrush was moved gently up and down for 5 min to detach ciliary cells from the brush. Samples were then spread onto non coated glass slides, air dried, and stored at -80°C until use. Slides were then fixed, washed and stained using mouse anti-acetylated α-tubulin primary antibody following the same protocol above.

2.15. *Xenopus leaves* egg fertilization

Xenopus leaves female frog ovulation was induced by injecting them subcutaneously with 800-1000 units of human chorionic gonadotropin (Sigma-Aldrich, USA, Cat. No. CG10-IVL) into the dorsal lymph sacs, near the lateral line, "stitch" marks. Both pigmented and albino females with a big belly and a red cloaca were used. Frogs were kept in plastic tanks filled with water at room temperature until they started to lay about 9-10 hours later. After ovulation, female frogs were rested for at least 3 months before being used again.

In the second day morning, the females were transferred to another tank with 1X high salt Barth's solution (10X high salt Barth's solution: 1.095 M NaCl; 10 mM KCl; 24 mM NaHCO3; 8 mM MgSO4.7H2O; 100 mM Hepes; 3.4 mM Ca(NO3) 2.4H2O; 4 mM CaCl2.2H2O pH7.7; up to 4000 ml nanopure H$_2$O). After 1-2 hours, eggs were collected gently using a 25 ml pipet set to

the slow speed to avoid any perturbations of the eggs and finely transferred into a 100 mm glass Petri dish (1/3 the surface of the plate). It is possible to collect eggs every 1 hour.

To fertilize the eggs, testes were excised from a male frog and kept at 4^0C in 1.5 ml microcentrifuge tube. About 1 ml of Steinberg's solution (10X Steinberg's Solution: 581 mM NaCl; 6.7 mM KCl; 3.3. mM Ca(NO3)2.4H2O; 8 mM MgSO4.7H2O; 0.01% Kanamycin; 50 mM Tris Base pH 7.45; up to 1000 ml nanopure H_2O) was added to the testes and crushed into small pieces with scissors in the tube. 5 to 10 drops of minced testes solution were then added onto the eggs after drawing off the 1X Barth's solution using a Pasteur pipet. Kimwipes were used to suck up extra buffer. The eggs were then incubated at room temperature for 5 min. After that, 0.1X Barth's solution (10X Barth's Solution: 889 mM NaCl; 10 mM KCl; 24 mM NaHCO3; 100 mM Hepes; 8 mM MgSO4.7H2O; 3.3 mM Ca(NO3)2.4H2O; 4.1 mM CaCl2.2H2O pH7.6 ; up to 500 ml pure H_2O) was added to the eggs and incubated at room temperature for 20 min. Sperm enters the eggs once adding 0.1X Barth's solution. Barth solution was then removed with Pasteur pipet and replaced with fresh 2% Cysteine Solution (800 ml with 0.1X Barth's; 16 g L-Cysteine Hydrochloride Monohydrate (Sigma-Aldrich, USA, Cat. No. C7880-500G) pH 7.8; up to 1000 ml pure H_2O) and incubated for 8 min at room temperature. This step is required to complete removal of protective glycoprotein jelly surrounding the eggs. Floating eggs were gently submerged by the finger. After incubation, the Cysteine Solution was drawn off and replaced with fresh solution and incubated for 3 min. Eggs were then washed approximately 6 times with 0.1X Barth's solutions and incubated in 0.1X

Barth. The embryos were placed in the incubator under low temperature to slow down the development of the fertilized embryos. The embryos were finally cultured in 0.1X Barth's solution in 50 mm plastic petridish lined with 1% agarose solution for injection.

Note that chemicals used in this experiment, were purchased from Sigma-Aldrich, USA unless otherwise stated.

2.16.   *Xenopus* **morpholino design and microinjection**

Splicing and translation blocking morpholino antisense oligos were designed and synthesized by Gene Tools, LLC (Oregon, USA) were re-suspended in RNase free water to a concentration of 1 mM. MO was injected at 25, 123 ng per embryo at the 2-4 cell stage. Western blot and PCR analysis of protein and RNA extracted from morpholino-injected embryos (morphants) were carried out to confirm the efficiency of the gene knock-down. Sequences of morpholinos are given in Appendix 1.

Embryos at desired stages of development were collected and fixed in 1X MEMFA (10 ml of 10X MEM (100mM MOPS (pH 7.4); 2mM EGTA; 1mM MgSO4; pH 7.4, filtered) + 10 ml of Formaldehyde + 80 ml dH$_2$O) for at least 2 hours at room temperature (or overnight at 4°C). After that, they were dehydrated through series of methanol (24%, 50%, 75%, and 100%) in 1X PBS (10X PBS: 80 g NaCl; 2 g KCl; 14.4 g Na2HPO4; 2.4 g KH2PO4; up to 1000 ml ddH$_2$O, pH 7.4, 0.1% DEPC) for 5 min each. Embryos were then kept in 100% methanol at -20°C until use.

Note that chemicals used in the given work, were purchased from Sigma-Aldrich, USA unless otherwise stated.

2.17.   Whole mount antibody staining in *Xenopus*

Embryos at desired stages of development were collected and fixed in 1X MEMFA for at least 2 hours at room temperature (or overnight at 4°C). After that, they were dehydrated through series of methanol (24%, 50%, 75%, and 100%) in 1X PBS. Embryos were bleached in bleaching solution (2/3 Methanol 100%; 1/3 Hydroxide Peroxide 31.5% (Calbiochem, Germany, Cat. No. 386790) for 2 hours to remove the melanin pigment, in order to get white embryos. Embryos were then stored in 100% Methanol at -20^{0}C until use.

On the first day, embryos were rehydrated in PBS-Methanol series (75%, 50%, 25%), 5 min each and incubated for 30 min in 1M glycine pH7-8. After incubation, embryos were washed for 30 min in 1X PBS and incubated in PBS + 3% H_2O_2 for 10 min. Embryos then washed 5 times in PBST (0.2% BSA, 0.1% Triton X-100 in PBS) (fast wash, 2 times, 5 min and 2 times, 30 min) and incubate in PBSTN for 30 min. After that, PBSTN (5% normal goat serum in PBST) was replaced with appropriate amount of primary antibody diluted in PBSTN at 4°C overnight on rotator.

On the second day, embryos were washed 8 times in PBST (fast wash, 3 times, 5 min and 4 times, 30 min) and incubated in PBSTN for at least 30 min. An appropriate amount of secondary antibodies conjugated with peroxidase diluted in PBSTN in a final dilution 1:400 and incubated for 2 hours at 25°C or overnight at 4°C. After incubation, embryos were washed 7 times in PBST (fast wash, times, 5 min and 4 times, 30 min). Embryos can be kept in PBST at 4°C, rocking.

On the third day, embryos were incubated in fresh DAB Peroxidase Substrate (Sigma-Aldrich, Germany, Cat. No. D4418) (1 tab of each gold and silver in 5ml water, vortex and use immediately). The color reaction must be check carefully within 1 to 5 min. After that, embryos were washed with PBS followed by PBS / 2mM EDTA to stop definitively the reaction. Embryos were then dehydrated through a methanol series (25%, 50%, 75% and 100%) in PBS, 5 min each and kept protected from light at 4ºC, rocking.

2.18. Whole mount *in situ* hybridization (WISH) of *Xenopus*

2.18.1. Synthesis of anti-sense RNA probe

Around 20 µg of plasmids containing cDNA of interest were first linearization by digestion with 50 U of suitable restriction enzyme (50 µl total reaction). Digestion was run on 1% gel and purified using a PCR purification kit. 2 µg of the linearized DNA template were transcribed using 4 µl of 10X digoxigenin (DIG) RNA labeling mix (Roche Diagnostics, USA, Cat. No. 1277073), 2 µl DTT, 1 µl RNase inhibitor, 40 U of (SP6 or T7) RNA polymerase (Roche Diagnostics, USA, Cat. No. SP6, 810 274; T7, 881767), 4 µl transcription buffer and dH2O (40 µl total reaction). After 3 hours of incubation at 37^0C, sample was treated with 2 µl of DNase I for 20 min at 37^0C to remove any of DNA plasmid. Unincorporated, free nucleotides were removed by adding 100 µl of isopropanol (100%) + 10 µl of LiCl (in ice), mixed, and incubated overnight at -20°C to allow precipitation of RNA. Sample was then centrifuged at 4°C, max speed for 30 min. The pellet was rinsed with 400 µl of iced ethanol 70% and spun down at 4°C, max speed for 10 min. The pellet was then air dried and resuspended in 30 µl of RNAse free water. Probe quality

was checked on agarose gel and quantified with Nanodrop spectrophotometer. Probe was stored at -80°C until use. Probes were used in *Xenopus* include *ccdc19* for multi-ciliated cells (MCC), *xeel* for mucus secreting cells (MSC), *xema* for ion-secreting cells (ISC), *nkx2.5* for heart tissues, *twist* for cranial neural crest, *asun* and *pkhd1l1*.

2.18.2. WISH

Embryos were first rehydrated in PBS-methanol series (75%, 50%, 25%) in 0.1% Tween-20 (PBSw) (10X PBS: 80 g NaCl; 2 g KCl; 14.4 g Na2HPO4; 2.4 g KH2PO4; up to 1000 ml ddH$_2$O, pH 7.4, 0.1% DEPC) for 5 min each, followed by 3 washes in 1X PBSw, 5 min each. Subsequently, embryos were digested in 10 µg/ml Proteinase K (Invitrogen, USA, Cat. No. 25530-049) / 1X PBSw for 8 min at room temperature. Digestion was stopped by washing the embryos with 2 mg/ml of glycine in PBSw. After 3 subsequent washes in 1X PBSw, 5 min each, embryos were fixed in fresh 4% paraformaldehyde / 0.2% glutaraldehyde in PBSw for 15 min. After fixing, embryos were washed in PBSw again, 3 times 5 min each, followed by washing for 3 min with 50% PBSw / 50% hybridization solution (HS) (10 g Boehringer block; 500 ml formamide; 250 ml 20x SSC, heat at 65ºC for 1 hour. Add 120 ml DEPC treated water; 100 ml Torula RNA (10 mg/ml in filtered water); 2 ml Heparin (50 mg/ml in 1X SSC); 5 ml 20% Tween-20; 10 ml 10% CHAPS; 10 ml 0.5 M EDTA). Then, embryos were again washed in HS (100%) for 3 min and then incubated with 400 µl of HS for 3 hours at 65ºC. Hybridization was started by replacing the HS with 2 µg of DIG-labeled RNA probes diluted in 100 µl of HS. Embryos were then incubated for overnight at 70ºC.

On the second day, probes were replaced with 800 μl of HS for 5 min at 70ºC, followed by subsequent washing of embryos with 400μl of 2X SSC (pH4.5) (20X SSC: 175.3 g NaCl; 88.2 g Sodium Citrate; up to 1000 ml ddH$_2$O DEPC treated), 3 washes for 5 min each at 70ºC; (final volume = 800 μl + 400 μl + 400 μl + 400 μl = 2000 μl). The embryos were then washed with 2X SSC (pH7) / 0.1% CHAPS (2 times, 30 min, at 70ºC), MAB (100 mM Maleic Acid; 150 mM NaCl pH 7.5) (2 times, 10 min, at room temperature), followed by (2 times, 30 min, at 70ºC) in MAB, (2 times, 10 min, at room temperature) in PBS, and finally (1 time, 5 min, at room temperature) in PBSw. After that, embryos were incubated in 1ml Antibody Buffer (10% heat inactivated goat serum; 10% Boehringer blocking stock solution (Roche Diagnostics, USA, Cat. No. 1096176) / 80% PBSw. Heat at 70°C for 10 min, vortex, cool on ice and filter at 4ºC, on a rocking platform, for 2 hours. In the same time, the antibody anti-DIG-alkaline phosphatase (Roche Diagnostics, USA, Cat. No. 1093274) diluted at 1:5000 from a stock of 150 units/200 μl was pre-blocked in antibody buffer at 4ºC, on a rocking platform. After 2 hours, the antibody buffer was replaced with 1.5 ml of pre-blocked antibody and incubated at 4ºC, overnight, rocking.

On the third day, embryos were quickly washed with 0.1% BSA in PBSw, followed by washing (5 times, 1 hour, at room temperature, rocking) in 0.1% BSA in PBSw. Embryos were then washed (2 times, 30 min, at room temperature) in PBSw, (2 times, 10 min, at room temperature) in AP1 Buffer (0.1 M NaCl; 0.1 M Tris pH 9.5; 50 mM MgCl2). AP1 Buffer was then replaced with 1 ml BM Purple (Roche Diagnostics, USA, Cat. No. 1442074).

The reaction was developed in the dark until desired intensity (overnight) at 4ºC with rocking.

The color reaction was stopped by washing at least 2 times in Stop Solution (100 mM Tris pH 7.4; 1 mM EDTA) for 15 min each. Subsequently, embryos were dehydrated through a methanol series (25%, 50%, 75% and 100%), 5 min each and kept at 4ºC. For better visualization of the signals, pigmentation or excess background were removed by incubating embryos in fresh bleaching solution (2/3 methanol 100%; 1/3 hydroxide peroxide 31.5%). Images of embryos were taken by a stereomicroscope M205 FA equipped with an ICD camera (Leica) and assembled using Adobe Photoshop (CS5).

Note that chemicals used in this experiment, were purchased from Sigma-Aldrich, USA unless otherwise stated.

2.19.   Assessment of ciliary beating on skin of live embryo

At desired stages of development (Tadpole stages onward), live imaging of wild type and injected live embryos was taken by using high-speed cameras. On the other hand, drops of a diluted trypan blue dye (Sigma-Aldrich, USA, Cat. No. T8154) was applied on the surface of embryos. The visualization of fluid flow was observed under a dissecting microscope equipped with digital camera. Movie was edited using ImageJ (NIH).

2.20.   Scanning electron microscopy (SEM)

Embryos at the desired stages were fixed in 3% PBS-glutaraldehyde, pH 7.4, for 4 hours with agitation. Embryos were then washed 3 times PBS buffer, 5 min with agitation, followed by 3 washes with ddH2O, 5 min each, with

agitation. After that, embryos were dehydrated through series of ethanol concentrations in ddH2O (25%, 50%, 70%, 90%, 100%), 30 min each, with agitation. Embryos can be kept at 4°C in 70% for several days.

Embryos were embedded in Epon 812. Sections (50-60 nm) were prepared and contrasted with 4% uranyl acetate in 50% EtOH and 2.6% lead nitrate in 1 M NaOH. Embryos were scanned using a Hitachi 7000 electron microscope (Hitachi, Tokyo, Japan). SEM scanning was performed at electron microscopy facility (Institute of molecular and cell biology (IMCB), A*STAR, Singapore).

2.21.   Morpholino injection and testing in zebrafish

Splice blocking morpholinos were designed and synthesized by Gene Tools (Data S3). Variable amounts of diluted morpholinos were tested in 1-2 cell stage embryos to determine the maximum sub lethal dose. Sequences of morpholinos are given in Appendix 1.

Morphant embryo phenotypes were analyzed at different developmental stages using a dissection stereomicroscope. Otolith defects were assessed at 20-22 hours post fertilization (hpf). Hydrocephaly and curved body axis were detected at 48 hpf. Cardiac oedema was scored at 4-5 days post fertilization (dpf). Two independent injections were performed to assess the observed phenotypes. The number of embryos in each trial (wild-type, morpholino-a (MO-a), morpholino-b (MO-b) was as follows: Otolith defects, (60,160, 200) embryos; curved body and hydrocephaly (50, 130, 155) embryos; cardiac edema, (55, 90, 80) embryos. The Fisher's Exact Test (2 x 2 matrix, two-tailed) was used to evaluate significance, by comparing the MO-injected

embryos to wild-type embryos. Morphants phenotypes were considered positives with a minimum percentage of affected embryos and a maximum p-value compared to wild type embryos. For curved body: positives; >15% aberrant embryos, with a p-value $< 3.0 \times 10^{-10}$. For otolith defects: positives; >20% aberrant embryos, with a p-value $< 4.0 \times 10^{-7}$. For hydrocephaly: positives; >10% aberrant embryos, with a p-value $< 3.0 \times 10^{-11}$. For edema: positives; >20% aberrant embryos, with a p-value $< 4.0 \times 10^{-5}$.

2.22.   *In situ* hybridization in zebrafish

Embryos at desired stages were fixed in 4% PFA overnight with rocking at 4°C, followed by washing twice in PBST, 5 min each. Embryos were then dechorionated in PBST, dehydrated in methanol series in PBST (25%, 50%, 75%, 100%), 10 min each and stored in 100% methanol at -20°C until use. In the first day, embryos were rehydrated in PBST-methanol series (75%, 50%, 25%), for 5 min with rocking followed by washing 3 times in PBST for 5 min each. Embryos were then treated with Proteinase K in PBST at room temperature (~1 ml per tube) as follow: 24 hours embryos: 3-4 µg/ml Proteinase K in PBST, 5-6 min, <24 hour embryos: 3 µg/ml Proteinase K in PBST, 3-5 min, <100% epiboly embryos: 1 µg/ml Proteinase K in PBST, 2-3 min. After that, embryos were fixed again in 4% PFA for 20 min at room temperature followed by washing 2 times in PBST for 5 min each. After washing, embryos were incubated in 200µl (50% PBST/50% HS) for 5 min at 65°C followed by incubation at 65°C for 4 hours with fresh prehybridization buffer. Hybridization was started by replacing the prehybridization solution

with 2 µg of DIG-labeled RNA probes diluted in 100 µl of HS. Embryos were then incubated at 65ºC, overnight.

On the second day, probes were removed and replaced with FS solution (50% Formamide, 5X SSC) and wash at 65°C for 10 min followed by subsequent washing of embryos through a FS series in 2X SSCT (75%, 50%, 25%) at 65°C for 10 min each. The embryos were then washed with 3X SSSC at 65°C for 10 min and 2 times in 0.2X SSCT at 65°C for 30 min each. Embryos were then wash through 0.2X SSCT series in MABT (1 M Maleic Acid; 5 M NaCl pH 7.5; 0.1% Tween-20, up to 1000 ml ddH$_2$O, pH 7.1-7.6) (75%, 50%, 25%) at room temperature for 5 min each followed by washing 3 times in 100% MABT at room temperature, 5 min each. Embryos were then incubated with 0.5% blocking solution at room temperature, for a minimum of 1 hour with rocking. After incubation, the blocking solution was replaced with antibody solution, anti-DIG-alkaline phosphatase or anti-fluorescent-alkaline phosphatase in blocking buffer and incubated with rocking at 4°C overnight.

On the third day, embryos were quickly washed with 10X in MABT, for 10 min each followed by washing 3 times in fresh NTMT (1 ml 100 mM NaCl; 5ml 100 mM Tris (pH9.5); 2.5 ml 50 mM MgCl$_2$; 50 µl 0.1% Tween-20; 41.5 ml ddH$_2$O), for 5 min each. The NTMT was then replaced with 500 µl of BM Purple substrate, covered with aluminum foil and incubated with rocking until desired staining is reached. The reaction was stopped by washing in PBST for 10-15 min. Finally, embryos were fixed with 4% PFA overnight.

On the fourth day, embryos were washed 3 times with PBST, for 10 min each and then stored at 4°C with 50% Glycerol:PBST. WISH with an antisense probe for the asymmetrically expressed gene *lefty2* was used in this study.

Note that chemicals used in this experiment, were purchased from Sigma-Aldrich, USA unless otherwise stated.

2.23. Co-immunoprecipitation (co-IP)

Co-IP technique is used to analyze protein interactions. Co-IP experiments were processed with anti-Protein C Affinity Matrix (Roche Diagnostics, USA, Cat. No. 11815024001). These agarose beads are coupled to the antibody anti-Protein C (Roche Diagnostics, USA, Cat. No. 11814516001) that recognizes the epitope EDQVDPRLIDGK, also called PC-tag.

To prepare cell lysate, HEK293T cells were transfected with full-length *ASUN*, *INT5* and *CEP170* cDNAs subcloned in pCS2+ plasmid tagged at the N-terminal with PC for *ASUN* and with heamaglutinin (HA) for both *INT5* and *CEP170*. Cells were also transfected with empty vector as a negative control to assess whether the interaction observed between PC-tag protein and the target protein was specific. After 48 hours of expression, cells were lysed on ice using a lysis RIPA buffer (50 mM Tris HCl pH 7.5; 150 mM NaCl; 0.1% NP-40; 0.05% Na-deoxycholate) containing 1mM $CaCl_2$ (Ca^{2+} increase the efficiency of binding of antibody to PC epitope) supplemented with complete Protease Inhibitor. In order to use the equivalent amount of proteins in the Co-IP, the quantity of over-expressed proteins were estimated first by western blot analysis.

The immunoprecipitation was performed as follows: The PC-tagged protein was immunoprecipitated to PC-beads in 1.5 ml microcentrifuge tube (MAXYMum recovery tubes) (Axygen, USA, Cat. No. MCT-150-L-C) rotating for 4 hours at 4°C. After incubation, the PC-beads were washed on ice in lysis RIPA buffer, 3 times for 5 min each, and beads were spun down at 4000 rpm. Then, 150 µl of target protein which was expected to bind was added on each immunoprecipitated complex. Samples were then incubated overnight at 4°C with rotating. After that, the samples were centrifuged at 4°C, 3000 rpm for 1 min and washed 1 time in 1 ml of lysis RIPA buffer followed by 3 washes on ice with high salt wash buffer (20 mM Tris HCl pH 7.5; 0.5 M to 1 M NaCl; 1 mM $CaCl_2$), 5 min each in order to remove the unspecific proteins from the beads. Then, the beads were denatured to dissociate the purified complexes from the PC-beads by addition of 200 µl of 2X reducing loading buffer (1X stacking gel buffer; 4% SDS; 20% Glycerol; 10 mg bromophenol blue; 1.65 g DTT; ddH_2O to 50 ml) and heated at 95°C for 10 min. After that, beads were precipitated by centrifugation at 4000 rpm for 1 min and the supernatant was carefully collected and run on a NuPAGE Novex 4% to 12% Bis-Tris SDS-PAGE gel. The interaction of proteins was assessed by immunoblotting.

Note that chemicals used in this experiment, were purchased from Sigma-Aldrich, USA unless otherwise stated.

2.24.   Statistical analysis

Statistical analyses used are described in the figure legends. Calculations and graphing were compiled using Microsoft Excel software. Student's t-test was

used to calculate two-tailed 'P' values. Values < 0.05 (*) or < 0.005 (**) were considered statistically significant unless otherwise specified in the legend of individual figures.

Chapter 3: Results and Discussion

3.1. Detailed clinical manifestations in the two affected girls diagnosed with Mohr syndrome

A consanguineous family from Jordan was diagnosed with Mohr syndrome. Out of five children, two females (patients IV.6 and IV.7) are affected and displayed typical features of Mohr syndrome, including craniofacial dysmorphisms, abnormalities in the oral cavity, digit malformations and heart defects, in addition to other medical problems (Table 3). The two sisters were born at term with an uneventful pregnancy and via normal vaginal delivery. From medical records, birth weight was around 3.5 kg for each. During infancy, patients were admitted to a neonatal intensive care unit (NICU) for about 1 month because of feeding difficulties. The unaffected parents are maternal first cousins whose parents are also first cousins (Figure 12a). Although, consanguineous marriages are common within the family relatives, there is no further history of congenital deformities or genetic diseases in the extended family.

Upon physical examination, the two sisters displayed similar phenotypes consisting of craniofacial dysmorphisms including a bilateral CL, microcephaly, hypertelorism, epicanthal fold, broad nasal root with depressed nasal tip, large and low set ears, long philtrum and thick septum (Figure 12b). They presented with apparent bilateral CP, omega shape epiglottis, under developed epiglottic folds and hypertrophied false vocal cords. Oral frenula and tongue anomalies or tongue hamartomas were absent. Dental abnormalities were also observed such as central median upper incisor in one

girl and single central upper incisor in the other affected sister and dental caries. Supernumerary teeth were also observed only in one girl (IV.6) (Figure 12b). Mild digit malformations were present such as short broad fingers, clinodactyly of the 4th and 5th fingers and toes in both hands and feet. Pre-axial polydactyly, was observed in one hand of one affected girl only (IV.6). Bilateral simian creases on both hands and rough hair were also observed in both patients (Figure 12j,k). Both patients underwent multiple surgical operations to correct the CL/P and to remove the extra finger. Hallux duplication, which is a common feature in Mohr syndrome was unremarkable in the two patients (Arroyo Carrera et al., 2013; Gurrieri et al., 2007; Pradhan et al., 2007; Siebert, 2008). Audiologic examination for the two girls revealed the presence of tympanic membrane retraction and calcification (myringosclerosis). Ear discharge was also frequently seen, which could be associated with impaired hearing and recurrent ear infections in the two girls. Physical examination of the eyes, showed the presence of racemose angioma (dilated retinal vessels) and crowded optic disk (Figure 22e,f). Patients were reported to have chronic urinary tract infection and recurrent respiratory tract infections with chronic cough. Interestingly, patient IV.7 had supravalvular pulmonary stenosis and partial anomalous pulmonary venous return, soon after birth, which is not a common feature of Mohr or OFDS. On the contrary, central nervous system (CNS) malformations, which are frequently observed in Mohr syndrome, were absent in the two patients (Balci et al., 1999; Liu et al., 2012). Both patients started to walk at 1.5 years old and started to make sentences after 3 years of age. Currently, patients have normal performance and development for their age despite their speech abnormality. Ultrasound

scan of abdomen revealed normal internal organs. Brain magnetic resonance imaging (MRI) and computer tomogram (CT) scan were done and revealed no abnormalities. Patient (IV.6) recently suffered from pancreatitis and chronic renal failure. These are new findings of Mohr syndrome which have not been seen in any other reported cases.

Taken together, both patients share the cardinal features of Mohr syndrome and exhibit a wide range of clinical manifestations detailed in table 3. Inter- and intra- familial variations have been reported in Mohr syndrome and were clearly observed between the two probands. We therefore decided to study this family because many clinical features are unique to this family, suggesting that it may be a new form of OFD, with a novel genetic aetiology.
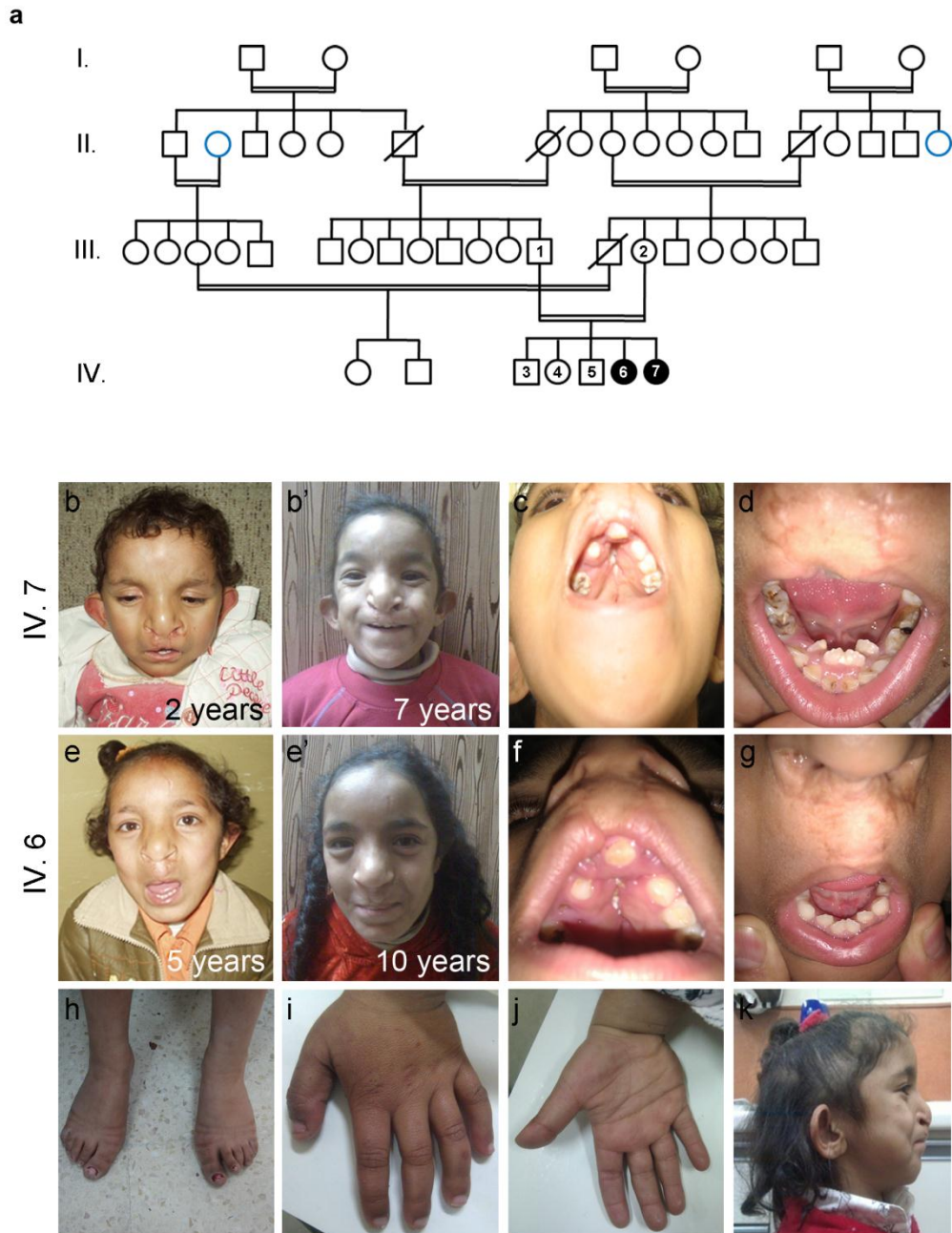
Figure 12: Clinical features of the 2 Jordanian probands with Mohr syndrome.
(a) Pedigree of the Jordanian family. Males and females are represented by squares and circles, respectively. Open and black symbols indicate normal and affected (IV.6, IV.7) individuals, respectively. Blue circle represents the same individual. Crossed symbols indicate deceased individuals. (b-d,k) Pictures of the patient IV.7 at different ages. (e-h) Pictures of the patient IV.6 at different ages. (b-f) Craniofacial dysmorphisms including bilateral cleft lip and palate (corrected after multiple surgical operations). (b,b',e,e') Hypertelorism and broad nasal bridge. (g) Flat philtrum. (c,d,f,g) Dental abnormalities. (h,i) Digit anomalies. (j) Simian creases. (k) Large low ears and rough hair. Patients' parent gave consent for publication of all photos.

96

Table 3 — Clinical phenotype of the two probands compared to other Mohr syndrome reported cases (OFDSII; MIM 252100)

Clinical synopsis	Jordan (ASUN)	Jordan (ASUN)	China[1]	Sweden[2]	Croatia[3]	Italy[4]	India[5]	India[6]	India[7]	India[8]	India[9]	Brazil[10]	Turkey[11]	Japan[12]	Lebanon[13]	Albania[14]
Gender	F	F	M	F	M	F	F	M	M	M	M	F	F	F	M	M
Age of diagnosis			17m	21y	4y	8m	1m	<2y	11y	7d	29y	days	7y	3d	22w	6m	3y	18m
Patient number (refer to pedigree)	IV-6	IV-7														
Oral																
Cleft / high arched palate	Bi	Bi	Bi	+	Bi	+	+	+	+	+	+	+	+	-	+	+
Tongue anomalies / hamartoma	-	-	Bi	+	+	+	+	-	+	+	+	+	+	+	+	+
Incisors absent	+*	+	n.d.	-	+	+	-*	+	-	+*	+*	-	-	n.d.	-*	-
Teeth abnormalities	+*	+	+	+	+	+	+	+	+	+*	+*	+*	+	+	+	n.d.
Oral frenulae/ Ankyloglossia	-	-	-	-	+	+	-	-	+	+	+	+	+	+	+	+
Epiglottis	+	+	-	-	-	-	-	-	-	-	-	-	-	-	-	-
Craniofacial																
Microcephaly	+	+	+	+	n.d.	+	-	-	+	+	n.d.	+	-	n.d.	+	n.d.
Hypertelorism/telecanthus	+	+	+	+	n.d.	+	+	+	+	+	+	+	+	+	+	+
Median cleft lip	Bi	Bi	Bi	-	Bi	-	-	-	-	-	-	-	-	-	-	-
Broad nasal bridge / nasal tip anomalies	+	+	+	+	n.d.	+	+	+	+	+	+	+	+	+	+	+
Ear manifestations																
Low set ears	+	+	+	+	n.d.	-	+	+	+	-	+	+	-	n.d.	+	-
Tympanic membrane pathogenesis	+	+	+	+	n.d.	-	+	-	+	n.d.	n.d.	n.d.	n.d.	n.d.	+	-
Hearing problem	+	+	+	+	n.d.	-	n.d.	+	+	+	+	+	+	n.d.	+	-
Hands																
Syndactyly	-	+	+	+	n.d.	+	-	-	+	+	+	+	+	-	+	+
Clinodactyly	+	+	+	+	+	+	+*	-	+	+	n.d.	+	-	-	+*	+*
Polydactyly (pre-, post-axial)	+	+	+	+	+	+	+	+	+	n.d.	+	+	+	+	+	+
Bifid/duplicated thumb	-	-	+	-	n.d.	+	-	+	+	+	+	+	+	-	+*	-
Feet																
Syndactyly	+	+	+	+	+	+	+	-	+	+	+	+	+	+	+*	+*
Clinodactyly	-	-	+	+	n.d.	-	+*	+	+	+	+	+	-	+	+*	+*
Polydactyly (pre-, post-axial)	+	+	+	+	+	+	+	+	+	n.d.	+	+	+	+	+	+
Bilateral hallux duplication	-	-	-	+	+	+	+$	-	+	n.d.	n.d.	-	+	+	-	+
Clubfoot (CTEV)	-	-	-	-	+	-	+$	-	+	+	n.d.	+	+	-	-*	+
Skeletal																
Short/enlarge humerus/short stature	-	-	-	-	+	-	n.d.	-	+	-	+	+	-	-	-	+
Pectus excavatum	-	-	n.d.	-	-	-	-	-	-	n.d.	n.d.	n.d.	n.d.	n.d.	-	-
Systemic																
Congenital heart defects	-	+	-	+	+	+	+	+	-	+	+	+	+	-	-	-
CNS Abnormalities	-	-	+	+	+	-	n.d.	-	-	+	-	-	+	+	+	n.d.
Mental retardation	-	-	n.d.	+	n.d.	-	n.d.	+	-	n.d.	n.d.	-	-	-	-	n.d.
Psychomotor defects (hypotonia, reflexes)	-	n.d.	n.d.	+	n.d.	-	n.d.	-	-	-	+	+	-	+	+	+
Additional Findings																
Eye manifestations	+	+	n.d.	n.d.	n.d.	n.d.	n.d.	+	+	+	n.d.	n.d.	n.d.	n.d.	+	+
Speech abnormality	+	+	n.d.	+	+	n.d.	n.d.	-	n.d.	+	+	+	-	-	-	+
Respiratory infections and cough	+	+	+	n.d.	n.d.	n.d.	n.d.	-	n.d.	-	n.d.	+	+	-	-	n.d.
Long philtrum	+	+*	+*	n.d.	+	n.d.	n.d.	n.d.	-	n.d.	n.d.	n.d.	n.d.	n.d.	-	-
Frontal bossing	-	-	-	-	n.d.	-	n.d.	n.d.	-	n.d.	-	n.d.	-	+	-	-
Epicanthal fold	+	-	n.d.	-	n.d.	-	+	+	n.d.	-	n.d.	n.d.	-	+	-	n.d.
Micrognathia/retrognathia	n.d.	n.d.	n.d.	+	+	+	-	-	+	+	+	+	-	-	+	+

Unique features present in the present cases:
- Alveolar pulmonary stenosis
- Omega shaped epiglottis
- Underdeveloped aryepiglottic folds
- Hypertrophied false vocal cords
- Thick septum
- Racemose Angioma
- Crowded optic disc
- Rough and sparse hair
- Adenoid hypertrophy
- Opacification of mastoid and ethmoid cells
- Presence of single central upper incisor
- Flat foot
- Bilateral simian creases

1. Liu et al., 2012; 2. G. Amiem et al., (1990); 3. Velepic et al., 2004; 4. Digilio Maria Cristina et al., (1996); 5. PHK Goudar et al., (2012); 6. Dave et al., (2013); 7. Pradhan M et al., (2007); 8. Kalyan et al., (2012); 9. Biswas et al., (2009); 10. Carla de Souza Lage et al., (1989); 11. Balci et al., (1999); 12. Sakai et al., (2002); 13. Ghossaini et al., (2002); 14. Sukarova-Angelovska et al., (2012)

Table 3: Clinical phenotype of the two probands compared to other Mohr syndrome reported cases. n.d., not determined; +, affirmative; -, negative; M, male; F, female. $, bilateral hallux triplication.

3.2.   Identification of the Mohr syndrome causative gene

We searched for genetic lesion by combining linkage analysis (GWL), using homozygosity mapping with exon capture and massively parallel sequencing. This approach has been successful to find the causative genes for many diseases in single and multiple families (Bonnard et al., 2012; Reversade et al., 2009; Thiel et al., 2011; Thomas et al., 2012).

3.2.1.   SNP genotyping and homozygosity mapping of the family

The 2 cases were born to consanguineous unaffected parents, suggesting an autosomal recessive mode of inheritance. To identify the homozygous and identical by descent (IBD) regions of the genome that may contain the causative allele for this disease, we first performed homozygosity mapping. We detected many segments of homozygosity located on autosomal chromosomes and shared between the family members, confirming consanguinity in the family. Homozygous segments shared by affected and unaffected siblings were excluded. As a result, five candidate IBD regions were defined as being homozygous and identical in the two affected individuals. None of these IBD blocks were found in unaffected family members (Figure 13).

The 5 IBD loci with a total size of 45.7 Mb containing 395 genes (Appendix 2) were as follow:

-      Ch6q27: (chr6:167,901,317-170,287,795)   (~2.4 Mb)

-      Ch8q23.1-q24.12: (chr8:106,743,988-122,186,235   (~15.4 Mb)

-       Ch12p13.2-p11.22: (chr12:12,129,350-28,091,505)   (~16 Mb)

-       Ch13q12.11-q12.13: (chr13:21,704,404-26,337,017)   (~4.6 Mb)

-       Ch16q21: (chr16:58,296,974-65,631,053)   (~7.3 Mb)

Mohr syndrome could be caused either by point mutations or indels or copy number variations present within these 5 loci particularly in the coding region of one of these 395 genes. After identifying the candidate regions, the next step was to sequence all genes present in the 5 IBD regions.
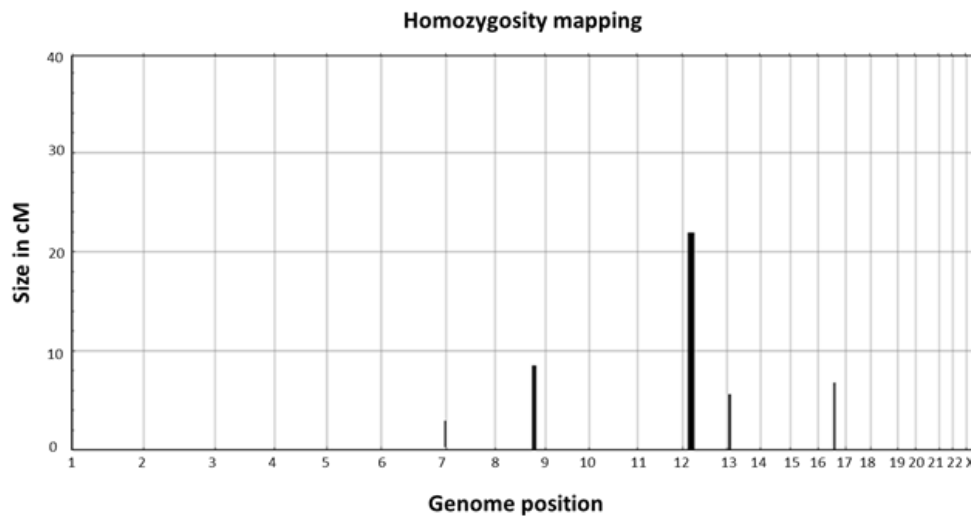
Figure 13: Homozygosity mapping in the Jordanian family identifies 5 IBD regions. Homozygous blocks were found across all the autosomal chromosomes. The position of candidate loci on each chromosome is indicated along the y-axis. The size of each locus is given in centiMorgan (cM) and the respective chromosome is indicated on the x-axis. Five homozygous and identical regions were found in the two probands on chromosome 16 (Ch6q27), chromosome 8 (Ch8q23.1-q24.12), chromosome 12 (Ch12p13.2-p11.22), chromosome 13 (Ch13q12.11-q12.13) and chromosome 16 (Ch16q21). Graphs were generated by Dr. Merriman (2009).

3.2.2. Capture array and re-sequencing of 395 genes

In order to find the causative gene, we sequenced all the 5 homozygous IBD regions in patient IV.6. A custom array (Agilent 610K) was designed to target all coding exons and exon-intron boundaries regions of the 395 genes present in the 5 regions. A DNA library from patient IV.6 was prepared and hybridized to the array according to the Agilent array protocol.

After high-throughput sequencing, 2328 contigs found in the 5 common IBD regions were targeted, captured and sequenced. A total of 894 mismatches were identified when aligned to the human reference genome (UCSC hg18) (Figure 14). Out of 849 mismatches, 735 variants were homozygous and reported in dbSNP129. The remaining 114 variants were homozygous novel and not reported in the dbSNP129. Of the 114 variants, 71 were novel and within transcribed regions. Of these, using SeqWare tools and the "knownGene" gene model from the UCSC hg18, we found that only 22 were localized in transcribed regions of UCSC known genes. Finally, we narrowed down the list of 22 to only 7 homozygous, non-synonymous mutations (Those causing amino acids sequence changes that potentially affect protein function).
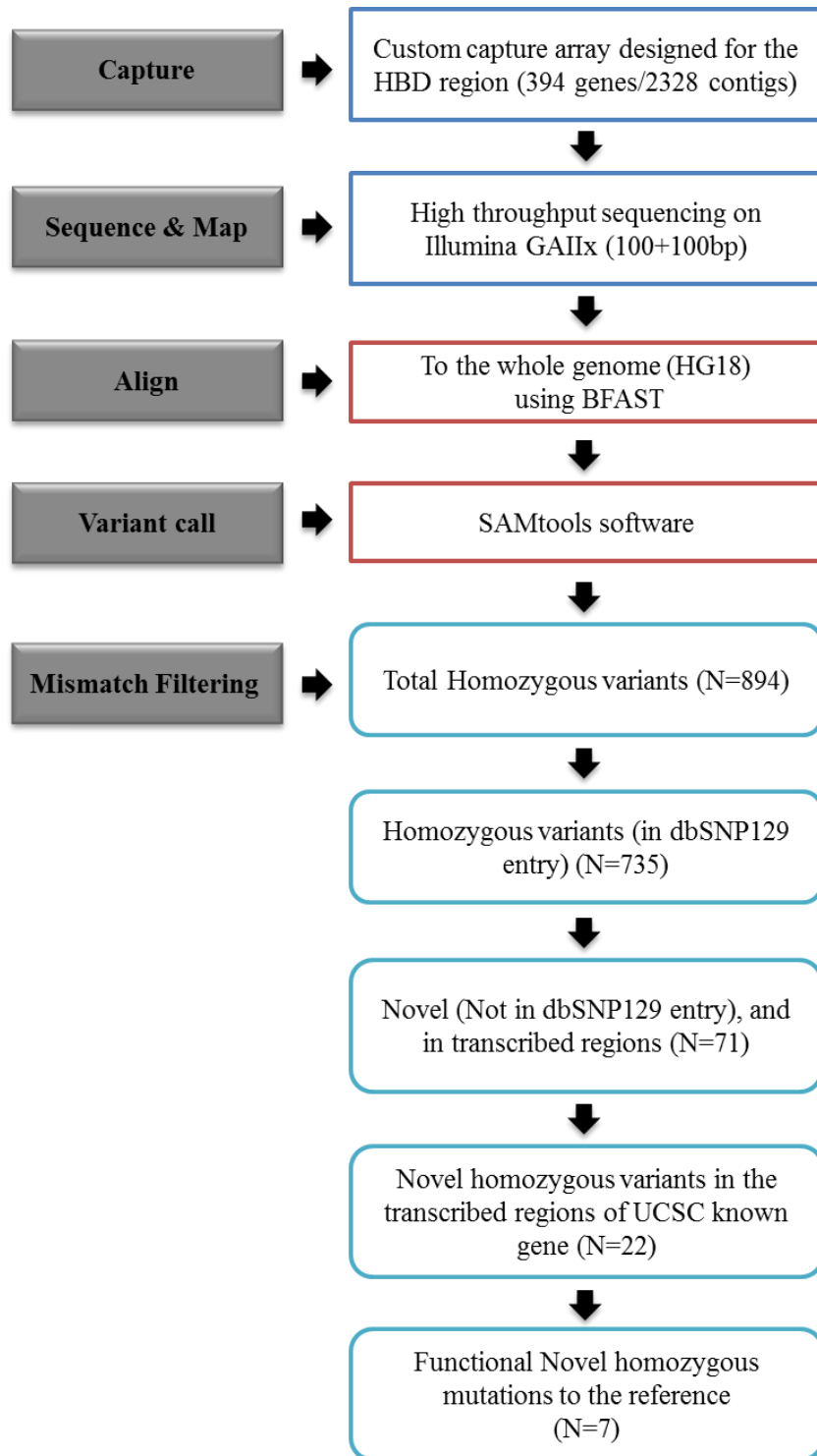
Figure 14: Sequencing workflow and number of mismatches found following loci-capturing and re-sequencing of the five genomic candidate regions. Detail of the sequenced genes is provided in Appendix 2.

Of the 7 mutations 5 were missense, 1 frameshift and 1 splice site mutations located in 6 distinct genes as summarized in Table 4.

Ch.	Gene	Mutation	Position	Consequence
6	*MLLT4*	c.3923A>T	168094827	Missense
6	*DACT2*	c.515G>A	168453763	Missense
6	*THBS2*	c.389T>C	169390657	Missense
8	*PKHD1L1*	c.6406T>G	110533684	Missense
		c.6507+1g>a	110533586	Splice site
12	*ASUN*	c.2004delA	26950579	Frameshift
13	*SAC2*	c.4335A>T	22809430	Missense

Table 4: The candidate genes list. Homozygosity mapping defined five candidate regions covering 395 genes. Using loci capture assay followed by high throughput re-sequencing in patient IV.6, we identified 6 non-synonymous variants and 1 splice site mutation.

We validated the high-throughput results by Sanger sequencing of the family members. All unaffected siblings were found to be heterozygous or wild-type and the parents were heterozygous for all 7 mutations. Hence, all 7 mutations segregated with the disease in the family with an autosomal recessive mode of inheritance.

To further narrow down the candidate gene list, we extended our sequencing to unaffected siblings of the parents. To this end, we collected saliva from 34 parent's brothers, sisters and their children: 7 from the father's siblings, 27 from the mother's side (Supplementary Figure 1). After sequencing the 7 variants in each of these samples, we uncovered 4 unaffected siblings who were homozygous for one or two mutations found in *DACT2, PKHD1L1, MLLT4* and *THBS2,* allowing us to exclude these four genes (Supplementary Table). We also eliminated *SACS* because it has been implicated in autosomal recessive spastic ataxia (MIM 604490) (Duquette et al., 2013; Synofzik et al., 2013), a disease with distinct manifestations from Mohr syndrome. Finally, one candidate gene *ASUN* remains (Table 4).

3.2.3. Identification of c.2004delA in *ASUN* as the disease-causing mutation

We first verified that the *ASUN* mutation segregates with the disease status in all family members using Sanger sequencing. PCR primers are given in Appendix 1. The homozygous deletion c.2004delA in *ASUN* gene was confirmed in the two affected patients. Based on the autosomal recessive mode of inheritance of the causative allele, both parents and the unaffected sister were found to be heterozygous (unaffected carriers) (Figure 15). The other 34

family members were either heterozygous or homozygous non-carrier. The c.2004delA variant in *ASUN* is therefore most likely a disease-causing in the affected probands.
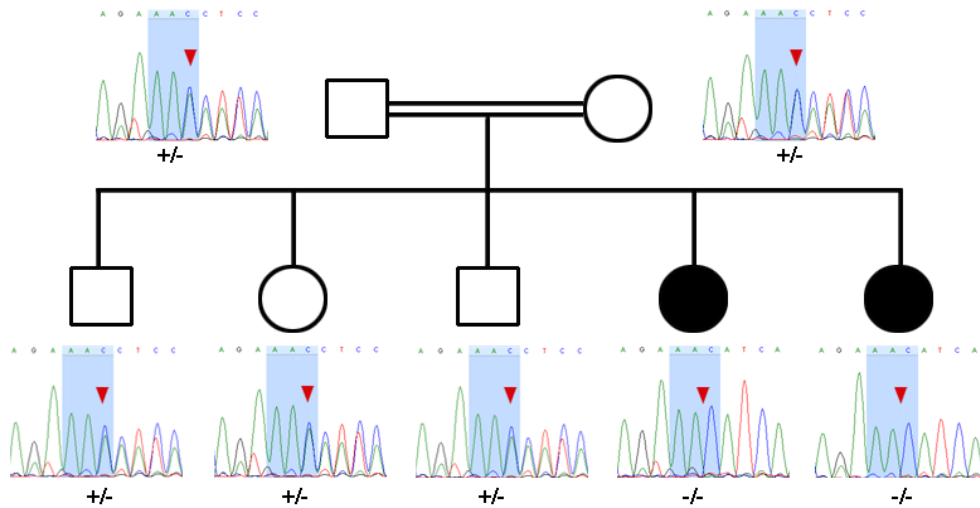
Figure 15: Electropherogram of the *ASUN* mutation in the family siblings obtained by Sanger sequencing. Electropherograms of the parents (heterozygous/carriers), the unaffected siblings (heterozygous/carriers), and the two affected cases (homozygous mutant) for c.2004delA mutation. The red arrowheads indicate the position of the mutation.

The one base pair (bp) deletion c.2004delA, located in exon 16 of *ASUN* (NM_018164.2), causes a frameshift (Table 4). *In silico* analysis using a computer prediction software SIFT (http://sift.bii.a-star.edu.sg/) predicted that this mutation may create a premature termination codon (PTC) 8 amino acids from the site of mutation, resulting in deletion of the remaining 31 amino acids of the ASUN protein (Figure 16a). This *ASUN* mutation led to the amino acid change p.K668Nfs*9. It is also predicted that c.2004delA in exon 16 may induce nonsense-mediated mRNA decay (NMD) (Figure 16b).

a

Chr. 12p11.23

↓

26950578-26950579
VAR: delA

↓

ASUN

c.2004delA

↓

ASUN

p.K668Nfs*9

ASUN

ATG   ... exons 1-17 ...   TGA

c.2004delA
PTC
STOP

16   17

Disrupted frame

. . RINTANSRKHQEFAGR LNSVNNRAELYQHLKEENGMETTENGKASRQ
. . RINTANSR NIRNLLDV ....

b

Mutation	Amino acids substitution	Region	dbSNP ID	Causes NMD
c.2004delA	TANSRnirnlldv*	EXON 16	Novel	Yes
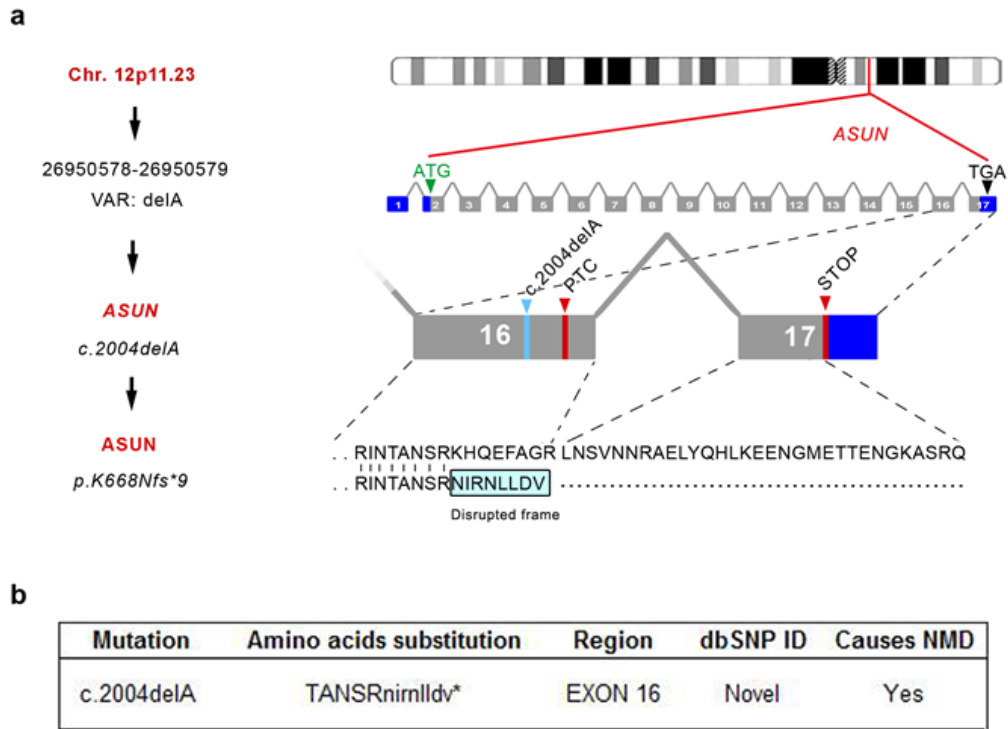
Figure 16: Overview of the chromosomal localization of the *ASUN* gene (hg 18), genomic structure and schematic representation of the frameshift mutation. (a) The ASUN gene is located in chromosome 12 (Ch12p13.2-p11.22) and consists of 17 exons. A frameshift mutation is detected in *ASUN* gene as a disease causing mutation. The c.2004delA (p.K668Nfs*9) mutation caused by single base pair deletion in exon 16 predicted to introduce a PTC which may disrupt the reading frame and deletes the rest of around 31 amino acids from mutated protein. (b) *In silico* analysis using SIFT software also predicted that this mutation could induce NMD.

3.2.4. *ASUN* gene and ASUN protein functions SNP genotyping

ASUN, also known as a spermatogenesis regulator homolog, referred to its basic function in *Drosophila* and later it was given a name asunder (set apart in position or space) based on its phenotypes. *ASUN* is encoded by a 32.8 kb genomic region (12p11-p12) and comprises 17 exons (Figure 16a). *ASUN* has an open reading frame of 2.97 kb and encodes a 706 amino acids protein known as ASUNDER (ASUN) with predicted molecular weight of 76 kDa. This protein belongs to a cell cycle regulator Mat89Bb (Maternal transcript 89Bb) family due to its maternal expression in *Drosophila* embryo (Lee et al., 2005; Stebbings et al., 1998).

Bourdon and colleagues found that ASUN was expressed in all normal human tissues with high expression in testicular seminomas (Bourdon et al., 2002). Using a genome scale *in vitro* expression cloning (IVEC) technique in *Drosophila*, Lee and her group identified several genes including *asun*, whose encoded proteins function as substrates for the PAN GU (PNG) kinase that regulates *Drosophila* cell cycles. Subsequent functional analysis of ASUN was then performed in *Drosophila*, *Xenopus* and human epithelial cervical cancer cells (HeLa), showed that ASUN plays a biological function in HeLa cell cycle as well as animal models embryonic development (Lee et al., 2005). Loss-of-function approach of Asun resulted in disruption of development in *Xenopus* and *Drosophila* and cell cycle defects in both models and cultured cells. By these findings, authors suggested that ASUN has a conserved function in cell cycle control and embryonic development in these animal models.

In 2009, functional analysis of ASUN in *Drosophila* revealed that *asun* regulates spermatogenesis, a process required to generate mature and functional sperm (Anderson et al., 2009). While, loss-of-function analysis had no defects in either spermatogonial cell proliferation or overall appearance of *Drosophila* males, the seminal vesicles of male testis had few mature sperm which were mostly immotile. Furthermore, most of the spermatocytes were arrested during prophase I and contained free centrosomes. The cells that escaped cell cycle arrest displayed severe defects such as spindle assembly, chromosome segregation, and cytokinesis. They also showed that the failure of nucleus-centrosome coupling at the onset of meiotic cell cycle caused by disruption of normal nuclear localization of dynein-dynactin in mutant spermatocytes and spermatids (Anderson et al., 2009). The mechanism by which asun regulates spermatogenesis through recruitment of dynein-dynactin to the nuclear surface however could not be determined.

This work was followed by two more studies explaining the previous mechanism. The results showed that *Drosophila* asun co-localized and interacted with *Drosophila* lissencephaly 1 (lis1), a dynein adaptor (Sitaram et al., 2012). This interaction was found to be conserved between the mammalian homologues. Down-regulation of *ASUN* in cultured human cells resulted in reduction of perinuclear dynein during prophase of mitosis, nucleus-centrosome uncoupling and downstream cell cycle defects (Jodoin et al., 2012). These findings suggested that ASUN interaction with dynein in the cytoplasm via LIS1 required for the proper dynein-dynactin perinuclear localization, a step that is necessary for the nucleus-centrosome coupling at the onset of meiotic G2/M transition in *Drosophila* primary spermatocytes and

mitotic cell cycle in cultured human cells (Jodoin et al., 2012; Sitaram et al., 2012). These studies suggested that besides asun and lis1 interaction, other unknown protein partners may be required for the proper function; a proposition that has yet to be determined.

A genome-wide RNAi screen in *Drosophila* S2 cells performed by Chen and coworkers has elucidated a new function of asun. It was shown that asun is required for the formation of the 3'-end of small nuclear RNAs (snRNAs), a process normally mediated by a complex of proteins known as integrator complex (INT) (Chen et al., 2012). snRNAs are non-coding RNA molecules that play vital roles in pre-mRNA splicing via removing of introns and further processing of pre-mRNAs (Matera et al., 2007). Additional biochemical analysis demonstrated that ASUN is a core component of INT. 14 INT subunits (INT) were found to be evolutionarily conserved, including ASUN, which is referenced as INT13 (Chen et al., 2012).

Subsequent experiments were carried out on HeLa cells in order to understand the mechanism of dynein localization and to determine the precise role of ASUN and other INT in this process (Jodoin et al., 2013b). The experimental results showed that INT required for dynein enrichment at the nuclear envelope. Knock-down (KD) of several individual INT in HeLa cells resulted in similar reduction of perinuclear dynein as in ASUN-siRNA cells. Structural analysis of ASUN revealed the presence of a specific conserved sequence at the C-terminus that mediates the nuclear localization of ASUN. These findings confirmed that ASUN and many INT interact to regulate the recruitment of dynein to the nucleus at specific time of the cell division. Taken together,

these results established that INT complex is essential for nuclear dynein localization, possibly through snRNA processing. This discovery paved the way for the following studies of role of INT in ciliogenesis.

Jodoin and colleagues found that several INT were essential for primary cilia formation (Jodoin et al., 2013a). Using siRNA-mediated KD of individual INT in human retinal pigmented epithelial (RPE) cells, led to the absence of primary cilia and defects in centriole coupling. These results were limited to a group of INT. Interestingly; depletion of several INT did not affect other proteins required for primary cilia formation or for dynein recruitment to the nuclear envelope. Subsequent siRNA-mediated down-regulation experiments of other proteins that regulate perinuclear dynein showed no defects in ciliogenesis, although one of these proteins (CENP) displayed longer cilia. These results have demonstrated that primary cilia formation is independent on dynein recruitment to the nuclear envelope even though both processes are regulated by INT (Jodoin et al., 2013a). A recent study in *Drosophila* has confirmed the role of asun in the regulation of dynein localization and subsequent processes during oogenesis (Sitaram et al., 2013).

3.2.5. ASUN is highly conserved across vertebrate species

Highly conserved protein sequence across different species indicates a crucial function of this protein and a high evolutionary significant (Giudice, 2001). By amino acid alignment of ASUN proteins found in amphibians, fish and mammals, we found a high degree of sequence similarity among these animals. Moreover, we found that mutated residues reside within a highly conserved sequence of ASUN protein (Figure 17), suggesting that alteration of

these amino acids may lead to a pathogenic function of ASUN protein. A full sized ASUN protein alignment (Supplementary Figure 2) is given in appendix 3.

Figure 17: Amino acid sequence alignment of ASUN in different speicies. Partial amino acid alignment of ASUN proteins shows high homology across vertebrate species. The amino acid sequences were retrieved from http://www.ncbi.nlm.nih.gov/protein/ website, using the following accession numbers: *Homo sapiens* (NP_060634.2), *Gallus gallus* (XP_416439.2), *Xenopus leaves* (NP_001086192.1), zebrafish (NP_956177.1), *Rattus norvegicus* (NP_001103078.1). Alignment performed using http://multalin.toulouse.inra.fr/multalin/. Asterisk (*) referred to the position of the mutation found in the two patients.

3.2.6. The c.2004delA mutation causes down-regulation of *ASUN* mRNA expression

Quantitative reverse transcriptase PCRs (qRT-PCR) were performed using cDNAs generated from RNA extracted from patient and control cells. The level of *ASUN* transcripts was found to be significantly down-regulated in patient's fibroblast cells compared to control cells Figure 18a). This suggests that *ASUN* mRNA was targeted for degradation by a nonsense-mediated decay (NMD). NMD is an evolutionary conserved mRNA surveillance mechanism which selectively degrades mRNAs that carry premature termination codons (PTCs) (Chang et al., 2007; Culbertson, 1999). The qRT-PCR was repeated in other cell types derived from patients and controls such as Epstein Barr virus-transformed B-lymphoblastoid (EBV-LYB) cells and peripheral blood mononuclear cells (PBMC). The expression level of *ASUN* mRNA was also down-regulated in EBV-LYB, while the level of mRNA transcripts was unchanged in PBMC (Figure 18b,c). This might be due to the differences of number of white blood cells between both patients and control; therefore the abundance of mRNA transcripts will be different. To test whether the reduction in mRNA level in patient's cells was caused by NMD, the cultured cells were treated with cycloheximide (CHX) (Sigma), a translational inhibitor that inhibits NMD. A qRT-PCR was then performed on total mRNA to determine the mutant transcript levels. The results showed that the level of mutant mRNA was increased in EBV-LYB cells following CHX treatment, while levels were unchanged in fibroblast cells. This suggests that the mutant *ASUN* mRNA was susceptible to NMD (Figure 18d).
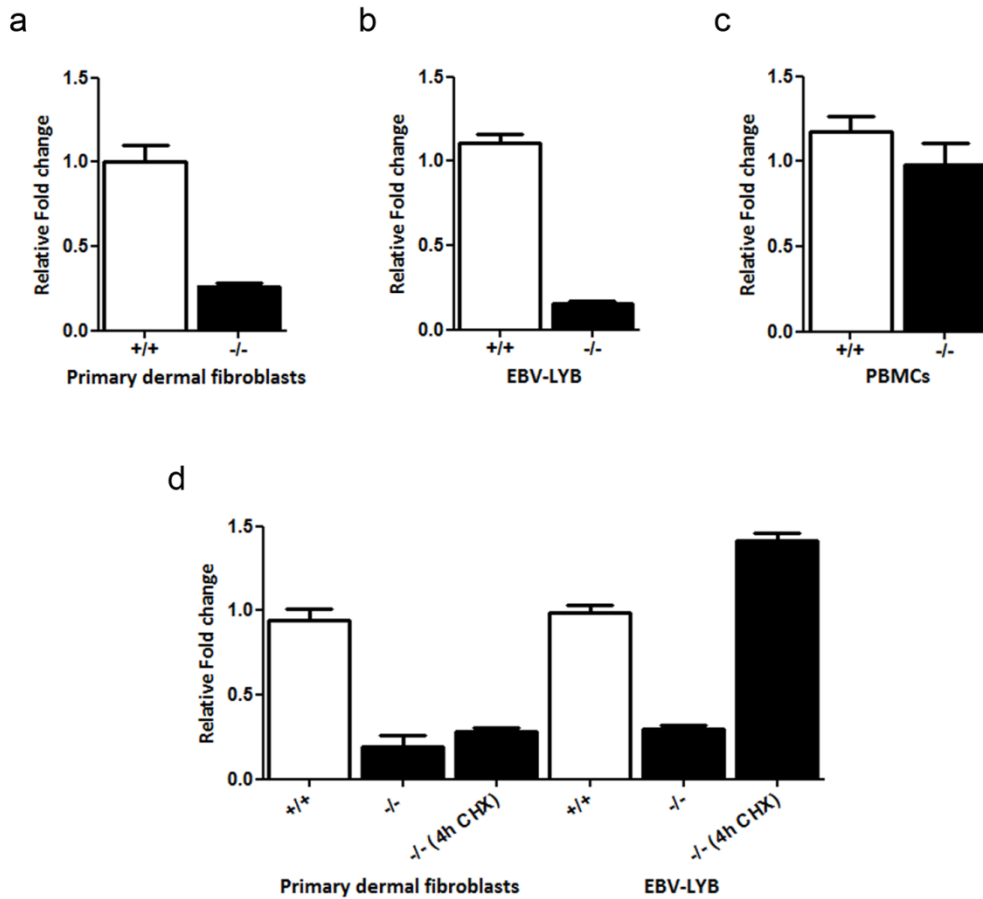
Figure 18: Quantitative real time PCR (qRT-PCR) in different cell lines. (a,b) The ASUN expression is down-regulated in patient's primary dermal fibroblasts & EBV-LYB cells, respectively relative to control cells. (c) Whereas, there is no significant difference between the affected and control PBMC. (d) Primary dermal fibroblast and EBV-LYB were treated with cycloheximide (CHX) (100 g/ml) for 4 h. Following treatment with CHX, a transcript level is increased in EBV-LYB relative to untreated cells; however it is unchanged in fibroblast cells. Error bars indicate SEM.

3.2.7. The c.2004delA mutation results in a truncated protein

To evaluate the effect of *ASUN* gene mutation on the encoded protein, western blot of cell lysates made from patients and control fibroblasts was performed. We designed two high affinity purified polyclonal antibodies against N-terminal and C-terminal peptides of human ASUN (rabbit anti-M and anti-C, respectively) (Jodoin et al., 2012) (Figure 19a). These antibodies were used to determine the presence or absence of a truncated protein, respectively. The results displayed the presence of a truncated protein in patient cells compared to control cells by anti-M antibody. No product however was observed by anti-C antibody, consistent with the genetic mutation we discovered (Figure 19b). This result was further confirmed in RPE cells, these were generated using induced pluripotent stem (iPS) cells derived from patient's fibroblast cells (Figure 19b). This suggests that a truncated ASUN protein is made in the patient cells, consistent of the reduced level of mRNA as a result of NMD.
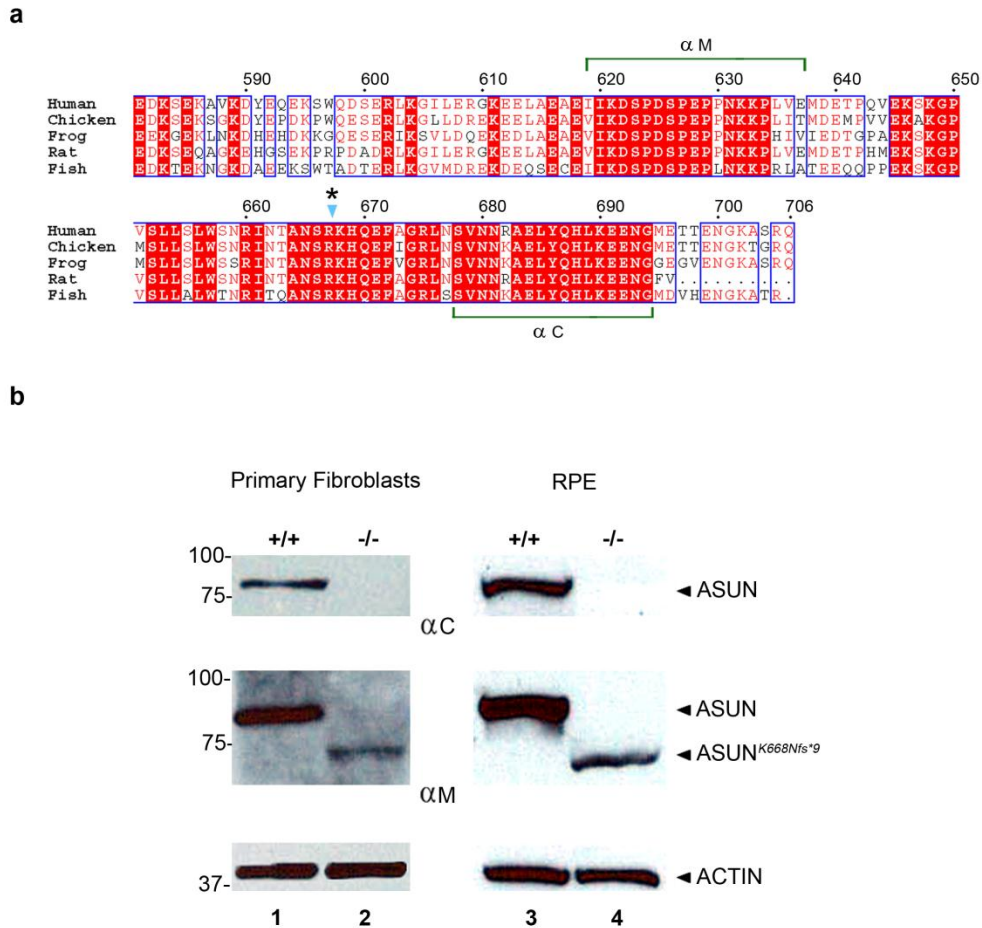
Figure 19: The c.2004delA mutation resulted in a truncated protein. (a) The position of peptide sequence of ASUN polyclonal antibodies. (b) Western blot analysis in primary dermal fibroblast and RPE cells using anti-ASUN (M & C) antibodies. The results show the presence of a truncated product of ASUN in the affected fibroblast cells (Lane 2) and RPE (Lane 4) when probed with the α-M antibody but there is no product is observed with the α-C antibody compared to the control fibroblast cells and RPE (Lane 1,3, respectively). Actin was used as a loading control.

3.2.8. Conclusions

Using a homozygosity mapping and loci capture assay, we identified a single base pair deletion in *ASUN* gene that leads to a rare congenital disorder called Mohr syndrome or OFDII affecting the face, the oral cavity and the digits in addition to other organs.

The *ASUN* mutation reported in the two patients leads to a frameshift that results in a PTC in the *ASUN* mRNA; that should, in theory, detects the mutant mRNA to be degraded by NMD, thus the transcript level is predicted to be reduced. Therefore, we proposed that patient's phenotypes are primarily caused by changes in activity of the remaining truncated ASUN protein. Therefore, the next step was to investigate the impact of c.2004delA mutation experimentally. A quantitative real-time PCR (qPCR) and western blot analysis were carried out to examine the levels of both *ASUN* mRNA and the encoded protein as a result of this mutation.

The qPCR, findings indicated the existence of tissue-specific NMD for *ASUN* gene, which was confirmed by CHX treatments. The western blot analysis revealed the presence of a truncated product of ASUN in the affected fibroblasts. These findings suggest that the disease phenotype could be either due to loss of ASUN protein or as a result of truncated protein.

To investigate the function of *ASUN* and its encoded protein in patients' cells, we first need to determine the localization pattern of the endogenous protein. Moreover, Identification of a crucial role of several OFD genes (*CXORF5*, *TCTN3*, *TBC1D32* and *SCLT1*) in cilia formation and function suggests that Mohr syndrome and even the other OFD could be ciliopathies as well.

Additionally, the fundamental role of several INT in ciliogenesis provides further evidence that is ASUN could be implicated in cilia formation and/or function. To investigate this hypothesis and to gain insight into the possible role of ASUN in ciliary processes, biochemical experiments on patients' cells and other cell lines were undertaken.

3.3.   Subcellular localization of ASUN

3.3.1.   ASUN is ubiquitously localized in human and mouse cell lines

ASUN has been reported to localize in *Drosophila* spermatocytes and its localization ranges from predominantly nuclear to being apportioned between the nucleus and cytoplasm (Anderson et al., 2009; Jodoin et al., 2012). Similar patterns were also observed in cultured HeLa cells. To assess the subcellular localization of ASUN in cultured primary dermal fibroblasts, we carried out immunofluorescence staining using ASUN α-M and α-C, respectively and DAPI to visualize DNA. The results showed that ASUN is localized both to the nucleus, and to the cytoplasm by α-M, similar to which have been reported in *Drosophila* spermatocytes and HeLa cells (Figure 20a,b). Whereas, using α-C antibody, ASUN localization was predominantly to the cytoplasm with a background of unspecific staining. We repeated the experiment using other cell lines such as mouse embryonic fibroblast cells (NIH3T3) and human embryonic kidney 293 (HEK293T) cells, which showed similar localization patterns of ASUN (Figure 20c-e). Both ASUN antibodies showed inconsistency between cells which could be due to a cross reactivity of these antibodies to non-specific antigens in immunofluorescence although these antibodies were successfully validated by immunoblotting

3.3.2.   ASUN is localized to primary cilia in primary dermal fibroblasts

To investigate the possible role of ASUN in ciliogenesis, and whether the primary cilia are affected in patient's cells, immunofluorescence staining in primary fibroblast cells was undertaken using ASUN (α-M & α-C) and anti-

acetylated α-tubulin antibodies that marks ciliary axoneme. Upon analysis, the

results showed that the ASUN signal was overlapped with acetylated α-tubulin

(Figure 20a-e). These findings suggest a conserved function of ASUN

throughout evolution as a mediator of ciliogenesis or ciliary function.
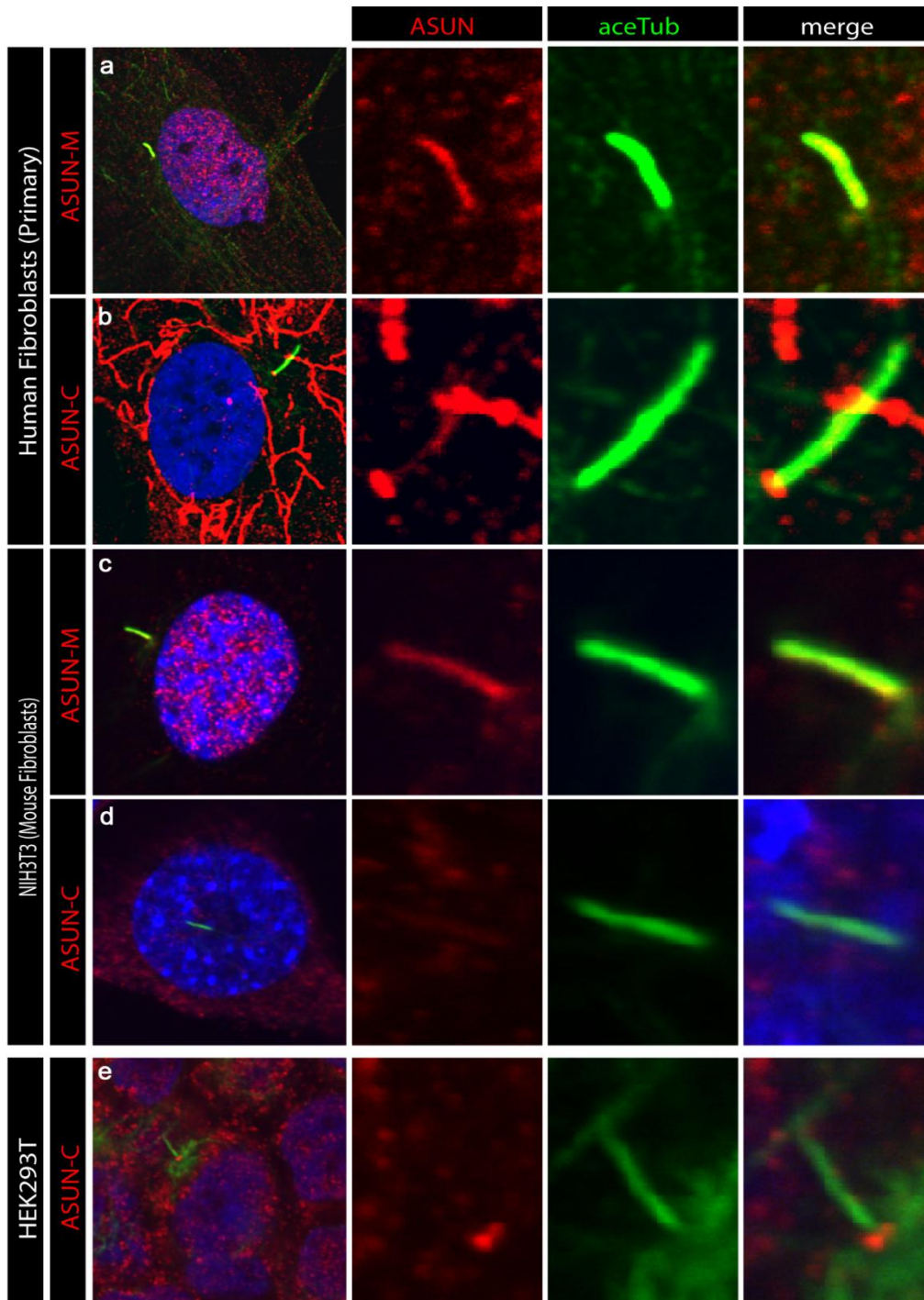
Figure 20: Cytoplasmic, nuclear and primary cilia localization of ASUN in different cell lines. ASUN localization in human and mouse cell lines. (a,b) Immunofluorescence staining for ASUN in human primary fibroblasts, (c,d) NIH3T3 and (e) HEK293T cells. ASUN (α-C & α-M) and acetylated α-tubulin antibodies were used in this experiment. ASUN displays cytoplasmic and nuclear localization in all cell types. Additionally, ASUN is also co-localized with the acetylated α-tubulin that labels cilia axoneme.

3.3.3. Primary cilia assembly is not affected in patient's cells

Given the localization of ASUN to primary cilia, we decided to examine whether its localization is affected in patient's cells as a result of a frameshift mutation. To test this, cultured fibroblasts derived from patient and from unaffected age-matched control were seeded until they become confluent, followed by incubation with serum free medium for 72 hours to promote ciliogenesis. We next performed immunofluorescence staining with ASUN antibodies and other antibodies against axonemal (acetylated α-tubulin) and centrosomal (pericentrin and CEP170) proteins. Unfortunately, we were unable to discern significant differences with respect to cilia formation, morphology and number in the patient's cells compared to control cells, although many patient's cells displayed either no cilia or longer cilia (Figure 21a,b). Similarly, patient's RPE cells were normally ciliated compared to control cells (Figure 21c). The plausible explanation for this could be due to that *ASUN* mRNA escaped NMD leading to the production of truncated ASUN protein which might be hypomorphic or neomorphic rather than loss-of-function. On other hand, there was a significant reduction in the nuclear expression of ASUN protein between patient and control fibroblast cells, using ASUN (α-M) antibody, while the cytoplasmic expression ASUN was unchanged (Figure 21a). Therefore, we sought to address primary cilia formation following depletion of *ASUN* using siRNA-mediated down-regulation.
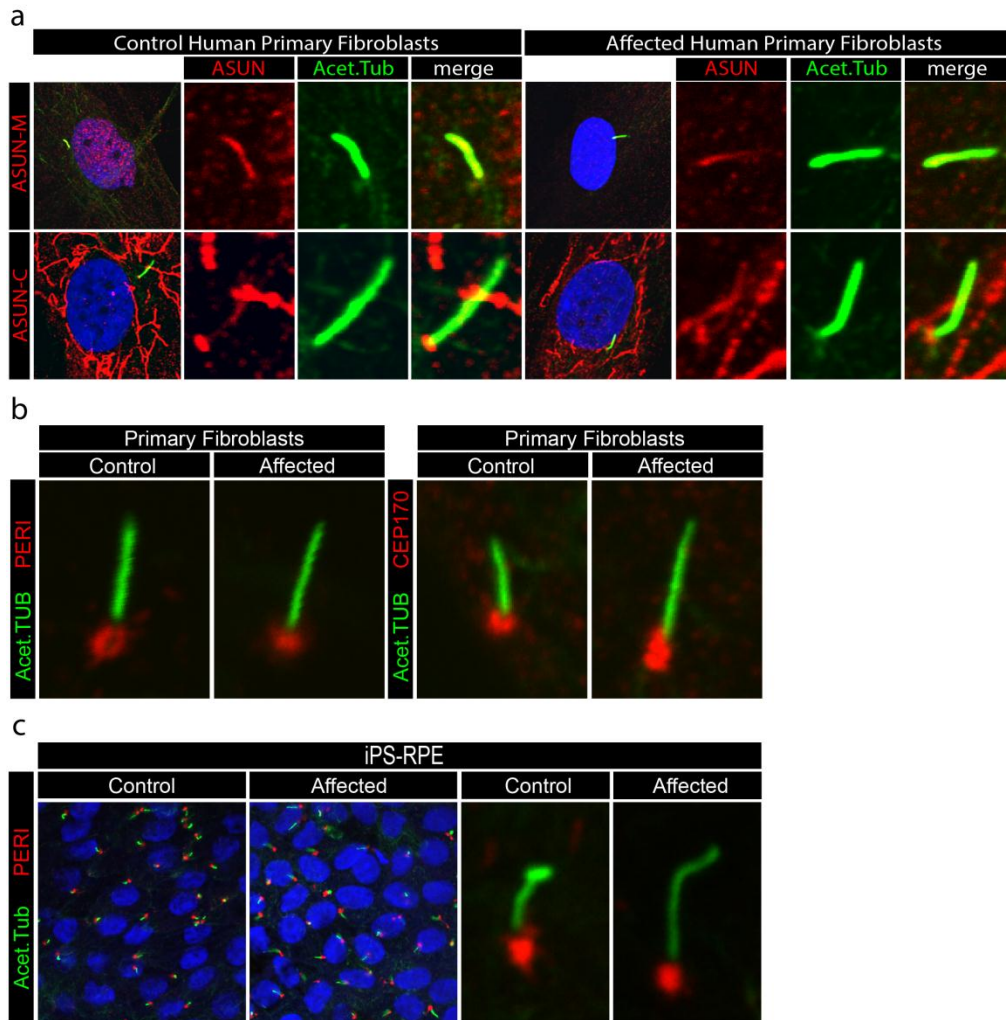
Figure 21: Normal primary cilia formation in patient's cells. Immunofluorescence staining in control and patient's cells using acetylated α-tubulin, pericentrin, CEP170 and ASUN antibodies. (a) Patient fibroblasts display normal cilia formation with marked reduction in a nuclear localization of ASUN, while no change in its localization to primary cilia. (b) Many individual patient's cells possess variable length of cilia compared to control cells. (c) Patient RPE cells show no significant difference in primary cilia morphology and number as well as ASUN localization compared to control cells.

3.3.4. *ASUN* depletion through RNA interference (RNAi)

To gain insight into the function of ASUN in ciliogenesis, we performed siRNA-mediated depletion for *ASUN* in primary dermal fibroblasts and RPE cell as another cell line that normally form primary cilia when they become confluent. RNAi is a highly conserved pathway involving a gene silencing mediated by introduction of exogenous short double-stranded RNA (Campbell and Choy, 2005). By this technique, we examined the consequences of *ASUN* depletion in ciliogenesis in human cells.

3.3.5. *ASUN* down-regulation shows no defect in primary cilia formation in cultured dermal fibroblasts

Since we did not find ciliogenesis defects in patient's cells, we postulated that KD of *ASUN* in fibroblast cells could cause obvious ciliary defect compared to the patient mutation. Fibroblasts were transfected with *ASUN*-siRNA followed by immunofluorescence staining with anti-acetylated α-tubulin antibody to visualize primary cilia formation. Unfortunately, we found that reduction of ASUN levels had no overt effect on primary cilia formation; cilia were present and formed normally from the surface of fibroblast cells after 48 hours of serum starvation.

3.3.6. *ASUN* depletion results in loss of primary cilia in retinal epithelial cells (RPE)

To preclude the possibility of tissue-specific requirement of ASUN in primary cilia formation, we repeated these experiments in retinal epithelial cells (RPE). We chose RPE since ophthalmological assessment in both patients revealed the presence of racemose angioma (dilated retinal vessels) and crowded optic disk (Figure 22e,f), raising the possibility that these manifestations could be related to ciliary dysfunction as a result of *ASUN* mutation. Therefore, we addressed the consequence of *ASUN* depletion on ciliogenesis in RPE cells. Performing siRNA-down-regulation of ASUN, followed by incubation with low serum medium for 24 hours to promote ciliogenesis. For rescue experiment, cells were transfected with another ASUN-siRNA duplex designed against 3'UTR together with wild-type and mutant ASUN-tagged with Myc epitope to detect fusion proteins. Immunofluorescence staining using antibodies against acetylated α-acetylated tubulin and γ-tubulin was then carried out which showed most of *ASUN*-siRNA transfected cells did not form cilia compared to the control cells (Figure 22a-d,g). The experiment was repeated four times and gave similar findings. Besides that ASUN is indispensable for primary cilia formation, these findings also indicate a tissue specific function of this protein. The plausible explanation for this heterogeneity between fibroblasts and RPE could be due to a difference in the level of ASUN expression between these cells. The level of ASUN protein was assessed by western blot analysis to validate the KD efficiency (Figure 22h). ASUN depletion in RPE cells was carried out by our collaborator Dr.

Laura A. Lee lab, Department of Cell and Developmental Biology, Vanderbilt
University Medical Centre, Nashville.
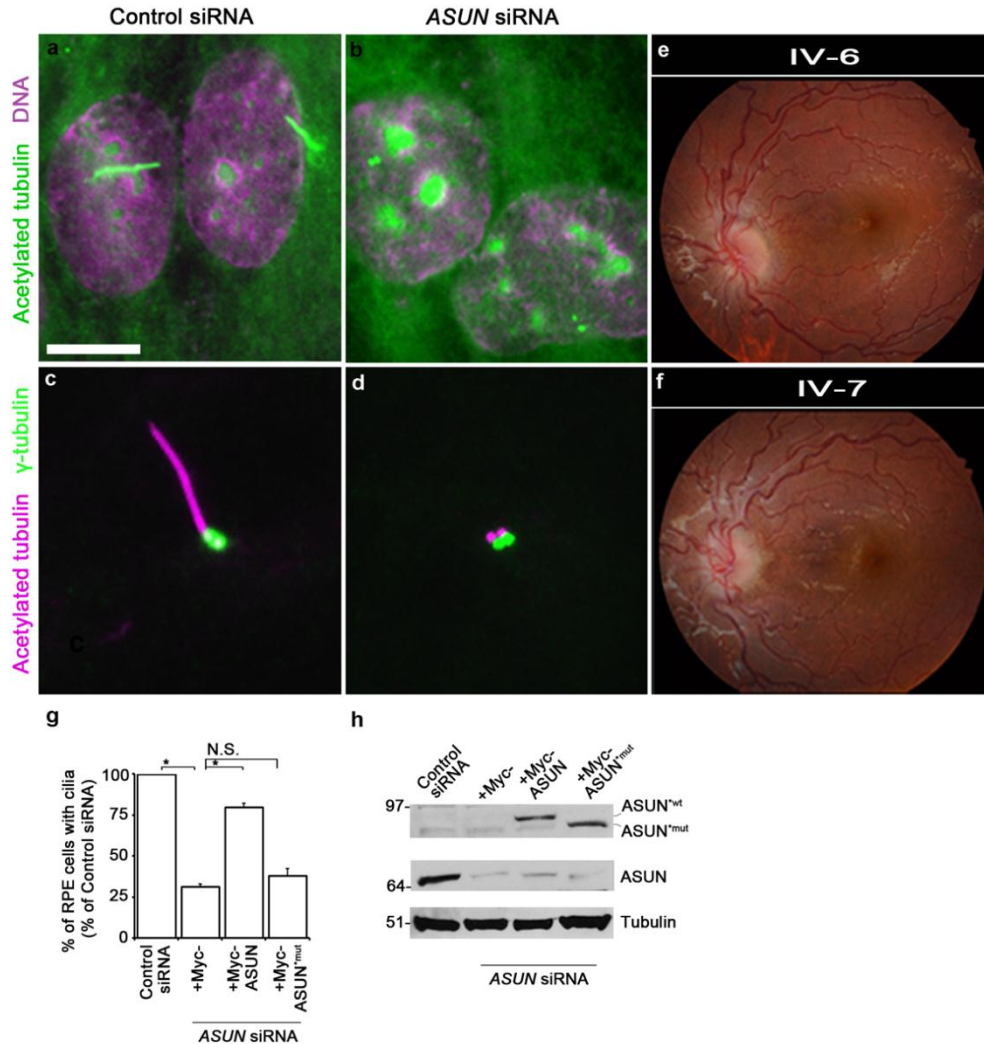
Figure 22: Loss of primary cilia in RPE cells following ASUN-KD. (a) RPE cells transfected with control siRNA plus vector DNA display primary cilia. (b,d) Cells transfected with ASUN-siRNA plus vector DNA display no cilia. Furthermore, loss of hASUN causes an even more sever degree of multinucleation. (c) Cells transfected with ASUN siRNA directed against 3'UTR plus a Myc tagged-ASUN expression construct ("Rescue") show restored cilia. Cells were fixed and stained for acetylated α-tubulin (labels cilia) and γ-tubulin (labels basal bodies). Scale bars, 20 μm. (e,f) Fundus appearance in both patients shows dilated retinal vessels and crowded optic disk. (g) Quantification of cells with primary cilia. Almost all control-siRNA cells had cilia compared to 30% of ASUN-siRNA cells. All experiments were performed a minimum of four times with at least 300 cells scored per condition. Error bars indicate SEM. "NS" stands for not significant. Asterisk, $p < 0.0001$ (Student's unpaired t test). (h) Immunoblotting of cell lysates confirms the efficient KD of ASUN. Tubulin was used as loading control.

3.3.7. Multi-cilia are perturbed in patients' nasal epithelia

The epithelia lining the upper and lower respiratory tract are densely covered with motile cilia that are responsible for the clearance of the airway. Reduction of mucociliary clearance of the airway is related to cilia dysfunction, often resulting in recurrent respiratory tract infections. Both patients suffer from recurrent respiratory tract infection and chronic cough. We assumed the ciliary defect could be behind these phenotypes. So, we obtained respiratory epithelial cells from the two patients and the mother to assess the cilia formation and performance. Immunofluorescence staining was performed using anti-acetylated α-tubulin antibody. The average length of nasal cilia was then scored. The results revealed shorter, fewer and disorganized cilia compared to that of the heterozygous mother, which may explain the recurrent respiratory tract infections in the two affected patients (Figure 23).
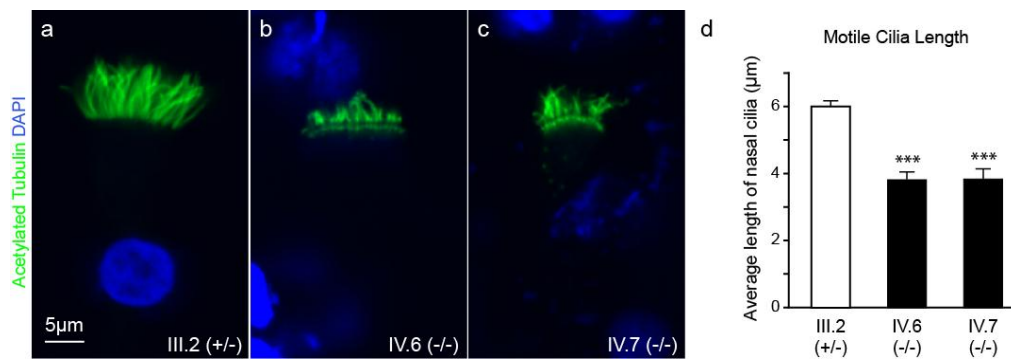
Figure 23: Immunofluorescence of multiciliated cells after nasal biopsies. (a-c) Morphological appearance of respiratory epithelial multi-cilia in the mother and the two patients' cells, respectively. (d) Average length of nasal cilia in 200 cells of both control and patient. Cilia look shorter, less dense and disorganized in most epithelial ciliated cells of both patients compared to their unaffected mother.

3.3.8. Alteration of Sonic hedgehog (SHH) signaling in patient's cells

Although the out-of-frame mutation of *ASUN* had no effect on primary cilia formation, the overall appearance of patients' phenotypes suggests a possible ciliary dysfunction. Example of these phenotypes including, hypertelorism, polydactyly and teeth duplication, all suggesting SHH defects. We postulate that in spite of normal ciliation in patients' cells, the effect of *ASUN* mutation could be restricted to cilia function. Therefore, we addressed whether a frameshift mutation alters the activity of SHH. Patient's and control fibroblasts were seeded till confluency and incubated with low serum media for 72h. At 48h incubation, cells were treated with hedgehog agonist (SAG) and further incubated for the last 24h. A qRT-PCR was carried out to examine the expression levels of *Ptch1* and *Gli1*, SHH target genes to give a read out of SHH signaling pathway activity (Caspary et al., 2007). Interestingly, the results showed that SAG treatment was able to induce SHH signaling pathway in patient's cells to a level higher and comparable between control- and *ASUN*-siRNA transfected cells (Figure 24). We observed an up-regulation of *Gli1* expression following SAG treatment in patient's cells more than either the control or the ASUN-depleted cells. For *Ptch1*, We did not observe a significant change of its level in both control and patient's cells. However, these findings suggest that the frameshift mutation could be a hypomorphic, which while allowing primary cilia formation, does not lead to fully functional cilia. Alternatively, the truncated ASUN mutant protein could have a neomorphic function in promoting SHH signaling, either directly or indirectly through molecular alterations to ciliary function activity of *ASUN* mutation, the result need to be validated using patient's RPE cells (Figure 24).
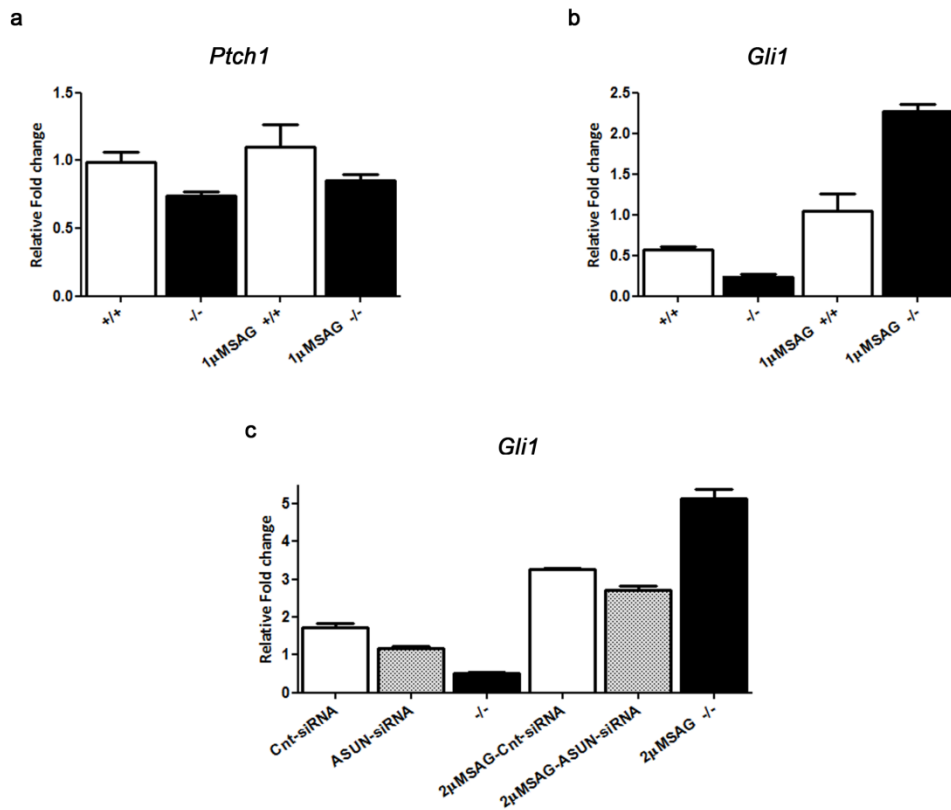
Figure 24: Disruption of SHH in patient's cells. A qRT-PCR for SHH target genes, *Ptch1 and Gli1* before and after Sonic hedgehog (SAG) treatment. (a) The level of *Ptch1* transcript is not significantly changed after 1 μM SAG treatment. (b) The level of *Gli1* transcript is markedly up-regulated after SAG treatment. (c) The level of *Gli1* expression at higher dose of SAG (2 μM) in patient's cells compared to control- and *ASUN*-siRNA transfected cells, shows dosage dependent of *Gli1*. Surprisingly, *Gli1* transcript level in patient's cells is highly up-regulated compared to control-siRNA and even to *ASUN*-siRNA transfected cells. Error bars indicate SEM.

3.3.9. Conclusions

The *ASUN* depletion in human cell lines indicated the essential role of this protein in cilia formation, although insignificant effect of *ASUN* frameshift mutation in patient's cells. Despite normal ciliation of patient's cells, our findings showed alteration in SHH signaling pathway, which argued for us to characterize the function of this gene in animal models.

To gain insight into the pathophysiological mechanism behind the clinical features of individuals with Mohr syndrome, different animal models such as zebrafish, *Xenopus* and *Drosophila* were utilized to investigate the role of ASUN during embryogenesis. My objective was to better understand how the *ASUN* mutation responsible for the disease could lead to such a pathogenic course.

3.4. *In vivo* animal modeling of ASUN

3.4.1. *ASUN c*.2004delA failed to rescue *asun*-mutant *Drosophila* phenotypes

This experiment was carried out by our collaborator Dr. Laura A. Lee. Her group had previously generated an *asun*-mutant *Drosophila* line (*asun*[f02815] males) carrying a truncated *asun* transcript in germ cells of the testes which displayed spermatogenesis phenotypes (Anderson et al., 2009; Jodoin et al., 2012). The biochemical analysis of *asun*-mutant *Drosophila* revealed severe reduction of perinuclear dynein, loss of nucleus-centrosome coupling and multinucleation in the spermatids (Jodoin et al., 2012). ASUN protein is highly conserved from *C. elegans* to human. The human ASUN protein shares 61% similarity and 36% identity with its *Drosophila* orthologue (Lee et al., 2005). *Drosophila* asun mutants expressing the wild-type of either *Drosophila asun* or human *ASUN* were able to rescue the aforementioned phenotypes (Anderson et al., 2009). Given this functional conservation of ASUN, we therefore attempted to examine whether the *ASUN* c.2004delA mutation could restore the resulted *Drosophila asun* mutant phenotypes.

A mutated human *ASUN* construct (pCS^{2+}-*ASUN*[c.2004delA]) was generated by introducing a frameshift mutation into the wild type pCS^{2+}-*ASUN* using site-specific mutagenesis. Mutated construct was verified by sequencing (this part was performed by me in our lab). Both mutant and wild-type constructs were then subcloned into testis expression vector tv3 tagged with Cherry (CHY) at the N-terminal. Transgenic lines of *asun* mutants expressing either the wild-type human CHY-tagged *ASUN* or CHY-tagged *ASUN*[c.2004delA] were

generated. Then perinuclear dynein, nucleus-centrosome coupling and multinucleation in *asun* spermatocytes were assessed in each line. Rewardingly, the results showed that unlike the CHY-*ASUN*, the CHY-*ASUN*$^{c.2004delA}$ transgene failed to rescue *Drosophila asun* prototypical phenotypes (Figure 25). These findings strongly support that *ASUN* frameshift mutation is most likely a disease-causative mutation.
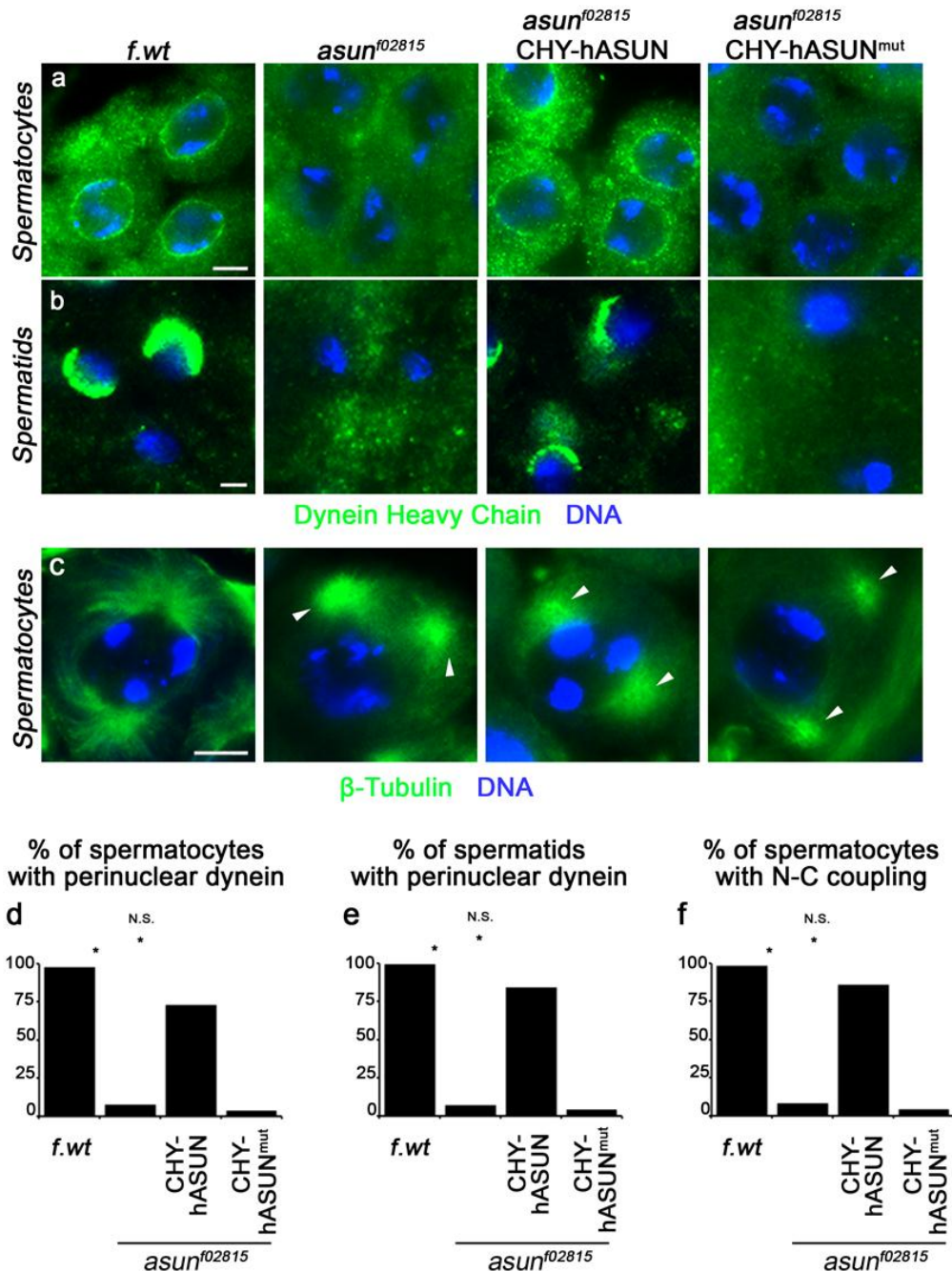
Figure 25: Mutant ASUN failed to rescue *Drosophila asun*-mutant phenotype.
(a,b) Germline CHY-*ASUN* expression restored perinuclear dynein in *asun* primary spermatocytes and spermatids, respectively, while *ASUN*[c.2004delA] (CHY-*ASUN*[mut]) did not. (d,e) Representative G2 spermatocytes stained for dynein heavy chain (DHC) and DNA are shown with bar graphs describing percentages of spermatocytes or spermatids exhibiting properly localized DHC. (c,f) Germline CHY-*ASUN* expression restored nucleus-centrosome coupling in *asun* primary spermatocytes, while CHY-*ASUN*[mut] failed to. (c) Prophase I spermatocytes stained for β-tubulin and DNA. (f) Quantification of nucleus-centrosome coupling in prophase spermatocytes. Arrowheads indicate centrosome positions, f.wt (*asun-Drosophila* wild-type). Asterisks, $p<0.0001$. Scale bars, 10 μm.

135

3.4.2. Modeling of Asun loss-of-function in zebrafish

After we identified the causative gene for Mohr syndrome, the next step is to understand its function. In order to recapitulate the disease phenotypes and explore the role of ASUN *in vivo*, we chose to use a zebrafish model, which has been well established as a suitable vertebrate model system to explore ciliopathies (Bisgrove et al., 2005; Hildebrandt and Zhou, 2007; Otto et al., 2010; Sayer et al., 2006; Simms et al., 2012; Valente et al., 2010). One *asun* paralogue has been annotated in zebrafish and showed high amino acid sequences similarity to other vertebrates. We first determined the expression pattern of *asun* at different developmental stages and then performed loss of function experiments. Zebrafish work was carried out by our collaborators Dr. Sudipto Roy and Dr. Semil Choksi, Institute of Molecular Cell Biology (IMCB), A*STAR, Singapore.

3.4.2.1. Endogenous *asun* is expressed ubiquitously throughout zebrafish development

Whole embryo *in situ* hybridization was performed to examine spatiotemporal expression pattern of *asun* in zebrafish at different embryonic developmental stages. We found that *asun* was constitutively and ubiquitously expressed throughout development. Figure 26 shows that the expression of *asun* at 24 hours post fertilization (hpf) is ubiquitous, while being enriched in the anterior regions of the embryo, including the brain and the eye (Figure 26a). Whole mount immunofluorescence staining using ASUN (α-C, α-M) antibodies and GFP-tagged Asun protein revealed that the endogenous protein is mainly

expressed in the cytoplasm, while the exogenous proteins showed a nuclear expression (Figure 26b-d).
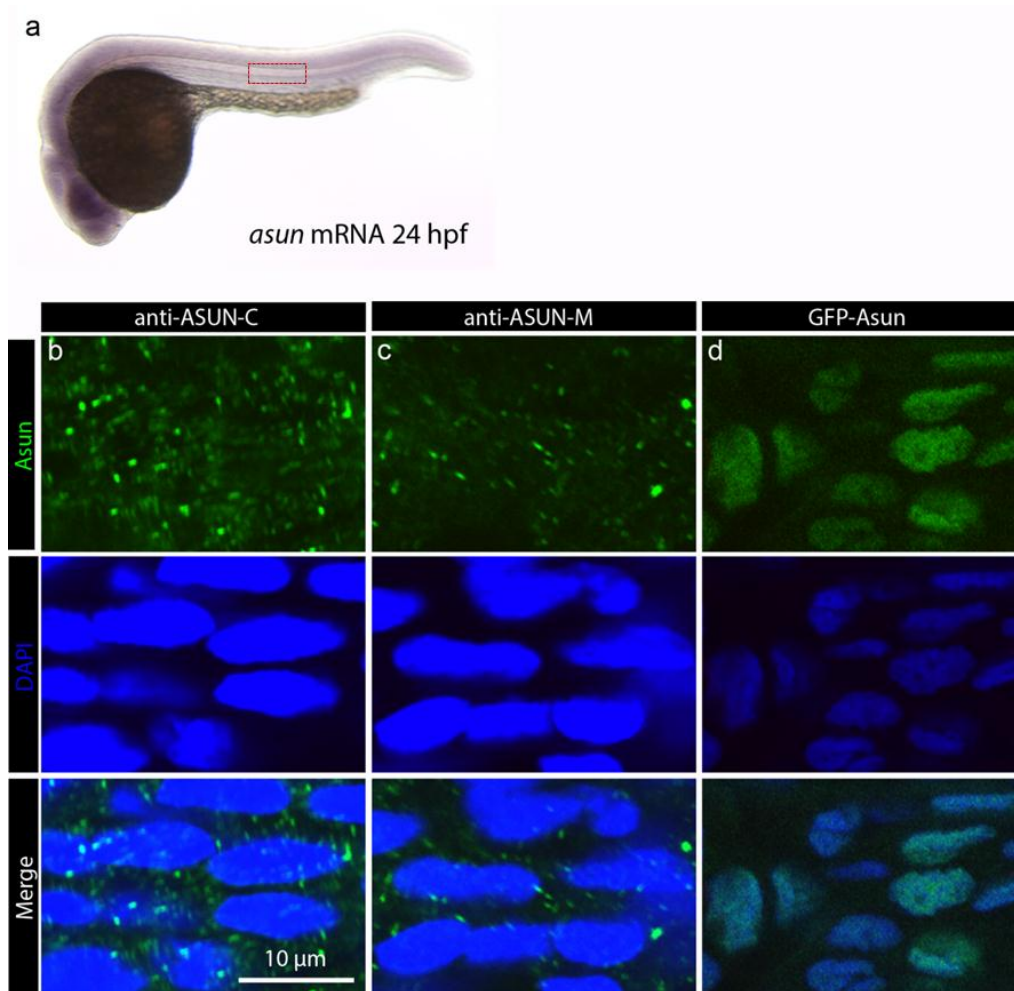
Figure 26: Expression pattern of asun/Asun in zebrafish embryos. (a) *In situ* hybridization in zebrafish at 24 hpf revealed an ubiquitous expression of *asun* transcripts. The red box represents the position of cells, which were used for Immunofluorescence. (b-d) Immunofluorescence analysis using ASUN antibodies (α-C, α-M) and an overexpression of a GFP-tagged Asun, respectively. The result shows cytoplasmic localization of Asun using α-C, α-M, whereas it is predominantly localized to nucleus using GFP-tagged fusion protein.

3.4.2.2. Loss of Asun function in zebrafish causes ciliary defects

To assess whether the loss of Asun resulted in ciliary and embryonic defects in zebrafish, we performed transient depletion of Asun protein. Splice blocking morpholinos (MO), anti-sense oligonucleotide sequence, were designed against *asun* mRNA to disrupt its normal splicing. Two different splicing-MO (MOa & MOb) were injected separately into the animal pole of zebrafish embryos at the 1-cell stage. We observed that morphant embryos were severely malformed, displaying small head, shortened and curved body axis, hydrocephalus and otolith defects (fused) (Figure 27c,d,g) and cardiac oedema developed at 3 days post fertilization (dpf) (Figure 27f; Figure 28). Almost all morphants did not survive after 5 dpf due to a massive edema. Both MO gave similar phenotypes, but phenotypes were more severe with *asun*-MOa than with *asun*-MOb (Figure 27g). RT-PCR was performed to verify aberrant splicing for each MO (Figure 27h). These phenotypes are collectively considered as typical ciliary defects, suggesting a crucial role of Asun in ciliary function during early developmental stages (Austin-Tse et al., 2013; Ferrante et al., 2009; Lee et al., 2012; Lunt et al., 2009).
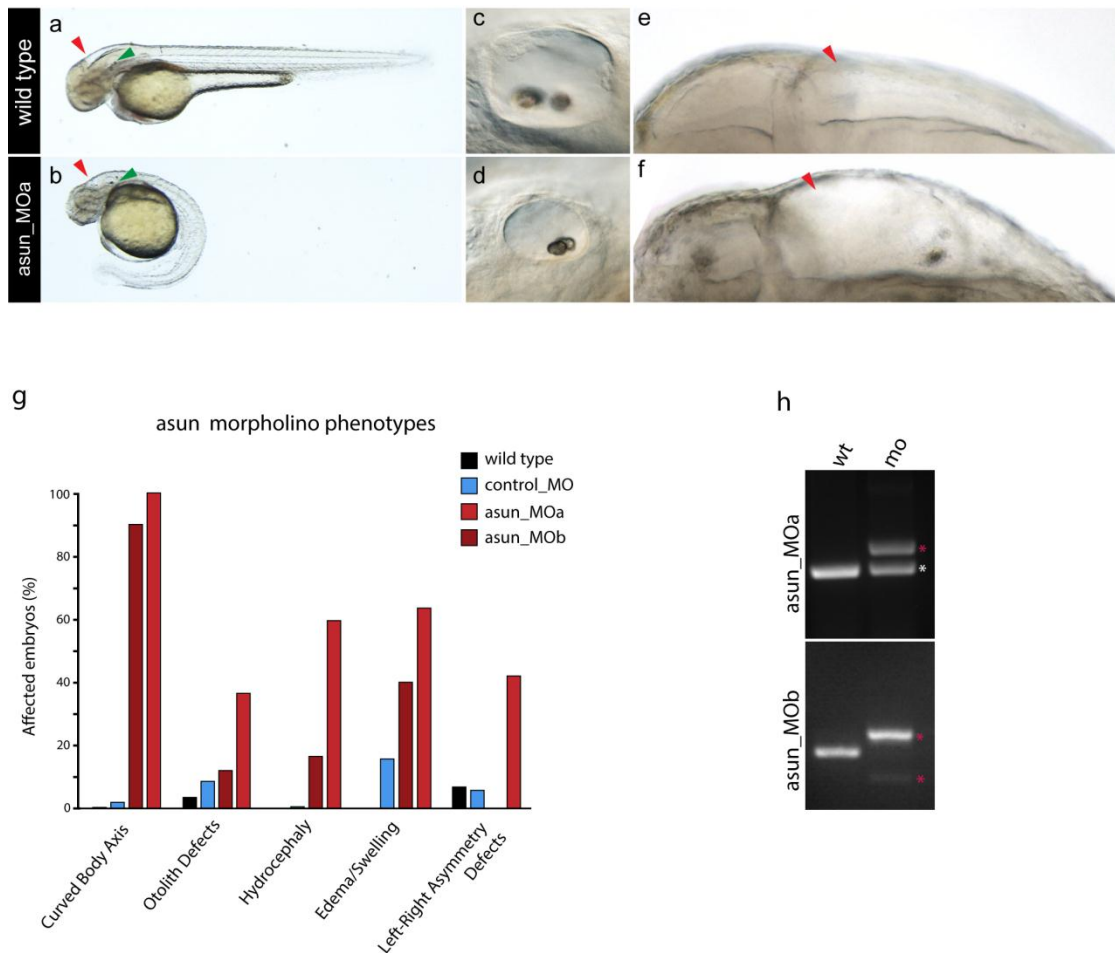
Figure 27: Morphological phenotypes of asun MO-injected zebrafish embryos.
(a,c,e) Lateral views of 48 hpf controls. (b,d,f) Time-matched views of asun morphant embryos. (b) Embryo injected with asun-MO display small head, short and bent body axis. (c) In control embryos, two otoliths are found in the otic vesicle, whereas the two otoliths are often fused in morphant embryos (d). (e,f) Morphant embryos also display marked hydrocephaly compared to the control embryos (red arrow head). (g) The percentage of observed phenotypes using two different splicing-MO injected in 100 embryos. (h) RT-PCR for splicing-MO (MOa & MOb) shows that MOa is more effective than Mob, consistent with overall resulted phenotypes in (g).

3.4.2.3. KD of *asun* in zebrafish causes craniofacial patterning defects

Craniofacial development is conserved throughout different species and particularly between human and zebrafish as shown in several studies, zebrafish is thus, a suitable model to address craniofacial defects (Duldulao et al., 2009; Ferrante et al., 2009; Tobin and Beales, 2009; Tobin et al., 2008). Moreover, many developmental signaling pathways (e.g. Shh and Wnt) that are essential for the development of craniofacial structures were found to be conserved between fish and mammals. We therefore examined the craniofacial morphology in larval zebrafish Asun morphants using alcian blue (AB) staining. We observed severe craniofacial disruption; craniofacial cartilage was totally absent at majority of the injected embryos, and morphants exhibited a small head with variable severity of hypotelorism (Figure 28), consistent with the expression pattern of *asun*. Given that Asun is important for the formation of normal head structures, one can hypothesize that it is involved in cranial neural crest cells (CNCC) migration and suggests a potential defect in the Shh signaling pathway.
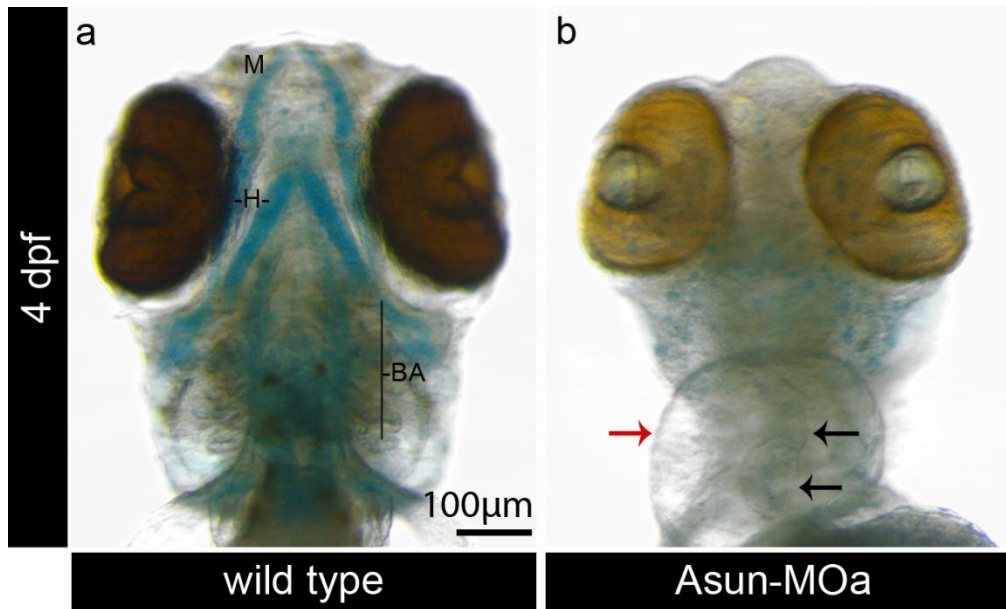
Figure 28: Severe carniofacial defects in Asun-depleted embryos. Ventral view of representative wild-type and Asun-morphant embryos stained with AB at 4 dpf. (a) wild-type embryo with intact craniofacial structures. (b) Asun-morphant with sever craniofacial defects including small head, hypotelorism and complete absence craniofacial cartilage. Branchial (BA), mandibular (M) and hyoid arches (H). Red and black arrows indicate a cardiac oedema, and heart looping randomization, respectively.

3.4.2.4. Asun is required to establish normal left-right asymmetry in zebrafish

The left-right (LR) axis specification in zebrafish is mainly controlled by the Kupffer's vesicle (KV). KV is equivalent to the mammalian node and is conserved among all teleost fish. Between 12 and 16 hpf, KV originates from a group of cells, the dorsal forerunner cells, which migrate at the posterior end of the embryo during gastrulation (Essner et al., 2002). This transient structure filled with cilia that rotate clockwise to generate a directional fluid flow, which is essential to determine the LR asymmetry in fish (Kramer-Zucker et al., 2005; Kreiling et al., 2007; Melby et al., 1996). Randomization of fluid flow as a result of defects in cilia formation and/or function has been shown to cause laterality defects in the internal organs of zebrafish (Ferrante et al., 2009). Therefore, we sought to address whether the *asun*-MO would cause laterality defects. This can be examined by determining the position of heart looping with the ventricle and atrium in the right and left side of the embryo, respectively and the position of the pancreas, liver and gut looping (Levin, 2005; McGrath and Brueckner, 2003).

We performed *in situ* hybridization with an antisense probe for the asymmetrically expressed gene *lefty2,* a nodal pathway gene which is specifically expressed to the left side of zebrafish embryos (Bisgrove et al., 1999; Liang et al., 2000; Long et al., 2003) (Figure 29).

Upon analysis, we observed that *lefty2* expression pattern was disrupted in the lateral plate mesoderm. The majority of uninjected embryos displayed normal

left-side expression, while around 45% of Asun-depleted embryos exhibited bilateral, absent or right-sided expression, indicating situs randomization (Figure 29). These findings indicate that a loss of Asun expression perturbs the establishment of LR asymmetry, which could be a result of malfunctioning KV cilia leading to a defective fluid flow.
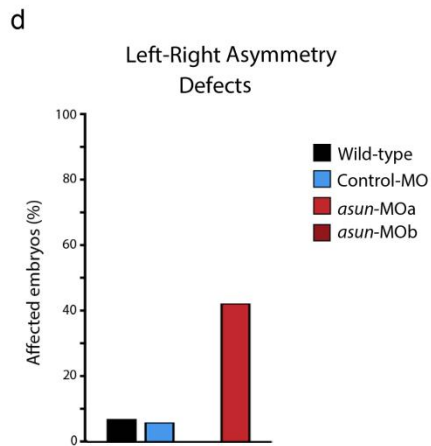
Figure 29: KD of *asun* causes laterality defects in zebrafish embryos. *In situ* hybridization for *lefty2* at 24 hpf embryos. (a) In wild-type embryos, the expression of *lefty2* is observed on the left side of the embryos (b,c) Expression of *lefty2* in Asun morphant, is detected either bilaterally or absent (b) or at the right side only (c). (d) Percentage of embryos with laterality defect, around 45% of Asun morphants show randomization of *lefty* expression. Arrow in (a) indicates expression in the left lateral plate mesoderm, the normal position.

3.4.2.5. Asun is essential for normal formation of otoliths in the developing ear

In addition to laterality defects, otoliths malformation was remarkably observed in zebrafish morphant embryos (Figure 28c,d,g). Functionally, zebrafish inner ear is analogous to the mammalian counterpart; they are important for hearing, gravity sensation and balance (Hughes et al., 2006; Malicki et al., 1996; Supatto and Vermot, 2011). Zebrafish otoliths usually develop at stages 18-24 hpf when the otic placode invaginates to form the otocyst; a fluid filled cavity (Hughes et al., 2006; Stooke-Vaughan et al., 2012). Within each otic vesicle (OV), specialized mechanosensory hair cells are then formed. These hair cells harbor a single specialized long non-motile cilium, known as the kinocilium and cluster of actin-based protrusions, referred to as stereocilia that are densely packed and arranged to form a bundle. These hair cells kinocilia also known as mature tether cells, attach to otoliths at the poles of the OV. These cilia are non-motile, surrounded by clusters of motile cilia which undergo beating that contribute to the formation and correct nucleation of otoliths (Riley et al., 1997; Stooke-Vaughan et al., 2012; Wu et al., 2011; Yu et al., 2011). The rest of the OV epithelia are lined with non-motile cilia (Stooke-Vaughan et al., 2012). Otoliths are equivalent to otoconia in mammals; both are mineral-rich structures composed mainly of calcium carbonate ($CaCO_3$) and proteins. In the zebrafish at 18-22 hpf, they appear as irregular clumps with continuous deposition of mineralized precursors and by 24 hpf, two small round otoliths are formed, attached to tether cells. Defects in ciliary beating has been reported to cause abnormalities in the shape, number and formation of otoliths (Ferrante et al., 2009; Lee et

al., 2012; Neugebauer et al., 2009; Schibler and Malicki, 2007; Stooke-Vaughan et al., 2012; Yu et al., 2011).

Asun morphants displayed otoliths defects as early as 20-22 hpf. For most MO-injected embryos, otoliths were formed; however they were miss-localized and fused to each other, as compared to the uninjected embryos (Figure 28c,d,g). Defects in otoliths formation and laterality as well as pericardial oedema indicated a ciliary disruption in zebrafish morphant embryos.

3.4.2.6. Conclusions

Expression analysis and Loss of function experiments of Asun in zebrafish revealed typical ciliary phenotypes. *In situ* hybridization analysis of *lefty2* expression confirms the laterality defects. We suggest that abnormal left-right asymmetry establishment and other ciliary related phenotypes including cardiac oedema, fused otoliths and hydrocephalus could be due to disruption of ciliary beating which in turn caused impairment of fluid flow in KV, inner ear, spinal cord and pronephric duct. Furthermore, examining the cartilage of morphant embryos showed marked defects in craniofacial structures.

Because Asun is highly conserved among vertebrates, it is expected that this gene would play a similar function in embryogenesis. Therefore, we investigated the role of Asun in *Xenopus* as another model for studying ciliogenesis and ciliary function that would correlate with human disease phenotypes.

3.4.3. Loss of ASUN function modeling in *Xenopus*

3.4.3.1. Expression patterns of *asun* during *Xenopus* embryonic development

To provide a complementary evidence for ASUN function in embryonic development, and ciliary function, we used *Xenopus* as another appropriate *in vivo* model to address ciliopathies (Fakhro et al., 2011; Hagenlocher et al., 2013; Mitchell et al., 2009; Park et al., 2006; Schweickert et al., 2007; Vincensini et al., 2011a, b).

We first characterized the spatial and temporal expression pattern of *asun* in developing embryos, using whole embryo *in situ* hybridization (WISH) with DIG-labeled antisense RNA probes.

By examining the expression pattern of *asun* in *Xenopus* our aim was to get an overview about its functions during embryonic development. The expression of *asun* was found to be ubiquitous during early cleavage, gastrula and even in the late stages, suggesting both a maternal and zygotic expression of this gene in *Xenopus* (Figure 30a-f). At early cleavage stages, *asun* transcripts were restricted to the animal half, but they were absent in the vegetal hemisphere (Figure 30a). At these stages, only the maternal transcripts are present since the zygotic expression begins at the mid blastula transition (MBT) stage 9 (Kerns et al., 2012; Newport and Kirschner, 1982; Tadros and Lipshitz, 2009). At gastrula (stage 12), the expression of *asun* was enriched in ectoderm cells with no expression in the endodermal cells (Figure 30b). At early neurula (stage 17), *asun* expression was enriched in the neural tube and the neural folds (Figure 30c). From tadpole stages onwards, *asun* transcripts were

abundantly observed in specific tissues including the brain, branchial arches, pronephros, eye vesicles, otic vesicles and a diffuse staining of the whole head was also observed (Figure 30d,e).

Moreover, staining was also found to cover the whole skin of the embryos in a punctate pattern at stage 22 onward (Figure 30d,e). Punctate staining was also extended to the head tissues, including the brain regions, eye, and ear. This punctate pattern is demonstrative of ciliated cells located in the epidermis of the embryo, which are better observed with whole mount immunostaining, performed with our custom polyclonal ASUN (α-M) antibody (Figure 30f).

To conclude, *asun* is a maternally expressed gene with ubiquitous expression at gastrula stage. At later stages, *asun* displays a tissue specific expression raising the possibility that *asun* could have a role in tissue morphogenesis. The expression pattern of *asun* in frog embryos significantly overlaps with the one observed in zebrafish embryos, suggesting a conserved function of Asun protein during evolution. The expression of *asun* overall the epidermis of skin embryos is overlapping with the expression of ciliated cells genes (Park et al., 2006). These results provide further support to our hypothesis that *ASUN* could be involved in ciliogenesis. The similar expression pattern of *asun* in frog and zebrafish animal models was consistent with the ubiquitous expression of *ASUN* in human adult tissues (Bourdon et al., 2002), suggesting that ASUN is evolutionary conserved, and thus suggesting a role for Asun during vertebrate development. Therefore, to gain further insights into the role played by *asun* in these specific organs and tissues, we performed loss-of-function analysis in *Xenopus*.
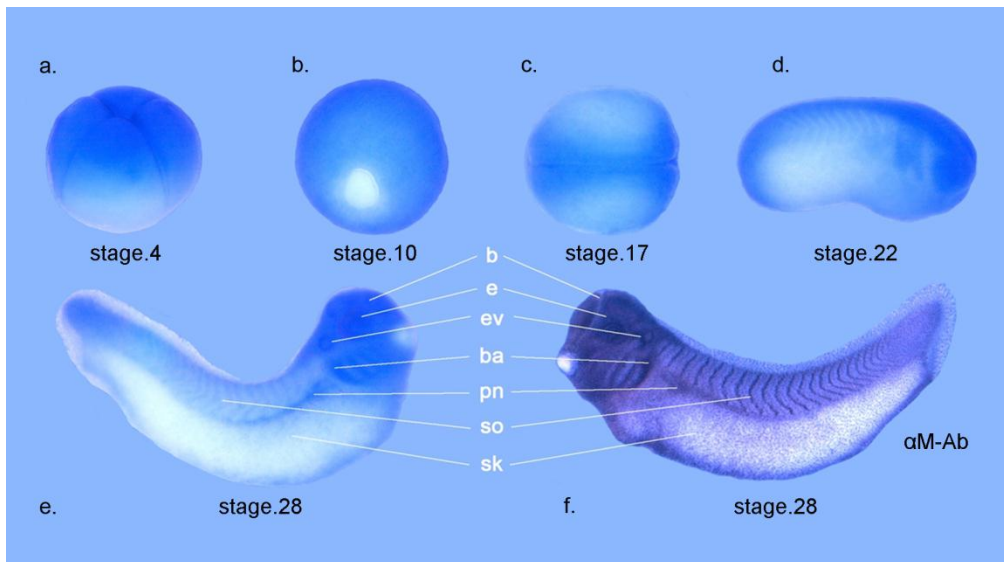
Figure 30: Detailed expression pattern of *asun*/Asun in *Xenopus* embryos analyzed by WISH and whole mount immunostaining. *asun* has both maternal and zygotic. (a) Stage 4, *asun* transcripts are localized within the animal half. (b) Stage 12, its expression covers the whole embryo except the blastopore. (c) Stage 17, *asun* is observed in neural tube and neural folds. Lateral view, anterior is right (d) Stage 22 *asun* starts to be enriched in brain(b), branchial arches (ba), pronephros (pn), eye vesicles (ev), ear (e), skin cells (sk) and somites (so). Lateral view, anterior is right (e) Stage 32 *asun* expression is also detected in ear (e), skin cells (sk) and pronephros (pn). Lateral view, anterior is left. (f) Correlation of transcript localization of Asun protein by whole mount embryo antibody staining using a custom polyclonal ASUN (α-M) antibody at tadpole stage.

3.4.3.2. Morpholino design, microinjection and validation

In order to gain more insight into the precise function of ASUN during *Xenopus* embryonic development, anti-sense morpholino (MO) oligonucleotides against *asun* mRNA were designed either to block the translation or disrupt the normal splicing of *asun* mRNA.

The ATG-targeted antisense MO was previously published (Lee et al., 2005) (Figure 31a). For a splicing MO, the DNA sequence of the exon-intron boundaries that mimic the position of patients' mutation was obtained by PCR amplification. *Xenopus* embryos were microinjected with 4 nl of pure *asun*-MO (123 ng) into each blastomere of 2 to 4-cell stages (Figure 31b).

The efficiency of the ATG-MO was verified by western blot analysis of lysate from wild-type and morphant embryos using human ASUN antibodies and confirmed the complete reduction of Asun protein in Asun morphant embryos (Figure 31c). For *asun* splicing-MO, we confirmed the splicing defects by RT-PCR analysis of RNA extracted from wild-type and MO-injected embryos using pair of primers flanking the MO binding site. PCR products were run on 1% agarose to confirm the splicing alteration (Figure 31d). Compared to control transcript, *asun*-MO injection significantly disrupted the normal splicing of *asun* mRNA. These results suggest that both ATG-MO and splicing-MO successfully block the translation and disrupt the normal splicing of *asun* mRNA, respectively.
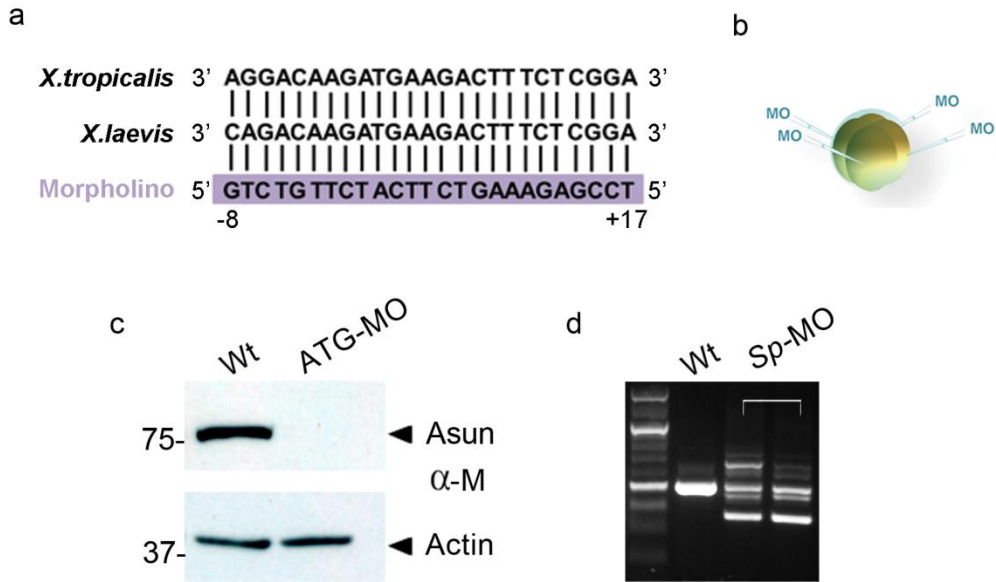
Figure 31: Morpholinos design, microinjection and validation. (a,b) The sequences of asun ATG-MO and the site of injection in 2- and 4-cell stage *Xenopus* embryo. (c) Immunoblotting for ATG-MO morphants and uninjected embryos lysate using ASUN (α-M) antibody shows effective depletion of Asun protein. Actin used as a loading control. (d) RT-PCR for a splice-blocking (Sp) MO shows effective splicing.

3.4.3.3. Knock-down (KD) of *asun* in *Xenopus* partially recapitulates human disease

In the past 8 years, the functions of ASUN in vertebrates have already been addressed in *Xenopus leaves*. ASUN has a crucial function in cell cycle control and development (Lee et al., 2005). For instance, the *asun* gene is required for normal convergent extension (CE), a process involved in tissue movements during gastrulation and neurulation. Down-regulation of *asun* using MO injection resulted in developmental delay, shortened body axis, polyploidy and early developmental arrest in *Xenopus* morphants. These defects are consistent with disruption of gastrulation and cell cycle events. In this study, we confirmed gastrulation defects as a result of *asun* depletion in *Xenopus* that were discovered previously (Lee et al., 2005). More importantly, we describe for the first time that Asun was also involved in ciliogenesis and craniofacial, heart and muscle development.

To further examine the loss of *Xenopus* Asun function phenotypes during *Xenopus* development, embryos were closely examined at different stages following MO injection. We observed that MO-injected embryos were severely affected and exhibited small head, big belly and convergent extension defects such as irregular somites, shortened and curved body axis and bent tail compared to wild-type embryos(Figure 32a',b',b'',c'). Moreover, cardiac oedema and massive developmental delay were also noted in morphant embryos (Figure 32). These phenotypes were more severe with the ATG-MO. These results suggest that a translation-blocking MO causes phenotypes more consistent with loss-of-function interference, whereas the splice-blocking MO

generates hypomorphic phenotypes. The weaker defects observed in splicing-

MO are likely to be due to a deposition of maternal RNA in the oocyte.
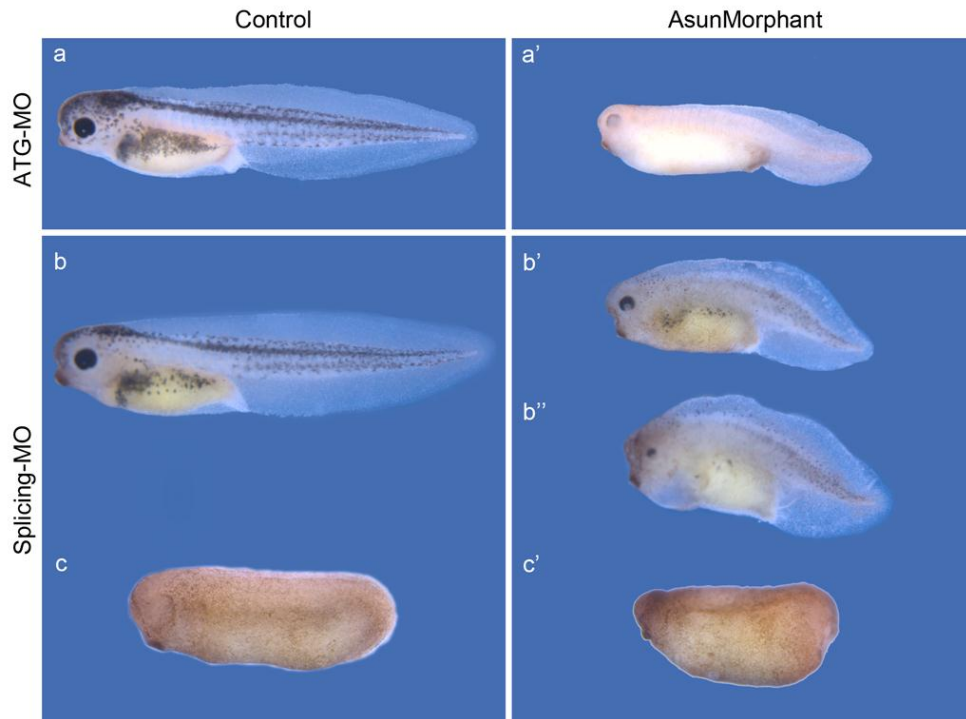
Figure 32: Common phenotypes in *asun*-depleted *Xenopus* embryos. (a-c) Control embryos at tadpole stage (a, b) and stage 24 (c). (a'-c') *Xenopus* embryos injected separately with *asun* ATG-MO and splicing-MO. Morphant embryos display severe developmental defects including a small head, big belly, short and down curved-body axes, cardiac oedema (b") and massive developmental delay compared to control embryos.

3.4.3.4. *asun* depletion affects heart morphogenesis

Congenital heart defects (CHD) have been reported in many patients with Mohr syndrome, including aortic coarctation, aortic stenosis, atrial septal defect, atrioventricular canal defect, hypoplastic left ventricle, truncus arteriosus, mitral atresia, endocardial cushion defects and tetralogy of Fallot (Digilio et al., 1999; Digilio et al., 1996; Ghossaini et al., 2002; Orstavik et al., 1992; Shashi et al., 1995). In the Jordanian family, one of the affected girls (IV.7) had supravalvular pulmonary stenosis. To our knowledge, this defect has never been observed in previously reported cases of Mohr syndrome. KD of *asun* in *Xenopus* showed cardiac edema; therefore it is worth it to examine the role of Asun in heart development. To examine this, we performed *in situ* hybridization using the *nkx2.5* (transcription factor); a heart specific marker (Tonissen et al., 1994). The results showed an increase in *nkx2.5* expression in morphants heart tissues compared to control embryos, suggesting that *asun* is involved in *Xenopus* heart development (Figure 33b-c').

3.4.3.5. Asun is required for CNCC migration in *Xenopus* embryos

In addition to heart defects, craniofacial dysmorphisms were also observed in the two patients. The characteristic features of Mohr syndrome and other OFD, suggest that *ASUN* gene could have a specific role in the development of CNCC. CNCC and cranial mesoderm are known to responsible for the formation of the majority of craniofacial bones in vertebrates (Trainor, 2005). Tobin and colleagues have demonstrated that migrating CNCC of zebrafish bear primary cilia. They highlighted that, craniofacial features in patients with

Bardet-Biedl syndrome (BBS) could be due to defects in CNCC migration (Tobin et al., 2008). Similarly, Brugmann and his group showed that mouse CNCC also express primary cilia, which were missing in knock-out intraflagellar transport protein Kif3 mouse cells (Brugmann et al., 2010a). These findings suggest that the craniofacial dysmorphisms presented in the two patients could possibly be attributed to a deficit in the migration of CNCC secondary to primary cilia perturbation.

In support of this, at *Xenopus* tailbud stage, we observed that Asun morphants displayed smaller heads compared to control embryos (Figure 32). During neurula stages, *asun* was found to be expressed in brachial arches, a neural tube and neural folds; at which CNCC undergo directional migration to form the craniofacial structures (Nichols, 1987; O'Rahilly and Muller, 2007).

Therefore, it is advisable to examine whether *asun* depletion in frog embryos causes changes in head development. *In situ* hybridization for embryos at early tailbud stages was carried out using a tissue-specific antisense RNA probe for cranial neural crest marker; *twist* (Betters et al., 2010). We observed that abrogation of *asun* expression reduces the expression of *twist* (Figure 33a,a'). This result demonstrates that *asun* depletion affects CNCC migration.

To conclude, the pleiotropic expression of *asun* in the head, heart and skin as well as the phenotypic appearance following *asun* depletion in *Xenopus* phenocopy the patient phenotypes.
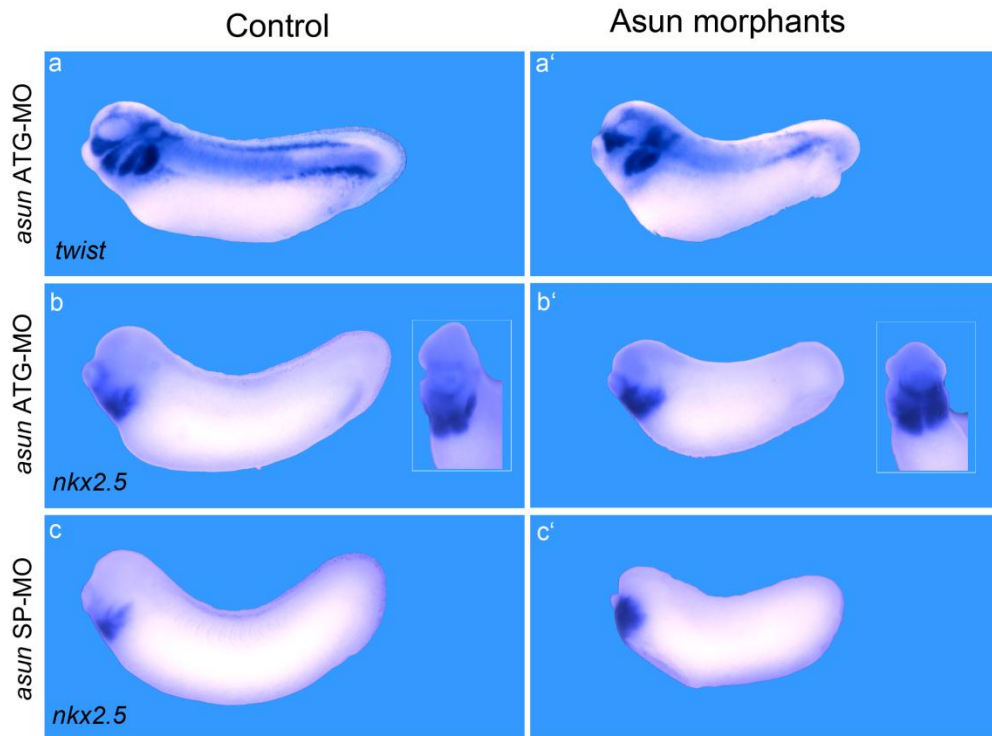
Figure 33: Asun is required for CNCC and heart development. Whole embryo *in situ* hybridization using CNCC marker (*twist*) and heart marker (*nkx2.5)* at stage 28. (a) Expression of *twist* reveals the CNCC population in the 4 branchial arches. (a') ATG-MO injected embryos display defective CNCC migration, especially in the second branchial arch (b-c') Impairment of *nkx2.5* expression is observed in both ATG-MO (b') and slicing-MO (c') injected embryos. The level of *nkx2.5* expression is increased in both morphants relative to control embryos.

3.4.3.6. Asun is also required for somites development in *Xenopus* embryos

During *Xenopus* gastrulation, cells undergo morphogenic movements and cell fate determination that will lead to the formation of the three germ layers: ectoderm, mesoderm, and endoderm. As a result of these movements, the embryonic axes are determined. For instance, the dorsal mesoderm develops into the axial mesoderm that form the notochord and paraxial mesoderm that undergo segmentation at both sides of notochord to form the somites (Keller et al., 2000).

In addition to heart defects and craniofacial dysmorphisms, Asun-depleted embryos displayed defects that were clearly observed in the developing somites from tadpole stages onwards. Whole mount antibody staining using anti-ASUN-M antibody showed disorganization and mislocalization in the majority of somites in ATG-MO injected embryos (Figure 34a). Whole mount antibody staining was further carried out for the somite specific marker (MyoD) (Rupp et al., 2002) to determine the role of Asun in somites development. The results showed that the expression of MyoD was reduced in the disrupted somite segments (Figure 34b). These results indicate that Asun is required for somites differentiation in *Xenopus.*
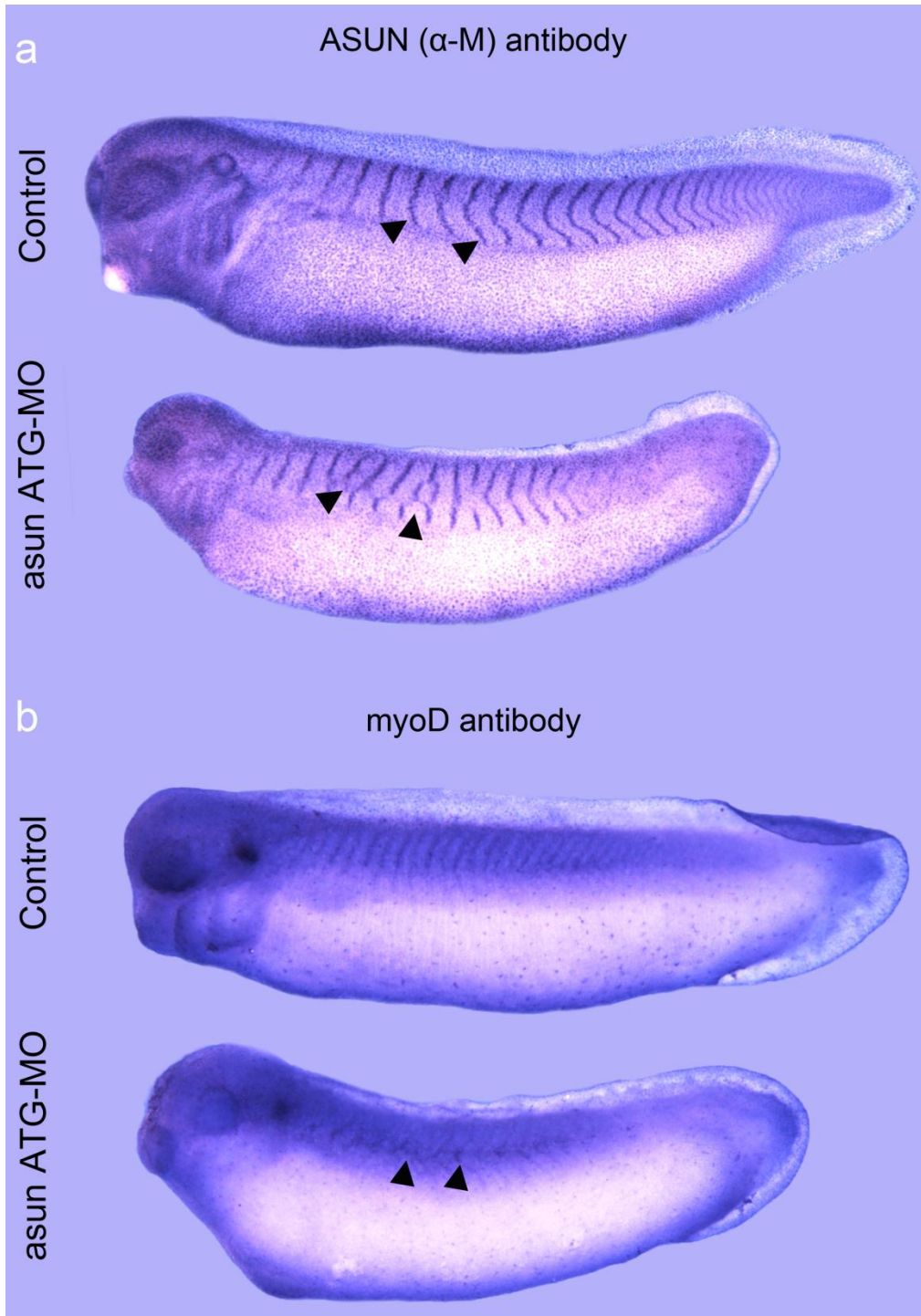
Figure 34: Asun is required for somites development in *Xenopus*. Whole mount antibody staining of *Xenopus* tailbud embryos (stage 32) using ASUN (α-M) antibody and a somite specific antibody, MyoD. (a) Expression of ASUN is observed in developing somites (black arrowhead) (b) MyoD immunostaining reveals that depletion of Asun affects both induction and segmentation of the somites in morphant embryos compared to controls.

3.4.3.7. Ciliary beating frequency is markedly reduced following *asun* depletion

Based on the biological function of ASUN in ciliogenesis in mammalian cells and the ubiquitous expression of *asun* mRNA throughout the *Xenopus* skin, we next examined the possibility that *asun* also affect multi-cilia formation and beating in *Xenopus* embryos.

Following MO injection, live imaging was performed to investigate whether Asun disrupts directional flow over the *Xenopus* epidermis, and to observe general embryonic development. In order to observe the flow across the epidermis of *Xenopus* embryos, both control and morphant embryos at desired stages, at which all multi-ciliated cells (MCC) are totally differentiated were collected in a Petri dish and a dye was added drop wise on the surface of embryos. A time-lapse movie was taken to assess for the performance of beating cilia in the skin of control and morphant embryos. In control embryos, the dye moved away very rapidly in one direction, from dorso-anterior region to ventral-posterior part. Interestingly, in ATG-MO injected embryos, the results showed that all morphants were completely unable to move liquid around their bodies. This suggests that ciliated cells were either unable to form cilia or that cilia were not functional in Asun morphants. However, when we used the splicing-MO, we observed disorganized movements of dye in different directions. Furthermore, the dye movement was significantly slower than controls suggesting that the fluid flow was disorganized. This also suggests that MCC either had few cilia or that cilia did not properly function in Asun-depleted embryos. To further observe the ciliary beating more clearly,

we recorded the cilia movement using a high-speed video microscopy. Images were taken at 200-250 frames per second. We found that MCC in morphant embryos seem to have fewer cilia with reduced beating frequency compared to control embryos (Figure 35). Moreover, the ciliary beating in Asun-depleted embryos was erratic and uncoordinated compared to control embryos.

Taken together, these data indicate that Asun is necessary for cilia formation and coordination of ciliary beat of cilia within ciliated cells, and is thereby responsible for the generation of the directional flow of embryos by MCC.
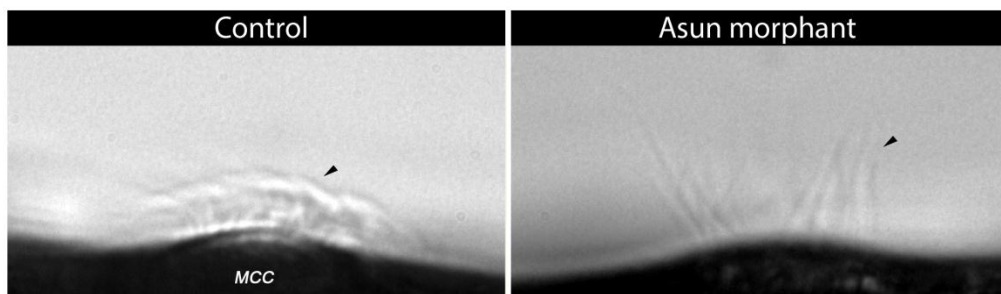
Figure 35: Ciliary formation and beating are disrupted following asun depletion. Time-laps pictures of multi-cilia beating using a high-speed video microscopy. MCC display less and disorganized cilia in morphant embryos. Moreover, cilia beating frequency is markedly reduced in Asun morphants compared to control embryos. Arrowhead indicates motile multi-cilia.

3.4.3.8. Ciliogenesis is markedly perturbed in Asun morphants

The reduced ciliary beating frequency in Asun morphants suggests that the morphology of cilia themselves could also be affected. Therefore, we performed *in situ* hybridization using specific MCC marker, *ccdc19* (Hayes et al., 2007) which showed reduction in the expression of *ccdc19* in Asun-depleted embryos compared to control embryos (Figure 36a,a'). To further investigate the effect of Asun on MCC, we also performed whole mount antibody staining for control and morphant embryos using acetylated α-tubulin. We found that morphant embryos displayed punctate pattern similar to control embryos but more shiny in control embryos (Figure 36b-c'), consistent with the *ccdc19* expression pattern. Furthermore, the distances between puncta were higher and irregular in Asun-depleted embryos. This suggests that the epidermis of Asun morphants could have either less differentiated ciliated cells and/or these cells express less cilia, indicating the important role of Asun on MCC.
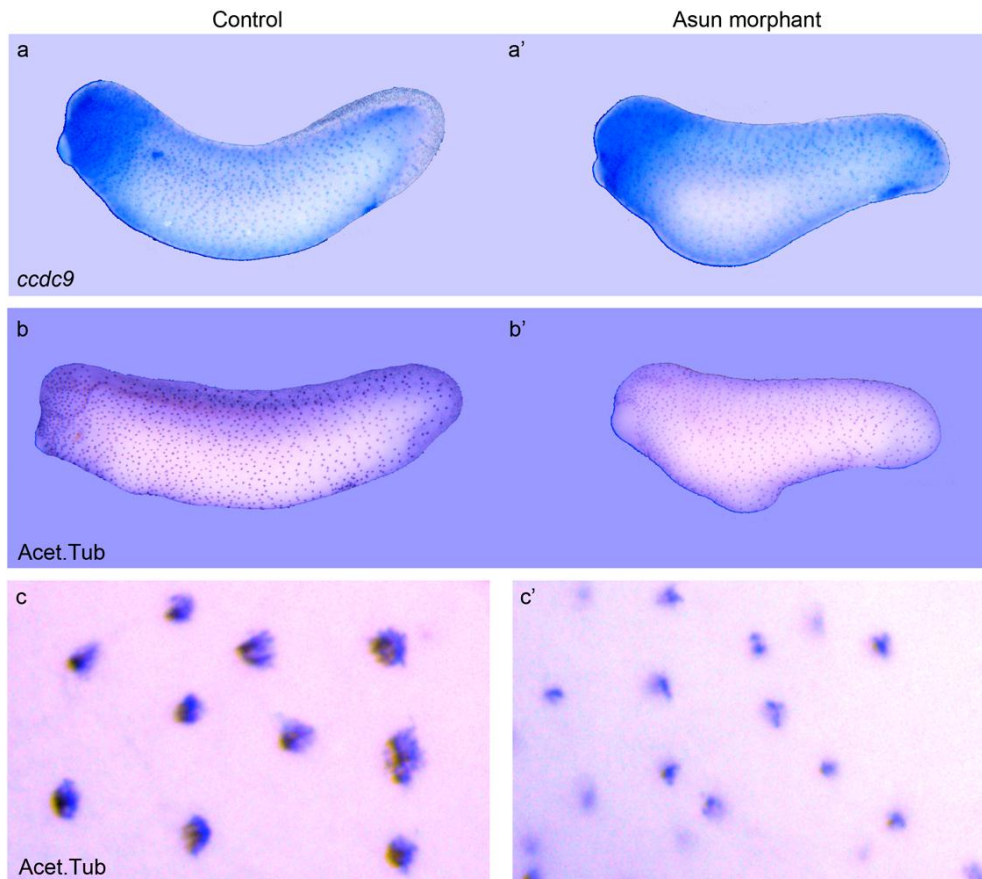
Figure 36: MCC differentiation and multi-cilia formation are affected in Asun-*Xenopus* morphants. (a,a') *In situ* hybridization in control and Asun morphant embryos using a specific probe for the MCC marker (*ccdc9*) shows reduction in ccdc9 expression in morphants' MCC compared to control embryos. (b,b') whole mount antibody staining with acetylated α-tubulin antibody shows punctate pattern similar to *ccdc9*. The punctate look more condense and stronger in control embryos. (c,c') High magnification view of MCC shows marked reduction in multi-cilia.

To gain further insights into the impact of *asun* KD on *Xenopus* MCC, we performed a scanning electron microscopy (SEM) for both Asun morphants and wild-type embryos. In this experiment, we used both the splicing blocking MO and the ATG-MO. For ATG-MO, the results showed that the major defect was in the MCC. Most MCC in ATG-MO injected embryos exhibited variable reduction in number of cilia, while few individual cells displayed no cilia. However, the length of cilia seemed to be normal in many ciliated cells, inconsistency was also observed within and between MCC (Figure 37). Moreover, cilia exhibited abnormalities in morphology, protrusion and direction (Figure 37). Interestingly, at the low magnification view, we observed fewer differentiated cells in Asun-depleted embryos compared to control embryos (Figure 37a-d). For splicing-MO, MCC showed mild ciliary defects compared to ATG-MO, cilia were either twisted and clumped to each other or spread in irregular directions in the majority of MCC (Supplementary Figure. 3). Interestingly, we detected no abnormal cilia in many cells, while many expressed no cilia and variability in length of cilia on individual cells was also observed.

Taken together, these data demonstrate that Asun is required for MCC differentiation as well as cilia formation and function which could explain the reasons behind the improper cilia motility in Asun-depleted embryos as documented by time-laps movies. On the other hand, the similarity between human airway lining cells and *Xenopus* skin cells suggest that the phenotypic appearance in patients' respiratory system could be due to defects in MCC that cover the airway system.
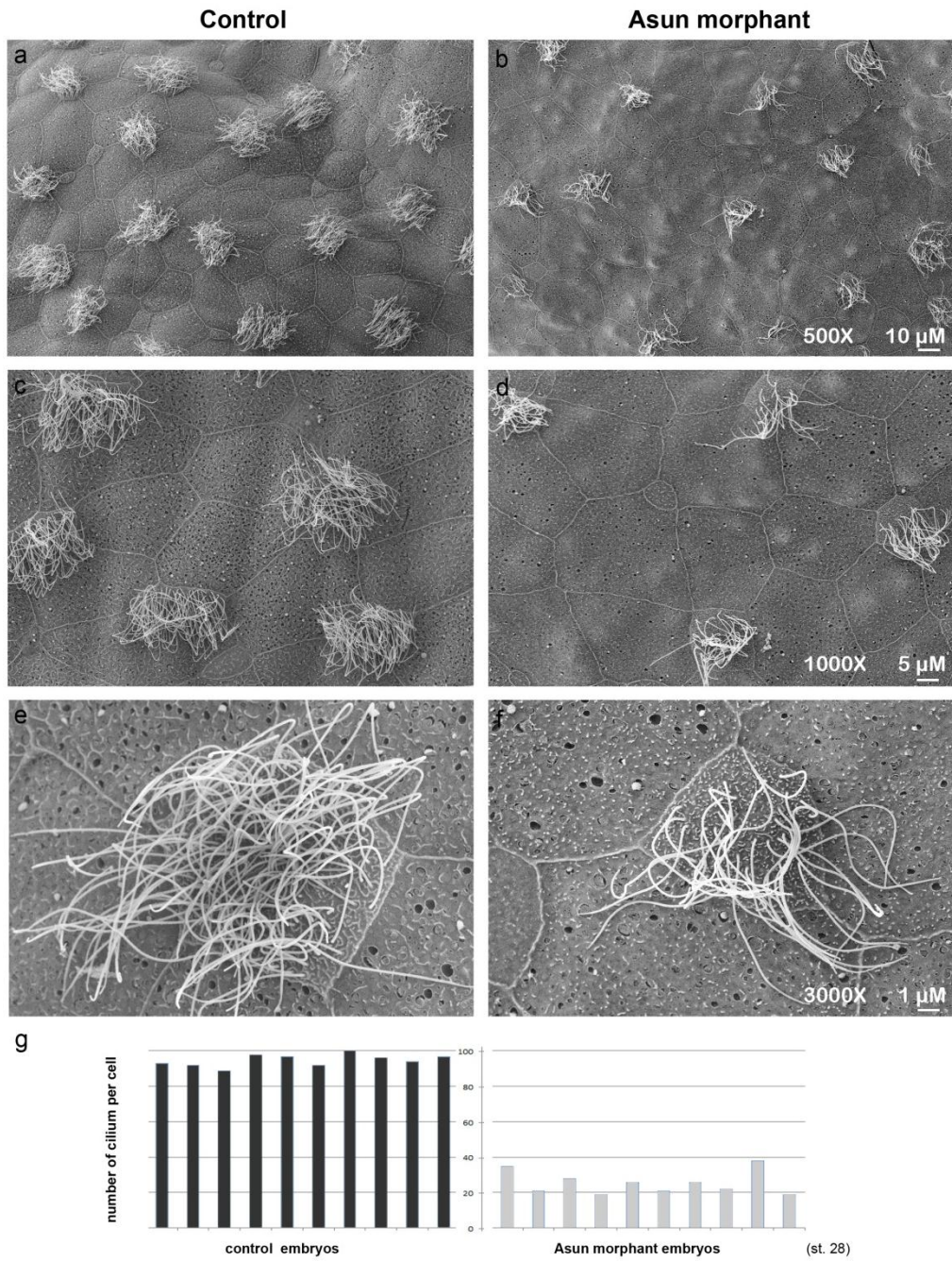
Figure 37: Multi-cilia are markedly perturbed in MCC of *Xenopus* morphants. Ultrastructure of the *Xenopus* MCC at different magnification using SEM at embryonic stage 28. (a,c,e) MCC of control embryo possess multiple, long cilia. (b,d,f) Asun morphant MCC display few, short and disorganized cilia. (c-f) At high magnification view, it seem that the length of cilia is not severely affected in Asun morphant, however MCC appear less differentiated in morphant embryo compared to control embryo. (g) The average number of cilia in individual MCC is markedly reduced in Asun morphants compared to control embryos.

166

3.4.3.9. Loss of Asun affects the development of mucus secreted cells (MSC) and ion-secreting cells (ISC)

In addition to MCC defects in frog morphants, SEM analysis also revealed marked defects in other epidermal cells. In control embryos, we clearly observed that *Xenopus* skin covered with extensive small round exocytic vesicles or empty vacuoles spread at the apical surface of MSC. The ultrastructure of MSC seemed to be affected and the number of secretory vesicles was remarkably reduced in the majority of morphants MSC (Figure 38b,d,f). On the other hand, we also observed less ISC in morphants compared to control embryos (Figure 38b).

To conclude, these findings demonstrate that beside the indispensable role of Asun for MCC development, it is also required for both MSC and ISC function and differentiation, respectively. Indeed, we were unable to interpret the precise effect of Asun in ISC by SEM because the small size of these cells compared to others. To gain a greater insight into the impact of *asun* depletion on epidermal cells, it would be interesting to carry out *in situ* hybridization using specific markers; *xeel* (Hayes et al., 2007) for MSC and *xema* (Mir et al., 2007) for ISC together with a transmission electron microscopy analysis (TEM).
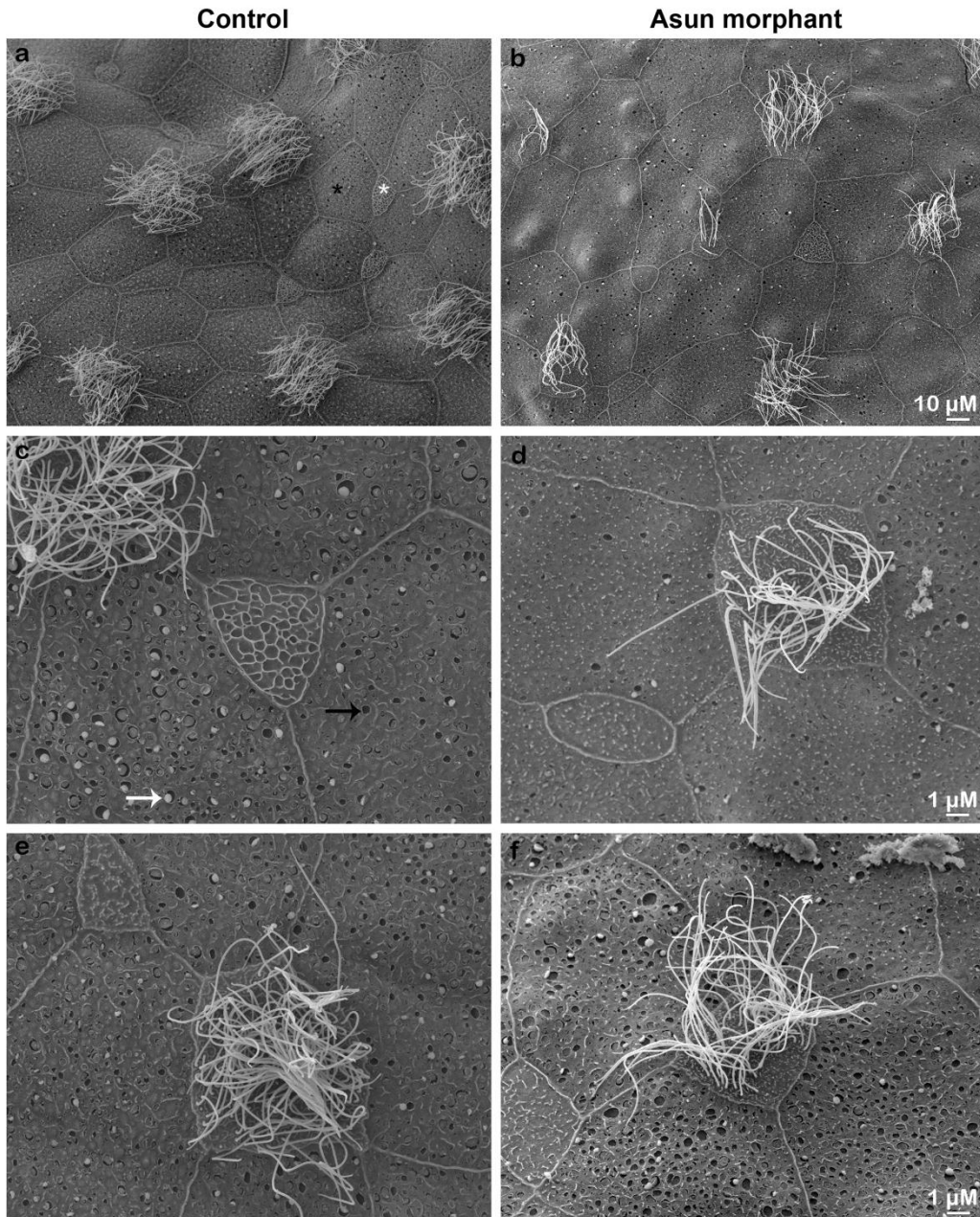
Figure 38: *asun* **depletion results in variable defects in** *Xenopus* **skin MSC and ISC.** Ultrastructure of the *Xenopus* MSC and ISC at different magnification using SEM at embryonic stage 28. (a,c,e) Control embryos possess numerous MSC with secretory vesicles (white arrow) and empty vesicles (black arrows) at their apical surface. (b,d,f) Asun morphants MSC display small and marked reduction in secretory vesicles. Black and white asterisk indicate to MSC and ISC, respectively.

3.4.3.10. Conclusions

Loss-of-function analysis of Asun in *Xenopus* showed typical ciliary phenotypes including irregular somites, shortened and curved body axis, bent tail and cardiac edema. Defects in multi-cilia formation and beating were also apparent; all are consistent with the expression analysis in embryonic tissues. These phenotypes are common in genes that are associated with cilia formation and function. First, *in situ* hybridization analysis showed an obvious overlap between the expression of *asun* and the ciliated cells marker (*ccdc19*). Additionally, whole mount antibody staining for Asun in *Xenopus* embryos also showed similar expression to the ciliary protein (acetylated α-tubulin). Depletion of *asun* confirmed the defect in these cells and the other epidermal cell types. Using *in situ* hybridization together with live imaging and SEM analyses showed apparent defects in cilia formation, morphology and beating, indicating that Asun is indispensable for MCC differentiation and multi-cilia biogenesis. Furthermore, SEM analysis in *Xenopus* revealed possible defects in MSC and ISC as well. These results indicated that Asun is required for the development and differentiation of epidermal cells especially the MCC. Beside ciliary defects in the MCC, Asun-depleted embryos displayed shortened and curved body axis, small head, bent tail and developmental delay. More severe phenotypes were also highlighted by *in situ* hybridization and immunohistochemistry experiments including defects in heart development, developing somites and craniofacial structures. These phenotypes were less severe in embryos injected with a splicing-MO as compared to ATG-MO.

Altogether, analysis of *asun* expression during embryonic development stages together with *asun* KD experiments in *Xenopus* confirmed that *asun* gene played a crucial role in the development of heart, somites craniofacial structures as well as playing a pivotal role in development, differentiation and function of MCC.

To conclude, KD of *asun* in both *Xenopus* and zebrafish animal models recapitulate the patients' phenotypes to a reasonable extent. Additionally, functional analysis of Asun in *Xenopus* and zebrafish helped us to elucidate roles for this protein in the regulation of cilia function, and embryonic development. However, the molecular mechanism by which Asun controls these events is still unknown.

3.5.   A possible modifier affect on patients' phenotypes

Genetic and phenotypic overlaps have been widely observed among ciliopathies arguing strongly for the presence of genetic factors that could influence disease manifestations. In ciliopathies, it is not uncommon to find mutations in a given gene which can function as causal mutations for disease phenotypes or as modifying factors that modulate disease manifestations. These findings have provided further evidence for the contribution of second-site genetic modifiers on the phenotypic variability of ciliopathies including OFD. For instance, the ciliary gene, Retinitis pigmentosa GTPase regulator interacting protein 1-like gene (RPGRIP1L; MIM 610937) mutated in JBTS, NPHP and MKS. However, the pathogenic effect of *RPGRIP1L* in these disorders, it has been shown that a common mutation that function as a second-site modifier allele of the retinal degeneration in patients with other ciliopathies (Delous et al., 2007; Fahim et al., 2012; Khanna et al., 2009). Mutations in *OFD1* gene resulted in variable phenotypes in X-linked JBTS10, X-linked RP and SGBS2 syndromes (Bisschoff et al., 2013; Coene et al., 2009; Field et al., 2012). Similarly, mutations in *CEP290* (MIM 610142) can cause SLSN, NPHP, LCA, JBTS, BBS, and MKS (Baala et al., 2007; Coppieters et al., 2010; Helou et al., 2007) and mutations in *MKS3* are found to cause JBTS, MKS, BBS and NPHP (Cardenas-Rodriguez and Badano, 2009; Leitch et al., 2008). Mutations in Abelson helper integration site 1 (AHI; MIM 608894) have also been found to cause NPHP or JBTS but also function as a modifier of retinal degeneration (Louie et al., 2010; Utsch et al., 2006).

Altogether, these data indicate that the phenotypic spectrum of ciliopathies is governed by mutation type, position, and the total mutational load within different ciliary genes that cause variable effects on gene and protein function. Furthermore, the phenotypic differences of the disease in the expression or penetrance also suggest the presence of disease modifying alleles that could exacerbate or modulate the disease phenotypes.

Among all reported Mohr syndrome cases, we observed intra- and inter-familial phenotypic variability and severity, which were apparent in the two affected patients in this study. For instance, heart defect, polydactyly, duplicated teeth were only observed in one of either probands. Otitis media, bronchitis and urinary tract infection were more sever in one patient than another. Moreover, new manifestations like chronic renal failure and chronic pancreatitis have recently developed in patient IV.6, which could correspond to an age dependent phenotype.

In this context, we asked whether mutations in other genes could be associated with the phenotypic variability observed in patients affected with Mohr syndrome. Therefore, we first looked back at our candidate genes list and checked whether any of these genes could be involved in ciliary biogenesis. One of these genes, known as Polycystic Kidney and Hepatic Disease Like-1 (*PKHD1L1)* as a potential good candidate. It is a very large and complex gene, located on chromosome 8q23.1-q23.2. It spans a genomic segment of ~168 kb, contains 79 exons and encodes a protein known as Fibrocystin-Like1 (Hogan et al., 2003). Human Fibrocystin-L is a large protein (4243 amino acids; 466 kDa) and has homology to Fibrocystin (PKHD1, MIM 606702) over the

extracellular portion of the protein with overall identity of 25% and similarity of 41.5% (Hogan et al., 2003). The protein homolog Fibrocystin is localized to the basal bodies of primary cilia, and the loss of this protein is associated with cilia morphology and function defects (Masyuk et al., 2003; Wang et al., 2007; Zhang et al., 2004). Fibrocystin-L is predicted to be the ancestral Fibrocystin protein and this implies that Fibrocystin-L could have a similar function of Fibrocystin.

In *PKHD1L1* gene we found 1 missense mutation that leads to non-conservative amino acid substitution in exon 42 and 1 splice site mutation located in intron 42 (Table 4). The c.6507+1g>a mutation predicted to disrupt the normal splicing of mRNA which in turn could create a PTC. We therefore sought to address the effect of c.6507+1g>a mutation on the function of PKHD1L1 in patients' cells and animal model using a combination of molecular and biochemical tools.

3.5.1. *In silico* splicing and qRT-PCR analyses

In silico analysis using human splice site finder (HSF) (http://www.umd.be/HSF/), a tool which predicts the effects of splice site mutations on mRNA splicing, showed that this mutation generates various high score cryptic splice sites in both exon 42 and intron 42. These cryptic splice sites could be preferentially used as an alternative to the canonical 5' splice site, thereby resulting in partial exon deletion or partial intron retention. A qRT-PCR analysis showed that *PKHD1L1* gene was not expressed in fibroblast cells of patient and control cells. We repeated qRT-PCR in different patient's cell lines including EBV-LYB and PBMC. Upon analysis, the

expression level of *PKHD1L1* was significantly down-regulated in patients'

EBV-LYB and PBMC compared to control cells (Figure 39). These findings

indicate the NMD mechanism for *PKHD1L1* gene.
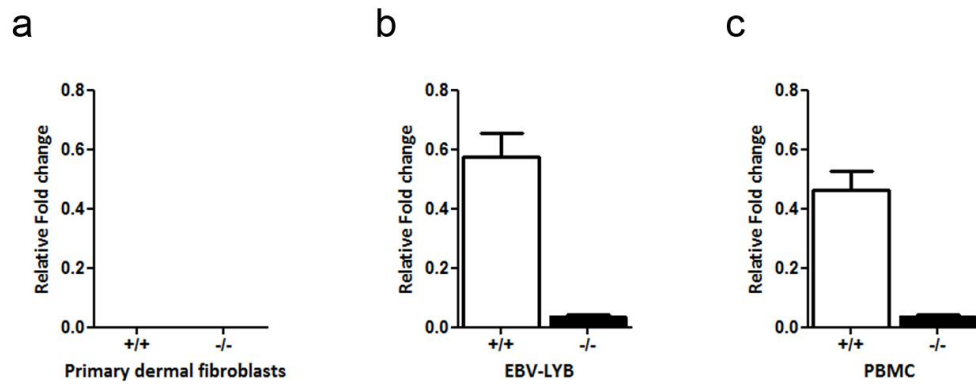
Figure 39: QRT-PCR for *PKHD1L1* in different cell lines. (a) The *PKHD1L1* is not expressed in primary fibroblasts. However, it is expression is down-regulated in patient's EBV-LYB (b) & PBMC (c) cells relative to control cells. Error bars indicate SEM.

3.5.2. *pkhd1l1* is expressed in cilia related tissues in *Xenopus*

To examine the endogenous *pkhd1l1* expression pattern during development, I performed whole mount *in situ* hybridization in *Xenopus* embryos. The results showed that the *pkhd1l1* expression exclusively zygotic and began at the end of neurulation. Its expression was confined to a subset of skin cells and was concentrated in gills, cement gland, proctodaeum and along the ventral fin. The results indicated that the expression of *pkhd1l1* was overlapping with the expression of ciliated cells genes. These results give us complementary evidence that Pkhd1l1 is a ciliary protein (Figure 40).
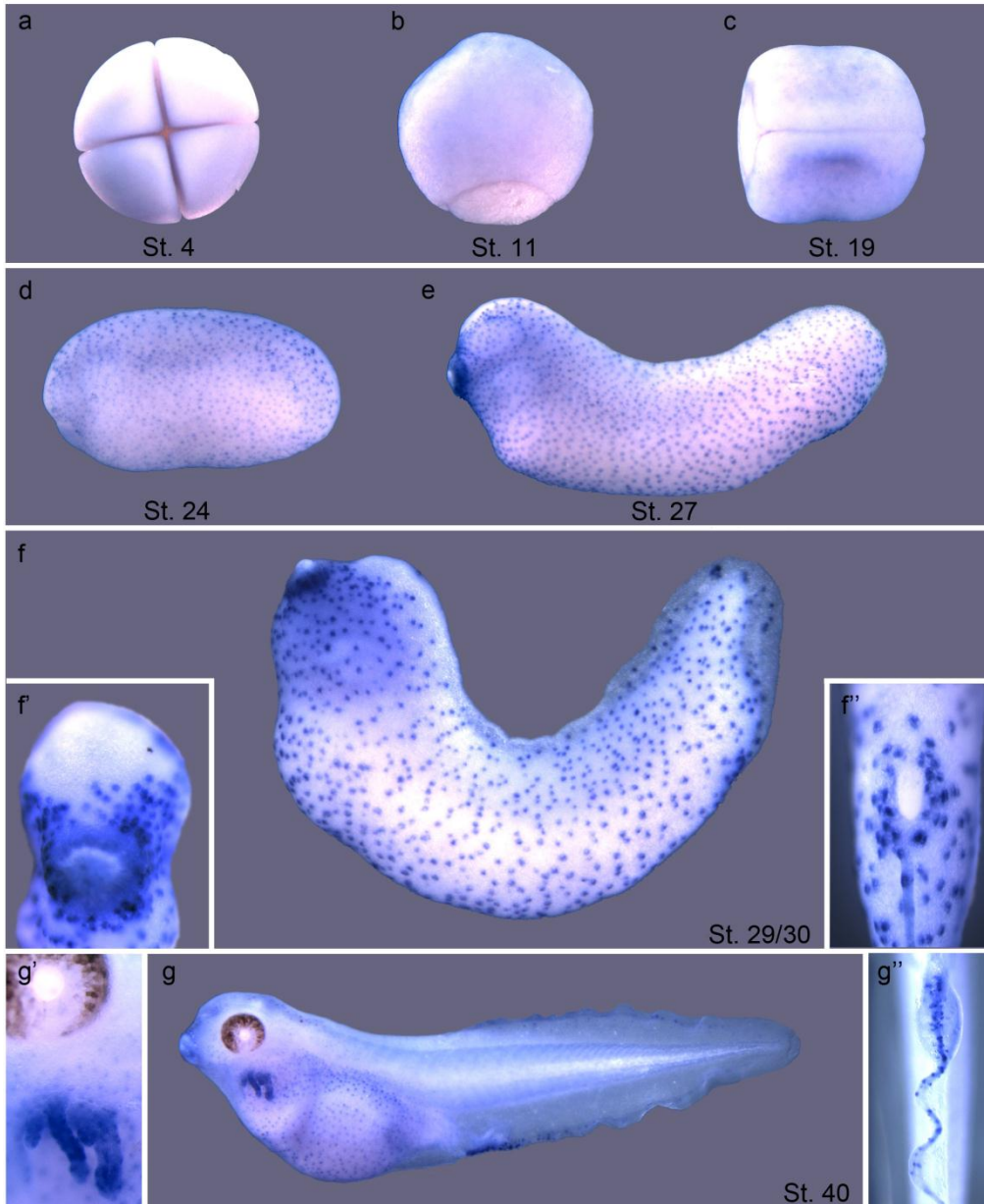
Figure 40: Expression pattern of *pkhd1l1* during *Xenopus* developmental stages. *In situ* hybridization analysis shows the zygotic expression of *pkhd1l1*. This gene is not expressed in early stages: cleavage (a), gastrula (b), and neurula stages (c). The expression is observed during early tailbud stages onward with majority in the epidermis particularly the MCC (d-g). *pkhd1l1* transcripts are also seen in cement gland, proctodaeum, gills and ventral fin (f'-g''), respectively.

3.5.3. Loss-of-function analysis

To investigate the precise role of *pkhd1l1* gene in *Xenopus*, we next knocked-down its translation using MO-mediated down-regulation. A partial sequence of *Xenopus leaves pkhd1l1* was identified using 5' RACE (Rapid Amplification of CDNA Ends) and specific primers were designed from the closely related *Xenopus tropicalis* sequence.

3.5.4. Pkhd1l1 is required for *Xenopus* epidermal cells differentiation and multi-cilia formation

Xenopus embryos were injected at the 2 to 4-cell stage. At a desired stage of embryonic development, live imaging was taken to assess the performance of beating cilia following *pkhd1l1* depletion in *Xenopus*. The result showed that the Pkhd1l1 morphants were completely unable to move liquid around their bodies compared to wild-type embryos. This suggests that ciliated cells were either unable to form cilia or that cilia were not functional in Pkhd1l1-depleted embryos. We further assessed the role of Pkhd1l1 in MCC and other cell types using *in situ* hybridization for epidermal cells markers for MCC, MSC and ISC. The results showed that the expression of all three epidermal cell types was markedly impaired in Pkhd1l1 morphants relative to controls (Figure 41). Moreover, we noted a developmental delay in morphants. These results were further confirmed by SEM (Figure 42) which showed that the major defect was in MCC. The multi-cilia were found to be absent compared to wild-type embryos. Moreover, MSC seem to be affected as well, there are an empty vesicles and vesicles with secretory granules in the wild type embryos, which are missing in the Pkhd1l1 morphants. Furthermore, ISC were

also affected; these cells are microvilli-rich cells, seemed to be compromised

in the Pkhd1l1 morphants compared to the wild type embryos (Figure 42).
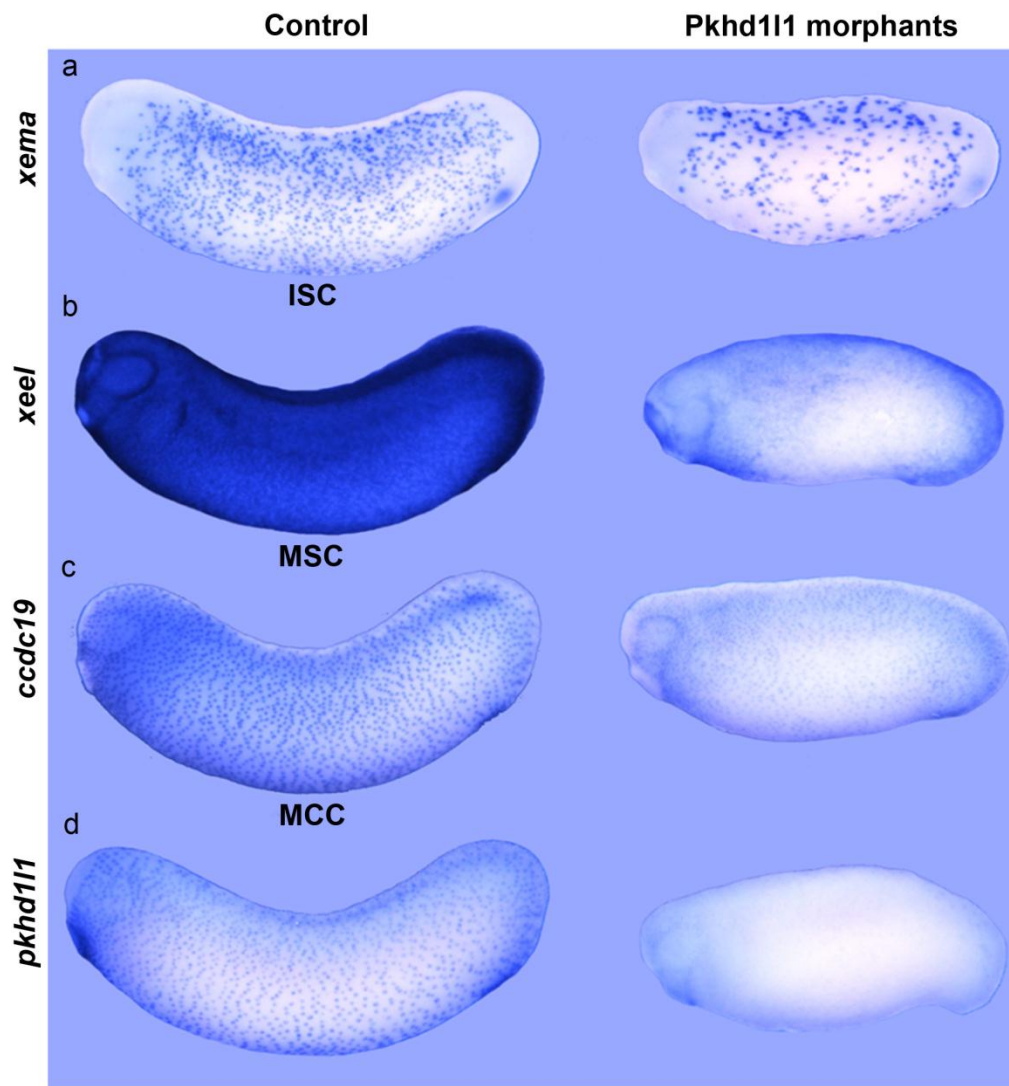
Figure 41: ***Xenopus* epidermal cells defects following *pkhd1l1* depletion.** *In situ* hybridization analysis for *Xenopus* skin markers following *pkhd1l1* depletion at stage 28. ISC mark by *xema*, (a), MSC mark by *xeel* (b) and MCC mark by *ccdc19* and *pkhd1l1* (c,d), all are markedly reduced in numbers in Pkhd1l1-MO injected embryos relative to controls. This is indicative of skin hypoplasia following *pkhd1l1* depletion.
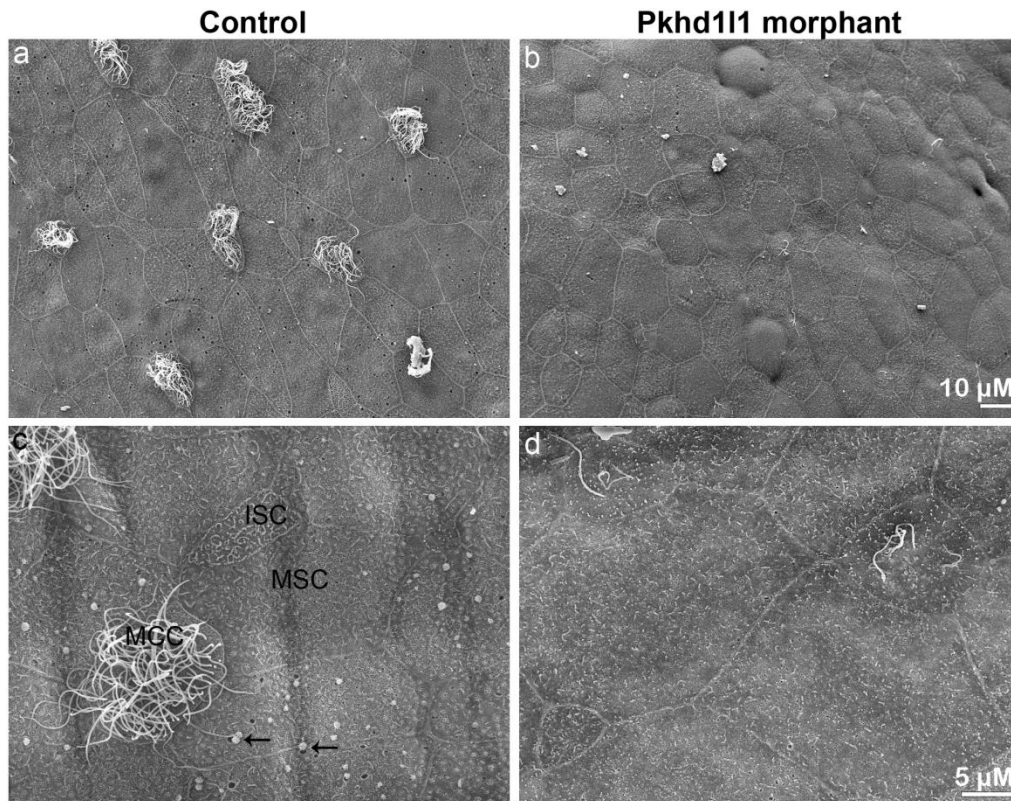
Figure 42: SEM skin surface of stage 28 *Xenopus* embryo upon *pkhd1l1* depletion. (a,b) View of *Xenopus* epidermal cell types at low magnification in control and morphant embryos, respectively. Ciliogenesis is severely compromised in overall MCC of Pkhd1l1 morphant. (c,d) At high magnification view, cilia are nearly absent, the remaining cilia seem to be shorter and disturbed in the Pkhd1l1 morphants relative to control. Moreover, MSC in control embryos contain empty vesicles and vesicles with secretory granules (black arrows) which are missing in Pkhd1l1 morphant. ISC appear to be affected as well compared to control embryo.

3.5.5. Conclusions

In conclusion, the *PKHD1L1* splice site mutation causes aberrant splicing resulted in multiple illegitimate transcripts. These abnormal transcripts could lead to production of a truncated protein or could potentially be degraded by NMD pathway as anticipated from qRT-PCR results in PBMC and immortalized B-lymphocytes. Moreover, the *pkhd1l1* causes an observable ciliary perturbation in *Xenopus* epidermis which gives us further evidence that PKHD1L1 is indispensable for ciliogenesis. However, the obvious effect of the donor splice site mutation in *PKHD1L1* mRNA processing and protein function, we found this mutation unable to display disease phenotypes in the unaffected sibling who carries the homozygous alleles.

Taken together, our work on PKHD1L1 suggests that it is not sufficient for pathogenesis although it may contribute to aggravating the phenotype caused by the *ASUN* mutation.

Chapter 4: Conclusions and Perspectives

4.1.   Aims, results and significance

The goal of this thesis was to identify the molecular genetics, biochemical and functional aetiology of a disorder known as Oral-facial-digital syndrome type II (OFDII) or Mohr syndrome. The main aims of this study were to find the causative gene of this syndrome, to explore its function during the development and determine if the disease phenotypes are attributed to ciliary defects. In this chapter, I will give a summary and discussion of my findings and their implications, as well as future perspectives which stem from this study.

A frameshift mutation in *ASUN* gene causes Mohr syndrome

A single base pair deletion mutation in *ASUN* gene was identified in two affected girls of Jordanian family. ASUN is a core component of INT family and was found to be required for *Drosophila* spermatogenesis and oogenesis, snRNA processing, and dynein localization (Anderson et al., 2009; Chen et al., 2012; Jodoin et al., 2013a; Jodoin et al., 2012; Jodoin et al., 2013b; Sitaram et al., 2012; Sitaram et al., 2013). In this study we identified an additional role of ASUN in ciliogenesis and embryonic development. To the best of my knowledge this is the first report of a human genetic disorder caused by mutations in *ASUN*.

The out-of-frame mutation in *ASUN* gene found to introduce a premature termination codon (PTC) in the penultimate exon, resulting in the deletion of the last 31 amino acid residues of the protein. These residues are highly

conserved across both vertebrate and invertebrate species, suggesting that they are functionally indispensable. The corollary is a likely pathogenicity of this novel mutation. Based on qRT-PCR and western blot analyses, we confirmed that this mutation caused marked reduction in *ASUN* mRNA levels and produced a truncated protein. Rescue experiment analysis in *Drosophila* revealed that expression of the truncated *ASUN* allele in an *asun*-mutant line failed to restore the mutant phenotypes. These phenotypes include loss of dynein recruitment to the nuclear surface, loss of nucleus-centrosome coupling and cell cycle defects. Accordingly, this finding suggests that c.2004delA is most likely the causative mutation for Mohr syndrome and patients' phenotypes likely due to loss of function of ASUN protein as a result of this mutation.

ASUN as a new player in cilia function and formation

At the inception of this thesis project, the genetic aetiology of Mohr syndrome was unknown. However, the genetic lesions for many OFD syndromes including OFDI, OFDIV, OFDV, OFDVI OFDIX and OFDXIV had been identified. For OFDI, OFDIV, OFDIX and OFDXIV, their encoded proteins were found to be localized in primary cilia and essential for cilia formation and function. However, *DDX59*, the gene involved in OFDV does not have a role in primary cilia formation, but it was found instead to have an effect on SHH, a ciliary related signaling pathway. Lastly, the contribution of C5ORF42 which causes OFDVI, to ciliary function, has yet to be confirmed or disproved. In addition to ciliary conspicuous link between cilia link and OFD syndromes, recent findings have established the role played by several INT in

ciliogenesis. These data, led us to hypothesize that ASUN could be involved in ciliary processes, and thus Mohr syndrome could therefore be a ciliopathy similar to other OFD syndromes. Besides being localized to the nucleus and cytoplasm in mammalian cells, we also found that ASUN is localized to primary cilia. Despite our finding that the mutation results in decreased *ASUN* mRNA in patient's cell compared to control cells, we were unable to observe a significant difference in its expression to primary cilia, using two different ASUN specific polyclonal antibodies. Conversely, we detect marked reduction in ASUN nuclear localization in patient's cells using ASUN (α-M) antibody. These findings showed absence of consistency of ASUN antibodies in immunostaining, which confounded the reliability of these results. One plausible explanation for this inconsistency is due to a cross reactivity of these antibodies to non-specific antigens in immunofluorescence although these antibodies were successfully validated by immunoblotting. Therefor *in vivo* animal modeling would hopefully provide clarification. We further assessed whether there are ciliary defects in patient's cells using immunofluorescence analysis with ciliary markers. Unexpectedly, we also did not detect overt differences in cilia formation and morphology, both fibroblasts and RPE cells from the affected individuals were normally ciliated. This result suggests that ASUN could be dispensable for cilia formation and it is role could be restricted to cilia function after the cilia have been formed. Alternatively, the frameshift mutation could behave as hypomorphic variant, and thus a truncated protein allows ciliogenesis in an *in vitro* setting. Conversely, we did detect dysgenesis of motile cilia in nasal biopsies of our patients. To investigate whether total loss of ASUN affects ciliogenesis, we performed

siRNA-based down-regulation of ASUN in primary fibroblasts. Immunofluorescence staining of these cells showed no overt defects in ciliogenesis. These results suggest even with low level of ASUN, cells are able to form cilia. In an attempt to explain these findings, we sought to deplete ASUN using siRNA in RPE cells, another human ciliated cell line. *ASUN* depletion in RPE cells revealed marked loss of primary cilia in ASUN-siRNA cells compared to control siRNA cells however primary cilia were formed in siRNA primary fibroblasts, suggesting the fundamental role of ASUN in primary cilia formation in RPE cells. The discordance between fibroblasts and RPE suggests a probable cell type-specific requirement of ASUN during ciliogenesis. Variation in cilia morphology between these cells also suggests that loss of ASUN proteins may have different effects in different ciliated cell types. In addition, normal ciliation does not always guarantee normal cilia function, differences in the rate of ciliary growth and turnover could lead to morphological and functional variation. On the other hand, ciliary related signaling defects could be observed even with normal cilia formation. Several studies on ciliary genes showed ciliary function defects despite normal cilia formation. For instance, a hypomorphic mouse model of intraflagellar transport 80 (*Ift80*) which causes autosomal recessive JATD and SRPIII (MIM: 263510) syndromes resulted in normal cilia formation accompanied with Shh pathway alteration in the embryonic fibroblast cells (Rix et al., 2011). Moreover, mutation in *CCDC65*, which causes primary ciliary dyskinesia (PCD) syndrome, did not cause ciliary morphological defects but impaired cilia beating (Horani et al., 2013). Additionally, same scenario was recently observed in an OFDV gene (*DDX59*) which gives further support for

possible ciliary signaling defects even with normal primary cilia assembly (Shamseldin et al., 2013).

SHH signaling is potentially altered in patient's cells

For the reasons mentioned above, we asked if the cilia in patient's cells are functionally defective despite being normally formed. Since one of the main functions of primary cilia is to mediate signaling transduction pathways including SHH, we therefore assessed the response of our patient's ciliated fibroblasts to a Hedgehog agonist (SAG). Surprisingly, patient's cells displayed increased response toward SAG, suggesting an increase in SHH signaling. This was not observed in ASUN-depleted cells. These findings suggest a neomorphic activity of the truncated ASUN mutant protein encoded by the mutant *ASUN* allele in patient's cells. To validate this hypothesis, we will need to reproduce these results using patient's RPE cells and examine the localization and levels of SHH targets at the protein level. These findings indicate that a truncated ASUN does not affect ciliogenesis in patient's fibroblasts, but might be able to cause HEDGEHOG signaling defects.

ASUN displays conserved expression patterns during *Xenopus* and zebrafish embryonic development

Using whole embryo antibody staining in *Xenopus* and *in situ* hybridization in both *Xenopus* and zebrafish, we delineated the spatiotemporal expression of *asun* during early development. My results confirmed the maternal and zygotic expression of *asun* which was constitutive and ubiquitous throughout development. *asun* is specially expressed in tissues preferentially containing cilia or rely on cilia biogenesis to develop including neural tube, epidermal

multi-ciliated cells (MCC), ear, eye, brain, head, somite and pronephros. This broad expression pattern suggests that *asun* could play a fundamental role during embryonic development as well as ciliary processes.

The pathophysiology of Mohr syndrome is partially recapitulated by *in vivo* animal modeling

The phenotypes of Mohr syndrome patients suggest that it is a ciliopathy. Hence, ASUN probably function in ciliary biogenesis and/or function during embryogenesis in humans. To describe the function of the *asun* gene during embryonic development, *in vivo* animal modeling of this syndrome was performed using morpholino (MO)-based knock-down (KD) of *asun* in zebrafish and *Xenopus leaves* embryos. Embryos microinjected with different antisense MOs designed against *asun* displayed developmental defects partially reminiscent of the disease phenotypes in the affected patients.

asun depletion in *Xenopus* and zebrafish resulted in morphological phenotypes not observed in wild-type embryos, including shortened and curved body axis, disrupted somites, cardiac edema, developmental delay and randomization of left-right (LR) asymmetry. Collectively, these phenotypes are similar to common phenotypes caused by mutations in genes that are involved in cilia biogenesis. Additionally, *asun* is expressed in the developing head, eye, ear, skin and heart in *Xenopus*, which are the tissues that exhibit defects in the human syndrome. This suggests that patients' phenotypes might be due to altered cilia formation and/or function as a consequence of impaired ASUN function.

First, the congenital heart defect diagnosed in one proband, could be phenocopied by Asun-depleted *Xenopus* embryos that displayed impaired expression of heart marker *nkx2.5*. *asun* depletion in zebrafish embryos also caused randomization of heart looping/jogging associated with pericardial oedema. These phenotypes provide support that Asun is required for establishment of LR asymmetry, which is directly dependent on normal cilia function.

In addition to cardiac phenotypes, Asun-depleted *Xenopus* and zebrafish embryos also displayed a small head and dysmorphic head structures in zebrafish. These defects were previously found to be caused by migration defect of the cranial neural crest cells (CNCC) in branchial arches (BAs) similar to what we established in this study by a CNCC marker *twist* in *Xenopus*. This likely indicates defects in primary cilia that cover the migratory CNCC.

Further investigation of craniofacial structures of zebrafish morphants revealed severe defects including lack of cartilage structures and variable degrees of hypotelorism. Additional ciliary-related phenotypes observed in Asun-depleted zebrafish embryos include otolith malformation and hydrocephaly. Furthermore, *Xenopus* morphants also exhibited somitic dysgenesis which was clearly observed by whole embryo immunostaining using ASUN (α-M) antibody and confirmed by the somites specific marker MyoD. All these phenotypes demonstrate the pivotal role of Asun in cilia biogenesis and function.

Asun is required for ciliary differentiation and proper motility in *Xenopus* epidermis

Besides the fundamental role of ASUN in ciliogenesis in mammalian cells, our results also identified Asun as an essential player in cilia assembly and function in MCC of *Xenopus*. As described earlier, *in situ* hybridization analysis revealed ubiquitous expression of *asun/*Asun throughout embryonic skin in a punctate pattern reminiscent to a ciliary marker, acetylated α-tubulin and other MCC expressing genes (Dubaissi and Papalopulu, 2011; Hayes et al., 2007). KD of *asun* in *Xenopus* resulted in prominent defects in MCC. The majority of MCC in Asun-depleted embryos failed to express normal cilia, and showed an obvious perturbation of multi-cilia beating. Cilia were fewer in number, relatively shorter and lack a normal orientation. Immunofluorescence staining using acetylated α-tubulin together with live imaging delineated less cilia and abnormal beating frequency of MCC multi-cilia, respectively.

To gain a further insight into the impact of *asun* depletion on the ultrastructure of the epidermal cells specifically the MCC, morphant embryos were then analyzed by scanning electron microscopy (SEM). We demonstrated that besides MCC defects, both mucus-secreting cells (MSC) ion-secreting cells (ISC) seemed to be affected as well. We found fewer secretory vesicles on the apical surface of MSC, which were also smaller in size compared to wild-type embryos. Moreover, the number of ISC was reduced in morphant embryos, suggesting that Asun affects normal differentiation of these cells. MSC and ISC defects could be secondary to MCC perturbation. Alternatively, a recent study on *Xenopus* epidermis showed that depletion of ISC resulted in strong

defect in MCC development and differentiation similar to what we observed in Asun-depleted embryos (Dubaissi and Papalopulu, 2011). These findings indicate a strong interaction between these cells.

The observation of *Xenopus* epidermal cells might provide an explanation for the recurrent, respiratory tract infections and cough reported in Mohr syndrome patients, including the present two probands. This finding suggests the presence of ciliary defects in epithelial cells that line human airway particularly the ciliated cells. Immunofluorescence staining on patients' nasal epithelial cells revealed an alteration in cilia formation and morphology, consistent with the observed ciliary defects in MCC of *Xenopus* morphant embryos. The conserved structure of airway lining cells among vertebrates, suggesting a possible defect in the MSC and ISC as well. Moreover, *Xenopus* ISC were found to be analogous to those found in transporting epithelia of the collecting duct of mammalian kidney (α and β intercalated cells) (Batlle et al., 2001; Wagner et al., 2009). These cells are ion secreting cells also known as ionocytes, proton-secreting cells, and mitochondria-rich cells that regulate ionic balance in order to control the epithelial surface liquid. Several human diseases arise as a result of defective ISC and MSC, including Inflammatory bowel disease, Pseudomyxoma peritonei, Cystic fibrosis and Distal renal acidosis (Dubaissi and Papalopulu, 2011; Kim and Ho, 2010).

To gain a greater insight on the impact of Asun on epidermal cells, it would therefore be important to perform *in situ* hybridization of markers specifically expressed in these cells. Furthermore, it will be important to visualize the

entire ultrastructure of each of the cells by transmission electron microscopy (TEM), which is currently underway.

PKHD1L1 splicing mutation as a modifier in Mohr syndrome

In addition to the *ASUN* mutation, our probands were also homozygous for a splicing mutation in *PKHD1L1* that was able to disrupt the normal splicing of *PKHD1L1* mRNA. Consequently, the expression level of *PKHD1L1* mRNA was significantly down-regulated and alternative transcript isoforms were produced as a result of defective splicing. However, this mutation was also found in a healthy, unaffected aunt with no signs of disease manifestations. As we described before, the phenotypic variability in patients affected by Mohr syndrome is notable within and between families, which is also very obvious in the two patients. These observations suggest the existence of modifier alleles that modulate the disease severity. Several studies have shown that splicing defects can influence the severity of the disease (Garcia-Blanco et al., 2004; Nissim-Rafinia and Kerem, 2002, 2005).

The phenotypic spectrum of Mohr syndrome could possibly be due to tissue-specific *PKHD1l1* splicing concomitant with ubiquitous expression of ASUN. We postulate that *PKHD1L1* splicing could influence disease phenotypes caused by ASUN deficiency in certain tissues, thereby modifying the expressivity of *ASUN* mutation. In addition, reduction of nuclear localization of ASUN in patient's cells, suggesting that some of the clinical manifestations observed in Mohr patients could be related to the nuclear function of ASUN protein.

4.2.   Future perspectives

Searching for potential interactors with ASUN

Mohr syndrome and other OFD syndromes are pleotropic disorders characterized by multiple organ defects. Inter- and intra-familial phenotypic variations have been described in patients with Mohr syndrome as well as in the two patients we studied. Moreover, the phenotypic overlap between OFD and other ciliopathies imply that a similar underlying aetiology may cause these pathologies.

It has been shown that different genes that share spatio-temporal expression or that encode proteins with similar functional domains or motifs, may act in common pathways. Several proteomic analyses revealed that many ciliary proteins are components of multi-protein complexes. The dysfunction of any of these proteins may affect the function of the other complex components, which would therefore result in a variable degree of phenotypic severity (Adams et al., 2008; Cardenas-Rodriguez and Badano, 2009; Deltas and Papagregoriou, 2010). For instance, mutations in the *OFDI* (*CXORF5*) gene have been associated to a variety of diseases such as with X-linked JBTS10, X-linked RP and SGBS2 syndromes (Bisschoff et al., 2013; Coene et al., 2009; Field et al., 2012). The phenotypic variability among OFDI was correlated with differences of interaction affinity between CXORF5 protein and its partner, the LCA protein (Lebercilin). This level of interaction was shown to depend on the types and the positions of mutation in *CXORF5* gene (Coene et al., 2009). Likewise, mutations in the centrosomal protein CEP290 resulted in variable phenotypic appearance among several ciliopathies such as

Senior-Loken syndrome (SLSN; MIM 266900), NPHP, LCA, JBTS, BBS, and MKS (Coppieters et al., 2010). This wide range of phenotypes caused by CEP290 was confirmed by its interaction with these disorder-associated proteins that are all localized at the TZ of cilium (Garcia-Gonzalo et al., 2011). As such, the phenotypic severity and variability could be explained by differences in binding of different mutated proteins with their interacting partners (Zaghloul and Katsanis, 2010). Further examples of protein-protein interactions were mentioned in section 1.10.

To find possible proteins that interact with ASUN, we performed a mass spectrometry (MS) analysis in NIH3T3 cells followed by a pull down experiment using a specific ASUN antibody. Several proteins were enriched by immunoprecipitation, especially components of INT subunits (INT 1, 3, 5 and 10) (Table 5). This confirms our finding that ASUN is a functional component of the integrator complex.

#	Protein symbol	Accession #	Fold Change by Sample (Fold Change)	ASUN IP (anti-M)	ASUN IP (anti-V5)	Total Peptides
479	Cep170	H7BX26	95% (5)	5	0	5
114	Int1	K3W4P2	95% (INF)	17	0	17
431	Int3	Q7TPD0	95% (4)	4	1	5
202	Int5	Q8CHT3	95% (3)	3	1	4
84	Int10	E9Q360	95% (2.6)	12	4	16
20	Snrnp200	Q6P4T2	95% (74)	47	1	48
13	Ddx5	Q61656	95% (13)	20	4	24
58	Ddx1	Q91VR5	95% (4)	17	6	23

Table 5: The list of proteins that are enriched with ASUN antibody using MS

Concurrently, we also searched through, a web-based resource of Affymetrix microarray data (http://genome.ucla.edu/~jdong/GeneCorr.html), the genes

that were highly correlated in term of their expression. This tool gave us an estimation of genes that may act in similar biological pathways (Table 6). In order to verify whether these proteins are putative interactors of ASUN, co-immunoprecipitation (co-IP) using tagged INT5 and CEP170 are currently being performed.

Correlation with *ASUNDER* chr12:26949384-26961934

Chromosome position	Gene title	Gene symbol	Probe Set.ID	correlation coefficients	Average
chr7:1476438-1500014	integrator complex subunit 1	INTS1	212210_at	0.135	0.12825
chr7:1476438-1500014	integrator complex subunit 1	INTS1	212212_s_at	0.1215	
chr17:57297512-57360159	integrator complex subunit 2	INTS2	224308_s_at	0.3872	0.3872
chr1:152001922-152013179	integrator complex subunit 3	INTS3	202809_s_at	0.0798	0.0798
chr11:77267415-77383360	integrator complex subunit 4	INTS4	225169_at	0.3237	0.3237
chr11:62170898-62174171	integrator complex subunit 5	INTS5	221818_at	0.262	0.2934
chr11:62170898-62171381	integrator complex subunit 5	INTS5	53968_at	0.3248	
chr13:50837642-50854200	integrator complex subunit 6	INTS6	222239_s_at	0.2455	0.2455
chr1:210181320-210275485	integrator complex subunit 7	INTS7	222250_s_at	0.65	0.35
chr1:210180367-210247362	integrator complex subunit 7	INTS7	218783_at	0.2401	
chr1:210246976-210248475	integrator complex subunit 7	INTS7	1570173_at	0.1593	
chr8:95930909-95961714	integrator complex subunit 8	INTS8	218905_at	0.3974	0.3974
chr8:28681098-28803398	integrator complex subunit 9	INTS9	203941_at	0.4748	0.4748
chr8:19752917-19753858	integrator complex subunit 10	INTS10	229632_s_at	0.2865	0.2865
chr4:106823235-106840620	integrator complex subunit 12	INTS12	218616_at	0.5445	0.5445

Table 6: Correlation of *ASUN* gene with genes encoding CEP170, INT (1-10, 12) according to gene-gene correlation tool. 1: correlated, indicative of co-expression; 0: not correlated.

4.3. Limitations and perspectives

Although the expression of *ASUN* is ubiquitous in most tissues and cilia are widely spread, we may ask why that the loss of ASUN caused defects only in certain organs or body parts of Mohr syndrome patients. Chronic kidney failure and pancreatitis have been recently reported in the older patient, suggesting that additional phenotypes could be observed over age. Therefore, the possibility for the youngest patient to display these defects still remains. The potential role of ASUN protein in kidney and pancreas should therefore be investigated.

Our results delineate *ASUN* as a causative gene for multi-organ phenotype ciliopathies. Gene augmentation therapy may be used to correct the genetic lesion by injecting an adenoviral-mediated expression of the wild-type gene to the affected target tissue. This technique was effective to restore vision of human and animal models with non-syndromic retinal ciliopathies as well as restoring of olfactory function in mouse model (Estrada-Cuzcano et al., 2012; Hufnagel et al., 2012; McIntyre et al., 2012) . Similarly, delivery of the wild-type gene using the same approach was able to restore ciliary beating in patient with PCD whose airway epithelium cells express non-motile cilia (Estrada-Cuzcano et al., 2012). Although this technique is not accessible for multi-organ defects, it may be used to cure specific affected organs.

Induced pluripotent stem cells (iPS) may also be a promising approach to examine the role of ASUN *in vitro*. We have already generated iPS from the patient's primary fibroblasts and different ciliated lineages such as neural

precursor cells (NPC), kidney and pancreatic cells are currently being generating. With the help of Institute of Medical Biology (IMB) Stem Cell Bank, Singapore, these reprogrammed cells were successfully differentiated into RPE cells. Besides disease modeling, the iPS cells generated from matched unaffected siblings can also be transplanted into the patient for therapy purpose (Phillips, 2012; Zou et al., 2011). The patients' respiratory tract defect could therefore be cured by this approach.

Moreover, the role of ASUN during spermatogenesis and oogenesis in *Drosophila* drives us to examine the role of ASUN in human male and female reproductive system. Since *ASUN* is expressed in human testis and based on the essential role of *asun* for fertility in *Drosophila* male embryos, we could hypothesize that males present with Mohr syndrome may have reduced fertility. Unfortunately, this possible phenotype could not be investigated during my thesis since the two probands are females. Recently, the role of *asun* in *Drosophila* oogenesis has been also elucidated, suggesting a similar effect in human female's patients (Sitaram et al., 2013).

In line with this, *ASUN* showed high expression in testicular seminomas (Bourdon et al., 2002), suggesting a possible role of ASUN in cancer development that could be seen at late onset.

Based on the medical examination of the two patients, laterality defects were not observed in these patients. In this work, we cannot exclude the probability of LR asymmetry randomization in humans as a result of *ASUN* mutation.

Finally, since Asun-depleted *Xenopus* and zebrafish embryos displayed convergent extension (CE) defects, we suggest that the planar cell polarity

(PCP) pathway may be defective. As convergent extension (CE) movements are regulated by non-canonical / Wnt PCP signaling, it would therefore be interesting to investigate whether Asun plays a role in this signaling pathway.

To conclude, I have in part achieved my initial objectives and successfully determined the genetic aetiology of Mohr Syndrome. I am well aware that it is critical that other cases diagnosed with this rare disease be sequenced in order to uncover distinct pathogenic variant in *ASUN*. This will provide independent confirmation of our findings which are for the moment most pertinent to this particular Jordanian family. Nonetheless, my functional studies and animal modeling lend support to the notion that ASUN is indeed involved in ciliary function in humans, fish and frogs. I trust that the results presented in my thesis lay a sound foundation for future investigations on the role of ASUN in the context of embryonic development and cilia biology.

Bibliography

Adams, M., Smith, U.M., Logan, C.V., and Johnson, C.A. (2008). Recent advances in the molecular pathology, cell biology and genetics of ciliopathies. J Med Genet *45*, 257-267.

Adly, N., Alhashem, A., Ammari, A., and Alkuraya, F.S. (2014). Ciliary Genes TBC1D32/C6orf170 and SCLT1 are Mutated in Patients with OFD Type IX. Human mutation *35*, 36-40.

Afzelius, B.A. (1976). A human syndrome caused by immotile cilia. Science *193*, 317-319.

Al-Halabi, H., Nantel, A., Klekner, A., Guiot, M.C., Albrecht, S., Hauser, P., Garami, M., Bognar, L., Kavan, P., Gerges, N.*, et al.* (2011). Preponderance of sonic hedgehog pathway activation characterizes adult medulloblastoma. Acta Neuropathol *121*, 229-239.

al-Qattan, M.M., and Hassanain, J.M. (1997). Classification of limb anomalies in oral-facial-digital syndromes. Journal of hand surgery *22*, 250-252.

Alazami, A.M., Alshammari, M.J., Salih, M.A., Alzahrani, F., Hijazi, H., Seidahmed, M.Z., Abu Safieh, L., Aldosary, M., Khan, A.O., and Alkuraya, F.S. (2012). Molecular characterization of Joubert syndrome in Saudi Arabia. Human mutation *33*, 1423-1428.

Alman, B.A. (2008). Skeletal dysplasias and the growth plate. Clinical genetics *73*, 24-30.

Anderhub, S.J., Kramer, A., and Maier, B. (2012). Centrosome amplification in tumorigenesis. Cancer letters *322*, 8-17.

Anderson, M.A., Jodoin, J.N., Lee, E., Hales, K.G., Hays, T.S., and Lee, L.A. (2009). Asunder is a critical regulator of dynein-dynactin localization during Drosophila spermatogenesis. Molecular biology of the cell *20*, 2709-2721.

Andrae, J., Gallini, R., and Betsholtz, C. (2008). Role of platelet-derived growth factors in physiology and medicine. Genes Dev *22*, 1276-1312.

Anneren, G., Arvidson, B., Gustavson, K.H., Jorulf, H., and Carlsson, G. (1984). Oro-facio-digital syndromes I and II: radiological methods for diagnosis and the clinical variations. Clinical genetics *26*, 178-186.

Ansley, S.J., Badano, J.L., Blacque, O.E., Hill, J., Hoskins, B.E., Leitch, C.C., Kim, J.C., Ross, A.J., Eichers, E.R., Teslovich, T.M.*, et al.* (2003). Basal body dysfunction is a likely cause of pleiotropic Bardet-Biedl syndrome. Nature *425*, 628-633.

Arnaiz, O., Malinowska, A., Klotz, C., Sperling, L., Dadlez, M., Koll, F., and Cohen, J. (2009). Cildb: a knowledgebase for centrosomes and cilia. Database : the journal of biological databases and curation *2009*, 1758-0463.

Arroyo Carrera, I., Lopez Cuesta, M.J., Lozano Rodriguez, J.A., and Martinez-Fernandez, M.L. (2013). [Oral-facial-digital syndrome type ii: Clinical case and differential diagnosis.]. Anales de pediatria *80*, 1695-9531.

Arts, H.H., and Knoers, N.V. (2013). Current insights into renal ciliopathies: what can genetics teach us? Pediatric nephrology *28*, 863-874.

Austin-Tse, C., Halbritter, J., Zariwala, M.A., Gilberti, R.M., Gee, H.Y., Hellman, N., Pathak, N., Liu, Y., Panizzi, J.R., Patel-King, R.S.*, et al.* (2013). Zebrafish Ciliopathy

Screen Plus Human Mutational Analysis Identifies C21orf59 and CCDC65 Defects as Causing Primary Ciliary Dyskinesia. Am J Hum Genet *93*, 672-686.

Baala, L., Audollent, S., Martinovic, J., Ozilou, C., Babron, M.C., Sivanandamoorthy, S., Saunier, S., Salomon, R., Gonzales, M., Rattenberry, E*., et al.* (2007). Pleiotropic effects of CEP290 (NPHP6) mutations extend to Meckel syndrome. Am J Hum Genet *81*, 170-179.

Badano, J.L., Mitsuma, N., Beales, P.L., and Katsanis, N. (2006). The ciliopathies: an emerging class of human genetic disorders. Annu Rev Genomics Hum Genet *7*, 125-148.

Badano, J.L., Teslovich, T.M., and Katsanis, N. (2005). The centrosome in human genetic disease. Nat Rev Genet *6*, 194-205.

Baker, K., and Beales, P.L. (2009). Making sense of cilia in disease: the human ciliopathies. American journal of medical genetics Part C, Seminars in medical genetics *151C*, 281-295.

Balci, S., Guler, G., Kale, G., Soylemezoglu, F., and Besim, A. (1999). Mohr syndrome in two sisters: prenatal diagnosis in a 22-week-old fetus with post-mortem findings in both. Prenatal diagnosis *19*, 827-831.

Baraitser, M. (1986). The orofaciodigital (OFD) syndromes. J Med Genet *23*, 116-119.

Baraitser, M., Burn, J., and Fixsen, J. (1983). A female infant with features of Mohr and Majewski syndromes: variable expression, a genetic compound, or a distinct entity? J Med Genet *20*, 65-67.

Basten, S.G., and Giles, R.H. (2013). Functional aspects of primary cilia in signaling, cell cycle and tumorigenesis. Cilia *2*, 2046-2530.

Batlle, D., Ghanekar, H., Jain, S., and Mitra, A. (2001). Hereditary distal renal tubular acidosis: new understandings. Annual review of medicine *52*, 471-484.

Bell, P.D., Fitzgibbon, W., Sas, K., Stenbit, A.E., Amria, M., Houston, A., Reichert, R., Gilley, S., Siegal, G.P., Bissler, J*., et al.* (2011). Loss of primary cilia upregulates renal hypertrophic signaling and promotes cystogenesis. Journal of the American Society of Nephrology : JASN *22*, 839-848.

Benzing, T., and Schermer, B. (2011). Transition zone proteins and cilia dynamics. Nat Genet *43*, 723-724.

Berbari, N.F., Johnson, A.D., Lewis, J.S., Askwith, C.C., and Mykytyn, K. (2008a). Identification of ciliary localization sequences within the third intracellular loop of G protein-coupled receptors. Molecular biology of the cell *19*, 1540-1547.

Berbari, N.F., Lewis, J.S., Bishop, G.A., Askwith, C.C., and Mykytyn, K. (2008b). Bardet-Biedl syndrome proteins are required for the localization of G protein-coupled receptors to primary cilia. Proc Natl Acad Sci U S A *105*, 4242-4246.

Berbari, N.F., O'Connor, A.K., Haycraft, C.J., and Yoder, B.K. (2009). The primary cilium as a complex signaling center. Curr Biol *19*, R526-535.

Bettencourt-Dias, M., and Glover, D.M. (2007). Centrosome biogenesis and function: centrosomics brings new understanding. Nat Rev Mol Cell Biol *8*, 451-463.

Betters, E., Liu, Y., Kjaeldgaard, A., Sundstrom, E., and Garcia-Castro, M.I. (2010). Analysis of early human neural crest development. Dev Biol *344*, 578-592.

Billett, F.S., and Gould, R.P. (1971). Fine structural changes in the differentiating epidermis of Xenopus laevis embryos. Journal of anatomy *108*, 465-480.

Bisgrove, B.W., Essner, J.J., and Yost, H.J. (1999). Regulation of midline development by antagonism of lefty and nodal signaling. Development *126*, 3253-3262.

Bisgrove, B.W., Snarr, B.S., Emrazian, A., and Yost, H.J. (2005). Polaris and Polycystin-2 in dorsal forerunner cells and Kupffer's vesicle are required for specification of the zebrafish left-right axis. Dev Biol *287*, 274-288.

Bisschoff, I.J., Zeschnigk, C., Horn, D., Wellek, B., Riess, A., Wessels, M., Willems, P., Jensen, P., Busche, A., Bekkebraten, J*., et al.* (2013). Novel mutations including deletions of the entire OFD1 gene in 30 families with type 1 orofaciodigital syndrome: a study of the extensive clinical variability. Human mutation *34*, 237-247.

Bitgood, M.J., Shen, L., and McMahon, A.P. (1996). Sertoli cell signaling by Desert hedgehog regulates the male germline. Curr Biol *6*, 298-304.

Blagden, S.P., and Glover, D.M. (2003). Polar expeditions--provisioning the centrosome for mitosis. Nat Cell Biol *5*, 505-511.

Boehlke, C., Kotsis, F., Patel, V., Braeg, S., Voelker, H., Bredt, S., Beyer, T., Janusch, H., Hamann, C., Godel, M*., et al.* (2010). Primary cilia regulate mTORC1 activity and cell size through Lkb1. Nat Cell Biol *12*, 1115-1122.

Boesger, J., Wagner, V., Weisheit, W., and Mittag, M. (2009). Analysis of flagellar phosphoproteins from Chlamydomonas reinhardtii. Eukaryotic cell *8*, 922-932.

Boldt, K., van Reeuwijk, J., Gloeckner, C.J., Ueffing, M., and Roepman, R. (2009). Tandem affinity purification of ciliopathy-associated protein complexes. Methods in cell biology *91*, 143-160.

Bonnard, C., Strobl, A.C., Shboul, M., Lee, H., Merriman, B., Nelson, S.F., Ababneh, O.H., Uz, E., Guran, T., Kayserili, H*., et al.* (2012). Mutations in IRX5 impair craniofacial development and germ cell migration via SDF1. Nat Genet *44*, 709-713.

Bornens, M. (2002). Centrosome composition and microtubule anchoring mechanisms. Curr Opin Cell Biol *14*, 25-34.

Bourdon, V., Naef, F., Rao, P.H., Reuter, V., Mok, S.C., Bosl, G.J., Koul, S., Murty, V.V., Kucherlapati, R.S., and Chaganti, R.S. (2002). Genomic and expression analysis of the 12p11-p12 amplicon using EST arrays identifies two novel amplified and overexpressed genes. Cancer research *62*, 6218-6223.

Broekhuis, J.R., Leong, W.Y., and Jansen, G. (2013). Regulation of cilium length and intraflagellar transport. International review of cell and molecular biology *303*, 101-138.

Brugmann, S.A., Allen, N.C., James, A.W., Mekonnen, Z., Madan, E., and Helms, J.A. (2010a). A primary cilia-dependent etiology for midline facial disorders. Hum Mol Genet *19*, 1577-1592.

Brugmann, S.A., Cordero, D.R., and Helms, J.A. (2010b). Craniofacial ciliopathies: A new classification for craniofacial disorders. American journal of medical genetics Part A *152A*, 2995-3006.

Budny, B., Chen, W., Omran, H., Fliegauf, M., Tzschach, A., Wisniewska, M., Jensen, L.R., Raynaud, M., Shoichet, S.A., Badura, M*., et al.* (2006). A novel X-linked recessive mental retardation syndrome comprising macrocephaly and ciliary dysfunction is allelic to oral-facial-digital type I syndrome. Human genetics *120*, 171-178.

Camera, G., Marasini, M., Pozzolo, S., and Camera, A. (1994). Oral-facial-digital syndrome: report on a transitional type between the Mohr and Varadi syndromes in a fetus. American journal of medical genetics *53*, 196-198.

Campbell, T.N., and Choy, F.Y. (2005). RNA interference: past, present and future. Current issues in molecular biology *7*, 1-6.

Cano, D.A., Murcia, N.S., Pazour, G.J., and Hebrok, M. (2004). Orpk mouse model of polycystic kidney disease reveals essential role of primary cilia in pancreatic tissue organization. Development *131*, 3457-3467.

Cardenas-Rodriguez, M., and Badano, J.L. (2009). Ciliary biology: understanding the cellular and genetic basis of human ciliopathies. American journal of medical genetics Part C, Seminars in medical genetics *151C*, 263-280.

Caspary, T., Larkins, C.E., and Anderson, K.V. (2007). The graded response to Sonic Hedgehog depends on cilia architecture. Developmental cell *12*, 767-778.

Chang, Y.F., Imam, J.S., and Wilkinson, M.F. (2007). The nonsense-mediated decay RNA surveillance pathway. Annual review of biochemistry *76*, 51-74.

Chari, N.S., and McDonnell, T.J. (2007). The sonic hedgehog signaling network in development and neoplasia. Adv Anat Pathol *14*, 344-352.

Chen, J., Ezzeddine, N., Waltenspiel, B., Albrecht, T.R., Warren, W.D., Marzluff, W.F., and Wagner, E.J. (2012). An RNAi screen identifies additional members of the Drosophila Integrator complex and a requirement for cyclin C/Cdk8 in snRNA 3'-end formation. Rna *18*, 2148-2156.

Christensen, S.T., Clement, C.A., Satir, P., and Pedersen, L.B. (2012). Primary cilia and coordination of receptor tyrosine kinase (RTK) signalling. The Journal of pathology *226*, 172-184.

Christensen, S.T., Pedersen, L.B., Schneider, L., and Satir, P. (2007). Sensory cilia and integration of signal transduction in human health and disease. Traffic *8*, 97-109.

Chung, W.Y., and Chung, L.P. (1999). A case of oral-facial-digital syndrome with overlapping manifestations of type V and type VI: a possible new OFD syndrome. Pediatric radiology *29*, 268-271.

Coene, K.L., Mans, D.A., Boldt, K., Gloeckner, C.J., van Reeuwijk, J., Bolat, E., Roosing, S., Letteboer, S.J., Peters, T.A., Cremers, F.P.*, et al.* (2011). The ciliopathy-associated protein homologs RPGRIP1 and RPGRIP1L are linked to cilium integrity through interaction with Nek4 serine/threonine kinase. Hum Mol Genet *20*, 3592-3605.

Coene, K.L., Roepman, R., Doherty, D., Afroze, B., Kroes, H.Y., Letteboer, S.J., Ngu, L.H., Budny, B., van Wijk, E., Gorden, N.T.*, et al.* (2009). OFD1 is mutated in X-linked Joubert syndrome and interacts with LCA5-encoded lebercilin. Am J Hum Genet *85*, 465-481.

Colantonio, J.R., Vermot, J., Wu, D., Langenbacher, A.D., Fraser, S., Chen, J.N., and Hill, K.L. (2009). The dynein regulatory complex is required for ciliary motility and otolith biogenesis in the inner ear. Nature *457*, 205-209.

Cole, D.G., Diener, D.R., Himelblau, A.L., Beech, P.L., Fuster, J.C., and Rosenbaum, J.L. (1998). Chlamydomonas kinesin-II-dependent intraflagellar transport (IFT): IFT particles contain proteins required for ciliary assembly in Caenorhabditis elegans sensory neurons. J Cell Biol *141*, 993-1008.

Conduit, S.E., Dyson, J.M., and Mitchell, C.A. (2012). Inositol polyphosphate 5-phosphatases; new players in the regulation of cilia and ciliopathies. FEBS letters *586*, 2846-2857.

Coppieters, F., Lefever, S., Leroy, B.P., and De Baere, E. (2010). CEP290, a gene with many faces: mutation overview and presentation of CEP290base. Human mutation *31*, 1097-1108.

Corbit, K.C., Aanstad, P., Singla, V., Norman, A.R., Stainier, D.Y., and Reiter, J.F. (2005). Vertebrate Smoothened functions at the primary cilium. Nature *437*, 1018-1021.

Corbit, K.C., Shyer, A.E., Dowdle, W.E., Gaulden, J., Singla, V., Chen, M.H., Chuang, P.T., and Reiter, J.F. (2008). Kif3a constrains beta-catenin-dependent Wnt signalling through dual ciliary and non-ciliary mechanisms. Nat Cell Biol *10*, 70-76.

Culbertson, M.R. (1999). RNA surveillance. Unforeseen consequences for gene expression, inherited genetic disorders and cancer. Trends Genet *15*, 74-80.

Dabdoub, A., and Kelley, M.W. (2005). Planar cell polarity and a potential role for a Wnt morphogen gradient in stereociliary bundle orientation in the mammalian inner ear. J Neurobiol *64*, 446-457.

Davenport, J.R., and Yoder, B.K. (2005). An incredible decade for the primary cilium: a look at a once-forgotten organelle. American journal of physiology Renal physiology *289*, F1159-1169.

Debec, A., Sullivan, W., and Bettencourt-Dias, M. (2010). Centrioles: active players or passengers during mitosis? Cellular and molecular life sciences : CMLS *67*, 2173-2194.

Deblandre, G.A., Wettstein, D.A., Koyano-Nakagawa, N., and Kintner, C. (1999). A two-step mechanism generates the spacing pattern of the ciliated cells in the skin of Xenopus embryos. Development *126*, 4715-4728.

Degner, D., Bleich, S., Riegel, A., and Ruther, E. (1999). [Orofaciodigital syndrome--a new variant? Psychiatric, neurologic and neuroradiological findings]. Fortschr Neurol Psychiatr *67*, 525-528.

Delous, M., Baala, L., Salomon, R., Laclef, C., Vierkotten, J., Tory, K., Golzio, C., Lacoste, T., Besse, L., Ozilou, C.*, et al.* (2007). The ciliary gene RPGRIP1L is mutated in cerebello-oculo-renal syndrome (Joubert syndrome type B) and Meckel syndrome. Nat Genet *39*, 875-881.

Deltas, C., and Papagregoriou, G. (2010). Cystic diseases of the kidney: molecular biology and genetics. Archives of pathology & laboratory medicine *134*, 569-582.

DeSimone, D.W., Davidson, L., Marsden, M., and Alfandari, D. (2005). The Xenopus embryo as a model system for studies of cell migration. Methods in molecular biology *294*, 235-245.

Digilio, M.C., Marino, B., Ammirati, A., Borzaga, U., Giannotti, A., and Dallapiccola, B. (1999). Cardiac malformations in patients with oral-facial-skeletal syndromes: clinical similarities with heterotaxia. American journal of medical genetics *84*, 350-356.

Digilio, M.C., Marino, B., Giannotti, A., and Dallapiccola, B. (1996). Orocardiodigital syndrome: an oral-facial-digital type II variant associated with atrioventricular canal. J Med Genet *33*, 416-418.

Dixon, M.J., Marazita, M.L., Beaty, T.H., and Murray, J.C. (2011). Cleft lip and palate: understanding genetic and environmental influences. Nat Rev Genet *12*, 167-178.

Dode, C., Levilliers, J., Dupont, J.M., De Paepe, A., Le Du, N., Soussi-Yanicostas, N., Coimbra, R.S., Delmaghani, S., Compain-Nouaille, S., Baverel, F., *et al.* (2003). Loss-of-function mutations in FGFR1 cause autosomal dominant Kallmann syndrome. Nat Genet *33*, 463-465.

Drummond, I.A. (2012). Cilia functions in development. Curr Opin Cell Biol *24*, 24-30.

Dubaissi, E., and Papalopulu, N. (2011). Embryonic frog epidermis: a model for the study of cell-cell interactions in the development of mucociliary disease. Disease models & mechanisms *4*, 179-192.

Duldulao, N.A., Lee, S., and Sun, Z. (2009). Cilia localization is essential for in vivo functions of the Joubert syndrome protein Arl13b/Scorpion. Development *136*, 4033-4042.

Duquette, A., Brais, B., Bouchard, J.P., and Mathieu, J. (2013). Clinical presentation and early evolution of spastic ataxia of Charlevoix-Saguenay. Movement disorders : official journal of the Movement Disorder Society *28*, 2011-2014.

Edwards, M., Mulcahy, D., and Turner, G. (1988). X-linked recessive inheritance of an orofaciodigital syndrome with partial expression in females and survival of affected males. Clinical genetics *34*, 325-332.

Eggenschwiler, J.T., and Anderson, K.V. (2007). Cilia and developmental signaling. Annu Rev Cell Dev Biol *23*, 345-373.

Eley, L., Yates, L.M., and Goodship, J.A. (2005). Cilia and disease. Curr Opin Genet Dev *15*, 308-314.

Essner, J.J., Amack, J.D., Nyholm, M.K., Harris, E.B., and Yost, H.J. (2005). Kupffer's vesicle is a ciliated organ of asymmetry in the zebrafish embryo that initiates left-right development of the brain, heart and gut. Development *132*, 1247-1260.

Essner, J.J., Vogan, K.J., Wagner, M.K., Tabin, C.J., Yost, H.J., and Brueckner, M. (2002). Conserved function for embryonic nodal cilia. Nature *418*, 37-38.

Estrada-Cuzcano, A., Roepman, R., Cremers, F.P., den Hollander, A.I., and Mans, D.A. (2012). Non-syndromic retinal ciliopathies: translating gene discovery into therapy. Hum Mol Genet *21*, R111-124.

Eswarakumar, V.P., Lax, I., and Schlessinger, J. (2005). Cellular signaling by fibroblast growth factor receptors. Cytokine Growth Factor Rev *16*, 139-149.

Evans, J.E., Snow, J.J., Gunnarson, A.L., Ou, G., Stahlberg, H., McDonald, K.L., and Scholey, J.M. (2006). Functional modulation of IFT kinesins extends the sensory repertoire of ciliated neurons in Caenorhabditis elegans. J Cell Biol *172*, 663-669.

Ezratty, E.J., Stokes, N., Chai, S., Shah, A.S., Williams, S.E., and Fuchs, E. (2011). A role for the primary cilium in Notch signaling and epidermal differentiation during skin development. Cell *145*, 1129-1141.

Fahim, A.T., Bowne, S.J., Sullivan, L.S., Webb, K.D., Williams, J.T., Wheaton, D.K., Birch, D.G., and Daiger, S.P. (2012). Polymorphic variation of RPGRIP1L and IQCB1 as modifiers of X-linked retinitis pigmentosa caused by mutations in RPGR. Advances in experimental medicine and biology *723*, 313-320.

Fakhro, K.A., Choi, M., Ware, S.M., Belmont, J.W., Towbin, J.A., Lifton, R.P., Khokha, M.K., and Brueckner, M. (2011). Rare copy number variations in congenital heart disease patients identify unique genes in left-right patterning. Proc Natl Acad Sci U S A *108*, 2915-2920.

Feistel, K., and Blum, M. (2006). Three types of cilia including a novel 9+4 axoneme on the notochordal plate of the rabbit embryo. Dev Dyn *235*, 3348-3358.

Ferkol, T.W., and Leigh, M.W. (2012). Ciliopathies: the central role of cilia in a spectrum of pediatric disorders. The Journal of pediatrics *160*, 366-371.

Ferrante, M.I., Giorgio, G., Feather, S.A., Bulfone, A., Wright, V., Ghiani, M., Selicorni, A., Gammaro, L., Scolari, F., Woolf, A.S.*, et al.* (2001). Identification of the gene for oral-facial-digital type I syndrome. Am J Hum Genet *68*, 569-576.

Ferrante, M.I., Romio, L., Castro, S., Collins, J.E., Goulding, D.A., Stemple, D.L., Woolf, A.S., and Wilson, S.W. (2009). Convergent extension movements and ciliary function are mediated by ofd1, a zebrafish orthologue of the human oral-facial-digital type 1 syndrome gene. Hum Mol Genet *18*, 289-303.

Ferrante, M.I., Zullo, A., Barra, A., Bimonte, S., Messaddeq, N., Studer, M., Dolle, P., and Franco, B. (2006). Oral-facial-digital type I protein is required for primary cilia formation and left-right axis specification. Nat Genet *38*, 112-117.

Field, M., Scheffer, I.E., Gill, D., Wilson, M., Christie, L., Shaw, M., Gardner, A., Glubb, G., Hobson, L., Corbett, M.*, et al.* (2012). Expanding the molecular basis and phenotypic spectrum of X-linked Joubert syndrome associated with OFD1 mutations. European journal of human genetics : EJHG *20*, 806-809.

Figuera, L.E., Rivas, F., and Cantu, J.M. (1993). Oral-facial-digital syndrome with fibular aplasia: a new variant. Clinical genetics *44*, 190-192.

Fliegauf, M., Benzing, T., and Omran, H. (2007). When cilia go bad: cilia defects and ciliopathies. Nat Rev Mol Cell Biol *8*, 880-893.

Fliegauf, M., and Omran, H. (2006). Novel tools to unravel molecular mechanisms in cilia-related disorders. Trends Genet *22*, 241-245.

Gabrielli, O., Ficcadenti, A., Fabrizzi, G., Perri, P., Mercuri, A., Coppa, G.V., and Giorgi, P. (1994). Child with oral, facial, digital, and skeletal anomalies and psychomotor delay: a new OFDS form? American journal of medical genetics *53*, 290-293.

Garcia-Blanco, M.A., Baraniak, A.P., and Lasda, E.L. (2004). Alternative splicing in disease and therapy. Nature biotechnology *22*, 535-546.

Garcia-Gonzalo, F.R., Corbit, K.C., Sirerol-Piquer, M.S., Ramaswami, G., Otto, E.A., Noriega, T.R., Seol, A.D., Robinson, J.F., Bennett, C.L., Josifova, D.J.*, et al.* (2011). A transition zone complex regulates mammalian ciliogenesis and ciliary membrane composition. Nat Genet *43*, 776-784.

Geerts, W.J., Vocking, K., Schoonen, N., Haarbosch, L., van Donselaar, E.G., Regan-Klapisz, E., and Post, J.A. (2011). Cobblestone HUVECs: a human model system for studying primary ciliogenesis. J Struct Biol *176*, 350-359.

Gerdes, J.M., Davis, E.E., and Katsanis, N. (2009). The vertebrate primary cilium in development, homeostasis, and disease. Cell *137*, 32-45.

Gerdes, J.M., and Katsanis, N. (2008). Ciliary function and Wnt signal modulation. Curr Top Dev Biol *85*, 175-195.

Gerdes, J.M., Liu, Y., Zaghloul, N.A., Leitch, C.C., Lawson, S.S., Kato, M., Beachy, P.A., Beales, P.L., DeMartino, G.N., Fisher, S.*, et al.* (2007). Disruption of the basal

body compromises proteasomal function and perturbs intracellular Wnt response. Nat Genet *39*, 1350-1360.

Gherman, A., Davis, E.E., and Katsanis, N. (2006). The ciliary proteome database: an integrated community resource for the genetic and functional dissection of cilia. Nat Genet *38*, 961-962.

Ghossaini, S.N., Hadi, U., and Tawil, A. (2002). Oral-facial-digital syndrome type II variant associated with congenital tongue lipoma. Oral surgery, oral medicine, oral pathology, oral radiology, and endodontics *94*, 324-327.

Ginger, M.L., Portman, N., and McKean, P.G. (2008). Swimming with protists: perception, motility and flagellum assembly. Nat Rev Microbiol *6*, 838-850.

Giudice, G. (2001). Conserved cellular and molecular mechanisms in development. Cell Biol Int *25*, 1081-1090.

Gluenz, E., Hoog, J.L., Smith, A.E., Dawe, H.R., Shaw, M.K., and Gull, K. (2010). Beyond 9+0: noncanonical axoneme structures characterize sensory cilia from protists to humans. FASEB J *24*, 3117-3121.

Goetz, S.C., and Anderson, K.V. (2010). The primary cilium: a signalling centre during vertebrate development. Nat Rev Genet *11*, 331-344.

Gong, Y., Mo, C., and Fraser, S.E. (2004). Planar cell polarity signalling controls cell division orientation during zebrafish gastrulation. Nature *430*, 689-693.

Gorden, N.T., Arts, H.H., Parisi, M.A., Coene, K.L., Letteboer, S.J., van Beersum, S.E., Mans, D.A., Hikida, A., Eckert, M., Knutzen, D.*, et al.* (2008). CC2D2A is mutated in Joubert syndrome and interacts with the ciliopathy-associated basal body protein CEP290. Am J Hum Genet *83*, 559-571.

Gurrieri, F., Franco, B., Toriello, H., and Neri, G. (2007). Oral-facial-digital syndromes: review and diagnostic guidelines. American journal of medical genetics Part A *143A*, 3314-3323.

Gurrieri, F., Sammito, V., Ricci, B., Iossa, M., Bellussi, A., and Neri, G. (1992). Possible new type of oral-facial-digital syndrome with retinal abnormalities: OFDS type (VIII). American journal of medical genetics *42*, 789-792.

Gustavson, K.H., Kreuger, A., and Petersson, P.O. (1971). Syndrome characterized by lingual malformation, polydactyly, tachypnea, and psychomotor retardation (Mohr syndrome). Clinical genetics *2*, 261-266.

Habbig, S., Bartram, M.P., Muller, R.U., Schwarz, R., Andriopoulos, N., Chen, S., Sagmuller, J.G., Hoehne, M., Burst, V., Liebau, M.C.*, et al.* (2011). NPHP4, a cilia-associated protein, negatively regulates the Hippo pathway. J Cell Biol *193*, 633-642.

Hagenlocher, C., Walentek, P., C, M.L., Thumberger, T., and Feistel, K. (2013). Ciliogenesis and cerebrospinal fluid flow in the developing Xenopus brain are regulated by foxj1. Cilia *2*, 2046-2530.

Han, Y.G., and Alvarez-Buylla, A. (2010). Role of primary cilia in brain development and cancer. Curr Opin Neurobiol *20*, 58-67.

Hari, L., Brault, V., Kleber, M., Lee, H.Y., Ille, F., Leimeroth, R., Paratore, C., Suter, U., Kemler, R., and Sommer, L. (2002). Lineage-specific requirements of beta-catenin in neural crest development. J Cell Biol *159*, 867-880.

Haumont, D., and Pelc, S. (1983). The Mohr syndrome: are there two variants? Clinical genetics *24*, 41-46.

Haycraft, C.J., Banizs, B., Aydin-Son, Y., Zhang, Q., Michaud, E.J., and Yoder, B.K. (2005). Gli2 and Gli3 localize to cilia and require the intraflagellar transport protein polaris for processing and function. PLoS Genet *1*, 1553-7404

Hayes, J.M., Kim, S.K., Abitua, P.B., Park, T.J., Herrington, E.R., Kitayama, A., Grow, M.W., Ueno, N., and Wallingford, J.B. (2007). Identification of novel ciliogenesis factors using a new in vivo model for mucociliary epithelial development. Dev Biol *312*, 115-130.

Helou, J., Otto, E.A., Attanasio, M., Allen, S.J., Parisi, M.A., Glass, I., Utsch, B., Hashmi, S., Fazzi, E., Omran, H.*, et al.* (2007). Mutation analysis of NPHP6/CEP290 in patients with Joubert syndrome and Senior-Loken syndrome. J Med Genet *44*, 657-663.

Hildebrandt, F., Benzing, T., and Katsanis, N. (2011). Ciliopathies. The New England journal of medicine *364*, 1533-1543.

Hildebrandt, F., and Zhou, W. (2007). Nephronophthisis-associated ciliopathies. Journal of the American Society of Nephrology : JASN *18*, 1855-1871.

Hilton, M.J., Tu, X., Cook, J., Hu, H., and Long, F. (2005). Ihh controls cartilage development by antagonizing Gli3, but requires additional effectors to regulate osteoblast and vascular development. Development *132*, 4339-4351.

Hirokawa, N., Tanaka, Y., Okada, Y., and Takeda, S. (2006). Nodal flow and the generation of left-right asymmetry. Cell *125*, 33-45.

Hogan, M.C., Griffin, M.D., Rossetti, S., Torres, V.E., Ward, C.J., and Harris, P.C. (2003). PKHDL1, a homolog of the autosomal recessive polycystic kidney disease gene, encodes a receptor with inducible T lymphocyte expression. Hum Mol Genet *12*, 685-698.

Hong, S.K., and Dawid, I.B. (2009). FGF-dependent left-right asymmetry patterning in zebrafish is mediated by Ier2 and Fibp1. Proc Natl Acad Sci U S A *106*, 2230-2235.

Hoover, A.N., Wynkoop, A., Zeng, H., Jia, J., Niswander, L.A., and Liu, A. (2008). C2cd3 is required for cilia formation and Hedgehog signaling in mouse. Development *135*, 4049-4058.

Horani, A., Brody, S.L., Ferkol, T.W., Shoseyov, D., Wasserman, M.G., Ta-shma, A., Wilson, K.S., Bayly, P.V., Amirav, I., Cohen-Cymberknoh, M.*, et al.* (2013). CCDC65 mutation causes primary ciliary dyskinesia with normal ultrastructure and hyperkinetic cilia. PLoS One *8*, 1932-6203.

Huangfu, D., and Anderson, K.V. (2005). Cilia and Hedgehog responsiveness in the mouse. Proc Natl Acad Sci U S A *102*, 11325-11330.

Huangfu, D., Liu, A., Rakeman, A.S., Murcia, N.S., Niswander, L., and Anderson, K.V. (2003). Hedgehog signalling in the mouse requires intraflagellar transport proteins. Nature *426*, 83-87.

Hufnagel, R.B., Ahmed, Z.M., Correa, Z.M., and Sisk, R.A. (2012). Gene therapy for Leber congenital amaurosis: advances and future directions. Graefe's archive for clinical and experimental ophthalmology = Albrecht von Graefes Archiv fur klinische und experimentelle Ophthalmologie *250*, 1117-1128.

Hughes, I., Thalmann, I., Thalmann, R., and Ornitz, D.M. (2006). Mixing model systems: using zebrafish and mouse inner ear mutants and other organ systems to unravel the mystery of otoconial development. Brain research *1091*, 58-74.

Hunkapiller, J., Singla, V., Seol, A., and Reiter, J.F. (2011). The ciliogenic protein Oral-Facial-Digital 1 regulates the neuronal differentiation of embryonic stem cells. Stem cells and development *20*, 831-841.

Ibanez-Tallon, I., Heintz, N., and Omran, H. (2003). To beat or not to beat: roles of cilia in development and disease. Hum Mol Genet *12 Spec No 1*, R27-35.

Ikegawa, S. (2006). Genetic analysis of skeletal dysplasia: recent advances and perspectives in the post-genome-sequence era. Journal of human genetics *51*, 581-586.

Inglis, P.N., Boroevich, K.A., and Leroux, M.R. (2006). Piecing together a ciliome. Trends Genet *22*, 491-500.

Insinna, C., and Besharse, J.C. (2008). Intraflagellar transport and the sensory outer segment of vertebrate photoreceptors. Dev Dyn *237*, 1982-1992.

Ishikawa, H., Kubo, A., Tsukita, S., and Tsukita, S. (2005). Odf2-deficient mother centrioles lack distal/subdistal appendages and the ability to generate primary cilia. Nat Cell Biol *7*, 517-524.

Ishikawa, H., and Marshall, W.F. (2011). Ciliogenesis: building the cell's antenna. Nat Rev Mol Cell Biol *12*, 222-234.

Ishikawa, H., Thompson, J., Yates, J.R., 3rd, and Marshall, W.F. (2012). Proteomic analysis of mammalian primary cilia. Curr Biol *22*, 414-419.

Iso, T., Kedes, L., and Hamamori, Y. (2003). HES and HERP families: multiple effectors of the Notch signaling pathway. J Cell Physiol *194*, 237-255.

Jamieson, R., and Collins, F. (1993). Oral-facial-digital syndrome and retinal abnormalities with autosomal recessive inheritance. American journal of medical genetics *47*, 304-306.

Jensen, C.G., Poole, C.A., McGlashan, S.R., Marko, M., Issa, Z.I., Vujcich, K.V., and Bowser, S.S. (2004). Ultrastructural, tomographic and confocal imaging of the chondrocyte primary cilium in situ. Cell Biol Int *28*, 101-110.

Jin, H., White, S.R., Shida, T., Schulz, S., Aguiar, M., Gygi, S.P., Bazan, J.F., and Nachury, M.V. (2010). The conserved Bardet-Biedl syndrome proteins assemble a coat that traffics membrane proteins to cilia. Cell *141*, 1208-1219.

Jodoin, J.N., Shboul, M., Albrecht, T.R., Lee, E., Wagner, E.J., Reversade, B., and Lee, L.A. (2013a). The snRNA-processing complex, Integrator, is required for ciliogenesis and dynein recruitment to the nuclear envelope via distinct mechanisms. Biology open *2*, 1390-1396.

Jodoin, J.N., Shboul, M., Sitaram, P., Zein-Sabatto, H., Reversade, B., Lee, E., and Lee, L.A. (2012). Human Asunder promotes dynein recruitment and centrosomal tethering to the nucleus at mitotic entry. Molecular biology of the cell *23*, 4713-4724.

Jodoin, J.N., Sitaram, P., Albrecht, T.R., May, S.B., Shboul, M., Lee, E., Reversade, B., Wagner, E.J., and Lee, L.A. (2013b). Nuclear-localized Asunder regulates cytoplasmic dynein localization via its role in the integrator complex. Molecular biology of the cell *24*, 2954-2965.

Johnson, E.T., Nicola, T., Roarty, K., Yoder, B.K., Haycraft, C.J., and Serra, R. (2008). Role for primary cilia in the regulation of mouse ovarian function. Dev Dyn *237*, 2053-2060.

Jones, C., and Chen, P. (2007). Planar cell polarity signaling in vertebrates. Bioessays *29*, 120-132.

Jones, C., Roper, V.C., Foucher, I., Qian, D., Banizs, B., Petit, C., Yoder, B.K., and Chen, P. (2008). Ciliary proteins link basal body polarization to planar cell polarity regulation. Nat Genet *40*, 69-77.

Jugessur, A., and Murray, J.C. (2005). Orofacial clefting: recent insights into a complex trait. Curr Opin Genet Dev *15*, 270-278.

Kalter, H., and Warkany, J. (1983). Medical progress. Congenital malformations: etiologic factors and their role in prevention (first of two parts). The New England journal of medicine *308*, 424-431.

Kalyan, M., Kanitkar, S., John, R., Gireesh, G., Bhate, A., and Mithun, M. (2012). Oro-facial-digital syndrome type II. The Journal of the Association of Physicians of India *60*, 50-52.

Kayserili, H., Uz, E., Niessen, C., Vargel, I., Alanay, Y., Tuncbilek, G., Yigit, G., Uyguner, O., Candan, S., Okur, H.*, et al.* (2009). ALX4 dysfunction disrupts craniofacial and epidermal development. Hum Mol Genet *18*, 4357-4366.

Keller, R., Davidson, L., Edlund, A., Elul, T., Ezin, M., Shook, D., and Skoglund, P. (2000). Mechanisms of convergence and extension by cell intercalation. Philosophical transactions of the Royal Society of London Series B, Biological sciences *355*, 897-922.

Kelly, M., and Chen, P. (2007). Shaping the mammalian auditory sensory organ by the planar cell polarity pathway. Int J Dev Biol *51*, 535-547.

Kerns, S.L., Schultz, K.M., Barry, K.A., Thorne, T.M., and McGarry, T.J. (2012). Geminin is required for zygotic gene expression at the Xenopus mid-blastula transition. PLoS One *7*, 1932-6203.

Khanna, H., Davis, E.E., Murga-Zamalloa, C.A., Estrada-Cuzcano, A., Lopez, I., den Hollander, A.I., Zonneveld, M.N., Othman, M.I., Waseem, N., Chakarova, C.F.*, et al.* (2009). A common allele in RPGRIP1L is a modifier of retinal degeneration in ciliopathies. Nat Genet *41*, 739-745.

Kim, G.H., and Han, J.K. (2005). JNK and ROKalpha function in the noncanonical Wnt/RhoA signaling pathway to regulate Xenopus convergent extension movements. Dev Dyn *232*, 958-968.

Kim, H.G., Herrick, S.R., Lemyre, E., Kishikawa, S., Salisz, J.A., Seminara, S., MacDonald, M.E., Bruns, G.A., Morton, C.C., Quade, B.J.*, et al.* (2005). Hypogonadotropic hypogonadism and cleft lip and palate caused by a balanced translocation producing haploinsufficiency for FGFR1. J Med Genet *42*, 666-672.

Kim, S., and Dynlacht, B.D. (2013). Assembling a primary cilium. Curr Opin Cell Biol *25*, 506-511.

Kim, Y.S., and Ho, S.B. (2010). Intestinal goblet cells and mucins in health and disease: recent insights and progress. Current gastroenterology reports *12*, 319-330.

Kimonis, V., Gold, J.A., Hoffman, T.L., Panchal, J., and Boyadjiev, S.A. (2007). Genetics of craniosynostosis. Semin Pediatr Neurol *14*, 150-161.

Ko, H.W., Norman, R.X., Tran, J., Fuller, K.P., Fukuda, M., and Eggenschwiler, J.T. (2010). Broad-minded links cell cycle-related kinase to cilia assembly and hedgehog signal transduction. Developmental cell *18*, 237-247.

Kobayashi, T., Tsang, W.Y., Li, J., Lane, W., and Dynlacht, B.D. (2011). Centriolar kinesin Kif24 interacts with CP110 to remodel microtubules and regulate ciliogenesis. Cell *145*, 914-925.

Komiya, Y., and Habas, R. (2008). Wnt signal transduction pathways. Organogenesis *4*, 68-75.

Kramer-Zucker, A.G., Olale, F., Haycraft, C.J., Yoder, B.K., Schier, A.F., and Drummond, I.A. (2005). Cilia-driven fluid flow in the zebrafish pronephros, brain and Kupffer's vesicle is required for normal organogenesis. Development *132*, 1907-1921.

Krawczak, M., Chuzhanova, N.A., Stenson, P.D., Johansen, B.N., Ball, E.V., and Cooper, D.N. (2000). Changes in primary DNA sequence complexity influence the phenotypic consequences of mutations in human gene regulatory regions. Human genetics *107*, 362-365.

Kreiling, J.A., Prabhat, Williams, G., and Creton, R. (2007). Analysis of Kupffer's vesicle in zebrafish embryos using a cave automated virtual environment. Dev Dyn *236*, 1963-1969.

Lee, H., O'Connor, B.D., Merriman, B., Funari, V.A., Homer, N., Chen, Z., Cohn, D.H., and Nelson, S.F. (2009). Improving the efficiency of genomic loci capture using oligonucleotide arrays for high throughput resequencing. BMC genomics *10*, 1471-2164.

Lee, J.E., and Gleeson, J.G. (2011). A systems-biology approach to understanding the ciliopathy disorders. Genome medicine *3*, 1756-1994X.

Lee, J.E., Silhavy, J.L., Zaki, M.S., Schroth, J., Bielas, S.L., Marsh, S.E., Olvera, J., Brancati, F., Iannicelli, M., Ikegami, K.*, et al.* (2012). CEP41 is mutated in Joubert syndrome and is required for tubulin glutamylation at the cilium. Nat Genet *44*, 193-199.

Lee, L.A., Lee, E., Anderson, M.A., Vardy, L., Tahinci, E., Ali, S.M., Kashevsky, H., Benasutti, M., Kirschner, M.W., and Orr-Weaver, T.L. (2005). Drosophila genome-scale screen for PAN GU kinase substrates identifies Mat89Bb as a cell cycle regulator. Developmental cell *8*, 435-442.

Leightner, A.C., Hommerding, C.J., Peng, Y., Salisbury, J.L., Gainullin, V.G., Czarnecki, P.G., Sussman, C.R., and Harris, P.C. (2013). The Meckel syndrome protein meckelin (TMEM67) is a key regulator of cilia function but is not required for tissue planar polarity. Hum Mol Genet *22*, 2024-2040.

Leitch, C.C., Zaghloul, N.A., Davis, E.E., Stoetzel, C., Diaz-Font, A., Rix, S., Alfadhel, M., Lewis, R.A., Eyaid, W., Banin, E.*, et al.* (2008). Hypomorphic mutations in syndromic encephalocele genes are associated with Bardet-Biedl syndrome. Nat Genet *40*, 443-448.

Levin, M. (2005). Left-right asymmetry in embryonic development: a comprehensive review. Mechanisms of development *122*, 3-25.

Li, F., Chong, Z.Z., and Maiese, K. (2006). Winding through the WNT pathway during cellular development and demise. Histol Histopathol *21*, 103-124.

Liang, J.O., Etheridge, A., Hantsoo, L., Rubinstein, A.L., Nowak, S.J., Izpisua Belmonte, J.C., and Halpern, M.E. (2000). Asymmetric nodal signaling in the zebrafish diencephalon positions the pineal organ. Development *127*, 5101-5112.

Lindemann, C.B., and Lesich, K.A. (2010). Flagellar and ciliary beating: the proven and the possible. J Cell Sci *123*, 519-528.

Lipinski, R.J., Song, C., Sulik, K.K., Everson, J.L., Gipp, J.J., Yan, D., Bushman, W., and Rowland, I.J. (2010). Cleft lip and palate results from Hedgehog signaling antagonism in the mouse: Phenotypic characterization and clinical implications. Birth Defects Res A Clin Mol Teratol *88*, 232-240.

Liu, Y., Pathak, N., Kramer-Zucker, A., and Drummond, I.A. (2007). Notch signaling controls the differentiation of transporting epithelia and multiciliated cells in the zebrafish pronephros. Development *134*, 1111-1122.

Liu, Y.B., Xing, Z.K., Yang, L., Li, L.J., Liu, Y., and Liu, X.W. (2012). Bilateral cleft lip: a potential variant form of orofaciodigital syndrome type II? Journal of oral and maxillofacial surgery : official journal of the American Association of Oral and Maxillofacial Surgeons *70*, 2669-2673.

Long, S., Ahmad, N., and Rebagliati, M. (2003). The zebrafish nodal-related gene southpaw is required for visceral and diencephalic left-right asymmetry. Development *130*, 2303-2316.

Lopes, S.S., Lourenco, R., Pacheco, L., Moreno, N., Kreiling, J., and Saude, L. (2010). Notch signalling regulates left-right asymmetry through ciliary length control. Development *137*, 3625-3632.

Lopez, E., Thauvin-Robinet, C., Reversade, B., Khartoufi, N.E., Devisme, L., Holder, M., Ansart-Franquet, H., Avila, M., Lacombe, D., Kleinfinger, P*., et al.* (2013). C5orf42 is the major gene responsible for OFD syndrome type VI. Human genetics.

Louie, C.M., Caridi, G., Lopes, V.S., Brancati, F., Kispert, A., Lancaster, M.A., Schlossman, A.M., Otto, E.A., Leitges, M., Grone, H.J*., et al.* (2010). AHI1 is required for photoreceptor outer segment development and is a modifier for retinal degeneration in nephronophthisis. Nat Genet *42*, 175-180.

Lucker, B.F., Behal, R.H., Qin, H., Siron, L.C., Taggart, W.D., Rosenbaum, J.L., and Cole, D.G. (2005). Characterization of the intraflagellar transport complex B core: direct interaction of the IFT81 and IFT74/72 subunits. J Biol Chem *280*, 27688-27696.

Lunt, S.C., Haynes, T., and Perkins, B.D. (2009). Zebrafish ift57, ift88, and ift172 intraflagellar transport mutants disrupt cilia but do not affect hedgehog signaling. Dev Dyn *238*, 1744-1759.

Maffucci, T., Raimondi, C., Abu-Hayyeh, S., Dominguez, V., Sala, G., Zachary, I., and Falasca, M. (2009). A phosphoinositide 3-kinase/phospholipase Cgamma1 pathway regulates fibroblast growth factor-induced capillary tube formation. PLoS One *4*, 1932-6203.

Malicki, J., Avanesov, A., Li, J., Yuan, S., and Sun, Z. (2011). Analysis of cilia structure and function in zebrafish. Methods in cell biology *101*, 39-74.

Malicki, J., Schier, A.F., Solnica-Krezel, L., Stemple, D.L., Neuhauss, S.C., Stainier, D.Y., Abdelilah, S., Rangini, Z., Zwartkruis, F., and Driever, W. (1996). Mutations affecting development of the zebrafish ear. Development *123*, 275-283.

Mangold, E., Ludwig, K.U., and Nothen, M.M. (2011). Breakthroughs in the genetics of orofacial clefting. Trends in molecular medicine *17*, 725-733.

Mans, D.A., Voest, E.E., and Giles, R.H. (2008). All along the watchtower: is the cilium a tumor suppressor organelle? Biochim Biophys Acta *1786*, 114-125.

Marcet, B., Chevalier, B., Luxardi, G., Coraux, C., Zaragosi, L.E., Cibois, M., Robbe-Sermesant, K., Jolly, T., Cardinaud, B., Moreilhon, C*., et al.* (2011). Control of vertebrate multiciliogenesis by miR-449 through direct repression of the Delta/Notch pathway. Nat Cell Biol *13*, 693-699.

Marques, S.R., Lee, Y., Poss, K.D., and Yelon, D. (2008). Reiterative roles for FGF signaling in the establishment of size and proportion of the zebrafish heart. Dev Biol *321*, 397-406.

Marshall, W.F., and Nonaka, S. (2006). Cilia: tuning in to the cell's antenna. Curr Biol *16*, R604-614.

Martin, C., Babin, J.P., Camier, P., Lorin, J.C., and Cazauran, J.M. (1971). [Orofaciodigital syndrome with severe cardiopathy]. Arch Fr Pediatr *28*, 992-993.

Martinot, V.L., Manouvrier, S., Anastassov, Y., Ribiere, J., and Pellerin, P.N. (1994). Orodigitofacial syndromes type I and II: clinical and surgical studies. The Cleft palate-craniofacial journal : official publication of the American Cleft Palate-Craniofacial Association *31*, 401-408.

Mason, I. (2007). Initiation to end point: the multiple roles of fibroblast growth factors in neural development. Nature reviews Neuroscience *8*, 583-596.

Masyuk, A.I., Masyuk, T.V., and LaRusso, N.F. (2008). Cholangiocyte primary cilia in liver health and disease. Dev Dyn *237*, 2007-2012.

Masyuk, T.V., Huang, B.Q., Ward, C.J., Masyuk, A.I., Yuan, D., Splinter, P.L., Punyashthiti, R., Ritman, E.L., Torres, V.E., Harris, P.C.*, et al.* (2003). Defects in cholangiocyte fibrocystin expression and ciliary structure in the PCK rat. Gastroenterology *125*, 1303-1310.

Matera, A.G., Terns, R.M., and Terns, M.P. (2007). Non-coding RNAs: lessons from the small nuclear and small nucleolar RNAs. Nat Rev Mol Cell Biol *8*, 209-220.

Matthews, H.K., Marchant, L., Carmona-Fontaine, C., Kuriyama, S., Larrain, J., Holt, M.R., Parsons, M., and Mayor, R. (2008). Directional migration of neural crest cells in vivo is regulated by Syndecan-4/Rac1 and non-canonical Wnt signaling/RhoA. Development *135*, 1771-1780.

May-Simera, H.L., and Kelley, M.W. (2012). Cilia, Wnt signaling, and the cytoskeleton. Cilia *1*, 2046-2530

Mayer, U., Kuller, A., Daiber, P.C., Neudorf, I., Warnken, U., Schnolzer, M., Frings, S., and Mohrlen, F. (2009). The proteome of rat olfactory sensory cilia. Proteomics *9*, 322-334.

McDermott, K.M., Liu, B.Y., Tlsty, T.D., and Pazour, G.J. (2010). Primary cilia regulate branching morphogenesis during mammary gland development. Curr Biol *20*, 731-737.

McEwen, D.P., Jenkins, P.M., and Martens, J.R. (2008). Olfactory cilia: our direct neuronal connection to the external world. Curr Top Dev Biol *85*, 333-370.

McGrath, J., and Brueckner, M. (2003). Cilia are at the heart of vertebrate left-right asymmetry. Curr Opin Genet Dev *13*, 385-392.

McGrath, J., Somlo, S., Makova, S., Tian, X., and Brueckner, M. (2003). Two populations of node monocilia initiate left-right asymmetry in the mouse. Cell *114*, 61-73.

McIntyre, J.C., Davis, E.E., Joiner, A., Williams, C.L., Tsai, I.C., Jenkins, P.M., McEwen, D.P., Zhang, L., Escobado, J., Thomas, S.*, et al.* (2012). Gene therapy rescues cilia defects and restores olfactory function in a mammalian ciliopathy model. Nature medicine *18*, 1423-1428.

Melby, A.E., Warga, R.M., and Kimmel, C.B. (1996). Specification of cell fates at the dorsal margin of the zebrafish gastrula. Development *122*, 2225-2237.

Menezes, L.F., and Germino, G.G. (2009). Polycystic kidney disease, cilia, and planar polarity. Methods in cell biology *94*, 273-297.

Michaud, E.J., and Yoder, B.K. (2006). The primary cilium in cell signaling and cancer. Cancer research *66*, 6463-6467.

Mir, A., Kofron, M., Zorn, A.M., Bajzer, M., Haque, M., Heasman, J., and Wylie, C.C. (2007). FoxI1e activates ectoderm formation and controls cell position in the Xenopus blastula. Development *134*, 779-788.

Mitchell, B., Jacobs, R., Li, J., Chien, S., and Kintner, C. (2007). A positive feedback mechanism governs the polarity and motion of motile cilia. Nature *447*, 97-101.

Mitchell, B., Stubbs, J.L., Huisman, F., Taborek, P., Yu, C., and Kintner, C. (2009). The PCP pathway instructs the planar orientation of ciliated cells in the Xenopus larval skin. Curr Biol *19*, 924-929.

Montcouquiol, M., Rachel, R.A., Lanford, P.J., Copeland, N.G., Jenkins, N.A., and Kelley, M.W. (2003). Identification of Vangl2 and Scrb1 as planar polarity genes in mammals. Nature *423*, 173-177.

Moran-Barroso, V., Valdes Flores, M., Garcia-Cavazos, R., Kofman-Alfaro, S., and Saavedra-Ontiveros, D. (1998). Oral-facial-digital (OFD) syndrome with associated features: a new syndrome or genetic heterogeneity and variability? Clinical dysmorphology *7*, 55-57.

Moran, D.T., Rowley, J.C., 3rd, Jafek, B.W., and Lovell, M.A. (1982). The fine structure of the olfactory mucosa in man. J Neurocytol *11*, 721-746.

Moser, J.J., Fritzler, M.J., Ou, Y., and Rattner, J.B. (2010). The PCM-basal body/primary cilium coalition. Semin Cell Dev Biol *21*, 148-155.

Muller, U. (2008). Cadherins and mechanotransduction by hair cells. Curr Opin Cell Biol *20*, 557-566.

Nachury, M.V., Loktev, A.V., Zhang, Q., Westlake, C.J., Peranen, J., Merdes, A., Slusarski, D.C., Scheller, R.H., Bazan, J.F., Sheffield, V.C.*, et al.* (2007). A core complex of BBS proteins cooperates with the GTPase Rab8 to promote ciliary membrane biogenesis. Cell *129*, 1201-1213.

Nagai, K., Nagao, M., Yanai, S., Minagawa, K., Takahashi, Y., Takekoshi, Y., Ishizaka, A., Matsuzono, Y., Kobayashi, O., and Itagaki, T. (1998). Oral-facial-digital syndrome type IX in a patient with Dandy-Walker malformation. J Med Genet *35*, 342-344.

Nakayama, Y., Miyake, A., Nakagawa, Y., Mido, T., Yoshikawa, M., Konishi, M., and Itoh, N. (2008). Fgf19 is required for zebrafish lens and retina development. Dev Biol *313*, 752-766.

Nauli, S.M., Alenghat, F.J., Luo, Y., Williams, E., Vassilev, P., Li, X., Elia, A.E., Lu, W., Brown, E.M., Quinn, S.J.*, et al.* (2003). Polycystins 1 and 2 mediate mechanosensation in the primary cilium of kidney cells. Nat Genet *33*, 129-137.

Nayak, G.D., Ratnayaka, H.S., Goodyear, R.J., and Richardson, G.P. (2007). Development of the hair bundle and mechanotransduction. Int J Dev Biol *51*, 597-608.

Neugebauer, J.M., Amack, J.D., Peterson, A.G., Bisgrove, B.W., and Yost, H.J. (2009). FGF signalling during embryo development regulates cilia length in diverse epithelia. Nature *458*, 651-654.

Newport, J., and Kirschner, M. (1982). A major developmental transition in early Xenopus embryos: II. Control of the onset of transcription. Cell *30*, 687-696.

Nie, X., Luukko, K., and Kettunen, P. (2006). FGF signalling in craniofacial development and developmental disorders. Oral Dis *12*, 102-111.

Nigg, E.A., and Raff, J.W. (2009). Centrioles, centrosomes, and cilia in health and disease. Cell *139*, 663-678.

Nissim-Rafinia, M., and Kerem, B. (2002). Splicing regulation as a potential genetic modifier. Trends Genet *18*, 123-127.

Nissim-Rafinia, M., and Kerem, B. (2005). The splicing machinery is a genetic modifier of disease severity. Trends Genet *21*, 480-483.

Nogales-Cadenas, R., Abascal, F., Diez-Perez, J., Carazo, J.M., and Pascual-Montano, A. (2009). CentrosomeDB: a human centrosomal proteins database. Nucleic acids research *37*, D175-180.

Nonaka, S., Tanaka, Y., Okada, Y., Takeda, S., Harada, A., Kanai, Y., Kido, M., and Hirokawa, N. (1998). Randomization of left-right asymmetry due to loss of nodal cilia generating leftward flow of extraembryonic fluid in mice lacking KIF3B motor protein. Cell *95*, 829-837.

Nowaczyk, M.J., Zeesman, S., Whelan, D.T., Wright, V., and Feather, S.A. (2003). Oral-facial-digital syndrome VII is oral-facial-digital syndrome I: a clarification. American journal of medical genetics Part A *123A*, 179-182.

Nozawa, Y.I., Lin, C., and Chuang, P.T. (2013). Hedgehog signaling from the primary cilium to the nucleus: an emerging picture of ciliary localization, trafficking and transduction. Curr Opin Genet Dev *23*, 429-437.

Nusslein-Volhard, C., and Wieschaus, E. (1980). Mutations affecting segment number and polarity in Drosophila. Nature *287*, 795-801.

O'Connor, B.D., Merriman, B., and Nelson, S.F. (2010). SeqWare Query Engine: storing and searching sequence data in the cloud. BMC bioinformatics *12*, 1471-2105.

Oh, E.C., and Katsanis, N. (2012). Cilia in vertebrate development and disease. Development *139*, 443-448.

Okada, Y., Takeda, S., Tanaka, Y., Izpisua Belmonte, J.C., and Hirokawa, N. (2005). Mechanism of nodal flow: a conserved symmetry breaking event in left-right axis determination. Cell *121*, 633-644.

Omran, H. (2010). NPHP proteins: gatekeepers of the ciliary compartment. J Cell Biol *190*, 715-717.

Orstavik, K.H., Lindemann, R., Solberg, L.A., Foerster, A., and Sorland, S.J. (1992). Congenital heart defects, hamartomas of the tongue and polysyndactyly in a sister and brother. Clinical genetics *42*, 19-21.

Otto, E.A., Hurd, T.W., Airik, R., Chaki, M., Zhou, W., Stoetzel, C., Patil, S.B., Levy, S., Ghosh, A.K., Murga-Zamalloa, C.A.*, et al.* (2010). Candidate exome capture identifies mutation of SDCCAG8 as the cause of a retinal-renal ciliopathy. Nat Genet *42*, 840-850.

Pan, A., Chang, L., Nguyen, A., and James, A.W. (2013). A review of hedgehog signaling in cranial bone development. Front Physiol *4*, 1664-1042X.

Pan, J., and Snell, W. (2007). The primary cilium: keeper of the key to cell division. Cell *129*, 1255-1257.

Pan, J., You, Y., Huang, T., and Brody, S.L. (2007). RhoA-mediated apical actin enrichment is required for ciliogenesis and promoted by Foxj1. J Cell Sci *120*, 1868-1876.

Panigrahi, I., Das, R.R., Kulkarni, K.P., and Marwaha, R.K. (2013). Overlapping phenotypes in OFD type II and OFD type VI: report of two cases. Clinical dysmorphology *22*, 109-114.

Park, T.J., Haigo, S.L., and Wallingford, J.B. (2006). Ciliogenesis defects in embryos lacking inturned or fuzzy function are associated with failure of planar cell polarity and Hedgehog signaling. Nat Genet *38*, 303-311.

Park, T.J., Mitchell, B.J., Abitua, P.B., Kintner, C., and Wallingford, J.B. (2008). Dishevelled controls apical docking and planar polarization of basal bodies in ciliated epithelial cells. Nat Genet *40*, 871-879.

Pasca di Magliano, M., and Hebrok, M. (2003). Hedgehog signalling in cancer formation and maintenance. Nat Rev Cancer *3*, 903-911.

Patapoutian, A., and Reichardt, L.F. (2000). Roles of Wnt proteins in neural development and maintenance. Curr Opin Neurobiol *10*, 392-399.

Patzke, S., Redick, S., Warsame, A., Murga-Zamalloa, C.A., Khanna, H., Doxsey, S., and Stokke, T. (2010). CSPP is a ciliary protein interacting with Nephrocystin 8 and required for cilia formation. Molecular biology of the cell *21*, 2555-2567.

Pecina-Slaus, N. (2010). Wnt signal transduction pathway and apoptosis: a review. Cancer Cell Int *10*, 1475-2867.

Pedersen, L.B., and Rosenbaum, J.L. (2008). Intraflagellar transport (IFT) role in ciliary assembly, resorption and signalling. Curr Top Dev Biol *85*, 23-61.

Pedersen, L.B., Schroder, J.M., Satir, P., and Christensen, S.T. (2012). The ciliary cytoskeleton. Comprehensive Physiology *2*, 779-803.

Perrault, I., Saunier, S., Hanein, S., Filhol, E., Bizet, A.A., Collins, F., Salih, M.A., Gerber, S., Delphin, N., Bigot, K.*, et al.* (2012). Mainzer-Saldino syndrome is a ciliopathy caused by IFT140 mutations. Am J Hum Genet *90*, 864-870.

Phadke, S.R., Pahi, J., Pandey, A., and Agarwal, S.S. (1999). Oral-facial-digital syndrome with acromelic short stature: a new variant--overlap with Ellis Van Creveld syndrome. Clinical dysmorphology *8*, 185-188.

Phillips, M.I. (2012). Gene, Stem Cell, and Future Therapies for Orphan Diseases. Clinical pharmacology and therapeutics *92*, 182-192.

Pirvola, U., Spencer-Dene, B., Xing-Qun, L., Kettunen, P., Thesleff, I., Fritzsch, B., Dickson, C., and Ylikoski, J. (2000). FGF/FGFR-2(IIIb) signaling is essential for inner ear morphogenesis. J Neurosci *20*, 6125-6134.

Pochynyuk, O., Zaika, O., O'Neil, R.G., and Mamenko, M. (2013). Novel insights into TRPV4 function in the kidney. Pflugers Archiv : European journal of physiology *465*, 177-186.

Pradhan, M., Manisha, and Sankar, H. (2007). Short humerus: an additional antenatal sonographic feature of OFDS type II. Journal of clinical ultrasound : JCU *35*, 390-394.

Praetorius, H.A., and Spring, K.R. (2005). A physiological view of the primary cilium. Annu Rev Physiol *67*, 515-529.

Pratt, K.G., and Khakhalin, A.S. (2013). Modeling human neurodevelopmental disorders in the Xenopus tadpole: from mechanisms to therapeutic targets. Disease models & mechanisms *6*, 1057-1065.

Prpic, I., Cekada, S., and Franulovic, J. (1995). Mohr syndrome (oro-facial-digital syndrome II)--a familial case with different phenotypic findings. Clinical genetics *48*, 304-307.

Quarmby, L.M., and Parker, J.D. (2005). Cilia and the cell cycle? J Cell Biol *169*, 707-710.

Quigley, I.K., Stubbs, J.L., and Kintner, C. (2011). Specification of ion transport cells in the Xenopus larval skin. Development *138*, 705-714.

Raya, A., and Izpisua Belmonte, J.C. (2006). Left-right asymmetry in the vertebrate embryo: from early information to higher-level integration. Nat Rev Genet *7*, 283-293.

Reardon, W., Harbord, M.G., Hall-Craggs, M.A., Kendall, B., Brett, E.M., and Baraitser, M. (1989). Central nervous system malformations in Mohr's syndrome. J Med Genet *26*, 659-663.

Reversade, B., Escande-Beillard, N., Dimopoulou, A., Fischer, B., Chng, S.C., Li, Y., Shboul, M., Tham, P.Y., Kayserili, H., Al-Gazali, L.*, et al.* (2009). Mutations in PYCR1 cause cutis laxa with progeroid features. Nat Genet *41*, 1016-1021.

Reya, T., and Clevers, H. (2005). Wnt signalling in stem cells and cancer. Nature *434*, 843-850.

Richardson, G.P., de Monvel, J.B., and Petit, C. (2011). How the genetics of deafness illuminates auditory physiology. Annu Rev Physiol *73*, 311-334.

Riley, B.B., Zhu, C., Janetopoulos, C., and Aufderheide, K.J. (1997). A critical period of ear development controlled by distinct populations of ciliated cells in the zebrafish. Dev Biol *191*, 191-201.

Riley, B.M., Mansilla, M.A., Ma, J., Daack-Hirsch, S., Maher, B.S., Raffensperger, L.M., Russo, E.T., Vieira, A.R., Dode, C., Mohammadi, M.*, et al.* (2007). Impaired FGF signaling contributes to cleft lip and palate. Proc Natl Acad Sci U S A *104*, 4512-4517.

Rix, S., Calmont, A., Scambler, P.J., and Beales, P.L. (2011). An Ift80 mouse model of short rib polydactyly syndromes shows defects in hedgehog signalling without loss or malformation of cilia. Hum Mol Genet *20*, 1306-1314.

Rohatgi, R., Milenkovic, L., and Scott, M.P. (2007). Patched1 regulates hedgehog signaling at the primary cilium. Science *317*, 372-376.

Rohatgi, R., and Snell, W.J. (2010). The ciliary membrane. Curr Opin Cell Biol *22*, 541-546.

Ross, A.J., May-Simera, H., Eichers, E.R., Kai, M., Hill, J., Jagger, D.J., Leitch, C.C., Chapple, J.P., Munro, P.M., Fisher, S.*, et al.* (2005). Disruption of Bardet-Biedl syndrome ciliary proteins perturbs planar cell polarity in vertebrates. Nat Genet *37*, 1135-1140.

Rupp, R.A., Singhal, N., and Veenstra, G.J. (2002). When the embryonic genome flexes its muscles. European journal of biochemistry / FEBS *269*, 2294-2299.

Saito-Diaz, K., Chen, T.W., Wang, X., Thorne, C.A., Wallace, H.A., Page-McCaw, A., and Lee, E. (2013). The way Wnt works: components and mechanism. Growth Factors *31*, 1-31.

Sakai, N., Nakakita, N., Yamazaki, Y., Ui, K., and Uchinuma, E. (2002). Oral-facial-digital syndrome type II (Mohr syndrome): clinical and genetic manifestations. The Journal of craniofacial surgery *13*, 321-326.

Sang, L., Miller, J.J., Corbit, K.C., Giles, R.H., Brauer, M.J., Otto, E.A., Baye, L.M., Wen, X., Scales, S.J., Kwong, M.*, et al.* (2011). Mapping the NPHP-JBTS-MKS protein network reveals ciliopathy disease genes and pathways. Cell *145*, 513-528.

Satir, P. (1995). Landmarks in cilia research from Leeuwenhoek to us. Cell Motil Cytoskeleton *32*, 90-94.

Satir, P., and Christensen, S.T. (2007). Overview of structure and function of mammalian cilia. Annu Rev Physiol *69*, 377-400.

Sayer, J.A., Otto, E.A., O'Toole, J.F., Nurnberg, G., Kennedy, M.A., Becker, C., Hennies, H.C., Helou, J., Attanasio, M., Fausett, B.V.*, et al.* (2006). The centrosomal protein nephrocystin-6 is mutated in Joubert syndrome and activates transcription factor ATF4. Nat Genet *38*, 674-681.

Schibler, A., and Malicki, J. (2007). A screen for genetic defects of the zebrafish ear. Mechanisms of development *124*, 592-604.

Schmidt, K.N., Kuhns, S., Neuner, A., Hub, B., Zentgraf, H., and Pereira, G. (2012). Cep164 mediates vesicular docking to the mother centriole during early steps of ciliogenesis. J Cell Biol *199*, 1083-1101.

Schneider, L., Cammer, M., Lehman, J., Nielsen, S.K., Guerra, C.F., Veland, I.R., Stock, C., Hoffmann, E.K., Yoder, B.K., Schwab, A.*, et al.* (2010). Directional cell migration and chemotaxis in wound healing response to PDGF-AA are coordinated by the primary cilium in fibroblasts. Cellular physiology and biochemistry : international journal of experimental cellular physiology, biochemistry, and pharmacology *25*, 279-292.

Schneider, L., Clement, C.A., Teilmann, S.C., Pazour, G.J., Hoffmann, E.K., Satir, P., and Christensen, S.T. (2005). PDGFRalphaalpha signaling is regulated through the primary cilium in fibroblasts. Curr Biol *15*, 1861-1866.

Scholey, J.M. (2008). Intraflagellar transport motors in cilia: moving along the cell's antenna. J Cell Biol *180*, 23-29.

Scholey, J.M., and Anderson, K.V. (2006). Intraflagellar transport and cilium-based signaling. Cell *125*, 439-442.

Schweickert, A., Weber, T., Beyer, T., Vick, P., Bogusch, S., Feistel, K., and Blum, M. (2007). Cilia-driven leftward flow determines laterality in Xenopus. Curr Biol *17*, 60-66.

Shah, A.S., Ben-Shahar, Y., Moninger, T.O., Kline, J.N., and Welsh, M.J. (2009). Motile cilia of human airway epithelia are chemosensory. Science *325*, 1131-1134.

Shaheen, R., Faqeih, E., Alshammari, M.J., Swaid, A., Al-Gazali, L., Mardawi, E., Ansari, S., Sogaty, S., Seidahmed, M.Z., AlMotairi, M.I.*, et al.* (2013). Genomic analysis of Meckel-Gruber syndrome in Arabs reveals marked genetic heterogeneity and novel candidate genes. European journal of human genetics : EJHG *21*, 762-768.

Shamseldin, H.E., Rajab, A., Alhashem, A., Shaheen, R., Al-Shidi, T., Alamro, R., Al Harassi, S., and Alkuraya, F.S. (2013). Mutations in DDX59 implicate RNA helicase in the pathogenesis of orofaciodigital syndrome. Am J Hum Genet *93*, 555-560.

Sharma, N., Berbari, N.F., and Yoder, B.K. (2008). Ciliary dysfunction in developmental abnormalities and diseases. Curr Top Dev Biol *85*, 371-427.

Shashi, V., Clark, P., Rogol, A.D., and Wilson, W.G. (1995). Absent pituitary gland in two brothers with an oral-facial-digital syndrome resembling OFDS II and VI: a new type of OFDS? American journal of medical genetics *57*, 22-26.

Shiratori, H., and Hamada, H. (2006). The left-right axis in the mouse: from origin to morphology. Development *133*, 2095-2104.

Siebert, J.R. (2008). The oral-facial-digital syndromes. Handbook of clinical neurology *87*, 341-351.

Siggins, S.L., Nguyen, N.Y., McCormack, M.P., Vasudevan, S., Villani, R., Jane, S.M., Wainwright, B.J., and Curtis, D.J. (2009). The Hedgehog receptor Patched1 regulates myeloid and lymphoid progenitors by distinct cell-extrinsic mechanisms. Blood *114*, 995-1004.

Silengo, M.C., Bell, G.L., Biagioli, M., and Franceschini, P. (1987). Oro-facial-digital syndrome II. Transitional type between the Mohr and the Majewski syndromes: report of two new cases. Clinical genetics *31*, 331-336.

Simms, R.J., Hynes, A.M., Eley, L., Inglis, D., Chaudhry, B., Dawe, H.R., and Sayer, J.A. (2012). Modelling a ciliopathy: Ahi1 knockdown in model systems reveals an essential role in brain, retinal, and renal development. Cellular and molecular life sciences : CMLS *69*, 993-1009.

Simons, M., Gloy, J., Ganner, A., Bullerkotte, A., Bashkurov, M., Kronig, C., Schermer, B., Benzing, T., Cabello, O.A., Jenny, A.*, et al.* (2005). Inversin, the gene product mutated in nephronophthisis type II, functions as a molecular switch between Wnt signaling pathways. Nat Genet *37*, 537-543.

Singla, V., and Reiter, J.F. (2006). The primary cilium as the cell's antenna: signaling at a sensory organelle. Science *313*, 629-633.

Singla, V., Romaguera-Ros, M., Garcia-Verdugo, J.M., and Reiter, J.F. (2010). Ofd1, a human disease gene, regulates the length and distal structure of centrioles. Developmental cell *18*, 410-424.

Sitaram, P., Anderson, M.A., Jodoin, J.N., Lee, E., and Lee, L.A. (2012). Regulation of dynein localization and centrosome positioning by Lis-1 and asunder during Drosophila spermatogenesis. Development *139*, 2945-2954.

Sitaram, P., Merkle, J.A., Lee, E., and Lee, L.A. (2013). Asunder is required for dynein localization and dorsal fate determination during Drosophila oogenesis. Dev Biol *383*, 42-52.

Slaney, S.F., Oldridge, M., Hurst, J.A., Moriss-Kay, G.M., Hall, C.M., Poole, M.D., and Wilkie, A.O. (1996). Differential effects of FGFR2 mutations on syndactyly and cleft palate in Apert syndrome. Am J Hum Genet *58*, 923-932.

Sloboda, R.D. (2005). Intraflagellar transport and the flagellar tip complex. J Cell Biochem *94*, 266-272.

Smith, K.R., Kieserman, E.K., Wang, P.I., Basten, S.G., Giles, R.H., Marcotte, E.M., and Wallingford, J.B. (2011). A role for central spindle proteins in cilia structure and function. Cytoskeleton *68*, 112-124.

Snell, W.J., Pan, J., and Wang, Q. (2004). Cilia and flagella revealed: from flagellar assembly in Chlamydomonas to human obesity disorders. Cell *117*, 693-697.

Song, Z., Yue, W., Wei, B., Wang, N., Li, T., Guan, L., Shi, S., Zeng, Q., Pei, X., and Chen, L. (2011). Sonic hedgehog pathway is essential for maintenance of cancer stem-like cells in human gastric cancer. PLoS One *6*, 1932-6203.

Spektor, A., Tsang, W.Y., Khoo, D., and Dynlacht, B.D. (2007). Cep97 and CP110 suppress a cilia assembly program. Cell *130*, 678-690.

Srour, M., Hamdan, F.F., Schwartzentruber, J.A., Patry, L., Ospina, L.H., Shevell, M.I., Desilets, V., Dobrzeniecka, S., Mathonnet, G., Lemyre, E.*, et al.* (2012a).

Mutations in TMEM231 cause Joubert syndrome in French Canadians. J Med Genet *49*, 636-641.

Srour, M., Schwartzentruber, J., Hamdan, F.F., Ospina, L.H., Patry, L., Labuda, D., Massicotte, C., Dobrzeniecka, S., Capo-Chichi, J.M., Papillon-Cavanagh, S.*, et al.* (2012b). Mutations in C5ORF42 cause Joubert syndrome in the French Canadian population. Am J Hum Genet *90*, 693-700.

Stebbings, L., Grimes, B.R., and Bownes, M. (1998). A testis-specifically expressed gene is embedded within a cluster of maternally expressed genes at 89B in Drosophila melanogaster. Development genes and evolution *208*, 523-530.

Stephan, A., Vaughan, S., Shaw, M.K., Gull, K., and McKean, P.G. (2007). An essential quality control mechanism at the eukaryotic basal body prior to intraflagellar transport. Traffic *8*, 1323-1330.

Stooke-Vaughan, G.A., Huang, P., Hammond, K.L., Schier, A.F., and Whitfield, T.T. (2012). The role of hair cells, cilia and ciliary motility in otolith formation in the zebrafish otic vesicle. Development *139*, 1777-1787.

Stubbs, J.L., Davidson, L., Keller, R., and Kintner, C. (2006). Radial intercalation of ciliated cells during Xenopus skin development. Development *133*, 2507-2515.

Supatto, W., and Vermot, J. (2011). From cilia hydrodynamics to zebrafish embryonic development. Curr Top Dev Biol *95*, 33-66.

Synofzik, M., Soehn, A.S., Gburek-Augustat, J., Schicks, J., Karle, K.N., Schule, R., Haack, T.B., Schoning, M., Biskup, S., Rudnik-Schoneborn, S.*, et al.* (2013). Autosomal recessive spastic ataxia of Charlevoix Saguenay (ARSACS): expanding the genetic, clinical and imaging spectrum. Orphanet journal of rare diseases *8*, 1750-1172.

Tadros, W., and Lipshitz, H.D. (2009). The maternal-to-zygotic transition: a play in two acts. Development *136*, 3033-3042.

Takeda, S., Yonekawa, Y., Tanaka, Y., Okada, Y., Nonaka, S., and Hirokawa, N. (1999). Left-right asymmetry and kinesin superfamily protein KIF3A: new insights in determination of laterality and mesoderm induction by kif3A-/- mice analysis. J Cell Biol *145*, 825-836.

Tanaka, Y., Okada, Y., and Hirokawa, N. (2005). FGF-induced vesicular release of Sonic hedgehog and retinoic acid in leftward nodal flow is critical for left-right determination. Nature *435*, 172-177.

Tanos, B.E., Yang, H.J., Soni, R., Wang, W.J., Macaluso, F.P., Asara, J.M., and Tsou, M.F. (2013). Centriole distal appendages promote membrane docking, leading to cilia initiation. Genes Dev *27*, 163-168.

Tasouri, E., and Tucker, K.L. (2011). Primary cilia and organogenesis: is Hedgehog the only sculptor? Cell and tissue research *345*, 21-40.

Tayeh, M.K., Yen, H.J., Beck, J.S., Searby, C.C., Westfall, T.A., Griesbach, H., Sheffield, V.C., and Slusarski, D.C. (2008). Genetic interaction between Bardet-Biedl syndrome genes and implications for limb patterning. Hum Mol Genet *17*, 1956-1967.

Teilmann, S.C., and Christensen, S.T. (2005). Localization of the angiopoietin receptors Tie-1 and Tie-2 on the primary cilia in the female reproductive organs. Cell Biol Int *29*, 340-346.

Teilmann, S.C., Clement, C.A., Thorup, J., Byskov, A.G., and Christensen, S.T. (2006). Expression and localization of the progesterone receptor in mouse and human reproductive organs. The Journal of endocrinology *191*, 525-535.

Thauvin-Robinet, C., Lee, J.S., Lopez, E., Herranz-Perez, V., Shida, T., Franco, B., Jego, L., Ye, F., Pasquier, L., Loget, P.*, et al.* (2014). The oral-facial-digital syndrome gene C2CD3 encodes a positive regulator of centriole elongation. Nat Genet *46*, 905-911.

Thiel, C., Kessler, K., Giessl, A., Dimmler, A., Shalev, S.A., von der Haar, S., Zenker, M., Zahnleiter, D., Stoss, H., Beinder, E.*, et al.* (2011). NEK1 mutations cause short-rib polydactyly syndrome type majewski. Am J Hum Genet *88*, 106-114.

Thomas, S., Legendre, M., Saunier, S., Bessieres, B., Alby, C., Bonniere, M., Toutain, A., Loeuillet, L., Szymanska, K., Jossic, F.*, et al.* (2012). TCTN3 mutations cause Mohr-Majewski syndrome. Am J Hum Genet *91*, 372-378.

Tobin, J.L., and Beales, P.L. (2009). The nonmotile ciliopathies. Genetics in medicine : official journal of the American College of Medical Genetics *11*, 386-402.

Tobin, J.L., Di Franco, M., Eichers, E., May-Simera, H., Garcia, M., Yan, J., Quinlan, R., Justice, M.J., Hennekam, R.C., Briscoe, J.*, et al.* (2008). Inhibition of neural crest migration underlies craniofacial dysmorphology and Hirschsprung's disease in Bardet-Biedl syndrome. Proc Natl Acad Sci U S A *105*, 6714-6719.

Tonissen, K.F., Drysdale, T.A., Lints, T.J., Harvey, R.P., and Krieg, P.A. (1994). XNkx-2.5, a Xenopus gene related to Nkx-2.5 and tinman: evidence for a conserved role in cardiac development. Dev Biol *162*, 325-328.

Toriello, H.V. (1988). Heterogeneity and variability in the oral-facial-digital syndromes. American journal of medical genetics Supplement *4*, 149-159.

Toriello, H.V. (2009). Are the oral-facial-digital syndromes ciliopathies? American journal of medical genetics Part A *149A*, 1089-1095.

Toriello, H.V., Carey, J.C., Suslak, E., Desposito, F.R., Leonard, B., Lipson, M., Friedman, B.D., and Hoyme, H.E. (1997). Six patients with oral-facial-digital syndrome IV: the case for heterogeneity. American journal of medical genetics *69*, 250-260.

Toriello, H.V., and Parisi, M.A. (2009). Cilia and the ciliopathies: an introduction. American journal of medical genetics Part C, Seminars in medical genetics *151C*, 261-262.

Trainor, P.A. (2005). Specification and patterning of neural crest cells during craniofacial development. Brain, behavior and evolution *66*, 266-280.

Tsao, P.N., Vasconcelos, M., Izvolsky, K.I., Qian, J., Lu, J., and Cardoso, W.V. (2009). Notch signaling controls the balance of ciliated and secretory cell fates in developing airways. Development *136*, 2297-2307.

Utsch, B., Sayer, J.A., Attanasio, M., Pereira, R.R., Eccles, M., Hennies, H.C., Otto, E.A., and Hildebrandt, F. (2006). Identification of the first AHI1 gene mutations in nephronophthisis-associated Joubert syndrome. Pediatric nephrology *21*, 32-35.

Valente, E.M., Logan, C.V., Mougou-Zerelli, S., Lee, J.H., Silhavy, J.L., Brancati, F., Iannicelli, M., Travaglini, L., Romani, S., Illi, B.*, et al.* (2010). Mutations in TMEM216 perturb ciliogenesis and cause Joubert, Meckel and related syndromes. Nat Genet *42*, 619-625.

van Reeuwijk, J., Arts, H.H., and Roepman, R. (2011). Scrutinizing ciliopathies by unraveling ciliary interaction networks. Hum Mol Genet *20*, R149-157.

Veland, I.R., Awan, A., Pedersen, L.B., Yoder, B.K., and Christensen, S.T. (2009). Primary cilia and signaling pathways in mammalian development, health and disease. Nephron Physiol *111*, p39-53.

Vincensini, L., Blisnick, T., and Bastin, P. (2011a). 1001 model organisms to study cilia and flagella. Biol Cell *103*, 109-130.

Vincensini, L., Blisnick, T., and Bastin, P. (2011b). [The importance of model organisms to study cilia and flagella biology]. Biologie aujourd'hui *205*, 5-28.

Vlad, A., Rohrs, S., Klein-Hitpass, L., and Muller, O. (2008). The first five years of the Wnt targetome. Cell Signal *20*, 795-802.

Wagner, C.A., Devuyst, O., Bourgeois, S., and Mohebbi, N. (2009). Regulated acid-base transport in the collecting duct. Pflugers Archiv : European journal of physiology *458*, 137-156.

Wallace, V.A., and Raff, M.C. (1999). A role for Sonic hedgehog in axon-to-astrocyte signalling in the rodent optic nerve. Development *126*, 2901-2909.

Wallingford, J.B. (2010). Planar cell polarity signaling, cilia and polarized ciliary beating. Curr Opin Cell Biol *22*, 597-604.

Wang, B., Sinha, T., Jiao, K., Serra, R., and Wang, J. (2011). Disruption of PCP signaling causes limb morphogenesis and skeletal defects and may underlie Robinow syndrome and brachydactyly type B. Hum Mol Genet *20*, 271-285.

Wang, S., Zhang, J., Nauli, S.M., Li, X., Starremans, P.G., Luo, Y., Roberts, K.A., and Zhou, J. (2007). Fibrocystin/polyductin, found in the same protein complex with polycystin-2, regulates calcium responses in kidney epithelia. Molecular and cellular biology *27*, 3241-3252.

Waters, A.M., and Beales, P.L. (2011). Ciliopathies: an expanding disease spectrum. Pediatric nephrology *26*, 1039-1056.

Webb, T.R., Parfitt, D.A., Gardner, J.C., Martinez, A., Bevilacqua, D., Davidson, A.E., Zito, I., Thiselton, D.L., Ressa, J.H., Apergi, M.*, et al.* (2012). Deep intronic mutation in OFD1, identified by targeted genomic next-generation sequencing, causes a severe form of X-linked retinitis pigmentosa (RP23). Hum Mol Genet *21*, 3647-3654.

Werner, M.E., and Mitchell, B.J. (2012). Understanding ciliated epithelia: the power of Xenopus. Genesis *50*, 176-185.

Werner, M.E., and Mitchell, B.J. (2013). Using Xenopus skin to study cilia development and function. Methods in enzymology *525*, 191-217.

Westlake, C.J., Baye, L.M., Nachury, M.V., Wright, K.J., Ervin, K.E., Phu, L., Chalouni, C., Beck, J.S., Kirkpatrick, D.S., Slusarski, D.C.*, et al.* (2011). Primary cilia membrane assembly is initiated by Rab11 and transport protein particle II (TRAPPII) complex-dependent trafficking of Rabin8 to the centrosome. Proc Natl Acad Sci U S A *108*, 2759-2764.

Whitfield, J.F. (2003). Primary cilium--is it an osteocyte's strain-sensing flowmeter? J Cell Biochem *89*, 233-237.

Widelitz, R. (2005). Wnt signaling through canonical and non-canonical pathways: recent progress. Growth Factors *23*, 111-116.

Williams, C.L., Li, C., Kida, K., Inglis, P.N., Mohan, S., Semenec, L., Bialas, N.J., Stupay, R.M., Chen, N., Blacque, O.E.*, et al.* (2011). MKS and NPHP modules cooperate to establish basal body/transition zone membrane associations and ciliary gate function during ciliogenesis. J Cell Biol *192*, 1023-1041.

Wilson, C.W., and Stainier, D.Y. (2010). Vertebrate Hedgehog signaling: cilia rule. BMC biology *8*, 1741-7007.

Wu, D., Freund, J.B., Fraser, S.E., and Vermot, J. (2011). Mechanistic basis of otolith formation during teleost inner ear development. Developmental cell *20*, 271-278.

Yamanaka, H., Moriguchi, T., Masuyama, N., Kusakabe, M., Hanafusa, H., Takada, R., Takada, S., and Nishida, E. (2002). JNK functions in the non-canonical Wnt pathway to regulate convergent extension movements in vertebrates. EMBO Rep *3*, 69-75.

Yamauchi, H., Miyakawa, N., Miyake, A., and Itoh, N. (2009). Fgf4 is required for left-right patterning of visceral organs in zebrafish. Dev Biol *332*, 177-185.

Ybot-Gonzalez, P., Savery, D., Gerrelli, D., Signore, M., Mitchell, C.E., Faux, C.H., Greene, N.D., and Copp, A.J. (2007). Convergent extension, planar-cell-polarity signalling and initiation of mouse neural tube closure. Development *134*, 789-799.

Ye, X., Zeng, H., Ning, G., Reiter, J.F., and Liu, A. (2014). C2cd3 is critical for centriolar distal appendage assembly and ciliary vesicle docking in mammals. Proc Natl Acad Sci U S A *111*, 2164-2169.

Yu, X., Lau, D., Ng, C.P., and Roy, S. (2011). Cilia-driven fluid flow as an epigenetic cue for otolith biomineralization on sensory hair cells of the inner ear. Development *138*, 487-494.

Yuan, K., Frolova, N., Xie, Y., Wang, D., Cook, L., Kwon, Y.J., Steg, A.D., Serra, R., and Frost, A.R. (2010). Primary cilia are decreased in breast cancer: analysis of a collection of human breast cancer cell lines and tissues. The journal of histochemistry and cytochemistry : official journal of the Histochemistry Society *58*, 857-870.

Zaghloul, N.A., and Katsanis, N. (2010). Functional modules, mutational load and human genetic disease. Trends Genet *26*, 168-176.

Zhang, M.Z., Mai, W., Li, C., Cho, S.Y., Hao, C., Moeckel, G., Zhao, R., Kim, I., Wang, J., Xiong, H.*, et al.* (2004). PKHD1 protein encoded by the gene for autosomal recessive polycystic kidney disease associates with basal bodies and primary cilia in renal epithelial cells. Proc Natl Acad Sci U S A *101*, 2311-2316.

Zou, J., Mali, P., Huang, X., Dowey, S.N., and Cheng, L. (2011). Site-specific gene correction of a point mutation in human iPS cells derived from an adult patient with sickle cell disease. Blood *118*, 4599-4608.

Zou, S.S., Li, Z., and Hu, H.L. (2012). [Desert hedgehog regulates the proliferation and differentiation of Leydig cells: an update]. Zhonghua Nan Ke Xue *18*, 172-175.

Appendices

Appendix 1

(a) The list of primers used for different experiments.

Primer	5'>3' sequence	Location
gDNA amplification of Exon 16 (human)		
ASUN-E16 (Fwd)	AGTCACTGAACTAGTGGTTGCTCTT	Intron 16
ASUN-E16 (Rev)	CTGCTTATGGGGAACATGTATTAG	Intron 17
cDNA amplification (human)		
ASUN-CDNA-5'	CCTTTTCCAGAGAGGCTGTG	5'UTR
ASUN-CDNA-3'	AACCAGTCCAGGCAACATAAC	3'UTR
PKHD1L1-P1 (Fwd)	AGCTGAGCAAGCCTGTGAA	Exon 41
PKHD1L1-P1 (Rev)	CATCAGGGAGTGTGACCGTA	Exon 47
PKHD1L1-P2 (Fwd)	TGCATGACAGATGCCCATAC	Exon 42
PKHD1L1-P2 (Rev)	TGCCTGGAGTTCAATGTCAG	Exon 44
QRT-PCR (human)		
ASUN-q (Fwd)	TTGCAGCAGTGGAAACTCTC	Exon 3
ASUN-q (Rev)	GTCTTCAAGCATTCGCACAT	Exon 4
PKHD1L1-q8 (Fwd)	AGGCCAGTTTAATCCTGTGG	Exon 63
PKHD1L1-q8 (Rev)	GCTGGCATGTAAATCATTGG	Exon 65
PTCH1-q (Fwd)	GCTGCACTACTTCAGAGACTGG	Exon 15
PTCH1-q (Rev)	CACCAGGAGTTTGTAGGCAAGG	Exon 16
Gli1-q (Fwd)	AGCCTTCAGCAATGCCAGTGAC	Exon 9
Gli1-q (Rev)	GTCAGGACCATGCACTGTCTTG	Exon 10
B-Actin (Fwd)	CATGTACGTTGCTATCCAGGC	Exon 4
B-Actin (Rev)	CTCCTTAATGTCACGCACGAT	Exon 4
GAPDH (Fwd)	GGAGCGAGATCCCTCCAAAAT	Exon 5
GAPDH (Rev)	GGCTGTTGTCATACTTCTCATGG	Exon 6
5'RACE-PCR primers (Xenopus)		
PKHD1L1-p86-deg2 (Fwd)	GCGCGGAATTC ATGTTYCARACNTAYGCN GA	5'UTR
PKHD1L1-p264-deg1 (Rev)	GCGCGCAAGCTT YTCNGCRTANGTYTGRAACAT	5'UTR
PKHD1L1-5UTR	GTGCAACAGGCAAGTGTGAG	5'UTR
PKHD1L1 (Rev)	CCTGGAGTTCCAGAGAATGG	Open reading frame
QRT-PCR (Xenopus & zebrafish)		
asun-slpicing-MO (Fwd)	GCCGAGGTGATCAAAGACTC	Exon 15
asun-slpicing-MO (Rev)	CCAGCGACAGAACAAAGTGA	3'UTR
asun_Moa (Fwd)	GGAAGCAGGAGGATCAAAATAC	
asun_Moa (Rev)	TGTATGGTTTCCAGCACACAGT	
asun_Mob (Fwd)	AGGATCCTGAATGCTGCAGTG	
asun_Mob (Rev)	GTCTGAGACCAGAGTGTCATCC	
Cloning in PCS2		
EcoRI-ASUN (Fwd)	CCGGAATTCCCAGGCACGAAAGTTAAAACA	5'UTR
StuI-ASUN (Rev)	AAAAGGCCTTTCTTCAAGTCACTCTTCACTGC	3'UTR
pCS2+_SP6	ATTTAGGTGACACTATAG	
pCS2+_T7	TAATACGACTCACTATAG GG	
Site-directed mutagenesis		
ASUN-del2004delA (Fwd)	AATAGAATCAATACTGCCAATTCCAGAAACATCAGGAATTTGCTG	Exon 16
ASUN-del2004delA (Rev)	CAGCAAATTCCTGATGTTTCTGGAATTGGCAGTATTGATTCTATT	Exon 16
Co-Immunoprecipitation		
EcoRI-PC-ASUN (Fwd)	CCGGAATTCATGGAAGATCAGGTAGATCCACGGTTAATCGATGGTAAG AAGATTTTTTCTGAATCTCATAAAACAGTGTTTGTTGTGGATCACTGC	Exon 1
ASUN-StuI (Rev)	AAAAGGCCTTCACTGCCGGCTGGCTTTTCC	3'UTR
ClaI-ATG-HA-CEP170 (Fwd)	CCCATCGATATGTACCCCTACGACGTCCCCGACTACGCAAGCTTAACAT CCTGGTTTTTGG	Exon 1
XhoI-TGA-CEP170 (Rev)	CCGCTCGAGTCATTCTTGTACTGTAACATCTTCCTCTTCCCCATCGG	3'UTR
EcoRI-HA-INTS-5 (Fwd)	CCGGAATTCATGTACCCCTACGACGTCCCCGACTACGCATCCGCGCTGT GCGACCCTC	Exon 1
INTS-5-XhoI-3 (Rev)	CCGGAATTCCTACGTCCCCTGTCGAAGGAGAGTGG	3'UTR

(b) The list of morpholino oligonucleotides (MO), siRNA and sequences.

Name	5'>3' sequence	Reference
Morpholino (MO)		
asun-ATG-MO	TCCGAGAAAGTCTTCATCTTGTCTG	Lee et al., 2005
asun-splicing-MO	TGCACAGGGACGGCACTCACCCATT	
asun-Moa	ATGAGCTAAACACACCACAGACATA	
asun-Mob	ACAGAGATATTAGAAGCTACCTGTC	
siRNA		
ASUN-siRNA-5' ORF	GGAAAUAGAGGACGAAUAA	Jodoin et al., 2012
ASUN-siRNA-3' UTR	cagcaagaugguataguua	Jodoin et al., 2012

(c) The list of primary and secondary antibodies.

Antibodies	Dillution	Company
Immunofluorscent staining		
Anti-Mouse Acetylated-α-tubulin	1: 500	Sigma-Aldrich, USA, (Cat. No. T6074)
Anti-Rabbit γ-tubulin	1: 500	Sigma-Aldrich, USA, (Cat. No. T5192)
Anti-Rabbit Pericentrin	1: 1000	Abcam, USA, (Cat. No. ab4448)
Anti-Rabbit Cep170	1: 1000	Abcam, USA, (Cat. No. ab84545)
Anti-Rabbit DHC	1: 120	Jodoin et al., 2013
Anti-Mouse MyoD	1: 500	Developmental Studies Hybridoma Bank, USA, (Cat. No. D7F2)
Immunoblotting		
Anti-Mouse Actin	1: 1000	Sigma-Aldrich, USA, (Cat. No. A4700)
Anti-Mouse β-tubulin	1: 500	Developmental Studies Hybridoma Bank, USA, (Cat. No. AA12.1)
Monoclonal Anti-PC Tag	1: 1000	Roche Diagnostics, Germany, (Cat. No. 11-814-508-001)
Monoclonal Anti-myc Tag	1: 4000	Sigma-Aldrich, USA, (Cat. No. H4439)
Donkey Anti-Rabbit-HRP	1: 4000	Jackson ImmunoResearch Laboratories, USA, (Cat. No. 711-035-152)
Donkey Anti-Mouse-HRP	1: 4000	Jackson ImmunoResearch Laboratories, USA, (Cat. No. 715-035-150)
Monoclonal Anti-HA-HRP	1: 4000	Sigma-Aldrich, USA, (Cat. No. H6533)

Appendix 2

The list of the 395 genes in the 5 IBD regions found by homozygosity mapping of the family. The 5 candidate genes are highlighted in blue.

#	Gene	Position	Discription
1	LOC401286	6q27	uncharacterized LOC401286
2	LOC100422263		serine palmitoyltransferase, long chain base subunit 2 pseudogene
3	C6orf123	6q27	chromosome 6 open reading frame 123
4	LOC441179	6q27	uncharacterized LOC441179
5	MLLT4-AS1	6q27	MLLT4 antisense RNA 1 (head to head)
6	MLLT4	6q27	myeloid/lymphoid or mixed-lineage leukemia
7	HGC6.3	6q27	uncharacterized LOC100128124
8	KIF25-AS1	6q27	KIF25 antisense RNA 1
9	KIF25	6q27	kinesin family member 25
10	FRMD1	6q27	FERM domain containing 1
11	LOC101929420		uncharacterized LOC101929420
12	CTAGE13P		CTAGE family, member 13, pseudogene
13	DACT2	6q27	dishevelled-binding antagonist of beta-catenin 2
14	SMOC2	6q27	SPARC related modular calcium binding 2
15	LOC101929442		uncharacterized LOC101929442
16	LOC101929460		uncharacterized LOC101929460
17	LOC101929484		uncharacterized LOC101929484
18	LOC101929504		uncharacterized LOC101929504
19	LOC101929523		uncharacterized LOC101929523
20	THBS2	6q27	thrombospondin 2
21	WDR27	6q27	WD repeat domain 27
22	LOC101929569		uncharacterized LOC101929569
23	LOC101929543		uncharacterized LOC101929543
24	C6orf120	6q27	chromosome 6 open reading frame 120
25	PHF10	6q27	PHD finger protein 10
26	TCTE3	6q27	t-complex-associated-testis-expressed 3
27	ERMARD	6q27	ER membrane-associated RNA degradation
28	LINC00242	6q27	long intergenic non-protein coding RNA 242
29	LINC00574	6q27	long intergenic non-protein coding RNA 574
30	ZFPM2	8q23	zinc finger protein, FOG family member 2
31	RPL12P24	8q23	ribosomal protein L12 pseudogene 24
32	SLC16A14P1	8q23.1	solute carrier family 16, member 14 pseudogene 1
33	OXR1	8q23	oxidation resistance 1
34	TAGLN2P1	8q23.1	transgelin 2 pseudogene 1
35	RNU7-84P	8q23.1	RNA, U7 small nuclear 84 pseudogene
36	ABRA	8q23.1	actin-binding Rho activating protein
37	LOC100419978		high mobility group box 1 pseudogene 46
38	ANGPT1	8q23.1	angiopoietin 1
39	PGAM1P13	8q23.1	phosphoglycerate mutase 1 pseudogene 13
40	RNA5SP275		RNA, 5S ribosomal pseudogene 275
41	RSPO2	8q23.1	R-spondin 2
42	NRBF2P4	8q23.1	nuclear receptor binding factor 2 pseudogene 4
43	AURKBPS1	8q23.1	aurora kinase B pseudogene 1
44	EIF3E	8q22-q23	eukaryotic translation initiation factor 3, subunit E
45	RPS17P14	8q23.1	ribosomal protein S17 pseudogene 14
46	EMC2	8q23.1	ER membrane protein complex subunit 2
47	LOC101060000		dnaJ homolog subfamily B member 6-like
48	LOC101060002		tRNA methyltransferase 10 homolog B-like
49	TMEM74	8q23.1	transmembrane protein 74
50	LOC101927413		uncharacterized LOC101927413
51	TRHR	8q23	thyrotropin-releasing hormone receptor
52	NUDCD1	8q23	NudC domain containing 1
53	ENY2	8q23.1	enhancer of yellow 2 homolog (Drosophila)
54	PKHD1L1	8q23	polycystic kidney and hepatic disease 1 (autosomal recessive)-like 1

#	Gene	Position	Discription
55	LOC100420748		suppressor of cytokine signaling 5 pseudogene
56	MAPK6PS5	8q23.1	mitogen-activated protein kinase 6 pseudogene 5
57	EBAG9	8q23	estrogen receptor binding site associated, antigen, 9
58	SYBU	8q23.2	syntabulin (syntaxin-interacting)
59	LOC100132813	8q23.2	uncharacterized LOC100132813
60	LOC644335	8q23.2	SMG5 nonsense mediated mRNA decay factor pseudogene
61	RPL18P6	8q23.2	ribosomal protein L18 pseudogene 6
62	KCNV1	8q23.2	potassium channel, subfamily V, member 1
63	RPSAP48	8q23.2	ribosomal protein SA pseudogene 48
64	LOC100132280	8q23.2	ataxin 3 pseudogene
65	LOC100129370	8q23.2	NADH dehydrogenase 1 beta subcomplex, 9, 22kDa pseudogene
66	LOC101927459		uncharacterized LOC101927459
67	LOC101927487		uncharacterized LOC101927487
68	EEF1A1P37		eukaryotic translation elongation factor 1 alpha 1 pseudogene 37
69	CSMD3	8q23.3	CUB and Sushi multiple domains 3
70	RPL30P16	8q23.3	ribosomal protein L30 pseudogene 16
71	MIR2053		microRNA 2053
72	RPL18P7	8q23.3	ribosomal protein L18 pseudogene 7
73	LOC100420746	8q23.3	NADH dehydrogenase complex I, assembly factor 7 pseudogene
74	TRPS1	8q24.12	trichorhinophalangeal syndrome I
75	LINC00536	8q23.3	long intergenic non-protein coding RNA 536
76	EIF3H	8q24.11	eukaryotic translation initiation factor 3, subunit H
77	UTP23	8q24.11	UTP23, small subunit (SSU) processome component, homolog (yeast)
78	RAD21	8q24	RAD21 homolog (S. pombe)
79	RAD21-AS1	8q24.11	RAD21 antisense RNA 1
80	MIR3610		microRNA 3610
81	AARD	8q24.11	alanine and arginine rich domain containing protein
82	SLC30A8	8q24.11	solute carrier family 30 (zinc transporter), member 8
83	MED30	8q24.11	mediator complex subunit 30
84	RPS10P16	8q24.11	ribosomal protein S10 pseudogene 16
85	EXT1	8q24.11	exostosin glycosyltransferase 1
86	SAMD12	8q24.12	sterile alpha motif domain containing 12
87	SAMD12-AS1	8q24.12	SAMD12 antisense RNA 1
88	RPS26P35	8q24.12	ribosomal protein S26 pseudogene 35
89	TNFRSF11B	8q24	tumor necrosis factor receptor superfamily, member 11b
90	COLEC10	8q23-q24.1	collectin sub-family member 10 (C-type lectin)
91	LOC100286746		GABA(A) receptor-associated protein-like 2 pseudogene
92	LOC101927513		uncharacterized LOC101927513
93	MAL2	8q23	mal, T-cell differentiation protein 2 (gene/pseudogene)
94	NOV	8q24.1	OTTHUMP00000228107
95	LOC392264	8q24.12	zinc finger protein 532 pseudogene
96	ENPP2	8q24.1	ectonucleotide pyrophosphatase/phosphodiesterase 2
97	CYCSP23	8q24.12	cytochrome c, somatic pseudogene 23
98	TAF2	8q24.12	TAF2 RNA polymerase II
99	DSCC1	8q24.12	DNA replication and sister chromatid cohesion 1
100	DEPTOR	8q24.12	DEP domain containing MTOR-interacting protein
101	RNA5SP277		RNA, 5S ribosomal pseudogene 277
102	COL14A1	8q23	collagen, type XIV, alpha 1
103	MRPL13	8q22.1-q22.3	mitochondrial ribosomal protein L13
104	MTBP	8q24.12	Mdm2, transformed 3T3 cell double minute 2, p53 binding protein
105	SNTB1	8q23-q24	syntrophin, beta 1 (dystrophin-associated protein A1, basic component 1)
106	LOC100421096		non-SMC condensin I complex, subunit G pseudogene
107	LOC101927561		uncharacterized LOC101927561
108	LOC101927543		uncharacterized LOC101927543
109	LOC100133147	8q24.12	glucosamine-phosphate N-acetyltransferase 1 pseudogene
110	LOC101928224		uncharacterized LOC101928224
111	BCL2L14	12p13-p12	BCL2-like 14 (apoptosis facilitator)
112	LOC100506248		prothymosin alpha-like
113	LRP6	12p13.2	low density lipoprotein receptor-related protein 6
114	RPL21P100	12p13.2	ribosomal protein L21 pseudogene 100
115	MORF4LP2	12p13.2	mortality factor 4 like 1 pseudogene 2

#	Gene	Position	Discription
116	LOC101929053		ubiquitin-conjugating enzyme E2 variant 1-like
117	MANSC1	12p13.2	MANSC domain containing 1
118	RPL23AP66	12p12	ribosomal protein L23a pseudogene 66
119	LOH12CR2	12p13.2	loss of heterozygosity, 12, chromosomal region 2 (non-protein coding)
120	LOH12CR1	12p12	loss of heterozygosity, 12, chromosomal region 1
121	DUSP16	12p13	dual specificity phosphatase 16
122	RPL19P17	12p13	ribosomal protein L19 pseudogene 17
123	CREBL2	12p13	cAMP responsive element binding protein-like 2
124	LOC100419521		ribosomal protein L21 pseudogene
125	GPR19	12p12.3	GPR-NGA
126	LOC101929220		caskin-2-like
127	CDKN1B	12p13.1-p12	cyclin-dependent kinase inhibitor 1B (p27, Kip1)
128	APOLD1	12p13.1	apolipoprotein L domain containing 1
129	MIR613	12p13.1	microRNA 613
130	LOC100423046		syntaxin 8 pseudogene
131	DDX47	12p13.1	DEAD (Asp-Glu-Ala-Asp) box polypeptide 47
132	RPL37AP9	12p13.1	ribosomal protein L37a pseudogene 9
133	RPS6P1	12p13.1	ribosomal protein S6 pseudogene 1
134	RPL13AP20	12p13.1	ribosomal protein L13a pseudogene 20
135	GPRC5A	12p13-p12.3	G protein-coupled receptor, family C, group 5, member A
136	MIR614	12p13.1	microRNA 614
137	GPRC5D	12p13.3	G protein-coupled receptor, family C, group 5, member D
138	HEBP1	12p13.1	heme binding protein 1
139	LOC100506314		uncharacterized LOC100506314
140	HTR7P1	12p13.1	5-hydroxytryptamine (serotonin) receptor 7 pseudogene 1
141	RPS26P46	12p13.1	ribosomal protein S26 pseudogene 46
142	KIAA1467	12p13.1	KIAA1467
143	GSG1	12p13.1	germ cell associated 1
144	EMP1	12p12.3	epithelial membrane protein 1
145	C12orf36	12p13.1	chromosome 12 open reading frame 36
146	RNA5SP353		RNA, 5S ribosomal pseudogene 353
147	GRIN2B	12p12	glutamate receptor, ionotropic, N-methyl D-aspartate 2B
148	HMGN1P23		high mobility group nucleosome binding domain 1 pseudogene 23
149	MRPS18CP4	12p13.31	mitochondrial ribosomal protein S18C pseudogene 4
150	GNAI2L	12p13.1	guanine nucleotide binding protein , alpha inhibiting activity polypeptide 2 pseudogene 1
151	RPL30P11	12p13.1	ribosomal protein L30 pseudogene 11
152	ATF7IP	12p13.1	activating transcription factor 7 interacting protein
153	PLBD1	12p13.1	phospholipase B domain containing 1
154	LOC101928317		uncharacterized LOC101928317
155	LOC101928290		uncharacterized LOC101928290
156	GUCY2C	12p12	guanylate cyclase 2C (heat stable enterotoxin receptor)
157	HIST4H4	12p12.3	histone cluster 4, H4
158	H2AFJ	12p12.3	H2A histone family, member J
159	WBP11	12p12.3	WW domain binding protein 11
160	C12orf60	12p12.3	chromosome 12 open reading frame 60
161	SMCO3	12p12.3	single-pass membrane protein with coiled-coil domains 3
162	ART4	12p13-p12	ADP-ribosyltransferase 4 (Dombrock blood group)
163	MGP	12p12.3	matrix Gla protein
164	ERP27	12p12.3	endoplasmic reticulum protein 27
165	ARHGDIB	12p12.3	Rho GDP dissociation inhibitor (GDI) beta
166	PDE6H	12p13	phosphodiesterase 6H, cGMP-specific, cone, gamma
167	LOC101928340		uncharacterized LOC101928340
168	RERG	12p12.3	RAS-like, estrogen-regulated, growth inhibitor
169	LOC728996	12p12.3	methyltransferase like 8 pseudogene
170	PTPRO	12p13-p12	protein tyrosine phosphatase, receptor type, O
171	RPS2P42	12p13.3-p13.	ribosomal protein S2 pseudogene 42
172	EPS8	12p12.3	epidermal growth factor receptor pathway substrate 8
173	MRPS7P2	12p13.1	mitochondrial ribosomal protein S7 pseudogene 2
174	STRAP	12p12.3	serine/threonine kinase receptor associated protein
175	DERA	12p12.3	deoxyribose-phosphate aldolase (putative)

#	Gene	Position	Discription
176	LOC100420503		egl-9 family hypoxia-inducible factor 3 pseudogene
177	SLC15A5	12p12.3	OTTHUMP00000239482
178	LOC101928362		uncharacterized LOC101928362
179	MGST1	12p12.3-p12.	microsomal glutathione S-transferase 1
180	SUPT16HP1	12p12.3	suppressor of Ty 16 homolog (S. cerevisiae) pseudogene 1
181	LOC121520	12p12.3	glutamic-oxaloacetic transaminase 2 pseudogene 4
182	LMO3	12p12.3	LIM domain only 3 (rhombotin-like 2)
183	SKP1P2	12p12.3	S-phase kinase-associated protein 1 pseudogene 2
184	LOC387845	12p12.3	eukaryotic translation elongation factor 1 alpha 1 pseudogene 16
185	RPL7P40	12p12.3	ribosomal protein L7 pseudogene 40
186	PSMC1P8	12p12.3	proteasome (prosome, macropain) 26S subunit, ATPase, 1 pseudogene 8
187	LOC390298	12p12.3	translocase of inner mitochondrial membrane 17 homolog B (yeast) pseudogene
188	MIR3974		microRNA 3974
189	RERGL	12p12.3	RERG/RAS-like
190	PIK3C2G	12p12	phosphatidylinositol-4-phosphate 3-kinase, catalytic subunit type 2 gamma
191	LOC100420792		Nedd4 family interacting protein 1 pseudogene
192	LOC100419827		zinc finger with KRAB and SCAN domains 7 pseudogene
193	PLCZ1	12p12.3	phospholipase C, zeta 1
194	PSMC1P9	12p12.3	proteasome (prosome, macropain) 26S subunit, ATPase, 1 pseudogene 9
195	CAPZA3	12p12.3	capping protein (actin filament) muscle Z-line, alpha 3
196	RPL7P6	12p12.3	ribosomal protein L7 pseudogene 6
197	LOC100128109	12p12.3	MEF2B neighbor pseudogene
198	PLEKHA5	12p12	pleckstrin homology domain containing, family A member 5
199	LOC100421296		serine/arginine-rich splicing factor 11 pseudogene
200	LOC100527946		programmed cell death 5 pseudogene
201	AEBP2	12p12.3	AE binding protein 2
202	EEF1A1P4	12p12.3	eukaryotic translation elongation factor 1 alpha 1 pseudogene 4
203	RPL34P25	12p12	ribosomal protein L34 pseudogene 25
204	LOC101928387		uncharacterized LOC101928387
205	TCP1P3	12p12.2	t-complex 1 pseudogene 3
206	LOC100506393	12p12	uncharacterized LOC100506393
207	PDE3A	12p12	phosphodiesterase 3A, cGMP-inhibited
208	UBE2L2	12q12	ubiquitin-conjugating enzyme E2L 2 (pseudogene)
209	hCG_23738	12p12.2	ubiquitin-like, containing PHD and RING finger domains, 1 pseudogene
210	SLCO1C1	12p12.2	solute carrier organic anion transporter family, member 1C1
211	SLCO1B3	12p12	solute carrier organic anion transporter family, member 1B3
212	SLCO1B7	12p12.2	solute carrier organic anion transporter family, member 1B7 (non-functional)
213	SLCO1B1	12p	solute carrier organic anion transporter family, member 1B1
214	SLCO1A2	12p12	solute carrier organic anion transporter family, member 1A2
215	IAPP	12p12.1	islet amyloid polypeptide
216	PYROXD1	12p12.1	pyridine nucleotide-disulphide oxidoreductase domain 1
217	TCEB1P31		transcription elongation factor B (SIII), polypeptide 1 pseudogene 31
218	RECQL	12p12	RecQ protein-like (DNA helicase Q1-like)
219	GOLT1B	12p12.1	golgi transport 1B
220	C12orf39	12p12.1	chromosome 12 open reading frame 39
221	GYS2	12p12.2	glycogen synthase 2 (liver)
222	LDHB	12p12.2-p12.	lactate dehydrogenase B
223	KCNJ8	12p11.23	potassium inwardly-rectifying channel, subfamily J, member 8
224	ABCC9	12p12.1	ATP-binding cassette, sub-family C (CFTR/MRP), member 9
225	THEM4P1	12p12.1	thioesterase superfamily member 4 pseudogene 1
226	CMAS	12p12.1	CMP-N-acetylneuraminic acid synthetase
227	ST8SIA1	12p12.1-p11.	ST8 alpha-N-acetyl-neuraminide alpha-2,8-sialyltransferase 1
228	LOC101928412		uncharacterized LOC101928412
229	C2CD5	12p12.1	C2 calcium-dependent domain containing 5
230	LOC100288378	12p12.1	leucine rich repeat containing 34 pseudogene
231	ETNK1	12p12.1	ethanolamine kinase 1
232	RPS27P22	12p12.1	ribosomal protein S27 pseudogene 22
233	LOC101928441		uncharacterized LOC101928441
234	SOX5	12p12.1	SRY (sex determining region Y)-box 5
235	MIR920	12p12.1	microRNA 920

226

| #	Gene	Position	Discription
236	LOC101928471		uncharacterized LOC101928471
237	LINC00477	12p12.1	long intergenic non-protein coding RNA 477
238	KNOP1P1	12p12.1	lysine-rich nucleolar protein 1 pseudogene 1
239	RPL21P102	12p12.1	ribosomal protein L21 pseudogene 102
240	BCAT1	12p12.1	branched chain amino-acid transaminase 1, cytosolic
241	DAD1L	12p12.1	defender against cell death 1 pseudogene 1
242	BRI3P2	12p12.1	brain protein I3 pseudogene 2
243	C12orf77	12p12.1	chromosome 12 open reading frame 77
244	LOC645177	12p12.1	protein KASH5-like
245	LRMP	12p12.1	lymphoid-restricted membrane protein
246	LOC100419930		centromere protein U pseudogene
247	CASC1	12p12.1	cancer susceptibility candidate 1
248	LYRM5	12p12.1	LYR motif containing 5
249	KRAS	12p12.1	Kirsten rat sarcoma viral oncogene homolog
250	RPL39P27	12p12.1	ribosomal protein L39 pseudogene 27
251	LOC100421617		family with sequence similarity 133, member A pseudogene
252	IFLTD1	12p12.1	intermediate filament tail domain containing 1
253	LOC645233	12p12.1	thymine-DNA glycosylase pseudogene
254	MIR4302		microRNA 4302
255	RASSF8-AS1		RASSF8 atnisense RNA 1
256	RASSF8	12p12.3	Ras association (RalGDS/AF-6) domain family (N-terminal) member 8
257	BHLHE41	12p12.1	basic helix-loop-helix family, member e41
258	SSPN	12p11.2	sarcospan (Kras oncogene-associated gene)
259	LOC101928554		uncharacterized LOC101928554
260	ITPR2	12p11	inositol 1,4,5-trisphosphate receptor, type 2
261	RNA5SP354		RNA, 5S ribosomal pseudogene 354
262	LOC101929091		enoyl-CoA hydratase domain-containing protein 2, mitochondrial-like
263	ASUN	12p11.23	asunder spermatogenesis regulator
264	FGFR1OP2	12p11.23	FGFR1 oncogene partner 2
265	TM7SF3	12q11-q12	transmembrane 7 superfamily member 3
266	MED21	12p11.23	mediator complex subunit 21
267	LOC101928625		uncharacterized LOC101928625
268	C12orf71	12p11.23	chromosome 12 open reading frame 71
269	LOC729222	12p11.23	liprin-beta-1-like
270	STK38L	12p11.23	serine/threonine kinase 38 like
271	ARNTL2	12p12.2-p11	aryl hydrocarbon receptor nuclear translocator-like 2
272	LOC101928646		uncharacterized LOC101928646
273	SMCO2	12p11.23	single-pass membrane protein with coiled-coil domains 2
274	LOC100419829		arginyl-tRNA synthetase pseudogene
275	PPFIBP1	12p12.1	PTPRF interacting protein, binding protein 1 (liprin beta 1)
276	LOC100506578		uncharacterized LOC100506578
277	REP15	12p11.22	RAB15 effector protein
278	LOC100420013		high mobility group box 1 pseudogene 49
279	MRPS35	12p11	mitochondrial ribosomal protein S35
280	MANSC4	12p11.22	MANSC domain containing 4
281	KLHL42	12p11.22	kelch-like family member 42
283	SAP18	13q12.11	Sin3A-associated protein, 18kDa
284	SKA3	13q12.11	spindle and kinetochore associated complex subunit 3
285	MRP63	13q12.11	mitochondrial ribosomal protein 63
286	ESRRAP2	13q12.11	estrogen-related receptor alpha pseudogene 2
287	LOC101928764		coiled-coil domain-containing protein 144C-like
288	MIPEPP3	13q12.11	mitochondrial intermediate peptidase pseudogene 3
289	LINC00539	13q12.11	long intergenic non-protein coding RNA 539
290	GRK6P1	13q12.11	G protein-coupled receptor kinase 6 pseudogene 1
291	GAPDHP52		glyceraldehyde 3 phosphate dehydrogenase pseudogene 52
292	RNA5SP25		RNA, 5S ribosomal pseudogene 25
293	ZDHHC20	13q12.11	zinc finger, DHHC-type containing 20
294	HIST1H2BPS3		histone cluster 1, H2b, pseudogene 3
295	MICU2	13q12.11	mitochondrial calcium uptake 2
296	FNTAP2	13q12.11	farnesyltransferase, CAAX box, alpha pseudogene 2
297	RNU6-59P		RNA, U6 small nuclear 59, pseudogene

#	Gene	Position	Discription
298	RPS7P10	13q12.11	ribosomal protein S7 pseudogene 10
299	FGF9	13q11-q12	FGF-9|HBGF-9|glia-activating factor|heparin-binding growth factor 9
300	LINC00424		long intergenic non-protein coding RNA 424
301	NME1P1		NME/NM23 nucleoside diphosphate kinase 1 pseudogene 1
302	MTND3P1		MT-ND3 pseudogene 1
303	LINC00540		long intergenic non-protein coding RNA 540
304	LOC101927298		uncharacterized LOC101927298
305	FTH1P7	13q12.11	ferritin, heavy polypeptide 1 pseudogene 7
306	DDX39AP1	13q12.11	DEAD (Asp-Glu-Ala-Asp) box polypeptide 39A pseudogene 1
307	RPL7AP73		ribosomal protein L7a pseudogene 73
308	IPMKP1	13q12.12	inositol polyphosphate multikinase pseudogene 1
309	LOC100129167	13q12.12	Rieske (Fe-S) domain containing pseudogene 1
310	BASP1P1	13q12.12	brain abundant, membrane attached signal protein 1 pseudogene 1
311	NUS1P2	13q12.12	nuclear undecaprenyl pyrophosphate synthase 1 homolog (S. cerevisiae) pseudogene 2
312	LOC100130029	13q12.12	high mobility group AT-hook 1 pseudogene 6
313	SGCG	13q12	sarcoglycan, gamma (35kDa dystrophin-associated glycoprotein)
314	RNU6-58P		RNA, U6 small nuclear 58, pseudogene
315	TATDN2P3		TatD DNase domain containing 2 pseudogene 3
316	SDAD1P4		SDA1 domain containing 1 pseudogene 4
317	SACS	13q12	spastic ataxia of Charlevoix-Saguenay (sacsin)
318	RPLP1P13		ribosomal protein, large, P1 pseudogene 13
319	SACS-AS1	13q12	SACS antisense RNA 1
320	LINC00327		long intergenic non-protein coding RNA 327
321	LOC101928839		uncharacterized LOC101928839
322	TNFRSF19	13q12.11-q12	tumor necrosis factor receptor superfamily, member 19
323	MIPEP	13q12	mitochondrial intermediate peptidase
324	MTCO3P2		MT-CO3 pseudogene 2
325	C1QTNF9B-AS	13q12	C1QTNF9B antisense RNA 1
326	C1QTNF9B	13q12.12	C1q and tumor necrosis factor related protein 9B
327	ANKRD20A19P	13q12.12	ankyrin repeat domain 20 family, member A19, pseudogene
328	SPATA13	13q12.12	spermatogenesis associated 13
329	RP11-309I15.2	13q12.12	importin 7 pseudogene 2
330	MIR2276		microRNA 2276
331	SPATA13-AS1		SPATA13 antisense RNA 1
332	C1QTNF9	13q12.12	C1q and tumor necrosis factor related protein 9
333	LOC100287275	13q12.12	protein PCOTH pseudogene
334	CEND1P2	13q12.12	cell cycle exit and neuronal differentiation 1 pseudogene 2
335	LOC101060086		cell cycle exit and neuronal differentiation protein 1-like
336	NUS1P3	13q12	nuclear undecaprenyl pyrophosphate synthase 1 homolog (S. cerevisiae) pseudogene 3
337	CYCSP33	13q12.12	cytochrome c, somatic pseudogene 33
338	PARP4	13q11	poly (ADP-ribose) polymerase family, member 4
339	LOC101927375		ankyrin repeat domain-containing protein 26-like
340	PSPC1P2		paraspeckle component 1 pseudogene 2
341	TPTE2P6	13q12.12	transmembrane phosphoinositide 3-phosphatase and tensin homolog 2 pseudogene 6
342	ATP12A	13q12.1-q12	ATPase, H+/K+ transporting, nongastric, alpha polypeptide
343	RPL26P34	13q12.12	ribosomal protein L26 pseudogene 34
344	LOC100418742		clustered mitochondria (cluA/CLU1) homolog pseudogene
345	IRX1P1	13q12.12	iroquois homeobox 1 pseudogene 1
346	LOC101928867		uncharacterized LOC101928867
347	ANKRD20A10P		ankyrin repeat domain 20 family, member A10, pseudogene
348	RNF17	13q12.12	ring finger protein 17
349	CENPJ	13q12.12	centromere protein J
350	LOC101928898		uncharacterized LOC101928898
351	TPTE2P1	13q12.13	transmembrane phosphoinositide 3-phosphatase and tensin homolog 2 pseudogene 1
352	LOC100422635		solute carrier family 25 (mitochondrial carrier; ornithine transporter) member 15 pseudogene 3
353	RPL34P27	13q12.12	ribosomal protein L34 pseudogene 27

| #	Gene	Position	Discription
354	LSP1P1	13q12.13	lymphocyte-specific protein 1 pseudogene 1
355	LOC100133284	13q12.13	striatin, calmodulin binding protein pseudogene
356	PABPC3	13q12-q13	poly(A) binding protein, cytoplasmic 3
357	AMER2	13q12.13	OTTHUMP00000018143
358	LOC101928922		uncharacterized LOC101928922
359	RPL23AP69	13q12.13	ribosomal protein L23a pseudogene 69
360	MTMR6	13q12	myotubularin related protein 6
361	NUPL1	13q12.13	nucleoporin like 1
362	TCEB2P1	13q12	transcription elongation factor B (SIII), polypeptide 2 (18kDa, elongin B) pseudogene 1
363	ATP8A2	13q12	ATPase, aminophospholipid transporter, class I, type 8A, member 2
364	RNU6-78P		RNA, U6 small nuclear 78, pseudogene
365	CCDC113	16q21	coiled-coil domain containing 113
366	PRSS54	16q21	protease, serine, 54
367	GINS3	16q21	GINS complex subunit 3 (Psf3 homolog)
368	NDRG4	16q21-q22.1	NDRG family member 4
369	SETD6	16q21	SET domain containing 6
370	CNOT1	16q21	CCR4-NOT transcription complex, subunit 1
371	SNORA46	16q21	small nucleolar RNA, H/ACA box 46
372	SNORA50	16q21	small nucleolar RNA, H/ACA box 50
373	SLC38A7	16q21	solute carrier family 38, member 7
374	GOT2	16q21	glutamic-oxaloacetic transaminase 2, mitochondrial
375	RNY5P9	16q21	RNA, Ro-associated Y5 pseudogene 9
376	GEMIN8P2	16q21	gem (nuclear organelle) associated protein 8 pseudogene 2
377	RPL12P36	16q21	ribosomal protein L12 pseudogene 36
378	RPS27P27	16q21	ribosomal protein S27 pseudogene 27
379	APOOP5	16q21	apolipoprotein O pseudogene 5
380	LOC101927580		uncharacterized LOC101927580
381	LOC100421258		NOP58 ribonucleoprotein homolog (yeast) pseudogene
382	LOC729159	16q21	UPF0607 protein ENSP00000381418-like
383	LOC101927605		uncharacterized LOC101927605
384	GNPATP	16q21	glyceronephosphate O-acyltransferase pseudogene
385	LOC100421593		family with sequence similarity 71, member A pseudogene
386	RPS27AP16	16q21	ribosomal protein S27a pseudogene 16
387	CDH8	16q22.1	cadherin 8, type 2
388	RNU6-21P		RNA, U6 small nuclear 21, pseudogene
389	LOC101060189		ubiquitin-conjugating enzyme E2F (putative) pseudogene
390	RPS15AP34	16q21	ribosomal protein S15a pseudogene 34
391	LOC101927629		uncharacterized LOC101927629
392	LOC729217	16q21	emopamil binding protein-like pseudogene
393	CDH11	16q21	cadherin 11, type 2, OB-cadherin (osteoblast)
394	LOC101927650		uncharacterized LOC101927650
395	LINC00922	16q21	long intergenic non-protein coding RNA 922

Appendix 3
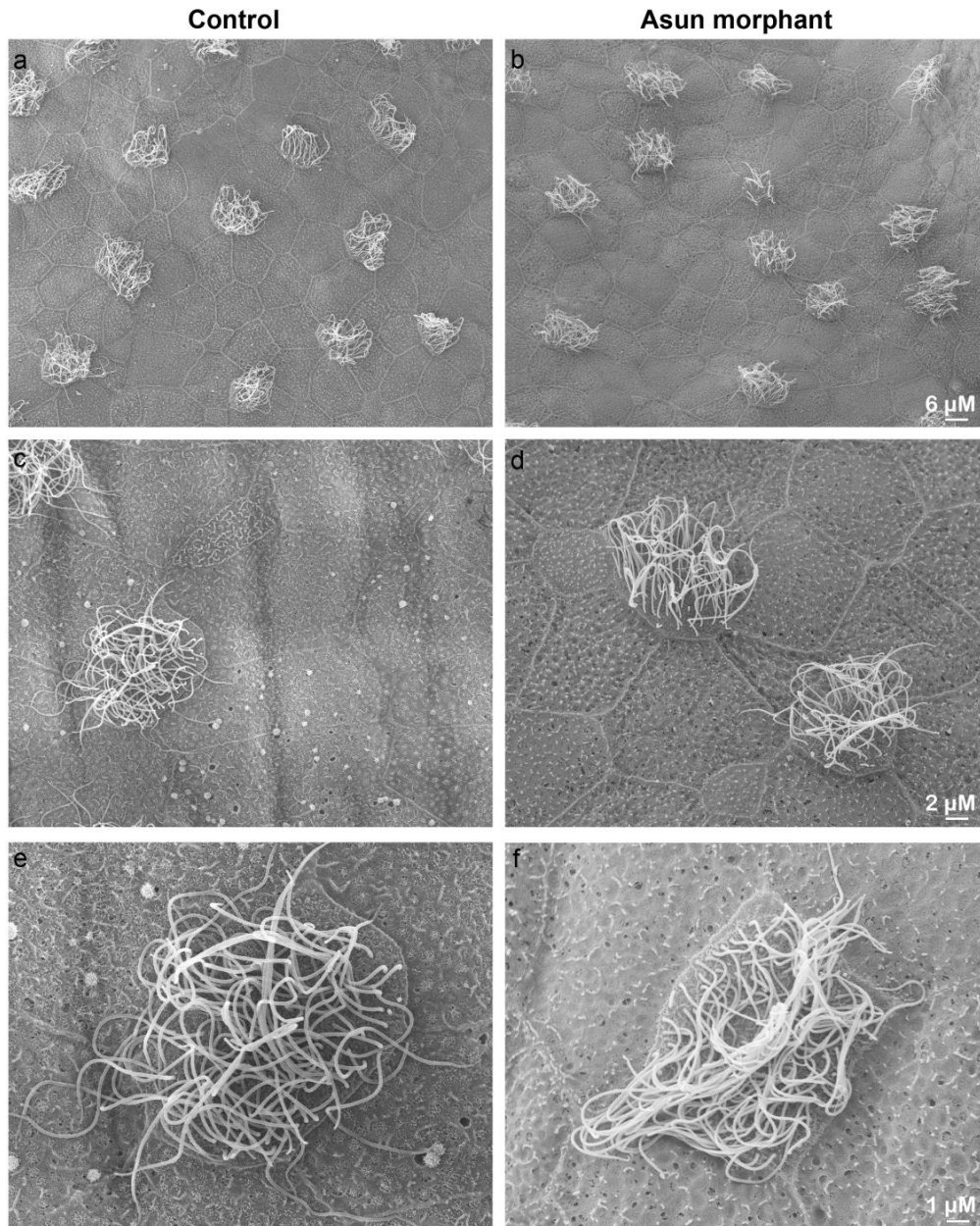
Supplementary Figures and Tables

Supplementary Figure 1: Full pedigree of the Jordanian family. Empty red boxes and circles indicate to parents' siblings whom we collected saliva samples for genotyping. Solid circles with similar color represet the same individual. Numbers indicate to the total number of males and females within each subfamily.
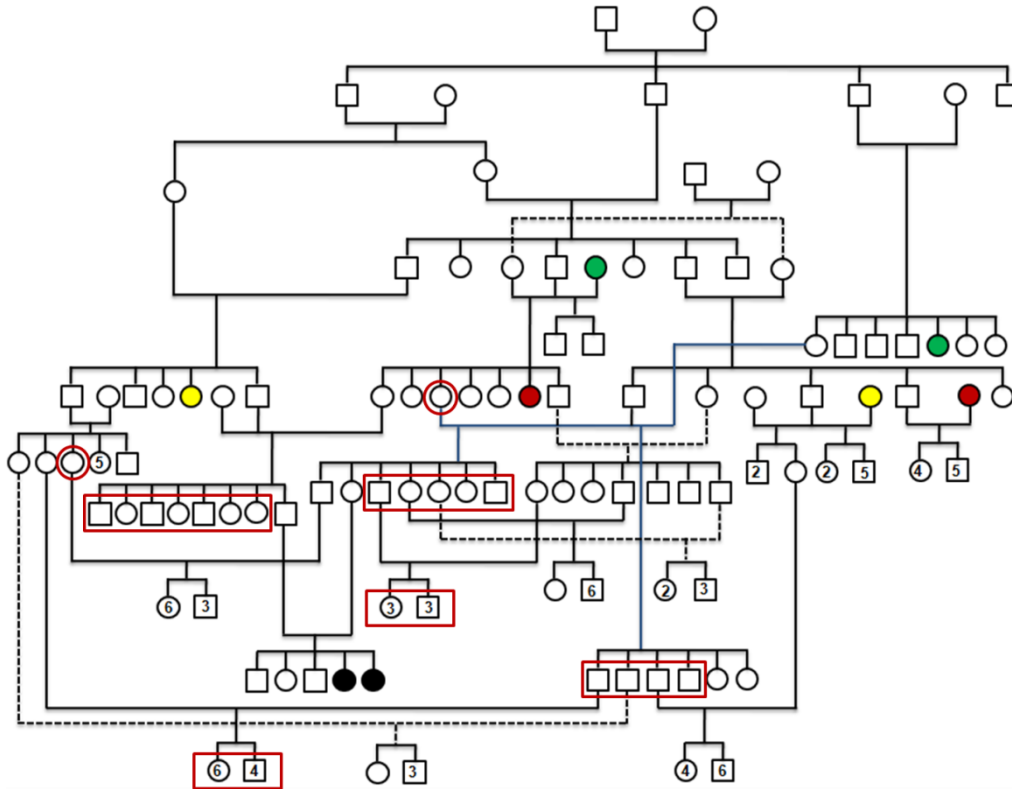
Supplementary Figure 2: Full sized ASUN protein alignment.
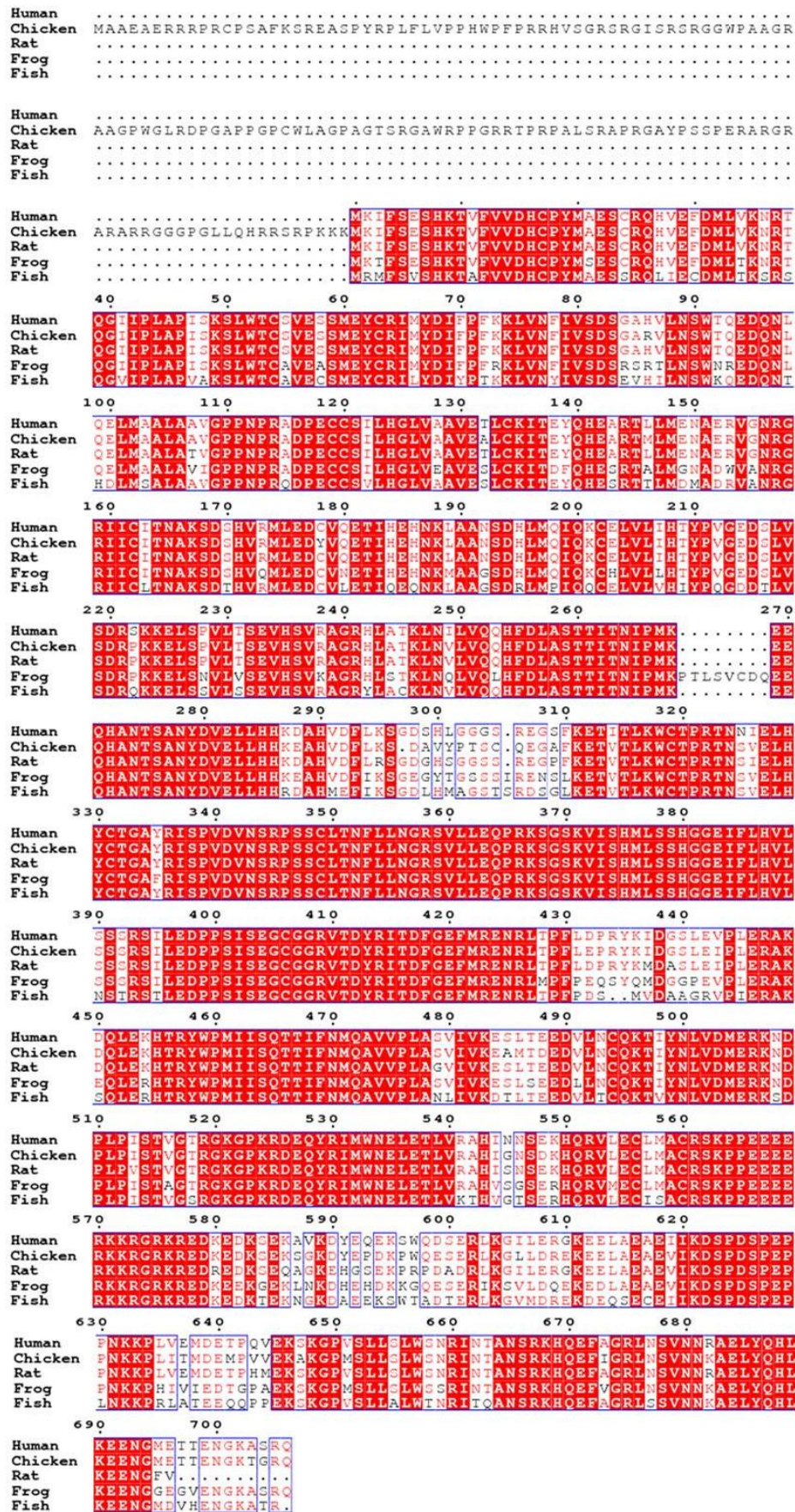
Supplementary Figure 3: A scanning electron microscopy for ciliated cells (MCC) of control and *asun*-splicing-MO injected embryos. (a,c,e) Low magnification view of control embryo MCC which display multiple, long cilia. (b,d,f) Low magnification view of Asun morphant MCC exhibit mild defect in multi-cilia although few MCC are not totally ciliated. (c-f) At high magnification view, it seems that the length of cilia is not affected in Asun morphant, however, few, malformed, disorganized and twisted to each other in individual cells.

Supplementary Figure 4: Nested RT-PCR analysis for *PKHD1L1* in lymphoblastoid cells of control, unaffected heterozygous brother and patients. (a) Primers position and the fragments size. Nested RT-PCR results display multiple and variable transcripts in both patients' cells. Wild-type transcript (Panels b and c, lane 1), heterozygous brother's transcripts (Panels b and c, lane 2), patients' transcripts carrying PTCs at different positions: patient IV.6 (Panel b, lanes 3-5); patient IV.7 (Panel c, lanes 3-5).
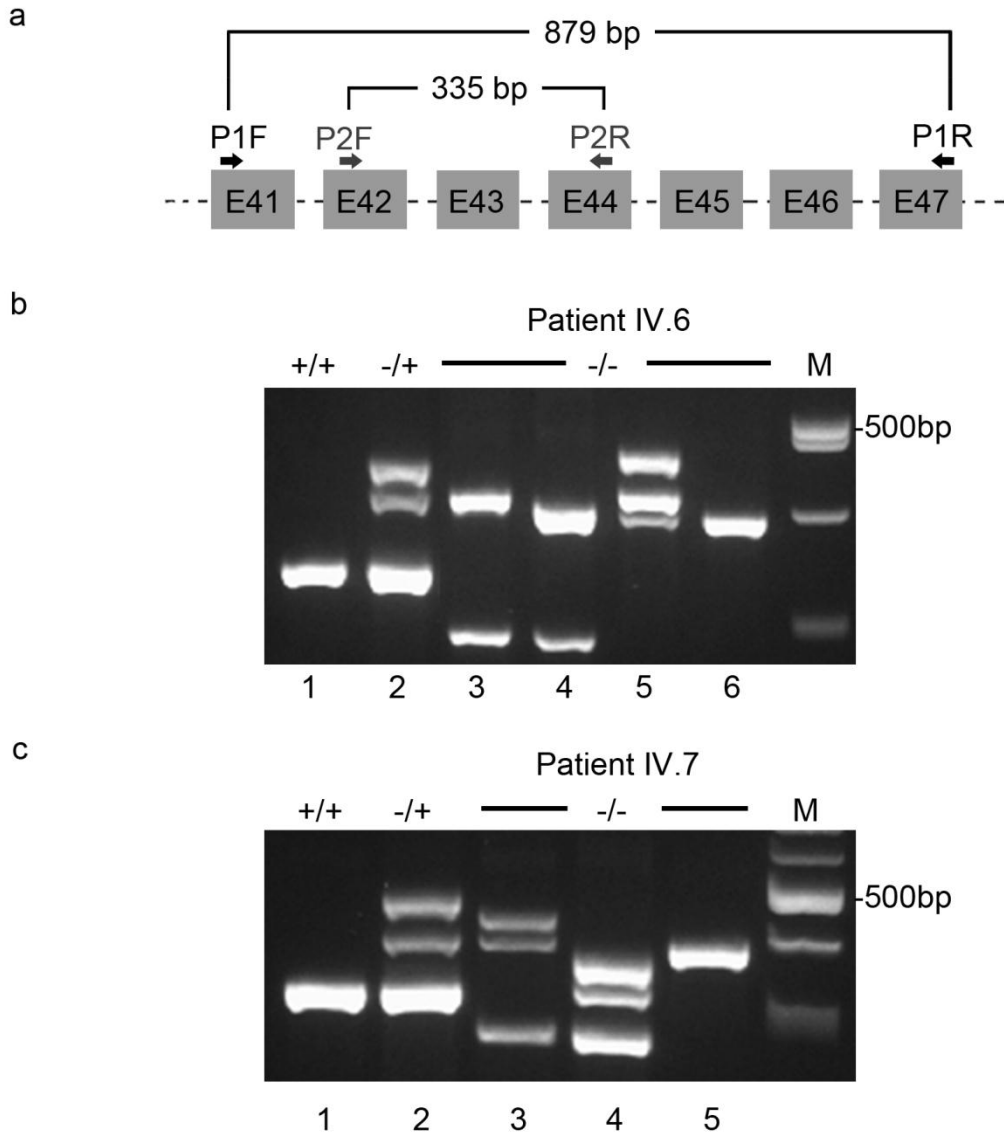
Supplementary Table: Mutation analysis of all candidate genes for 34 samples collected from parents' siblings. -/-, homozygous mutant; -/+, unaffected carrier; +/+, homozygous normal.

	Gene	*MLLT4*	*DACT2*	*THBS2*	*SAC2*	*PKHD1L1*	*ASUN*
	Mutation	c.3923A>T	c.515G>A	c.389T>C	c.4335A>T	c.6406T>G c.6507+1g>a	c.2004delA
Sample #	**Relation to patients**				**Results**		
	Father's siblings						
1	Uncle	-/+	-/-	-/-	+/+	-/+	+/+
2	Uncle	-/+	-/+	-/+	-/+	-/+	-/+
3	Uncle	-/-	+/+	-/-	-/+	-/+	+/+
4	Aunt	+/+	-/+	+/+	-/+	-/+	+/+
5	Aunt	-/+	+/+	-/+	+/+	-/+	+/+
6	Aunt	-/+	+/+	-/+	+/+	+/+	+/+
7	Aunt	+/+	+/+	+/+	+/+	-/+	+/+
8	Uncle	-/-	+/+	-/-	-/+	-/+	+/+
	Mother's siblings						
9	Grandmother	-/+	-/+	-/+	-/+	+/+	-/+
10	Uncle	+/+	+/+	+/+	-/+	+/+	-/+
11	Uncle	+/+	+/+	+/+	-/+	+/+	-/+
12	Aunt	+/+	+/+	+/+	+/+	+/+	-/+
13	Aunt	-/+	-/+	-/+	-/+	-/+	-/+
14	Aunt	+/+	+/+	+/+	-/+	-/+	-/+
15	Aunt	-/+	+/+	-/+	+/+	+/+	-/+
16	Uncle	+/+	+/+	-/+	+/+	+/+	+/+
17	Uncle	-/+	+/+	-/+	+/+	-/+	+/+
18	Cousin	+/+	+/+	+/+	-/+	-/+	+/+
19	Cousin	+/+	+/+	+/+	+/+	-/+	-/+
20	Cousin	+/+	+/+	+/+	-/+	-/+	+/+
21	Cousin	+/+	+/+	+/+	+/+	-/+	+/+
22	Cousin	+/+	+/+	+/+	-/+	-/+	+/+
23	Cousin	+/+	+/+	+/+	+/+	-/+	-/+
24	Cousin	+/+	+/+	+/+	-/+	-/+	+/+
25	Cousin	+/+	+/+	+/+	+/+	-/+	-/+
26	Uncle's wife	+/+	+/+	+/+	+/+	-/-	+/+
27	Cousin	+/+	+/+	+/+	-/+	+/+	-/+
28	Cousin	+/+	+/+	+/+	-/+	-/+	-/+
29	Cousin	+/+	+/+	+/+	+/+	-/+	-/+
30	Cousin	+/+	+/+	+/+	+/+	-/+	-/+
31	Cousin	+/+	+/+	+/+	-/+	-/+	-/+
32	Cousin	+/+	+/+	+/+	-/+	+/+	+/+
33	Uncle's wife	+/+	+/+	+/+	+/+	-/+	+/+
34	Cousin	+/+	+/+	+/+	+/+	-/+	+/+

234

Appendix 4

My co-author publications in different journals before and during my research work.

1. Zimoń M1, Battaloğlu E, Parman Y, Erdem S, Baets J, De Vriendt E, Atkinson D, Almeida-Souza L, Deconinck T, Ozes B, Goossens D, Cirak S,Van Damme P, **Shboul M**, Voit T, Van Maldergem L, Dan B, El-Khateeb MS, Guergueltcheva V, Lopez-Laso E, Goemans N, Masri A, Züchner S, Timmerman V, Topaloğlu H, De Jonghe P, Jordanova A. (2014). Unraveling the genetic landscape of autosomal recessive Charcot-Marie-Tooth neuropathies using a homozygosity mapping approach. Neurogenetics. PubMed PMID: 25231362.

2. Lopez E, Thauvin-Robinet C, Reversade B, Khartoufi NE, Devisme L, Holder M, Ansart-Franquet H, Avila M, Lacombe D, Kleinfinger P, Kaori I, Takanashi JI, Le Merrer M, Martinovic J, Noël C, **Shboul M**, Ho L, Güven Y, Razavi F, Burglen L, Gigot N, Darmency-Stamboul V, Thevenon J, Aral B, Kayserili H, Huet F, Lyonnet S, Le Caignec C, Franco B, Rivière JB, Faivre L, Attié-Bitach T. (2013). C5orf42 is the major gene responsible for OFD syndrome type VI. Human genetics 133, 367-377.

3. Jodoin, J.N., **Shboul, M.**, Albrecht, T.R., Lee, E., Wagner, E.J., Reversade, B., and Lee, L.A. (2013a). The snRNA-processing complex, Integrator, is required for ciliogenesis and dynein recruitment to the nuclear envelope via distinct mechanisms. Biology open 2, 1390-1396.

4. Jodoin, J.N., Sitaram, P., Albrecht, T.R., May, S.B., Shboul, M., Lee, E., Reversade, B., Wagner, E.J., and Lee, L.A. (2013b). Nuclear-localized Asunder regulates cytoplasmic dynein localization via its role in the integrator complex. Molecular biology of the cell 24, 2954-2965.

5. Jodoin, J.N., **Shboul, M.**, Sitaram, P., Zein-Sabatto, H., Reversade, B., Lee, E., and Lee, L.A. (2012). Human Asunder promotes dynein recruitment and centrosomal tethering to the nucleus at mitotic entry. Molecular biology of the cell 23, 4713-4724.

6. Pohler E, Mamai O, Hirst J, Zamiri M, Horn H, Nomura T, Irvine AD, Moran B, Wilson NJ, Smith FJ, Goh CS, Sandilands A, Cole C, Barton GJ, Evans AT, Shimizu H, Akiyama M, Suehiro M, Konohana I, **Shboul M**, Teissier S, Boussofara L, Denguezli M, Saad A, Gribaa M, Dopping-Hepenstal PJ, McGrath JA, Brown SJ, Goudie DR, Reversade B, Munro CS, McLean WH. (2012). Haploinsufficiency for AAGAB causes clinically heterogeneous forms of punctate palmoplantar keratoderma. Nat Genet 44, 1272-1276.

7. Bonnard C, Strobl AC, **Shboul M**, Lee H, Merriman B, Nelson SF, Ababneh OH, Uz E, Güran T, Kayserili H, Hamamy H, Reversade B. (2012). Mutations in IRX5 impair craniofacial development and germ cell migration via SDF1. Nat Genet 44, 709-713.

8. Kroos M, Hoogeveen-Westerveld M, Michelakakis H, Pomponio R, Van der Ploeg A, Halley D, Reuser A; GAA Database Consortium. (2012). Update of the pompe disease mutation database with 60 novel GAA sequence variants and additional studies on the functional effect of 34 previously reported variants. Hum Mut 33, 1161-1165.

9. Dajani R, Fatahallah R, Dajani A, **Al-Shboul M**, Khader Y. (2012). Prevalence of coagulation factor II G20210A and factor V G1691A Leiden polymorphisms

in Chechans, a genetically isolated population in Jordan. Molecular Biology Reports 39, 9133-9138.

10. Albaramki J, Akl K, Al-Muhtaseb A, **Al-Shboul M**, Mahmoud T, El-Khateeb M, Hamamy H. (2012). Sanjad Sakati syndrome: a case series from Jordan. East Mediterranean Health J 18, 527-531.

11. Samia Temtamy, Mona Aglan, A. Kemal Topaloglu, Bernd Wollnik, Khalda Amr, Tarek H. El-Badry, Gamal A. Hosny, Nermine Salah Eldin, **Mohammad Shboul**, Mustafa Herdem, Junxian Ong, Bruno Reversade and Jing Tian. (2012). Definition of the phenotypic spectrum of Temtamy Preaxial brachydactyly syndrome associated with autosomal recessive CHYS1 mutations. Middle East Journal of Medical Genetics 1, 64-70.

12. Huang L, Szymanska K, Jensen VL, Janecke AR, Innes AM, Davis EE, Frosk P, Li C, Willer JR, Chodirker BN, Greenberg CR, McLeod DR, Bernier FP, Chudley AE, Müller T, Shboul M, Logan CV, Loucks CM, Beaulieu CL, Bowie RV, Bell SM, Adkins J, Zuniga FI, Ross KD, Wang J, Ban MR, Becker C, Nürnberg P, Douglas S, Craft CM, Akimenko MA, Hegele RA, Ober C, **Shboul M**, Utermann G, Bolz HJ, Bulman DE, Katsanis N, Blacque OE, Doherty D, Parboosingh JS, Leroux MR, Johnson CA, Boycott KM. (2011). TMEM237 is mutated in individuals with a Joubert syndrome related disorder and expands the role of the TMEM family at the ciliary transition zone. Am J Hum Genet 89,713-730.

13. Tian J, Ling L, **Shboul M**, Lee H, O'Connor B, Merriman B, Nelson SF, Cool S, Ababneh OH, Al-Hadidy A, Masri A, Hamamy H, Reversade B. Loss of CHSY1, a secreted FRINGE enzyme, causes syndromic brachydactyly in humans via increased NOTCH signaling. (2010). Am J Hum Genet 87, 768-778.

14. Shammas C, Papasavva T, Felekis X, Christophorou C, Roomere H, Synodinos JT, Kanavakis E, El-Khateeb M, Hamamy H, Mahmoud T, **Shboul M**, El Beshlawy A, Filon D, Hussein IR, Galanello R, Romeo G, Kleanthous M. (2010). ThalassoChip, an array mutation and single nucleotide polymorphism detection tool for the diagnosis of β-thalassaemia. Clin Chem Lab Med 48, 1713-1718.

15. Reversade B, Escande-Beillard N, Dimopoulou A, Fischer B, Chng SC, Li Y, **Shboul M**, Tham PY, Kayserili H, Al-Gazali L, Shahwan M, Brancati F, Lee H, O'Connor BD, Schmidt-von Kegler M, Merriman B, Nelson SF, Masri A, Alkazaleh F, Guerra D, Ferrari P, Nanda A, Rajab A, Markie D, Gray M, Nelson J, Grix A, Sommer A, Savarirayan R, Janecke AR, Steichen E, Sillence D, Hausser I, Budde B, Nürnberg G, Nürnberg P, Seemann P, Kunkel D, Zambruno G, Dallapiccola B, Schuelke M, Robertson S, Hamamy H, Wollnik B, Van Maldergem L, Mundlos S, Kornak U. (2009). Mutations in PYCR1 cause cutis laxa with progeroid features. Nat Genet 4, 1016-21.

ORIGINAL ARTICLE

Unraveling the genetic landscape of autosomal recessive Charcot-Marie-Tooth neuropathies using a homozygosity mapping approach

**Magdalena Zimoń · Esra Battaloğlu · Yesim Parman · Sevim Erdem · Jonathan Baets ·
Els De Vriendt · Derek Atkinson · Leonardo Almeida-Souza · Tine Deconinck ·
Burcak Ozes · Dirk Goossens · Sebahattin Cirak · Philip Van Damme ·
Mohammad Shboul · Thomas Voit · Lionel Van Maldergem · Bernard Dan ·
Mohammed S. El-Khateeb · Velina Guergueltcheva · Eduardo Lopez-Laso ·
Nathalie Goemans · Amira Masri · Stephan Züchner · Vincent Timmerman ·
Haluk Topaloğlu · Peter De Jonghe · Albena Jordanova**

Abstract Autosomal recessive forms of Charcot-Marie-Tooth disease (ARCMT) are rare but severe disorders of the peripheral nervous system. Their molecular basis is poorly understood due to the extensive genetic and clinical heterogeneity, posing considerable challenges for patients, physicians, and researchers. We report on the genetic findings from a systematic study of a large collection of 174 independent ARCMT families. Initial sequencing of the three most common ARCMT genes (*ganglioside-induced differentiation protein 1—GDAP1*, *SH3 domain and tetratricopeptide repeats-containing protein 2—SH3TC2*, *histidine-triad nucleotide binding protein 1—HINT1*) identified pathogenic mutations

M. Zimoń · E. De Vriendt · D. Atkinson · A. Jordanova (✉)
Molecular Neurogenomics Group, VIB Department of Molecular Genetics, University of Antwerp, Universiteitsplein 1, 2610 Antwerp, Belgium
e-mail: albena.jordanova@molgen.vib-ua.be

M. Zimoń · J. Baets · E. De Vriendt · D. Atkinson ·
L. Almeida-Souza · T. Deconinck · V. Timmerman · P. De Jonghe ·
A. Jordanova
Neurogenetics Laboratory, Institute Born-Bunge, University of Antwerp, Antwerp, Belgium

E. Battaloğlu · B. Ozes
Department of Molecular Biology and Genetics, Bogazici University, Istanbul, Turkey

Y. Parman
Department of Neurology, Istanbul Medical Faculty, Istanbul University, Istanbul, Turkey

S. Erdem
Department of Neurology, Faculty of Medicine, Hacettepe University, Ankara, Turkey

J. Baets · T. Deconinck · P. De Jonghe
Neurogenetics Group, VIB Department of Molecular Genetics, University of Antwerp, Antwerp, Belgium

J. Baets · P. De Jonghe
Department of Neurology, Antwerp University Hospital, Antwerp, Belgium

L. Almeida-Souza · V. Timmerman
Peripheral Neuropathy Group, VIB Department of Molecular Genetics, University of Antwerp, Antwerp, Belgium

D. Goossens
Applied Molecular Genomics Unit, VIB Department of Molecular Genetics, University of Antwerp, Antwerp, Belgium

S. Cirak
Research Center for Genetic Medicine, Children's National Medical Center, Washington, DC, USA

P. Van Damme
Experimental Neurology and Leuven Institute for Neurodegenerative Disorders (LIND), University of Leuven, Leuven, Belgium

in 41 patients. Subsequently, 87 selected nuclear families underwent single nucleotide polymorphism (SNP) genotyping and homozygosity mapping, followed by targeted screening of known ARCMT genes. This strategy provided molecular diagnosis to 22 % of the families. Altogether, our unbiased genetic approach identified pathogenic mutations in ten ARCMT genes in a total of 41.3 % patients. Apart from a newly described founder mutation in *GDAP1*, the majority of variants constitute private molecular defects. Since the gene testing was independent of the clinical phenotype of the patients, we identified mutations in patients with unusual or additional clinical features, extending the phenotypic spectrum of the *SH3TC2* gene. Our study provides an overview of the ARCMT genetic landscape and proposes guidelines for tackling the genetic heterogeneity of this group of hereditary neuropathies.

Introduction

Charcot-Marie-Tooth disease (CMT) represents a group of degenerative disorders of the peripheral nervous system, characterized by progressive weakness and atrophy of distal limb muscles and sensory abnormalities. CMT is the most common type of inherited peripheral neuropathy affecting 1 in 2,500 individuals worldwide [1]. Autosomal recessive CMT (ARCMT) is considered to be rare in the European CMT population accounting for less than 10 % of patients. This frequency is most likely underestimated due to the small size of sibships, with many ARCMT patients being unrecognized and considered as sporadic cases. ARCMT, similarly to other rare recessive disorders, is more frequent (30–50 % of CMT patients) in populations with high prevalence of consanguineous marriages (e.g., in the Mediterranean basin or in the Middle East) [2].

ARCMT can be divided into demyelinating (CMT4), axonal (ARCMT2), or intermediate types based on clinical, electrophysiological, and neuropathological criteria. Clinical presentation of patients is similar to that of other types of CMT; however, it has a more severe disease course. The first symptoms are early in life (can be even congenital or in early infancy) and result in delayed developmental milestones. Progression of muscle atrophy and weakness often leads to loss of ambulation. The widespread involvement of peripheral nerves is frequently associated with vocal fold paralysis, sensorineural deafness, bulbar, facial and diaphragmatic weakness, and can lead to early death in the most severely affected patients. Accompanying phenotypic features, like scoliosis, glaucoma,

P. Van Damme
Vesalius Research Center, VIB, Leuven, Belgium

P. Van Damme
Department of Neurology, University Hospital Leuven, University of Leuven, Leuven, Belgium

M. Shboul
Institute of Medical Biology, A*STAR, Singapore, Singapore

T. Voit
Unité de Morphologie Neuromusculaire, Institut de Myologie, Université Pierre et Marie Curie-Paris, Paris, France

L. Van Maldergem
Centre de Génétique Humaine, Université de Franche-Comté, Besançon, France

B. Dan
Department of Neurology, Hôpital Universitaire des Enfants Reine Fabiola, Université Libre de Bruxelles (ULB), Brussels, Belgium

M. S. El-Khateeb
Genetic Laboratory, Faculty of Medicine, University of Jordan, Amman, Jordan

V. Guergueltcheva
Department of Neurology, Medical University-Sofia, Sofia, Bulgaria

E. Lopez-Laso
Pediatric Neurology Unity, University Hospital Reina Sofia, Cordoba, Spain

N. Goemans
Department of Pediatric Neurology, University Hospital Leuven, Leuven, Belgium

A. Masri
Pediatric Department, Division of Child Neurology, Faculty of Medicine, University of Jordan, Amman, Jordan

S. Züchner
Department of Human Genetics and Hussman Institute for Human Genomics, University of Miami Miller School of Medicine, Miami, FL, USA

H. Topaloğlu
Department of Pediatric Neurology, Faculty of Medicine, Hacettepe University, Ankara, Turkey

A. Jordanova
Department of Medical Chemistry and Biochemistry, Molecular Medicine Center, Medical University-Sofia, Sofia, Bulgaria

Present Address:
M. Zimoń
Cell Biology and Biophysics Unit, European Molecular Biology Laboratory (EMBL), Meyerhofstraße 1, 69117 Heidelberg, Germany

Present Address:
L. Almeida-Souza
MRC Laboratory of Molecular Biology, Hills Road, Cambridge, UK

myelin outfoldings, or neuromyotonia, can guide the correct genetic diagnosis of some ARCMT subtypes [3–6].

Up until now, 27 genes were causally associated with ARCMT, which however explain only a small proportion of cases. The known genes have been identified mainly by linkage analyses and candidate gene screenings in large pedigrees or in specific ethnic minorities (e.g., Gypsies), while the smaller families often remained undiagnosed. Furthermore, there is no single gene or mutation accounting for the majority of patients, and most of them carry private defects in rare genes. This extensive non-allelic heterogeneity challenges the molecular genetic diagnosis and follow-up of the ARCMT patients and hampers the development of effective treatment strategies.

In the current study, we analyzed a cohort of 174 nuclear families or isolated patients diagnosed with autosomal recessive Charcot-Marie-Tooth disease. Combining gene-based screening with homozygosity mapping and mutation analysis of positional CMT candidates, we were able to provide a molecular diagnosis to 41.3 % of the families. The gene screening was guided by genetic rather than clinical criteria, and we were able to expand the phenotypic spectrum of mutations in the SH3TC2 gene. Also, homozygosity mapping allowed estimating the actual degree of inbreeding and the corresponding size and number of homozygous regions in each patient or family, which facilitated mutation identification. Our results present an overview on the ARCMT genetic architecture and provide guidelines for future gene screenings in ARCMT patient cohorts.

Materials and methods

Standard protocol approvals, registrations, and patient consents

All patients or their legal representatives signed an informed consent form prior to enrolment. This study was approved by the local institutional review boards.

Patient cohort

In this study, we included 174 index patients with peripheral neuropathies either inherited in autosomal recessive fashion or sporadic patients, descendants from consanguineous marriages. Diagnosis of CMT in the probands was established by an experienced physician and was based on neurological examination and electrophysiological evaluation.

In 87 selected families, we performed SNP genotyping and subsequent candidate gene sequencing. The patients in the genotyped cohort were diagnosed with CMT1 (38), CMT2 (25), CMT-intermediate (2), hereditary motor neuropathy (2),

and hereditary neuropathy of unspecified type (20). Families included in this part of the study were of Turkish (83 %), Arab (5.7 %), Roma (4.5 %), or other (6.8 %) origin. We had data on parental consanguinity for 34 pedigrees, including double first cousins (2), first cousins (23), first cousins once removed (6), second cousins (2), and second cousins once removed (1) marriages. Other 23 families had unknown degree of relatedness, for 12 no information on parental consanguinity was available and for 18 no consanguinity was reported.

SNP genotyping and homozygosity mapping

Whole genome SNP genotyping on 155 individuals from 87 ARCMT families was performed with the Illumina Human660W-Quad (42 families) or OmniExpress (45) platforms. Data analysis was based on the human genome reference hg18 and hg19, respectively. We used the GenomeStudio software to calculate individual call rates (CR) and prepare files for bioinformatics analysis. Our quality filtering eliminated from further analysis samples with CR<98 %. Subsequent filtering steps were conducted with the PLINK software [7]. We excluded SNPs with low genotyping rate (uncalled in more than 10 % of individuals) and with low heterozygosity (minor allele frequency <0.05). Runs of homozygosity (ROH) in PLINK scanned the genome with a window of 50 consecutive SNPs, of which 94 % had to be homozygous and allowing 3 heterozygous SNPs. Overlap between sliding windows was 5 %. Acceptable missingness was three SNPs that were not called within the window. Allowed gap between SNPs was 1,000 kb. Subsequently, we selected only regions ≥1 Mb in size and containing minimum 100 SNPs. In the intra-familial analysis, overlapping homozygous segments were compared pairwise and were considered to be shared between individuals if allelic matching was declared for 95 % of all jointly homozygous and non-missing SNPs. Individual homozygous regions and the shared ones were visualized in Microsoft Excel using in-house developed Perl scripts. We developed Microsoft Excel-based script in order to automatically investigate the presence within selected homozygous regions of known CMT genes and genes involved in autosomal recessive forms of either ataxia or hereditary spastic paraplegia associated with peripheral neuropathy symptoms.

Mutation analysis

Total genomic DNA was isolated from peripheral blood samples and used as a template in the polymerase chain reactions (PCR). All coding exons and exon–intron boundaries of HINT1, GDAP1, SH3TC2, MTMR2, PRX, FGD4, MFN2, SBF2, NEFL, LMNA, NDRG1, HK1, and LRSAM were amplified using primer oligonucleotides designed with Primer3

(primer sequences and PCR conditions are available upon request). Subsequently, PCR products were purified with the exonuclease I-shrimp alkaline phosphatase enzymes (USB, Cleveland, USA) and sequenced in both directions using the BigDye® Terminator v3.1 Cycle Sequencing Kit (Applied Biosystems, Foster City, USA). Electrophoretic separation of fragments was performed on an ABI3730xl DNA Analyzer (Applied Biosystems, Foster City, USA). Sequences were analyzed with SeqMan™ II (DNASTAR Inc., Madison, USA) program. Mutations were described according to the latest conventions of the HGVS nomenclature (http://www.hgvs.org/mutnomen) with nucleotide numbering based on the published online (www.ncbi.nlm.nih.gov/) protein and mRNA sequences: HINT1 (NM_005340.5, NP_005331.1), GDAP1 (NM_018972, NP_061845), SH3TC2 (NM_024577.3, NP_078853.2), MTMR2 (NM_016156.5, NP_057240.3), PRX (NM_181882, NP_870998.2), FGD4 (NM_139241.2, NP_640334.2), MFN2 (NM_014874.3, NP_055689.1), SBF2 (NM_030962.3, NP_112224.1), NDRG1 (NM_001135242.1, NP_001128714.1), and HK1 (NM_033498.2, NP_277033.1). All sequence variants were confirmed by an independent PCR and resequencing of the original or newly obtained DNA samples. Segregation analysis of the mutations with the disease phenotype was performed in all available family members. For the newly identified mutations, 100 ethnically (Turkish, Belgian, Bulgarian) matched control individuals were screened.

Haplotype analysis

Haplotype sharing between families with the common GDAP1 deletion was ascertained with four highly informative short tandem repeat (STR) markers surrounding the gene (D8S286, D8S551, D8S1144, D8S548). STRs were first PCR-amplified with fluorescently labeled primer pairs (sequences are available at www.ncbi.nlm.nih.gov/), and fragments were subsequently combined with a formamide and GeneScan™ 500 Liz® Size Standard (Applied Biosystems, Foster City, USA) mixture (ratio 1:30) and size-separated on an ABI3730xl DNA Analyzer. Genotyping results were analyzed with Local Genotype Viewer, an in-house developed software program (http://www.vibgeneticservicefacility.be/).

Multiplex amplicon quantification assay (MAQ)

The presence of 3′-end partial deletion in GDAP1 was investigated by the MAQ assay (http://www.multiplicon.com/). In this assay, we performed multiplex PCR of ten fluorescently labeled amplicons targeting the genomic region of GDAP1 and six reference amplicons located at randomly selected genomic positions outside the GDAP1 region and other known copy number variations (CNVs). PCR fragments

were mixed with a formamide and GeneScan™ 500 Liz® Size Standard (Applied Biosystems, Foster City, USA) solution (ratio 1:30) and size-separated on ABI3730xl DNA Analyzer. The ratio of peak areas between the target and the reference amplicons was calculated. Comparison of the normalized peak area values between patients and control individuals allowed determination of a dosage quotient (DQ) for each target amplicon, calculated by the MAQ-S package (http://www.multiplicon.com/). DQ values below 0.75 were considered indicative for amplicon deletion.

Results

Mutation analysis of the most common ARCMT genes

Initially, we performed systematic analysis of 156 ARCMT families with unknown molecular defects (Fig. 1). We screened this cohort for the most frequently mutated ARCMT genes known to date, independent of the clinical phenotype of the patients. Mutation analysis of the coding regions and exon–intron boundaries of GDAP1 and HINT1 and the known hotspot mutations (R954* and R1190*) in SH3TC2 identified 15, 17, and 9 molecular defects, respectively. Some of the mutations were described previously [5, 8–12], and the novel or known pathogenic defects in non-reported pedigrees are presented in Table 1.

Additionally, 12 patients with known Roma ethnic background were screened for the private founder mutations in NDRG1 (R148*) and HK1 (AltT2 G>C + G>A intron). We identified ten individuals homozygous for the NDRG1 mutation and two for the HK1 alterations.

Collectively, this analysis provided molecular diagnosis to 53 out of the 156 families (33.9 %).

Homozygosity mapping analysis

As the remaining known ARCMT genes have very low frequency (<2 %) or are described in single families, we opted for an approach that would allow identification of the underlying defects in the rest of the patients while respecting the genetic heterogeneity of the CMT disease. To this end, we selected 69 ARCMT pedigrees from the initial cohort, based on the available genealogical information, reported consanguinity, ethnical, or geographic clustering. Additional 18 consanguineous families were included only at this stage of the study and therefore were not pre-screened for any gene (Fig. 1).

We performed genotyping with high-density SNP arrays of 155 individuals from these 87 families, followed by homozygosity mapping. We determined the median number of homozygous segments ≥1 Mb in size per affected

Fig. 1 Project strategy scheme
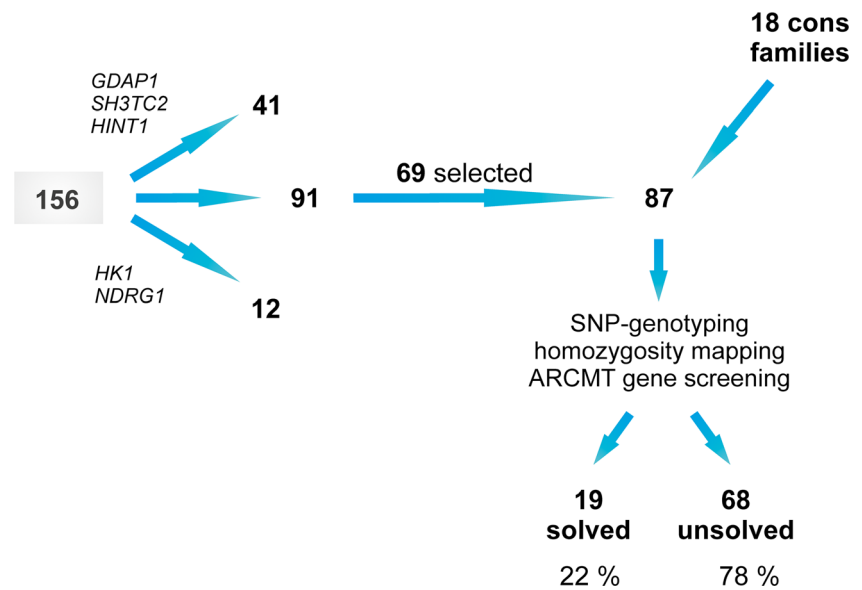
individual. This number progressively decreased from 61 for patients, whose parents were double first cousins, to 48 for first cousins, 35 for first cousins once removed, and to 40 for second cousins. The average sizes of the homozygous SNP blocks were 7.1, 5.4, 4.7, and 2.6 Mb, respectively (Supplementary Table 1).

We also correlated the proportion of homozygous autosomal genome with the degree of consanguinity. In descendants from first cousin marriages, the observed median genome homozygosity was 8.2 %, while the theoretical predictions suggest 6 % (1/16). Similarly, the calculated median values were higher by at least 2–3 % than the expected ones for all other consanguinity groups (Supplementary Table 1). Interestingly, patients with ARCMT and no documented history of consanguinity showed increased homozygosity of their genome that was often higher than the homozygosity observed in descendants from second cousin marriages (Supplementary Fig. 1).

To reduce the number and the size of homozygous regions containing putative ARCMT-causing mutations, we included the genotypes of additional sibs, available in 36 % of the families. Combined analysis of two affected individuals decreased the number and size of homozygous blocks by ~60 %. Inclusion of unaffected sibs also decreased the percentage of homozygous genome (and number of homozygous blocks) by 12 (33) %, 48 (50) %, or 73 (68) %, respectively for one, two, or three unaffected individuals.

Furthermore, we could not identify large autozygous regions shared by two affected individuals in the Belgian family cmt68, thus suggesting the presence of compound heterozygous mutations. Subsequent linkage analysis combined with whole genome sequencing revealed two compound heterozygous mutations in the novel at that time *HINT1* gene [6].

Gene and mutation contribution to ARCMT

We used the homozygosity data, rather than clinical features of the patients, to Sanger sequence any known ARCMT gene located within a large (>1 Mb) homozygous region. With this approach, we successfully identified mutations in 19 out of 87 families (22.9 %) (Table 1). We found mutations in *SH3TC2* (four), *HINT1* (two), *GDAP1* (two), *FGD4* (two), *MFN2* (two), *PRX* (two), *SBF2* (two), *MTMR2* (two), and *NDRG1* (one). Although *NEFL*, *LMNA*, and *LRSAM1* were located in large homozygous regions in several families, we could not find mutations in the coding regions of these genes.

In total, our screening efforts resulted in identification of 14 non-reported sequence variations in *GDAP1* (five), *SH3TC2* (three), *SBF2* (two), *MTMR2* (two), and *FGD4* (two) (Table 1). Importantly, we found a partial homozygous deletion of *GDAP1* in three presumably unrelated families originating from different parts of Turkey (cmt131, cmt239, and cmt1226). Haplotype analysis with flanking microsatellite markers revealed a shared chromosomal region surrounding *GDAP1*, suggesting a founder effect (Supplementary Fig. 2a). The deleted genomic segment encompasses intron 5, exon 6, and three prime untranslated region (3′ UTR) of the gene. Heterozygosity of this deletion in the parents was confirmed by the MAQ assay (Supplementary Fig. 2b).

For all variants, we confirmed segregation with the disease phenotype in available family members. Presence of the newly identified mutations in ethnically matched control individuals was also excluded.

The phenotypic characteristics of the patients with newly identified mutations are presented in Supplementary Table 2.

Our combined target- and homozygosity-based gene screening approach identified disease-causing mutations in

Table 1 Mutations identified by the gene-based screening of *HINT1*, *GDAP1*, and *SH3TC2* and after homozygosity mapping

Family	Origin	Diagnosis	Gene	Nucleotide change	Protein change	ROH size [kb]	ROH rank	Largest ROH [KB]	Publication
Mutations identified by the gene-based screening of *HINT1*, *GDAP1*, and *SH3TC2*									
cmt1326	American	HMSN II	HINT1	c.110G>C	p.R37P				Zimoń et al. (2012)
cmt238	Turkish	HMSN I	SH3TC2	c.2860 C>T	p.R954*				Senderek et al. (2003)
PN1781	Belgian	HMSN I							
cmt1226	Turkish	HMSN I	GDAP1	intron5+exon6+3' UTR deletion					This study
cmt239	Turkish	HMSN I							
cmt1233	Turkish	HMSN II		c.482G>A	p.R161H				Baxter et al. (2002)
cmt851	Bulgarian	HMSN II		c.[679A>G];[715C>T]	p.[N227D];[L239F]				This study; Ammar et al. (2003)
cmt926	Turkish	HMSN I		c.174insT;176_177CC>TG]	p.P59Vfs*4				Auer-Grumbach et al. (2008)
PN1015	Turkish	HMSN I		c.99_100insT	p.S34Ffs*16				This study
PN1850	Jordan	HMSN I		c.836A>G	p.Y279C				Rougeot et al. (2008)
Mutations identified after homozygosity mapping									
cmt209	Belgian	HMSN II	MFN2	c.2119C>T	p.R707W	11,958	4	29,645	rs119103267, Nicholson et al. (2008)
cmt1264	Turkish	HMSN II				19,773	3	25,544	
cmt1207	Gypsy	HMSN II	HINT1	c.334C>A	p.H112N	14,224	1	14,224	Zimoń et al. (2012)
cmt162	Turkish	HMSN II		c.110G>C	p.R37P	21,644	1	21,644	Zimoń et al. (2012)
cmt1236	Turkish	HMSN I	SH3TC2	c.1914delG	p.A639Pfs*6	4,422	12	44,170	This study
cmt1147	Jordan	HN		c.3202C>T	p.Q1068*	7,293	1	7,293	This study
cmt1224	Turkish	HMSN II		c.2339T>C	p.L780P	27,074	2	36,985	This study
cmt1261	Turkish	HMSN I		c.1894-1897delGAGGinsAAA	p.E632Kfs*13	27,585	1	27,585	Fisher et al. (2012)
cmt1107	Pakistani	HMSN II	GDAP1	c.840delC	p.Y280*	23,439	3	43,653	This study
cmt131	Turkish	HMSN I		Intron5+exon6+3' UTR deletion		26,733	1	26,733	This study
cmt1240	Turkish	HN	SBF2	c.862-2A>G	Splice site	4,976	3	12,582	This study
cmt1083	Moroccan	HMSN I		c.374C>T	p.S125P	9,139	5	18,584	This study
cmt1242	Turkish	HMSN I	MTMR2	c.358-2A>T	Splice site	28,964	1	28,964	This study
cmt1250	Turkish	HMSN I		c.1343 T>C	p.L448P	57,370	1	57,370	This study
cmt1254	Turkish	HMSN I	FGD4	c.1887-1891delAAAAG	p.K630Nfs*5	5,054	4	9,216	This study
cmt1249	Turkish	HMSN I		c.1772G>A	p.W591*	9,263	2	13,892	This study
cmt112	Turkish	HMSN I	PRX	c.2098delG	p.A700Pfs*17	1,768	16	24,322	Auer-Grumbach et al. (2008)
cmt1246	Turkish	HMSN I		c.2289delT	p.D765Tfs*10	11,394	21	45,581	Boerkoel et al. (2001)
cmt1252	Gypsy	HMSN I	NDRG1	c.442C>T	p.R148*	2,039	9	7,482	Kalaydjieva et al. (2000)

ROH runs of homozygosity

73 ARCMT families and provided molecular diagnosis to 41.3 % of the 174 ARCMT index patients analyzed (Fig. 2).

Discussion

ARCMT is a disorder found in all ethnic groups; however, its prevalence varies significantly between populations and is rather low in the Western societies, when compared to autosomal dominant CMT forms. ARCMT patients are dispersed among clinical and research centers and very few large patient collections exist worldwide. Accordingly, the majority of studies performed so far focused on single ARCMT genes, specific phenotypes, or populations. Here, we present the findings in 174 nuclear families and sporadic patients diagnosed with ARCMT. To our knowledge, this is the first systematic study providing a general overview on the genetic landscape of ARCMT in a large cohort of patients.

Considering the extensive clinical and genetic heterogeneity of ARCMT, we pursued a genetic approach to unravel the molecular defects in our patients. Initially, we examined them for *GDAP1*, *SH3TC2*, and the recently discovered *HINT1*, followed by homozygosity-based CMT gene screening. In the ARCMT field, application of homozygosity mapping and/or linkage analyses have been proven successful in small diagnostic studies [13] and in identification of novel genes [6, 14–16]. Therefore, we SNP-genotyped the affected patients of 87 families with high-density arrays, providing 550,000–700,000 equally spaced genetic markers per individual. We

selected autozygous stretches ≥1 Mb in size and containing at least 100 consecutive homozygous SNPs. We used the number of SNPs as an inclusion criterion, as in non-random locations of the human genome with low recombination rates, regions of increased homozygosity-by-state are present that are characterized by low number of polymorphic markers [17]. Using these parameters, the average size of a homozygous block per ARCMT individual, whose parents are first cousins, was 5.5 Mb and the average number of homozygous regions was 48. These numbers could be further reduced by including additional affected or non-affected family members, when available.

We applied homozygosity mapping as an unbiased prioritization tool for analysis of the numerous known ARCMT loci. We sequenced a total of 12 CMT genes located within homozygous regions larger than 1 Mb and found mutations in nine of them, i.e., *SH3TC2*, *HINT1*, *GDAP1*, *FGD4*, *MFN2*, *PRX*, *SBF2*, *MTMR2*, and *NDRG1*. Genes with identified mutations were residing in the largest shared homozygous block in 35 % of families. In patients, whose parents were first cousins, the average size of the disease-associated homozygous region was 19 Mb ($n=8$, range 4.4–45 Mb). Notably, in family cmt112, in which we detected high degree of relatedness of the parents (calculated autosomal genome homozygosity of ~5 %), the disease-associated region was only 1.7 Mb in size. This finding has important practical consequences, particularly in light of the numerous reports recommending the mutation search to be focused primarily on genes residing in one of the largest homozygous regions [18]. One should consider the genetic map density and the

Fig. 2 Gene contribution to ARCMT in the studied cohort
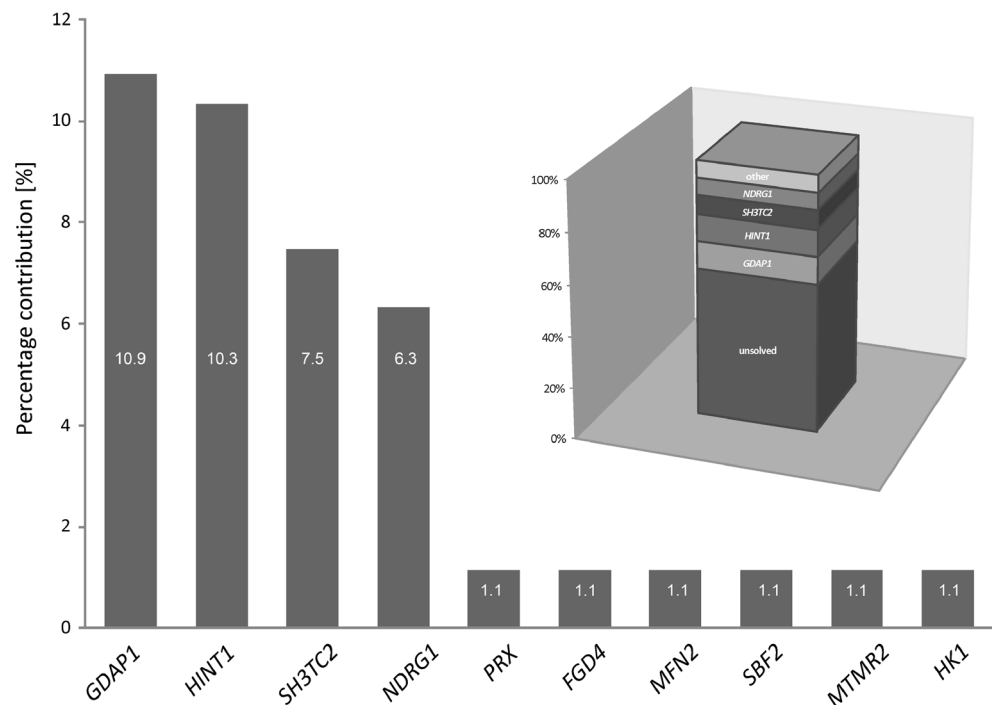
criteria for homozygosity in order not to miss small homozygous stretches that could also contain a disease-causing mutation.

Homozygosity analysis facilitated the molecular diagnosis of 22 % of patients in the genotyped cohort. Our success rate is lower in comparison with a recently published study [13], in which homozygosity mapping provided ARCMT diagnosis in 63 % of the cases. Fischer et al. however investigated only 24 index patients, while our cohort is substantially larger. Also, the fact that 7/24 patients with known ARCMT mutations were retrospectively analyzed for homozygosity could inflate the detection rate. Despite the differences in sensitivity, outcomes of both studies are complementary in showing that homozygosity mapping is an efficient tool in providing molecular diagnosis for a highly heterogeneous genetic disease, like ARCMT.

We identified 14 novel ARCMT mutations. New sequence variations were found in *GDAP1* (five), *SH3TC2* (three), *SBF2* (two), *FGD4* (two), and *MTMR2* (two). Homozygous partial deletion in *GDAP1* was identified in three Turkish families. STR marker analysis showed ancestral haplotype sharing between them, thus revealing a new *GDAP1* founder mutation in the Turkish population. Importantly, since the deletion encompasses intron 5, exon 6, and 3′ UTR, this small copy number variation can be easily missed if only parents are analyzed (e.g., the index patient is deceased) or if it occurs in *trans* with another heterozygous mutation. Thus, dosage analysis of exon 6 should be considered for ARCMT patients having only one heterozygous *GDAP1* mutation.

The probands carrying the *GDAP1* deletion showed an early onset phenotype and had walking difficulties requiring supports. In cmt239, *Pectus carinatum* was present, which could be considered as a skeletal deformity due to CMT, along with hoarseness and hypophonia. Although the patients had the same mutation, electrophysiological differences were observed between them. While cmt1226 and cmt239 had severely reduced or unrecordable nerve conduction velocities, cmt131 had considerably higher NCVs. Similar clinical heterogeneity was documented for other *GDAP1* mutation, even among patients within the same pedigree [10]. The peripheral nerve biopsies were characterized by absence of large myelinated fibers and overt signs of demyelination and axonal degeneration. Overall, this partial *GDAP1* deletion was characterized by mixed features, highlighting *GDAP1* as a gene causing an intermediate CMT phenotype.

Interestingly, our unbiased genetic approach allowed establishing of important genotype–phenotype correlations. In family, cmt1224 with the novel p.L780P *SH3TC2* mutation the proband had median NCVs values ≥40 m/s. The conduction velocities of patients with *SH3TC2* mutations reported so far are usually within the range 4–34 m/s (http://neuromuscular.wustl.edu/time/hmsn.html). In the available literature, the only two exceptions are a CMT patient with median

motor NCVs of 42.0 m/s, amplitude of 1.9 mV, and unexcitable median sensory nerves [12] and a patient reported by ref. [19] with median motor NCVs of 39.8 m/s, amplitude of 6.6 mV and median sensory NCVs of 43.0 m/s, and amplitude of 2.9 mV. Our findings extend the electrophysiological spectrum of *SH3TC2* mutations and suggest that along with intermediate conduction velocities, also patients with axonal electroneurographic findings should be considered for testing of this gene.

In patient cmt1236 with the novel p.A639Pfs*6 *SH3TC2* mutation, cerebellar dysfunction (tremor, bilateral horizontal nystagmus, titubation of the head with cerebellar dysmetria) was apparent. This type of central nervous system involvement has not been associated with *SH3TC2* mutations so far. We cannot exclude, however, that an additional gene might cause the cerebellar features in the patient.

The clinical phenotype of the remaining patients with newly identified mutations was in agreement with the genotype–phenotype correlations reported in the literature.

Our extensive screening efforts could not identify genetic defects in 58 % of the patients. Overall, there were no major clinical differences between the CMT individuals with known and unknown genetic causes. We cannot exclude that mutations located in unknown regulatory regions or deep-intronic sequences could have been missed by focusing on protein-coding regions. Furthermore, mutations in genes associated with other neuromuscular disorders that mimic CMT clinically could cause the disease in part of the families. Nevertheless, our findings underscore the heterogeneous molecular etiology of ARCMT and imply many unidentified disease-causing genes to exist.

The findings in this large-scale study allow us to suggest some guidelines for molecular genetic analysis of patients with ARCMT. Three genes are distinguished as major players in our ARCMT cohort, namely *GDAP1* (10.9 %), *HINT1* (10.3 %), and *SH3TC2* (7.5 %). Sanger or panel sequencing of these genes, which consist of only six, three, and two hotspot exons, respectively, would provide molecular diagnosis in ~25 % of the cases. It is also meaningful to first exclude known population-specific founder mutations. For example, the overall contribution of *NDRG1* is only 6.3 %; however, it reaches 17.9 % in the Gypsy population and should be tested in any patient with this ethnicity and demyelinating type of CMT [20]. The remaining known ARCMT genes have rather limited contribution to this disease (~1 %). Therefore, after screening the three most common genes, in view of constantly decreasing running costs, one could directly proceed with whole exome sequencing (WES) of the index patient. WES presents an interesting future alternative of the application of CMT gene panels, provided that the capturing and coverage will be improved. This way, finding of known genetic causes and searching for variations in new candidate genes can be performed simultaneously.

Homozygosity mapping with extracted SNPs from whole exome sequencing data can be used as a prioritization tool, pointing the regions encompassing known or novel ARCMT genes [21, 22]. WES-based homozygosity approach, however, will only identify autozygous loci that are located within regions containing a sufficient number of informative SNPs. Therefore, an alternative could be SNP genotyping of at least one affected individual prior to whole exome sequencing. Our data suggest that in patients originating from populations with prolonged history of consanguinity, the percentage of homozygous autosomal genome might be at least 2–3 % higher than the theoretical predictions [23]. Woods et al. by studying patients with autosomal recessive disorders originating from Pakistani and Arab populations reported similar findings [18]. In their study, mainly patients from first cousin marriages ($n=$ 38) were analyzed, and the percentage of homozygous autosomal genome was on average 11 %, while for us, this equals to 8.6 % ($n=27$). Interestingly, among the ARCMT patients with identified mutations, but no data or negative data for consanguinity, the percentage of homozygosity was also increased and could be as high as for descendants of a second cousin marriage. Therefore, in sporadic patients with increased degree of homozygosity, a recessive CMT inheritance should primarily be suspected. Contrastingly, lack of large in size (>1 Mb) or number of homozygous regions in any ARCMT family will be indicative of most likely compound heterozygous mutation underlying the phenotype.

In conclusion, our findings contribute to the knowledge on the molecular basis of ARCMT by providing an overview of the ARCMT genetic landscape, updating the ARCMT gene frequencies and broadening the mutation and clinical spectrum of known genes, like *GDAP1*, *SH3TC2*, *MTMR2*, *SBF2*, and *FGD4*. Furthermore, we propose guidelines for molecular investigation of ARCMT patients considering recent technological advances. Our findings have major implications for future molecular diagnostics and research in the field of peripheral neuropathies and other disorders with extensive genetic heterogeneity.

References

1. Skre H (1974) Genetic and clinical aspects of Charcot-Marie-Tooth's disease. Clin Genet 6:98–118
2. Dubourg O, Azzedine H, Verny C, Durosier G, Birouk N, Gouider R, Salih M, Bouhouche A, Thiam A, Grid D, Mayer M, Ruberg M, Tazir M, Brice A, LeGuern E (2006) Autosomal-recessive forms of demyelinating Charcot-Marie-Tooth disease. Neuromol Med 8:75–86
3. Bolino A, Muglia M, Conforti FL, LeGuern E, Salih MA, Georgiou DM, Christodoulou K, Hausmanowa-Petrusewicz I, Mandich P, Schenone A, Gambardella A, Bono F, Quattrone A, Devoto M, Monaco AP (2000) Charcot-Marie-Tooth type 4B is caused by mutations in the gene encoding myotubularin-related protein-2. Nat Genet 25:17–19
4. Azzedine H, Ruberg M, Ente D, Gilardeau C, Perie S, Wechsler B, Brice A, LeGuern E, Dubourg O (2003) Variability of disease progression in a family with autosomal recessive CMT associated with a S194X and new R310Q mutation in the GDAP1 gene. Neuromuscul Disord 13:341–346
5. Senderek J, Bergmann C, Stendel C, Kirfel J, Verpoorten N, De Jonghe P, Timmerman V, Chrast R, Verheijen MH, Lemke G, Battaloglu E, Parman Y, Erdem S, Tan E, Topaloglu H, Hahn A, Muller-Felber W, Rizzuto N, Fabrizi GM, Stuhrmann M, Rudnik-Schoneborn S, Zuchner S, Michael SJ, Buchheim E, Straub V, Klepper J, Huehne K, Rautenstrauss B, Buttner R, Nelis E, Zerres K (2003) Mutations in a gene encoding a novel SH3/TPR domain protein cause autosomal recessive Charcot-Marie-Tooth type 4C neuropathy. Am J Hum Genet 73:1106–1119
6. Zimon M, Baets J, Almeida-Souza L, De VE, Nikodinovic J, Parman Y, Battaloglu E, Matur Z, Guergueltcheva V, Tournev I, Auer-Grumbach M, De Rijk P, Petersen BS, Muller T, Fransen E, Van Damme P, Loscher WN, Barisic N, Mitrovic Z, Previtali SC, Topaloglu H, Bernert G, Beleza-Meireles A, Todorovic S, Savic-Pavicevic D, Ishpekova B, Lechner S, Peeters K, Ooms T, Hahn AF, Zuchner S, Timmerman V, Van DP, Rasic VM, Janecke AR, De Jonghe P, Jordanova A (2012) Loss-of-function mutations in HINT1 cause axonal neuropathy with neuromyotonia. Nat Genet 44:1080–1083
7. Purcell S, Neale B, Todd-Brown K, Thomas L, Ferreira MA, Bender D, Maller J, Sklar P, de Bakker PI, Daly MJ, Sham PC (2007) PLINK: a tool set for whole-genome association and population-based linkage analyses. Am J Hum Genet 81:559–575
8. Senderek J, Bergmann C, Ramaekers VT, Nelis E, Bernert G, Makowski A, Zuchner S, De Jonghe P, Rudnik-Schoneborn S, Zerres K, Schroder JM (2003) Mutations in the ganglioside-induced differentiation-associated protein-1 (GDAP1) gene in intermediate type autosomal recessive Charcot-Marie-Tooth neuropathy. Brain 126:642–649
9. Ammar N, Nelis E, Merlini L, Barisic N, Amouri R, Ceuterick C, Martin JJ, Timmerman V, Hentati F, De Jonghe P (2003) Identification of novel GDAP1 mutations causing autosomal recessive Charcot-Marie-Tooth disease. Neuromuscul Disord 13:720–728
10. Nelis E, Erdem S, Van Den Bergh PY, Belpaire-Dethiou MC, Ceuterick C, Van Gerwen V, Cuesta A, Pedrola L, Palau F, Gabreels-Festen AA, Verellen C, Tan E, Demirci M, Van BC, De Jonghe P, Topaloglu H, Timmerman V (2002) Mutations in GDAP1: autosomal recessive CMT with demyelination and axonopathy. Neurology 59:1865–1872

11. Kabzinska D, Strugalska-Cynowska H, Kostera-Pruszczyk A, Ryniewicz B, Posmyk R, Midro A, Seeman P, Barankova L, Zimon M, Baets J, Timmerman V, Guergueltcheva V, Tournev I, Sarafov S, De Jonghe P, Jordanova A, Hausmanowa-Petrusewicz I, Kochanski A (2010) L239F founder mutation in GDAP1 is associated with a mild Charcot-Marie-Tooth type 4C4 (CMT4C4) phenotype. Neurogenetics 11:357–366

12. Baets J, Deconinck T, De VE, Zimon M, Yperzeele L, Van HK, Peeters K, Spiegel R, Parman Y, Ceulemans B, Van Bogaert P, Pou-Serradell A, Bernert G, Dinopoulos A, Auer-Grumbach M, Sallinen SL, Fabrizi GM, Pauly F, Van den Bergh P, Bilir B, Battaloglu E, Madrid RE, Kabzinska D, Kochanski A, Topaloglu H, Miller G, Jordanova A, Timmerman V, De Jonghe P (2011) Genetic spectrum of hereditary neuropathies with onset in the first year of life. Brain 134:2664–2676

13. Fischer C, Trajanoski S, Papic L, Windpassinger C, Bernert G, Freilinger M, Schabhuttl M, Arslan-Kirchner M, Javaher-Haghighi P, Plecko B, Senderek J, Rauscher C, Loscher WN, Pieber TR, Janecke AR, Auer-Grumbach M (2012) SNP array-based whole genome homozygosity mapping as the first step to a molecular diagnosis in patients with Charcot-Marie-Tooth disease. J Neurol 259:515–523

14. Jenkinson EM, Rehman AU, Walsh T, Clayton-Smith J, Lee K, Morell RJ, Drummond MC, Khan SN, Naeem MA, Rauf B, Billington N, Schultz JM, Urquhart JE, Lee MK, Berry A, Hanley NA, Mehta S, Cilliers D, Clayton PE, Kingston H, Smith MJ, Warner TT, Black GC, Trump D, Davis JR, Ahmad W, Leal SM, Riazuddin S, King MC, Friedman TB, Newman WG (2013) Perrault syndrome is caused by recessive mutations in CLPP, encoding a mitochondrial ATP-dependent chambered protease. Am J Hum Genet 92:605–613

15. Bilguvar K, Tyagi NK, Ozkara C, Tuysuz B, Bakircioglu M, Choi M, Delil S, Caglayan AO, Baranoski JF, Erturk O, Yalcinkaya C, Karacorlu M, Dincer A, Johnson MH, Mane S, Chandra SS, Louvi A, Boggon TJ, Lifton RP, Horwich AL, Gunel M (2013) Recessive loss of function of the neuronal ubiquitin hydrolase UCHL1 leads to early-onset progressive neurodegeneration. Proc Natl Acad Sci U S A 110:3489–3494

16. Hammer MB, Eleuch-Fayache G, Schottlaender LV, Nehdi H, Gibbs JR, Arepalli SK, Chong SB, Hernandez DG, Sailer A, Liu G, Mistry PK, Cai H, Shrader G, Sassi C, Bouhlal Y, Houlden H, Hentati F, Amouri R, Singleton AB (2013) Mutations in GBA2 cause autosomal-recessive cerebellar ataxia with spasticity. Am J Hum Genet 92:245–251

17. Curtis D, Vine AE, Knight J (2008) Study of regions of extended homozygosity provides a powerful method to explore haplotype structure of human populations. Ann Hum Genet 72:261–278

18. Woods CG, Cox J, Springell K, Hampshire DJ, Mohamed MD, McKibbin M, Stern R, Raymond FL, Sandford R, Malik SS, Karbani G, Ahmed M, Bond J, Clayton D, Inglehearn CF (2006) Quantification of homozygosity in consanguineous individuals with autosomal recessive disease. Am J Hum Genet 78:889–896

19. Gosselin I, Thiffault I, Tetreault M, Chau V, Dicaire MJ, Loisel L, Emond M, Senderek J, Mathieu J, Dupre N, Vanasse M, Puymirat J, Brais B (2008) Founder SH3TC2 mutations are responsible for a CMT4C French-Canadians cluster. Neuromuscul Disord 18:483–492

20. Kalaydjieva L, Gresham D, Gooding R, Heather L, Baas F, de Jonge R,Blechschmidt K, Angelicheva D, Chandler D, Worsley P, Rosenthal A, King RH,Thomas PK (2000) N-myc downstream-regulated gene 1 is mutated in hereditary motor and sensory neuropathy-Lom. Am J Hum Genet 67:47–58

21. Pippucci T, Benelli M, Magi A, Martelli PL, Magini P, Torricelli F, Casadio R, Seri M, Romeo G (2011) EX-HOM (EXome HOMozygosity): a proof of principle. Hum Hered 72:45–53

22. Becker J, Semler O, Gilissen C, Li Y, Bolz HJ, Giunta C, Bergmann C, Rohrbach M, Koerber F, Zimmermann K, de Vries P, Wirth B, Schoenau E, Wollnik B, Veltman JA, Hoischen A, Netzer C (2011) Exome sequencing identifies truncating mutations in human SERPINF1 in autosomal-recessive osteogenesis imperfecta. Am J Hum Genet 88:362–371

23. Lander ES, Botstein D (1987) Homozygosity mapping: a way to map human recessive traits with the DNA of inbred children. Science 236: 1567–1570

ORIGINAL INVESTIGATION

C5orf42 is the major gene responsible for OFD syndrome type VI

Estelle Lopez · Christel Thauvin-Robinet · Bruno Reversade · Nadia El Khartoufi · Louise Devisme · Muriel Holder · Hélène Ansart-Franquet · Magali Avila · Didier Lacombe · Pascale Kleinfinger · Irahara Kaori · Jun-Ichi Takanashi · Martine Le Merrer · Jelena Martinovic · Catherine Noël · Mohammad Shboul · Lena Ho · Yeliz Güven · Ferechté Razavi · Lydie Burglen · Nadège Gigot · Véronique Darmency-Stamboul · Julien Thevenon · Bernard Aral · Hülya Kayserili · Frédéric Huet · Stanislas Lyonnet · Cédric Le Caignec · Brunella Franco · Jean-Baptiste Rivière · Laurence Faivre · Tania Attié-Bitach

Abstract Oral-facial-digital syndrome type VI (OFD VI) is a recessive ciliopathy defined by two diagnostic criteria: molar tooth sign (MTS) and one or more of the following: (1) tongue hamartoma (s) and/or additional frenula and/or upper lip notch; (2) mesoaxial polydactyly of one or more hands or feet; (3) hypothalamic hamartoma. Because of the MTS, OFD VI belongs to the "Joubert syndrome related disorders". Its genetic aetiology remains largely unknown although mutations in the *TMEM216* gene, responsible for Joubert (JBS2) and Meckel-Gruber (MKS2) syndromes, have been reported in two OFD VI patients. To explore the molecular cause(s) of OFD VI syndrome, we used an exome sequencing strategy in six unrelated families followed by Sanger sequencing. We identified a total of 14 novel mutations in the *C5orf42* gene in 9/11 families with positive OFD VI diagnostic criteria including a severe fetal case with microphthalmia, cerebellar hypoplasia, corpus callosum agenesis, polydactyly and skeletal dysplasia. *C5orf42* mutations have already been reported in Joubert syndrome confirming that OFD VI and JBS are allelic disorders, thus enhancing our knowledge of the complex, highly heterogeneous nature of ciliopathies.

Introduction

Oral-facial-digital syndrome type VI (OFD VI) or Varadi-Papp syndrome (OMIM 277170) belongs to the heterogeneous group of 13 OFD syndromes defined by the association of malformations of the face, the oral cavity, and the extremities (Gurrieri et al. 2007) and has been distinguished from other OFD subtypes by cerebellar

E. Lopez · C. Thauvin-Robinet (✉) · M. Avila · N. Gigot ·
J. Thevenon · B. Aral · F. Huet · J.-B. Rivière · L. Faivre
Equipe d'accueil EA 4271 GAD "Génétique des Anomalies du
Développement", IFR Santé STIC, Université de Bourgogne,
Dijon, France
e-mail: christel.thauvin@chu-dijon.fr

E. Lopez
e-mail: estl_l@yahoo.fr

C. Thauvin-Robinet · J. Thevenon · L. Faivre
Centre de Référence Anomalies de Développement et
Syndromes Malformatifs de l'interrégion Grand-Est, Hôpital
d'Enfants, CHU, Dijon, France

C. Thauvin-Robinet · N. Gigot · J. Thevenon · L. Faivre
FHU-TRANSLAD, Centre de Génétique, Hôpital d'Enfants,
CHU, 10 Bd du Maréchal de Lattre de Tassigny,
21034 Dijon Cedex, France

B. Reversade · L. Ho
Laboratory of Human Embryology, Institute of Medical Biology,
Agency for Science, Technology and Research (A*STAR),
Singapore, Singapore

N. E. Khartoufi · M. Le Merrer · F. Razavi · S. Lyonnet ·
T. Attié-Bitach
Département de Génétique, Hôpital Necker-Enfants Malades,
APHP, Paris, France

L. Devisme · H. Ansart-Franquet
Département d'Anatomo-Pathologie, Centre de Biologie et de
Pathologie, CHRU, Lille, France

M. Holder
Service de Génétique Clinique, Hôpital Jeanne de Flandre et
Service de Neurologie Pédiatrique, Roger Salengro, CHRU,
Lille, France

malformation, metacarpal abnomalities with mesoaxial polydactyly and severe intellectual disability (Doss et al. 1998; McPherson et al. 2006; Varadi et al. 1980). Hypothalamic hamartomas have also been described (Poretti et al. 2012; Stephan et al. 1994). Recently, diagnostic criteria for OFD VI have been defined as: molar tooth sign (MTS) and one or more of the following: (1) tongue hamartoma and/or additional frenula and/or upper lip notch; (2) mesoaxial polydactyly of one or more hands or feet and (3) hypothalamic hamartoma (Poretti et al. 2012).

The MTS on axial brain MRI argues in favor of OFD VI being a Joubert syndrome related disorder (JSRD) (Gleeson et al. 2004). To date, mutations in 20 genes (Brancati et al. 2010) (*INPP5E* [MIM613037], *TMEM216* [MIM613277], *AHI1* [MIM608894], *NPHP1* [MIM607100], *CEP290* [MIM610142], *TMEM67* [MIM609884], *RPGRIP1L* [MIM610937], *ARL13B* [MIM608922]), *CC2D2A* [MIM612013], *OFD1* [MIM300170], *KIF7* [MIM611254], *TCTN1* [MIM609863], *TCTN2* [MIM613846], *TMEM237* [MIM614423], *CEP41* [MIM610523] (Lee et al. 2012a), *TMEM138* [MIM614459] (Lee et al. 2012b), *C5orf42* [MIM614571] (Srour et al. 2012a), *TCTN3* [MIM614815] (Thomas et al. 2012), *ZNF423* [MIM604557] (Chaki et al. 2012) and *TMEM231* [MIM614949] (Srour et al. 2012b) have been identified in patients with a JSRD. Most of the encoded proteins are predicted or known to be involved in the function of the primary cilium/basal body.

OFD VI usually follows an autosomal recessive mode of inheritance with mainly unknown molecular basis. Indeed, mutations in the *TMEM216* gene, also responsible for Joubert (JS) and Meckel (MKS) syndromes, have been identified in only two JS patients with oral frenula and polydactyly (Valente et al. 2010). A few mutations in the X-linked *OFD1* gene have also been reported in male JS patients with oral defects (Coene et al. 2009) or female patients with OFD syndrome and mild MTS (Bisschoff et al. 2013; Darmency-Stamboul et al. 2013).

In this study, we used exome sequencing to identify *C5orf42* as the major gene responsible for OFD VI, and we delineated the clinical spectrum associated with mutations in this gene.

Patients and methods

Patients

We ascertained eight cases (six males and six females) from six unrelated sibships with clinical features meeting OFD VI diagnostic criteria (Table 1) (Darmency-Stamboul et al. 2013; Poretti et al. 2008). Informed consent for research investigations was obtained from the affected individuals, legal representatives, or relatives. The research protocol was approved by the local ethics committees.

Among the eight cases, 4/8 were fetuses including one deceased sibship and 4/8 were living including a second

D. Lacombe
Service de Génétique Médicale et Centre de Référence
Anomalies du Développement et Syndromes Malformatifs,
CHU de Bordeaux, Laboratoire MRGM, EA4576,
Université de Bordeaux, Bordeaux, France

P. Kleinfinger
Département de génétique, Laboratoire Cerba,
Saint-Ouen l'Aumone, France

P. Kleinfinger · C. Noël
Service de Gynécologie-Obstétrique, Hopital R. Dubos,
Pontoise, France

I. Kaori
Department of Pediatrics, Shimada Center for Rehabilitation
and Neurodevelopmental Intervention, Tama, Tokyo, Japan

J.-I. Takanashi
Department of Pediatrics, Kameda Medical Center,
Kamogawa, Japan

M. Le Merrer · F. Razavi · S. Lyonnet · T. Attié-Bitach
Unité INSERM U781 et Fondation IMAGINE,
Hôpital Necker Enfants-Malades, Paris, France

J. Martinovic
Unité de Foetopathologie, AP-HP, Hôpital Antoine Béclère,
Clamart, France

J. Martinovic
Département de Foetopathologie et Anatomopathologie,
Laboratoire Cerba, Saint-Ouen l'Aumone, France

M. Shboul · Y. Güven
Department of Pedodontics, Faculty of Dentistry, Istanbul
University, Istanbul, Turkey

F. Razavi · S. Lyonnet · T. Attié-Bitach
Université Paris Descartes, Sorbonne Paris Cité, Paris, France

F. Razavi · S. Lyonnet · T. Attié-Bitach
Hôpital Necker-Enfants Malades, Paris, France

L. Burglen
Service de Génétique, Hôpital Armand Trousseau,
AP-HP, Paris, France

L. Burglen
Centre de Référence des malformations et maladies congénitales
du cervelet, Hôpital Armand Trousseau, Paris, France

N. Gigot · B. Aral · J.-B. Rivière
Laboratoire de Génétique Moléculaire, Plateau Technique de
Biologie, CHU Dijon, France

V. Darmency-Stamboul · F. Huet
Service de Pédiatrie 1, Hôpital d'Enfants, CHU, Dijon, France

sibship. All living patients presented with MTS upon brain MRI (Fig. 1). The phenotype also included oral abnormalities (tongue hamartoma(s) and/or an additional frenula and/or upper lip notch) (5/7 cases), facial dysmorphism (4/6 cases), mesoaxial polydactyly (4/8 cases), Y-shaped metacarpal abnormality (2/5 cases), preaxial polydactyly (7/7 cases), postaxial polydactyly (5/7 cases), and hypothalamic hamartoma (4/8 cases) (Figs. 1, 2; Table 1). Standard chromosomal analysis and array-CGH (Agilent® 60, 105 or 244 K) were normal in all individuals. No mutation or genomic rearrangement in the *TMEM216* and *OFD1* genes was identified by Sanger sequencing of exons and intron–exon boundaries and quantitative PCR (primers and PCR conditions available on request).

An additional series of nine families was collected including 5/9 with OFD VI positive diagnostic criteria and possible atypical clinical features (short femurs, occipital meningocele, right fibular agenesis, tibial bowing and microphthalmia). One severe fetus (case 8) presented with facial dysmorphism, microphthalmia, cerebellar vermis hypoplasia, corpus callosum agenesis, bilateral hand and feet preaxial and postaxial polydactyly, unilateral hand mesoaxial polydactyly with Y-shaped metacarpal phalange, and severe skeletal dysplasia with right fibular agenesis and tibial bowing but absent oral manifestations. The four other families presented with an overlapping phenotype including polydactyly and at least one of the following features: oral defects, cerebellar hypoplasia, and hypothalamic hamartoma (3/4 with pituitary gland abnormality with hypothalamic hamartoma, 1/4 with normal central nervous system, but mesoaxial polydactyly and Y-shaped metacarpal phalanges).

Methods

Exome sequencing

Exome sequencing was performed by IntegraGen using the Agilent SureSelect Human All Exon kit v2 (Agilent, France). DNA samples were prepared according to the platform recommendations. Genomic DNA was captured

H. Kayserili
Medical Genetics Department, Istanbul Medical Faculty, Istanbul University, Istanbul, Turkey

C. Le Caignec
Service de Génétique Médicale, CHU, Nantes, France

B. Franco
Telethon Institute of Genetics and Medicine, Naples, Italy

B. Franco
Medical Genetics, Department of Medical Translational Sciences, University of Napoli Federico II, Naples, Italy

with a biotinylated oligonucleotide probe library (Agilent, France), followed by 75 bp paired-end massively parallel sequencing on an Illumina HiSEQ 2000 (Gnirke et al. 2009). Briefly, 3 µg of each genomic DNA sample was fragmented by sonication and purified to yield fragments of 150–200 bp. Paired-end adaptor oligonucleotides from Illumina were then ligated to the shared genomic DNA. Five hundred nanograms of these tailed fragments were then hybridized to the SureSelect probe library. Each DNA sample was sequenced on an Illumina HiSEQ 2000 as paired-end 75 bp reads. Image analysis and base calling were performed using Illumina real time analysis (RTA) pipeline version 1.8 with default parameters.

Reads were aligned to the human reference genome (GRCh37/hg19) with the burrows-wheeler aligner (BWA) (Li et al. 2009) and potential duplicate paired-end reads were removed with Picard v.1.22 (see Web Resources). The Genome Analysis Toolkit (GATK) v.1.0.57 was used for base quality-score recalibration and indel realignment as well as for single-nucleotide-variant and indel discovery and genotyping with the use of standard hard-filtering parameters (DePristo et al. 2011). Variants with a quality score <30, allele balance >0.75, sequencing depth <4, quality-to-depth ratio <5.0, length of homopolymer run >5.0, and strand bias >−0.10 were flagged and excluded from subsequent analyses. We used the GATK depth of coverage tool to assess coverage by ignoring reads with a mapping quality <20 and by ignoring bases with a base quality <30. All variants identified in the affected individuals were annotated with SeattleSeq SNP annotation (see Web resources). Candidate mutational events were then inspected with the integrative genomics viewer (see Web resources) (Robinson et al. 2011). The resulting variants were excluded when the frequency was over 1/1,000 in exome variant server (EVS) (see web Resources). The analyses were focused on genes with at least two heterozygous variants (missense, nonsense, and splice-site variants and coding indels).

Sanger sequencing

Exons containing the sequence variations of the *C5orf42* gene (NM_023073.3) were amplified using a 65°–55° touchdown protocol with primers designed to amplify all the 51 exons and intron–exon boundaries (Supplementary Table 1). PCR fragments were purified using the multiscreen Vacuum Manifold system (Millipore, Merck, France) or Exosap (Affymetrix, USB products, USA). Sequencing was performed using an ABI BigDye Terminator Cycle Sequencing kit (v3.1) (Applied Biosystems, France) in an ABI 3130 sequencer. Sequence data were analyzed with SeqScape v2.7 (Applied Biosystems, France) and Sequencer v4.1. The pathogenicity of missense mutations was tested with PolyPhen-2 and SIFT online software (see Web Resources) (Adzhubei et al. 2010).

Table 1 Clinical features and molecular data of individuals with *C5orf42* mutations in our series

Cases	Origin	Sex	Age	OFD VI diagnosis criteria	Oral features	Facial dysmorphism	Distal limbs abnormalities Hands	Distal limbs abnormalities Feet	Y-shaped metacarpal abnormalities Hands	Y-shaped metacarpal abnormalities Feet	CNS malformation	Intellectual deficiency	Other features	C5orf42 mutations cDNA	C5orf42 mutations Protein	Inheritance
1[a]	Japan	F	17 years	+	BF	+	–	PreP (L)	–	–	MTS HH	+	Breathing abnormality, Porencephaly, arachnoid cysts, nodular heterotopia, polymicrogyria	c.3557delA, c.3577C > T	p.Lys1186Argfs[a]21 p.Arg1193Cys	NA NA
2	France	F	f 29 wg	+	–	–	MP (bil) PoP (R)	S PreP (bil)	+	–	MTS[c] HH	NA	11 pairs of ribs	c.3550C > T, c.9121C > T	p.Arg1184Cys p.Gln3041[a]	Pat mat
3a[d]	Iraqi Kurdish	F	13 years	+	LT BF TH TA	+ ULN	B PoP (bil)	S PreP (bil)	NA	NA	MTS HH	+	Corpus callosum agenesis, mega cisterna magna, short stature, cubitus valgus (R), limited supination (L),	c.3150-1G > T, c.3150-1G > T	Splice acceptor Splice acceptor	Pat Mat
3b[d]	Iraqi Kurdish	F	4 years	+	CT LT BF TH TA	+ ULN	B PoP (bil) PoP (R)	S PreP (bil)	–	–	MTS	+	Epilepsy, short stature, microcephaly	c.3150-1G > T, c.3150-1G > T	Splice acceptor Splice acceptor	Pat Mat
4[b]	France Portugal	F	10 years	+	LT BF TH CP	+	PoP (bil)	S PreP (bil)	–	–	MTS	+	Arachnoid cysts	c.493delA, c.3290-2A > G	p.Ile165Tyrfs[a]17 Splice acceptor	Pat Mat
5	France	M	f 27 wg	+	SF	–	S MP (bil)	S PreP (bil)	+	–	MTS[c] HH	NA	–	c.2377C > T, c.8509G > T	p.Gln793[a] p.Val2837Leu	Pat Mat
6a[e]	France	F	f 12 wg	+	NA	NA	PoD	PreP	NA	NA	MTS[c]	NA	Fetal death Left ventricular hypoplasia	DNA not available		
6b[e]	France	M	f 26 wg	+	–	+	MP (bil) PreP (bil)	S PreP	+	–	MTS[c]	NA		c.493delA, c.3380C > T	p.Ile165Tyrfs[a]17 p.Ser1127Leu	Pat Mat
7a[f]	France	M	f 34 wg	+	–	NA	MP (R) PoP (L)	S PreP (L)	+	–	MTS[c]	NA	Aortic coarctation, short femurs	c.3380C > T, c.3859G > C	p.Ser1127Leu p.Asp1287His	Pat Mat

Table 1 continued

Cases	Origin	Sex	Age	OFD VI diagnosis criteria	Oral features	Facial dysmorphism	Distal limbs abnormalities		Y-shaped metacarpal abnormalities		CNS malformation	Intellectual deficiency	Other features	C5orf42 mutations		Inheritance
							Hands	Feet	Hands	Feet				c.DNA	Protein	
7b[f]	France	F	f 27 wg	+	−	NA	MP (R)	PreP (bil) PoP (bil)	+	−	MTS[c]	NA	Occipital meningocele, Uterus septation	c.3380C > T, c.3859G > C	p.Ser1127Leu, p.Asp1287His	Pat, Mat
8	France	F	f 14 wg	+	NA	+	PreP (bil) MP(L) PoP (R)	PreP (bil) PoP (bil)	+	−	MTS[c]	NA	CCA, hydrocephalus, Right fibular agenesis, Tibial bowing, Microphthalmia	c.3859G > C, c.7476delT	p.Asp1287His, p.Arg2493Aspfs[a]6	NA, NA
9	France		f 23 wg	+	BF	+	PoP	PreP	NA	NA	MTS[c] HH	NA	Occipital meningocele, arhinencephaly, common mesentery	c.6898delC, c.7402C > T	p.Gln2300ArgfsX8, p.Gln2468[a]	NA, NA

B brachydactyly, BF additional buccal frenulae, bil bilateral, CNS central nervous system, CP cleft palate, CT cleft tongue, f fetus, F female, HH hypothalamic hamartoma, L left, LT lobulated tongue, M male, MP mesoaxial polydactyly, MTS molar tooth sign, NA not available, PD polydactyly, PoP postaxial polydactyly, PreP preaxial polydactyly, R right, S syndactyly, SF short buccal frenula, TA tooth abnormalities, TH tongue hamartoma, ULN upper lip notch, y years, wg weeks of gestation, Mat maternal, Pat paternal

[a] Firstly reported by Poretti et al. (2012)

[b] First described by Darmency-Stamboul et al. (2013)

[c] Neuropathological examination evidenced cerebellar vermis hypoplasia compatible with MTS

[d] First sibship, parents had also a pair of male DZ twins, now deceased, with similar OFD clinical presentations

[e] Second sibship

[f] Third sibship
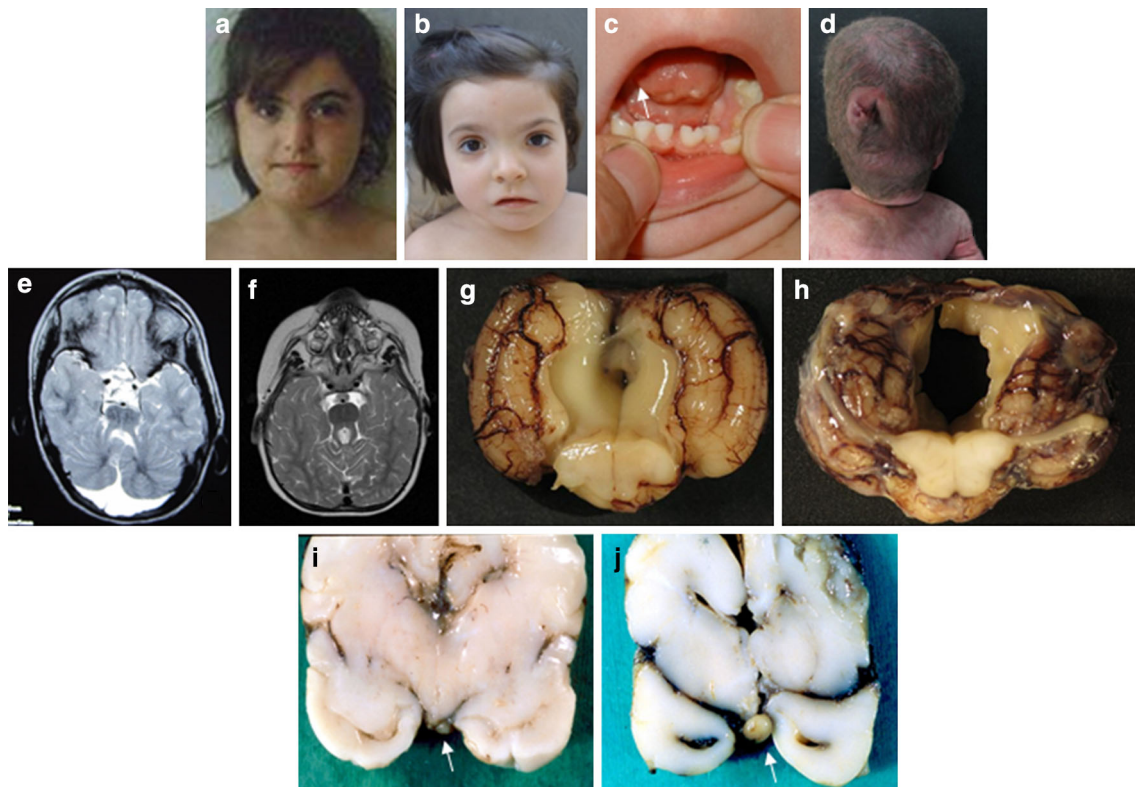
Fig. 1 Clinical and neuroimaging features of individuals with *C5orf42* mutations (case 1 (**e**), case 2 (**i**), case 3b (**a**), case 4 (**b**, **c**, **f**), case 5 (**j**), case 6b (**g**) and case 7b (**d**, **h**)), with facial dysmorphism with hypertelorism (**a**, **b**), oral hamartoma (**c**), occipital encephalocele (**d**), molar tooth sign (**e**, **f**), cerebellar hypoplasia (**g**, **h**) and hypothalamic hamartoma (**i**, **j**)

Results

To identify the molecular defect(s) underling this condition, we performed exome analysis in six index cases with OFD VI positive diagnostic criteria. After applying variant calling filters, we identified two causal mutations in the *C5orf42* gene in three out of six cases: one frameshift and one missense in patient 1, one nonsense and one missense in fetus 2 and one homozygous splice acceptor mutation in patient 3a. We also identified one causal heterozygous mutation in the 3/6 other individuals: one splice-site mutation in fetus 4 and one missense in fetus 5 and in case 6 (Table 1, Supplementary Table 2).

Since 2 transcripts of *C5orf42* are described in ensembl, we checked the exome coverage and noticed that the first 18 exons of the *C5orf42* (NM_023073) gene were not covered by v2 of the Agilent SureSelect Human All Exon library. *C5orf42* Sanger sequencing analysis of the first 18 exons was performed in individuals 4, 5, 6 allowing the identification of the same second causal mutation in cases 4 and 6 (p.Ile165Tyrfs*17) and one nonsense mutation in case 5.

Screening of nine additional individuals with OFD VI or overlapping phenotypes revealed three other families with *C5orf42* recessive mutations. In family seven, two missense mutations were found, including the same one as had been identified in case 6. In fetus 8, one missense (the same as that found in case 7) and one frameshift were found (Table 1 and Supplementary Table 3), while two unique mutations were identified in case 9. All variants were confirmed in all individuals and affected sibs by Sanger sequencing. Parental segregation analysis confirmed heterozygosity in parents in families 2, 3, 4, 5, 6 and 7. We also analyzed 5 microsatellite markers at the *C5orf42* locus and found that cases 6 and 7 share a common haplotype for D5S1994, D5S2021, D5S1964 and D5S2105 segregating with Ser1127Leu, suggesting a founder effect for this mutation. However, there was no evidence of linkage disequilibrium around the Ile165Thrfs*17 mutation shared by cases 4 and 6.

Altogether, a total of 14 distinct *C5orf42* mutations (four frameshift, three nonsense, five missense and two splice site, Table 1 and Supplementary Table 3) were identified in 9/11 unrelated families. Detailed clinical features of 12 individuals are presented in Table 1.

Fig. 2 Clinical and radiological distal limb abnormalities of individuals with *C5orf42* mutations (case 1 (**a–f**), case 2 (**h–j**), case 3b (**k–n**), case 4 (**g**), case 5 (**o–r**), case 6b (**s–v**) case 7b (**w–z**) and case 8 (**α-ζ**)), with hand polydactyly (**h, o, s, w, α**), hallux valgus or foot preaxial polydactyly (**d, g, j, m, q, u, y, γ**), Y-shaped metacarpal abnormality (**i, p, t, x, β**), and right fibula agenesis with tibial incurvation (**ζ**)

Discussion

In this study, we identified causal *C5orf42* mutations in 9/11 families meeting OFD VI diagnostic criteria, but no mutation in individuals with partly overlapping features. Thus, all presented the diagnostic criteria characterized by MTS and one or more of the following: (1) tongue hamartoma and/or an additional frenula and/or upper lip notch; (2) mesoaxial polydactyly of one or more hands or feet; (3) hypothalamic hamartoma (Poretti et al. 2012). Common distal limb abnormalities in the 12 cases with *C5orf42* mutations included constant feet preaxial polydactyly (12/12 cases) and frequent mesoaxial polydactyly (7/12 cases) and at least one distal extremity with Y–shaped metacarpal abnormality (6/9 cases) (Table 1; Fig. 2). Hypothalamic hamartoma was frequent (5/12 cases). Intellectual disability was constant (4/4 cases) in contrast with two other frequent OFD subtypes, i.e., OFD I and II (Gurrieri et al. 2007). OFD VI belongs to the JSRD (Gleeson et al. 2004). Remarkably, additional features usually reported in this group of ciliopathies such as polycystic kidney disease and retinal disease are absent in the cases with *C5orf42* mutations.

C5orf42 mutations were also found in atypical cases, such as fetus 7a with short femurs, fetuses 7b and 9 with occipital meningocele and fetus 8 with microphthalmia and severe skeletal dysplasia with right tibial bowing and fibular agenesis (Table 1; Fig. 2). Occipital meningocele, a feature of the lethal Meckel syndrome (MIM 249000) and rarely JBS, was also previously described in two JBS individuals with *C5orf42* mutations, but without renal involvement or polydactyly (Alazami et al. 2012; Shaheen et al. 2012). The absence of characteristic renal involvement seems, therefore, a discriminating feature of *C5orf42*-mutated individuals reported thus far. Tibial bowing and fibular agenesis have already been described in other ciliopathies, including short ribs polydactyly, OFD IV or OFD X syndromes (Figuera et al. 1993; Toriello et al. 1997). Moreover, OFD VI was diagnosed in 4/9 cases because of the association of mesoaxial polydactyly and MTS despite the absence of oral abnormalities (Gurrieri et al. 2007). Among the 15 previous reported cases with *C5orf42*

Hum Genet (2014) 133:367–377

Table 2 Main clinical features of individuals with *C5orf42* mutations reported thus far

Diagnosis	JBS					OFD VI
References	Srour et al. (2012a) (n = 10)	Alazami et al. (2012) (n = 3)	Srour et al. (2012b) (n = 1)	Shaheen et al. (2012) (n = 1)	Total (n = 15)	Present cases (n = 12)
Molar tooth sign	9/9	3/3	1/1	0/1	13/14	12/12
Oral abnormalities	NA	NA	NA	1/1[c]	1/1	6/10
Polydactyly	1/10	0/3	0/1	0/1	1/15	12/12
Hypothalamic hamartoma	0/9	0/3	0/1	0/1	0/14	5/12
Developmental delay	10/10	3/3	1/1	f	14/14	4/4
Oculomotor apraxia	9/10	3/3	0/1	f	12/14	0/4
Breathing abnormality	8/10	NA	1/1	f	9/11	1/4
Retinal involvement	0/10	1/3	0/1	f	1/14	0/4
Renal involvement	0/10	0/3	0/1	NA	0/14	0/12
Occipital encephalocele	0/10	1/3[b]	0/1	1/1	2/15	2/12
OFD VI positive diagnosis criteria	NA[a]	NA[a]	NA[a]	0/1	0/1	12/12
Mutations	p.Arg1336Trp	p.Arg2660[a]	c.7400 + 1G > A	p.Gly2663Alafs[a]40	p.Arg1336Trp	p.Ile165Tyrfs[a]17
	p.Ala1564Trp	p.Gly2663Alafs[a]40	p.Lys2753Lysfs[a]9		p.Ala1564Trp	p.Gln793[a]
	p.Arg1602[a]				p.Arg1602[a]	p.Gln2300ArgfsX8
	p.Pro2136Hisfs[a]31				p.Pro2136Hisfs[a]31	p.Gln2468[a]
	c.7400 + 1G > A				c.7400 + 1G > A	c.3150-1G > T
	p.Arg2493[a]				p.Arg2493[a]	c.3290-2A> G
					p.Arg2660[a]	p.Ser1127Leu
					p.Gly2663Alafs[a]40	p.Arg1184Cys
					p.Lys2753Lysfs[a]9	p.Lys1186Argfs[a]21
						p.Arg1193Cys
						p.Asp1287His
						p.Arg2493Aspfs[a]6
						p.Val2837Leu
						p.Gln3041[a]

JBS Joubert syndrome, *OFD VI* oral-facial-digital syndrome type VI

[a] Oral features are not available

[b] With no hepatic fibrosis and no kidney involvement

[c] Cleft lip and palate

mutations, hypothalamic hamartoma and mesoaxial poly-dactyly were absent. Oral examination has only been described in one case presenting with cleft lip and palate, and is therefore a rare but possible feature of OFD VI (2 cases of our series).

We identified a total of 14 novel *C5orf42* mutations in 9 families, mostly truncating (4 frameshift, 3 nonsense, 5 missense and 2 splice) including 3 recurrent mutations in unrelated cases. Thus far, 11 pathogenic *C5orf42* mutations have been reported in 15 patients (Table 2) (Alazami et al. 2012; Shaheen et al. 2012; Srour et al. 2012a, b). It is likely that at least one truncating mutation is necessary to induce JSRD or OFD VI as suggested by the high rate of mutations of this type (16/23 mutations, i.e., 70 %), contrasting with most JSRD causative genes (Mougou-Zerelli et al. 2009). Missense mutations identified in the compound heterozygous state are also predicted to alter splicing (Supplementary Table 3). While few patients with *TMEM216* mutations display OFD features, *C5orf42* appears the major gene for OFD VI in our series (9/11). Such genetic homogeneity will be helpful for molecular analysis and genetic counseling of patients with OFD VI diagnostic criteria.

The ciliopathy protein network implicated in the JSRD clinical spectrum involves three distinct, but connected modules: the ciliary transition zone, the centrosome and the Hedgehog signaling pathway (Sang et al. 2011). This network appears distinct from the BBsome and IFT complexes, implicated in other ciliopathies (Wei et al. 2012). *C5orf42* encodes a 3,198-amino acid protein, but very little is known about its function (Srour et al. 2012a). The Gene Ontology project suggests that it might be a transmembrane protein and ProtoNet predicts a coiled-coil structure within the protein. Analysis of EST, microarray, and other databases predict widespread expression of *C5orf42*, including in brain. The predicted protein sequence appears well conserved as close *C5orf42* orthologs are detected in several vertebrates. Additional studies will be required to identify the role of *C5orf42* in the ciliopathy protein network.

Overall, we report the identification of *C5orf42* as the major gene responsible for OFD VI. Mutations are associated with a broad clinical spectrum that extends from a viable to severe, lethal phenotype with skeletal dysplasia. These results also confirm that OFD VI and JBS are allelic disorders, thereby improving our understanding of the complex, frequently allelic and highly heterogeneous nature of ciliopathies.

Web resources

The URLs for data presented herein are as follows: Broad Institute Integrated Genomics Viewer (IGV), http://www.broadinstitute.org/igv/; NHLBI Exome Sequencing Project (ESP) Exome Variant Server (EVS), http://evs.gs.washington.edu/EVS/; Online Mendelian Inheritance in Man (OMIM), http://www.omim.org/; Picard, http://picard.sourceforge.net/; PolyPhen-2, http://genetics.bwh.harvard.edu/pph2/; Primer3, http://frodo.wi.mit.edu/primer3/; SeattleSeq Annotation 131, http://snp.gs.washington.edu/SeattleSeqAnnotation131/; SIFT, http://sift.bii.a-star.edu.sg/; Human Splicing Finder (HSF), http://www.umd.be/HSF/.

References

Adzhubei IA, Schmidt S, Peshkin L, Ramensky VE, Gerasimova A, Bork P, Kondrashov AS, Sunyaev SR (2010) A method and server for predicting damaging missense mutations. Nat Methods 7:248–249

Alazami AM, Alshammari MJ, Salih MA, Alzahrani F, Hijazi H, Seidahmed MZ, Abu Safieh L, Aldosary M, Khan AO, Alkuraya FS (2012) Molecular characterization of Joubert syndrome in Saudi Arabia. Human mutation 33:1423–1428

Bisschoff IJ, Zeschnigk C, Horn D, Wellek B, Riess A, Wessels M, Willems P, Jensen P, Busche A, Bekkebraten J, Chopra M, Hove HD, Evers C, Heimdal K, Kaiser AS, Kunstmann E, Robinson KL, Linne M, Martin P, McGrath J, Pradel W, Prescott KE, Roesler B, Rudolf G, Siebers-Renelt U, Tyshchenko N, Wieczorek D, Wolff G, Dobyns WB, Morris-Rosendahl DJ (2013) Novel mutations including deletions of the entire OFD1 gene in 30 families with type 1 orofaciodigital syndrome: a study of the extensive clinical variability. Hum Mutat 34:237–247

Brancati F, Dallapiccola B, Valente EM (2010) Joubert syndrome and related disorders. Orphanet J Rare Dis 5:20

Chaki M, Airik R, Ghosh AK, Giles RH, Chen R, Slaats GG, Wang H, Hurd TW, Zhou W, Cluckey A, Gee HY, Ramaswami G, Hong CJ, Hamilton BA, Cervenka I, Ganji RS, Bryja V, Arts HH, van Reeuwijk J, Oud MM, Letteboer SJ, Roepman R, Husson H, Ibraghimov-Beskrovnaya O, Yasunaga T, Walz G, Eley L, Sayer JA, Schermer B, Liebau MC, Benzing T, Le Corre S, Drummond I, Janssen S, Allen SJ, Natarajan S, O'Toole JF, Attanasio M, Saunier S, Antignac C, Koenekoop RK, Ren H, Lopez I, Nayir A, Stoetzel C, Dollfus H, Massoudi R, Gleeson JG, Andreoli SP, Doherty DG, Lindstrad A, Golzio C, Katsanis N, Pape L, Abboud EB, Al-Rajhi AA, Lewis RA, Omran H, Lee

EY, Wang S, Sekiguchi JM, Saunders R, Johnson CA, Garner E, Vanselow K, Andersen JS, Shlomai J, Nurnberg G, Nurnberg P, Levy S, Smogorzewska A, Otto EA, Hildebrandt F (2012) Exome capture reveals ZNF423 and CEP164 mutations, linking renal ciliopathies to DNA damage response signaling. Cell 150:533–548

Coene KL, Roepman R, Doherty D, Afroze B, Kroes HY, Letteboer SJ, Ngu LH, Budny B, van Wijk E, Gorden NT, Azhimi M, Thauvin-Robinet C, Veltman JA, Boink M, Kleefstra T, Cremers FP, van Bokhoven H, de Brouwer AP (2009) OFD1 is mutated in X-linked Joubert syndrome and interacts with LCA5-encoded lebercilin. Am J Hum Genet 85:465–481

Darmency-Stamboul V, Burglen L, Lopez E, Mejean N, Dean J, Franco B, Rodriguez D, Lacombe D, Desguerres I, Cormier-Daire V, Doray B, Pasquier L, Gonzales M, Pastore M, Crenshaw ML, Huet F, Gigot N, Aral B, Callier P, Faivre L, Attie-Bitach T, Thauvin-Robinet C (2013) Detailed clinical, genetic and neuroimaging characterization of OFD VI syndrome. Eur J Med Genet

DePristo MA, Banks E, Poplin R, Garimella KV, Maguire JR, Hartl C, Philippakis AA, del Angel G, Rivas MA, Hanna M, McKenna A, Fennell TJ, Kernytsky AM, Sivachenko AY, Cibulskis K, Gabriel SB, Altshuler D, Daly MJ (2011) A framework for variation discovery and genotyping using next-generation DNA sequencing data. Nat Genet 43:491–498

Doss BJ, Jolly S, Qureshi F, Jacques SM, Evans MI, Johnson MP, Lampinen J, Kupsky WJ (1998) Neuropathologic findings in a case of OFDS type VI (Varadi syndrome). Am J Med Genet 77:38–42

Figuera LE, Rivas F, Cantu JM (1993) Oral-facial-digital syndrome with fibular aplasia: a new variant. Clin Genet 44:190–192

Gleeson JG, Keeler LC, Parisi MA, Marsh SE, Chance PF, Glass IA, Graham JM Jr, Maria BL, Barkovich AJ, Dobyns WB (2004) Molar tooth sign of the midbrain-hindbrain junction: occurrence in multiple distinct syndromes. Am J Med Genet A 125:125–134 (discussion 117)

Gnirke A, Melnikov A, Maguire J, Rogov P, LeProust EM, Brockman W, Fennell T, Giannoukos G, Fisher S, Russ C, Gabriel S, Jaffe DB, Lander ES, Nusbaum C (2009) Solution hybrid selection with ultra-long oligonucleotides for massively parallel targeted sequencing. Nat Biotechnol 27:182–189

Gurrieri F, Franco B, Toriello H, Neri G (2007) Oral-facial-digital syndromes: review and diagnostic guidelines. Am J Med Genet A 143A:3314–3323

Lee JE, Silhavy JL, Zaki MS, Schroth J, Bielas SL, Marsh SE, Olvera J, Brancati F, Iannicelli M, Ikegami K, Schlossman AM, Merriman B, Attie-Bitach T, Logan CV, Glass IA, Cluckey A, Louie CM, Lee JH, Raynes HR, Rapin I, Castroviejo IP, Setou M, Barbot C, Boltshauser E, Nelson SF, Hildebrandt F, Johnson CA, Doherty DA, Valente EM, Gleeson JG (2012a) CEP41 is mutated in Joubert syndrome and is required for tubulin glutamylation at the cilium. Nat Genet 44:193–199

Lee JH, Silhavy JL, Lee JE, Al-Gazali L, Thomas S, Davis EE, Bielas SL, Hill KJ, Iannicelli M, Brancati F, Gabriel SB, Russ C, Logan CV, Sharif SM, Bennett CP, Abe M, Hildebrandt F, Diplas BH, Attie-Bitach T, Katsanis N, Rajab A, Koul R, Sztriha L, Waters ER, Ferro-Novick S, Woods CG, Johnson CA, Valente EM, Zaki MS, Gleeson JG (2012b) Evolutionarily assembled cis-regulatory module at a human ciliopathy locus. Science 335:966–969

Li H, Handsaker B, Wysoker A, Fennell T, Ruan J, Homer N, Marth G, Abecasis G, Durbin R (2009) The sequence alignment/map format and SAMtools. Bioinformatics 25:2078–2079

McPherson E, Zaleski C, Mascola M (2006) Prenatal diagnosis of episodic tachypnea in an infant with OFD VI. Am J Med Genet A 140:2146–2149

Mougou-Zerelli S, Thomas S, Szenker E, Audollent S, Elkhartoufi N, Babarit C, Romano S, Salomon R, Amiel J, Esculpavit C, Gonzales M, Escudier E, Leheup B, Loget P, Odent S, Roume J, Gerard M, Delezoide AL, Khung S, Patrier S, Cordier MP, Bouvier R, Martinovic J, Gubler MC, Boddaert N, Munnich A, Encha-Razavi F, Valente EM, Saad A, Saunier S, Vekemans M, Attie-Bitach T (2009) CC2D2A mutations in Meckel and Joubert syndromes indicate a genotype-phenotype correlation. Hum Mutat 30:1574–1582

Poretti A, Brehmer U, Scheer I, Bernet V, Boltshauser E (2008) Prenatal and neonatal MR imaging findings in oral-facial-digital syndrome type VI. AJNR Am J Neuroradiol 29:1090–1091

Poretti A, Vitiello G, Hennekam RC, Arrigoni F, Bertini E, Borgatti R, Brancati F, D'Arrigo S, Faravelli F, Giordano L, Huisman TA, Iannicelli M, Kluger G, Kyllerman M, Landgren M, Lees MM, Pinelli L, Romaniello R, Scheer I, Schwarz CE, Spiegel R, Tibussek D, Valente EM, Boltshauser E (2012) Delineation and diagnostic criteria of Oral-facial-digital syndrome type VI. Orphanet J Rare Dis 7:4

Robinson JT, Thorvaldsdottir H, Winckler W, Guttman M, Lander ES, Getz G, Mesirov JP (2011) Integrative genomics viewer. Nat Biotechnol 29:24–26

Sang L, Miller JJ, Corbit KC, Giles RH, Brauer MJ, Otto EA, Baye LM, Wen X, Scales SJ, Kwong M, Huntzicker EG, Sfakianos MK, Sandoval W, Bazan JF, Kulkarni P, Garcia-Gonzalo FR, Seol AD, O'Toole JF, Held S, Reutter HM, Lane WS, Rafiq MA, Noor A, Ansar M, Devi AR, Sheffield VC, Slusarski DC, Vincent JB, Doherty DA, Hildebrandt F, Reiter JF, Jackson PK (2011) Mapping the NPHP-JBTS-MKS protein network reveals ciliopathy disease genes and pathways. Cell 145:513–528

Shaheen R, Faqeih E, Alshammari MJ, Swaid A, Al-Gazali L, Mardawi E, Ansari S, Sogaty S, Seidahmed MZ, Almotairi MI, Farra C, Kurdi W, Al-Rasheed S, Alkuraya FS (2012) Genomic analysis of Meckel-Gruber syndrome in Arabs reveals marked genetic heterogeneity and novel candidate genes. Eur J Human Genet EJHG

Srour M, Hamdan FF, Schwartzentruber JA, Patry L, Ospina LH, Shevell MI, Desilets V, Dobrzeniecka S, Mathonnet G, Lemyre E, Massicotte C, Labuda D, Amrom D, Andermann E, Sebire G, Maranda B, Rouleau GA, Majewski J, Michaud JL (2012a) Mutations in TMEM231 cause Joubert syndrome in French Canadians. J Med Genet 49:636–641

Srour M, Schwartzentruber J, Hamdan FF, Ospina LH, Patry L, Labuda D, Massicotte C, Dobrzeniecka S, Capo-Chichi JM, Papillon-Cavanagh S, Samuels ME, Boycott KM, Shevell MI, Laframboise R, Desilets V, Maranda B, Rouleau GA, Majewski J, Michaud JL (2012b) Mutations in C5ORF42 cause Joubert syndrome in the French Canadian population. Am J Hum Genet 90:693–700

Stephan MJ, Brooks KL, Moore DC, Coll EJ, Goho C (1994) Hypothalamic hamartoma in oral-facial-digital syndrome type VI (Varadi syndrome). Am J Med Genet 51:131–136

Thomas S, Legendre M, Saunier S, Bessieres B, Alby C, Bonniere M, Toutain A, Loeuillet L, Szymanska K, Jossic F, Gaillard D, Yacoubi MT, Mougou-Zerelli S, David A, Barthez MA, Ville Y, Bole-Feysot C, Nitschke P, Lyonnet S, Munnich A, Johnson CA, Encha-Razavi F, Cormier-Daire V, Thauvin-Robinet C, Vekemans M, Attie-Bitach T (2012) TCTN3 mutations cause Mohr-Majewski syndrome. Am J Hum Genet 91:372–378

Toriello HV, Carey JC, Suslak E, Desposito FR, Leonard B, Lipson M, Friedman BD, Hoyme HE (1997) Six patients with oral-facial-digital syndrome IV: the case for heterogeneity. Am J Med Genet 69:250–260

Valente EM, Logan CV, Mougou-Zerelli S, Lee JH, Silhavy JL, Brancati F, Iannicelli M, Travaglini L, Romani S, Illi B, Adams

M, Szymanska K, Mazzotta A, Lee JE, Tolentino JC, Swistun D, Salpietro CD, Fede C, Gabriel S, Russ C, Cibulskis K, Sougnez C, Hildebrandt F, Otto EA, Held S, Diplas BH, Davis EE, Mikula M, Strom CM, Ben-Zeev B, Lev D, Sagie TL, Michelson M, Yaron Y, Krause A, Boltshauser E, Elkhartoufi N, Roume J, Shalev S, Munnich A, Saunier S, Inglehearn C, Saad A, Alkindy A, Thomas S, Vekemans M, Dallapiccola B, Katsanis N, Johnson CA, Attie-Bitach T, Gleeson JG (2010) Mutations in TMEM216 perturb ciliogenesis and cause Joubert, Meckel and related syndromes. Nat Genet 42:619–625

Varadi V, Szabo L, Papp Z (1980) Syndrome of polydactyly, cleft lip/palate or lingual lump, and psychomotor retardation in endogamic gypsies. J Med Genet 17:119–122

Wei Q, Zhang Y, Li Y, Zhang Q, Ling K, Hu J (2012) The BBSome controls IFT assembly and turnaround in cilia. Nat Cell Biol 14:950–957

The snRNA-processing complex, Integrator, is required for ciliogenesis and dynein recruitment to the nuclear envelope via distinct mechanisms

Jeanne N. Jodoin[1], Mohammad Shboul[2], Todd R. Albrecht[3], Ethan Lee[1], Eric J. Wagner[3], Bruno Reversade[2,4] and Laura A. Lee[1,*]

[1]Department of Cell and Developmental Biology, Vanderbilt University Medical Center, Nashville, TN 37232-8240, USA
[2]Institute of Medical Biology, A*STAR, Singapore138648, Singapore
[3]Department of Biochemistry and Molecular Biology, The University of Texas Medical School at Houston, Houston, TX 77030, USA
[4]Department of Pediatrics, National University of Singapore, Singapore 119228

*Author for correspondence (laura.a.lee@vanderbilt.edu)

Summary

We previously reported that the small nuclear RNA processing complex, Integrator, is required for dynein recruitment to the nuclear envelope at mitotic onset in cultured human cells. We now report an additional role for INT in ciliogenesis. Depletion of INT subunits from cultured human cells results in loss of primary cilia. We provide evidence that the requirements for INT in dynein localization and ciliogenesis are uncoupled: proteins essential for ciliogenesis are not essential for dynein recruitment to the nuclear envelope, while depletion of known regulators of perinuclear dynein has minimal effects on ciliogenesis. Taken together, our data support a model in which INT ensures proper processing of distinct pools of transcripts encoding components that independently promote perinuclear dynein enrichment and ciliogenesis.

Key words: Primary cilia, RNA processing, Dynein

Introduction

Cytoplasmic dynein is a large, multimeric, minus-end-directed motor complex that associates with the dynein-activating complex, dynactin. (Holzbaur and Vallee, 1994; Kardon and Vale, 2009; Schroer, 2004). Two forms of cytoplasmic dynein exist within cells: dynein-1 and dynein-2. Dynein-1 is required for a variety of essential functions such as cargo transport along microtubules, centrosome assembly, organelle positioning, mitotic spindle positioning, and ciliogenesis, whereas dynein-2 is required for retrograde transport of cargo along primary cilia (PC) and maintenance of PC length (Palmer et al., 2011; Rajagopalan et al., 2009). Dynein complexes are subject to multiple layers of regulation, including binding of accessory proteins, phosphorylation, variations in subunit composition, and subcellular localization (Kardon and Vale, 2009).

During G2/M of cell division in multiple species, a pool of dynein anchored to the nuclear envelope (NE) facilitates nucleus-centrosome coupling, an essential step for proper mitotic spindle formation (Anderson et al., 2009; Bolhy et al., 2011; Gönczy et al., 1999; Jodoin et al., 2012; Malone et al., 2003; Robinson et al., 1999; Sitaram et al., 2012; Splinter et al., 2010; Vaisberg et al., 1993). Three components are known to be required for dynein accumulation on the NE and subsequent nucleus-centrosome coupling in human cells. The first two components,

Bicaudal D2 (BICD2) and Centromere protein F (CENP-F), independently bind dynein subunits/adaptor proteins and nucleoporins to stably tether dynein complexes to the NE (Bolhy et al., 2011; Splinter et al., 2010). The third recently identified component, the small nuclear RNA (snRNA) complex, Integrator (INT), likely regulates dynein recruitment to the NE in an indirect manner distinct from that of BICD2 and CENP-F (Jodoin et al., 2013).

INT, a highly conserved nuclear complex consisting of 14 subunits, interacts with the C-terminal tail of the largest subunit of RNA-polymerase II to promote 3′-snRNA processing (Baillat et al., 2005; Chen and Wagner, 2010). These processed snRNAs play critical roles in gene expression via intron removal and further pre-mRNA processing (Matera et al., 2007). Analysis of INT has revealed that the complex must be intact to perform its RNA processing function: loss of individual INT subunits, with the exception of IntS10, leads to a nonfunctional complex (Chen et al., 2012). Various cellular functions have been ascribed to INT in cultured mammalian cells. IntS4 is required for formation of Cajal bodies (Takata et al., 2012) and IntS6 and IntS11 ensure proper differentiation of adipocytes (Otani et al., 2013). INT has additionally been reported to be required for developmental functions in vivo. IntS7 is essential for normal craniofacial development in both zebrafish and C. elegans as well as

abdominal formation in *Drosophila* (Golling et al., 2002; Kamath et al., 2003; Rutkowski and Warren, 2009). In zebrafish, IntS5, IntS9, and IntS11 are required for *smad1* and *smad5* mRNA processing (Tao et al., 2009). We recently reported an essential role for INT in recruitment of dynein to the NE at G2/M (Jodoin et al., 2013).

PC are non-motile appendages that form in the majority of vertebrate cells. These structures act as sensory organelles and play essential roles in sensing and processing signals from the extracellular environment (Basten and Giles, 2013; Ko, 2012; Salisbury, 2004). To initiate primary ciliogenesis during G1, one of the two centrioles migrates to the plasma membrane, where it will dock and mature into a basal body (BB) that nucleates the PC (Kim and Dynlacht, 2013). Prior to mitotic entry, the PC is resorbed to allow for the formation of the bipolar spindle (Wang et al., 2013). Across phyla, dynein has been shown to be required for ciliogenesis (Kim and Dynlacht, 2013; Kim et al., 2011; Kong et al., 2013). Loss of dynein heavy chain, which results in decay of the complex, hinders PC formation (Draviam et al., 2006; Rajagopalan et al., 2009). Additionally, dynein is required for retrograde movement of proteins along the PC and regulation of PC length (Rajagopalan et al., 2009). While many centrosomal and interflagellar trafficking proteins are known to be critical for PC formation, more are hypothesized to exist (Graser et al., 2007; Kim and Dynlacht, 2013).

In this work, we sought to determine if INT is required for additional dynein-dependent events within cultured human cells. We herein report a role for INT in promoting ciliogenesis. We propose a model in which INT regulates dynein localization during G2/M and ciliogenesis during G1 through distinct mechanisms.

Results and Discussion

Individual INT subunits are required for PC formation

Given the role of INT in dynein recruitment to the NE at G2/M, we asked whether INT plays a broader role in regulating dynein-related functions. Specifically, we sought to determine if INT is required for PC formation, another dynein-dependent process. We performed siRNA-mediated down-regulation of individual INT subunits in human retinal pigment epithelial (RPE) cells and assessed PC formation. Prior to fixation and immunostaining for acetylated tubulin and γ-tubulin (to mark cilia and centrioles, respectively), the confluent monolayer of cells was subjected to serum starvation for 24 hours to stimulate PC formation.

Under these conditions, the frequency of non-targeting (NT)-siRNA cells with PC ranged from ~60–80% (data not shown). Primary ciliogenesis data are presented as the percentage of NT-siRNA cells. As a positive control, cells were depleted of Centrin-2 (CETN2), a centriolar component required for ciliogenesis (Graser et al., 2007; Salisbury, 2004). Following individual knockdown of most INT subunits tested (IntS1, 3, 4, 9, 11, or 12), we observed loss of PC to a degree comparable to that of CETN2-siRNA cells, suggesting that INT plays a critical role in PC formation (Fig. 1). We observed essentially identical results using a second independent siRNA for a subset of INT subunits, confirming that the loss of PC is not due to an off-target effect (supplementary material Fig. S1). Knockdown of IntS10, which is dispensable for both snRNA processing and dynein localization, similarly had no effect on PC formation, further confirming that this subunit is not a critical component of the INT complex. Data are conflicting for only one INT subunit, IntS7,
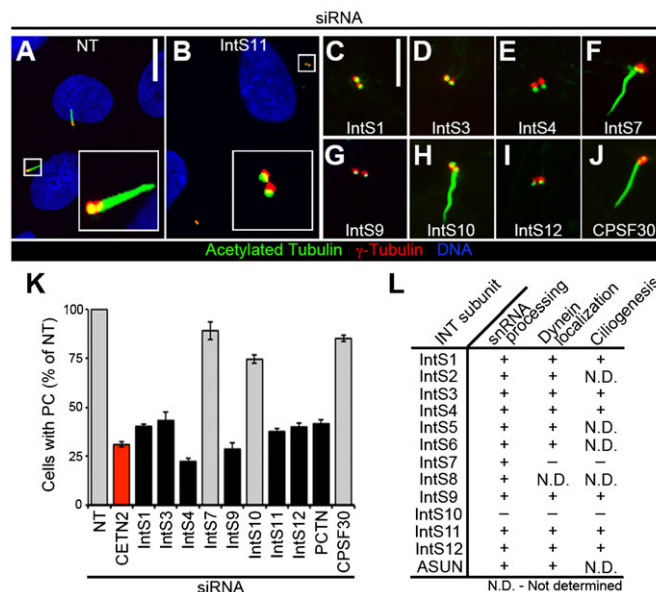

Fig. 1. Loss of PC following INT depletion. RPE cells were transfected with siRNA, serum-starved, fixed, and stained for acetylated tubulin, γ-tubulin, and DNA. (A–J) Representative images show decreased PC formation after knockdown of most INT subunits tested. Scale bars, 10 (A,B) or 5 (C–J) μm. (K) Quantification of PC formation (normalized to NT-siRNA) in INT-depleted cells. Gray, *P*<0.0001; black, not significant (both relative to CETN2-siRNA, red). (L) Comparison of INT subunit requirements in snRNA processing (Chen et al., 2012), dynein localization, and ciliogenesis (presented herein). (+), required; (−), not required; (N.D.), not determined.

which was previously reported to be required for snRNA processing, but not for dynein localization; we found that depletion of IntS7 had no effect on PC formation (Chen et al., 2012; Ezzeddine et al., 2011; Jodoin et al., 2013) (Fig. 1). A possible explanation for this discrepancy is that the snRNA-processing assay might be more sensitive than the assays designed to assess cytoplasmic events (perinuclear dynein accumulation and PC formation) that are presumably downstream of RNA processing. Efficient knockdown of all siRNA-targeted endogenous proteins in experiments presented herein was confirmed by immunoblotting (supplementary material Fig. S2).

To test whether the loss of PC in INT-depleted cells is specific to disruption of INT-mediated snRNA processing, and not secondary to a general disruption of RNA processing, we down-regulated Cleavage Polyadenylation Specificity Factor 30 (CPSF30) in cells and assessed PC formation. CPSF30 is a component of a complex required for the recruitment of machinery that mediates 3′-mRNA cleavage and poly(A) tail synthesis; depletion of CPSF30 leads to a deficiency, but not a complete loss, of poly(A) 3′-end formation in cells (Barabino et al., 1997). We found no significant effect on PC formation, however, in CPSF30-siRNA cells, suggesting a specific role for INT-mediated snRNA processing in PC formation (Fig. 1).

In addition to loss of PC, we observed increased centriole separation following individual knockdown of most INT subunits tested (IntS1, 3, 4, 9, 11, or 12) (results for IntS4 and IntS11 shown in supplementary material Fig. S3; data not shown for other listed subunits). This phenotype has been reported in cells depleted of a subset of ciliogenesis regulators, although a strict correlation between the separation of centrioles and loss of PC has not been observed; hence, the functional significance of this

phenotype is unclear (Graser et al., 2007; Salisbury, 2004). As for PC formation, we did not observe defects in centriole coupling following IntS7 or IntS10 depletion (results for IntS10 shown in supplementary material Fig. S3; data not shown for IntS7).

We considered the possibility that the lack of PC in INT-depleted cells could be secondary to a failure of these cells to arrest in G1 upon serum starvation. We previously showed that down-regulation of individual INT subunits does not lead to any gross defects in cell-cycle phasing under normal growth conditions (Jodoin et al., 2013). To confirm that INT-depleted cells respond normally to serum starvation by arresting in G1, we performed fluorescence-activated cell sorting analysis. In contrast to INT-depleted cells growing asynchronously in 10% fetal bovine serum, INT-depleted cells arrested in G1 following serum starvation in the same manner as control cells (supplementary material Fig. S4). Taken together, these data reveal that INT is required for PC formation and centriole coupling, thereby adding to the growing list of INT-dependent cellular processes. We propose a model in which INT mediates processing of snRNA required for normal production of mRNA encoding a critical regulator of ciliogenesis.

INT depletion does not affect a subset of proteins required for BB maturation and assembly

We considered the possibility that loss of PC following INT depletion could result from failure of BB maturation and/or abnormal BB composition. The process of BB maturation includes assembly of the distal appendage, which projects radially from the distal end of the cilium, serving to anchor the BB and cilium to the plasma membrane. Centrosomal protein 164 (Cep164), Centrosomal protein 89 (Cep89), and Fas-binding factor 1 (FBF-1) are distal appendage components required for PC production (Sillibourne et al., 2011; Tanos et al., 2013). We observed normal localization of these proteins to the base of the PC in INT-depleted cells (Fig. 2A–C, quantified in

supplementary material Fig. S5A–C). We next evaluated several core BB proteins essential for PC formation: CETN2, Pericentrin (PCTN), and Ninein (Graser et al., 2007; Salisbury, 2004). We found their localizations and intensities to be comparable in INT-depleted and control cells (Fig. 2D–F; quantified in Fig. S5D–F). We also found that γ-tubulin localized normally to BB in INT-siRNA cells (Fig. 1A–I). Taken together, these data suggest that loss of PC in INT-depleted cells is unlikely to be secondary to defective processing of transcripts encoding the studied proteins.

PC formation is not required for dynein recruitment to the NE

We have identified two dynein-mediated processes that require INT: PC formation during G1 and dynein recruitment to the NE at G2/M (Fig. 1) (Jodoin et al., 2013). We reasoned that INT might ensure production of a single transcript encoding a common regulator of these processes or distinct transcripts that independently regulate each process. To help distinguish between these two possibilities, we sought to determine whether dynein enrichment on the NE and PC formation are interdependent or uncoupled events.

We first asked whether proteins essential for PC formation are also generally required for dynein recruitment to the NE. We performed siRNA-mediated knockdown of CETN2 and PCTN in HeLa cells and assessed dynein localization during prophase. We used the following criteria to identify prophase cells: positively immunostained for phosphorylated histone H3 (PH3) with an intact NE. HeLa cells have commonly been used to study the regulation of perinuclear dynein due to their highly enriched pool of dynein on the NE at G2/M (Bolhy et al., 2011; Jodoin et al., 2012; Jodoin et al., 2013; Splinter et al., 2010). Prior to fixation and immunostaining for dynein intermediate chain (DIC) and PH3, siRNA-treated cells were incubated with 5 µM nocodazole to stimulate recruitment of dynein-dynactin complexes and their accessory proteins to the nuclear surface. This brief nocodazole
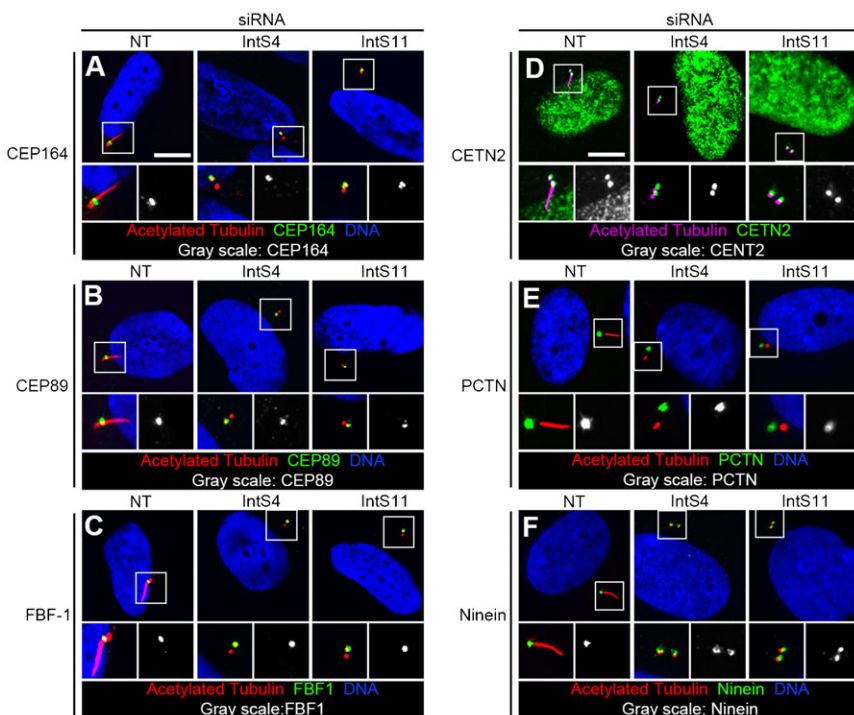

Fig. 2. **Normal BB composition following INT depletion.** RPE cells were transfected with siRNA, serum-starved, fixed, and stained for acetylated tubulin, BB markers, and DNA. Representative images show normal localization of BB markers in INT-depleted cells. Higher-magnification views (bottom micrographs) of BB correspond with regions enclosed by white boxes. Scale bars, 10 µm.

treatment has been documented to enrich for functional dynein complexes on the NE in non-G1 cells (Beswick et al., 2006; Bolhy et al., 2011; Hebbar et al., 2008; Jodoin et al., 2012; Jodoin et al., 2013; Splinter et al., 2010).

Consistent with our previous report, we observed drastic reduction of the fraction of cells with dynein accumulation on the NE following INT depletion: only 24% of IntS11-siRNA prophase cells exhibited perinuclear dynein compared to 92% of NT-siRNA prophase cells (Fig. 3A,C) (Jodoin et al., 2012). We chose to focus on IntS11 for this experiment based on its role as the catalytic subunit of the INT complex (Chen and Wagner, 2010). In contrast, the fraction of prophase cells with perinuclear

dynein following depletion of other ciliogenesis regulators, CETN2 or PCTN, was comparable to that of NT-siRNA cells (90% and 88%, respectively; Fig. 3A,C). We have previously reported that this NE-anchored pool of dynein is found in RPE cells (Jodoin et al., 2012). To determine if INT is required for dynein recruitment (in addition to primary ciliogenesis) in RPE cells, we assessed perinuclear dynein following down-regulation of IntS11. Dynein accumulation on the NE was found in 77% of NT-siRNA RPE prophase cells following treatment with 10 μM nocodazole (Fig. 3B,D). Similar to our results with HeLa cells, we observed a severe reduction in the percentage of RPE prophase cells with NE-anchored dynein (down to 7%) following
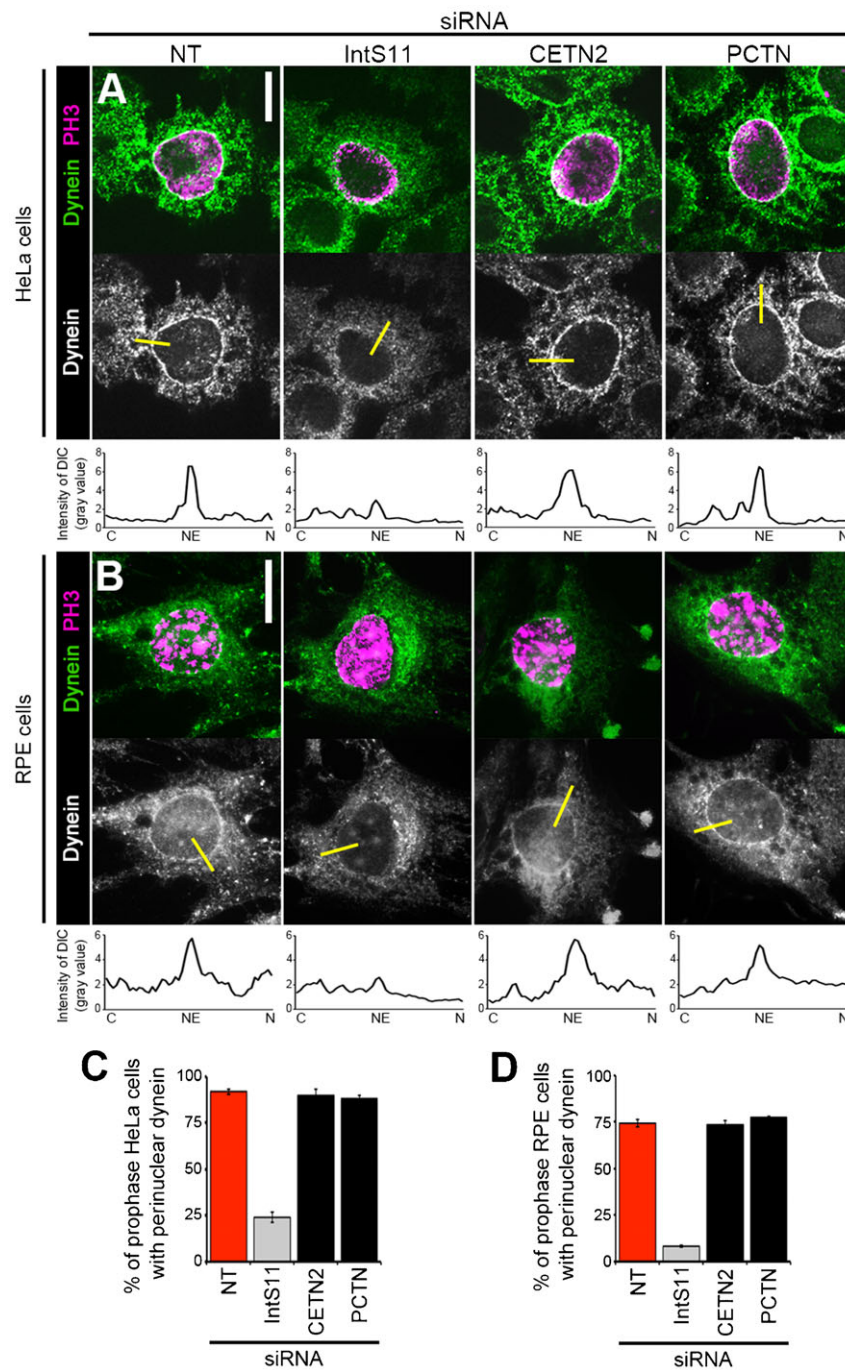
Fig. 3. Ciliogenesis regulators are not required for perinuclear dynein recrutiment. HeLa cells (A,C) or RPE cells (B,D) were transfected with siRNA, nocodazole-treated, fixed, and stained for dynein (DIC) and PH3. (A,B) Representative images show perinuclear dynein in prophase HeLa (A) or RPE cells (B) after indicated knockdowns. Yellow bars represent line scans that span the cytoplasm (C), nuclear envelope (NE), and nucleus (N) to measure peak DIC intensity on the NE; corresponding plots are shown below each micrograph. (C,D) Quantification of perinuclear dynein in HeLa (C) or RPE (D) prophase cells (PH3-positive with intact NE). Scale bars, 10 μm. Gray, $P<0.0001$; black bar, not significant (both relative to NT-siRNA, red).

depletion of IntS11 (Fig. 3B,D). This finding suggests that the role for INT in promoting perinuclear dynein is conserved and is not a consequence of the transformed nature of HeLa cells. As for HeLa cells, we found that the primary ciliogenesis regulators tested were not required for perinuclear dynein in RPE cells: loss of CETN2 or PCTN recapitulated what was observed in NT-siRNA cells (with PC formation in 76% and 78%, respectively, of siRNA-treated cells; Fig. 3B,D).

As further confirmation of these findings, we quantified DIC immunofluorescence signals on the NE versus the cytoplasm and the average peak DIC intensity on the NE in both cell lines and found them greatly reduced in IntS11 cells as previously described, but unchanged in cells depleted of CETN2 or PCTN compared to NT-siRNA cells (supplementary material Fig. S6) (Jodoin et al., 2012; Jodoin et al., 2013). These data reveal that INT differs from CETN2 and PCTN, two other proteins essential for ciliogenesis, in that it has a dual function in promoting perinuclear accumulation of dynein.

Perinuclear dynein is not required for PC formation

We next asked whether other proteins essential for perinuclear dynein accumulation are, like the INT complex, also required for

primary ciliogenesis. BICD2 and CENP-F directly anchor dynein motors to the NE, whereas RanBP2 serves as the binding site for BICD2 within the nuclear pore complex; depletion of any of these proteins results in loss of perinuclear dynein in HeLa cells (Bolhy et al., 2011; Splinter et al., 2010). We confirmed that these known regulators of perinuclear dynein in HeLa cells are similarly required for NE-anchoring of dynein in cells capable of forming PC: depletion of BICD2, CENP-F, or RanBP2 in RPE cells resulted in a marked loss of perinuclear dynein compared to NT-siRNA cells (Fig. 4A,C).

We disrupted the pool of dynein anchored on the NE in RPE cells by depleting proteins required for this process and assessed PC formation. Following siRNA treatment, cells were serum-starved and evaluated for the presence of PC. Loss of BICD2, CENP-F, or RanBP2 resulted in only a slight reduction in the fraction of cells with PC (80%, 91%, and 81% of NT-siRNA cells, respectively) compared to loss of INT subunits (e.g. 38% of NT-siRNA cells for IntS11; Fig. 1K; Fig. 4B,D). Additionally we confirmed the previously reported requirement for dynein in PC formation: down-regulation of DHC resulted in the absence of PC in a majority of cells (Fig. 4B,D) (Rajagopalan et al., 2009). These data suggest that, in contrast to the INT complex, other
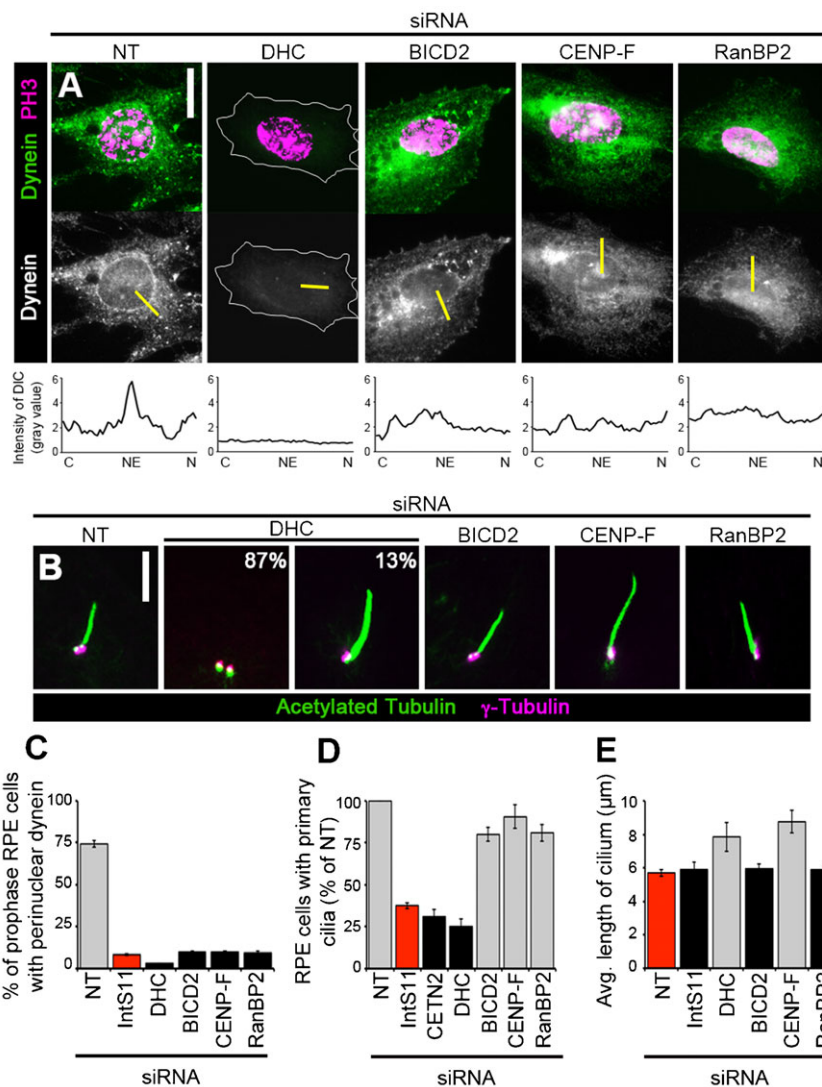
Fig. 4. Perinuclear dynein regulators are not required for primary ciliogenesis. RPE cells were transfected with siRNA and either nocodazole-treated, fixed, and stained for dynein (DIC) and PH3 (A,C) or serum-starved, fixed, and immunostained for acetylated tubulin and γ-tubulin (B,D,E). (A) Representative images show perinuclear dynein in prophase cells (PH3-positive and intact NE) after indicated knockdowns. Yellow bars represent line scans that span the cytoplasm (C), nuclear envelope (NE), and nucleus (N) to measure peak DIC intensity on the NE; corresponding plots are shown below each micrograph. (B) Representative images show PC after indicated knockdowns. Percentages in the DHC-siRNA micrographs indicate frequency at which each phenotype (no cilium, left; elongated cilium, right) was observed. (C–E) Quantification of prophase cells with perinuclear dynein (C), PC presence (D), or average PC length (E) after indicated knockdowns. Gray, $P<0.0001$; black bar, not significant (relative to IntS11-siRNA (C,D) or NT (E), red). Scale bars, 10 μm (A) or 5 μm (B).
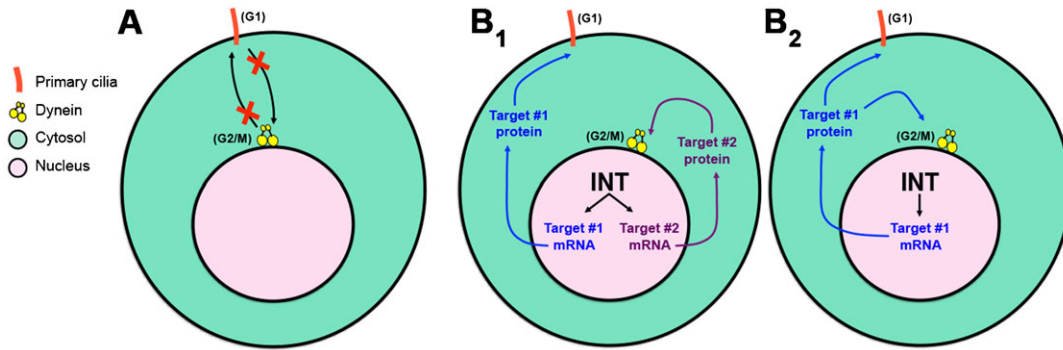
Fig. 5. Model for independent regulation of dynein recruitment and ciliogenesis by INT. See text for details.

known regulators of perinuclear dynein accumulation are not strictly required for generation of PC.

For the subset of cells with PC, we also assessed PC length in these experiments. As previously reported, we observed increased PC length following depletion of dynein when the PC was present (Fig. 4B,E) (Palmer et al., 2011). Similarly, CENP-F-siRNA cells exhibited longer PC compared to NT-siRNA cells, although BICD2 or RanBP2 depletion had no effect (Fig. 4B,E). These data suggest that CENP-F, while not required for PC formation, has a role in regulating PC length; a role for CENP-F in this process has not been previously reported to our knowledge. We speculate that CENP-F may influence PC length through its regulation of cytoplasmic dynein-2, which is essential for maintaining normal PC length (Palmer et al., 2011; Rajagopalan et al., 2009). No change in PC length, however, was observed in cells depleted of IntS11 (Fig. 1B; Fig. 4E). This finding suggests that INT promotes PC formation via a dynein-independent mechanism.

Taken together, the data presented herein showing that the pool of dynein anchored on the NE at the G2/M transition is not required for promoting primary ciliogenesis in G1, and vice versa, supports our hypothesis that dynein recruitment to the NE and PC formation are regulated by distinct INT-dependent mechanisms (Figs 3, 4; Fig. 5A). We propose the following model to explain how INT may regulate these two cytoplasmic events that occur at different cell-cycle stages. INT is required for proper processing of snRNAs, which in turn are required for efficient processing of mRNAs encoding at least two critical proteins that independently promote ciliogenesis in G1 and dynein recruitment to the NE at G2/M (Fig. 5B1). We cannot, however, exclude an alternative model in which INT functions through a common critical target required to mediate both of these events. In this case, INT would ensure efficient processing of transcripts encoding a single (as yet unidentified) protein that plays essential roles in promoting both ciliogenesis during G1 and perinuclear dynein accumulation at G2/M (Fig. 5B2). Further studies will be required to identify the critical target(s) of the INT complex that mediate these and other important cellular processes.

Materials and Methods

Cell culture, immunostaining, and microscopy

Cell lines were maintained at 37°C and 5% CO_2 in DMEM (Life Technologies, Carlsbad, CA) containing 10% FBS, 1% L-glutamine, 100 µg/ml streptomycin, and 100 U/ml penicillin. siGENOME NT siRNA#5 (Dharmacon, Lafayette, CO) was used as negative control. siRNA oligonucleotides used herein for specific knockdowns have been previously described as follows: INT subunits (Jodoin et al., 2012), CETN2 and PCTN (Graser et al., 2007), BICD2 and RanBP2

(Splinter et al., 2010), CENP-F (Bolhy et al., 2011), and DHC (Rajagopalan et al., 2009). siRNA oligonucleotides were obtained from Dharmacon or Sigma-Aldrich (St. Louis, MO). Independent siRNA oligonucleotides used to silence IntS3 (IntS3 #2; SASI_Hs01_00063141), IntS4 (IntS4 #2; 5′-CAG CAU UGU UCU CAG AUC A-3′), IntS9 (IntS9 #2; 5′-GUG AAC UCU GCC CUU AGU A-3′), and IntS11 (IntS11 #2; SASI_Hs02_00350804) were obtained from Sigma-Aldrich. Immunoblot signals for INT subunit protein levels following siRNA treatment were quantified relative to tubulin using ImageJ.

Cells were transfected with siRNA oligonucleotides using DharmaFECT 1 transfection reagent (Dharmacon) and analyzed at 72 h post-siRNA treatment in all cases. To stimulate PC formation under conditions of serum starvation, cells at 100% confluence and at 48 h post-siRNA treatment were incubated in DMEM plus 0.5% FBS for 24 h prior to fixation. Where indicated, siRNA-treated cells in normal growth medium were incubated in 5 µg/ml (16.6 µM) nocodazole (Sigma-Aldrich) for 3 h (HeLa cells) or 10 µg/ml (33.2 µM) nocodazole for 1 h (RPE cells) prior to fixation at 72 h post-siRNA treatment to enhance perinuclear localization of dynein. Primary antibodies were used as follows: acetylated tubulin (6-11B-1, 1:500, Sigma-Aldrich), γ-Tubulin (ab16504, 1:500, Abcam, Cambridge, MA), CEP164 (NBP-77006, 1:100, Novus Biologicals, Littleton, CO), CEP89 (HPA040056, 1:100, Sigma), FBF-1 (HPA023677; 1:100, Sigma), CETN2 (N-17-R, 1:200, Santa Cruz Biotechnology, Dallas, TX), PCTN (ab4448, 1:2000, Abcam), Ninein (ab4447, 1:500, Abcam), dynein intermediate chain (74.1, 1:500, Abcam), and PH3 (Mitosis Marker, 1:1000, Millipore, Billerica, MA). Wide-field and confocal fluorescence microscopy methods were previously described (Efimov et al., 2007; Jodoin et al., 2013).

PC length (visualized by acetylated tubulin staining) was measured from base to tip using ImageJ (National Institutes of Health, Bethesda, MD); at least 100 cells were scored per condition. For determination of the percentage of cells with PC or perinuclear dynein, experiments were performed ≥3 times with ≥200 cells scored per condition. For quantification of perinuclear dynein intensity, 10 representative cells were measured per condition; for each cell, 12 line scans distributed equally around the nuclear circumference were obtained. Line scan analyses were performed using ImageJ. Line scans presented within figures are 50 pixels in length and are oriented with the cytoplasmic end of each line to the left and the intranuclear end of each line to the right. Statistical analyses of data were performed using Student's unpaired t-test. For bar graphs, error bars indicate s.e.m.

Immunoblotting

Immunoblotting of cell lysates was performed as previously described (Jodoin et al., 2013). The following primary antibodies were used: c-Myc (9E10, 1:1000), β-tubulin (E7, 1:1000, Developmental Studies Hybridoma Bank, University of Iowa, Iowa City, IA), CENP-F (14C10 1D8, 1:500, Abcam), BICD2 (1:2500; gift from A. Akhmanova) (Splinter et al., 2010), dynein intermediate chain (74.1, 1:500, Santa Cruz Biotechnology), PCTN (ab4448, 1:2000, Abcam), CETN2 (N-17-R, 1:200, Santa Cruz Biotechnology), RanBP2 (ab64276, 1:1000, Abcam), IntS1, IntS4, IntS7, IntS9, IntS10, IntS11, IntS12, and CPSF30 (1:1000, Bethyl Labs, Montgomery, TX).

References

Anderson, M. A., Jodoin, J. N., Lee, E., Hales, K. G., Hays, T. S. and Lee, L. A. (2009). Asunder is a critical regulator of dynein-dynactin localization during Drosophila spermatogenesis. *Mol. Biol. Cell* **20**, 2709-2721.

Baillat, D., Hakimi, M. A., Näär, A. M., Shilatifard, A., Cooch, N. and Shiekhattar, R. (2005). Integrator, a multiprotein mediator of small nuclear RNA processing, associates with the C-terminal repeat of RNA polymerase II. *Cell* **123**, 265-276.

Barabino, S. M., Hübner, W., Jenny, A., Minvielle-Sebastia, L. and Keller, W. (1997). The 30-kD subunit of mammalian cleavage and polyadenylation specificity factor and its yeast homolog are RNA-binding zinc finger proteins. *Genes Dev.* **11**, 1703-1716.

Basten, S. G. and Giles, R. H. (2013). Functional aspects of primary cilia in signaling, cell cycle and tumorigenesis. *Cilia* **2**, 6.

Beswick, R. W., Ambrose, H. E. and Wagner, S. D. (2006). Nocodazole, a microtubule de-polymerising agent, induces apoptosis of chronic lymphocytic leukaemia cells associated with changes in Bcl-2 phosphorylation and expression. *Leuk. Res.* **30**, 427-436.

Bolhy, S., Bouhlel, I., Dultz, E., Nayak, T., Zuccolo, M., Gatti, X., Vallee, R., Ellenberg, J. and Doye, V. (2011). A Nup133-dependent NPC-anchored network tethers centrosomes to the nuclear envelope in prophase. *J. Cell Biol.* **192**, 855-871.

Chen, J. and Wagner, E. J. (2010). snRNA 3′ end formation: the dawn of the Integrator complex. *Biochem. Soc. Trans.* **38**, 1082-1087.

Chen, J., Ezzeddine, N., Waltenspiel, B., Albrecht, T. R., Warren, W. D., Marzluff, W. F. and Wagner, E. J. (2012). An RNAi screen identifies additional members of the Drosophila Integrator complex and a requirement for cyclin C/Cdk8 in snRNA 3′-end formation. *RNA* **18**, 2148-2156.

Draviam, V. M., Shapiro, I., Aldridge, B. and Sorger, P. K. (2006). Misorientation and reduced stretching of aligned sister kinetochores promote chromosome missegregation in EB1- or APC-depleted cells. *EMBO J.* **25**, 2814-2827.

Efimov, A., Kharitonov, A., Efimova, N., Loncarek, J., Miller, P. M., Andreyeva, N., Gleeson, P., Galjart, N., Maia, A. R., McLeod, I. X. et al. (2007). Asymmetric CLASP-dependent nucleation of noncentrosomal microtubules at the trans-Golgi network. *Dev. Cell* **12**, 917-930.

Ezzeddine, N., Chen, J., Waltenspiel, B., Burch, B., Albrecht, T., Zhuo, M., Warren, W. D., Marzluff, W. F. and Wagner, E. J. (2011). A subset of Drosophila integrator proteins is essential for efficient U7 snRNA and spliceosomal snRNA 3′-end formation. *Mol. Cell. Biol.* **31**, 328-341.

Golling, G., Amsterdam, A., Sun, Z., Antonelli, M., Maldonado, E., Chen, W., Burgess, S., Haldi, M., Artzt, K., Farrington, S. et al. (2002). Insertional mutagenesis in zebrafish rapidly identifies genes essential for early vertebrate development. *Nat. Genet.* **31**, 135-140.

Gönczy, P., Pichler, S., Kirkham, M. and Hyman, A. A. (1999). Cytoplasmic dynein is required for distinct aspects of MTOC positioning, including centrosome separation, in the one cell stage Caenorhabditis elegans embryo. *J. Cell Biol.* **147**, 135-150.

Graser, S., Stierhof, Y. D., Lavoie, S. B., Gassner, O. S., Lamla, S., Le Clech, M. and Nigg, E. A. (2007). Cep164, a novel centriole appendage protein required for primary cilium formation. *J. Cell Biol.* **179**, 321-330.

Hebbar, S., Mesngon, M. T., Guillotte, A. M., Desai, B., Ayala, R. and Smith, D. S. (2008). Lis1 and Ndel1 influence the timing of nuclear envelope breakdown in neural stem cells. *J. Cell Biol.* **182**, 1063-1071.

Holzbaur, E. L. and Vallee, R. B. (1994). DYNEINS: molecular structure and cellular function. *Annu. Rev. Cell Biol.* **10**, 339-372.

Jodoin, J. N., Shboul, M., Sitaram, P., Zein-Sabatto, H., Reversade, B., Lee, E. and Lee, L. A. (2012). Human Asunder promotes dynein recruitment and centrosomal tethering to the nucleus at mitotic entry. *Mol. Biol. Cell* **23**, 4713-4724.

Jodoin, J. N., Sitaram, P., Albrecht, T. R., May, S. B., Shboul, M., Lee, E., Reversade, B., Wagner, E. J. and Lee, L. A. (2013). Nuclear-localized Asunder regulates cytoplasmic dynein localization via its role in the integrator complex. *Mol. Biol. Cell* **24**, 2954-2965.

Kamath, R. S., Fraser, A. G., Dong, Y., Poulin, G., Durbin, R., Gotta, M., Kanapin, A., Le Bot, N., Moreno, S., Sohrmann, M. et al. (2003). Systematic functional analysis of the Caenorhabditis elegans genome using RNAi. *Nature* **421**, 231-237.

Kardon, J. R. and Vale, R. D. (2009). Regulators of the cytoplasmic dynein motor. *Nat. Rev. Mol. Cell Biol.* **10**, 854-865.

Kim, S. and Dynlacht, B. D. (2013). Assembling a primary cilium. *Curr. Opin. Cell Biol.* **25**, 506-511.

Kim, S., Zaghloul, N. A., Bubenshchikova, E., Oh, E. C., Rankin, S., Katsanis, N., Obara, T. and Tsiokas, L. (2011). Nde1-mediated inhibition of ciliogenesis affects cell cycle re-entry. *Nat. Cell Biol.* **13**, 351-360.

Ko, H. W. (2012). The primary cilium as a multiple cellular signaling scaffold in development and disease. *BMB Rep* **45**, 427-432.

Kong, S., Du, X., Peng, C., Wu, Y., Li, H., Jin, X., Hou, L., Deng, K., Xu, T. and Tao, W. (2013). Dlic1 deficiency impairs ciliogenesis of photoreceptors by destabilizing dynein. *Cell Res.* **23**, 835-850.

Malone, C. J., Misner, L., Le Bot, N., Tsai, M. C., Campbell, J. M., Ahringer, J. and White, J. G. (2003). The C. elegans hook protein, ZYG-12, mediates the essential attachment between the centrosome and nucleus. *Cell* **115**, 825-836.

Matera, A. G., Terns, R. M. and Terns, M. P. (2007). Non-coding RNAs: lessons from the small nuclear and small nucleolar RNAs. *Nat. Rev. Mol. Cell Biol.* **8**, 209-220.

Otani, Y., Nakatsu, Y., Sakoda, H., Fukushima, T., Fujishiro, M., Kushiyama, A., Okubo, H., Tsuchiya, Y., Ohno, H., Takahashi, S. et al. (2013). Integrator complex plays an essential role in adipose differentiation. *Biochem. Biophys. Res. Commun.* **434**, 197-202.

Palmer, K. J., MacCarthy-Morrogh, L., Smyllie, N. and Stephens, D. J. (2011). A role for Tctex-1 (DYNLT1) in controlling primary cilium length. *Eur. J. Cell Biol.* **90**, 865-871.

Rajagopalan, V., Subramanian, A., Wilkes, D. E., Pennock, D. G. and Asai, D. J. (2009). Dynein-2 affects the regulation of ciliary length but is not required for ciliogenesis in Tetrahymena thermophila. *Mol. Biol. Cell* **20**, 708-720.

Robinson, J. T., Wojcik, E. J., Sanders, M. A., McGrail, M. and Hays, T. S. (1999). Cytoplasmic dynein is required for the nuclear attachment and migration of centrosomes during mitosis in Drosophila. *J. Cell Biol.* **146**, 597-608.

Rutkowski, R. J. and Warren, W. D. (2009). Phenotypic analysis of deflated/Ints7 function in Drosophila development. *Dev. Dyn.* **238**, 1131-1139.

Salisbury, J. L. (2004). Primary cilia: putting sensors together. *Curr. Biol.* **14**, R765-R767.

Schroer, T. A. (2004). Dynactin. *Annu. Rev. Cell Dev. Biol.* **20**, 759-779.

Sillibourne, J. E., Specht, C. G., Izeddin, I., Hurbain, I., Tran, P., Triller, A., Darzacq, X., Dahan, M. and Bornens, M. (2011). Assessing the localization of centrosomal proteins by PALM/STORM nanoscopy. *Cytoskeleton (Hoboken)* **68**, 619-627.

Sitaram, P., Anderson, M. A., Jodoin, J. N., Lee, E. and Lee, L. A. (2012). Regulation of dynein localization and centrosome positioning by Lis-1 and asunder during Drosophila spermatogenesis. *Development* **139**, 2945-2954.

Splinter, D., Tanenbaum, M. E., Lindqvist, A., Jaarsma, D., Flotho, A., Yu, K. L., Grigoriev, I., Engelsma, D., Haasdijk, E. D., Keijzer, N. et al. (2010). Bicaudal D2, dynein, and kinesin-1 associate with nuclear pore complexes and regulate centrosome and nuclear positioning during mitotic entry. *PLoS Biol.* **8**, e1000350.

Takata, H., Nishijima, H., Maeshima, K. and Shibahara, K. (2012). The integrator complex is required for integrity of Cajal bodies. *J. Cell Sci.* **125**, 166-175.

Tanos, B. E., Yang, H. J., Soni, R., Wang, W. J., Macaluso, F. P., Asara, J. M. and Tsou, M. F. (2013). Centriole distal appendages promote membrane docking, leading to cilia initiation. *Genes Dev.* **27**, 163-168.

Tao, S., Cai, Y. and Sampath, K. (2009). The Integrator subunits function in hematopoiesis by modulating Smad/BMP signaling. *Development* **136**, 2757-2765.

Vaisberg, E. A., Koonce, M. P. and McIntosh, J. R. (1993). Cytoplasmic dynein plays a role in mammalian mitotic spindle formation. *J. Cell Biol.* **123**, 849-858.

Wang, G., Chen, Q., Zhang, X., Zhang, B., Zhuo, X., Liu, J., Jiang, Q. and Zhang, C. (2013). PCM1 recruits Plk1 to the pericentriolar matrix to promote primary cilia disassembly before mitotic entry. *J. Cell Sci.* **126**, 1355-1365.
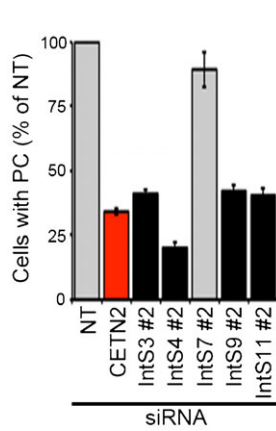
Supplementary Material

Fig. S1. Loss of PC following INT down-regulation by independent siRNA sequences. RPE cells were transfected with indicated siRNAs, serum-starved, fixed, and stained for acetylated tubulin, γ-tubulin, and DNA. Quantification of PC formation (normalized to NT-siRNA) in siRNA-depleted cells. Gray, $P<0.001$; black, not significant (relative to CETN2-siRNA, red).
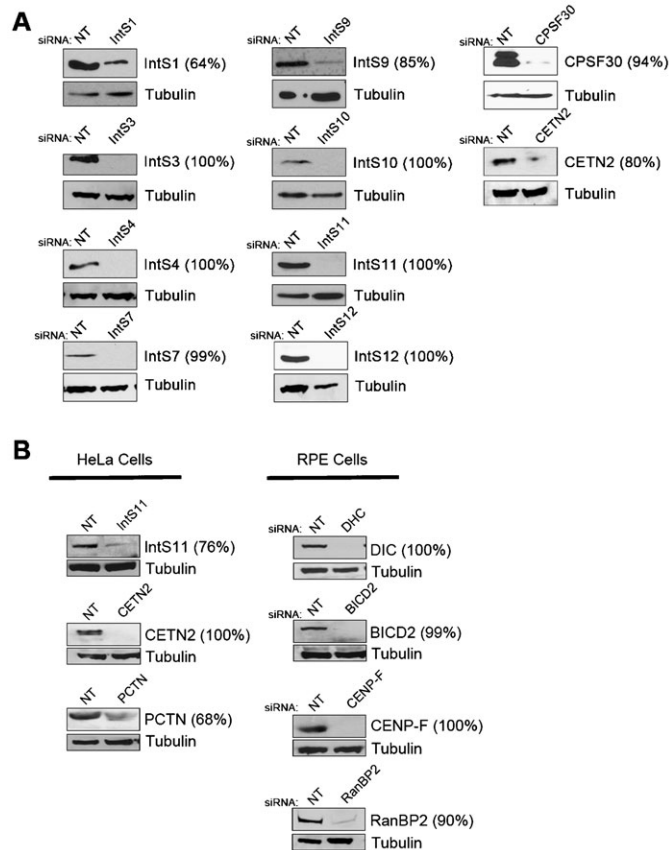

Fig. S3. Increased frequency and degree of centriole pair separation following loss of INT activity. RPE cells were transfected with siRNA as indicated. Following siRNA treatment, PC formation was stimulated by serum starvation. After fixation, cells were stained for acetylated tubulin, g-tubulin, and DNA. (A) Separation of centriole pairs was observed following INT subunit-siRNA treatment. (B) Higher magnification of region enclosed within white box shows scoring system used to measure distance between centriole pairs (yellow bars). (C) Quantification of the average distance between centriole pairs following indicated siRNA treatment. Gray bars, $P<0.0001$; black, not significant (both relative to NT-siRNA, red). Distance between the outer borders of basal body pairs (marked by g-tubulin staining) was measured using ImageJ. Basal body pairs in at least 100 cells were scored per condition.

Fig. S2. Confirmation of efficient knockdown of proteins by siRNA. RPE or Hela cells were transfected with siRNA as indicated. Immunoblots of cell lysates were probed with antibodies against INT subunits, perinuclear dynein regulators, ciliogenesis regulators, or related controls corresponding to data presented in Figs 1 and 3 (A) or Figs 3 and 4 (B). Depletion of each protein targeted by siRNA was confirmed. Tubulin was used as loading control. Percent of protein depletion following targeted knock down indicated next to each antibody.

Fig. S4. Confirmation of G1 arrest in serum-starved RPE cells following INT subunit knockdown. RPE cells were transfected with siRNA as indicated, serum-starved, fixed, and stained with propidium iodide. DNA content was analyzed by FACS as previously described (Jodoin et al., 2013). (A) Cell-cycle profile of NT-siRNA cells grown under normal medium conditions (plus 10% FBS). (B) Cell-cycle profiles of NT-siRNA and INT-depleted cells following serum starvation revealed a similar degree of G1 arrest.
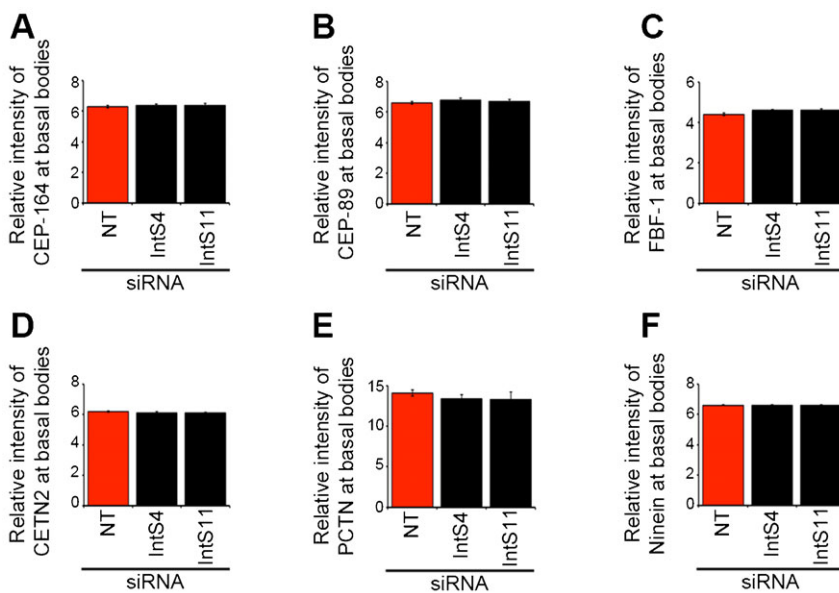
Fig. S5. Characterization of basal body markers. Quantification of distal appendage (A–C) and basal body (D–F) signals for indicated markers (normalized to signals for acetylated tubulin). No significant changes in intensity were observed following depletion of individual INT subunits. Intensity of antibody signals on basal bodies was determined using ImageJ. Basal bodies in at least 100 cells were scored per condition. Black bar, not significant (relative to NT-siRNA, red).
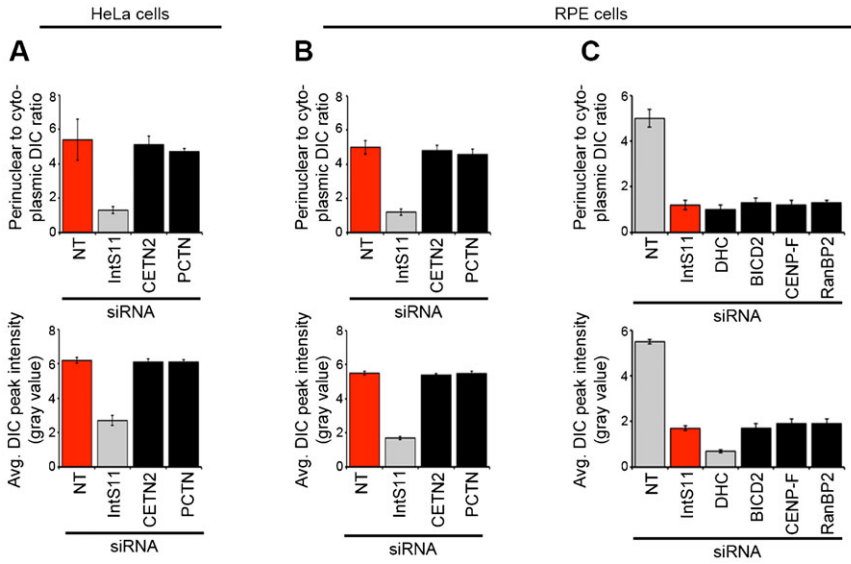
Fig. S6. Quantification of perinuclear dynein following knockdown of ciliogenesis regulators. Bar graphs correspond to representative images of immunostained HeLa (A) or RPE (B,C) cells presented in Fig. 3A,B and Fig. 4A. Line scans were drawn from the cytoplasm to inside the nucleus. Ratios of the intensity of the dynein signal on the NE to the cytoplasm (top) and average peak intensities of perinuclear dynein (bottom) are shown. Samples with $P<0.0001$ are shown in gray; black, not significant (relative to NT-siRNA (A,B) or IntS11-siRNA (C), red).

Nuclear-localized Asunder regulates cytoplasmic dynein localization via its role in the Integrator complex

Jeanne N. Jodoin[a], Poojitha Sitaram[a], Todd R. Albrecht[b], Sarah B. May[b], Mohammad Shboul[c], Ethan Lee[a], Bruno Reversade[c,d], Eric J. Wagner[b], and Laura A. Lee[a]

[a]Department of Cell and Developmental Biology, Vanderbilt University Medical Center, Nashville, TN 37232-8240; [b]Department of Biochemistry and Molecular Biology, University of Texas Medical School at Houston, Houston, TX 77030; [c]Institute of Medical Biology, A*STAR, Singapore 138648; [d]Department of Pediatrics, National University of Singapore, Singapore 119228

ABSTRACT We previously reported that Asunder (ASUN) is essential for recruitment of dynein motors to the nuclear envelope (NE) and nucleus–centrosome coupling at the onset of cell division in cultured human cells and *Drosophila* spermatocytes, although the mechanisms underlying this regulation remain unknown. We also identified ASUN as a functional component of Integrator (INT), a multisubunit complex required for 3′-end processing of small nuclear RNAs. We now provide evidence that ASUN acts in the nucleus in concert with other INT components to mediate recruitment of dynein to the NE. Knockdown of other individual INT subunits in HeLa cells recapitulates the loss of perinuclear dynein in ASUN–small interfering RNA cells. Forced localization of ASUN to the cytoplasm via mutation of its nuclear localization sequence blocks its capacity to restore perinuclear dynein in both cultured human cells lacking ASUN and *Drosophila asun* spermatocytes. In addition, the levels of several INT subunits are reduced at G2/M when dynein is recruited to the NE, suggesting that INT does not directly mediate this step. Taken together, our data support a model in which a nuclear INT complex promotes recruitment of cytoplasmic dynein to the NE, possibly via a mechanism involving RNA processing.

INTRODUCTION

Dynein, a minus end–directed molecular motor, is a large multimeric complex that can be divided into distinct regions (Holzbaur and Vallee, 1994; Kardon and Vale, 2009). Protruding from the head region are two microtubule-binding domains that allow the motor to walk processively along the microtubule toward its minus end. This movement is driven by the force-generating ATPase activity of the catalytic domains found within the head region of the motor. The stem region, consisting of multiple light, light intermediate, and intermediate chains, is the most variable and is widely considered to serve as the binding site for dynein adaptors.

Within the cell, dynein exists in association with its activating complex, dynactin (Schroer, 2004). The dynein–dynactin complex performs diverse functions within the cell, ranging from cargo transport, centrosome assembly, and organelle positioning to roles in chromosome alignment and spindle positioning during mitosis (Holzbaur and Vallee, 1994; Kardon and Vale, 2009). Dynein–dynactin complexes are subject to multiple layers of regulation, including binding of accessory proteins, phosphorylation, subunit composition, and subcellular localization (Kardon and Vale, 2009). Localized pools of dynein were identified and shown to be required for critical processes in the cell, although the mechanisms underlying the control of dynein localization are poorly understood (Kardon and Vale, 2009).

Abbreviations used: ASUN, Asunder; BICD2, Bicaudal D2; CDK1, cyclin-dependent kinase 1; CENP-F, centromere protein F; CHY, mCherry; CPSF30, cleavage polyadenylation specificity factor 30; dASUN, *Drosophila* Asunder; DIC, dynein IC; GFP, green fluorescent protein; hASUN, human Asunder; INT, Integrator complex; IntS, Integrator subunit; mASUN, mouse Asunder; NE, nuclear envelope; NEBD, nuclear envelope breakdown; NLS, nuclear localization sequence; NT, nontargeting; siRNA, small interfering RNA; snRNA, small nuclear RNA.

Across phyla, a stably anchored subpopulation of dynein exists on the nuclear envelope (NE) of cells (Gonczy *et al.*, 1999; Robinson *et al.*, 1999; Salina *et al.*, 2002; Payne *et al.*, 2003; Anderson *et al.*, 2009). This pool of dynein is required for both stable attachment of centrosomes to the NE before nuclear envelope breakdown (NEBD) and migration of centrosomes to opposite sides of the nucleus, thereby ensuring proper positioning of the bipolar spindle (Vaisberg *et al.*, 1993; Gonczy *et al.*, 1999; Robinson *et al.*, 1999; Malone *et al.*, 2003; Anderson *et al.*, 2009; Splinter *et al.*, 2010; Bolhy *et al.*, 2011; Jodoin *et al.*, 2012; Sitaram *et al.*, 2012). In addition, this pool of dynein appears to facilitate NEBD by forcibly tearing the NE, although the precise mechanism remains unknown (Beaudouin *et al.*, 2002; Salina *et al.*, 2002).

Two proteins, Bicaudal D2 (BICD2) and centromere protein F (CENP-F), have been shown to directly anchor dynein to the nuclear surface at the G2/M transition in HeLa cells (Splinter *et al.*, 2010; Bolhy *et al.*, 2011). BICD2, a dynein adaptor protein, directly binds dynein and nucleoporin RanBP2, thereby anchoring the motors to the NE (Splinter *et al.*, 2010). CENP-F directly interacts with dynein adaptor proteins NudE/EL and nucleoporin Nup133 to effectively anchor dynein to the NE (Bolhy *et al.*, 2011). In both *Drosophila* spermatocytes and cultured human cells, we previously identified ASUN as an additional regulator of dynein recruitment to the NE at G2/M of meiosis and mitosis, respectively, although physical interaction between ASUN and dynein has not been demonstrated (Anderson *et al.*, 2009; Jodoin *et al.*, 2012).

Spermatocytes within the testes of *Drosophila asun* males arrest at prophase of meiosis I with a severely reduced pool of perinuclear dynein and centrosomes that are not attached to the nuclear surface (hence the name "*asunder*"; Anderson *et al.*, 2009). Spermatocytes that progress beyond this arrest exhibit defects in spindle assembly, chromosome segregation, and cytokinesis during the meiotic divisions. Using cultured human cells, we found that small interfering RNA (siRNA)–mediated down-regulation of the human homologue of Asunder (hASUN) similarly resulted in reduction of perinuclear dynein during prophase of mitosis (Jodoin *et al.*, 2012). Additional defects observed after loss of hASUN included nucleus–centrosome uncoupling, abnormal mitotic spindles, and impaired progression through mitosis.

In either *Drosophila* or cultured human cells, a direct mechanism for promotion of perinuclear dynein by ASUN has not been elucidated, although localization changes in ASUN coincide with the accumulation of dynein on the NE. *Drosophila* ASUN (dASUN) is largely restricted within the nucleus of early G2 spermatocytes and first appears in the cytoplasm during late G2, roughly coincident with the initiation of dynein recruitment to the nuclear surface (Anderson *et al.*, 2009). Similarly, in prophase HeLa cells, when a perinuclear pool of dynein forms transiently at G2/M, hASUN is diffusely present in the cytoplasm (Jodoin *et al.*, 2012). On the basis of these temporal associations of the localizations of ASUN and perinuclear dynein, we previously proposed that the cytoplasmic pool of ASUN likely mediates recruitment of dynein motors to the NE (Anderson *et al.*, 2009; Jodoin *et al.*, 2012).

Integrator complex (INT) is an evolutionarily conserved complex consisting of 14 subunits, although its biology is poorly understood (reviewed in Chen and Wagner, 2010). INT was originally identified due to its association with the C-terminal tail of RNA polymerase II and was subsequently shown to be required for 3′-end processing of small nuclear RNAs (snRNAs; Baillat *et al.*, 2005). These processed snRNAs play roles in gene expression via intron removal and further processing of pre-mRNAs (Matera *et al.*, 2007). To discover novel components of INT that are required for its snRNA-processing

function, a cell-based assay was developed in which generation of a green fluorescent protein (GFP) signal due to incomplete processing of a reporter U7 snRNA served as a readout of INT activity (Chen *et al.*, 2012). With this approach, dASUN was identified as a functional component of INT: down-regulation of dASUN led to increase misprocessing of U7 and spliceosomal snRNA, indicating its requirement for activity of the complex (Chen *et al.*, 2012). Furthermore, dASUN was shown to biochemically interact with INT in a stoichiometric manner, an association that it is conserved in humans (Malovannaya *et al.*, 2010; Chen *et al.*, 2012). Collectively these data provide compelling evidence that ASUN is a core Integrator subunit.

Given the divergent nature of the known activities of ASUN—critical regulator of cytoplasmic dynein localization and essential component of a nuclear snRNA-processing complex—we sought to determine whether these roles are independent of each other or derived from a common function. We find that depletion of individual INT components from HeLa cells results in loss of perinuclear dynein, recapitulating the phenotype observed in hASUN-siRNA cells (Jodoin *et al.*, 2012). In addition, we find that forced localization of either hASUN or dASUN to the cytoplasm inhibits its capacity to recruit dynein to the NE in the absence of endogenous ASUN. We present a model in which ASUN acts within the nucleus in concert with other subunits of the Integrator complex, likely via processing of a critical RNA target(s), to promote recruitment of cytoplasmic dynein motors to the NE at G2/M.

RESULTS
Multiple INT subunits are required for dynein recruitment to the NE

Two ASUN-dependent cellular functions have been reported: dynein recruitment to the NE at G2/M, and proper processing of snRNA by INT (Chen *et al.*, 2012; Jodoin *et al.*, 2012). We hypothesized that other components of the INT complex, such as hASUN, may be required to promote dynein recruitment to the NE. To test this hypothesis, we performed siRNA-mediated knockdown of individual INT subunits in HeLa cells and assessed dynein localization. Before fixation and immunostaining for dynein IC (DIC), siRNA-treated cells were incubated briefly with 5 µM nocodazole to stimulate recruitment of dynein–dynactin complexes to the NE. This treatment has been documented to recapitulate, in non-G1 cells, the enrichment of functional dynein–dynactin complexes on the NE that normally occurs at G2/M, making this an ideal assay for identifying factors involved in dynein localization (Beswick *et al.*, 2006; Hebbar *et al.*, 2008; Splinter *et al.*, 2010; Bolhy *et al.*, 2011; Jodoin *et al.*, 2012).

Consistent with our previous report, we found that 78% of non-targeting (NT) control siRNA cells had a striking enrichment of dynein on the NE after brief nocodazole treatment (Figure 1, A and O); in contrast, the percentage of cells with perinuclear dynein was reduced to 20% after hASUN depletion (Figure 1, C and O; Jodoin *et al.*, 2012). In most cases, we found that treatment of cells with siRNA targeting individual INT subunits (IntS, each followed by a unique identifying number) resulted in a similar reduction of cells with perinuclear dynein (Figure 1, D–I, K, M, and N). Of importance, we did not observe any overt effect on cellular health or growth after treatment with INT-targeting siRNAs, arguing against any potential reduction in cellular fitness as the cause of reduced perinuclear dynein. To further quantify the dynein phenotype, we compared the DIC immunofluorescence signals on the NE to that of the cytoplasm and also determined the average peak DIC intensity on the NE for each knockdown as previously described (Supplemental Figure S1;
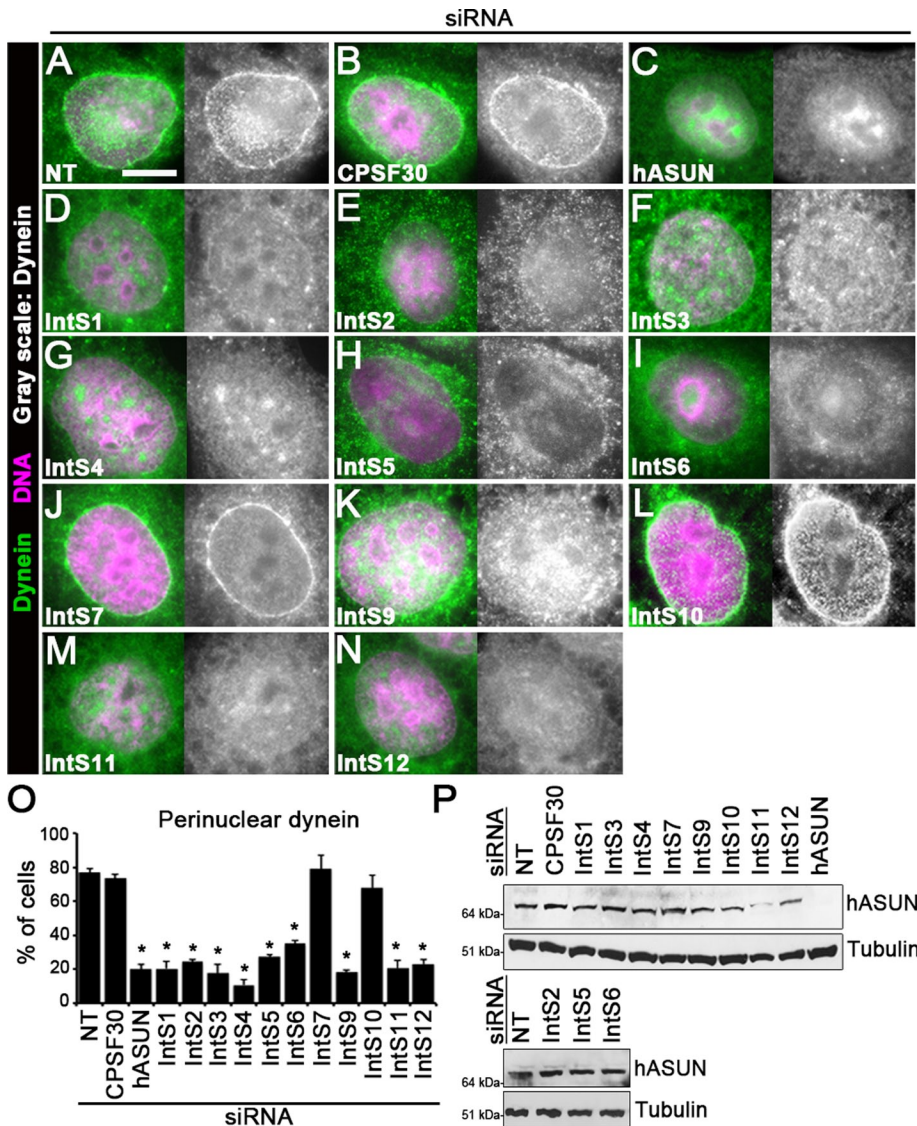
FIGURE 1: INT subunits are individually required for dynein recruitment to the NE. HeLa cells were transfected with siRNA as indicated. (A–N) After siRNA treatment, cells were incubated in nocodazole, fixed, and stained for DIC and DNA. Loss of perinuclear dynein was observed upon individual knockdown of the majority of INT subunits. Scale bar, 10 μm. (O) Quantification of perinuclear dynein in cells after knockdown of individual INT subunits. *$p < 0.0001$ (compared with NT control). (P) hASUN immunoblot analysis of cell lysates after knockdown of individual INT subunits. Tubulin was used as loading control.

analysis of DNA-stained HeLa cells after knockdown of individual INT subunits (Supplemental Figure S3). We observed no differences between the cell cycle profile of hASUN- or other INT subunit-siRNA cells and that of control NT-siRNA cells (Supplemental Figure S3A). We previously reported that hASUN depletion from HeLa cells results in a slightly increased mitotic index (Jodoin et al., 2012); we show here that depletion of other INT subunits has a similar effect (Supplemental Figure S3B). We also found that the percentage of prophase cells, the stage at which dynein normally accumulates on the NE, is slightly increased upon knockdown of ASUN or other INT subunits from HeLa cells (Supplemental Figure S3C). These results indicate that loss of dynein recruitment to the NE in cells depleted of INT is not due to any substantial cell cycle perturbation.

Table 1 summarizes our observations of the requirements for INT subunits in dynein localization and the previously reported requirements for INT subunits in snRNA processing (Ezzeddine et al., 2011; Chen et al., 2012). The two data sets compare favorably in that, for both processes, most INT subunits are required, whereas IntS10 is expendable. IntS7, however, was the sole exception, in that it is required for snRNA processing, yet we found no effect of its down-regulation on dynein recruitment to the NE (Chen et al., 2012). Overall these data are consistent with a model in which hASUN regulates dynein localization in an INT complex–dependent manner.

To show that loss of dynein localization is specific to disruption of an INT-mediated RNA processing event and not secondary to a general disruption of RNA processing, we depleted cells of cleavage polyadenylation specificity factor 30 (CPSF30) and assessed perinuclear dynein. CPSF30 is involved in the recruitment of machinery that mediates 3'-mRNA cleavage and poly(A) tail synthesis (Barabino et al., 1997). We found that siRNA-mediated down-regulation of CPSF30 had no effect on perinuclear dynein accumulation, suggesting a specific role for INT in this process (Figure 1, B and O, and Supplemental Figure S1).

hASUN levels are normal after depletion of INT

Given the established role of INT in snRNA processing, we considered the possibility that hASUN could be a downstream target (i.e., formation/splicing of mature *hASUN* transcripts might require a functional INT complex). In this case, lack of perinuclear dynein in cells with INT down-regulation would be secondary to a reduction in hASUN levels. To test this idea, we used previously generated anti-hASUN antibodies to probe immunoblots of lysates of HeLa cells after depletion of individual INT subunits (Jodoin et al., 2012). We found that hASUN protein levels remained largely unchanged in all lysates tested, with the exception of a slight reduction after IntS11

Jodoin et al., 2012). Depletion of IntS1–6, 9, 11, or 12 resulted in a marked decrease in both the ratio of NE to cytoplasmic dynein and the peak intensity of DIC on the NE, comparable to that observed for hASUN. IntS7 and IntS10 were the two exceptions: depletion of either of these INT subunits had no effect on perinuclear dynein accumulation compared with control cells (Figure 1, J, L, and O, and Supplemental Figure S1). We confirmed that all targeted proteins were efficiently depleted by immunoblotting of cell lysates after siRNA treatment or by a second, nonoverlapping, siRNA (Supplemental Figure S2). Taken together, these data show that the majority of the individual INT subunits are required for dynein recruitment to the NE.

We considered the possibility that loss of dynein accumulation on the NE upon INT depletion could be secondary to cell cycle arrest. We performed fluorescence-activated cell sorting (FACS)

Subunit	snRNA processing[a]	Dynein localization[b]
hASUN	+	+
IntS1	+	+
IntS2	+	+
IntS3	+	+
IntS4	+	+
IntS5	+	+
IntS6	+	+
IntS7	+	−
IntS8	+	N.D.
IntS9	+	+
IntS10	−	−
IntS11	+	+
IntS12	+	+

+, Required; −, not required; N.D., not determined.
[a]Analysis of requirements for INT subunits in U7 snRNA processing was previously reported (Chen et al. 2012).
[b]Analysis of requirements for INT subunits in dynein recruitment to the NE is presented here (Figure 1).

TABLE 1: Comparison of INT subunit requirements in snRNA processing versus dynein localization.

depletion (Figure 1P). We next assessed the reciprocal possibility that hASUN might be required for stability of the INT complex. By immunoblotting, we observed decreased levels of IntS3, 4, 7, 10, and 11 in lysates of hASUN-siRNA HeLa cells relative to control cells (Supplemental Figure S2). This observation is consistent with a recent report showing that levels of *Drosophila* IntS1 and 12 are interdependent, which may be due to their direct association within the complex (Chen et al., 2013). Taken together, these data indicate that failure of dynein localization in INT-depleted cells is not due to decreased hASUN production and hASUN is required for the stability of several other subunits of the INT complex.

INT subunits exhibit a range of subcellular localizations

We previously showed that *Drosophila* ASUN exhibits a dynamic localization pattern: in the *Drosophila* testes, mCherry-tagged dASUN (CHY-dASUN) expressed via a transgene shifts from exclusively nuclear in early G2 to diffusely present throughout the spermatocyte by late G2 (Anderson et al., 2009). Similar localizations (ranging from nuclear to cytoplasmic to diffuse throughout the cell) were observed when GFP-tagged dASUN was expressed in HeLa cells (Anderson et al., 2009). Similarly, we find in the present study that Myc-tagged hASUN expressed in HeLa cells localizes to the nucleus and/or cytoplasm, albeit with a predominantly nuclear pattern in most cells (Figure 2, A1–A3; quantified in Table 2 and later in Figure 4D).

In both fly testes and HeLa cells, we previously observed a temporal correlation in which a pool of cytoplasmic ASUN is present at the onset of dynein accumulation on the NE at G2/M (Anderson et al., 2009; Jodoin et al., 2012). In fly spermatocytes, dASUN undergoes a shift from nuclear to first appearing in the cytoplasm during late G2, roughly coinciding with dynein recruitment to the NE (Anderson et al., 2009). In HeLa cells, hASUN localizes to the cytoplasm at prophase, a cell cycle stage at which dynein is enriched on the NE (Jodoin et al., 2012). Owing to this correlation, we previously hypothesized that a cytoplasmic pool of ASUN is

required for recruitment of dynein motors to the NE at G2/M (Jodoin et al., 2012).

We considered the possibility that the INT complex might function within the cytoplasm to promote dynein recruitment to the NE in a manner independent of its role in snRNA processing within the nucleus. A broad survey of subcellular localization patterns of INT subunits has not been previously reported. To address whether the INT complex exists in the cytoplasm, we expressed GFP fusions of the majority of individual INT subunits in HeLa cells to visualize their localizations. We confirmed by immunoblotting for GFP that fusion proteins of the predicted sizes were stably expressed in transfected cells (Figure 2M).

We divided the INT subunits into three categories based on their localization: predominantly nuclear (hASUN; IntS4, 6, 9, 10, and 12), predominantly cytoplasmic (IntS2 and 7), or evenly distributed between the nucleus and cytoplasm (IntS3, 5, and 11; Figure 2, C–L; quantified in Table 2). Given these complex patterns, we could not exclude the possibility that the INT complex (or perhaps INT subcomplexes) could have potential roles in the cytoplasm in addition to its established role in snRNA processing in the nucleus. It is interesting to note, however, that knockdown of any of several INT subunits that localized predominantly to the nucleus (hASUN; IntS4, 6, 9, or 12; excluding the nonessential IntS10) resulted in loss of perinuclear dynein in HeLa cells; these observations suggest that a nuclear pool of INT might be required to promote recruitment of cytoplasmic dynein to the NE (Figures 1 and 2 and Table 2).

Reduced levels of several INT subunits at G2/M

We further considered the possibility that a cytoplasmic pool of the INT complex might be required for dynein localization. In this case, the simplest model would be that INT acts in the cytoplasm at G2/M to mediate dynein recruitment to the NE. As a test of this model, we asked whether INT subunits are present at G2/M. HeLa cells expressing tagged INT subunits were either left untreated (asynchronous population) or treated with an inhibitor of cyclin-dependent kinase 1 (CDK1; to obtain a G2/M-arrested population), followed by immunoblotting of cell lysates to assess fusion protein levels (Vassilev, 2006). Treated cells acquired a rounded morphology consistent with a G2/M arrest, confirming efficacy of CDK1 inhibition. We found that the levels of 60% (6 of 10) of the INT subunits tested were markedly decreased in G2/M-arrested cells compared with asynchronously dividing cells (Figure 3A). In contrast, levels of 4 INT subunits, including hASUN (both endogenous and tagged), were unchanged at G2/M (Figure 3B). Other known regulators of dynein recruitment, BICD2 (tagged) and CENP-F (endogenous), as well as a GFP control, showed no change in levels at G2/M (Figure 3C). Of note, four subunits required for dynein localization (IntS2, IntS5, IntS6, and IntS9) were present at relatively low levels at G2/M (Figures 1 and 3A). These data led us to conclude that INT is unlikely to directly mediate dynein recruitment to the NE at this stage. Instead, we propose that INT functions earlier in the cell cycle, possibly at the level of RNA processing during interphase, to subsequently affect dynein localization at G2/M.

Mammalian ASUN homologues contain a functional nuclear localization sequence

To determine whether dynein recruitment to the NE is promoted by cytoplasmic ASUN, as we originally hypothesized, or by nuclear ASUN, as suggested by data presented here, we needed a method to direct the localization of ASUN within cells to either of these two compartments (Jodoin et al., 2012). To identify critical regions of ASUN required for its nuclear localization, we began by performing
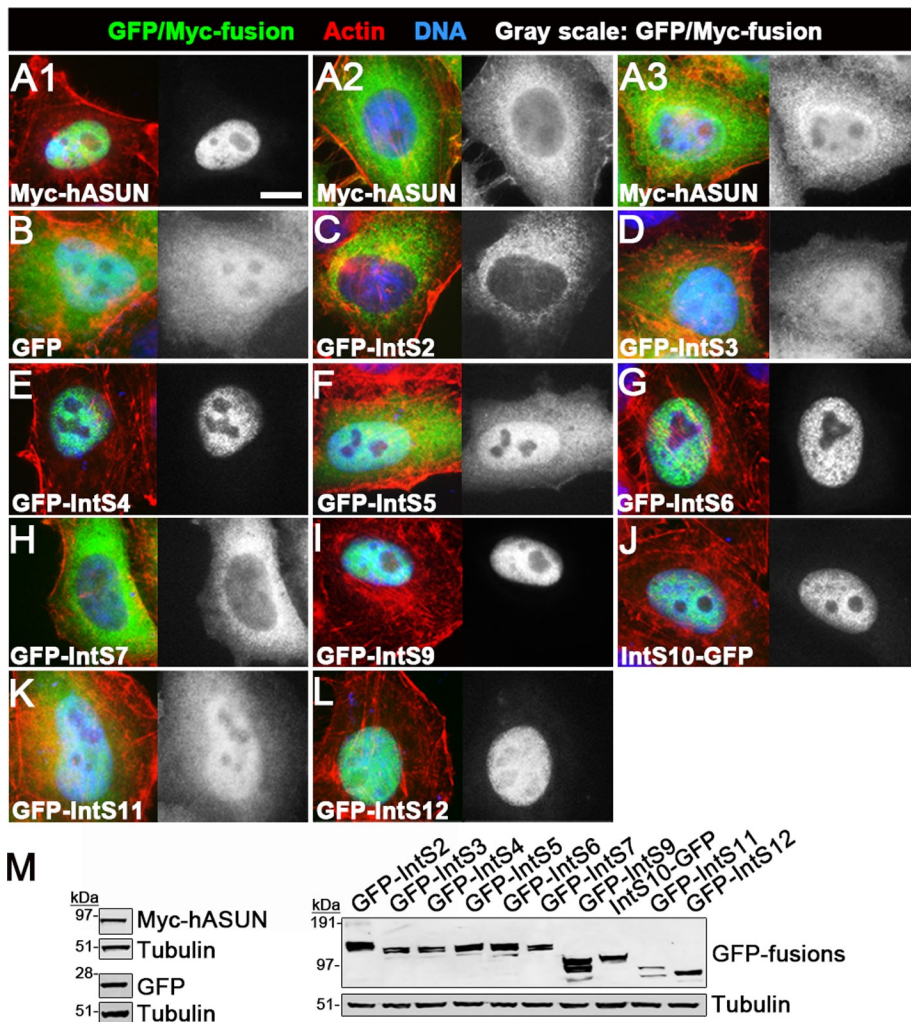
FIGURE 2: INT subunits localize to the nucleus, cytoplasm, or both. HeLa cells were transfected with the indicated expression constructs encoding tagged versions of INT subunits. (A–L) After fixation, cells were stained with phalloidin and DAPI; cells expressing Myc-hASUN were also immunostained for Myc. (A) Myc-hASUN was either exclusively nuclear (A1), predominantly cytoplasmic (A2), or distributed throughout the cell (A3). (B) GFP (control) was diffusely present throughout the cell. (C–L) GFP-tagged versions of other INT subunits localized to the nucleus (E, G, I, J, L), cytoplasm (C, H), or both (D, F). Scale bar, 10 μm. (M) Immunoblot analysis of lysates of transfected cells using antibodies against Myc or GFP tags revealed fusion proteins of the predicted sizes. Tubulin was used as loading control.

constructs used here, fusion proteins of the predicted sizes were observed by immunoblotting transfected HeLa cell lysates (Supplemental Figure S4B).

We used nuclear localization sequence (NLS) prediction software to identify a putative NLS in the C-terminal region of mASUN (Supplemental Figure S4A). We generated Myc-mASUN^{mutNLS} by performing site-directed mutagenesis to alter several charged residues to alanines within this region (Supplemental Figure S4A). When expressed in transfected HeLa cells, Myc-mASUN was predominantly nuclear, whereas Myc-mASUN^{mutNLS} was predominantly cytoplasmic, confirming functionality of the candidate NLS (Supplemental Figure S4, F and G).

We also used NLS prediction software to identify a putative NLS in the C-terminal region of the human ASUN homologue that was 100% identical to the verified NLS of mASUN (Figure 4A and Supplemental Figure S4A). We performed site-directed mutagenesis to change several charged residues in this sequence to alanines, thereby generating Myc-hASUN^{mutNLS} (Figure 4A). When expressed in HeLa cells, Myc-hASUN was predominantly nuclear, with some cytoplasmic or diffuse localization (Figure 2, A1–A3; quantified in Table 2 and Figure 4D). In contrast, Myc-hASUN^{mutNLS} was predominantly cytoplasmic, confirming that we had identified a functional NLS (Figure 4, C and D). For experiments presented later in Figure 6, we also generated constructs for addition of a strong exogenous NLS (PKKKRKV; derived from SV40 large T antigen) to both hASUN and hASUN^{mutNLS} (C-terminal to the Myc tag) to produce Myc-NLS-hASUN and Myc-NLS-hASUN^{mutNLS}, respectively (Figure 4A; Kalderon et al., 1984). As expected, both fusion proteins were predominantly nuclear when expressed in HeLa cells (Figure 4, C and D). We performed immunoblotting of lysates of transfected cells to confirm that all Myc-hASUN constructs used here produced fusion proteins of the predicted sizes (Figure 4B).

Drosophila ASUN contains a functional NLS

We also identified a putative NLS in the C-terminal region of dASUN by using NLS prediction software (Supplemental Figure S5A). We previously showed that GFP-tagged dASUN expressed in transfected HeLa cells localizes in the nucleus, cytoplasm, and between these two compartments, and we obtained similar results here using Myc-tagged dASUN (Supplemental Figure S5, A and B; Anderson et al., 2009). By site-directed mutagenesis, we changed several charged residues to alanines within the candidate NLS of Myc-dASUN to generate Myc-dASUN^{mutNLS} (Supplemental Figure S5A). Introduction of these mutations resulted in a significant shift of the fusion protein from the nucleus to the cytoplasm of transfected HeLa cells, verifying functionality of the putative NLS in this system
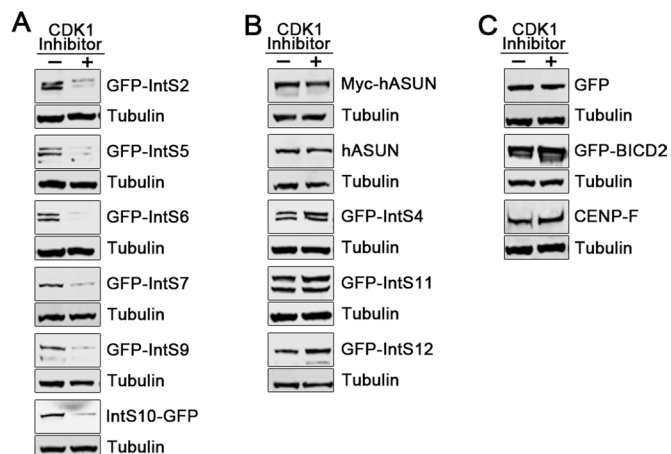
a structure–function analysis of the mouse ASUN homologue (mASUN). Full-length Myc-tagged mASUN expressed in transfected HeLa cells was concentrated in the nucleus, with some cells showing diffuse or cytoplasmic localization (Supplemental Figure S4, A and G). We divided full-length mASUN into three overlapping fragments (F1–F3) and generated constructs for expression of each fragment fused to GFP at its N-terminal end (Supplemental Figure S4A). On expression in transfected HeLa cells, we found that the three GFP-tagged mASUN fragments had distinct localization patterns. GFP-mASUN-F1 (N-terminal fragment) was present throughout the cell, with slight enrichment in the nucleus (Supplemental Figure S4, C and G), whereas GFP-mASUN-F2 (middle fragment) was predominantly cytoplasmic, with slight perinuclear enrichment (Supplemental Figure S4, D and G). GFP-mASUN-F3 (C-terminal fragment) appeared to be exclusively nuclear, suggesting that it likely contains critical sequences that mediate nuclear localization of full-length mASUN (Supplemental Figure S4, E and G). For all mASUN

FIGURE 3: Levels of a subset of INT subunits are reduced at G2/M. HeLa cells were transfected with the indicated GFP- or Myc-fusion constructs and either left untreated (asynchronous population; −) or treated with a CDK1 inhibitor (G2/M-arrested population; +) for 16 h. Immunoblot analysis of lysates of transfected cells using antibodies against GFP or Myc tags revealed decreased levels of several INT subunits at G2/M (A), whereas no changes were observed for other subunits (B). hASUN antibodies were used to assess endogenous hASUN levels. (C) No changes were observed in the levels of GFP (control), GFP-BICD2, or endogenous CENP-F at G2/M. Tubulin was used as loading control.

(Supplemental Figure S5B). For experiments presented later in this study, we also generated constructs encoding Myc-NLS-dASUN and Myc-NLS-dASUN^{mutNLS} (each containing a strong exogenous NLS placed C-terminal to the Myc tag) and confirmed that both of these fusion proteins were predominantly nuclear when expressed in HeLa cells (Supplemental Figure S5, A and B).

We next tested whether the NLS that we identified in dASUN using transfected HeLa cells was also functional in vivo. We previously established transgenic *Drosophila* lines with testes-specific expression of CHY-tagged dASUN and introduced a copy of this transgene into the *asun* background (Figure 5A; Anderson *et al.*, 2009). In G2 spermatocytes, CHY-dASUN was predominantly nuclear, with some diffuse localization (Figure 5, C and D). We used the same approach to express CHY-tagged dASUN^{mutNLS} (carrying mutations in the predicted NLS as described earlier) in *asun* testes (Figure 5A). CHY-dASUN^{mutNLS} was tightly localized to the cytoplasm of G2 spermatocytes, a pattern not observed for wild-type CHY-dASUN; thus, the NLS sequence we identified in dASUN using cultured human cells was also functional in vivo (Figure 5, C and D). For experiments presented later in Figure 7, to enrich for dASUN in the nucleus, we used the same approach to express CHY-dASUN with a strong exogenous NLS (NLS-CHY-dASUN) in *asun* testes (Figure 5A). The NLS-CHY-dASUN fusion was even more tightly localized to the nucleus of G2 spermatocytes than CHY-dASUN (Figure 5, C and D). For all CHY-dASUN constructs described here, fusion proteins of the predicted sizes were observed by immunoblotting of transgenic testes lysates (Figure 5B).

A nuclear pool of ASUN is required in HeLa cells for dynein localization

We used our hASUN expression constructs to address whether hASUN functions in the cytoplasm or nucleus of HeLa cells to promote dynein recruitment to the NE. We tested the capacity of cytoplasmic Myc-hASUN^{mutNLS} to restore perinuclear dynein to cells depleted of endogenous hASUN. Cells treated with NT or hASUN siRNA and transfected with Myc, Myc-hASUN, or Myc-hASUN^{mutNLS} constructs (refractory to hASUN siRNA) were analyzed using our dynein localization assay (Figure 6, A and B). As expected, we found that Myc-hASUN rescued the loss of perinuclear dynein caused by endogenous hASUN depletion (Figure 6A; quantified in Figure 6B). In contrast, dynein remained diffuse in the cytoplasm upon expression of Myc-hASUN^{mutNLS} in cells lacking endogenous hASUN, suggesting that hASUN may function in the nucleus to regulate dynein localization (Figure 6, A and B).

To further confirm that a nuclear pool of hASUN is required for dynein localization and rule out the trivial possibility that mutation of the NLS of hASUN might interfere with its activity in other ways (e.g., improper protein folding), we asked whether forced localization of Myc-hASUN^{mutNLS} to the nucleus via addition of an exogenous NLS would render it competent to restore perinuclear dynein in cells depleted of endogenous hASUN. Indeed, we found that dynein localized normally upon expression of Myc-NLS-hASUN or Myc-NLS-hASUN^{mutNLS} in hASUN-siRNA cells (Figure 6, A and B). These findings suggest that the mutations we introduced into the endogenous NLS of hASUN were not deleterious per se to the protein, but rather that nuclear residence is required for hASUN to exert its effect on dynein localization. Immunoblotting of cell lysates for endogenous hASUN and the Myc tag confirmed efficient depletion of hASUN by siRNA treatment and expression of all Myc-tagged hASUN fusions used here (Figure 6C).

We next used our dASUN constructs to test whether dASUN acts within the cytoplasm or nucleus of transfected HeLa cells to promote dynein localization. We previously reported that loss of perinuclear dynein in hASUN-depleted HeLa cells was rescued by expression of Cherry-dASUN, and similar results were obtained here by expressing Myc-dASUN in hASUN-siRNA cells (Supplemental Figure S5C; Anderson *et al.*, 2009). Consistent with our hASUN results, we found that expression of cytoplasmic-localized Myc-dASUN^{mutNLS} in hASUN-siRNA cells failed to restore perinuclear dynein, whereas

Subunit	Nuclear	Cytoplasmic	Diffuse
Myc-hASUN	87 ± 2.2	4 ± 1.9	9 ± 2.4
GFP-IntS2	—	100 ± 0	—
GFP-IntS3	—	—	100 ± 0
GFP-IntS4	97 ± 2.1	—	3 ± 2.1
GFP-IntS5	—	—	100 ± 0
GFP-IntS6	93 ± 1.4	—	7 ± 1
GFP-IntS7	—	93 ± 1	7 ± 1
GFP-IntS9	85 ± 2.5	—	15 ± 2.5
IntS10-GFP	81 ± 6.5	—	19 ± 6
GFP-IntS11	—	4 ± 0.5	96 ± 0
GFP-IntS12	100 ± 0	—	—

HeLa cells were transfected with the indicated expression constructs encoding GFP- or Myc-tagged versions of human INT subunits, fixed, and stained with phalloidin and DAPI. Cells expressing Myc-hASUN were also immunostained for Myc. Immunofluorescence microscopy was performed to assess localization patterns of INT fusion proteins (representative images presented in Figure 2, with quantification shown here). Localizations were scored as the percentage of cells with nuclear, cytoplasmic, or diffuse localization.

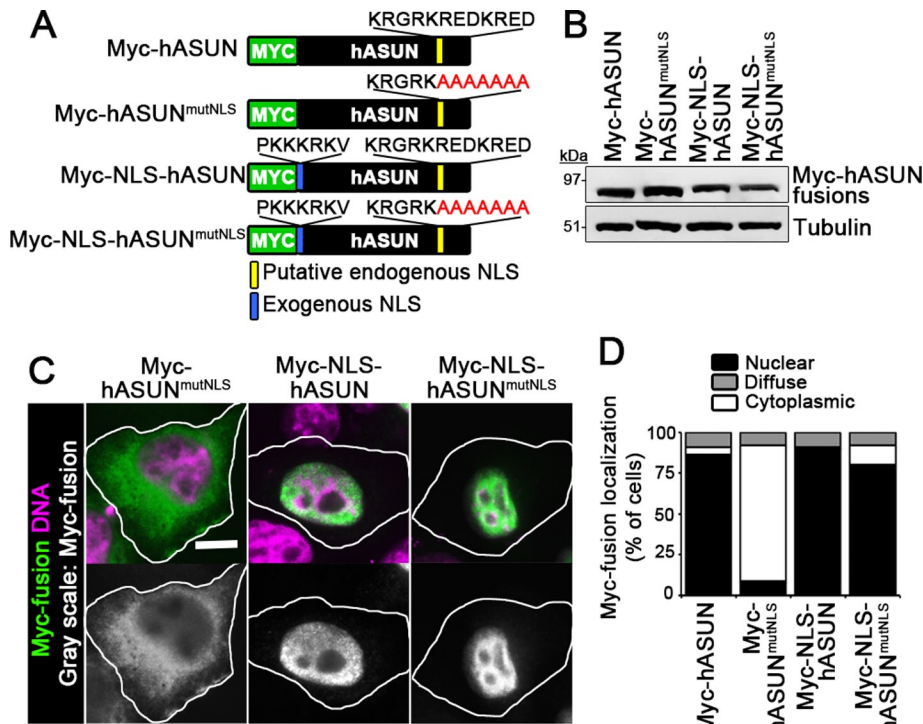**TABLE 2:** Quantification of localizations of tagged INT subunits in transfected HeLa cells.

FIGURE 4: Identification of a functional NLS in human ASUN. (A) Schematic of Myc-tagged hASUN with predicted NLS (yellow box) in the C-terminal region of the protein. Letter A (red) indicates each charged residue of the endogenous NLS mutated to alanine in Myc-hASUN^mutNLS and Myc-NLS-hASUN^mutNLS. An exogenous NLS (blue box) was added between the Myc tag and either hASUN or hASUN^mutNLS to generate Myc-NLS-hASUN and Myc-NLS-hASUN^mutNLS, respectively. (B) Myc immunoblot analysis of lysates of transfected HeLa cells revealed Myc-hASUN fusion proteins of the predicted sizes. Tubulin was used as loading control. (C) Representative images showing predominant localizations of Myc-hASUN fusions in transfected HeLa cells. Scale bars, 10 μm. (D) Quantification of localization patterns of Myc-hASUN fusion proteins in transfected HeLa cells.

nuclear-localized Myc-NLS-dASUN or Myc-NLS-dASUN^mutNLS were both competent to promote dynein localization (Supplemental Figure S5C). Immunoblotting of cell lysates for endogenous hASUN and the Myc tag confirmed efficient depletion of hASUN by siRNA treatment and expression of all Myc-tagged dASUN fusions used here (Supplemental Figure S5D). Taken together, these data provide further support for a model in which a nuclear pool of ASUN is required for recruitment of cytoplasmic dynein to the NE in cultured human cells and suggest that this mechanism might be conserved in *Drosophila*.

A nuclear pool of dASUN is required in *Drosophila* spermatocytes for dynein localization

We previously identified ASUN as a critical regulator of dynein localization during *Drosophila* spermatogenesis (Anderson *et al.*, 2009). We used this system to determine whether the requirement for nuclear ASUN in regulating cytoplasmic dynein localization that we observed in HeLa cells is conserved in vivo. Using transgenic *Drosophila* lines that we established (Figure 5A), we assessed the capacity of cytoplasmic CHY-dASUN^mutNLS or nuclear NLS-CHY-dASUN expressed in *asun* testes to promote dynein localization. As previously reported, we found that CHY-dASUN rescued loss of perinuclear dynein in *asun* spermatocytes (Figure 7, A and B; Anderson *et al.*, 2009). *asun* spermatocytes expressing CHY-dASUN^mutNLS, however, lacked perinuclear dynein; instead, dynein remained diffuse in the cytoplasm, similar to the phenotype

of *asun* spermatocytes lacking a transgenic rescue construct (Figure 7, A and B). Expression of NLS-CHY-dASUN in *asun* spermatocytes restored perinuclear dynein to nearly wild-type levels, suggesting that a nuclear pool of dASUN is responsible for regulating the localization of cytoplasmic dynein motors in this system.

In addition to the failure of dynein localization, *asun* mutants display a range of defects: spermatocytes arrested at prophase I with unattached centrosomes, impaired sperm bundling, and male sterility (Anderson *et al.*, 2009). This constellation of *asun* phenotypes is likely secondary to loss of perinuclear dynein in G2 spermatocytes, an event that occurred upstream of these defects. To determine whether restoration of dynein on the NE of *asun* spermatocytes by NLS-CHY-dASUN expression was sufficient to rescue the most downstream defect, male sterility, we scored the number of live progeny per fertile male. We found that NLS-CHY-dASUN could restore fertility to *asun* males to the same degree as the CHY-dASUN control, whereas only partial rescue was achieved with CHY-dASUN^mutNLS (Figure 7C).

Taken together, these data suggest that a nuclear pool of ASUN plays a conserved role, from *Drosophila* to humans, in the recruitment of cytoplasmic dynein motors to the NE at G2/M. Combined with evidence presented here that additional INT subunits likewise play an essential role in this recruitment step, we hypothesize that the Integrator complex mediates the processing of a critical RNA target(s) required for the production of a cytoplasmic protein that is directly involved in the regulation of dynein localization.

DISCUSSION

A newly identified role for Integrator in promoting dynein recruitment to the NE

We previously described an essential role for ASUN in regulating dynein localization in *Drosophila* spermatogenesis and cultured human cells (Anderson *et al.*, 2009; Jodoin *et al.*, 2012). Recent studies identified a second role for ASUN as an Integrator subunit required for snRNA-processing activity of the complex (Baillat *et al.*, 2005; Malovannaya *et al.*, 2010; Chen *et al.*, 2012). Owing to the seemingly divergent nature of these two roles, we initially speculated that ASUN might "moonlight" by performing cellular functions within the cytoplasm independently of INT. To disprove this model, we here asked whether additional INT subunits, such as ASUN, are required for dynein localization. Our finding that depletion of individual INT subunits recapitulates the loss of perinuclear dynein in hASUN-siRNA cells argues that ASUN functions within the Integrator complex to mediate this process as opposed to working independently. Given the established role of INT in snRNA processing, we considered that loss of perinuclear dynein in INT-depleted cells could be an indirect consequence of a failure to produce mature *ASUN* transcripts; our data, however, do not support this idea. Conversely, we find that ASUN is required for stability of several INT
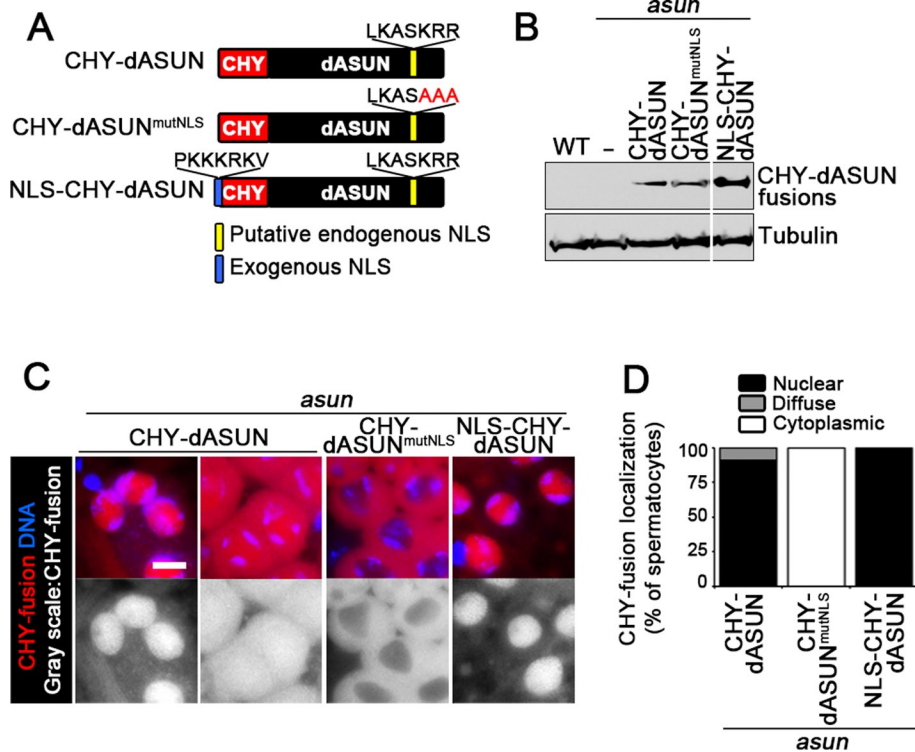
FIGURE 5: Functional NLS is conserved in *Drosophila* ASUN homologue. (A) Schematic of CHY-tagged dASUN with predicted NLS (yellow box) in the C-terminal region of the protein. Letter A indicates each charged residue of the endogenous NLS mutated to alanine in CHY-dASUN[mutNLS]. An exogenous NLS (blue box) was added to the N-terminal end of CHY-tagged dASUN to generate NLS-CHY-dASUN. (B) CHY immunoblot analysis of testes lysates from *asun* males with or without germline expression of CHY-dASUN fusions revealed proteins of the predicted sizes. An intervening lane just left of the last lane was removed. Wild-type (WT) males and *asun* males lacking a transgene were used as negative controls. Tubulin was used as loading control. (C) Representative images showing localizations of CHY-dASUN fusions in transgenic G2 spermatocytes. Scale bar, 10 μm. (D) Quantification of localization patterns of CHY-dASUN fusion proteins in transgenic G2 spermatocytes.

subunits, further underscoring its importance for functioning of the complex.

A model for regulation of dynein localization by integrator

We previously hypothesized that ASUN functions in the cytoplasm to promote redistribution of dynein from diffuse in the cytoplasm to NE anchored at G2/M (Anderson *et al.*, 2009; Jodoin *et al.*, 2012). We considered that a pool of Integrator might exist in the cytoplasm that could mediate dynein recruitment to the NE via a mechanism independent of its snRNA-processing role in the nucleus. Our finding that INT subunits exhibit a range of localization patterns in HeLa cells (predominantly nuclear to predominantly cytoplasmic) neither strongly supports nor refutes this model.

Our identification of a functional NLS in *Drosophila* and mammalian ASUN homologues allowed us to manipulate the subcellular compartmentalization of ASUN and assess effects on dynein localization. We find that forced cytoplasmic localization of ASUN (via endogenous NLS mutation) hinders its capacity to promote dynein recruitment to the NE, whereas redirection of this mutant protein into the nucleus (via exogenous NLS addition) restores its function. These data indicate that Integrator likely acts from within the nucleus to control dynein localization in the cytoplasm. Furthermore, our observation that levels of several INT subunits are paradoxically decreased at G2/M, the stage at which dynein normally accumu-

lates on the NE, suggests that Integrator may exert its effect on dynein by acting earlier in the cell cycle. We cannot exclude the possible existence of a subcomplex composed of a subset of INT subunits that are stable at G2/M; however, based on our finding that four subunits (IntS2, 5, 6, and 9) present at reduced levels at G2/M are nonetheless required for dynein localization, it is unlikely that any such subcomplex alone would be sufficient to mediate dynein recruitment to the NE.

We propose a model in which nuclear-localized Integrator complex, including ASUN, mediates 3′-end processing of snRNA, which in turn is required for normal processing of mRNA encoding a key regulator(s) of cytoplasmic dynein localization. When Integrator activity is compromised (e.g., by knockdown of an essential subunit), production of critical transcript(s) during interphase is impaired, leading to reduction of perinuclear dynein at G2/M. To further elucidate mechanisms underlying the temporal and spatial control of dynein, it will be important to identify critical target(s) of INT involved in this process.

What are the critical targets of Integrator that mediate dynein localization?

On the basis of data presented here, we hypothesize that transcripts encoding a key regulator(s) of dynein localization would be misprocessed after down-regulation of INT. In a preliminary effort to identify such a target(s), we performed a high-throughput RNA-seq screen using both control siRNA cells and IntS11-siRNA HeLa cells (T.R.A. and E.J.W., unpublished observations). We compared mRNA isolated from both populations, with an emphasis on identifying transcripts that were aberrantly spliced in the absence of functional INT. Although we observed several thousand alterations in splicing throughout the genome, we found no evidence for misprocessing of transcripts encoding 1) dynein–dynactin subunits or adaptor proteins or 2) components of the BICD2-RanBP2 or NudE/EL-CENP-F-Nup133 dynein-binding cassettes. We speculate that novel regulators of dynein localization could be the critical mRNA targets of INT involved in this process. The identification of *Drosophila* ASUN (also known as Mat89Bb) as a positive regulator of siRNA, endo-siRNA, and microRNA pathways in three high-throughput screens, however, suggests that the Integrator complex may impinge on other classes of small RNAs and highlights the need for further studies of its activities (Zhou *et al.*, 2008).

When comparing the list of individual INT subunits required for U7 snRNA processing and those required for dynein localization, only one discrepancy emerges (Table 1). IntS7 was previously shown to be essential for processing of U7 and spliceosomal snRNA using a cell-based reporter and through measurement of endogenous transcripts, but we find here that it is dispensable for dynein recruitment to the NE (Ezzeddine *et al.*, 2011; Chen *et al.*, 2012). Given that we observed significant RNA interference-mediated depletion
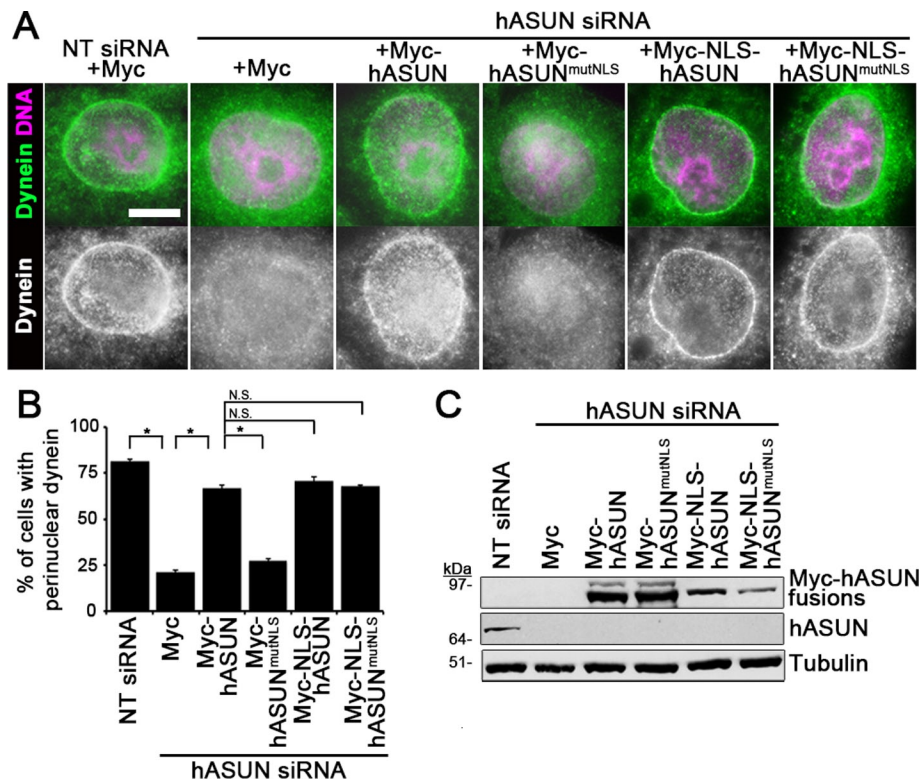
FIGURE 6: Nuclear pool of hASUN is required for dynein recruitment to the NE in HeLa cells. HeLa cells were transfected with NT or hASUN siRNA plus Myc (vector control) or Myc-hASUN expression constructs as indicated. (A) After nocodazole treatment, cells were fixed and stained for DIC and DNA. Representative images of cells. Perinuclear dynein was restored only by expression of hASUN fusion proteins with nuclear localization. Scale bar, 10 μm.
(B) Quantification of cells with perinuclear dynein after the indicated siRNA and DNA transfections. *p < 0.0001 (pairwise comparisons indicated). N.S., nonsignificant statistical differences. (C) hASUN immunoblot of lysates of transfected HeLa cells confirmed depletion of hASUN in hASUN-siRNA cells, and Myc immunoblot confirmed expression of Myc-hASUN fusion proteins of the predicted sizes. Tubulin was used as loading control.

(Supplemental Figure S2), one possible explanation for this differential requirement is that the assays used to measure RNA processing might be more sensitive to perturbations of INT function than the dynein localization assay, perhaps because the latter is a more downstream event.

Additional cellular and developmental roles of integrator
The Integrator complex mediates 3′-end processing of snRNAs that play essential roles in global gene expression. Given that Integrator is likely required for accurate production of a plethora of proteins, it is not surprising that loss of its activity is associated with a wide range of cellular and developmental phenotypes. It was recently reported that siRNA-mediated down-regulation of IntS4 leads to defects in formation of nuclear structures known as Cajal bodies (Takata et al., 2012). Another group found that IntS6 and IntS11 are required for proper differentiation of adipocytes in a cultured cell system; although the underlying mechanism is unknown, the authors hypothesized that U1 and U2 snRNAs are involved (Otani et al., 2013). In large-scale screens performed in zebrafish and *C. elegans*, *IntS7* homologues were shown to be required for normal craniofacial development (Golling et al., 2002; Kamath et al., 2003). Mutation of *Drosophila IntS7* (*deflated*) results in abdominal phenotypes due to cell cycle and signaling defects (Rutkowski and Warren, 2009). Integrator is also essential for hematopoiesis in zebrafish: down-regulation of IntS5, IntS9, or IntS11 causes aberrant

splicing of *smad1* and *smad5* transcripts, generating a dominant-negative form of Smad that disrupts erythrocyte differentiation (Tao et al., 2009).

What remains to be elucidated is how perturbations in snRNA 3′-end formation generate phenotypes so specific and yet so diverse. Although the favored hypothesis is that global reduction in snRNA biosynthesis negatively affects splicing of a subset of transcripts, the criteria for defining this set are unclear. It is likely that these sensitive transcripts will be enriched for either suboptimal splice sites, alternative splice sites, or minor spliceosome-dependent introns. Regardless of the root cause, our discovery of a new role for the Integrator complex in regulating dynein localization adds to the growing list of INT-dependent processes.

MATERIALS AND METHODS
Drosophila spermatocyte experiments
Flies were maintained at 25°C using standard techniques (Greenspan, 2004). *y w* flies obtained from Bloomington *Drosophila Stock* Center (Indiana University, Bloomington, IN) were used as the "wild-type" stock. The *asun^{f02815}* allele (Exelixis Collection, Harvard Medical School, Boston, MA) and a transgenic line with male germline–specific expression of CHY-tagged wild-type dASUN were previously described (Anderson et al., 2009). Transgenic lines for male germline–specific expression of CHY-tagged dASUN fusion proteins (constructs described later) were generated by *P*-element–mediated transformation via embryo injection (Rubin and Spradling, 1982). For each transgene, a single insertion mapping to the X chromosome was crossed into the *asun^{f02815}* background using standard genetic crosses.

To test male fertility, individual adult males (2 d old) were placed in vials with five wild-type females (2 d old) and allowed to mate for 5 d. The average number of live adult progeny produced per fertile male was scored (≥10 males tested per genotype). Statistical analysis was performed using an unpaired Student's *t* test.

Protein extracts were prepared by homogenizing dissected testes from newly eclosed males in SDS sample buffer. The equivalent of eight testes pairs was loaded per lane. After SDS–PAGE, immunoblotting was performed as described later.

Live testes cells were prepared for examination by fluorescence microscopy as described previously (Kemphues et al., 1980). Briefly, testes were dissected from newly eclosed adult males, placed in a drop of phosphate-buffered saline (PBS) on a microscopic slide, and gently squashed under a glass coverslip after making a small incision near the stem cell hub. Formaldehyde fixation was performed as described previously (Gunsalus et al., 1995). Briefly, slides of squashed testes were snap-frozen, immersed in 4% formaldehyde (in PBS with 0.1% Triton X-100) for 7 min at –20°C after coverslip removal, and washed three times in PBS. Mouse anti–dynein heavy chain primary antibody (P1H4, 1:120; gift from T. Hays, University of Minnesota, Minneapolis, MN) and Cy3-conjugated secondary antibody (Invitrogen, Carlsbad, CA) were used (McGrail and Hays,
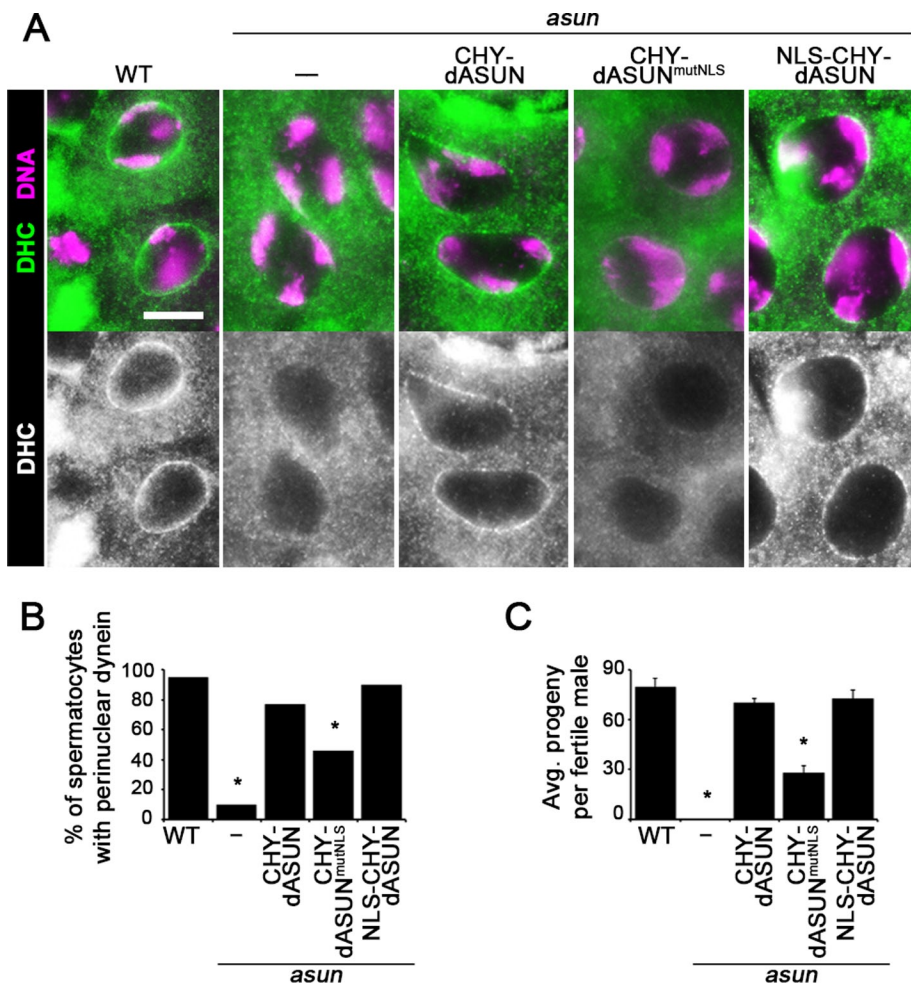
FIGURE 7: Nuclear pool of dASUN is required for dynein recruitment to the NE in *Drosophila* spermatocytes. (A, B) Testes dissected from wild-type (WT) or *asun* males with or without germline expression of CHY-tagged dASUN fusion proteins were stained for dynein heavy chain and DNA. (A) Representative images of G2 spermatocytes. Perinuclear dynein was restored to *asun* G2 spermatocytes only by expression of dASUN fusion proteins with nuclear localization. Scale bar, 10 μm. (B) Quantification of G2 spermatocytes with perinuclear dynein. (C) Fertility assay shows the average number of progeny per fertile male. *$p < 0.0001$ (compared with wild-type control).

1997). Fixed samples were mounted in PBS with 4′,6-diamidino-2-phenylindole (DAPI) to visualize DNA. Wide-field fluorescence images were obtained using an Eclipse 80i microscope (Nikon, Melville, NY) with Plan-Fluor 40× objective. In experiments to determine the percentage of late G2 spermatocytes with perinuclear dynein, at least 200 cells were scored per genotype. Statistical analysis was performed using Fisher's exact test.

Cell culture and treatments

HeLa cells were maintained at 37°C and 5% CO_2 in DMEM containing 10% fetal bovine serum, 1% L-glutamine, 100 μg/ml streptomycin, and 100 U/ml penicillin (Life Technologies, Carlsbad, CA). Plasmid DNA was transfected into cells using FuGENE HD (Promega, Madison, WI). siGENOME NT siRNA#5 (Dharmacon, Lafayette, CO) was used as negative control. siRNA used to silence hASUN (3′-UTR region; 5′-CAG CAA GAU GGU AUA GUU A-3′) was obtained from Dharmacon. siRNAs used to silence IntS1 (5′-CAU UUC UCC GUC GAU UAA A-3′), IntS2 (#1: 5′-CUC GUU UAG CUG UCA AUG U-3′ and #2: 5′-CCU UAA UCA GCG UUU CAG U-3′), IntS3 (5′-GAA GUA

CUG AGU UCA GAU A-3′), IntS4 (5′-CAG CAU UGU UCU CAG AUC A-3′), IntS5 (5′-CAA GUU UGU CCA GUC ACG U-3′), IntS6 (#1: 5′-CAC UAA UGA UUC GAU AAU A-3′ and #2: 5′-CCA UGA AGA GGU CAA UAC U-3′), IntS7 (5′-GGC UAA AUA GUU UGA AGG A-3′), IntS9 (5′-GAA AUG CUU UCU UGG ACA A-3′), IntS10 (5′-GGA UAC UUG GCU UUG GUU A-3′), IntS11 (Albrecht and Wagner, 2012), IntS12 (5′-GUC AAG ACA UCC ACA GUU A-3′), and CPSF30 (5′-GUG CCU AUA UCU GUG AUU U-3′) were obtained from Sigma-Aldrich (St. Louis, MO).

Cells were transfected with siRNA duplexes using DharmaFECT 1 transfection reagent (Dharmacon) and analyzed 3 d post-transfection. FuGENE HD transfection reagent was used for cotransfection of cells with siRNA and DNA constructs. Where indicated, cells were incubated in 5 μg/ml (16.6 μM) nocodazole (Sigma-Aldrich) for 3 h before fixation to enhance perinuclear localization of dynein. For G2/M arrest, cells were incubated for 16 h in 10 μM RO-3306 (Cdk1 inhibitor; Enzo Life Sciences, Plymouth, PA).

Cell fixation, immunostaining, and microscopy

Cells were fixed in methanol (5 min at −20°C followed by washing with Tris-buffered saline [TBS] plus 0.01% Triton X-100) and blocked in TBS plus 0.01% Triton X-100 and 0.02% bovine serum albumin before immunostaining. Primary antibodies were used as follows: DIC (clone 74.1, 1:500; Abcam, Cambridge, MA) and c-Myc (9E10, 1:1000). Alexa Fluor 546–conjugated phalloidin (1:1000; Invitrogen) was used to stain F-actin. Appropriate secondary antibodies conjugated to Alexa Fluor 488 or Cy3 were used (1:1000; Invitrogen). Cells were mounted in ProLong Gold Antifade Reagent with DAPI (Invitrogen). Wide-field fluorescence images were obtained using an Eclipse 80i microscope (Nikon) with Plano-Apo 100× objective.

Line scan analyses to quantify perinuclear dynein accumulation in HeLa cells were performed using ImageJ (National Institutes of Health, Bethesda, MD). Ten representative cells were measured per condition; for each cell, 12 line scans distributed equally around the nuclear circumference were obtained. To quantify the ratios of perinuclear to diffusely cytoplasmic DIC in stained HeLa cells, the average intensity of the DIC signal within a small rectangular region was sampled near the nuclear surface and in the surrounding cytoplasm using ImageJ. The ratio of the intensities was determined. At least 20 cells were scored per condition.

Statistical analyses of data from cultured cell experiments reported here were performed using Student's unpaired *t* test. Error bars indicate SEM for all bar graphs. All experiments were performed a minimum of three times with at least 200 cells scored per condition.

FACS analysis

siRNA-treated HeLa cells (~10^7) were fixed with 70% ethanol at 4°C for 24 h and incubated in PBS containing propidium iodide (20 µg/ml) and RNase A (0.2 mg/ml; Sigma-Aldrich) at 4°C for 24 h. FACS analysis was performed to determine propidium iodide intensity levels (a measure of DNA content). Gating was used to exclude cell debris and doublets from the DNA analysis. FACS experiments were performed in the Flow Cytometry Shared Resource of Vanderbilt University Medical Center.

DNA constructs

cDNA clones encoding mASUN and dASUN were previously described (Jodoin et al., 2012). The full-length hASUN open reading frame (ASUN; National Center for Biotechnology Information Reference Sequence, NM_018164 [gene], NP_060634.2 [protein]) was amplified from a human primary skin fibroblast cDNA library. The following forward and reverse primers were used to incorporate EcoRI and StuI restriction sites into the 5′ and 3′ ends, respectively, of the hASUN coding region, followed by subcloning of the digested, purified fragment into expression vector pCS2: 5′-CCG GAA TTC CCA GGC ACG AAA GTT AAA AC-3′ (ASUN-EcoRI-5′) and 5′-AAA AGG CCT TTC TTC AAG TCA CTC TTC ACT GC-3′ (ASUN-StuI-3′).

Constructs for expression in HeLa cells of the following N-terminally tagged proteins were generated by subcloning into vector pCS2-Myc: Myc-dASUN, Myc-mASUN (previously described in Jodoin et al. 2012), and Myc-hASUN. To generate pCS2-Myc-NLS vector, the following nucleotide sequence was engineered into the pCS2-Myc vector to add a strong exogenous NLS (PKKKRKV; derived from SV40 large T antigen) C-terminal to the Myc tag: CCC AAG AAG AAG CGC AAG GTC (Kalderon et al., 1984). hASUN and dASUN were subcloned into pCS2-Myc-NLS for production of Myc-NLS-hASUN and Myc-NLS-dASUN, respectively, in transfected cells. We used a PCR-based approach to generate mASUN fragments for subcloning into pCS2-GFP expression vector (N-terminal tag; illustrated in Supplemental Figure S4).

Vector tv3 (gift from J. Brill, The Hospital for Sick Children, Toronto, Canada) containing the testes-specific β2-tubulin promoter was used to make constructs for Drosophila transgenesis (Wong et al., 2005). Sequence encoding a strong exogenous NLS (described earlier) was engineered into a previously described tv3-CHY vector to generate tv3-NLS-CHY. dASUN was subcloned into modified tv3 vector to produce NLS-CHY-dASUN in transgenic fly testes.

We used NLStradamus software to identify putative NLS motifs in hASUN, mASUN, and dASUN (Nguyen Ba et al., 2009). We used the QuikChange II XL Site-Directed Mutagenesis Kit (Agilent Technologies, Santa Clara, CA) to mutate charged residues to alanines within these motifs of hASUN (Figure 4A), mASUN (Supplemental Figure S4A), and dASUN (Figure 5A and Supplemental Figure S5).

GFP-Integrator subunits were subcloned into pcDNA4/myc-His A (Invitrogen) using purchased cDNA templates (Open Biosystems/ Thermo Scientific, Huntsville, AL). The GFP-BICD2 expression construct was a gift from A. Akhmanova (Erasmus Medical Center, Rotterdam, Netherlands; Hoogenraad et al., 2001).

Immunoblotting

HeLa cell lysates were prepared using nondenaturing lysis buffer (50 mM Tris-Cl, pH 7.4, 300 mM NaCl, 5 mM EDTA, 1% Triton X-100). After SDS–PAGE, proteins were transferred to nitrocellulose for immunoblotting using standard techniques. Immunoblotting was performed using the following primary antibodies: c-Myc (9E10,

1:1000), β-tubulin (clone E7, 1:1000; Developmental Studies Hybridoma Bank, University of Iowa, Iowa City, IA), mCherry (1:500; Clontech, Mountain View, CA), CENP-F (clone 14C10 1D8, 1:500; Abcam), C-hASUN (1:300; Jodoin et al., 2012), GFP B-2 (1:1000; Santa Cruz Biotechnology, Dallas, TX), and IntS1, IntS4, IntS7, IntS9, IntS10, IntS11, IntS12, and CPSF30 (1:1000; Bethyl Labs, Montgomery, TX). Horseradish peroxidase–conjugated secondary antibodies (1:5000) and chemiluminescence were used to detect primary antibodies.

REFERENCES

Albrecht TR, Wagner EJ (2012). snRNA 3′ end formation requires heterodimeric association of integrator subunits. Mol Cell Biol 32, 1112–1123.

Anderson MA, Jodoin JN, Lee E, Hales KG, Hays TS, Lee LA (2009). Asunder is a critical regulator of dynein-dynactin localization during Drosophila spermatogenesis. Mol Biol Cell 20, 2709–2721.

Baillat D, Hakimi MA, Naar AM, Shilatifard A, Cooch N, Shiekhattar R (2005). Integrator, a multiprotein mediator of small nuclear RNA processing, associates with the C-terminal repeat of RNA polymerase II. Cell 123, 265–276.

Barabino SM, Hubner W, Jenny A, Minvielle-Sebastia L, Keller W (1997). The 30-kD subunit of mammalian cleavage and polyadenylation specificity factor and its yeast homolog are RNA-binding zinc finger proteins. Genes Dev 11, 1703–1716.

Beaudouin J, Gerlich D, Daigle N, Eils R, Ellenberg J (2002). Nuclear envelope breakdown proceeds by microtubule-induced tearing of the lamina. Cell 108, 83–96.

Beswick RW, Ambrose HE, Wagner SD (2006). Nocodazole, a microtubule de-polymerising agent, induces apoptosis of chronic lymphocytic leukaemia cells associated with changes in Bcl-2 phosphorylation and expression. Leuk Res 30, 427–436.

Bolhy S, Bouhlel I, Dultz E, Nayak T, Zuccolo M, Gatti X, Vallee R, Ellenberg J, Doye V (2011). A Nup133-dependent NPC-anchored network tethers centrosomes to the nuclear envelope in prophase. J Cell Biol 192, 855–871.

Chen J, Ezzeddine N, Waltenspiel B, Albrecht TR, Warren WD, Marzluff WF, Wagner EJ (2012). An RNAi screen identifies additional members of the Drosophila Integrator complex and a requirement for cyclin C/Cdk8 in snRNA 3′-end formation. RNA 18, 2148–2156.

Chen J, Wagner EJ (2010). snRNA 3′ end formation: the dawn of the Integrator complex. Biochem Soc Trans 38, 1082–1087.

Chen J, Waltenspiel B, Warren WD, Wagner EJ (2013). Functional analysis of the integrator subunit 12 identifies a microdomain that mediates activation of the Drosophila integrator complex. J Biol Chem 288, 4867–4877.

Ezzeddine N, Chen J, Waltenspiel B, Burch B, Albrecht T, Zhuo M, Warren WD, Marzluff WF, Wagner EJ (2011). A subset of Drosophila integrator proteins is essential for efficient U7 snRNA and spliceosomal snRNA 3′-end formation. Mol Cell Biol 31, 328–341.

Golling G et al. (2002). Insertional mutagenesis in zebrafish rapidly identifies genes essential for early vertebrate development. Nat Genet 31, 135–140.

Gonczy P, Pichler S, Kirkham M, Hyman AA (1999). Cytoplasmic dynein is required for distinct aspects of MTOC positioning, including centrosome separation, in the one cell stage Caenorhabditis elegans embryo. J Cell Biol 147, 135–150.

Greenspan RJ (2004). Fly Pushing: The Theory and Practice of Drosophila Genetics, Cold Spring Harbor, NY: Cold Spring Harbor Laboratory Press.

Gunsalus KC, Bonaccorsi S, Williams E, Verni F, Gatti M, Goldberg ML (1995). Mutations in twinstar, a Drosophila gene encoding a cofilin/ADF

homologue, result in defects in centrosome migration and cytokinesis. J Cell Biol 131, 1243–1259.

Hebbar S, Mesngon MT, Guillotte AM, Desai B, Ayala R, Smith DS (2008). Lis1 and Ndel1 influence the timing of nuclear envelope breakdown in neural stem cells. J Cell Biol 182, 1063–1071.

Holzbaur EL, Vallee RB (1994). Dyneins: molecular structure and cellular function. Annu Rev Cell Biol 10, 339–372.

Hoogenraad CC, Akhmanova A, Howell SA, Dortland BR, De Zeeuw CI, Willemsen R, Visser P, Grosveld F, Galjart N (2001). Mammalian Golgi-associated Bicaudal-D2 functions in the dynein-dynactin pathway by interacting with these complexes. EMBO J 20, 4041–4054.

Jodoin JN, Shboul M, Sitaram P, Zein-Sabatto H, Reversade B, Lee E, Lee LA (2012). Human Asunder promotes dynein recruitment and centrosomal tethering to the nucleus at mitotic entry. Mol Biol Cell 23, 4713–4724.

Kalderon D, Roberts BL, Richardson WD, Smith AE (1984). A short amino acid sequence able to specify nuclear location. Cell 39, 499–509.

Kamath RS *et al.* (2003). Systematic functional analysis of the *Caenorhabditis elegans* genome using RNAi. Nature 421, 231–237.

Kardon JR, Vale RD (2009). Regulators of the cytoplasmic dynein motor. Nat Rev Mol Cell Biol 10, 854–865.

Kemphues KJ, Raff EC, Raff RA, Kaufman TC (1980). Mutation in a testis-specific beta-tubulin in *Drosophila*: analysis of its effects on meiosis and map location of the gene. Cell 21, 445–451.

Malone CJ, Misner L, Le Bot N, Tsai MC, Campbell JM, Ahringer J, White JG (2003). The *C. elegans* hook protein, ZYG-12, mediates the essential attachment between the centrosome and nucleus. Cell 115, 825–836.

Malovannaya A, Li Y, Bulynko Y, Jung SY, Wang Y, Lanz RB, O'Malley BW, Qin J (2010). Streamlined analysis schema for high-throughput identification of endogenous protein complexes. Proc Nat Acad Sci USA 107, 2431–2436.

Matera AG, Terns RM, Terns MP (2007). Non-coding RNAs: lessons from the small nuclear and small nucleolar RNAs. Nat Rev Mol Cell Biol 8, 209–220.

McGrail M, Hays TS (1997). The microtubule motor cytoplasmic dynein is required for spindle orientation during germline cell divisions and oocyte differentiation in *Drosophila*. Development 124, 2409–2419.

Nguyen Ba AN, Pogoutse A, Provart N, Moses AM (2009). NLStradamus: a simple hidden Markov model for nuclear localization signal prediction. BMC Bioinformatics 10, 202.

Otani Y *et al.* (2013). Integrator complex plays an essential role in adipose differentiation. Biochem Biophys Res Commun 434, 197–202.

Payne C, Rawe V, Ramalho-Santos J, Simerly C, Schatten G (2003). Preferentially localized dynein and perinuclear dynactin associate with nuclear pore complex proteins to mediate genomic union during mammalian fertilization. J Cell Sci 116, 4727–4738.

Robinson JT, Wojcik EJ, Sanders MA, McGrail M, Hays TS (1999). Cytoplasmic dynein is required for the nuclear attachment and migration of centrosomes during mitosis in *Drosophila*. J Cell Biol 146, 597–608.

Rubin GM, Spradling AC (1982). Genetic transformation of *Drosophila* with transposable element vectors. Science 218, 348–353.

Rutkowski RJ, Warren WD (2009). Phenotypic analysis of deflated/Ints7 function in *Drosophila* development. Dev Dyn 238, 1131–1139.

Salina D, Bodoor K, Eckley DM, Schroer TA, Rattner JB, Burke B (2002). Cytoplasmic dynein as a facilitator of nuclear envelope breakdown. Cell 108, 97–107.

Schroer TA (2004). Dynactin. Annu Rev Cell Dev Biol 20, 759–779.

Sitaram P, Anderson MA, Jodoin JN, Lee E, Lee LA (2012). Regulation of dynein localization and centrosome positioning by Lis-1 and asunder during *Drosophila* spermatogenesis. Development 139, 2945–2954.

Splinter D *et al.* (2010). Bicaudal D2, dynein, and kinesin-1 associate with nuclear pore complexes and regulate centrosome and nuclear positioning during mitotic entry. PLoS Biol 8, e1000350.

Takata H, Nishijima H, Maeshima K, Shibahara K (2012). The integrator complex is required for integrity of Cajal bodies. J Cell Sci 125, 166–175.

Tao S, Cai Y, Sampath K (2009). The Integrator subunits function in hematopoiesis by modulating Smad/BMP signaling. Development 136, 2757–2765.

Vaisberg EA, Koonce MP, McIntosh JR (1993). Cytoplasmic dynein plays a role in mammalian mitotic spindle formation. J Cell Biol 123, 849–858.

Vassilev LT (2006). Cell cycle synchronization at the G2/M phase border by reversible inhibition of CDK1. Cell Cycle 5, 2555–2556.

Wong R, Hadjiyanni I, Wei HC, Polevoy G, McBride R, Sem KP, Brill JA (2005). PIP2 hydrolysis and calcium release are required for cytokinesis in *Drosophila* spermatocytes. Curr Biol 15, 1401–1406.

Zhou R, Hotta I, Denli AM, Hong P, Perrimon N, Hannon GJ (2008). Comparative analysis of argonaute-dependent small RNA pathways in *Drosophila*. Mol Cell 32, 592–599.

Human Asunder promotes dynein recruitment and centrosomal tethering to the nucleus at mitotic entry

Jeanne N. Jodoin[a], Mohammad Shboul[b], Poojitha Sitaram[a], Hala Zein-Sabatto[a], Bruno Reversade[b,c], Ethan Lee[a], and Laura A. Lee[a]

[a]Department of Cell and Developmental Biology, Vanderbilt University Medical Center, Nashville, TN 37232-8240; [b]Institute of Medical Biology, A*STAR, Singapore, Singapore 138648; [c]Department of Pediatrics, National University of Singapore, Singapore 119228

ABSTRACT Recruitment of dynein motors to the nuclear surface is an essential step for nucleus–centrosome coupling in prophase. In cultured human cells, this dynein pool is anchored to nuclear pore complexes through RanBP2–Bicaudal D2 (BICD2) and Nup133– centromere protein F (CENP-F) networks. We previously reported that the *asunder* (*asun*) gene is required in *Drosophila* spermatocytes for perinuclear dynein localization and nucleus–centrosome coupling at G2/M of male meiosis. We show here that male germline expression of mammalian Asunder (ASUN) protein rescues *asun* flies, demonstrating evolutionary conservation of function. In cultured human cells, we find that ASUN down-regulation causes reduction of perinuclear dynein in prophase of mitosis. Additional defects after loss of ASUN include nucleus–centrosome uncoupling, abnormal spindles, and multinucleation. Coimmunoprecipitation and overlapping localization patterns of ASUN and lissencephaly 1 (LIS1), a dynein adaptor, suggest that ASUN interacts with dynein in the cytoplasm via LIS1. Our data indicate that ASUN controls dynein localization via a mechanism distinct from that of either BICD2 or CENP-F. We present a model in which ASUN promotes perinuclear enrichment of dynein at G2/M that facilitates BICD2- and CENP-F-mediated anchoring of dynein to nuclear pore complexes.

INTRODUCTION

Cytoplasmic dynein plays critical roles in many cellular processes by carrying out minus end–directed transport along microtubules (Holzbaur and Vallee, 1994). Dynein is a multimeric complex composed of heavy, intermediate, light intermediate, and light chains. Each heavy chain contains six ATPase domains that power the motor. Noncatalytic subunits regulate dynein by linking the complex to its cargo and adaptor proteins. Dynein complexes approach 2 MDa in size, making dynein the largest of all known motor complexes. The composition of dynein complexes and the cellular events requiring these complexes have been defined, although a comprehensive understanding of the mechanisms by which these complexes are regulated within cells is lacking.

Dynein complexes are subject to several modes of regulation, including phosphorylation, subunit composition, subcellular localization, and binding of accessory proteins. Dynactin, another large multimeric complex, was identified through in vitro studies as an activator of dynein; subsequent work suggested that dynein requires dynactin to perform its cellular functions (Schroer, 2004). A dynein adaptor protein, lissencephaly 1 (LIS1), binds directly to dynein heavy chains and is essential for multiple dynein functions, including coupling of centrosomes to the nucleus during neuronal migration (Tanaka *et al.*, 2004; Kardon and Vale, 2009).

A dynein subpopulation stably anchored to the nuclear envelope (NE) at the G2/M transition is essential for proper nucleus–centrosome coupling in multiple systems (Malone *et al.*, 2003; Anderson *et al.*, 2009; Splinter *et al.*, 2010; Bolhy *et al.*, 2011). Minus end–directed movement of anchored dynein motors along astral microtubules has been hypothesized to draw centrosomes toward the nuclear surface to facilitate their attachment to the NE before nuclear envelope breakdown (NEBD; Burgess and Knight, 2004). This anchored pool of dynein has also been implicated in the process of NEBD (Beaudouin *et al.*, 2002; Salina *et al.*, 2002).

Although promotion of nucleus–centrosome coupling is a dynein-dependent function that is evolutionarily conserved, the exact molecular mechanisms appear to vary (Salina *et al.*, 2002). Dynein is anchored to the nuclear surface via KASH and SUN domain–containing proteins in *Caenorhabditis elegans* embryogenesis and during neuronal migration in mice (Malone *et al.*, 2003; Zhang *et al.*, 2009). In a cultured mammalian cell line (HeLa), at least two distinct pathways are required to ensure proper execution of this critical event. These pathways both employ nuclear pore complex (NPC) interactions to anchor dynein motors to the nuclear surface. The first pathway uses RanBP2, a nucleoporin that associates with the cytoplasmic face of NPCs, as the docking site for Bicaudal D2 (BICD2; Splinter *et al.*, 2010). BICD2, directly bound to dynein, moves in a minus-end direction toward the nuclear surface just before the G2/M transition, thereby anchoring dynein at the NE. The second pathway uses another nucleoporin, Nup133, as a docking site for centromere protein F (CENP-F; Bolhy *et al.*, 2011). Before G2/M, CENP-F directly binds dynein-bound NudE/EL; CENP-F then simultaneously binds Nup133 to anchor dynein, NudE/EL, and ultimately the centrosomes to the NE.

We previously identified *asunder* (*asun*; formerly known as *Mat89Bb*) as an essential regulator of dynein localization during *Drosophila* spermatogenesis (Anderson *et al.*, 2009). Spermatocytes of *asun* mutant testes arrest at prophase of meiosis I with centrosomes unattached to the nucleus. *asun* spermatocytes that progress beyond this arrest exhibit defects in meiotic spindle assembly, chromosome segregation, and cytokinesis. The severe loss of perinuclear dynein in *asun* spermatocytes is the likely basis for this constellation of defects. Our studies revealed that *Drosophila* ASUN (dASUN) plays a key role in recruiting dynein to the nuclear surface at G2/M, a critical step in establishing nucleus–centrosome coupling and fidelity of meiotic divisions.

The human homologue of *asun* (also known as *GCT1* or *C12ORF11*) was originally identified in a screen for genes up-regulated in testicular seminomas (Bourdon *et al.*, 2002). Whereas expression of *Drosophila asun* is limited to male and female germline cells, transcripts of the mouse homologue were detected in both germlines and all somatic cells surveyed (Stebbings *et al.*, 1998; Bourdon *et al.*, 2002). These findings suggested that Asunder (ASUN) might play a broader role in mammals.

To further investigate the mechanism by which ASUN regulates dynein, we examined the function of the human homologue of ASUN (hASUN) in this study. We find that, like BICD2 and CENP-F, hASUN is required in cultured cells for enrichment of dynein on the nuclear surface at the onset of mitosis. hASUN depletion leads to mitotic defects, which are likely secondary to failure of dynein localization. We present a model in which hASUN acts via a mechanism distinct from that of BICD2 and CENP-F to promote dynein recruitment to the nuclear surface at G2/M, a critical step to establishing nucleus–centrosome coupling and fidelity of mitotic divisions.

RESULTS

Mammalian ASUN can functionally replace dASUN during spermatogenesis

The predicted hASUN and mouse ASUN (mASUN) proteins are 95% identical and 97% similar to each other; comparison of the predicted mammalian and *Drosophila* ASUN proteins revealed that they are 43% identical and 64% similar. We sought to determine whether a mammalian form of ASUN could functionally replace dASUN in vivo. Using the *Drosophila* model system, we established transgenic lines expressing mCherry-tagged mASUN (CHY-mASUN) exclusively in the male germline (Figure 1A). We found that the presence of a single copy of the CHY-mASUN transgene significantly increased the percentage of *asun*[f02815] males (hypomorphic allele) that produced adult progeny (Figure 1B; Anderson *et al.*, 2009). We also observed a significant increase in the number of adult progeny produced per fertile male, albeit not to the level of wild-type controls (Figure 1C). We previously reported that germline expression of CHY-tagged dASUN fully rescued the sterility of *asun* males; the partial rescue obtained by germline expression of the mouse homologue might be due to the relatively low level of expression of this fusion protein in the fly testes (Figure 1A; Anderson *et al.*, 2009).

We previously identified a critical role for dASUN in recruitment of dynein motors to the nuclear surface and nucleus–centrosome coupling in *Drosophila* male germline cells (Anderson *et al.*, 2009). We next asked whether a mammalian form of ASUN could similarly regulate these events. The severe reduction of perinuclear dynein heavy chain (DHC) that is a hallmark feature of *asun* G2 spermatocytes and immature spermatids was almost fully restored to wild-type levels by transgenic CHY-mASUN expression (Figure 1, D–H). We also observed a significant increase in the degree of nucleus–centrosome coupling at prophase in *asun* spermatocytes harboring the CHY-mASUN transgene (Figure 1, I and J). Together these findings reveal that mASUN can functionally replace its *Drosophila* homologue in vivo to regulate dynein localization during spermatogenesis and suggest that the molecular function of ASUN is conserved across phyla.

hASUN is required for dynein anchoring to the NE at prophase

On the basis of the role of dASUN during male meiosis and the broader expression pattern of mASUN, we reasoned that vertebrate homologues of ASUN might promote dynein recruitment to the NE of somatic cells at the onset of mitosis. To test this hypothesis, we performed small interfering RNA (siRNA)–mediated knockdown of hASUN in HeLa cells. We confirmed that ASUN was efficiently depleted from cells by immunoblotting with antipeptide antibodies (M-hASUN antibody [Ab] and C-hASUN Ab) directed against distinct epitopes in the C-terminal region of hASUN (Supplemental Figure S1A). siRNA-treated cells were briefly incubated with nocodazole to enhance perinuclear localization of dynein–dynactin complexes and accessory proteins before fixation and immunostaining for dynein intermediate chain (DIC; Beswick *et al.*, 2006; Hebbar *et al.*, 2008; Splinter *et al.*, 2010; Bolhy *et al.*, 2011). We found that ~91% of NT-siRNA (nontargeting control) prophase cells showed strong perinuclear dynein staining (Figure 2, A and D–F). After hASUN knockdown, however, only ~30% of cells exhibited this pattern; instead, the majority of prophase cells displayed diffuse localization of dynein in the cytoplasm (Figure 2, B and D–F). Using a second independent hASUN-siRNA sequence that efficiently depleted ASUN from cells, we observed a similar reduction in the percentage of prophase cells with perinuclear dynein (Supplemental Figure S1, B–D).
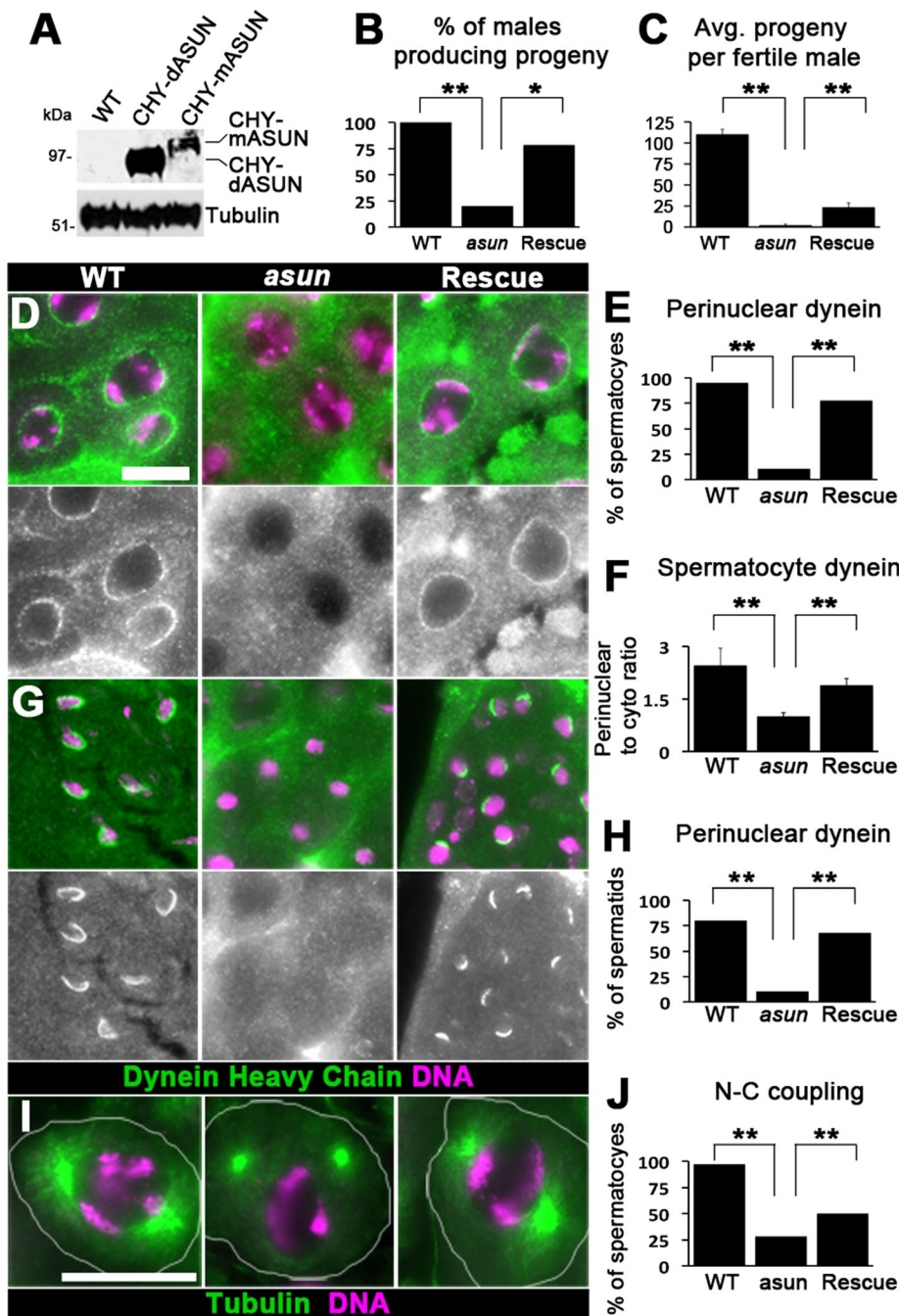
FIGURE 1: mASUN partially rescues spermatogenesis defects of *Drosophila asun* mutants. (A) Anti-CHY immunoblot of testes extracts from *Drosophila* wild-type (WT) males with or without germline expression of CHY-dASUN or CHY-mASUN; a relatively low expression level of a fusion protein of the expected size was observed for the latter. Tubulin was used as loading control. (B, C) Male fertility assays. "Rescue" indicates *asun* males with germline expression of CHY-mASUN, which increased the percentage of *asun* males producing progeny (B) and the average number of progeny per fertile male (C). (D–H) Germline CHY-mASUN expression restored perinuclear dynein in *asun* primary spermatocytes and spermatids. (D–F) Representative G2 spermatocytes stained for DHC and DNA are shown (D) with bar graphs depicting percentages of spermatocytes exhibiting perinuclear DHC (E) and average ratios of perinuclear to diffusely cytoplasmic DHC signal intensities (F). (G, H) Representative immature spermatids stained for DHC and DNA are shown (G) with bar graph depicting percentages of spermatids exhibiting perinuclear DHC (H). (I, J) Germline CHY-mASUN expression restored nucleus–centrosome coupling in *asun* primary spermatocytes. (I) Prophase I spermatocytes stained for β-tubulin and DNA. (J) Quantification of nucleus–centrosome coupling in prophase spermatocytes. **$p < 0.0001$, *$p < 0.001$. Scale bars, 50 μm.

We considered the possibility that hASUN might function to destabilize microtubules; in that case, down-regulation of hASUN could inhibit nocodazole-induced depolymerization of microtubules, thereby blocking access of dynein to the NE. We performed immunostaining experiments to assess whether microtubules undergo a normal degree of nocodazole-induced depolymerization after loss of hASUN. We observed essentially identical tubulin staining patterns for NT-siRNA versus hASUN-siRNA cells in response to nocodazole treatment, suggesting that the lack of perinuclear dynein observed in hASUN-siRNA cells is not secondary to gross alterations of the microtubule network (Supplemental Figure S2).

To further confirm that loss of perinuclear dynein in hASUN-siRNA HeLa cells was due to depletion of endogenous hASUN, we performed a rescue experiment by transiently expressing CHY-tagged dASUN (refractory to hASUN siRNA). CHY-dASUN restored perinuclear dynein in hASUN-siRNA prophase cells to levels similar to that of control cells (Figure 2, C–F). These results confirmed that loss of perinuclear dynein in hASUN-siRNA cells was specifically caused by hASUN depletion and demonstrated that dASUN can replace its human homologue to promote dynein recruitment to the NE at prophase.

We considered an alternative possibility that hASUN is required for stability of dynein–dynactin complexes rather than to promote their enrichment on the NE. Depletion of individual dynein–dynactin components can destabilize other subunits of these complexes (Schroer, 2004; Mische *et al.*, 2008). We immunoblotted for DIC and dynamitin (DMN; dynactin subunit) in extracts of HeLa cells after hASUN knockdown and found no changes in their cellular levels (Supplemental Figure S3A). We also performed sucrose density gradient analysis to assess whether dynein complexes remained intact after hASUN knockdown and found no change in migration profiles (Supplemental Figure S3B). Taken together, these data suggest that hASUN is not required to maintain the integrity of dynein–dynactin complexes.

hASUN is required for proper coupling of centrosomes to the NE at prophase

Perinuclear dynein is essential for proper tethering of centrosomes to the NE at G2/M (Splinter *et al.*, 2010; Tanenbaum *et al.*, 2010; Bolhy *et al.*, 2011). On the basis of the loss of perinuclear dynein we observed in hASUN-siRNA HeLa cells at prophase, we predicted that nucleus–centrosome coupling defects would ensue. We used the human osteosarcoma U2OS cell line for these
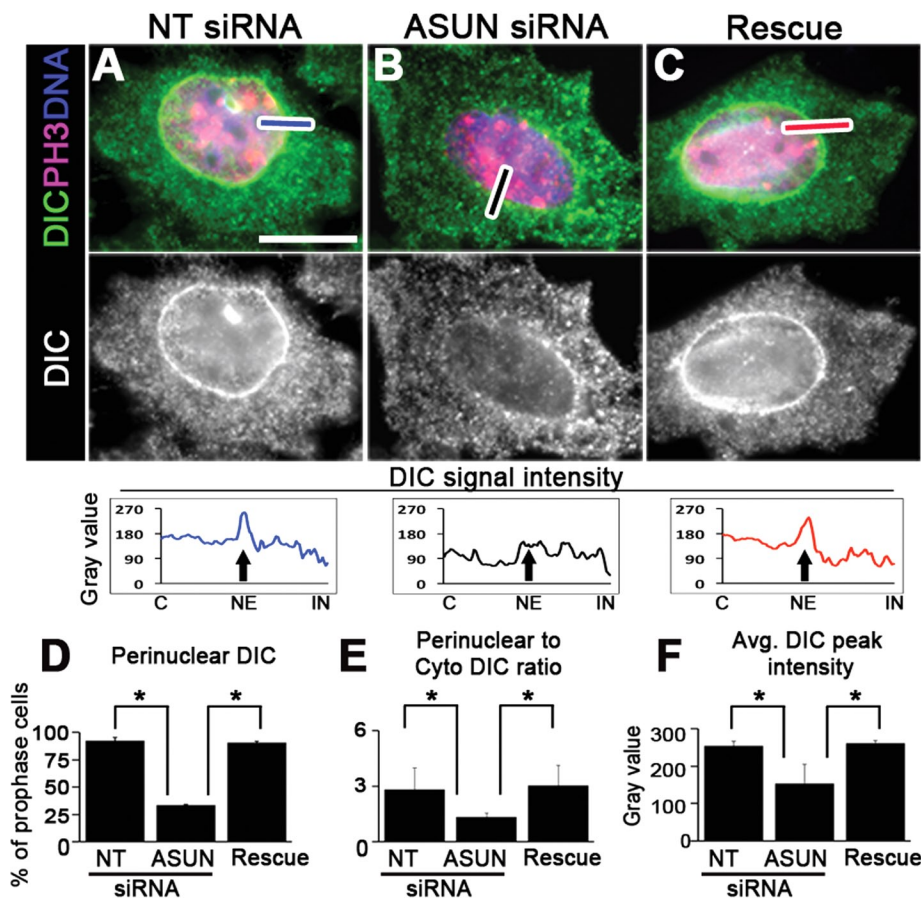
FIGURE 2: hASUN is required for localization of dynein to the NE at mitotic entry. (A–C) HeLa cells were transfected with NT siRNA, hASUN siRNA, or hASUN siRNA plus a CHY-dASUN expression construct ("Rescue"). After nocodazole treatment, cells were fixed and stained for DIC, PH3, and DNA. Both the percentage of prophase cells with perinuclear DIC and the ratio of perinuclear to cytoplasmic DIC signal intensity were reduced by hASUN knockdown (compare B to A); CHY-dASUN expression rescued these defects (C). Note that CHY-dASUN cannot be visualized in C because its signal intensity was much weaker than that of PH3 (visualized with Cy3-conjugated secondary antibodies). (D–F) Quantification of dynein localization defects in hASUN-siRNA cells. Representative line scans (corresponding to blue, black, and red lines in A– C, respectively) of DIC intensity centered at the NE (marked by arrows) are shown below each micrograph with average peak intensities plotted in F. C, cytoplasmic; IN, intranuclear. *p < 0.0001. Scale bars, 20 μm.

fidelity of subsequent mitotic events (Splinter et al., 2010; Tanenbaum et al., 2010). If centrosomes are improperly coupled to the NE at prophase, their separation to prospective poles before NEBD may be random, leaving room for errors in mitotic spindle assembly and chromosome segregation (Tanenbaum et al., 2010). Given our identification of a role for hASUN in dynein recruitment and centrosomal tethering to the NE at mitotic prophase, we assessed whether loss of hASUN in HeLa cells would induce downstream mitotic defects.

We tested the capacity of HeLa cells to form normal bipolar spindles after hASUN knockdown. To enrich for cells with mitotic spindles, we treated siRNA-transfected cells with a Cdk1 inhibitor (RO-3306) and released them into media containing a proteasome inhibitor (Vassilev, 2006). We found that ~35% of hASUN-siRNA metaphase cells exhibited mitotic spindle defects, including scattered chromosomes and broadened spindles; these phenotypes, which were seen in ~9% of NT-siRNA metaphase cells, were fully rescued by CHY-dASUN expression (Figure 4, A–C and G). Similarly, in the absence of drug treatment, we observed a nearly fourfold higher incidence of spindle defects in hASUN-siRNA metaphase cells compared with control cells (Supplemental Figure S4A). We found that hASUN-siRNA cells concomitantly exhibited a ~50% increase in the mitotic index (12.1 vs. 8.1% for control cells), suggesting that loss of hASUN can lead to a mild delay in progression through mitosis (Supplemental Figure S4B).

We also assessed DNA content after loss of hASUN by microscopic examination of DNA-stained HeLa cells. We previously noted the presence of multinucleated HeLa cells after hASUN down-regulation; this phenotype, however, was not quantified or further characterized (Lee et al., 2005). To quantify the multinucleation phenotype, we scored cells only if they contained more than two nuclei due to the common occurrence of binucleation in control HeLa cells. We found that ~37% of hASUN-siRNA cells were multinucleated (typically containing three nuclei), compared with ~9% of control cells, and this defect was fully rescued by CHY-dASUN expression (Figure 4, D–F and H). Furthermore, loss of hASUN caused an even more severe degree of multinucleation: ~6% of hASUN-siRNA cells contained more than four nuclei, which we never observed in control cells (12 of 177 and 0 of 165 cells, respectively; Figure 4F). Using a second independent siRNA sequence, we also observed multinucleation of HeLa cells after hASUN knockdown (Supplemental Figure S1E).

A common cause of multinucleation involves successful completion of chromosome segregation during mitosis, followed by a lack of cell division; increased centriole number is another indicator of cytokinesis failure (Godin and Humbert, 2011; Lacroix and Maddox, 2012). In addition to multinucleation, we observed supernumerary

studies. Owing to the relatively decreased density of the microtubule network in these cells, centrosomes undergo a more dramatic migration from the nucleus to the cortex at interphase and back to the nuclear surface at G2/M (Akhmanova and Hammer, 2010).

We found that ~19% of hASUN-siRNA U2OS cells exhibited loss of coupling of one or both centrosomes to the NE at prophase, compared with a baseline rate of ~4% in control cells (Figure 3, A–E, and Supplemental Figure S1A). We measured an average distance of ~8 μm between the nucleus and centrosomes in hASUN-siRNA cells, compared with a baseline distance of ~3 μm in control cells (Figure 3F). These data indicate that hASUN is required for normal linkage of centrosomes to the NE during prophase, and they further demonstrate evolutionary conservation of function of ASUN homologues.

hASUN is required for proper spindle formation and fidelity of mitotic divisions

The evidence suggests that the perinuclear pool of dynein mediating nucleus–centrosome coupling at G2/M is also required for the

NT siRNA

ASUN siRNA

A **B** **C** **D**

Pericentrin PH3 DNA

E Nucleus-centrosome
coupling defects

F Avg. distance of
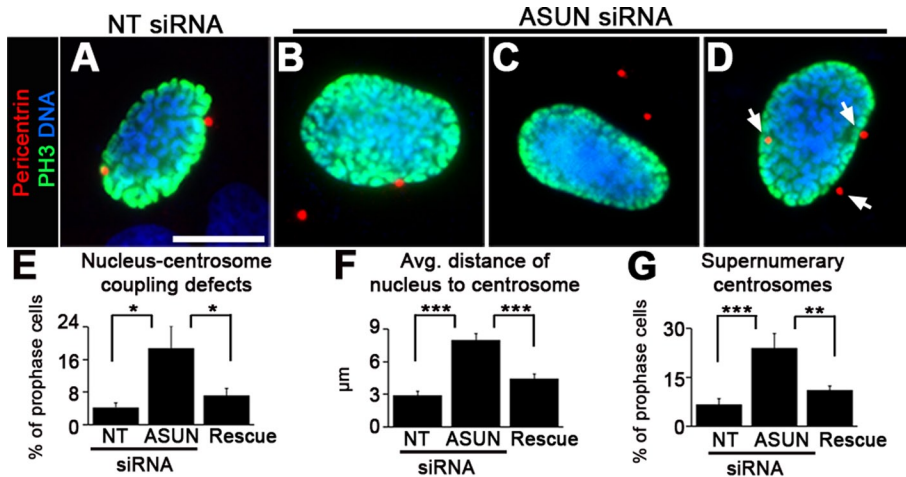nucleus to centrosome

G Supernumerary
centrosomes

FIGURE 3: hASUN is required for recruitment of centrosomes to the NE at mitotic entry. (A–D) U2OS cells were transfected with NT or hASUN siRNA, fixed, and stained for pericentrin (centrosomal marker), PH3, and DNA. hASUN knockdown yielded an increased percentage of prophase cells with loss of coupling of one (B) or both (C) centrosomes to the NE compared with control cells (A) as well as supernumerary centrosomes (arrows in D). (E–G) Quantification of centrosome defects in hASUN-siRNA cells. Expression of CHY-dASUN in hASUN-siRNA cells ("Rescue") corrected these defects. $***p < 0.0001$, $**p < 0.005$, $*p < 0.02$. Scale bar, 20 µm.

centrosomes in ~24% of prophase cells after hASUN knockdown, compared with ~5% of control cells; this defect was corrected by expression of CHY-dASUN (Figure 3, D and G). Our data are consis-

NT siRNA **ASUN siRNA**

A **B** **C**

G Abnormal spindle morphology

D **E** **F**

Tubulin DNA

H Multinucleation, > 2 nuclei

FIGURE 4: Loss of hASUN causes mitotic spindle defects and multinucleation. (A–F) HeLa cells were transfected with NT or hASUN siRNA, fixed, and stained for tubulin and DNA. (A–C) Mitotic spindles. To enrich for mitotic spindles, cells were arrested in metaphase before fixation. NT-siRNA cells had bipolar spindles with tight alignment of chromosomes at metaphase (A). hASUN-siRNA cells had an increased percentage of abnormal spindles with defects such as scattering of chromosomes along spindles (B) and broadened spindles (C). (D–F) Interphase cells. An increased percentage of hASUN-siRNA cells (E, F) were multinucleated (more than two nuclei) compared with NT-siRNA cells (D). We occasionally observed a more severe degree of multinucleation (more than four nuclei) in hASUN-siRNA cells (F). (G, H) Quantification of spindle morphology defects (G) and multinucleation (H) in hASUN-siRNA cells. Expression of CHY-dASUN in hASUN-siRNA cells ("Rescue") corrected these defects. $* p < 0.0001$. Scale bars, 20 µm.

tent with a possible role for hAUN in mitotic events downstream of nucleus–centrosome coupling: proper spindle formation and execution of cytokinesis.

hASUN is required for dynein anchoring to the NE at prophase in nontransformed cells

To confirm that the observed loss of NE-bound dynein after knockdown of hASUN is independent of the transformed nature of HeLa cells, we performed a similar analysis using human retinal pigment epithelial (RPE) cells, which are nontransformed. We detected strong perinuclear localization of dynein after nocodazole treatment in 59% of control RPE cells; in contrast, we observed this staining pattern in only 12% of cells after knockdown of hASUN (Figure 5, A–D). We observed an increased frequency of multinucleation in RPE cells after hASUN knockdown, possibly due to downstream mitotic defects caused by loss of perinuclear 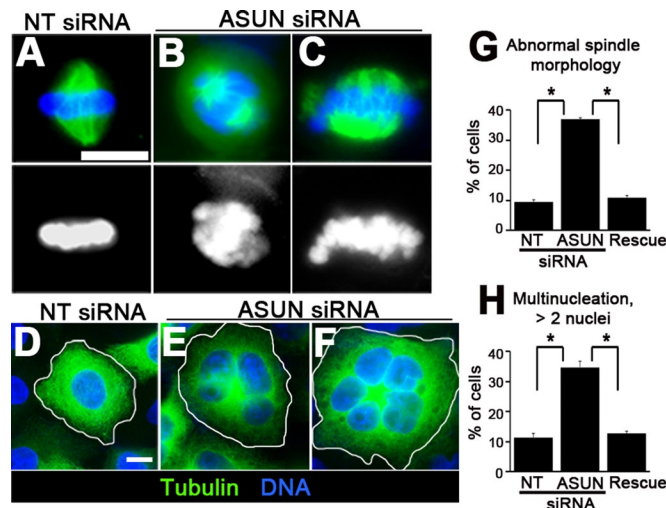dynein: ~35% of hASUN-siRNA cells had more than one nucleus, compared with ~10% of control cells (Figure 5, E–G). These data suggest that the role of hASUN in regulating recruitment of dynein to the nuclear surface is not limited to transformed cells.

hASUN is cytoplasmic at G2/M

We previously reported that a tagged form of dASUN exhibited a meiotic stage–specific localization pattern in *Drosophila* spermatocytes: intranuclear in early G2 and appearing in the cytoplasm in late G2, coincident with dynein recruitment to the nuclear surface (Anderson *et al.*, 2009). Tagged versions of dASUN and hASUN co-expressed in HeLa cells exhibited similar localization patterns during mitosis (Anderson *et al.*, 2009).

To further understand the mechanism by which ASUN controls dynein localization at G2/M, we sought to determine the localization pattern of the endogenous protein in cultured human cells during prophase. Using C-hASUN Ab for immunostaining of HeLa cells, we found endogenous hASUN to be localized to the cytoplasm in ~98% of prophase cells (85 of 87 cells; Figure 6A). We used the following criteria to identify prophase cells: phosphorylated histone (PH3)-positive DNA and intact NE.

To further confirm that this localization pattern reflects that of endogenous hASUN, we transfected HeLa cells with either control or hASUN siRNA, followed by immunostaining with C-hASUN Ab. The hASUN signal present in control cells was lost in hASUN-siRNA cells, demonstrating specificity (Figure 6, B and C). We confirmed these results with a second hASUN-siRNA sequence (Supplemental Figure S1C). We found that Myc-tagged mASUN transiently expressed in HeLa cells tightly colocalized with endogenous hASUN, indicating a conserved localization pattern of the human and mouse homologues, which are ~95% identical at the amino acid level (Figure 6D).

Two dynein-recruiting proteins, BICD2 and CENP-F, have recently been reported to bind NPCs at prophase via direct interactions with the NPC components RanBP2 and Nup133, respectively (Splinter *et al.*, 2010; Bolhy *et al.*, 2011). Owing to their similar functions in recruiting dynein complexes to the NE, we considered
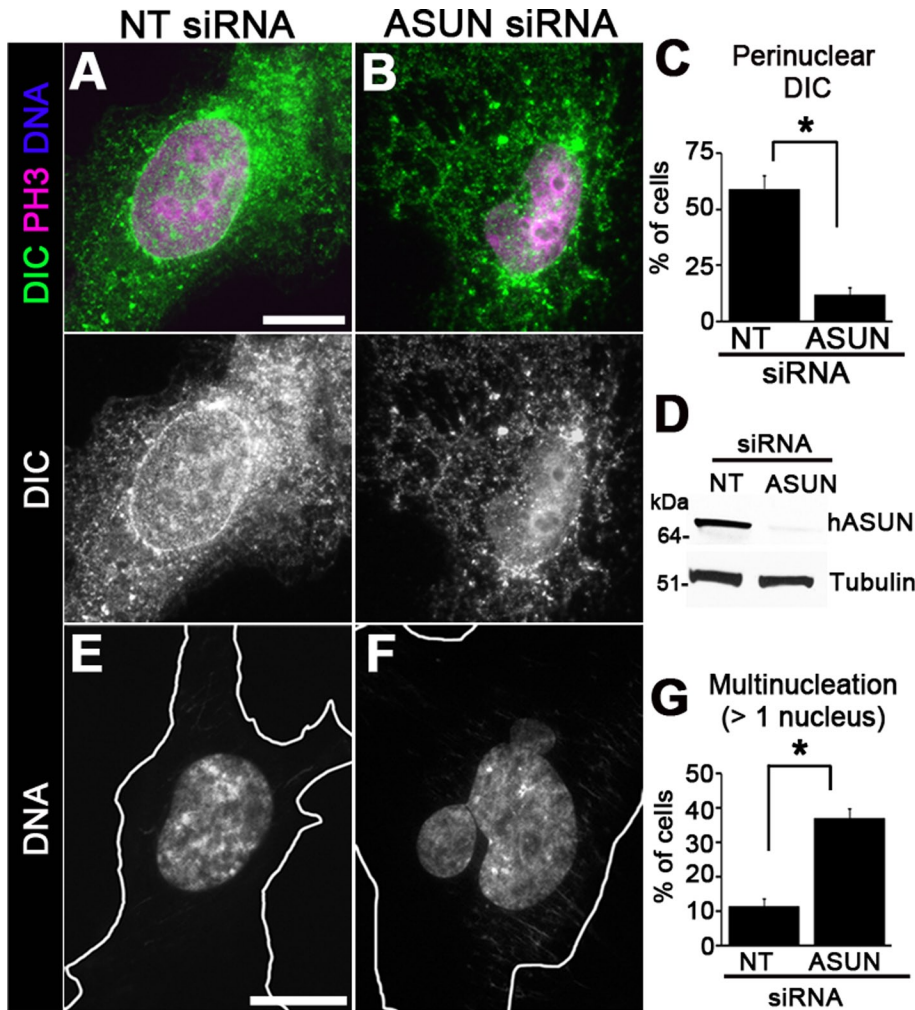
FIGURE 5: Loss of hASUN causes reduction of perinuclear dynein and multinucleation in nontransformed cells. (A–C) Dynein localization defects in hASUN-siRNA RPE cells. RPE cells were transfected with NT or hASUN siRNA. After nocodazole treatment, cells were fixed and stained for DIC, PH3, and DNA. The percentage of prophase cells with perinuclear DIC was reduced after hASUN knockdown (B) compared with control cells (A; quantified in C). (D) Immunoblotting of lysates confirmed down-regulation of hASUN. Tubulin was used as loading control. (E–G) A higher percentage of hASUN-siRNA RPE cells (F) were multinucleated (more than one nucleus per cell) compared with control cells (E; quantified in G). *p < 0.0005. Scale bars, 20 µm.

precipitation of human LIS1 and *Drosophila* ASUN proteins, further indicating evolutionary conservation of this interaction (Supplemental Figure S6). In further support of these data, we found that CHY-LIS1 colocalizes with endogenous hASUN in the perinuclear region of ~70% of nocodazole-treated HeLa cells (Figure 7, C and E). Line scans confirmed that hASUN and CHY-LIS1 have overlapping staining patterns, although tight colocalization was not consistently observed (Figure 7D). Despite the interaction observed between ASUN and LIS1, we did not detect coimmunoprecipitation of ASUN and dynein–dynactin subunits (Supplemental Figure S7A).

To further explore the nature of the relationship between ASUN and LIS1, we tested whether hASUN is required for perinuclear enrichment of LIS1 at G2/M. After nocodazole treatment, perinuclear CHY-LIS1 was detected in <25% of cells with loss of hASUN, compared with ~80% of control cells (Figure 7, F and G). Immunoblot analysis revealed no change in CHY-LIS1 levels after hASUN knockdown, suggesting that ASUN is not required to maintain steady-state levels of LIS1 within cells (Figure 7H). These data are consistent with a model in which hASUN acts via LIS1 to recruit dynein complexes to the NE at prophase. The localization of ASUN at G2/M, however, was not dependent on LIS1 (Figure 7, I and J, and Supplemental Figure S8).

hASUN, BICD2, and CENP-F localize independently of each other at prophase

Two pathways, BICD2–RanBP2 and NudE/EL–CENP-F–Nup133, have been described that appear to operate independently to anchor dynein to the NE and facilitate proper positioning of centrosomes at the G2/M transition (Splinter *et al.*, 2010; Bolhy *et al.*, 2011). We confirmed that BICD2 and CENP-F colocalize to the NE of prophase HeLa cells as we would predict on the basis of independent reports of their localization patterns (Figure 8A; Splinter *et al.*, 2010; Bolhy *et al.*, 2011). As expected from our demonstration that the hASUN immunostaining pattern excludes the NE, we observed essentially no overlap of endogenous hASUN and GFP-BICD2 signals (Figure 8B). Furthermore, we observed no coimmunoprecipitation from cell lysates of ASUN with either BICD2 or CENP-F (Supplemental Figure S7, B and C).

We asked whether knockdown of hASUN, BICD2, or CENP-F in HeLa cells would globally disrupt the structure of NPCs in such a way that docking of dynein motors to the nuclear surface might be blocked. In hASUN-siRNA cells exhibiting loss of dynein at the NE, nuclear pore morphology as assessed by immunostaining for an NPC marker resembled that of control cells; similarly, depletion of BICD2 or CENP-F caused loss of dynein at the NE without grossly disrupting NPCs (Figure 8C and Supplemental Figure S9).
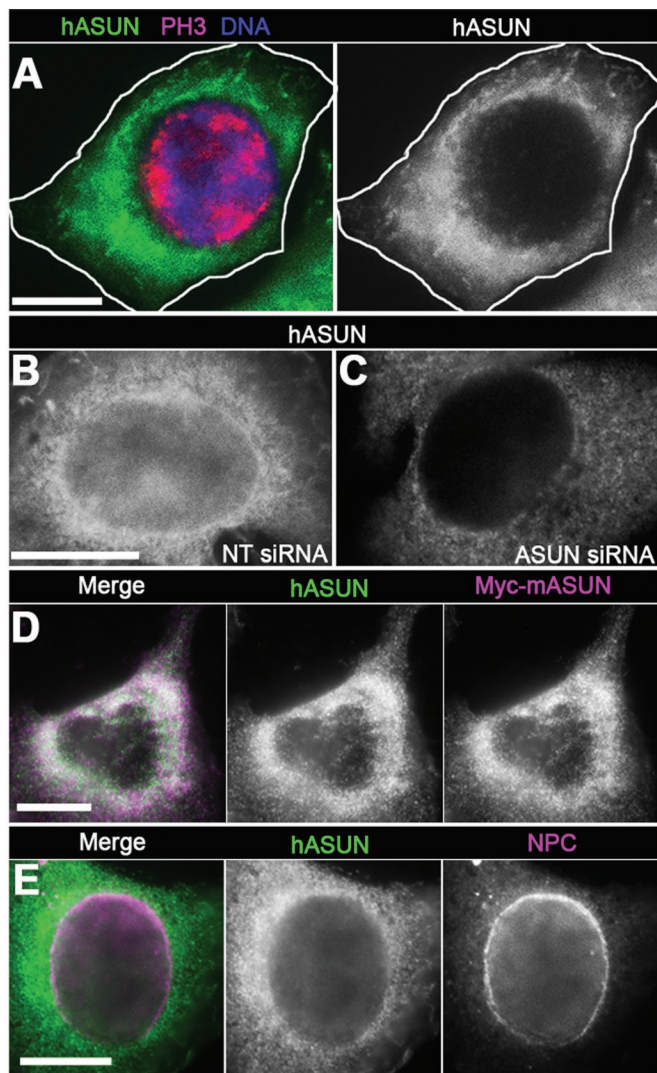
the possibility that hASUN might also bind to NPCs at prophase. We observed minimal colocalization, however, of endogenous hASUN and a marker for NPCs in costained cells (Figure 6E).

hASUN interacts with the dynein adaptor LIS1

We recently demonstrated a strong genetic interaction between *Drosophila asun* and *Lis-1*, coimmunoprecipitation and colocalization of dASUN and *Drosophila* LIS-1 proteins in cultured cells, and dependence of LIS-1 localization on dASUN during spermatogenesis (Sitaram *et al.*, 2012). On the basis of these findings, we considered the possibility that this interaction might be conserved between the mammalian homologues.

We showed coimmunoprecipitation of Myc-tagged mASUN and hemagglutinin (HA)-tagged human LIS1 after their coexpression in HEK293 cells, suggesting that these proteins exist within a complex; the capacity of these two proteins to coimmunoprecipitate was maintained when the affinity tags were switched (Figure 7, A and B, and Supplemental Figure S5). We also demonstrated coimmuno-

FIGURE 6: Subcellular localization of ASUN. HeLa cells were immunostained for endogenous hASUN using antipeptide antibodies (C-hASUN Ab). (A) PH3 costaining revealed endogenous hASUN localizes to the cytoplasm of prophase cells. (B, C) The hASUN signal of NT-siRNA cells (B) was lost in hASUN-siRNA cells (C), thereby demonstrating specificity. (D) Colocalization of endogenous hASUN and transiently expressed Myc-tagged mASUN. (E) Costaining of endogenous hASUN revealed no significant overlap with the NPC marker Mab414. Scale bars, 20 μm.

We next assessed whether hASUN, BICD2, or CENP-F is localized within HeLa cells in an interdependent manner (Figure 8D). We observed no change in the cytoplasmic localization pattern of hASUN after depletion of BICD2 or CENP-F. Conversely, BICD2 and CENP-F localized normally to the NE in hASUN-siRNA cells. We confirmed the previous observations of Bolhy et al. (2011) that BICD2 and CENP-F are not reciprocally required for their anchoring to the NE. Taken together, these data suggest that hASUN, BICD2, and CENP-F localize independently of each other at G2/M.

It was previously reported that inhibition of dynein function (via dynein antibody injection or dynactin subunit overexpression) does not disrupt the recruitment of BICD2 or CENP-F to the NE at G2/M (Splinter et al., 2010; Bolhy et al., 2011). We used siRNA-mediated knockdown to test whether the dynein adaptor LIS1 is required to

properly localize BICD2 or CENP-F. We observed no alteration in the localization patterns of BICD2 or CENP-F in prophase HeLa cells, providing further confirmation that functional dynein motors are not reciprocally required to recruit these proteins to the NE (Supplemental Figure S10).

hASUN, BICD2, and CENP-F cooperatively regulate dynein recruitment to the NE at prophase

We investigated possible cross-talk between hASUN, BICD2, and CENP-F in their regulation of dynein recruitment to the NE and nucleus–centrosome coupling at prophase. After knockdown of these three proteins, either individually or in combination, we assessed perinuclear dynein localization in nocodazole-treated HeLa cells and average nucleus–centrosome distances in U2OS cells (Figure 8, E and F). We did not observe additive or synergistic effects on these phenotypes in the double- or triple-knockdown cells. Bolhy et al. (2011) reported similar findings for the average nucleus–centrosome distances in U2OS cells with double knockdown of BICD2 and CENP-F. These observations suggest that hASUN, BICD2, and CENP-F operate via distinct molecular mechanisms but converge to regulate dynein localization and centrosomal tethering to the NE in prophase.

DISCUSSION
Proposed mechanism for hASUN-mediated recruitment of dynein to the NE during mitotic prophase

Two recent studies advanced our understanding of the mechanisms underlying the recruitment of dynein motors to the NE of cultured human cells at the onset of mitosis (Splinter et al., 2010; Bolhy et al., 2011). BICD2–RanBP2 and NudE/EL–CENP-F–Nup133 were identified as separate cassettes of proteins that provide sites to anchor dynein to the NE. We report here our findings that hASUN is a third protein required for this critical event in cultured cells. In contrast to the BICD2 and CENP-F cassettes, however, which can bind directly to components of dynein complexes, our data suggest that hASUN regulates the localization of dynein in an indirect manner via LIS1, an accessory protein of the motor. Another distinction is that BICD2 and CENP-F localize to NPCs within the NE, whereas hASUN localizes to the cytoplasm with exclusion of the NE.

We propose a model in which hASUN works in a manner distinct from that of BICD2 and CENP-F to mediate dynein recruitment to the NE at G2/M, a critical event required for nucleus–centrosome coupling before NEBD and faithful execution of mitotic divisions. Our data lead us to hypothesize that cytoplasmic hASUN transiently interacts with LIS1, which is bound to dynein heavy chains, to promote the enrichment and/or proper orientation of dynein complexes in the vicinity of the nuclear surface at G2/M. The BICD2–RanBP2 and NudE/EL–CENP-F–Nup133 cassettes then capture and stably anchor dynein complexes to NPCs. In the absence of hASUN, BICD2 and CENP-F are not sufficient to carry out the early steps in the process of dynein recruitment to the NE at G2/M; similarly, when either BICD2 or CENP-F is depleted from cells, hASUN can promote the enrichment/orientation of dynein complexes near the nuclear surface, but the complexes do not become stably anchored to the NE.

Why are so many factors required to carry out this important cellular process? A network of proteins might be required to move and properly orient dynein complexes at G2/M, given their large size and multisubunit composition. NudE, in addition to directly interacting with dynein motors, facilitates the interaction between LIS1 and dynein, suggesting that both ASUN and the NudE/EL–CENP-F–Nup133 cassette might converge on dynein through
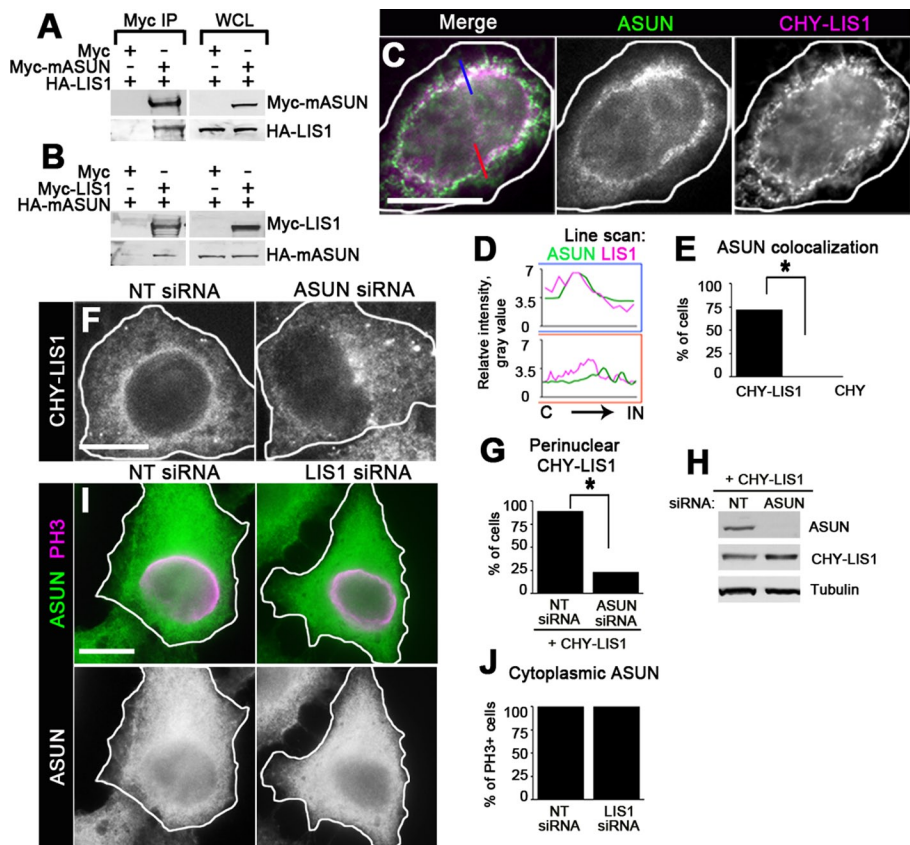
FIGURE 7: Interactions between ASUN and LIS1. (A, B) Coimmunoprecipitation experiments. (A, B) Lysates of HEK293 cells coexpressing the indicated tagged versions of mASUN and human LIS1 were used for Myc immunoprecipitation. Immunoblots of whole-cell lysates (WCL) and Myc immunoprecipitates (IP) were probed with HA and Myc antibodies. Representative blots are shown. (C–E) Overlapping localizations of hASUN and CHY-LIS1. Transfected HeLa cells expressing CHY-LIS1 were treated with nocodazole, fixed, and stained for hASUN. (C) Representative cell with partial overlap of hASUN and CHY-LIS1 in the perinuclear region is shown. (D) Line scans centered at the NE (corresponding to blue and red lines in D) confirmed colocalization of hASUN and CHY-LIS1 in some but not all areas. C, cytoplasmic; IN, intranuclear. (E) Quantification of overlap of perinuclear CHY-LIS1 (but not CHY) and hASUN in a majority of transfected cells. (F–H) Perinuclear localization of CHY-LIS1 is hASUN dependent. HeLa cells cotransfected with NT or hASUN siRNA plus CHY-LIS1 expression construct were treated with nocodazole and fixed. (F) Representative hASUN-siRNA cell with loss of perinuclear CHY-LIS1 compared with control. (G) Quantification of the loss of perinuclear CHY-LIS1 after hASUN knockdown. (H) Immunoblotting revealed no change in steady-state levels of CHY-LIS1 protein after hASUN knockdown. Tubulin was used as loading control. (I, J) ASUN localization at G2/M is independent of LIS1. HeLa cells transfected with NT or LIS1 siRNA were stained for PH3 and ASUN. (I) NT-siRNA and LIS1-siRNA cells showed comparable ASUN staining patterns. (J) Quantification of cytoplasmic ASUN localization in PH3+ cells after LIS1 knockdown. *$p < 0.0001$. Scale bars, 20 μm.

LIS1 at the onset of mitosis (McKenney *et al.*, 2010). It will be interesting to test in future experiments whether ASUN plays a role in promoting the interaction between CENP-F tethered to the NE and cytoplasmic NudE/EL–LIS1–dynein complexes at G2/M, a possible mechanism of action that would be consistent with our model.

Meiotic versus mitotic roles of ASUN

Whereas ASUN remained largely uncharacterized in human cells before this study, we previously showed that it has cell cycle and developmental roles in other organisms. In *Drosophila*, dASUN regulates dynein localization and centrosomal tethering to the nucleus during spermatogenesis, and it is required for male fertility (Anderson *et al.*, 2009). In *Xenopus*, we previously reported that the ASUN homo-

logue plays a role during embryonic development (Lee *et al.*, 2005). Down-regulation of ASUN in *Xenopus* embryos via morpholino oligonucleotide injection resulted in disruption of gastrulation and polyploidy; the latter phenotype suggested that ASUN might regulate the mitotic cell cycles of early blastomeres during vertebrate embryogenesis. We also showed conservation of function between *Xenopus* and human ASUN homologues by restoring proper developmental progression in *Xenopus* ASUN morphants via coinjection of mRNA encoding hASUN.

Drosophila asun mutants and HeLa cells depleted of ASUN exhibit strikingly similar disruptions of male meiosis and mitosis, respectively. These shared phenotypes underscore the likelihood that the transformed nature of the HeLa cell line is not responsible for the defects we observed. The reduction of dynein localized to the NE of prophase RPE cells after hASUN knockdown as reported here further validates this conclusion. One difference in the meiotic versus mitotic phenotypes is that *asun* spermatocytes exhibit delayed progression through meiosis, as evidenced by a large increase in the prophase fraction, whereas we report here that hASUN-siRNA HeLa cells have only a slightly increased mitotic index compared with control cells (Anderson *et al.*, 2009). We speculate that dynein localized to the nuclear surface might play a more important role in facilitating nuclear envelope breakdown at the end of prophase in *Drosophila* spermatocytes than in HeLa cells.

In contrast to *Drosophila asun*, which is expressed exclusively in germline tissues, mouse *ASUN* transcripts have been detected in all tissues, both somatic and germline, surveyed in a study by another group (Stebbings *et al.*, 1998; Bourdon *et al.*, 2002). The data we present here indicate that hASUN plays an important role in human somatic cells during mitosis. The human *ASUN* gene is located within a genomic region that is amplified in testicular seminomas, raising the possibility that

ASUN may also regulate division of male germline cells in vertebrates as it does in *Drosophila* (Bourdon *et al.*, 2002).

Why might ASUN expression be limited to germline cells in flies? The absence of dASUN expression within somatic cells may be related to the lack of an absolute requirement for centrosomes during most life cycle stages of *Drosophila*. Centrioles, although important for the formation of centrosomes (as well as cilia and flagella), play nonessential roles in development from an embryo to an adult fly, with the exception of early embryogenesis (Basto *et al.*, 2006; Stevens *et al.*, 2007). The process of spermatogenesis in adult male flies is also exceptional in that centrioles are required to form the cilium of spermatocytes and the axoneme of spermatids (Bettencourt-Dias *et al.*, 2005). Centrioles within G2 spermatocytes undergo major changes in
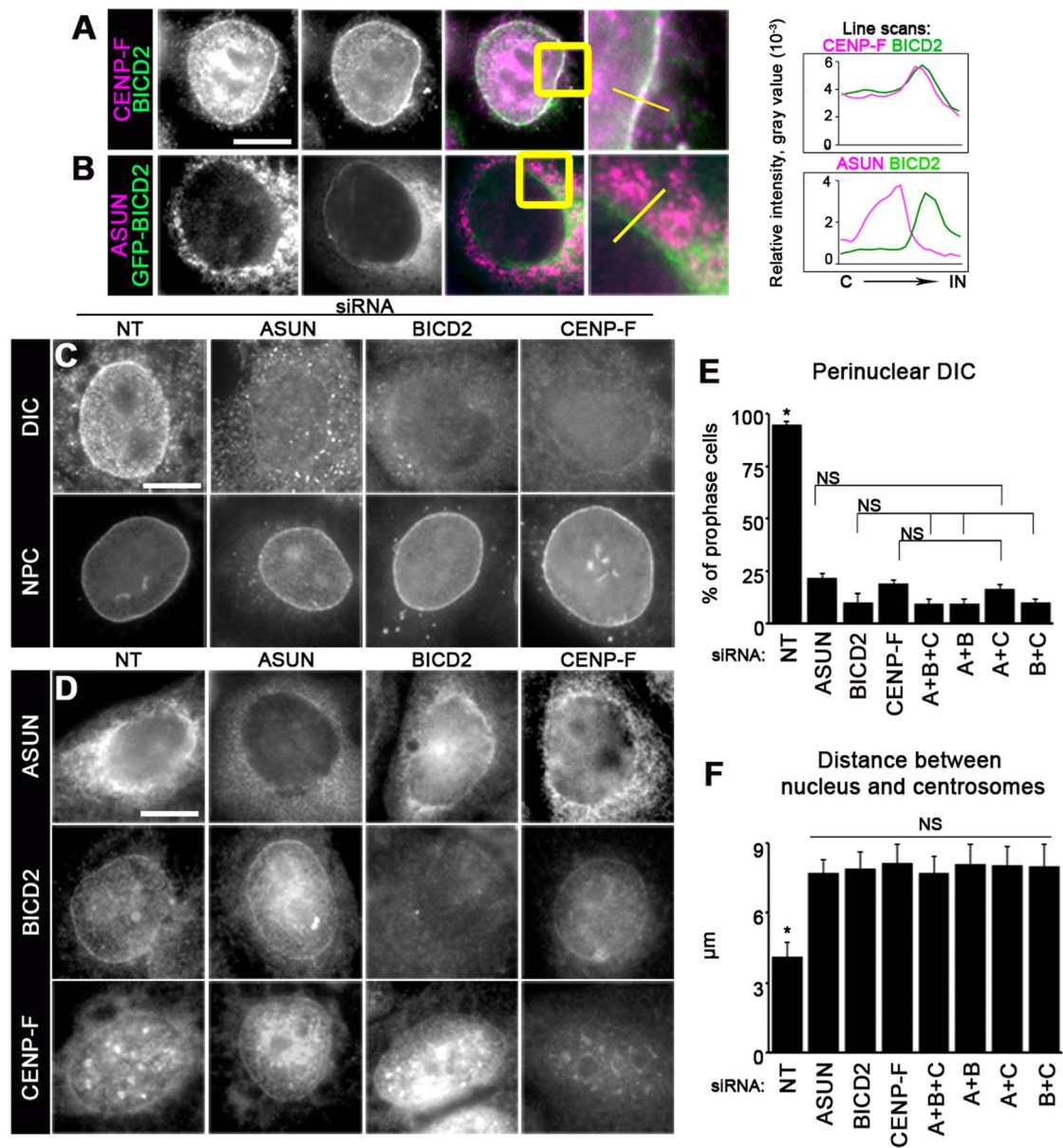
FIGURE 8: Relationship between hASUN, CENP-F, and BICD2 in recruiting dynein and centrosomes to the NE at mitotic entry. (A, B) HeLa cells were nocodazole treated, fixed, and immunostained as indicated. Endogenous CENP-F and BICD2 colocalized on the NE (A), but no colocalization was observed for GFP-BICD2 and endogenous hASUN (B). Higher-magnification views (micrographs on far right) of costained cells in the vicinity of the NE correspond to regions enclosed by yellow boxes. Line scans centered at the NE (corresponding to yellow lines in higher-magnification views) confirmed significant overlap of CENP-F and BICD2 signals but not hASUN and GFP-BICD2 signals. C, cytoplasmic; IN, intranuclear. (C–F) HeLa (C–E) or U2OS (F) cells were transfected with siRNA as indicated to down-regulate hASUN (A), BICD2 (B), and/or CENP-F (C). Transfected cells were nocodazole treated, fixed, and immunostained. (C) Perinuclear DIC was lost after hASUN, BICD2, or CENP-F knockdown without changes in the gross morphology of NPCs. (D) No change in hASUN, BICD2, or CENP-F localization was observed after knockdown of either of the other proteins. (E) Cells were immunostained for PH3, DIC, and DNA. Bar graph displays the percentage of prophase cells with perinuclear DIC for each knockdown condition. (F) Cells were immunostained for PH3, pericentrin, and DNA. Bar graph displays the mean nucleus–centrosome distance for each knockdown condition. $*p < 0.0001$. Scale bars, 20 µm.

their positioning, moving to the cortex during the extensive growth phase to elaborate a cilium and then back toward the nucleus at G2/M; the necessity to reestablish nucleus–centrosome coupling at the time of meiotic entry may impose a stringent requirement for dynein-localizing proteins such as ASUN in these cells (Fuller, 1993). Bicaudal, the *Drosophila* homologue of BICD2, is a potential candidate to cooperate with dASUN in dynein recruitment to the nuclear surface of G2 spermatocytes; our database searches, however, revealed no CENP-F homologues in flies.

Evolved mechanisms for dynein regulation in multicellular organisms

Cytoplasmic dynein, most commonly studied for its roles in trafficking of organelles and directed cell movement, is also required in

multicellular organisms for coordination of mitotic entry and exit (Dujardin *et al.*, 2003). Specifically, dynein promotes the coupling of centrosomes to the NE, has been hypothesized to assist in NEBD, and functions along the mitotic spindle to facilitate chromosome segregation at anaphase (Lippincott-Schwartz, 2002; Dujardin *et al.*, 2003; Tanenbaum *et al.*, 2010). In contrast, only one role for dynein has been identified in budding yeast: proper positioning of the spindle during mitosis (Stuchell-Brereton *et al.*, 2011).

It is interesting to note that none of the three proteins needed for localization of dynein to the NE of prophase HeLa cells (BICD2 and CENP-F as previously reported; hASUN as reported herein) have predicted homologues in either budding or fission yeast. The centrosome-like structure in yeast, known as the spindle pole body, is embedded into the nuclear surface throughout interphase and mitosis in budding yeast (Jaspersen and Winey, 2004). Similarly, in fission yeast, the spindle pole body is tethered to the nuclear surface throughout interphase and will embed at mitosis (Lim *et al.*, 2009). In both cases, dynein is not required for the process of spindle pole body–nucleus embedding (Jaspersen and Winey, 2004; Lim *et al.*, 2009). Thus metazoans appear to have evolved a finely tuned mechanism for regulating the localization of dynein complexes at the onset of mitosis, with at least three proteins required to execute the recruitment and docking of these motors to the NE.

MATERIALS AND METHODS

Drosophila experiments

Flies were maintained at 25°C using standard techniques (Greenspan, 2004). *y w* was obtained from the Bloomington *Drosophila* Stock Center (Indiana University, Bloomington, IN) and used as the "wild-type" stock. The *asun*^{f02815} allele (Exelixis Collection, Harvard Medical School, Boston, MA) and transgenic line with male germline–specific expression of CHY-dASUN were previously described (Anderson *et al.*, 2009). cDNA encoding mASUN (clone details provided later) with an N-terminal CHY tag was subcloned into vector tv3 (a gift from J. Brill, Hospital for Sick Children, Toronto, Canada) for expression of CHY-tagged mASUN under control of the testes-specific β2-*Tubulin* promoter (Wong *et al.*, 2005). Transgenic lines were generated by *P*-element–mediated transformation via embryo injection (Rubin and Spradling, 1982). A single transgene was mapped to the X chromosome and crossed into the *asun*^{f02815} background using standard genetic crosses.

To test male fertility, individual adult males (2 d old) were placed in vials with five wild-type females (2 d old) and allowed to mate for 5 d. The percentage of males producing adult progeny and the average number of live adult progeny produced per fertile male were scored (≥10 males tested per genotype). Statistical analyses were performed using Fisher's exact test (percentage of males producing progeny) or an unpaired Student's *t* test (average number of progeny per fertile male).

Protein extracts were prepared by homogenizing dissected testes from newly eclosed males in SDS sample buffer. The equivalent of eight testes pairs was loaded per lane. After SDS–PAGE, proteins were transferred to nitrocellulose for immunoblotting using standard techniques. Primary antibodies were used as follows: mCherry (1:500, Clontech, Mountain View, CA) and mouse anti–β-tubulin (E7, 1:5000; Developmental Studies Hybridoma Bank, University of Iowa, Iowa City, IA). Horseradish peroxidase (HRP)–conjugated secondary antibodies and chemiluminescence were used to detect primary antibodies.

Live testes cells were prepared for examination by fluorescence microscopy as described previously (Kemphues *et al.*, 1980). Briefly, testes were dissected from newly eclosed adult males, placed in a drop of phosphate-buffered saline (PBS) on a microscopic slide, and gently squashed under a glass coverslip after making a small incision near the stem cell hub. Formaldehyde fixation was performed as described previously (Gunsalus *et al.*, 1995). Briefly, slides of squashed testes were snap-frozen, immersed in 4% formaldehyde (in PBS with 0.1% Triton X-100) for 7 min at −20°C after coverslip removal, and washed three times in PBS. Primary antibodies were used as follows: mouse anti-DHC (P1H4, 1:120; a gift from T. Hays, University of Minnesota, Minneapolis, MN; McGrail and Hays, 1997) and rat anti–α-tubulin (Mca77G, 1:300; Accurate Chemical & Scientific, Westbury, NY). Fixed samples were mounted in PBS with 4′,6-diamidino-2-phenylindole (DAPI) to visualize DNA. Wide-field fluorescence images were obtained using an Eclipse 80i microscope (Nikon, Melville, NY) with Plan-Fluor 40× objective.

In experiments to determine the percentage of late G2 spermatocytes or immature spermatids with perinuclear dynein or the percentage of prophase I spermatocytes with nucleus–centrosome coupling, at least 200 cells were scored per genotype; statistical analyses were performed using Fisher's exact test. To quantify the ratios of perinuclear to diffusely cytoplasmic dynein in late G2 spermatocytes (testes stained for DHC), after image acquisition, the average intensity of the DHC signal within a small rectangular region was sampled near the nuclear surface and in the surrounding cytoplasm using Photoshop (Adobe, San Jose, CA). The ratio of the intensities was determined. At least 30 cells from a minimum of three testes pairs were scored per genotype. Statistical analysis was performed using an unpaired Student's *t* test.

Cell culture and treatments

Cell lines were maintained at 37°C and 5% CO_2 in DMEM (Life Technologies, Carlsbad, CA) containing 10% fetal bovine serum, 1% L-glutamine, 100 µg/ml streptomycin, and 100 U/ml penicillin. U2OS and RPE cells were cultured in antibiotic-free media. Plasmid DNA was transfected into cells using Lipofectamine 2000 (Invitrogen, Carlsbad, CA) or FuGENE HD (Promega, Madison, WI). siRNA duplexes were purchased from Dharmacon (Lafayette, CO). siGENOME NT siRNA#5 was used as negative control. siRNA sequences were designed to target human *ASUN* at its 5′-end (#1: 5′-GGAAAUAGAGGACGAAUAAUU-3′) or its 3′-end (#2: 5′-CAGAAGAGGAAGAACGAAA-3′; *LIS1* (5′-GAGTTGTGCTGAT-GACAAG-3′; Shu *et al.*, 2004); *CENP-F* (5′-CAGAATCTTAGTAGT-CAAGTA-3′; Bolhy *et al.*, 2011); or *BICD2* (5′-GGUGGACUAU-GAGGCUAUC-3′; Splinter *et al.*, 2010). hASUN siRNA#1 was used for all experiments in this study unless otherwise indicated. Cells were transfected with siRNA duplexes using DharmaFECT 1 transfection reagent (Dharmacon) in two successive rounds and analyzed 3 d later. Lipofectamine 2000 transfection reagent was used for cotransfection of cells with siRNA and DNA constructs. Where indicated, cells were incubated in 5 µg/ml (16.6 µM) nocodazole (Sigma-Aldrich, St. Louis, MO) for 3 h before fixation to enhance perinuclear localization of dynein. For metaphase arrest, cells were incubated for 16 h in 10 µM RO-3306 (Cdk1 inhibitor; Enzo Life Sciences, Plymouth, PA), followed by incubation for 3 h in 10 µM MG-132 (proteasome inhibitor; Calbiochem, La Jolla, CA). Approximately 80% of cells were arrested in metaphase under these conditions.

Fixation, immunostaining, and microscopy

Cells were fixed in either methanol (5 min at −20°C, followed by washing with Tris-buffered saline [TBS] plus 0.01% Triton X-100) or 4% formaldehyde (20 min at room temperature, followed by 20-min permeabilization step with TBS plus 0.05% Triton X-100). Cells were

blocked in TBS plus 0.01% Triton X-100 and 0.02% BSA before immunostaining. Primary antibodies were used as follows: C-hASUN (1:500), PH3 (Mitosis Marker, 1:1000, Millipore, Billerica, MA; or 1:2000, Abcam, Cambridge, MA), DIC (clone 74.1, 1:500; Abcam), pericentrin centriolar marker (clone 28144, 1:2000; Abcam), c-Myc (9E10, 1:1000), β-tubulin (clone E7, 1:1000; Developmental Studies Hybridoma Bank), CENP-F (clone 14C10 1D8, 1:200; Abcam), BICD2 (1:300; a gift from A. Akhmanova, Erasmus Medical Center, Rotterdam, Netherlands), and NPC marker (Mab414, 1:1000; Abcam). Appropriate secondary antibodies conjugated to Alexa Fluor 488 or Cy3 were used (1:1000; Invitrogen). Cells were mounted in ProLong Gold Antifade Reagent with DAPI (Invitrogen).

Wide-field fluorescence images were obtained using an Eclipse 80i microscope (Nikon) with Plano-Apo 100× objective. Confocal stacks were taken by a Yokogawa QLC-100/CSU-10 spinning disk head (Visitec assembled by Vashaw [Norcross, GA]) attached to a Nikon TE2000E microscope using a CFI PLAN APO VC 100× oil lens/numerical aperture 1.4, with or without 1.5× intermediate magnification, and a back-illuminated Cascade 512B electron-multiplying charge-coupled device camera (Photometrics, Tucson, AZ) driven by IPLab software (Scanalytics, Rockville, MD). A krypton–argon laser (75 mW 488/568; Melles Griot, Albuquerque, NM) with acousto-optic tunable filters was used for two-color excitation. Custom double dichroic mirror and filters (Chroma, Bellows Falls, VT) in a filter wheel (Ludl, Hawthorne, NY) were used in the emission light path. The Z-steps (0.2 μm) were driven by a Nikon built-in Z motor.

Line-scan analyses were performed using ImageJ (National Institutes of Health, Bethesda, MD). Ten representative cells were measured per condition; for each cell, 12 line scans distributed equally around the nuclear circumference were obtained. Lines scans presented within figures are 100 pixels in length and are oriented with the cytoplasmic end of each line to the left and the intranuclear end of each line to the right. To quantify the ratios of perinuclear to diffusely cytoplasmic DIC in stained HeLa cells, we sampled the average intensity of the DIC signal within a small rectangular region near the nuclear surface and in the surrounding cytoplasm using ImageJ. The ratio of the intensities was determined. At least 30 cells were scored per condition.

Statistical analyses of experiments reported here were performed using Student's unpaired t test unless otherwise noted. Error bars indicate SEM for all bar graphs. All experiments were performed a minimum of three times, with at least 100 cells scored per condition unless otherwise noted.

DNA constructs
cDNA clone LD33046 encoding ASUN was obtained from the *Drosophila* Gene Collection. IMAGE cDNA clones encoding mASUN (#4459471) and human LIS1 (#5786560) were obtained from the American Type Culture Collection (Manassas, VA). Constructs for expression of the following N-terminally tagged proteins were generated by subcloning into vector pCS2: HA- and CHY-dASUN; HA- and Myc-mASUN; and HA-, Myc-, and CHY-LIS1. The HA-LIS1 expression construct was a gift from Deanna Smith (University of South Carolina Biological Sciences, Columbia SC). The GFP-BICD2 expression construct was a gift from A. Akhmanova (Hoogenraad *et al.*, 2001). Mobyle@Pasteur, version 1.0.4, was used to determine the percentage identities and similarities between ASUN proteins from different species.

Anti-ASUN antibody production
Two rabbit polyclonal antibodies (M-hASUN Ab and C-hASUN Ab) were raised using synthetic peptides corresponding to the following

amino acid residues of hASUN: IIKDSPDSPEPPNKKPLVEC (619–637) and CSVNNRAELYQHLKEENG (678–694), respectively. Exogenous cysteine residues were added for conjugation and affinity purification purposes. After exsanguination, enzyme-linked immunosorbent assay–positive antisera were antigen-affinity purified to a final concentration of ~1 mg/ml.

Immunoblotting and coimmunoprecipitation
Lysates were prepared using nondenaturing lysis buffer (50 mM Tris-Cl, pH 7.4, 300 mM NaCl, 5 mM EDTA, 1% Triton X-100). After SDS–PAGE, proteins were transferred to nitrocellulose for immunoblotting using standard techniques. Immunoblotting was performed using the following primary antibodies: c-Myc (9E10, 1:1000), HA (CAS 12, 1:1000), β-tubulin (clone E7, 1:1000; Developmental Studies Hybridoma Bank), mCherry (1:500; Clontech), CENP-F (clone 14C10 1D8, 1:500; Abcam), DIC (clone 74.1, 1:500; Abcam), DMN (clone 25, 1:250; BD Biosciences, San Diego, CA), M-hASUN (1:300), and C-hASUN (1:500). BICD2 antibody (1:2500) was a gift from A. Akhmanova (Hoogenraad *et al.*, 2001). HRP-conjugated secondary antibodies (1:5000) and chemiluminescence were used to detect primary antibodies. For coimmunoprecipitation experiments, anti–c-Myc agarose beads (40 μl; Sigma-Aldrich) were incubated with lysates of transfected HEK293 cells (500 μg) for 1 h at 4°C with shaking and washed 3× in lysis buffer. Samples were boiled in 6× sample buffer, resolved by SDS–PAGE, and analyzed by immunoblotting.

Sucrose density gradients
HeLa cells were transfected with either NT or hASUN siRNA. At 3 d posttransfection, lysates were prepared using nondenaturing lysis buffer (as described earlier). Lysates were layered on top of sucrose gradients (5 ml) with equal volumes of 30, 20, 10, and 5% sucrose in PBS (137 mM NaCl, 7 mM Na$_2$HPO$_4$, and 3 mM NaH$_2$PO$_4$, pH 7.2). Samples were centrifuged at 46,000 rpm for 16 h in a swinging-bucket rotor (SW55ti; Beckman Coulter, Brea, CA). After centrifugation, fractions (167 μl) were collected and analyzed by immunoblotting. Molecular weight standards were obtained from Bio-Rad (Hercules, CA).

REFERENCES
Akhmanova A, Hammer JA 3rd (2010). Linking molecular motors to membrane cargo. Curr Opin Cell Biol 22, 479–487.

Anderson MA, Jodoin JN, Lee E, Hales KG, Hays TS, Lee LA (2009). Asunder is a critical regulator of dynein-dynactin localization during *Drosophila* spermatogenesis. Mol Biol Cell 20, 2709–2721.

Basto R, Lau J, Vinogradova T, Gardiol A, Woods CG, Khodjakov A, Raff JW (2006). Flies without centrioles. Cell 125, 1375–1386.

Beaudouin J, Gerlich D, Daigle N, Eils R, Ellenberg J (2002). Nuclear envelope breakdown proceeds by microtubule-induced tearing of the lamina. Cell 108, 83–96.

Beswick RW, Ambrose HE, Wagner SD (2006). Nocodazole, a microtubule de-polymerising agent, induces apoptosis of chronic lymphocytic leukaemia cells associated with changes in Bcl-2 phosphorylation and expression. Leuk Res 30, 427–436.

Bettencourt-Dias M, Rodrigues-Martins A, Carpenter L, Riparbelli M, Lehmann L, Gatt MK, Carmo N, Balloux F, Callaini G, Glover DM (2005). SAK/PLK4 is required for centriole duplication and flagella development. Curr Biol 15, 2199–2207.

Bolhy S, Bouhlel I, Dultz E, Nayak T, Zuccolo M, Gatti X, Vallee R, Ellenberg J, Doye V (2011). A Nup133-dependent NPC-anchored network tethers centrosomes to the nuclear envelope in prophase. J Cell Biol 192, 855–871.

Bourdon V, Naef F, Rao PH, Reuter V, Mok SC, Bosl GJ, Koul S, Murty VV, Kucherlapati RS, Chaganti RS (2002). Genomic and expression analysis of the 12p11-p12 amplicon using EST arrays identifies two novel amplified and overexpressed genes. Cancer Res 62, 6218–6223.

Burgess SA, Knight PJ (2004). Is the dynein motor a winch? Curr Opin Struct Biol 14, 138–146.

Dujardin DL, Barnhart LE, Stehman SA, Gomes ER, Gundersen GG, Vallee RB (2003). A role for cytoplasmic dynein and LIS1 in directed cell movement. J Cell Biol 163, 1205–1211.

Fuller MT (1993). Spermatogenesis. In: The Development of Drosophila melanogaster, ed. M Bate and A Martinez-Arias, Cold Spring Harbor, NY: Cold Spring Harbor Laboratory Press, 71–147.

Godin JD, Humbert S (2011). Mitotic spindle: focus on the function of huntingtin. Int J Biochem Cell Biol 43, 852–856.

Greenspan RJ (2004). Fly Pushing: The Theory and Practice of Drosophila Genetics, Cold Spring Harbor, NY: Cold Spring Harbor Laboratory Press.

Gunsalus KC, Bonaccorsi S, Williams E, Verni F, Gatti M, Goldberg ML (1995). Mutations in twinstar, a Drosophila gene encoding a cofilin/ADF homologue, result in defects in centrosome migration and cytokinesis. J Cell Biol 131, 1243–1259.

Hebbar S, Mesngon MT, Guillotte AM, Desai B, Ayala R, Smith DS (2008). Lis1 and Ndel1 influence the timing of nuclear envelope breakdown in neural stem cells. J Cell Biol 182, 1063–1071.

Holzbaur EL, Vallee RB (1994). DYNEINS: molecular structure and cellular function. Annu Rev Cell Biol 10, 339–372.

Hoogenraad CC, Akhmanova A, Howell SA, Dortland BR, De Zeeuw CI, Willemsen R, Visser P, Grosveld F, Galjart N (2001). Mammalian Golgi-associated bicaudal-D2 functions in the dynein-dynactin pathway by interacting with these complexes. EMBO J 20, 4041–4054.

Jaspersen SL, Winey M (2004). The budding yeast spindle pole body: structure, duplication, and function. Annu Rev Cell Dev Biol 20, 1–28.

Kardon JR, Vale RD (2009). Regulators of the cytoplasmic dynein motor. Nat Rev Mol Cell Biol 10, 854–865.

Kemphues KJ, Raff EC, Raff RA, Kaufman TC (1980). Mutation in a testis-specific beta-tubulin in Drosophila: analysis of its effects on meiosis and map location of the gene. Cell 21, 445–451.

Lacroix B, Maddox AS (2012). Cytokinesis, ploidy and aneuploidy. J Pathol 226, 338–351.

Lee LA, Lee E, Anderson MA, Vardy L, Tahinci E, Ali SM, Kashevsky H, Benasutti M, Kirschner MW, Orr-Weaver TL (2005). Drosophila genome-scale screen for PAN GU kinase substrates identifies Mat89Bb as a cell cycle regulator. Dev Cell 8, 435–442.

Lim HH, Zhang T, Surana U (2009). Regulation of centrosome separation in yeast and vertebrates: common threads. Trends Cell Biol 19, 325–333.

Lippincott-Schwartz J (2002). Cell biology: ripping up the nuclear envelope. Nature 416, 31–32.

Malone CJ, Misner L, Le Bot N, Tsai MC, Campbell JM, Ahringer J, White JG (2003). The C. elegans hook protein, ZYG-12, mediates the essential attachment between the centrosome and nucleus. Cell 115, 825–836.

McGrail M, Hays TS (1997). The microtubule motor cytoplasmic dynein is required for spindle orientation during germline cell divisions and oocyte differentiation in Drosophila. Development 124, 2409–2419.

McKenney RJ, Vershinin M, Kunwar A, Vallee RB, Gross SP (2010). LIS1 and NudE induce a persistent dynein force-producing state. Cell 141, 304–314.

Mische S, He Y, Ma L, Li M, Serr M, Hays TS (2008). Dynein light intermediate chain: an essential subunit that contributes to spindle checkpoint inactivation. Mol Biol Cell 19, 4918–4929.

Rubin GM, Spradling AC (1982). Genetic transformation of Drosophila with transposable element vectors. Science 218, 348–353.

Salina D, Bodoor K, Eckley DM, Schroer TA, Rattner JB, Burke B (2002). Cytoplasmic dynein as a facilitator of nuclear envelope breakdown. Cell 108, 97–107.

Schroer TA (2004). Dynactin. Annu Rev Cell Dev Biol 20, 759–779.

Shu T, Ayala R, Nguyen MD, Xie Z, Gleeson JG, Tsai LH (2004). Ndel1 operates in a common pathway with LIS1 and cytoplasmic dynein to regulate cortical neuronal positioning. Neuron 44, 263–277.

Sitaram P, Anderson MA, Jodoin JN, Lee E, Lee LA (2012). Regulation of dynein localization and centrosome positioning by Lis-1 and asunder during Drosophila spermatogenesis. Development 139, 2945–2954.

Splinter D et al. (2010). Bicaudal D2, dynein, and kinesin-1 associate with nuclear pore complexes and regulate centrosome and nuclear positioning during mitotic entry. PLoS Biol 8, e1000350.

Stebbings L, Grimes BR, Bownes M (1998). A testis-specifically expressed gene is embedded within a cluster of maternally expressed genes at 89B in Drosophila melanogaster. Dev Genes Evol 208, 523–530.

Stevens NR, Raposo AA, Basto R, St Johnston D, Raff JW (2007). From stem cell to embryo without centrioles. Curr Biol 17, 1498–1503.

Stuchell-Brereton MD, Siglin A, Li J, Moore JK, Ahmed S, Williams JC, Cooper JA (2011). Functional interaction between dynein light chain and intermediate chain is required for mitotic spindle positioning. Mol Biol Cell 22, 2690–2701.

Tanaka T, Serneo FF, Higgins C, Gambello MJ, Wynshaw-Boris A, Gleeson JG (2004). Lis1 and doublecortin function with dynein to mediate coupling of the nucleus to the centrosome in neuronal migration. J Cell Biol 165, 709–721.

Tanenbaum ME, Akhmanova A, Medema RH (2010). Dynein at the nuclear envelope. EMBO Rep 11, 649.

Vassilev LT (2006). Cell cycle synchronization at the G2/M phase border by reversible inhibition of CDK1. Cell Cycle 5, 2555–2556.

Wong R, Hadjiyanni I, Wei HC, Polevoy G, McBride R, Sem KP, Brill JA (2005). PIP2 hydrolysis and calcium release are required for cytokinesis in Drosophila spermatocytes. Curr Biol 15, 1401–1406.

Zhang X, Lei K, Yuan X, Wu X, Zhuang Y, Xu T, Xu R, Han M (2009). SUN1/2 and Syne/Nesprin-1/2 complexes connect centrosome to the nucleus during neurogenesis and neuronal migration in mice. Neuron 64, 173–187.

Haploinsufficiency for *AAGAB* causes clinically heterogeneous forms of punctate palmoplantar keratoderma

Elizabeth Pohler[1], Ons Mamai[2,3], Jennifer Hirst[4], Mozheh Zamiri[5], Helen Horn[6], Toshifumi Nomura[7], Alan D Irvine[8,9], Benvon Moran[8], Neil J Wilson[1], Frances J D Smith[1], Christabelle S M Goh[1], Aileen Sandilands[1], Christian Cole[1,10], Geoffrey J Barton[10], Alan T Evans[11], Hiroshi Shimizu[7], Masashi Akiyama[12], Mitsuhiro Suehiro[13], Izumi Konohana[14], Mohammad Shboul[3], Sebastien Teissier[3], Lobna Boussofara[15], Mohamed Denguezli[15], Ali Saad[2], Moez Gribaa[2], Patricia J Dopping-Hepenstal[16], John A McGrath[17], Sara J Brown[1], David R Goudie[18], Bruno Reversade[3,19], Colin S Munro[20] & W H Irwin McLean[1]

Palmoplantar keratodermas (PPKs) are a group of disorders that are diagnostically and therapeutically problematic in dermatogenetics[1–3]. Punctate PPKs are characterized by circumscribed hyperkeratotic lesions on the palms and soles with considerable heterogeneity. In 18 families with autosomal dominant punctate PPK, we report heterozygous loss-of-function mutations in *AAGAB*, encoding α- and γ-adaptin–binding protein p34, located at a previously linked locus at 15q22. α- and γ-adaptin–binding protein p34, a cytosolic protein with a Rab-like GTPase domain, was shown to bind both clathrin adaptor protein complexes, indicating a role in membrane trafficking. Ultrastructurally, lesional epidermis showed abnormalities in intracellular vesicle biology. Immunohistochemistry showed hyperproliferation within the punctate lesions. Knockdown of *AAGAB* in keratinocytes led to increased cell division, which was linked to greatly elevated epidermal growth factor receptor (EGFR) protein expression and tyrosine phosphorylation. We hypothesize that p34 deficiency may impair endocytic recycling of growth factor receptors such as EGFR, leading to increased signaling and cellular proliferation.

Palmoplantar keratoderma (MIM 148600) describes a group of hereditary skin disorders characterized by thickening (hyperkeratosis) of the epidermis of the palms and soles[1]. Historically, PPKs have been classified according to the pattern of lesions (diffuse, focal,

punctate and striate), as well as by histopathological changes (epidermolytic, non-epidermolytic and porokeratotic). Molecular genetics now allows for improved classification and diagnosis and for personalized approaches to treatment. Three distinct types of inherited punctate PPK are recognized by Online Mendelian Inheritance in Man (OMIM)[2]: PPKP1 (also known as the Buschke-Fischer-Brauer type; MIM 148600), for which the associated locus mapped to 15q22 (refs. 4–6); PPKP2 (porokeratotic type; MIM 175860), for which no locus has been mapped yet; and PPKP3 (also known as acrokeratoelastoidosis; MIM 101850), for which preliminary linkage suggests a possible associated locus at 2p25–p12 (ref. 7). An additional disease-associated locus was identified at 8q24.13–8q24.21 in two Chinese families whose phenotypes resemble PPKP1 clinically and histologically[8]. Here we studied a collection of 18 kindreds with PPKP1 from Scotland, Ireland, Japan and Tunisia, 11 of whom had a family history consistent with autosomal dominant inheritance (**Supplementary Fig. 1**). In our PPKP1 case collection, there was considerable phenotypic variation (**Fig. 1**). In all families, onset was typically during the first to second decade of life, with the appearance of small circumscribed lesions on the palms and soles. These lesions consistently increased in number with advancing age and coalesced later to form larger lesions. In some families, lesions remained subtle (**Fig. 1a,b**), whereas the phenotype in other families, resembling human papilloma virus (HPV)-induced papilloma-like lesions, was much more severe, painful and debilitating (**Fig. 1c,d**). Histology of lesional palmar epidermis from three unrelated kindreds (families 1,

[1]Centre for Dermatology and Genetic Medicine, College of Life Sciences and College of Medicine, Dentistry & Nursing, University of Dundee, Dundee, UK. [2]Laboratory of Human Cytogenetics, Molecular Genetics and Reproductive Biology, Farhat Hached University Hospital, Sousse, Tunisia. [3]Institute of Medical Biology, Agency for Science, Technology and Research (A*STAR), Singapore. [4]Cambridge Institute for Medical Research, University of Cambridge, Cambridge, UK. [5]Department of Dermatology, University Hospital Crosshouse, Kilmarnock, UK. [6]Department of Dermatology, Royal Infirmary of Edinburgh, Edinburgh, UK. [7]Department of Dermatology, Hokkaido University Graduate School of Medicine, Sapporo, Japan. [8]Department of Paediatric Dermatology, Our Lady's Children's Hospital, Dublin, Ireland. [9]Institute for Molecular Medicine, Trinity College Dublin, Dublin, Ireland. [10]Bioinformatics Research Group, Division of Biochemistry and Drug Discovery, College of Life Sciences, University of Dundee, Dundee, UK. [11]Department of Pathology, Ninewells Hospital and Medical School, Dundee, UK. [12]Department of Dermatology, Nagoya University Graduate School of Medicine, Nagoya, Japan. [13]Department of Dermatology, Otsu Municipal Hospital, Otsu, Japan. [14]Department of Dermatology, Hiratsuka Municipal Hospital, Hiratsuka, Japan. [15]Department of Dermatology and Venerology, Farhat Hached University Hospital, Sousse, Tunisia. [16]Guy's and St. Thomas' (GSTS) Pathology, St. Thomas' Hospital, London, UK. [17]St. John's Institute of Dermatology, King's College London, London, UK. [18]Human Genetics Unit, Ninewells Hospital and Medical School, Dundee, UK. [19]Department of Paediatrics, National University of Singapore, Singapore. [20]Department of Dermatology, Southern General Hospital, Glasgow, UK. Correspondence should be addressed to W.H.I.M. (w.h.i.mclean@dundee.ac.uk).

Figure 1 Clinical and histological features of punctate PPK. (**a**) The palm of the proband in family 1 with PPKP1 shows numerous small, hard, slightly indented hyperkeratotic lesions (arrow). Inset, magnified view of the lesion indicated by the arrow. (**b**) On the soles, lesions tend to coalesce at pressure points, and the presentation can therefore resemble a focal form of keratoderma. (**c**,**d**) In some cases, the phenotype is much more severe, as seen with the hand (**c**) and feet (**d**) of the proband from family 15. (**e**) Hematoxylin and eosin staining of a section showing a punch sample of skin incorporating a well-defined central epidermal depression associated with hypergranulosis and a prominent layer of overlying orthokeratosis. Scale bar, 500 µm. (**f**) Staining for the proliferation marker Ki67 highlights an increase in the number of keratinocytes in the cell cycle within the floor of the epidermal depression (arrowheads) compared to perilesional epidermis (arrow). Scale bar, 100 µm.

11 and 15) all showed very similar findings of a well-defined central epidermal depression associated with hypergranulosis and a prominent layer of overlying orthokeratosis (**Fig. 1e**). Immunohistochemical staining for the cell proliferation marker Ki67 showed continuous staining of the basal cell (proliferative) compartment of the epidermis beneath the hyperkeratotic lesions (**Fig. 1f**), indicative of a hyperproliferative form of hyperkeratosis rather than a retention hyperkeratosis due to defective desquamation.

Microsatellite linkage to the previously reported 15q22 locus was observed in a large Tunisian kindred originating from Saudi Arabia (**Supplementary Fig. 2**), with a maximum two-point logarithm of odds (LOD) score of 8.18 at recombination frequency (θ) = 0 obtained for D15S983 (**Supplementary Table 1**). The family was reported previously[9]. A 6.24-Mb key interval containing 80 RefSeq genes was defined by visible recombination with markers D15S993 (proximal) and D15S977 (distal). This locus overlaps the previously reported intervals associated with PPKP1 (**Supplementary Table 2**). In parallel, the proband in family 1 (of Scottish ancestry) was subjected to whole-exome sequencing. Of the 28,513 SNPs identified, we elected to concentrate on loss-of-function variants located within the key interval defined by our linkage data and that previously reported. Of 106 unique stop-gain SNPs in the exome data set, only 3 SNPs, all heterozygous in the proband, were located on chromosome 15 (**Supplementary Table 3**). Two were located well outside the interval, including a known SNP, rs57809907, in *DYX1C1*, c.1617C>T, predicted to cause a p.Glu417* alteration, and a second previously unreported variant of unknown consequence in *GABRG3*, c.1316T>A, predicted to cause a p.Leu439* alteration. The remaining variant, c.481C>T in *AAGAB*, predicted to cause a p.Arg161* alteration (mRNA, NM_024666; protein, NP_078942), fell within our linkage interval and that initially reported[5] but was just outside the interval reported in a Chinese kindred[6]. This variant was absent from current dbSNP and 1000 Genomes Project data sets (1 June 2012). The mutation was confirmed by conventional sequencing and cosegregated with the PPKP1 phenotype in family 1 (**Supplementary Fig. 3a,b**). By conventional sequencing, a second loss-of-function mutation, c.346_347delAG,

was identified and found to fully cosegregate with disease in the linked kindred and two additional Tunisian families (**Supplementary Fig. 3c,d**). Sequencing of the remaining 16 families identified a total of 8 mutations in *AAGAB* (2 nonsense, 5 frameshift and 1 splice-site mutation, as detailed in **Supplementary Table 4**). *AAGAB*, consisting of ten exons spanning 53,708 bp of genomic DNA, encodes α- and γ-adaptin–binding protein p34, which was identified in a yeast two-hybrid screen using a subunit of the adapter protein (AP)-1 complex as bait[10]. The positions of the predicted alterations in relation to the protein organization of p34 are shown (**Fig. 2**).

Conventional RT-PCR showed expression in palmoplantar epidermis comparable to that in abdominal skin (data not shown). By quantitative RT-PCR (qRT-PCR), we confirmed that *AAGAB* is expressed at broadly comparable levels in skin, HeLa cells, primary epidermal keratinocytes and the commonly used keratinocyte cell line, HaCaT[11] (**Fig. 3a**). Using qRT-PCR, we also showed that *AAGAB* message is very widely expressed across tissues, including
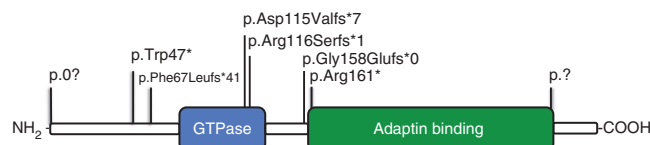

Figure 2 Identification of mutations in *AAGAB* in families with PPKP1. Protein domain organization of the p34 protein encoded by *AAGAB*, showing the positions of all eight alterations identified. Further details on the mutations are provided in **Supplementary Table 4**. Examples of sequence traces are shown in **Supplementary Figure 3**.

Figure 3 *AAGAB* is expressed in skin and keratinocytes and its depletion leads to increased cell numbers over time. (**a**) qRT-PCR showed that *AAGAB* mRNA is expressed in skin and is present at broadly comparable levels in primary epidermal keratinocytes. HeLa cells and the epidermal keratinocyte cell line HaCaT. (**b**) Protein blot showing that two independent siRNAs (designated *AAGAB* 1239 and 2164) potently lower p34 expression in HaCaT cells. NSC4, nonspecific control siRNA (inverted *lacZ* sequence). (**c**) *AAGAB* knockdown by either siRNA leads to an approximate twofold increase in HaCaT cell division 96 h after transfection. Error bars, s.d.
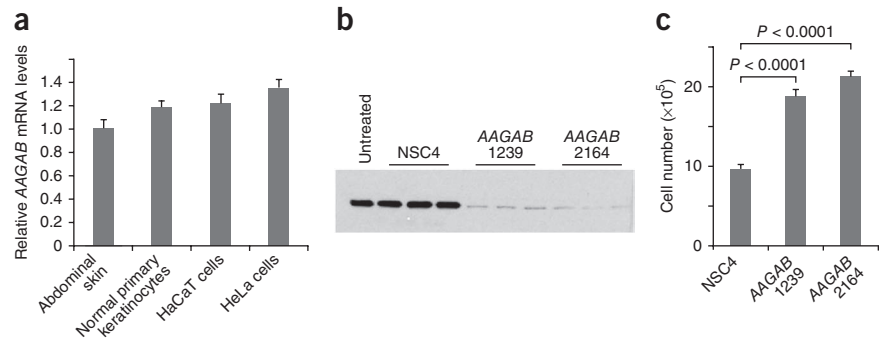
in the skin (**Supplementary Fig. 4**). Two independent small interfering RNAs (siRNAs) were developed that resulted in almost complete reduction of the amount of p34 protein in HaCaT cells (**Fig. 3b**). Treatment of HaCaT cells with either of these potent siRNAs resulted in an approximately twofold increase in cell number over time compared to cells transfected with a negative control siRNA (**Fig. 3c**), thus mirroring the high epidermal proliferation observed in lesional epidermis (**Fig. 1f**).

The coating of clathrin-coated vesicles consists of clathrin and adaptor complexes, both of which have to be recruited to the appropriate membrane from the cytoplasm[12,13]. The two most abundant types of adaptor protein complexes are AP-1, which is responsible for sorting proteins between the trans-Golgi network (TGN) and endosomes, and AP-2, which is responsible for sorting proteins at the plasma membrane. Both are heterotypic complexes, with AP-1 containing a γ-adaptin subunit and AP-2 containing an α-adaptin subunit. Although cDNA encoding p34 protein was the predominant species cloned from the original yeast two-hybrid screen[10], difficulty in obtaining antibodies specific to the p34 protein meant that further biochemical confirmation of these protein-protein interactions were not presented. Here, using two independent antibodies to p34 that were made in house, we confirmed by immunoprecipitation combined with protein blotting that this protein indeed interacts with both AP-1 and AP-2 complexes in the cytosol (**Fig. 4a**). Cytosolic localization was confirmed by immunocytochemistry using constructs encoding p34 fused to green fluorescent protein (GFP)

at either the N or C terminus (**Fig. 4b**), although fusion of GFP at the C terminus also led to some nuclear accumulation of the fusion protein. Cell fractionation studies showed that p34 protein is found in the cytosol but not in the membrane or clathrin-coated vesicle fractions in HeLa cells (**Fig. 4c**). Almost complete siRNA-mediated knockdown of *AAGAB* (**Fig. 4d**) did not lead to an obvious change in the plasma membrane or TGN localization of AP-2 or AP-1, respectively (**Fig. 4e**). Neither AP-1 nor AP-2 colocalized with the N- or C-terminal GFP fusions of p34 (**Supplementary Fig. 5**). Essentially identical diffuse cytoplasmic localization data were obtained in the keratinocyte cell line HaCaT (data not shown). Overall, these data confirm that p34 is a cytosolic protein that binds to AP-1 and AP-2; however, p34 does not follow these protein complexes into their membrane-associated vesicle populations on intracellular membranes or at the plasma membrane, respectively. This finding is consistent with a possible chaperone function for p34, as previously suggested[10]. For example, p34 might either prevent soluble clathrin from assembling with soluble adaptor complexes in the cytosol, be involved in vesicle uncoating or aid recruitment of soluble adaptors to membranes[10]. Bioinformatics analysis identified a GTPase domain in p34, which is most closely related to the Rab superfamily of vesicular trafficking proteins (**Fig. 2** and **Supplementary Fig. 6**). It is not known whether this GTPase domain is functional. If this is the case, our finding may be indicative of a role for p34 in the active transport of cytosolic adaptor complexes rather than a more passive chaperone function[14].

Ultrastructural analysis of lesional plantar skin showed mild acanthosis, a reduction in the granular cell layer and compact orthokeratosis (**Supplementary Fig. 7**). In basal keratinocytes (**Fig. 5**), there was a large increase in the number of small vesicles
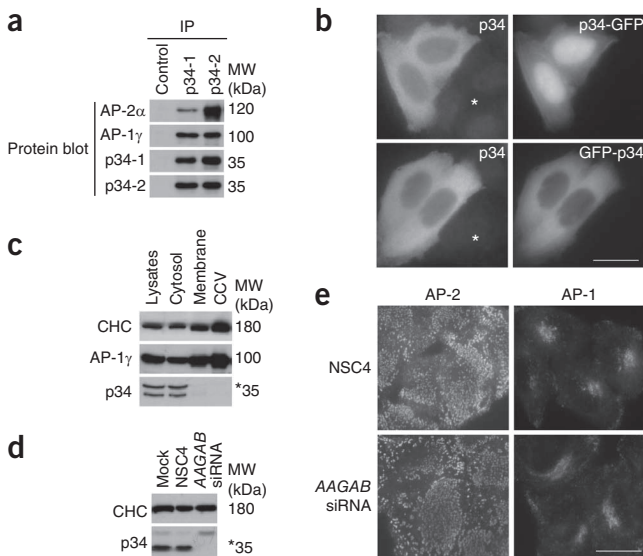

Figure 4 p34 associates with AP-1 and AP-2 in the cytosol. (**a**) Native immunoprecipitation of HeLa cytosolic extracts was performed with antibodies against p34, α-adaptin (detecting the AP-2 complex) and γ-adaptin (detecting the AP-1 complex). (**b**) HeLa cells were transiently transfected with constructs encoding p34 fused with GFP either at the C terminus (p34-GFP) or N terminus (GFP-p34). Both fusion proteins show a mainly cytosolic localization, consistent with the staining pattern (albeit faint) observed using antibody against p34 in either transfected or untransfected cells (*). (**c**) HeLa cell lysates were subjected to fractionation into cytosol, membrane and clathrin-coated vesicle (CCV) fractions, and protein blot analysis was performed for clathrin heavy chain (CHC), AP-1 and p34. *, cross-reacting band. (**d**) HeLa cells were treated with siRNA (SMARTpool, Thermo-Fisher) to reduce expression of p34, and protein blot analysis was performed for CHC and p34. *, cross-reacting band. The amount of p34 protein was reduced by >95% in cells transfected with *AAGAB* siRNA. (**e**) Localization of AP-1 and AP-2 visualized by immunofluorescence after knockdown of *AAGAB*. AP-2–containing membrane-associated vesicles and AP-1–TGN appear unperturbed. Scale bars, 20 μm.
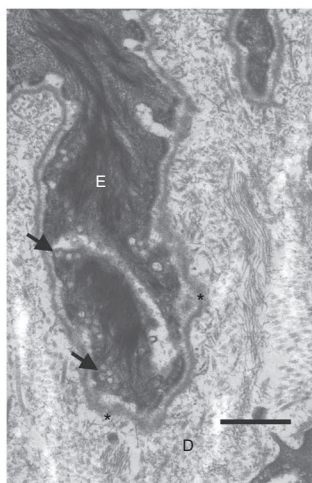
Figure 5 Transmission electron microscopy of lesional plantar skin shows vesicle abnormalities within basal keratinocytes. Transmission electron microscopy of a basal epidermal keratinocyte (E) within PPKP1 lesional epidermis shows an abnormal abundance of membrane-bound vesicles abutting the plasma membrane (arrows), close to the cutaneous basement membrane (*). D, dermis. Scale bar, 0.2 μm. Additional electron micrographs are shown in **Supplementary Figure 7**.

close to the cell membrane and prominent dilatation of the Golgi apparatus in lesional epidermis compared to normal, control skin (**Supplementary Fig. 7**). These ultrastructural features are consistent with a defect in vesicle transport.

We hypothesized that a mechanism whereby perturbation of vesicle trafficking could lead to increased epidermal proliferation might involve recycling of EGFR. EGFR is known to undergo rapid turnover in a process that requires a number of sorting steps, including clathrin- and AP-2–dependent endocytosis[15,16]. Internalized ligand-bound EGFR is either shuttled to late endosomes/lysosomes for degradation or into recycling endosomes, where, after removal of the bound ligand and dephosphorylation, the receptor is returned to the plasma membrane via vesicle fusion. Knockdown of *AAGAB* in HaCaT cells led to a modest ~2.5-fold increase in *EGFR* mRNA levels relative to cells transfected with control siRNA, as determined by qRT-PCR (data not shown); however, the amount of total EGFR protein was >10-fold higher in protein blot analysis (**Fig. 6a**), consistent with decreased EGFR turnover. Notably, phosphorylation of EGFR at Tyr992, indicating active EGFR signaling[17], was increased by >20-fold in cells with *AAGAB* knockdown (**Fig. 6b**). The regulation of EGFR signaling via clathrin-mediated endocytosis is a complex process mediated by Rab proteins[15], dynamin[18], AP-2 and the Grb2 adaptor protein that involves multiple mechanisms relating to post-translational modification of the receptor itself[19]. Disruption of EGFR endocytosis by double knockout of the *Dnm1* and *Dnm2* genes encoding the motor proteins dynamin-1 and dynamin-2, respectively, in mouse has been shown to result in decreased protein turnover with increased EGFR signaling[18], very similar to what we observed with knockdown of *AAGAB*.

Here, using a combination of genetic linkage analysis and whole-exome sequencing, we have identified mutations in the *AAGAB* gene, encoding p34, that cause the autosomal dominant form of punctate PPK that was previously linked to 15q22 known as PPKP1 (MIM 148600)[5,6,9]. AP-2 is known to be involved in EGFR endocytosis[19], and we confirmed here that p34 binds cytosolic AP-2 (**Fig. 4**) and show that p34 deficiency results in increased epidermal cell proliferation

(**Fig. 1f** and **Fig. 3**). Overall, p34 seems to have a hitherto unrecognized role in the control of cell division, possibly by contributing to normal endocytic recycling of receptor tyrosine kinases, such as EGFR[15,16,18,19]. Other genes involved in intracellular vesicle trafficking have been linked to inherited skin diseases where hyperkeratosis and/or keratoderma form part of the phenotypic constellation. These genes include *SNAP29* in cerebral dysgenesis, neuropathy, ichthyosis and keratoderma (CEDNIK) syndrome[20] and *VPS33B* in arthrogryposis, renal dysfunction and cholestasis (ARC) syndrome[21], both of which encode proteins required for vesicle membrane fusion in the epidermis and other tissues. Moreover, loss-of-function mutations in *AP1S1*, which encodes the small σ1A subunit of the AP-1 complex, have been shown to cause the recessive neurocutaneous disorder mental retardation, enteropathy, deafness, peripheral neuropathy, ichthyosis and keratodermia (MEDNIK)[22]. Similarly, defects in multiple proteins involved in melanosome transport and fusion lead to the pigmentation disorder Griscelli syndrome[23], and mutations in the gene encoding the AP-3 subunit protein β3A have been linked to Hermansky-Pudlak syndrome type 2, which consists of oculocutaneous albinism and other features[24]. Thus, mutations in a growing number of genes involved in vesicle transport have been linked to genetic skin disease, with or without extracutaneous phenotypes.

Disruption of EGFR signaling is a feature of neoplasia. There are anecdotal reports of cancer occurring in association with punctate PPK[25]; however, without genetic testing, we cannot determine whether the *AAGAB* gene was involved in those cases. Although a few cases of cancer were reported in the larger families studied here, we did not observe cosegregation with the *AAGAB* mutations, and, therefore, any causal link between *AAGAB* mutations and cancer remains unproven.

It remains unclear why haploinsufficiency for this widely expressed gene leads to a phenotype limited to palm and sole epidermis, although this is not unusual in hereditary skin disease. For example, haploinsufficiency for the *DSP* or *DSG1* genes encoding the desmosomal proteins desmoplakin and desmoglein-1, respectively (refs. 26,27), both of which are structural proteins expressed throughout the epidermis, lead to striate palmoplantar keratoderma[28]. Another unanswered question relates to why the hyperkeratotic lesions are focal. These lesions are late in onset, appearing in the first or second decade of life, and increase in number with advancing age. This pattern of appearance might be explained by a 'second hit' mutation in *AAGAB*, and we therefore sequenced the gene using genomic DNA derived from microdissected lesional tissue from more than one affected individual. We found neither loss of heterozygosity nor a
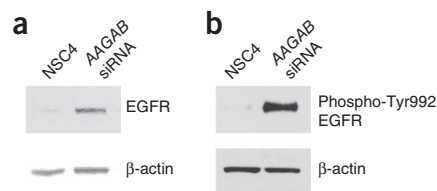

Figure 6 Knockdown of *AAGAB* greatly increases EGFR protein expression. (**a**) Knockdown of *AAGAB* with siRNA 1239 leads to greatly increased EGFR protein expression relative to cells transfected with NSC4. Part of the blot was stained for β-actin for a loading control and to normalize EGFR quantification. Using the LI-COR Odyssey system, the observed upregulation of EGFR was found to be greater than tenfold. (**b**) Knockdown of *AAGAB* with siRNA 1239 also leads to greatly increased phosphorylation of Tyr992 on the EGFR protein compared to transfection with NSC4. Using the LI-COR Odyssey system, the observed increase in phosphorylation of this residue was found to be >20-fold.

second compound heterozygous *AAGAB* mutation (data not shown). We also attempted immunohistochemistry; however, neither the in-house nor commercially available antibody to p34 gave a signal on fixed abdominal tissue from a normal control. It is also possible that a second somatic mutation might occur in a gene other than *AAGAB*.

In conclusion, this study expands the molecular diagnostic repertoire for keratodermas and shows that the p34 protein, which is associated with AP-1 and AP-2, is involved in regulating epidermal cell division.

URLs. The Eastern Sequence and Informatics Hub (EASIH), http://www.easih.ac.uk/; Pachyonychia Congenita Project, http://www.pachyonychia.org/.

METHODS
Methods and any associated references are available in the online version of the paper.

Note: Supplementary information is available in the online version of the paper.

COMPETING FINANCIAL INTERESTS
The authors declare no competing financial interests.

1. Itin, P.H. & Fistarol, S.K. Palmoplantar keratodermas. *Clin. Dermatol.* **23**, 15–22 (2005).
2. Stevens, H.P. *et al.* Linkage of an American pedigree with palmoplantar keratoderma and malignancy (palmoplantar ectodermal dysplasia type III) to 17q24. Literature survey and proposed updated classification of the keratodermas. *Arch. Dermatol.* **132**, 640–651 (1996).
3. Kelsell, D.P. & Stevens, H.P. The palmoplantar keratodermas: much more than palms and soles. *Mol. Med. Today* **5**, 107–113 (1999).
4. Emmert, S. *et al.* 47 patients in 14 families with the rare genodermatosis keratosis punctata palmoplantaris Buschke-Fischer-Brauer. *Eur. J. Dermatol.* **13**, 16–20 (2003).
5. Martinez-Mir, A. *et al.* Identification of a locus for type I punctate palmoplantar keratoderma on chromosome 15q22-q24. *J. Med. Genet.* **40**, 872–878 (2003).
6. Gao, M. *et al.* Refined localization of a punctate palmoplantar keratoderma gene to a 5.06-cM region at 15q22.2–15q22.31. *Br. J. Dermatol.* **152**, 874–878 (2005).
7. Jung, E.G. Acrokeratoelastoidosis. *Humangenetik* **17**, 357–358 (1973).
8. Zhang, X.J. *et al.* Identification of a locus for punctate palmoplantar keratodermas at chromosome 8q24.13–8q24.21. *J. Invest. Dermatol.* **122**, 1121–1125 (2004).
9. El Amri, I. *et al.* Clinical and genetic characteristics of Buschke-Fischer-Brauer's disease in a Tunisian family. *Ann. Dermatol. Venereol.* **137**, 269–275 (2010).
10. Page, L.J., Sowerby, P.J., Lui, W.W. & Robinson, M.S. γ-synergin: an EH domain–containing protein that interacts with γ-adaptin. *J. Cell Biol.* **146**, 993–1004 (1999).
11. Boukamp, P. *et al.* Normal keratinization in a spontaneously immortalized aneuploid human keratinocyte cell line. *J. Cell Biol.* **106**, 761–771 (1988).
12. Robinson, M.S. & Bonifacino, J.S. Adaptor-related proteins. *Curr. Opin. Cell Biol.* **13**, 444–453 (2001).
13. Robinson, M.S. Adaptable adaptors for coated vesicles. *Trends Cell Biol.* **14**, 167–174 (2004).
14. Horgan, C.P. & McCaffrey, M.W. Rab GTPases and microtubule motors. *Biochem. Soc. Trans.* **39**, 1202–1206 (2011).
15. Ceresa, B.P. Regulation of EGFR endocytic trafficking by rab proteins. *Histol. Histopathol.* **21**, 987–993 (2006).
16. Rappoport, J.Z. & Simon, S.M. Endocytic trafficking of activated EGFR is AP-2 dependent and occurs through preformed clathrin spots. *J. Cell Sci.* **122**, 1301–1305 (2009).
17. Downward, J., Parker, P. & Waterfield, M.D. Autophosphorylation sites on the epidermal growth factor receptor. *Nature* **311**, 483–485 (1984).
18. Sousa, L.P. *et al.* Suppression of EGFR endocytosis by dynamin depletion reveals that EGFR signaling occurs primarily at the plasma membrane. *Proc. Natl. Acad. Sci. USA* **109**, 4419–4424 (2012).
19. Goh, L.K., Huang, F., Kim, W., Gygi, S. & Sorkin, A. Multiple mechanisms collectively regulate clathrin-mediated endocytosis of the epidermal growth factor receptor. *J. Cell Biol.* **189**, 871–883 (2010).
20. Sprecher, E. *et al.* A mutation in *SNAP29*, coding for a SNARE protein involved in intracellular trafficking, causes a novel neurocutaneous syndrome characterized by cerebral dysgenesis, neuropathy, ichthyosis, and palmoplantar keratoderma. *Am. J. Hum. Genet.* **77**, 242–251 (2005).
21. Gissen, P. *et al.* Mutations in *VPS33B*, encoding a regulator of SNARE-dependent membrane fusion, cause arthrogryposis–renal dysfunction–cholestasis (ARC) syndrome. *Nat. Genet.* **36**, 400–404 (2004).
22. Montpetit, A. *et al.* Disruption of *AP1S1*, causing a novel neurocutaneous syndrome, perturbs development of the skin and spinal cord. *PLoS Genet.* **4**, e1000296 (2008).
23. Van Gele, M., Dynoodt, P. & Lambert, J. Griscelli syndrome: a model system to study vesicular trafficking. *Pigment Cell Melanoma Res.* **22**, 268–282 (2009).
24. Tarpey, P.S. *et al.* Mutations in the gene encoding the Sigma 2 subunit of the adaptor protein 1 complex, *AP1S2*, cause X-linked mental retardation. *Am. J. Hum. Genet.* **79**, 1119–1124 (2006).
25. Bennion, S.D. & Patterson, J.W. Keratosis punctata palmaris et plantaris and adenocarcinoma of the colon. A possible familial association of punctate keratoderma and gastrointestinal malignancy. *J. Am. Acad. Dermatol.* **10**, 587–591 (1984).
26. Armstrong, D.K. *et al.* Haploinsufficiency of desmoplakin causes a striate subtype of palmoplantar keratoderma. *Hum. Mol. Genet.* **8**, 143–148 (1999).
27. Wan, H. *et al.* Striate palmoplantar keratoderma arising from desmoplakin and desmoglein 1 mutations is associated with contrasting perturbations of desmosomes and the keratin filament network. *Br. J. Dermatol.* **150**, 878–891 (2004).
28. McLean, W.H. Genetic disorders of palm skin and nail. *J. Anat.* **202**, 133–141 (2003).

ONLINE METHODS

Affected individuals and phenotypes. Individuals from 18 apparently unrelated families presented with PPK at dermatology clinics in Scotland, Ireland, Japan and Tunisia. Clinical examination and histological analysis of affected persons was consistent with a diagnosis of the Buschke-Fischer-Brauer type of punctate PPK (PPKP1; MIM 148600)[2]. In severely affected cases, where keratoderma resembled plantar warts, the presence of HPV was excluded in the clinical work-up. Blood samples were obtained in tubes containing the anticoagulant EDTA from the affected individuals with written informed consent and approval from the institutional ethics committee (Tayside Committee on Research Ethics, Dundee, UK) that complied with the Declaration of Helsinki Principles. DNA was extracted using standard procedures.

Linkage analysis. Microsatellite genotypes were generated for members of family 15 using standard protocols. LOD scores were calculated using FASTLINK[29,30], assuming a mutant allele frequency of 1 in 50,000. The LOD scores were recalculated assuming a 10% chance of non-penetrance because of difficulty in obtaining a definitive clinical ascertainment in some individuals in family 15 (the family resides in a remote mountainous area of Tunisia).

Exome sequencing. Exome enrichment was performed using the Agilent SureSelect 50Mb exome enrichment system, using the protocol for Applied Biosystems SOLiD (Protocol version 1.0, May 2010). Sequencing was then performed on the ABI SOLiD platform (Applied Biosystems), with an average sequencing depth of >30× across the exome. Next-generation sequencing and SNP calling were performed by The Eastern Sequence and Informatics Hub (EASIH; see URLs). To simplify filtering of the exome data, all SNP calls were put into a MySQL database and queried via an in-house web-based django front-end.

Histology. Routine hematoxylin and eosin staining of paraffin-embedded tissue was performed using standard protocols. Immunohistochemical staining for the cell proliferation marker Ki67 was performed using polyclonal antibody HPA000451 (Sigma-Aldrich).

Mutation analysis of the *AAGAB* gene. The individual exons of *AAGAB* were amplified by PCR using genomic primers (sequences listed in **Supplementary Table 5**) and the following cycling conditions: 1 cycle at 94 °C for 5 min; 35 cycles at 94 °C for 30 s, 55 °C for 30 s and 72 °C for 1 min; and 1 final extension at 72 °C for 5 min.

Cell culture. HaCaT keratinocytes were maintained in a monolayer in 5% CO_2 in DMEM (Invitrogen) supplemented with 10% FCS. Normal human keratinocytes were obtained from CELLnTECH and cultured in the defined growth medium CnT57 (TCS Cellworks). HeLa cells were cultured in DMEM supplemented with 10% FCS, 2 mM L-glutamine, 50 U/ml penicillin and 50 μg/ml streptomycin (Sigma-Aldrich).

RT-PCR. Total RNA was extracted from cultured HaCaT cells and primary keratinocytes using the RNeasy Mini kit (Qiagen). RNA (1 μg) was reverse transcribed using AMV Reverse Transcriptase (Promega) and oligo(dT)$_{15}$ (Roche Diagnostics). We used 1 μl of the reaction mix in subsequent PCR with Expand High Fidelity PCR buffer containing 1.5 mM $MgCl_2$ and 0.5 U of High Fidelity DNA Polymerase (Roche Diagnostics). Primers AAGAB5intFor and AAGAB8intRev (see **Supplementary Table 5**) were used to amplify a 292-bp fragment with the following cycling conditions: 1 cycle at 94 °C for 5 min; 35 cycles at 94 °C for 30 s, 52 °C for 30 s and 72 °C for 30 s; and a final extension at 72 °C for 5 min.

Isolation of RNA and gene expression analysis. RNA was isolated from abdominal skin, primary keratinocytes, and HaCaT and HeLa cells using the RNeasy Mini kit and was treated with RNase-Free DNase (Qiagen) to remove any contaminating genomic DNA. We reverse transcribed 1 μg of each using the High-Capacity cDNA Reverse Transcription kit (Applied Biosystems). Then, 1 μl of each reaction was used in quantitative PCR performed with Perfecta qPCR ToughMix, ROX (Quanta Biosciences) on a 7900HT Fast Real-Time

PCR system (Applied Biosystems). TaqMan Gene Expression Assays (Life Technologies) for *AAGAB* (Hs01027607_m1) and *GAPDH* (4310884E) were used according to the manufacturer's recommendations.

Multiple-tissue expression analysis. A cDNA clone was generated and used to produce a standard curve for copy-number estimation by qRT-PCR. To make this construct, cDNA was generated by reverse transcription of RNA from HaCaT cells and was used as a template for the amplification of a 940-bp *AAGAB* cDNA fragment using the primers P34clone1 and P34clone2 (**Supplementary Table 5**). The cDNA was cloned as a fragment flanked by EcoRI and HindIII restriction endonuclease sites and was inserted into pcDNA3.1(-)/*myc*-His A (Life Technologies). A normalized cDNA panel from 48 different human tissues (Origene Technologies) was quantified by TaqMan Gene Expression Assay Hs01027607_m1. The standard used in this assay was plasmid DNA encoding wild-type *AAGAB*. The standard curve was calculated using the formulae described by Applied Biosystems.

siRNA knockdown of *AAGAB* in HaCaT cells. siRNA oligonucleotides targeting *AAGAB* and a scrambled negative control were obtained from Eurofins MWG Operon. The sequences of the siRNAs specific for *AAGAB* (designated AAGAB1239 and AAGAB2164) and the non-specific control siRNA (designated NSC4; a scrambled bacterial *lacZ* sequence) are shown in **Supplementary Table 5**. We plated 1.2×10^5 HaCaT cells in each well of a 6-well dish containing DMEM supplemented with 10% FCS and transfected the cells with siRNA at a final concentration of 5 nM using Lipofectamine RNAiMAX Reagent (Invitrogen). Cells were incubated for 72 or 96 h before harvesting for RNA extraction and protein isolation and for cell proliferation analysis.

Cell proliferation analysis. HaCaT cells were transfected with siRNA and incubated for 96 h. Cells were washed with PBS and detached from the dishes using 0.05% trypsin-EDTA. Counts of viable cells (after trypan blue staining) were obtained using a hemocytometer.

Antibodies to α- and γ-adaptin–binding protein p34. Two affinity-purified rabbit polyclonal antibodies, p34-1 and p34-2, were raised using a glutathione S-transferase (GST) fusion protein consisting of residues 142–315 (the C terminus) of rat α- and γ-adaptin–binding protein p34 (85% identical and 91% similar to the human protein). These antibodies were used for the HeLa cell experiments (protein blot analysis and immunofluorescence). For the HaCaT cell experiments, rabbit polyclonal antibody to α- and γ-adaptin–binding protein p34 was used (HPA040174, Sigma-Aldrich). Protein blotting and immunofluorescence of HeLa cells was repeated using the Sigma-Aldrich antibody with very similar results (data not shown). Similarly, protein blotting and immunofluorescence of HaCaT cells was repeated using p34-2 with similar results (data not shown).

Protein blotting of HaCaT lysates and EGFR quantification. Cells were rinsed in ice-cold PBS, lysed in SDS lysis buffer (1% SDS, 20 mM Tris-HCl, pH 8.0, 137 mM NaCl, 10% glycerol, 2 mM EDTA) with added protease inhibitor cocktail (Sigma-Aldrich), phosphatase inhibitor cocktail (Sigma-Aldrich) and 25 U/ml Benzonase (Merck) and incubated at room temperature for 10 min with agitation. Lysates were cleared by centrifugation at 10,000*g* for 10 min at 4 °C, and protein concentration was determined using the Bio-Rad Protein Assay. For each sample, 10 μg of total protein was separated on NuPAGE 4–12% Bis-Tris polyacrylamide gels (Invitrogen) in NuPAGE MOPS running buffer (Invitrogen) and blotted onto Hybond-C Extra (GE Healthcare). Membranes were probed with a 1:1,000 dilution of the appropriate primary antibody (rabbit antibody to α- and γ-adaptin–binding protein p34, Sigma-Aldrich), rabbit antibody to EGFR (4267P, Cell Signaling Technology) or a 1:10,000 dilution of mouse antibody to β-actin (A5441, Sigma-Aldrich). Membranes were then incubated with a 1:1,000 dilution of horseradish peroxidase (HRP)-conjugated goat secondary antibody to rabbit or HRP-conjugated rabbit secondary antibody to mouse (Dako). Immobilon Western Chemiluminescent HRP substrate (Millipore) was used for visualization. For detection of phosphorylated EGFR, blots were blocked in 3% BSA in PBS containing 0.1% Tween-20 (PBST) and 10 mM β-glycerophosphate for

1 h at room temperature and incubated overnight in a 1:1,000 dilution of antibody to phosphorylated EGFR (Tyr992; 2235, Cell Signaling Technology) in PBST containing 10 mM β-glycerophosphate at 4 °C. Blots were washed in three changes of PBST containing 10 mM β-glycerophosphate and incubated in a 1:1,000 dilution of HRP-conjugated goat secondary antibody to rabbit in PBST containing 10 mM β-glycerophosphate for 1 h at room temperature. After washing, blots were developed using enhanced chemiluminescence (ECL). For detection of β-actin, blots were blocked and antibodies were diluted in 5% non-fat milk in PBST under the same conditions as described above. A dilution of 1:10,000 was used for the antibody to actin (Sigma-Aldrich), and a 1:1,000 dilution was used for the secondary HRP-conjugated rabbit antibody to mouse. Quantification of protein bands on blots was performed using a LI-COR Odyssey infrared imaging system.

HeLa cell transfection. Transfection of HeLa cells with siRNA was achieved with Oligofectamine (Invitrogen) following the manufacturer's instructions, using 25 mM siRNA and incubating for 72 h. Knockdown of *AAGAB* was achieved using an siGENOME SMARTpool (M-0159891), and control knockdown was performed with a non-targeting siRNA (D-001810-10) (both from Thermo-Fisher). Transient transfections with plasmid DNA encoding GFP-tagged protein was achieved using HeLa Monster transfection reagent (Cambridge Bioscience) following the manufacturer's instructions and transfecting 48 h before imaging. For immunofluorescence, cells were grown on glass-bottom coverslips (MatTek), fixed in 3% formaldehyde in PBS at room temperature and permeabilized with 0.1% Triton X-100. Cells were imaged with a Zeiss Axiovert 200 inverted microscope using a Zeiss Plan Achromat 63× oil immersion objective, a Hamamatsu ORCA-ER2 camera and Improvision Openlab software (PerkinElmer).

Protein blot, immunofluorescence and immunoprecipitation in HeLa cells. These experiments were performed with antibodies raised in house, including to α- and γ-adaptin–binding protein p34 (p34-1, p34-2), AP-2α, AP-1γ and clathrin heavy chain[10]. Antibody p34-2 was used to detect α- and γ-adaptin–binding protein p34 unless otherwise specified. Constructs encoding N- and C-terminally tagged α- and γ-adaptin–binding protein p34 were constructed from rat cDNA[10] (human and rat AP-1γ share 99% amino-acid identity) by PCR amplification and cloned in frame into pEGFP-N3 (p34-GFP) or pEGFP-C1 (GFP-p34) (plasmids from Takara Bio Europe/Clontech) using HindIII and KpnI restriction sites. The sequences of both constructs were verified by Sanger sequencing analysis.

Immunoprecipitation and clathrin-coated vesicle isolation in HeLa cell extracts. For immunoprecipitation, cells were lysed in PBS containing 1% IGEPAL (Sigma-Aldrich). Lysates were cleared of debris by centrifugation, and antibody-protein complexes were captured using Protein A Sepharose (Pharmacia). Samples were then analyzed by PAGE and protein blotting. Blots were probed with various antibodies, and signals were visualized with the ECL Plus Western Blotting Detection System (GE Healthcare). Control clathrin-coated vesicle–enriched fractions were prepared as described previously[31], except that the final pelleting step was performed at 86,900*g* for 30 min to improve yield.

Ultrastructural analysis. Skin biopsy specimens were cut into small pieces (of <1 mm^3) and fixed in half-strength Karnovsky fixative for 4 h at room temperature. After washing in 0.1 M sodium phosphate buffer (pH 7.4), samples were immersed in 1.3% aqueous osmium tetroxide (TAAB Laboratories) for 2 h. Samples were then incubated in 2% uranyl acetate (Bio-Rad) and dehydrated in a graded ethanol series. We embedded the samples in epoxy resin via propylene oxide (TAAB Laboratories). Ultra-thin sections were stained with uranyl acetate and lead citrate and examined on a Philips CM10 transmission electron microscope.

29. Cottingham, R.W. Jr., Idury, R.M. & Schaffer, A.A. Faster sequential genetic linkage computations. *Am. J. Hum. Genet.* **53**, 252–263 (1993).
30. Schäffer, A.A., Gupta, S.K., Shriram, K. & Cottingham, R.W. Jr. Avoiding recomputation in linkage analysis. *Hum. Hered.* **44**, 225–237 (1994).
31. Hirst, J., Miller, S.E., Taylor, M.J., von Mollard, G.F. & Robinson, M.S. EpsinR is an adaptor for the SNARE protein Vti1b. *Mol. Biol. Cell* **15**, 5593–5602 (2004).

Mutations in *IRX5* impair craniofacial development and germ cell migration via SDF1

Carine Bonnard[1], Anna C Strobl[2], Mohammad Shboul[1], Hane Lee[3], Barry Merriman[3], Stanley F Nelson[3], Osama H Ababneh[4], Elif Uz[5,6], Tülay Güran[7], Hülya Kayserili[8], Hanan Hamamy[9,10] & Bruno Reversade[1,11]

Using homozygosity mapping and locus resequencing, we found that alterations in the homeodomain of the IRX5 transcription factor cause a recessive congenital disorder affecting face, brain, blood, heart, bone and gonad development. We found through *in vivo* modeling in *Xenopus laevis* embryos that Irx5 modulates the migration of progenitor cell populations in branchial arches and gonads by repressing *Sdf1*. We further found that transcriptional control by Irx5 is modulated by direct protein-protein interaction with two GATA zinc-finger proteins, GATA3 and TRPS1; disruptions of these proteins also cause craniofacial dysmorphisms. Our findings suggest that IRX proteins integrate combinatorial transcriptional inputs to regulate key signaling molecules involved in the ontogeny of multiple organs during embryogenesis and homeostasis.

Development and evolution of craniofacial structures are driven by a transient cell population of embryonic origin known as cranial neural crest cells (NCCs). Changes in their proliferation or migration have led to diverse head shapes among living or extinct species of fish, amphibians, reptiles, birds and mammals[1,2]. This phylogenetic plasticity is limited, however, by the need to develop cardinal organs in the head region for cognition, sight, smell, taste, hearing, balance and touch. NCCs also contribute to the morphogenesis of secondary organs such as dental, lacrimal, salivary and thyroid structures[3]. As a result, even small alterations in craniofacial morphogenesis can lead to substantial structural or functional congenital anomalies of the human head[4].

Here we report on the genetic, molecular and developmental etiology of a new autosomal recessive human syndrome[5] (MIM611174) that is marked by defective craniofacial morphogenesis and heart, blood, bone and germ cell ontogeny. In two consanguineous families, we diagnosed five probands (**Fig. 1a**) with a unique set of craniofacial dysmorphisms, including severe telecanthus, myopia, hypoplasia of the lacrimal-salivary apparatus, frontonasal anomalies, protruding ears and sensorineural hearing impairment (**Fig. 1b–e** and **Supplementary Fig. 1**). Skeletal anomalies with repeated fractures of long bones (**Fig. 1f** and **Supplementary Fig. 1**), hypodontia (**Fig. 1g**), microcytic hypochromic anemia (**Fig. 1h,i**) and congenital heart defects with intraventricular conduction delay (**Fig. 1j**) were also documented in all affected individuals. This syndrome includes a wide range of clinical symptoms (**Supplementary Table 1**).

Assuming a common etiology in both families, we carried out identical-by-descent (IBD) homozygosity mapping and delineated a single candidate locus of 9.2 Mb on chromosome 16. We used targeted genomic locus capturing followed by high-throughput resequencing[6,7] to screen the 73 candidate genes in this region (**Fig. 1k**). In the Jordanian family, we identified 204 genomic mismatches in subject 1; only two of these were newly identified homozygous and nonsynonymous in the *SLC12A3* and *IRX5* (c.498C>A) genes (**Fig. 1k** and **Supplementary Table 2**). In the Turkish family, we identified a distinct homozygous mutation (c.448G>C) in the *IRX5* gene (NM_005853.5) segregating with the disease. The Iroquois (*IRX*) genes encode a family of six conserved transcription factors (IRX1 to IRX6) that specify the identity of precise body parts via spatial and temporal regulation of target genes[8]. The *IRX5* variants, which were homozygous in the index cases but not in the unaffected relatives, led to the amino acid alterations p.Ala150Pro and p.Asn166Lys, altering two residues that are phylogenetically invariant in all known IRX paralogs and orthologs (**Fig. 2a** and **Supplementary Fig. 2**). Taken together, these results show that biallelic mutations in the *IRX5* homeobox cause a congenital disorder affecting the ontogeny and homeostasis of multiple organs.

To examine the allelic strength of these IRX5 missense variants, we carried out *in vitro* luciferase assays using mouse *Irx5* expression constructs and a rat *Kcnd2* promoter reporter[9]. Behaving like an *Irx5*

[1]Institute of Medical Biology, Agency for Science, Technology and Research (A*STAR), Singapore, Singapore. [2]Division of Systems Biology, Medical Research Council National Institute for Medical Research, London, UK. [3]Department of Human Genetics, David Geffen School of Medicine, University of California, Los Angeles, California, USA. [4]Department of Ophthalmology, Faculty of Medicine, University of Jordan, Amman, Jordan. [5]Department of Biology, Faculty of Arts and Sciences, Duzce University, Duzce, Turkey. [6]Gene Mapping Laboratory, Department of Medical Genetics, Hacettepe University Medical Faculty, Ankara, Turkey. [7]Pediatric Endocrinology and Diabetes, Marmara University Hospital, Istanbul, Turkey. [8]Medical Genetics Department, Istanbul Medical Faculty, Istanbul University, Istanbul, Turkey. [9]Department of Genetic Medicine and Development, Geneva University Hospital, Geneva, Switzerland. [10]National Center for Diabetes, Endocrinology and Genetics, Amman, Jordan. [11]Department of Pediatrics, National University of Singapore, Singapore. Correspondence should be addressed to B.R. (bruno@reversade.com).

Figure 1 Clinical and genetic findings in five probands diagnosed with Hamamy syndrome. (**a**) Pedigrees of two inbred families from Jordan and Turkey. Filled black symbols, affected individuals (1–5). Crossed symbols, individual deceased. Small black circle, miscarriage (sex unspecified). SB, stillborn. (**b–e**) Full facial photographs of affected individuals with common craniofacial dysmorphisms, including midface prominence, sparse lateral eyebrows, severe telecanthus, agenesis of lacrimal punctuae (**b**, inset), anteverted nostrils, pointed nasal tip, flat philtrum, thin upper vermillion border and protruding ears (**c,e**, inset). Participants gave consent for publication of all photos. (**f**) Femoral radiograph of subject 5 showing multiple fractures and corrective osteotomy. (**g**) Panoramic radiograph of maxilla and mandible of subject 5 showing loss of lamina dura and teeth malocclusion. (**h,i**) Blood cell separation by density-gradient centrifugation and blood smear of mother of subject 5 (**h**) and subject 5 (**i**) show hypochromic microcytic anemia. Scale bar, 10 μm. (**j**) Electrocardiogram of subjects 1–3 showing left intraventricular conduction delay (QRS complex >100 ms). V1, fourth intercostal right chest lead. (**k**) Homozygosity mapping delineated a single candidate locus encompassing 73 genes on chromosome 16q12.2-q21 (Chr. 16). Locus capture followed by massive parallel resequencing in subject 1 identified a single biallelic base pair change (c.498C>A) in the *IRX5* gene, leading to a missense alteration (p.Asn166Lys) in the IRX5 transcription factor.
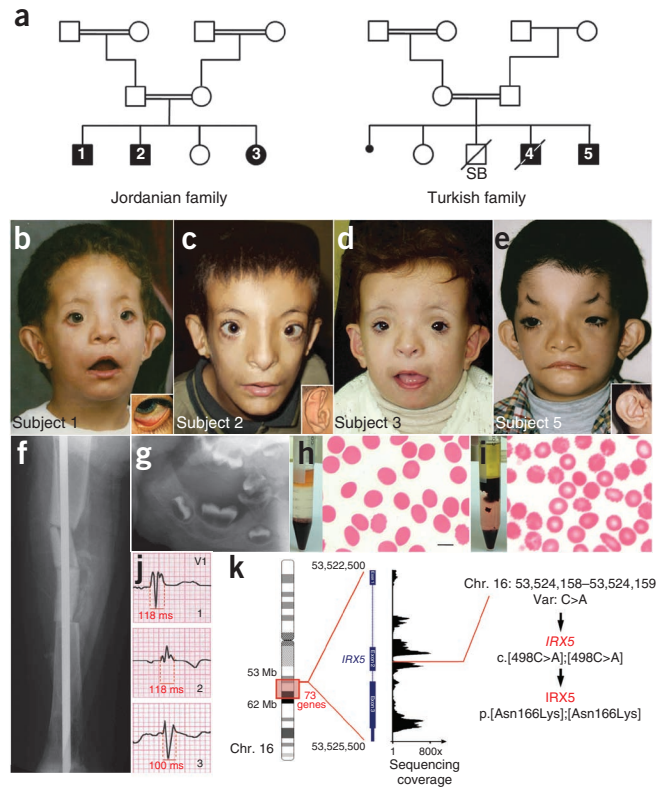
construct lacking its homeobox[9], the two Irx5 missense variants could not transactivate *Kcnd2*, in contrast with wild-type Irx5 (**Fig. 2b**). Whereas wild-type Irx5 and the p.Asn166Lys variant were stable, the p.Ala150Pro variant was rapidly degraded via ubiquitin-mediated proteolysis in cultured 10T1/2 cells (**Fig. 2c**). This is in agreement with earlier reports on alterations affecting the same homeodomain residues of helices 2 and 3, which affect protein stability and DNA binding, respectively[10].

To investigate the role of Irx5 during craniofacial development, we examined whether its depletion in *X. laevis* embryos could partly model the human syndrome. *Irx5* knockdown by morpholino injection[11] showed that blood, heart, germ cell and craniofacial anomalies could be recapitulated *in vivo* (**Fig. 3** and **Supplementary Fig. 3**). In particular, *Irx5* morphant embryos showed defective cranial NCC migration in the first branchial arch; this could be rescued by injection of wild-type mouse *Irx5* DNA but not p.Ala150Pro *Irx5* DNA (**Fig. 3a–d**).

However, the p.Asn166Lys variant, as compared with wild-type Irx5, allowed partial repopulation of NCCs to the first branchial arch of *Irx5* morphants (**Fig. 3c,e**). With all constructs being equally transcribed, the p.Ala150Pro Irx5 variant was unstable in embryos relative to wild-type Irx5 and the p.Asn166Lys Irx5 variant (**Fig. 3f**), in agreement with results obtained in cultured cells (**Fig. 2c**). Taken together, these data suggest that the p.Ala150Pro and p.Asn166Lys variants do not behave as null alleles. Rather, owing to their altered protein stability and DNA binding activity, these missense *IRX5* variants may act as hypomorphic alleles.

To gain mechanistic insight into the etiology of NCC defects observed in *Irx5* morphants, we conducted an exploratory microarray experiment comparing *Irx5* morpholino–injected and control embryos at neurulation. *Sdf1* (also known as *Cxcl12*), which encodes a chemokine essential for cranial NCC migration[12], was found nearly 20-fold upregulated in *Irx5*-depleted embryos relative to control embryos. Ectopic expression of *Sdf1* in developing head of *Irx5* morphants was confirmed by *in situ* hybridization (**Fig. 3g,h**).
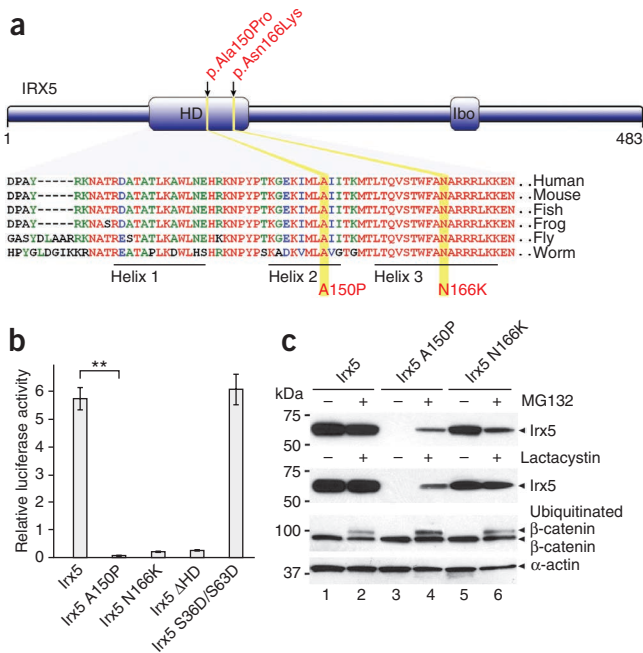
Figure 2 Homeodomain IRX5 missense variants behave as hypomorphs. (**a**) Human IRX5 contains two conserved regions, a homeodomain (HD) and an Iro box (Ibo). The p.Ala150Pro and p.Asn166Lys missense variants map to IRX5 homeodomain helices 2 and 3, respectively. These two residues are invariant in all vertebrate and invertebrate IRX5 homologs. (**b**) Transient cotransfections of 10T1/2 cells with constructs encoding mouse Irx5 A150P, N166K and ΔHD variants with an Irx5 reporter construct (rat *Kcnd2* promoter luciferase) show total abrogation of transcriptional activity relative to constructs for wild-type Irx5 or Irx5 S36D/S63D. Data are mean ± s.d. **$P < 0.005$ (one-tailed Student's *t* test). (**c**) In 10T1/2 cells, Irx5 A150P protein was not detected (lane 3) compared to wild-type Irx5 (lane 1) or Irx5 N166K (lane 5). However, Irx5 A150P protein was stabilized (lane 4) after the addition of proteosomal degradation inhibitors MG132 or lactacystin to the culture medium. β-catenin, ubiquitination control; α-actin, loading control.

Figure 3 *Irx5* orchestrates migration of cranial NCCs and primordial germ cells by repressing *Sdf1* expression. (**a**–**e**) Cranial NCC migration patterns visualized by *Twist1* expression in *X. laevis* embryos. Lateral view of head region of stage 26 embryos, anterior to the left. (**a**) Expression of *Twist1* demarcated NCCs in four branchial arches (1–4; n = 36/36). Dashed red line outlines eye vesicle and dashed white line outlines first branchial arch. Scale bar, 0.25 mm. (**b**) *Irx5* morpholino (MO)-injected embryos specifically lacked NCCs in first branchial arch (n = 23/38). Red arrowhead, ectopic NCC migration over eye vesicles. (**c**) Injection of wild-type mouse *Irx5* DNA in *Irx5* morphant embryos rescued NCC migration to first branchial arch (n = 30/40). (**d**) Injection of DNA encoding mouse Irx5 A150P in *Irx5* morphant embryos did not rescue NCC migration to first branchial arch (n = 27/48). (**e**) Injection of DNA encoding mouse Irx5 N166K partially rescued NCC migration in *Irx5* morphant embryos (n = 23/48). (**f**) Irx5 A150P protein was not detected in embryos injected with DNA encoding mouse Irx5 A150P compared to embryos injected with DNA encoding wild-type mouse Irx5. α-actin, loading control. Quantitative RT-PCR results show comparable transcription for each *Irx5* DNA construct injected. *Actb*, positive control. (**g,h**) At stage 25, *Sdf1* was markedly overexpressed in head region of *Irx5* morphants relative to control embryos (n = 18/18). Scale bar, 0.25 mm. (**i**) Injection of a human *SDF1* promoter reporter showed greater basal luciferase activity in *Irx5*-depleted embryos. Overexpression of mouse *Irx5* in MS5 cells repressed trans-activation of *SDF1* reporter. Data are mean ± s.d. *P < 0.05 (one-tailed Student's t test). (**j**) *Twist1* expression demarcated NCCs in four branchial

arches (1–4; n = 70/70). Dashed red line, eye vesicle. Scale bar, 0.25 mm. (**k**) *Sdf1* morpholino–injected embryos did not show overt NCC migration defects (n = 46/46). (**l**) *Irx5* morpholino–injected embryos lacked NCCs in first branchial arch (n = 37/58). Dashed black line, absence of first branchial arch. (**m**) Reduction of *Sdf1* by injection of *Sdf1* morpholino rescued NCC migration to first branchial arch of *Irx5* morphants (n = 42/58). (**n**) Defective migration of primordial germ cells marked by *Xpat* was seen in *Irx5* morphant embryos (n = 33/40). Scale bar, 0.5 mm.
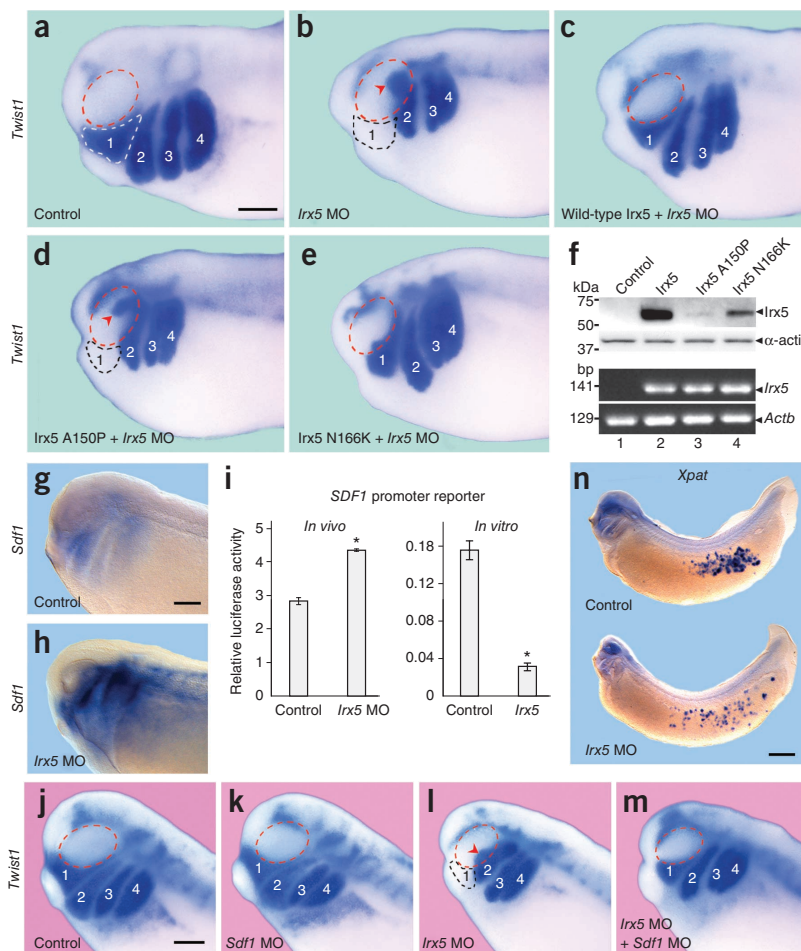
Injection of a human *SDF1* promoter luciferase reporter[13] into *Irx5*-depleted embryos led to greater luciferase activity compared with wild type (**Fig. 3i**). Conversely, overexpression of wild-type mouse *Irx5* DNA in cultured cells was sufficient to mediate *SDF1* promoter *trans*-repression (**Fig. 3i** and **Supplementary Fig. 4**). To test whether ectopic *Sdf1* expression in *Irx5* morphants was responsible for the defective NCC migration, we reduced endogenous Sdf1 levels by co-injection of an *Sdf1* morpholino[12]. We found that proper streaming of NCCs into the first branchial arch was recovered in double *Irx5*-*Sdf1* morpholino–injected embryos (**Fig. 3j**–**m**). Primordial germ cells, whose migration into gonads also depends on Sdf1 levels[14,15], were mislocalized and more scarce within *Irx5* morphants relative to control embryos (**Fig. 3n**). This prompted us to re-examine index cases for gonadal activity. Scintillography tests on all males with homozygous *IRX5* mutations showed minimal testis activity (**Supplementary Fig. 5**), consistent with observed hydrocele and cryptorchidism (**Supplementary Table 1**). These data suggest that IRX5 is required to repress *SDF1* expression for correct chemoattraction of migratory cell populations in branchial arches and gonads, raising the possibility that craniofacial and gonadal anomalies in individuals with homozygous *IRX5* mutations may stem, in part, from a gain of SDF1 signaling during human development.

To clarify the transcriptional output of IRX5, we searched for protein partners that could modulate its activity. In a meta-analysis of human Affymetrix microarrays[16], we noted that *IRX3*, *GATA3* and *TRPS1* defined a *syn*-expression group with *IRX5* (**Supplementary Table 3**). *IRX3* and *IRX5* are coexpressed and interact at the protein level[11,17]. Therefore, we focused on the two GATA zinc-finger transcription factors TRPS1 (ref. 18) and GATA3, which are disrupted in trichorhinophalangeal type 1 syndrome[19] (MIM190350) and hypoparathyroidism sensorineural deafness and renal disease[20] (MIM131320), respectively, two congenital disorders that share clinical features with IRX5 syndrome (**Supplementary Table 1**). *In situ* hybridization showed that *Trps1*, *Gata3* and *Irx5* share craniofacial domains of expression in *X. laevis* embryos at stage 33 (**Fig. 4a**–**d**). Biochemical experiments showed coimmunoprecipitation of Irx5 by Trps1 or by Gata3, consistent with possible protein-protein interactions during craniofacial development (**Fig. 4e,f**). Moreover, luciferase assays showed that Trps1 dose-dependently potentiated Irx5 transactivation (**Fig. 4g**), whereas Gata3 significantly decreased Irx5-mediated transactivation of the *Kcnd2* reporter (**Fig. 4h**). Gata3, which bound Trps1 alone (**Supplementary Fig. 6a**), could better coimmunoprecipitate Irx5 in the presence of increasing amount of Trps1, suggesting that these three proteins might form a heterotrimeric complex

Figure 4 Irx5 interacts with zinc-finger transcription factors Gata3 and Trps1 to regulate craniofacial morphogenesis. (a–c) *Irx5* (a), *Trps1* (b) and *Gata3* (c) were expressed in nested regions of developing *X. laevis* head at stage (st.) 33. (d) *Irx5*, *Trps1* and *Gata3* transcripts (pink) colocalized to ventral region of four branchial arches (1–4), otic vesicle (ov) and frontonasal process (fp). *Irx5* and *Trps1* (yellow) were coexpressed in most anterior three branchial arches (1–3). *Irx5* and *Gata3* mRNA (green) were seen in developing lens (le). (e) Irx5 coimmunoprecipitated with wild-type Trps1 (lane 2), and to a lesser extent with the variant[18] (lane 4). IP, immunoprecipitation; IB, immunoblot. Irx5 N166K protein was pulled down by wild-type Trps1 (lane 3). (f) Gata3 coimmunoprecipitated with wild-type Irx5 (lane 2), and to a lesser extent with mutant Irx5 N166K (lane 3). (g,h) Trps1 promoted Irx5-dependent transactivation of *Kcnd2* promoter luciferase construct. Conversely, Gata3 inhibited Irx5-dependent transactivation of *Kcnd2* reporter. Data are mean ± s.d. *$P < 0.05$; **$P < 0.005$; one-tailed Student's *t* test. (i) Increasing amounts of Trps1 dose-dependently enhanced binding of Gata3 to Irx5 (lanes 2–5). (j) Increasing amounts of Trps1 potentiated inhibitory role of Gata3 on Irx5-mediated transactivation of *Kcnd2* reporter.

Data are mean ± s.d. *$P < 0.05$; **$P < 0.005$ (one-tailed Student's *t* test). (k) Schematic of IRX5 and IRX3 proteins, in complex with comodulators TRPS1 and GATA3, tuning transcription of target genes such as *SDF1* for chemoattraction of migratory populations of NCCs and germ cells.
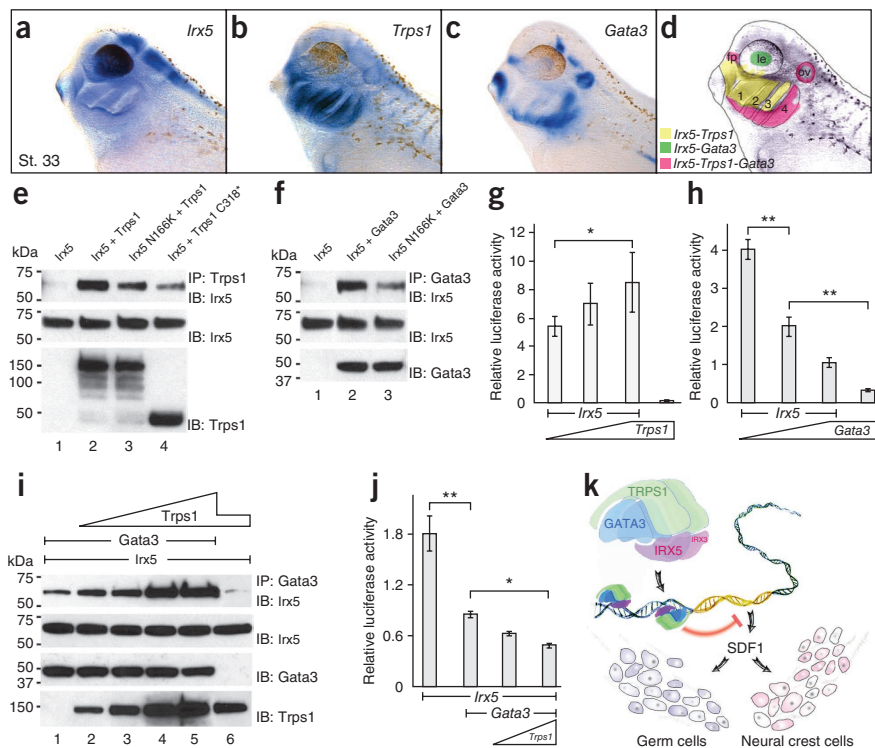
(**Fig. 4i**). In support of this hypothesis, we observed stronger transcriptional repression of both the *Kcnd2* and *SDF1* promoters when Trps1, Gata3 and Irx5 were coexpressed (**Fig. 4j** and **Supplementary Fig. 6b**). Finally, noting that the p.Asn166Lys Irx5 variant could still bind its protein partners (**Fig. 4e,f**), we examined whether it retained any activity using a Gata3-regulated *GCMB* reporter[21]. Notably, the p.Asn166Lys Irx5 variant exerted stronger *trans*-repression than wild-type Irx5 when coexpressed with Gata3 (**Supplementary Fig. 6c**). This indicates that the *IRX5* missense variants we identified may exhibit neomorphic properties, unlike *Irx5* knockout mice, which carry a null allele[9,22].

Our genetic, developmental and biochemical results suggest that the stoichiometry of GATA3, TRPS1 and presumably IRX3, bound individually or in a molecular complex to IRX5, can modulate its transcriptional activity, creating a wide spectrum of craniofacial features (**Fig. 4k**). Haploinsufficiency, which has been observed in hypoparathyroidism sensorineural deafness and renal disease as well as trichorhinophalangeal type 1 syndrome, supports a gene-dosage effect for these transcriptional regulators[19,20]. Likewise, monosomy of *IRX3*, *IRX5* and *IRX6* causes a disorder[23] similar to that of biallelic *IRX5* mutations, suggesting that *IRX3* and *IRX6* are needed to circumvent *IRX5* haploidy. A picture emerges in which the IRX proteins and their comodulators regulate the expression of key signaling molecules such as SDF1 during organogenesis and in the pathogenesis of this disorder, which we propose to call Hamamy syndrome (MIM611174) in recognition of the clinician who first described it[5]. Finally, children exposed to folate antagonists can share similar facial features to individuals with *IRX5* mutations[24]. There is strong correlation between expression of *IRX5* and *SLC39A6* (**Supplementary Table 3**), a transporter associated with uptake of the folate inhibitor methotrexate[25]. Similarly, the ear, dental and lacrimal anomalies observed in IRX5

probands are reminiscent of the lacrimoauriculodentodigital (MIM149730) syndrome caused by alterations affecting the FGF10 pathway[26], raising the possibility that the *SLC39A6* and *FGF10* genes may act in concert with or as direct targets of IRX5.

URLs. GenBank, http://www.ncbi.nlm.nih.gov/mapview/; Ensembl, http://www.ensembl.org/; University of California Santa Cruz (UCSC), human reference genome, build 18, http://genome.ucsc.edu/; Blat-like Fast Accurate Search Tool, https://secure.genome.ucla.edu/index.php/BFAST/; SAMTools, http://samtools.sourceforge.net/; SeqWare Pipeline, http://sourceforge.net/projects/seqware/; UGET, http://genome.ucla.edu/~jdong/GeneCorr.html; unabridged protocols, http://www.reversade-a.googlepages.com/protocols/.

METHODS

Methods and any associated references are available in the online version of the paper.

Accession codes. *Homo sapiens IRX5*, NM_005853.5; *Mus musculus Irx5*, NM_018826.2; *X. laevis Irx5*, NM_001085754.1.

Note: Supplementary information is available in the online version of the paper.

AUTHOR CONTRIBUTIONS
B.R. and C.B. designed the study. H.H. and H.K. diagnosed subjects. B.R., M.S., O.H.A., T.G., H.K. and H.H. collected clinical data and subject samples. C.B., B.M., H.L., S.F.N. and E.U. conducted genotyping, mapping and genomic loci capture. C.B. and A.C.S. did *X. laevis* work. C.B. did cell culture and biochemical studies. B.R. and C.B. wrote the manuscript.

COMPETING FINANCIAL INTERESTS
The authors declare no competing financial interests.

1. Gans, C. & Northcutt, R.G. Neural crest and the origin of vertebrates: a new head. *Science* **220**, 268–273 (1983).
2. Le Douarin, N.M., Brito, J.M. & Creuzet, S. Role of the neural crest in face and brain development. *Brain Res. Rev.* **55**, 237–247 (2007).
3. Hall, B.K. The neural crest and neural crest cells: discovery and significance for theories of embryonic organization. *J. Biosci.* **33**, 781–793 (2008).
4. Wilkie, A.O. & Morriss-Kay, G.M. Genetics of craniofacial development and malformation. *Nat. Rev. Genet.* **2**, 458–468 (2001).
5. Hamamy, H.A., Teebi, A.S., Oudjhane, K., Shegem, N.N. & Ajlouni, K.M. Severe hypertelorism, midface prominence, prominent/simple ears, severe myopia, borderline intelligence, and bone fragility in two brothers: new syndrome? *Am. J. Med. Genet. A.* **143**, 229–234 (2007).
6. Reversade, B. *et al.* Mutations in *PYCR1* cause cutis laxa with progeroid features. *Nat. Genet.* **41**, 1016–1021 (2009).
7. Tian, J. *et al.* Loss of CHSY1, a secreted FRINGE enzyme, causes syndromic brachydactyly in humans via increased NOTCH signaling. *Am. J. Hum. Genet.* **87**, 768–778 (2010).
8. Cavodeassi, F., Modolell, J. & Gomez-Skarmeta, J.L. The Iroquois family of genes: from body building to neural patterning. *Development* **128**, 2847–2855 (2001).
9. Costantini, D.L. *et al.* The homeodomain transcription factor Irx5 establishes the mouse cardiac ventricular repolarization gradient. *Cell* **123**, 347–358 (2005).
10. Chi, Y.I. Homeodomain revisited: a lesson from disease-causing mutations. *Hum. Genet.* **116**, 433–444 (2005).
11. Rodríguez-Seguel, E., Alarcon, P. & Gomez-Skarmeta, J.L. The *Xenopus Irx* genes are essential for neural patterning and define the border between prethalamus and thalamus through mutual antagonism with the anterior repressors Fezf and Arx. *Dev. Biol.* **329**, 258–268 (2009).
12. Theveneau, E. *et al.* Collective chemotaxis requires contact-dependent cell polarity. *Dev. Cell* **19**, 39–53 (2010).
13. García-Moruja, C. *et al.* Functional characterization of *SDF-1* proximal promoter. *J. Mol. Biol.* **348**, 43–62 (2005).
14. Takeuchi, T., Tanigawa, Y., Minamide, R., Ikenishi, K. & Komiya, T. Analysis of SDF-1/CXCR4 signaling in primordial germ cell migration and survival or differentiation in *Xenopus laevis. Mech. Dev.* **127**, 146–158 (2010).
15. Staton, A.A., Knaut, H. & Giraldez, A.J. miRNA regulation of Sdf1 chemokine signaling provides genetic robustness to germ cell migration. *Nat. Genet.* **43**, 204–211 (2011).
16. Day, A., Carlson, M.R., Dong, J., O'Connor, B.D. & Nelson, S.F. Celsius: a community resource for Affymetrix microarray data. *Genome Biol.* **8**, R112 (2007).
17. He, W., Jia, Y. & Takimoto, K. Interaction between transcription factors Iroquois proteins 4 and 5 controls cardiac potassium channel Kv4.2 gene transcription. *Cardiovasc. Res.* **81**, 64–71 (2009).
18. Malik, T.H. *et al.* Transcriptional repression and developmental functions of the atypical vertebrate GATA protein TRPS1. *EMBO J.* **20**, 1715–1725 (2001).
19. Momeni, P. *et al.* Mutations in a new gene, encoding a zinc-finger protein, cause tricho-rhino-phalangeal syndrome type I. *Nat. Genet.* **24**, 71–74 (2000).
20. Van Esch, H. *et al. GATA3* haplo-insufficiency causes human HDR syndrome. *Nature* **406**, 419–422 (2000).
21. Grigorieva, I.V. *et al.* Gata3-deficient mice develop parathyroid abnormalities due to dysregulation of the parathyroid-specific transcription factor Gcm2. *J. Clin. Invest.* **120**, 2144–2155 (2010).
22. Cheng, C.W. *et al.* The Iroquois homeobox gene, *Irx5*, is required for retinal cone bipolar cell development. *Dev. Biol.* **287**, 48–60 (2005).
23. Chang, C.F. *et al.* Identification of a submicroscopic 3.2 Mb chromosomal 16q12.2–13 deletion in a child with short stature, mild developmental delay, and craniofacial anomalies, by high-density oligonucleotide array-a recognizable syndrome. *Am. J. Med. Genet. A.* **152A**, 2365–2371 (2010).
24. Bawle, E.V., Conard, J.V. & Weiss, L. Adult and two children with fetal methotrexate syndrome. *Teratology* **57**, 51–55 (1998).
25. French, D. *et al.* Acquired variation outweighs inherited variation in whole genome analysis of methotrexate polyglutamate accumulation in leukemia. *Blood* **113**, 4512–4520 (2009).
26. Rohmann, E. *et al.* Mutations in different components of FGF signaling in LADD syndrome. *Nat. Genet.* **38**, 414–417 (2006).

ONLINE METHODS

Subjects and clinical assessment. Jordanian index cases were initially diagnosed at the Pediatrics Department in Jordan University Hospital by Hanan Hamamy[5]. The affected children in the Turkish family were clinically evaluated at the Medical Genetics Department, Istanbul Medical Faculty, by Hülya Kayserili. Ultrasound scanning, electrocardiogram, ophthalmic examination, magnetic resonance imaging and dacryoscintillography were undertaken to ascertain and document clinical symptoms associated with this syndrome. Each participant gave informed consent after approval by the local ethics commission. Additional information is provided in **Supplementary Note**.

Genotyping and homozygosity mapping. Genomic DNAs of Jordanian parents and children were extracted from saliva samples (Puregene DNA Purification Kit, Gentra Systems) and genotyped with Illumina Infinium HD Human 1M-Duo BeadChips according to manufacturer's instructions. Call rates were >98%, and gender and relationship were verified using Illumina BeadStudio software. Mapping was done by searching for shared regions that are homozygous and IBD in the three affected individuals using custom programs written in Mathematica (Wolfram Research) data analysis software. Confidence criteria to identify IBD blocks were a minimum of 3 cM and a SNP density over the fifth percentile. Centimorgan distances between SNPs were determined from the HapMap2 recombination rate map. Candidate regions were further refined by exclusion of common homozygous segments with any unaffected family members. Homozygosity mapping of the Turkish family was done using SNP genotyping data of the affected boy and unaffected parents and sibling generated from Affymetrix GeneChip Human Mapping NspI 250K arrays. The Visual Genome Studio (VIGENOS) program (Hemosoft) developed at the Gene Mapping Laboratory facility of Hacettepe University Medical Faculty was used for genome-wide haplotyping of SNP data[27].

Genomic loci capture. Briefly, custom arrays (Agilent 244K) were designed to target every exonic sequence of the genes present in the IBD region on chromosome 16 between genomic coordinates 52812847 and 61978673. In total, 730 contigs encompassing 208042 base pairs were targeted. A DNA library from subject 1 was prepared according to the Illumina library generation protocol version 2.3, hybridized to custom arrays according to the Agilent CGH 244K array protocol, and washed, eluted and amplified[28]. The sample was submitted to one channel of Illumina flow cell and sequenced by Illumina Genome Analyzer (GAII) using standard manufacturer's protocol. The image data was processed by the provided GA Pipeline (Firecrest version 1.3.4 and Bustard version 1.3.4) and all sequences were aligned to the human reference genome (UCSC, build 18; see URLs) by Blat-like Fast Accurate Search Tool (BFAST; see URLs). Variants were called using SAMtools pileup tool (SAMtools; see URLs) and the variants were submitted to an internal database for further filtration and annotation. Mismatches were filtered to identify variants seen ten or more times, in which the variant was called as homozygous and did not overlap with a known dbSNP129 entry mismatch. Nonsynonymous mutations were identified using additional SeqWare tools and the "knownGene" gene model from the UCSC hg18. The open source SeqWare project, which provides a Laboratory Information Management System (LIMS) tool for tracking samples (SeqWare LIMS) and a pipeline for sequence analysis (SeqWare Pipeline; see URLs), was used throughout this work[29].

Mutation analysis. Positional candidate genes were obtained from GenBank and Ensembl databases (see URLs). Flanking primers for each exon were manually designed and direct Sanger resequencing was done with the BigDye Terminator cycle sequencing kit (Applied Biosystems). Primer sequences are in **Supplementary Table 4**.

Luciferase assay. 10T1/2, 293T and MS5 cells were cotransfected with luciferase reporters and expression vectors (encoding mouse wild-type Irx5 and the A150P, N166K, HD and S36D/S63D variants) at 60–70% confluency using Fugene HD (Roche) in 24-well plates. After 48 h of incubation, firefly and *Renilla* luciferase assays were carried out on cell lysates using Dual-Luciferase Reporter 1000 Assay System (Promega), and enzyme activities were measured with Spectramax plate reader (Molecular Devices). For luciferase assays carried out *in vivo*, 55 pg of firefly and 3 pg of *Renilla* constructs were mixed in water or in pure *Irx5* morpholino and injected into two- to four-cell stage *X. laevis* embryos. Five embryos were lysed in 100 µl at stage 25 and analyzed in the same way.

Western blot analysis. Embryos or transfected cells were lysed in RIPA buffer supplemented with protease inhibitor cocktails (Roche). Extracted proteins were separated by electrophoresis on SDS polyacrylamide gels with DTT, followed by transfer on polyvinylidene difluoride membranes. The following antibodies were used for probing western blots: mouse antibody to Irx5 (Sigma; WH0010265M1), mouse antibody to actin (Chemicon; Mab1501R), mouse antibody to β-catenin (Sigma; C2206) and mouse antibody to Protein C (Roche; 11814508001). To block protein ubiquitin-dependent degradation, 10 µM lactacystin (Sigma) or MG132 (Calbiochem) was added to cultured cells overnight.

Quantitative PCR. We reverse transcribed 1 µg RNA isolated from transfected 10T1/2 cells using the Revert Aid kit (Fermentas) and oligo(dT) primer. Quantitative PCR was done with Power SYBR Green (Applied Biosystems). Primer sequences are in **Supplementary Table 4.**

Microinjection of morpholino oligonucleotides and DNAs. The *Irx5* morpholino[11] and *Sdf1* morpholino[12] synthesized by Gene Tools were resuspended in sterile water to a concentration of 1 mM. At the two- to four-cell stage, the *Irx5* morpholino was injected pure (123 ng per embryo) and *Sdf1* morpholino was injected at 25 ng per embryo. For rescue experiments, 80 pg of nonlinearized DNA in pCS2+ encoding wild-type mouse Irx5 or p.Ala150Pro and p.Asn166Lys Irx5 variants were co-injected with the *Irx5* morpholino. Morpholino sequences are in **Supplementary Table 4**.

Embryological methods. Protocols for fertilization, injections and whole-mount *in situ* hybridization are at our protocol website (see URLs). A stereomicroscope equipped with an integrated digital camera (Leica; M205 FA) was used to capture images of embryos in successive focal planes. Images were then merged into one picture with Photoshop CS4 (Adobe).

Coimmunoprecipitation. Proteins were extracted from transfected HEK293T with lysis buffer (50 mM Tris, pH 7.5, 150 mM NaCl, 0.1% Nonidet P-40; 0.05% deoxycholate, 1 mM CaCl$_2$) supplemented with protease inhibitor cocktails (Roche). Protein C–tagged proteins (Gata3 or Trps1) were first immunoprecipitated on Anti-Protein C Affinity Matrix (Roche) during 5 h at 4 °C. After several washes of the matrix with lysis buffer, untagged protein (Irx5 or Gata3) was co-incubated overnight at 4 °C. Bound proteins were eluted from the beads using a wash buffer (20 mM Tris, pH 7.5, 0.5 M NaCl, 1 mM CaCl$_2$). Proteins were dissociated in reducing loading buffer and analyzed by western blotting using the indicated antibodies.

Statistical analysis. Each experiment was repeated at least three times and data were expressed as mean ± s.d. Significance of pairwise comparisons was determined by Student's *t* test. Significant differences were considered as those with $P < 0.05$ (*) or $P < 0.005$ (**).

27. Kayserili, H. *et al.* ALX4 dysfunction disrupts craniofacial and epidermal development. *Hum. Mol. Genet.* **18**, 4357–4366 (2009).
28. Lee, H. *et al.* Improving the efficiency of genomic loci capture using oligonucleotide arrays for high throughput resequencing. *BMC Genomics* **10**, 646 (2009).
29. O'Connor, B.D., Merriman, B. & Nelson, S.F. SeqWare Query Engine: storing and searching sequence data in the cloud. *BMC Bioinformatics* **11** (suppl. 12), S2 (2010).

Update of the Pompe Disease Mutation Database with 60 Novel *GAA* Sequence Variants and Additional Studies on the Functional Effect of 34 Previously Reported Variants

Marian Kroos,[1] Marianne Hoogeveen-Westerveld,[1] Helen Michelakakis,[2] Robert Pomponio,[3] Ans Van der Ploeg,[1] Dicky Halley,[1] Arnold Reuser,[1]* and *GAA* Database Consortium[#]

[1]*Departments of Clinical Genetics and Paediatrics, Center for Lysosomal and Metabolic Diseases, Erasmus MC, Rotterdam, The Netherlands;*
[2]*Department of Enzymology and Cellular Function, Institute of Child Health, Athens, Greece;* [3]*Clinical Laboratory Science Group, Genzyme Corp. Framingham, Massachusetts*

ABSTRACT: Pompe disease is an autosomal recessive lysosomal glycogen storage disorder, characterized by progressive muscle weakness. Deficiency of acid α-glucosidase (EC; 3.2.1.20/3) can be caused by numerous pathogenic variants in the *GAA* gene. The Pompe Disease Mutation Database at http://www.pompecenter.nl aims to list all variants and their effect. This update reports on 94 variants. We examined 35 novel and 34 known mutations by site-directed mutagenesis and transient expression in COS-7 cells or HEK293T cells. Each of these mutations was given a severity rating using a previously published system, based on the level of acid α-glucosidase activity in medium and transfected cells and on the quantity and quality of the different molecular mass species in the posttranslational modification and transport of acid α-glucosidase. This approach enabled to classify 55 missense mutations as pathogenic and 13 as likely nonpathogenic. Based on their nature and the use of in silico analysis (Alamut® software), 12 of the additional 25 novel mutations were predicted to be pathogenic including 4 splicing mutations, 6 mutations leading to frameshift, and 2 point mutations causing stop codons. Seven of the additional mutations were considered nonpathogenic (4 silent and 3 occurring in intron regions), and 6 are still under investigation.
Hum Mutat 00:1–6, 2012. © 2012 Wiley Periodicals, Inc.

KEY WORDS: *GAA*; Pompe disease; α-glucosidase; acid maltase; glycogenosis; lysosomal storage disorder

Introduction

Pompe disease (MIM# 232300) also known as glycogen storage disease type II and acid maltase deficiency encompasses a contin-uous clinical spectrum with regard to the age at which the first symptoms occur. All patients eventually manifest progressive muscle weakness [Engel et al., 2004; Hirschhorn and Reuser, 2001; van der Ploeg and Reuser, 2008]. The most severely affected infants (classic-infantile Pompe disease) have hypertrophic cardiomyopathy as additional clinical characteristic. The average life expectancy of patients with classic-infantile Pompe disease is less than one year [Kishnani and Howell, 2004; Van den Hout et al., 2003]. Patients without cardiac involvement can present from early childhood to late adulthood and have a shorter life expectancy than unaffected individuals in the same age category [Gungor et al., 2011].

The Pompe Disease Mutation Database aims to list all α-glucosidase (GAA) variations and to describe their effect so to facilitate diagnosis and counseling in patients and families with Pompe disease. It also aims to provide insight in the genotype–phenotype correlation in this very heterogeneous disease. The 1 July (2011) edition of the Pompe Disease Mutation Database at http://www.pompecenter.nl provides a list of 372 sequence variants in the *GAA* gene (MIM# 606800; RefSeq NT_024871.11; NM_000152.3; NP 000143.2). Seventy-six of these variants are marked as nonpathogenic, 248 as pathogenic, 2 are presumably nonpathogenic, while the effect of 46 other variants is marked as unknown. One hundred and sixteen of the pathogenic mutations are listed as very severe, 91 as potentially less severe, 23 as less severe, and 18 as potentially mild. Since then many cases of Pompe disease patients have been diagnosed and analyzed in our collaborating centers and a wealth of new sequence variations has come to light. This update of the Pompe disease mutation database reports on the identification of 60 novel sequence variations including 3 deletions, 3 insertions, 2 nonsense mutations, 4 silent mutations, 4 splice site mutations, and 3 nonpathogenic intronic variations with predictable effect. Thirty-five novel missense mutations were investigated regarding their effect on the synthesis and function of acid α-glucosidase by site-directed mutagenesis and transient expression in COS-7 or HEK293T cells. Six mutations are still under investigation. This update further reports on the effect of 33 missense mutations and 1 in frame deletion that were published previously but were not yet investigated as to their functional effect.

Methods

The DNA analysis was performed as part of diagnostic practice with informed consent of the patients. One case in this study concerned mutation analysis in a proven carrier of Pompe disease.

All other cases were suspected to be affected with Pompe disease and diagnosed by a combination of clinical findings and enzymatic assay. The DNA was isolated from leukocytes or skin fibroblasts. The coding exons and the exon–intron boundaries of the acid α-glucosidase gene (*GAA*) were amplified and subsequently sequenced using an ABI 3730 DNA Analyser under GLP conditions as described [Kroos et al., 2008]. NM_000152.3 was used as reference sequence for the coding regions, whereby the "A" nucleotide of the ATG translation initiation codon at nucleotide position 368 constitutes +1 numbering of the cDNA sequence. This ATG codon represents +1 for the amino acid numbering as set forth by the acid α-glucosidase preprotein sequence NP_000143.2. The positions of intronic sequence variations were assigned based on the cDNA sequence and the genomic contig sequence NT_024871.11 whereby the "A" of the ATG start codon is at position 481925. The three reference sequences used in this study can be found at http://www.pompecenter.nl.

To investigate whether silent mutations and intronic variations not located in splice sites could possibly cause alternative splicing, we performed in silico analysis using the Alamut® software (Interactive Biosoftware, member of the Human Genome Variation Society and of the EBI SME Support Forum). Because all the missense mutations and the 9 bp deletion were found in the Caucasian *GAA**01-type allele, the single-base changes, and the deletion were introduced in the corresponding wild-type *GAA* cDNA expression construct pSHAG2 by site-directed mutagenesis according to the manufacturer's protocol (Stratagene® Quick Change Site-directed Mutagenesis kit number 200516). The integrity of the resulting mutant constructs was in each case confirmed by full-length sequencing of the *GAA* cDNA insert. Two independently obtained mutant constructs were used to transfect COS-7 or HEK293T cells and to express acid α-glucosidase. The wild-type *GAA* cDNA construct (pSHAG2) and a mock transfection with a plasmid containing a cDNA construct unrelated to *GAA* (pITA) served as a positive and a negative control. The cells were harvested 72 hr later and the acid α-glucosidase activity (EC: 3.2.1.20/3) was measured in the culture media and in the cell homogenates using 4-methylumbelliferyl-α-glucopyranoside as substrate. In addition to measuring the acid α-glucosidase activities in the media and the cells, the synthesis of acid α-glucosidase was studied by SDS-PAGE and immunoblotting. Cell homogenates were directly applied onto the gel. The enzyme in the media was first concentrated by immuno-precipitation with anti α-glucosidase antibodies and then applied [Hermans et al., 1998]. Different molecular mass species reflect the sequential, posttranslational, and modification steps of the enzyme during transport from the endoplasmic reticulum to the lysosomes [Hasilik and Neufeld, 1980]. The mutation severity rating that we used was as previously described and gives an account of the quality and the quantity of the different molecular mass species as well as the activity of acid α-glucosidase in the transfected cells and in the media [Kroos et al., 2008].

Results and Discussion

DNA analyis has become integrated part of the diagnosis of Pompe disease. Over the past two years, a large number of Pompe disease patients were seen in our clinical and metabolic diagnostic centers, and DNA analysis was performed in most cases. One case in this study concerned mutation analysis in a proven carrier of Pompe disease. All other cases were suspected to be affected with Pompe disease and diagnosed by a combination of clinical findings and enzymatic assay. The DNA was isolated from leukocytes or skin fibroblasts and DNA analysis was performed with informed consent of the patients. Table 1 lists a collection of 68 missense mutations

(Table 1A—novel mutations; and Table 1B—previously published mutations) and one in-frame deletion (Table 1C) that were investigated as to their effect. All these mutations were introduced in a wild-type *GAA* cDNA expression construct by site-directed mutagenesis to investigate their effect. The severity of the sequence variations is judged by a rating system as previously described [Kroos et al., 2008]. The system takes into account how much of each of the characteristic forms of acid α-glucosidase (processed and unprocessed) is detectable in transiently transfected cells and in the medium in which they are maintained. It also judges the quality of these forms in terms of having the proper molecular mass and includes the acid α-glucosidase activity in cells and media. The sum of these recordings results in a severity class, whereby A stands for "very severe," B for "potentially less severe," C for "less severe," D for "potentially mild," E for "presumably nonpathogenic," and F for "nonpathogenic" [Kroos et al., 2008]. Class A mutations are characterized by complete absence of any molecular form of acid α-glucosidase as detected by immunoblotting (Cross Reactive Immunologic Material-negative; CRIM-negative), and by lack of any residual acid α-glucosidase activity in a transient expression system. In contrast to class A mutations, class B, C, D, E, and F mutations are all CRIM-positive.

According to the method of severity rating, none of the 35 newly discovered missense mutations (Table 1A) received the label "very severe." Twenty-five mutations were classified as "potentially less severe" (class B), and one as "less severe" (class C) on basis of the relative height of the acid α-glucosidase activity in the transfected cells. One sequence variant was classified as "potentially mild" (class D) because that sequence variation allowed for more than 20% residual activity in the cells, and all molecular forms of acid α-glucosidase were clearly detectable by immunoblotting. Four missense mutations in this series were scored as "presumably nonpathogenic" (class E) and 4 as "nonpathogenic" (class F) since the introduction of these sequence variants in the wild-type *GAA* cDNA expression construct did not lead to a dramatic reduction of the acid α-glucosidase activity nor to abnormalities in the posttranslational modification.

Class B mutations are mutations that do not hamper the very first step of acid α-glucosidase synthesis. The 110 kD precursor protein is typically detectable in either normal or subnormal amount inside the cells, but not always in the medium. The apparent molecular mass can be either normal or abnormal due to differences in charge, folding, proteolytic processing or glycosylation. Processed forms of acid α-glucosidase can be absent or present, but are mostly catalytically inactive. Patients with Pompe disease carrying these mutations are classified as CRIM-positive patients as they express a molecular form of acid α-glucosidase that can be visualized by immunoblotting [Bali et al., 2011]. The adjective "potentially" less severe implies that these variants might behave differently in situ. In practice, however, most of these class B variants are very severe on the basis of available clinical data.

The missense mutations c.1A>T and c.2T>C both obliterate the start codon. Interestingly, it seems that in our in vitro system a downstream ATG is used as alternative start codon since a molecular species of approximately 85 kD was visible in very low amount in HEK293T cells transfected with these mutant constructs.

The missense mutation c.266G>A (p.Arg89His) was detected in combination with c.546+45G>C in both *GAA* alleles of a severely affected infant. However, when c.266G>A was analyzed by transient expression in HEK293T cells, it behaved like a class E variant. We are currently investigating the possibility that the combination of c.266G>A with c.546+45G>C is pathogenic.

A previous update of the Pompe Disease Mutation Database included 20 missense mutations and one deletion of three amino acids

Table 1A. Severity Rating of Novel Missense Mutations

Exon	Variant	Result	M110	C110	C95	C76	M%Wt	C%Wt	Class[b]	Nr
			Severity rating[a]							
2	c.1A>T	p.?	1,1	2,2[c]	1,1	1,1	1.0	0	B	1
2	c.2T>C	p.?	1,1	2,2[c]	1,1	1,1	3.6	0	B	2
2	c.221G>A	p.Arg74His	4,4	4,4	4,4	4,4	72	103	F	3
2	c.266G>A	p.Arg89His	3,4	3,4	3,4	3,4	20.0	43.5	E	4
2	c.307T>C	p.Cys103Arg	1,1	3,4	2,4	1,1	1,1	0	B	5
2	c.322T>G	p.Cys108Gly	1,1	3,4	3,4	1,1	1.3	8.2	B	6
2	c.380G>T	p.Cys127Phe	1,1	5,4	3,4	1,1	2.4	1.5	B	7
3	c.658G>T	p.Val220Leu	4,4	4,4	4,4	4,4	100	100	F	8
3	c.664G>A	p.Val222Met	4,4	4,4	4,4	4,4	112	98	F	9
3	c.671G>A	p.Arg224Gln	2,4	2,4	1,1	1,1	0.1	0.7	B	10
4	c.701C>G	p.Thr234Arg	1,1	3,4	3,4	1,1	5.3	1.6	B	11
4	c.701C>A	p.Thr234Lys	1,1	3,4	3,4	1,1	3.4	2.7	B	12
5	c.868A>G	p.Asn290Asp	4,4	4,4	4,4	4,4	38	71	E	13
5	c.947A>T	p.Asn316Ile	2,4	4,4	1,1	1,1	0	0	B	14
6	c.1004G>A	p.Gly335Glu	1,1	4,4	3,4	1,1	0.6	0.2	B	15
7	c.1082C>T	p.Pro361Leu	1,1	3,2	1,1	1,1	0.1	3.9	B	16
7	c.1190C>T	p.Pro397Leu	2,2	4,4	1,1	1,1	0	0	B	17
8	c.1256A>T	p.Asp419Val	3,4	3,4	3,4	3,4	5.1	21.3	D	18
9	c.1370C>A	p.Pro457His	1,1	3,4	2,4	1,1	0.5	0	B	19
9	c.1373A>G	p.Tyr458Cys	3,3	2,4	3,4	3,4	7.0	45	E	20
11	c.1568C>A	p.Ser523Tyr	4,4	4,4	2,4	2,4	0	0	B	21
12	c.1672T>A	p.Cys558Ser	3,3	4,3	1,1	1,1	0.3	4.8	B	22
12	c.1724A>G	p.Tyr575Cys	3,4	3,4	1,1	1,1	0.2	2	B	23
12	c.1726G>C	p.Gly576Arg	2,3	4,3	1,1	1,1	0.6	3.8	B	24
13	c.1781G>A	p.Arg594His	1,1	4,4	3,4	1,1	1.4	0.1	B	25
13	c.1802C>T	p.Ser601Leu	1,1	3,4	2,4	1,1	0.5	0.4	B	26
13	c.1804A>G	p.Thr602Ala	4,4	5,4	3,4	3,4	1.8	5.8	C	27
13	c.1879T>C	p.Ser627Pro	1,1	2,4	2,4	2,4	0.1	0.5	B	28
13	c.1886C>T	p.Pro629Leu	4,4	4,4	4,4	4,4	29.0	49	E	29
14	c.1943G>A	p.Gly648Asp	1,1	4,4	1,1	1,1	0	0	B	30
15	c.2105G>T	p.Arg702Leu	1,1	5,4	2,4	1,1	1.3	0.4	B	31
15	c.2152G>A	p.Val718Ile	4,4	4,4	4,4	4,4	158	127	F	32
16	c.2227C>A	p.Gln743Lys	1,1	3,4	3,4	1,1	1.1	4.1	B	33
17	c.2456G>C	p.Arg819Pro	1,1	5,4	3,4	1,1	2.0	0.4	B	34
19	c.2746G>T	p.Val916Phe	1,1	2,4	2,4	1,1	0	0	B	35

The nucleotide numbering reflects cDNA numbering with +1 corresponding to the A of the ATG initiation codon in RefSeq NM_000152.3; the amino acid numbering is according to NP 000143.2.

[a] The severity rating in digits reports on the quantity (first digit) and quality (second digit) of the precursor (110 kD), the intermediate (95 kD), and the mature (76 kD) forms of acid α-glucosidase as they are detectable in the medium (M) of transfected COS-7 and HEK293T cells and in the cell homogenates (C) by immunoblotting. First digit, quantity: 1 = not detectable; 2 = barely detectable; 3 = clearly present, but clearly less than normal; 4 = normal amount; Second digit, quality: 1 = too little present to judge; 2 = apparent molecular mass too low; 3 = apparent molecular mass too high; 4 = apparent molecular mass normal. The columns labeled M% and C% report on the acid α-glucosidase activity in the medium (M) and in the cells (C) as percentage of the wild-type activity (Wt).

[b] Class A mutations are "very severe," class B mutations are "potentially less severe," class C mutations are "less severe," class D mutations are "potentially mild," class E mutations are "presumably nonpathogenic," and class F mutations are "nonpathogenic."

[c] Only one molecular species with a mass of approximately 85 kD was detected.

with unknown functional effect [Kroos et al., 2008]. We have now analyzed also these mutations as to their effect by transient expression, and the results are presented in Tables 1B and 1C. The same was done for thirteen additional missense mutations that were recently reported in the literature (included in Table 1B). Twenty-five of those 33 missense mutations obtained the classification "potentially less severe" (class B) (Table 1B). Also the three amino acids deletion turned out to be a class B mutation (Table 1C). The class E and F mutations deserve attention as they were scored in our analysis as being "presumably nonpathogenic" (class E) or "nonpathogenic" (class F). However, our analysis does not test for splicing defects and it is notable that c.1075G>A and c.1754G>A are both located near a splice-site and are predicted by in silico analysis to cause abnormal splicing. Mutation c.2132C>G is located in *cis* on a *GAA* allele that contains a proven pathogenic mutation. The outcome of c.811A>G and c.136T>C as nonpathogenic class F mutations remains enigmatic as they were described in infants with Pompe disease having only one other proven pathogenic *GAA* mutation.

The deletion c.461_469del (Table 1C) results in an in-frame deletion of three amino acids. The precursor is smaller than 110 kD, less abundant, and is not further processed.

Twelve *GAA* sequence variations, other than missense mutations, were identified with a predictable pathogenic effect (Table 2). Among these were five mutations causing frame shift, four mutations located in either a splice acceptor or splice donor site, and two mutations introducing a premature stop codon. One of these latter two mutations, c.2242G>T (p.Glu748*) in exon 16, was transiently expressed in HEK293T cells to confirm its deleterious effect. In accordance with the position of the premature stop, we thereby detected a truncated form of acid α-glucosidase with a molecular mass of approximately 86 kD. In vivo, however, this nonsense mutation might lead to nonsense mediated mRNA decay. Furthermore, in silico analysis predicts that c.2242G>T might also lead to aberrant splicing.

Apart from pathogenic mutations we encountered seven sequence variations with a predictable nonpathogenic effect (Table 3A). Four of them were silent and three were located deeper in the introns. In silico analysis did not predict any of these sequence variations to be pathogenic.

Moreover, these variations were found in the DNA of patients who had two other clearly pathogenic sequence variations. Finally, Table 3B lists six novel *GAA* sequence variations that require

Table 1B.   Severity Rating of Previously Published Missense Mutations

Exon	Variant	Result	Severity rating[a]						Class[b]	Ref[c]
			M110	C110	C95	C76	M%Wt	C%Wt		
2	c.136T>C	p.Ser46Pro	4,4	4,4	4,4	4,4	85.3	100.2	F	b
3	c.569G>A	p.Arg190His	1,1	3,4	1,1	1,1	1.3	3.9	B	a
3	c. 650C>T	p.Pro217Leu	1,1	3,4	1,1	1,1	2.1	13.3	C	b
3	c. 671G>C	p.Arg224Pro	1,1	3,4	1,1	1,1	0.8	0	B	c
4	[c.752C>T+ c.761C>T]	[p.Ser251Leu+p.Ser254Leu]	1,1	3,4	1,1	1,1	1.7	3.3	B	c
4	c.811A>G	p.Thr271Ala	4,4	4,4	4,4	4,4	71.7	83.6	F	c
4	c.853C>T	p.Pro285Ser	3,4	3,4	3,4	3,4	0.2	4.8	C	a
5	c.871C>T	p.Leu291Phe	3,4	4,4	3,4	3,4	0.7	0.7	B	a
5	c.872T>C	p.Leu291Pro	3,4	4,4	3,4	2,4	1.4	0.7	B	a
5	c.953T>A	p.Met318Lys	1,1	3,4	2,4	1,1	0.2	3.2	B	a
6	c.1003G>A	p.Gly335Arg	1,1	4,4	3,4	1,1	0.4	0.8	B	a
6	c.1040C>G	p.Pro347Arg	2,4	2,4	1,1	1,1	0.8	1	B	a
6	c.1075G>A	p.Gly359Arg	2,4	3,4	3,4	3,4	14.2	54.3	E	d
10	c.1445C>G	p.Pro482Arg	2,3	4,4	2,4	1,1	0	0	B	a
10	c.1448G>T	p.Gly483Val	2,3	4,4	2,4	1,1	0	0	B	a
10	c.1456G>C	p.Ala486Pro	3,3	4,3	1,1	1,1	3,0	0	B	b
11	c.1561G>C	p.Glu521Gln	3,4	4,4	2,4	1,1	0	0	B	a
11	c.1564C>T	p.Pro522Ser	1,1	2,4	2,4	1,1	0.8	0.8	B	a
11	c.1574T>A	p.Phe525Tyr	4,4	4,4	4,4	4,4	9.8	13.4	D	c
12	c.1669A>T	p.Ile557Phe	2,4	3,3	2,4	2,4	0.3	2.7	B	c
12	c.1673G>C	p.Cys558Ser	2,4	3,3	2,4	2,4	0.3	2.1	B	e
12	c.1710C>G	p.Asn570Lys	1,1	3,4	2,4	1,1	0.5	0.9	B	a
12	c.1716C>G	p.His572Gln	2,3	3,3	1,1	1,1	0	0	B	a
12	c.1754G>A	p.Arg585Lys	4,4	4,4	4,4	4,4	89	94	F	a
13	c.1781G>C	p.Arg594Pro	1,1	3,4	2,4	1,1	0.2	1.2	B	a
13	c.1834C>T	p.His612Tyr	2,4	3,3	2,4	2,4	0.2	0.0	B	b
13	c.1841C>A	p.Thr614Lys	1,1	3,4	2,4	1,1	0.1	1.7	B	a
14	c.1905C>A	p.Asn635Lys	1,1	2,4	1,1	1,1	0.1	0.0	B	b
15	c.2132C>G	p.Thr711Arg	4,4	3,4	4,4	4,4	65.3	86.0	F	c
16	c.2210C>A	p.Thr737Asn	1,1	4,4	2,4	2,4	0	0	B	a
16	c.2228A>G	p.Gln743Arg	2,4	3,4	2,4	2,4	1.0	0.8	B	a
16	c.2237G>C	p.Trp746Ser	1,1	3,4	2,4	2,4	2.0	0.1	B	a
20	c.2804T>C	p.Leu935Pro	1,1	2,4	2,4	1,1	0.8	0.5	B	a

The nucleotide numbering reflects cDNA numbering with +1 corresponding to the A of the ATG initiation codon in RefSeq NM_000152.3; the amino acid numbering is according to NP 000143.2.

[a,b]Annotations are the same as those in Table 1A.

[c]The letters refer to publications first reporting on these variations: a (Kroos et al., 2008), b (Oba-Shinjo et al., 2009), c (Labrousse et al., 2009), d (Muller-Felber et al., 2007), and e (Alcantara-Ortigoza et al., 2010).

Table 1C.   Severity Rating of a Deletion of Three Amino Acids

Exon	Variant	Result	Severity rating[a]						Class[b]	Ref[c]
			M110	C110	C95	C76	M%Wt	C%Wt		
2	c.461_469del	p.Arg154_Thr156del	1,1	3,2	1,1	1,1	1.4	0.5	B	a

The nucleotide numbering reflects cDNA numbering with +1 corresponding to the A of the ATG initiation codon in RefSeq NM_000152.3; the amino acid numbering is according to NP 000143.2.

[a,b]Annotations are the same as those in Table 1A.

[c]The letter refers to the publication first reporting on this variation: a (Kroos et al., 2008 listed in Table 5).

further investigation. Among these are three novel missense mutations, one in frame deletion, and two intronic variations that can potentially affect splicing. For instance, 546+45G>C could be pathogenic as the patient was homozygous for this mutation and had only one other homozygous sequence variation, c.266G>A (p.Arg89His), which by itself was found to be nonpathogenic (Table 1A). Alternatively, the combination [c.546+45G>C+266G>A] might be pathogenic.

Conclusion

New mutations continuously emerge and add to the remarkably long list of sequence variations in the *GAA* gene coding for acid α-glucosidase, one of the many lysosomal enzymes. Sixty-eight of the 94 sequence variants, presented in this study, received the label "pathogenic" based on the nature of the mutations or on the effect they had on the synthesis and function of acid α-glucosidase when transiently expressed in cells transfected with mutated *GAA*-cDNA constructs. Eighty-one percent of the 68 missense mutations that we investigated were proven to be pathogenic and to hamper the synthesis or posttranslational processing of acid α-glucosidase, but none of these mutations blocked the synthesis completely (class B mutations). Patients with one of these mutations are likely to present as CRIM-positive individuals because their mutant acid α-glucosidase immunologically cross-reacts with antibodies raised against the normal human enzyme.

Table 2. Novel Frame Shifts, Premature Stops and Splice-Site Mutations

Position	Variant	Result	Predicted effect	Nr
Exon 2	c.186_196dup	p.Arg66Hisfs*80	Pathogenic	36
Exon 2	c.483dup	p.Lys162Glnfs*15	Pathogenic	37
Exon 4	c.836G>A	p.Trp279*	Pathogenic	38
Exon 8	c.1293_1312del	p.Gln433Aspfs*66	Pathogenic	39
Intron 10	c.1551+1G>T	r.0?	Pathogenic	40
Intron 11	c.1637-2A>G	r.0?	Pathogenic	41
Exon 13	c.1848dup	p.Val617Argfs*19	Pathogenic	42
Intron13–intron14	c.1889-27_2040+23del	p.Glu630_Leu680delfs	Pathogenic	43
Exon16	c.2242G>T	p.Glu748*	Pathogenic	44
Intron 17	c.2481+1G>A	r.0?	Pathogenic	45
Intron 17	c.2481+2T>C	r.0?	Pathogenic	46
Exon 18	c.2495_2496del	Thr832Asnfs*51	Pathogenic	47

The nucleotide numbering reflects cDNA numbering with +1 corresponding to the A of the ATG initiation codon in RefSeq NM_000152.3; the amino acid numbering is according to NP 000143.2.

Table 3A. Novel Silent Mutations and Intronic Variants

Position	Variant	Result	Predicted effect	Nr
Exon 2	c.54C>T	p.(=)	Nonpathogenic	48
Exon 5	c.861C>T	p.(=)	Nonpathogenic	49
Exon 5	c.915G>A	p.(=)	Nonpathogenic	50
Intron 7	c.1194+5G>A	–	Nonpathogenic	51
Exon 14	c.1923G>A	p.(=)	Nonpathogenic	52
Intron 14	c.2041-64del	–	Nonpathogenic	53
Intron 18	c.2646+39G>A	–	Nonpathogenic	54

The nucleotide numbering reflects cDNA numbering with +1 corresponding to the A of the ATG initiation codon in RefSeq NM_000152.3.

Table 3B. Novel Sequence Variations Still to be Investigated

Position	Variant	Result	Predicted effect	Nr
Intron 2	c.546+45G>C	r.spl?	–	55
Exon 5	c.929T>G	p.Val310Gly	–	56
Exon 7	c.1171A>G	p.Met391Val	–	57
Intron 8	c.1326+5G>A	r.spl?	–	58
Exon 13	c.1832G>A	p.Gly611Asp	–	59
Exon 15	c.2097_2102del	p.Thr700_Leu701del	–	60

The nucleotide numbering reflects cDNA numbering with +1 corresponding to the A of the ATG initiation codon in RefSeq NM_000152.3; the amino acid numbering is according to NP 000143.2.

These new findings will be entered in the Pompe Disease Mutation Database at www.pompecenter.nl with the aim to facilitate diagnosis and counseling of patients and families with Pompe disease and to provide better insight in the genotype–phenotype correlation and the effect of therapy in this very heterogeneous disease.

Acknowledgments

References

Alcantara-Ortigoza MA, Gonzalez-Del Angel A, Barrientos-Rios R, Cupples C, Garrido-Garcia LM, de Leon-Bojorge B, Alva-Chaire AD. 2010. Screening of late-onset Pompe disease in a sample of Mexican patients with myopathies of unknown etiology: identification of a novel mutation in the acid alpha-glucosidase gene. J Child Neurol 25:1034–7.

Bali DS, Tolun AA, Goldstein JL, Dai J, Kishnani PS. 2011. Molecular analysis and protein processing in late-onset pompe disease patients with low levels of acid alpha-glucosidase activity. Muscle Nerve 43:665–70.

Engel AG, Hirschhorn R, Huie ML. 2004. Acid maltase deficiency. In: Engel A and Franzini-Armstrong C, editors. Myology. New York: McGraw-Hill. p 1559–1586.

Gungor D, de Vries JM, Hop WC, Reuser AJ, van Doorn PA, van der Ploeg AT, Hagemans ML. 2011. Survival and associated factors in 268 adults with Pompe disease prior to treatment with enzyme replacement therapy. Orphanet J Rare Dis 6:34.

Hasilik A, Neufeld EF. 1980. Biosynthesis of lysosomal enzymes in fibroblasts. Synthesis as precursors of higher molecular weight. J Biol Chem 255:4937–4945.

Hermans MMP, Kroos MA, Smeitink JAM, van der Ploeg AT, Kleijer WJ, Reuser AJJ. 1998. Glycogen Storage Disease type II: genetic and biochemical analysis of novel mutations in infantile patients from Turkish ancestry. Hum Mutat 11:209–15.

Hirschhorn R, Reuser AJJ. 2001. Glycogen storage disease type II: acid alpha-glucosidase (acid maltase) deficiency. In: Scriver CR, Beaudet AL, Valle D, Sly WS, editors. The metabolic and molecular bases of inherited disease. New York: McGraw-Hill. p 3389–3420.

Kishnani PS, Howell RR. 2004. Pompe disease in infants and children. J Pediatr 144:S35–43.

Kroos M, Pomponio RJ, van Vliet L, Palmer RE, Phipps M, Van der Helm R, Halley D, Reuser A. 2008. Update of the Pompe disease mutation database with 107 sequence variants and a format for severity rating. Hum Mutat 29:E13–26.

Labrousse P, Chien YH, Pomponio RJ, Keutzer J, Lee NC, Akmaev VR, Scholl T, Hwu WL. 2009. Genetic heterozygosity and pseudodeficiency in the Pompe disease newborn screening pilot program. Mol Genet Metab 99:379–83.

Muller-Felber W, Horvath R, Gempel K, Podskarbi T, Shin Y, Pongratz D, Walter MC, Baethmann M, Schlotter-Weigel B, Lochmuller H, Schoser B. 2007. Late onset Pompe disease: clinical and neurophysiological spectrum of 38 patients including long-term follow-up in 18 patients. Neuromuscul Disord 17:698–706.

Oba-Shinjo SM, da Silva R, Andrade FG, Palmer RE, Pomponio RJ, Ciociola KM, S Carvalho M, Gutierrez PS, Porta G, Marrone CD et al. 2009. Pompe disease in a Brazilian series: clinical and molecular analyses with identification of nine new mutations. J Neurol 256:1881–90.

van den Hout HM, Hop W, Van Diggelen OP, Smeitink JA, Smit GP, Poll-The BT, Bakker HD, Loonen MC, de Klerk JB, Reuser AJJ, van der Ploeg AT. 2003. The natural course of infantile Pompe's disease: 20 original cases compared with 133 cases from the literature. Pediatrics 112:332–340.

van der Ploeg AT, Reuser AJ. 2008. Pompe's disease. Lancet 372:1342–53.

Prevalence of coagulation factor II G20210A and factor V G1691A Leiden polymorphisms in Chechans, a genetically isolated population in Jordan

Rana Dajani · Raja Fatahallah · Abdelrahman Dajani ·
Mohammad Al-Shboul · Yousef Khader

Abstract Background Coagulation factor II G20210A and coagulation factor V (Leiden) G1691A single nucleotide polymorphisms (SNPs) are major inherited risk factors of venous thromboembolism. In view of the heterogeneity in their world distribution and lack of sufficient information about their distribution among Chechans, we addressed the prevalence of these SNPs in the Chechan population in Jordan, a genetically isolated population. Methods and Results factor II G20210A and factor V Leiden SNPs were analysed by polymerase chain reaction and restriction fragment length polymorphism (PCR–RFLP) method and Amplification refractory mutation detection system (ARMS) respectively in 120 random unrelated subjects from the Chechan population in Jordan. Among the subjects studied for factor II G20210A mutation there were three individuals carrying this mutation as heterozygous (one female and two male), giving a prevalence of 2.5 % and an allele frequency of 1.25 %. No homozygous factor II allele was found. Factor V Leiden G1691A mutation was detected as heterozygous in 22 of 120 of individuals (17 female and five male) indicating a prevalence of 18.3 % and allele frequency of 9.2 %. No homozygous allele was found. Conclusion Our results indicated that prevalence of factor II G20210A mutation in the Chechan population is similar to prevalence in Jordan and Caucasian populations (1–6 %) while the prevalence of factor V Leiden was higher in the Chechan population compared to Jordan and Caucasian populations (2–15 %).

Keywords Genetic polymorphisms · Ethnicity · Thrombosis

R. Dajani (✉)
Department of Biology and Biotechnology, Hashemite University, Zarqa, Jordan
e-mail: rdajani@hu.edu.jo

R. Fatahallah
National Center for Diabetes, Endocrinology and Genetics, Amman, Jordan

A. Dajani
Faculty of Medicine, Hashemite University, Zarqa, Jordan

M. Al-Shboul
Laboratory of Human Embryology, Institute of Medical Biology, A*STAR, Singapore, Singapore

Y. Khader
Department of Community Medicine, Public Health and Family Medicine, Faculty of Medicine, Jordan University for Science and Technology, Irbid, Jordan

Introduction

Thrombosis represents one of the most common causes of morbidity and mortality in societies [1]. Haemostatic disequilibrium is the key mechanism for all types of thromboses. Venous thrombosis (VTE) is a common multifactorial disease involving the interaction of environmental factors such as aging, obesity, surgery, pregnancy and post-partum, and oral contraceptives or cancer, with genetic predisposing risk factors [1]. The most common genetic risk factors implicated in VTE, are the polymorphisms of the prothrombin G20210A and factor V Leiden [2–4]. The study of their frequencies in various populations provides perspectives for both clinical medicine, population genetics and biological anthropology [1].

Dahlback et al. [5]. reported activated protein C resistance (APCR) which until now has constituted the most frequently encountered genetic abnormality in patients with VTE (20–30 % of cases). This condition is due in

more than 90 % of cases to a single mutation (G1691A) in the factor V gene [2]. In 1996, Poort et al. [4] described factor II G20210A which is present in 8–10 % of thrombosis patients. The coinheritance of these relatively common genetic conditions, which is not a rare event, further increases the relative risk of thrombosis, i.e., factor V Leiden plus factor II G20210A [6, 7]. Similarly, the combination with an environmental risk factor is associated with a substantial increased risk of venous thromboembolism [8].

Flanking SNPs and microsatellites demonstrate a single origin for both factor II G20210A and factor V G1691A and indicate that the polymorphisms arose 1,050–1,200 generations ago (21,000–36,000 years ago for 20–30 year generations) [9, 10]. Based on the frequencies of the two polymorphisms, it has been suggested that they originated in the Middle East. Several studies argued that factor II G20210A and factor V G1691A were maintained at polymorphic frequencies among Caucasoids, because they conferred an evolutionary advantage of reduced bleeding [11]. The various prevalences of thrombophilia in different ethnic populations have been established. A high prevalence of the factor V Leiden mutation in Middle Eastern subjects and a virtual absence of this mutation in Asian population has been suggested [9]. The ethnic and geographic distribution prevalence of factor II G20210A and factor V Leiden among general population ranges from 1 to 4 and 3 to 15 %, respectively [1].

These genetic prothrombotic factors demonstrate peculiar patterns of geographical distribution and therefore represent valuable tools for population genetics. We are interested in studying the prevalence of these thrombophilic mutations in the Chechan population in Jordan. The Chechans, who call themselves Noxchii and their land Noxchiin moxk, are the largest indigenous nationality of the North Caucasus. Most of Chechans in Jordan belong to the Naqshbandi tariqat [12]. The Chechans immigrated to Jordan about 140 years ago and are genetically isolated because of cultural reasons. Chechans in Jordan have managed to keep their separate sense of identity and ethnicity during the last one hundred years, even after large waves of Bedouin and Palestinian immigration into Jordan over the course of the twentieth century. The Chechan population is around 10,000 [13]. Jaradat has confirmed that the mitochondrial DNA variation in the HV1 region is significantly different between the Chechan and Arab populations in Jordan (S. Jaradat, personal communication).

This study aimed to assess the prevalence of factor II G20210A and factor V Leiden in 120 unrelated random samples from the Chechan population, living in Jordan. We hypothesize that the prevalences of these thrombophilic mutations in this population are different from other populations because of their separate ethnicity. Since the prevalences of these thrombophilic mutations are studied in the Chechan population in Jordan we also wanted to compare the prevalences of these factors in the general Jordanian population and to other countries and world regions. This is the first report on the prevalence of these factors in the Chechan population.

Materials and methods

This study has been approved by the IRB committee at the Hashemite University.

A random sample of unrelated individuals ($N = 120$) of both sexes, mean age of 45 (range 13–81 years) from the Chechan population in Jordan were recruited after signing a consent form indicating their acceptance to participate in the study. The sample size was calculated based on the assumption that the prevalence of factor II mutation in the Caucasian population is 2 %. The sample size needed to estimate the prevalence of factor II mutation with a precision of 3 % at a level of confidence of 95 % is 88 subjects. The sample size was calculated using Epicalc 2000. The samples were taken during the period between August 2008 and March 2009. Each participant in the study filled out a survey that included pedigree information. The names and ethnicity of parents, grandparents, great grand parents both maternal and paternal and any individual with non Chechan heritage for even one person in his/her pedigree was excluded.

Sample collection

Nine millilitre of whole blood was drawn in EDTA tubes from 120 peoples by Vacutainer system. Genomic DNA was isolated from whole blood sample using the phenol–chloroform protocol [14].

PCR-reactions

The PCR-reactions [4] were performed in a final volume of 25 μL containing 5 μL from 5X Go Taq buffer (Promega) for factor II, and 10× buffer (Applied Biosystem) for factor V, 2.5 μL from 2 mM dNTPs (invitrogen) 15 μL sterile distilled water, 10 pmol forward and 10 pmol reverse primers (Alpha DNA, Canada), 1 U (5 U/μL) Taq polymerase (Go Taq® DNA polymerase, Promega) and 1.5 μL target DNA (50–100 μg/mL).

Detection of the G20210A polymorphism in factor II gene was performed by means of polymerase chain reaction followed by restriction enzyme analysis. The forward

primer for factor II (G20210A) is 5′-TCTAGAAA-CAGTTGCCTGGC-3′ and the reverse primer is 5′-ATA-GCACTGGGAGCATTGAAGC-3′ [4]. The thermal cycling conditions for factor II consisting of 5 min denaturation at 95° followed by 35 cycles of denaturation at 95 °C for 25 s, annealing at 55 °C for 25 s, extension at 72 °C for 40 s, then the final extension step at 72 °C for 5 min and kept at 4 °C until use. After overnight incubation with 5 U of *Hin*dIII restriction enzyme for the G20210A at 37 °C, PCR reactions were run on 3 % agarose gels for 1.30 h at 90 V stained with ethidium bromide. The factor II wild type had only one band: 345 bp, G20210A genotype had three bands: 345, 322 and 23 bp, and AA homozygote had two bands: 322 and 23 bp.

For factor V Leiden (G1691A) the PCR reaction were carried out by Amplification refractory mutation detection system (ARMS), the wild-type primer is 5′-GGA-CAAAATACCTGTATTCCTC-3′, the mutant primer is 5′-GGACAAAATACCTGTATTCCTT-3′, and the common primer is 5′-CTTTCAGGCAGGAACAACACC-3′ [15]. The thermal cycling conditions consisting of 5 min denaturation at 95° followed by 35 cycles of denaturation at 95 °C for 25 s, annealing at 61 °C for 25 s, extension at 72 °C for 40 s, then the final extension step at 72 °C for 5 min, kept at 4 °C until use. PCR reaction was run on 2 % agarose gel for 45 min at 150 V and stained with ethidium bromide, the product size was 233 bp.

Statistical analysis

Statistical analysis was performed using the Statistical Package for Social Sciences (SPSS), version 15. Frequencies, percentages, and means were used to describe data. Data were expressed as percentages of the mean or as frequency of the allele. Percentages were compared using χ^2-test or Fisher exact test wherever appropriate. A p value of less than 0.05 was considered statistically significant.

Results

The prevalences and allele frequencies of factor II G20210A and factor V Leiden G1691A were determined for 120 random unrelated Chechan subjects. The subjects were of both sexes 43 males (36 %) and 77 females (64 %) with a mean age of 45 (range 13–81 years).

Among the 120 individuals studied for factor II G20210A mutation there were three individuals carrying this mutation as heterozygous (one female and two male), giving a prevalence of 2.5 % (95 % CI: 0–5.3) and an allele frequency of 1.25 %. No homozygous factor II allele was found (Fig. 1). There was no significant difference in factor II G20210A frequency with respect to gender (4.7 % in males vs. 1.3 % in females) (Table 1). Furthermore, the observed homozygote to heterozygote ratio was consistent

Fig. 1 Detection of factor II gene mutation G20210A by PCR–RFLP analysis. *Hin*dIII digested fragment were separated by 3 % agarose gel electrophoresis and visualized by ethidium bromide staining. *Lanes 1, 3–9, 11–15* represent an individuals with normal factor II genotype, 345 bp. *Lanes 2, 10* represent an individuals with heterozygous for FII-G20210A digested by *Hin*dIII, 345 and 322 fragments
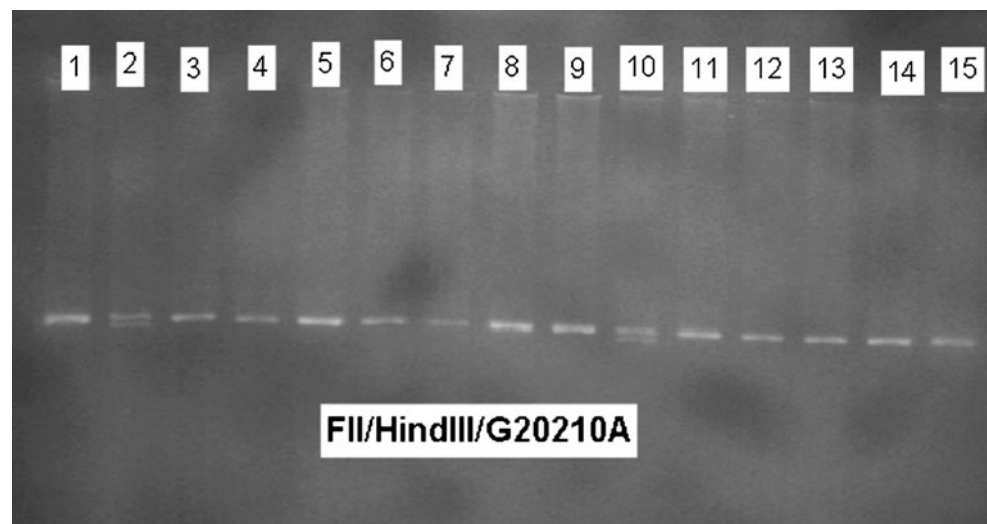
Table 1 Genotype and allele frequency of factor II G20210A mutation

Group	N	Genotype freq of G/G N (%)	Genotype freq of G/A N (%)	95 % confidence interval	p value for G/A (males vs. females)	Genotype freq of A/A %	Allele freq of A %
Total	120	117 (97.5)	3 (2.5)	0–5.3	0.292	0.00	1.25
Male	43	41 (95.3)	2 (4.7)	0–10.9		0.00	2.3
Female	77	76 (98.7)	1 (1.3)	0–3.8		0.00	0.65

with the Hardy–Weinberg equilibrium ($p = 0.975$, pq = 0.025, and q = 0) $\chi^2 = 0.02$, $p > 0.05$.

Factor V G1691A mutation was detected as heterozygous in 22 of 120 of individuals (17 female and five male) indicating a prevalence of 18.3 % (95 % CI 11.4–25.2) and allele frequency of 9.2 %. No homozygous allele was found, Fig. 2. There was no significant difference in factor V Leiden frequency with respect to gender (11.6 % in males vs. 22.1 % in females) (Table 2). Furthermore, the observed homozygote to heterozygote ratio was consistent with the Hardy–Weinberg equilibrium ($p = 0.817$, pq = 0.183, and q = 0.00) $\chi^2 = 0.99$, $p > 0.05$.

There are no subjects with both mutations in factor II and factor V Leiden.

Discussion

The prevalence of factor II mutation in the Caucasian population varies between 1 and 6 %, with an overall prevalence of about 2 % [1]. In Jordan the prevalence of factor II G20210A mutation was 2 % [16]. Our studies have found that the prevalence of factor II G20210A is 2.5 % in the Chechan population comparable to the prevalence in Jordan. The prevalence of factor II mutation is rarely seen in Asian populations [17]. Among Arab populations the allele frequency is 1.36 % in Lebanon, 1.28 % in Tunis, 0.52 % in Bahrain and 0.0 % in Saudi Arabia [18]. In a separate study on Middle Eastern Arab populations the prevalence has been reported to be 1.7 % [19].

Fig. 2 Detection of factor V Leiden gene mutation G1691A by polymerase chain reaction–Amplification refractory mutation system (PCR–ARMS) analysis. Bands were separated by 2 % agarose gel electrophoresis and visualized by ethidium bromide staining. *Lane M* represents a 100-bp molecular weight marker. Every *number* represents two *lanes*; *numbers 1, 3, 4–11, 13, 15–20* represents normal FV genotype with one band in *first lane* for every numbers (241 bp). *Numbers 2, 12*, and *14* represents heterozygous factor V Leiden mutation (R506Q) with two bands in both *lanes* for every number. *Number 21* represents positive control for factor V Leiden mutation. *Number 22* represents negative control for factor V Leiden mutation. *Number 23* represents blank
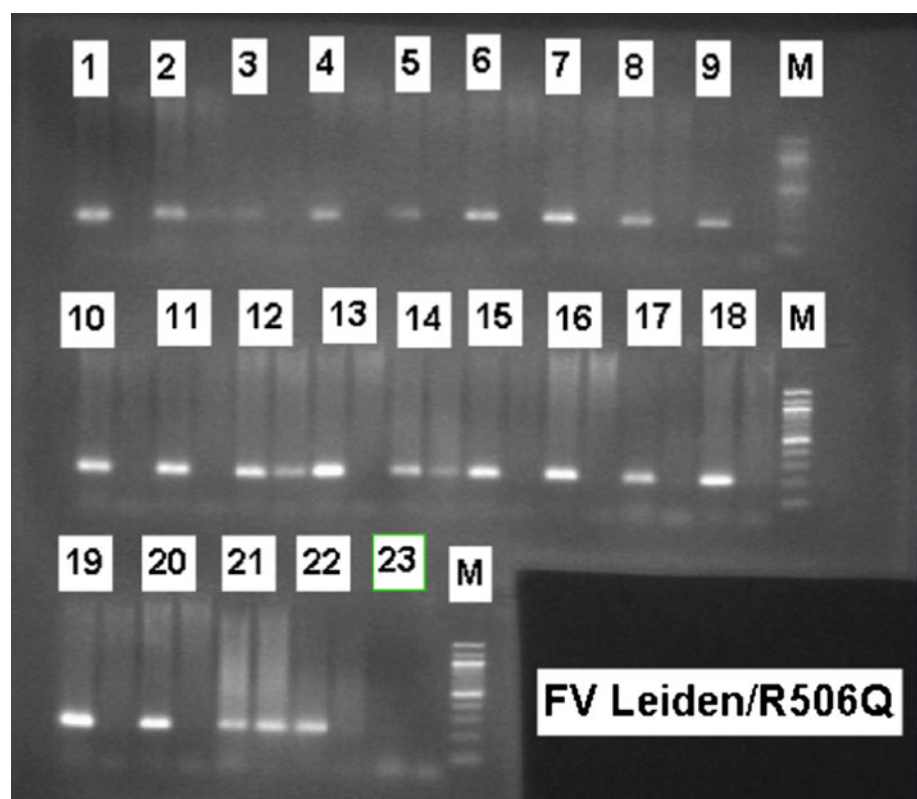
Table 2 Genotype and allele frequency of factor V Leiden mutation

Group	N	Genotype freq of G/G N (%)	Genotype freq of G/A N (%)	95 % confidence interval	p value for G/A (males vs. females)	Genotype freq of A/A %	Allele freq of A %
Total	120	98 (81.7)	22 (18.3)	11.4–25.2	0.156	0.0	9.2
Male	43	38 (88.4)	5 (11.6)	2.0–21.2		0.0	5.8
Female	77	60 (77.9)	17 (22.1)	12.8–31.3		0.0	11.0

Table 3 Genotype frequency of factor II G20210A mutation in different populations

Population	Prevalence (%)	Reference
Chechans	2.5	
Jordan	2	[16]
Lebanon	1.36	[18]
Tunis	1.28	[18]
Bahrain	0.52	[18]
Saudi Arabia	0.0	[18]
Turkish	1.37	[20]
Turk cypriotes	4.0	[20]
Southern Europeans	3	[21]
Northern Europeans	1.7	[21]
Asians	Rare	[17]

Table 4 Allele frequency of factor V Leiden mutation in different populations

Population	Allele frequency (%)	Reference
Chechans	9.2	
Jordan	8.5	[16]
Cyprus	12	[23]
Lebanon	7.88	[18]
Tunis	3.5	[18]
Bahrain	1.5	[18]
Saudi Arabia	1	[18]
Turkey	4.5–4.9	[23]
North India	1.9	[24]
Western Iran	2.97	[25]
Tehran	5.5	[25]
Sweden	15	[23]

The allele frequency of factor II in the Turkish population and Turkish Cypriotes is 1.37 and 4.0 % respectively [20]. Among southern Europeans a rate of 3 % for factor II polymorphism has been reported which is higher than the 1.7 % reported for northern European populations [21] (Table 3).

The prevalence of factor V Leiden varies between 2 and 15 % in the healthy Caucasian population [1]. The prevalence factor V Leiden in the Chechan population is 18.3 %. In comparison with percentage of prevalence for Jordanians 15 % [16] and more recently 21.8 % in a study done by Nusier et al. [22], the Chechans have a higher percentage than other populations. A high prevalence of factor V Leiden has been reported in Caucasians but not in non-Caucasians [1]. For example the allele frequency of factor V Leiden polymorphism among Caucasoid subpopulations ranges from 1 to 8.5 %. This polymorphism is not found among African blacks Chinese, Japanese and native North and South Americans or Greenland Inuits [9].

The mean allele frequency among European populations is 2.7 %. In Cyprus the incidence is 12 % and in Sweden is 15 % [23]. Among Arabs the highest frequency is in Lebanon 7.88 % followed by Tunis 3.5 %, Bahrain 1.5 % and Saudi Arabia 1.0 % [18]. The allele frequency in north India is 1.9 % [24], in western Iran 2.97 % and in Tehran 5.5 % [25]. The frequency in Turkey is 4.5–4.9 % [23]. The allele frequency in the Chechan population is 9.2 % which is high compared to other populations (Table 4). Thus suggesting a single origin of the mutation. The data obtained from different studies support and suggest that this mutation arose in the Eastern Mediterranean and migrated to European regions with the migrants [9]. This supports the history that states the Chechans to be more ancient as a race having a higher prevalence of factor V Leiden.

Thus, factor II G20210A and factor V Leiden are restricted to European populations, which tends to argue for their monocentric origin. Their founding effect is posterior to the separation of the Caucasoids and Mongoloids (21,000–34,000 years ago according to haplotype analysis) [9, 10] and their dispersion was probably associated with the Neolithic migrations into Europe [11]. In their review of about 6,000 individuals from 26 populations from Europe and neighbouring countries, Lucotte and Mercier [23] concluded that factor V Leiden may have expanded from the Anatolian region, close by the zone where the process of agriculture is thought to have begun.

Factor V Leiden is the largest inherited risk factor of VTE [26]. However, the pathogenesis of VTE is multifactorial [1]. Although our results do not support random screening for factor V Leiden, its high prevalence among apparently healthy individuals in the Chechan population recommends screening for factor V Leiden in relatives of factor V Leiden carriers, in individuals with family history of VTE, and in high-risk situations, including pregnancy, use of oral contraceptives, and surgery.

Thus, these two inherited prothrombotic polymorphisms represent interesting tools for population genetics studies. The knowledge of these frequencies in the Middle East region through population-based studies will contribute to a better understanding of the interaction between genetic and environmental risk factors underlying thrombosis. The relationship between venous thrombophilia and these mutations have to be further studied in the Chechan population.

Conflict of interest None.

References

1. Bauduer F, Lacombe D (2005) Factor V Leiden, prothrombin 20210A, methylenetetrahydrofolate reductase 677T, and population genetics. Mol Genet Metab 86(1–2):91–99
2. Bertina RM, Koeleman BP, Koster T, Rosendaal FR, Dirven RJ, de Ronde H, van der Velden PA, Reitsma PH (1994) Mutation in blood coagulation factor V associated with resistance to activated protein C. Nature 369(6475):64–67
3. Rosendaal FR, Koster T, Vandenbroucke JP, Reitsma PH (1995) High risk of thrombosis in patients homozygous for factor V Leiden (activated protein C resistance). Blood 85(6):1504–1508
4. Poort SR, Rosendaal FR, Reitsma PH, Bertina RM (1996) A common genetic variation in the 3′-untranslated region of the prothrombin gene is associated with elevated plasma prothrombin levels and an increase in venous thrombosis. Blood 88(10):3698–3703
5. Dahlback B, Carlsson M, Svensson PJ (1993) Familial thrombophilia due to a previously unrecognized mechanism characterized by poor anticoagulant response to activated protein C: prediction of a cofactor to activated protein C. Proc Natl Acad Sci USA 90(3):1004–1008
6. De Stefano V, Martinelli I, Mannucci PM, Paciaroni K, Chiusolo P, Casorelli I, Rossi E, Leone G (1999) The risk of recurrent deep venous thrombosis among heterozygous carriers of both factor V Leiden and the G20210A prothrombin mutation. N Engl J Med 341(11):801–806
7. Martinelli I, Bucciarelli P, Margaglione M, De Stefano V, Castaman G, Mannucci PM (2000) The risk of venous thromboembolism in family members with mutations in the genes of factor V or prothrombin or both. Br J Haematol 111(4):1223–1229
8. Rosendaal FR (1999) Venous thrombosis: a multicausal disease. Lancet 353(9159):1167–1173
9. Zivelin A, Griffin JH, Xu X, Pabinger I, Samama M, Conard J, Brenner B, Eldor A, Seligsohn U (1997) A single genetic origin for a common Caucasian risk factor for venous thrombosis. Blood 89(2):397–402
10. Zivelin A, Rosenberg N, Faier S, Kornbrot N, Peretz H, Mannhalter C, Horellou MH, Seligsohn U (1998) A single genetic origin for the common prothrombotic G20210A polymorphism in the prothrombin gene. Blood 92(4):1119–1124
11. Rees DC, Chapman NH, Webster MT, Guerreiro JF, Rochette J, Clegg JB (1999) Born to clot: the European burden. Br J Haematol 105(2):564–566
12. Nasidze I, Ling EY, Quinque D, Dupanloup I, Cordaux R, Rychkov S, Naumova O, Zhukova O, Sarraf-Zadegan N, Naderi GA, Asgary S, Sardas S, Farhud DD, Sarkisian T, Asadov C, Kerimov A, Stoneking M (2004) Mitochondrial DNA and Y-chromosome variation in the Caucasus. Ann Hum Genet 68(Pt 3):205–221
13. Kailani W (2002) Chechens in the Middle East: between original and host cultures. Caspian Studies Program

14. Poncz M, Solowiejczyk D, Harpel B, Mory Y, Schwartz E, Surrey S (1982) Construction of human gene libraries from small amounts of peripheral blood: analysis of beta-like globin genes. Hemoglobin 6(1):27–36
15. Bortolin S, Black M, Modi H, Boszko I, Kobler D, Fieldhouse D, Lopes E, Lacroix JM, Grimwood R, Wells P, Janeczko R, Zastawny R (2004) Analytical validation of the tag-it high-throughput microsphere-based universal array genotyping platform: application to the multiplex detection of a panel of thrombophilia-associated single-nucleotide polymorphisms. Clin Chem 50(11):2028–2036
16. Eid SS, Rihani G (2004) Prevalence of factor V Leiden, prothrombin G20210A, and MTHFR C677T mutations in 200 healthy Jordanians. Clin Lab Sci 17(4):200–202
17. Angchaisuksiri P, Pingsuthiwong S, Aryuchai K, Busabaratana M, Sura T, Atichartakarn V, Sritara P (2000) Prevalence of the G1691A mutation in the factor V gene (factor V Leiden) and the G20210A prothrombin gene mutation in the Thai population. Am J Hematol 65(2):119–122
18. Almawi WY, Keleshian SH, Borgi L, Fawaz NA, Abboud N, Mtiraoui N, Mahjoub T (2005) Varied prevalence of factor V G1691A (Leiden) and prothrombin G20210A single nucleotide polymorphisms among Arabs. J Thromb Thrombolysis 20(3):163–168
19. Abu-Amero KK, Wyngaard CA, Kambouris M, Dzimiri N (2002) Prevalence of the 20210 G->A prothrombin variant and its association with coronary artery disease in a Middle Eastern Arab population. Arch Pathol Lab Med 126(9):1087–1090
20. Akar N, Misirlioglu M, Akar E, Avcu F, Yalcin A, Sozuoz A (1998) Prothrombin gene 20210 G-A mutation in the Turkish population. Am J Hematol 58(3):249
21. Rosendaal FR, Doggen CJ, Zivelin A, Arruda VR, Aiach M, Siscovick DS, Hillarp A, Watzke HH, Bernardi F, Cumming AM, Preston FE, Reitsma PH (1998) Geographic distribution of the 20210 G to A prothrombin variant. Thromb Haemost 79(4):706–708
22. Nusier MK, Radaideh AM, Ababneh NA, Qaqish BM, Alzoubi R, Khader Y, Mersa JY, Irshaid NM, El-Khateeb M (2007) Prevalence of factor V G1691A (Leiden) and prothrombin G20210A polymorphisms among apparently healthy Jordanians. Neuroendocrinol Lett 28(5):699–703
23. Lucotte G, Mercier G (2001) Population genetics of factor V Leiden in Europe. Blood Cells Mol Dis 27(2):362–367
24. Garewal G, Das R, Trehan U (1997) Factor V Leiden: prevalence in the indigenous population and cases of thrombosis in North India. Br J Haematol 97(4):940
25. Rahimi Z, Vaisi-Raygani A, Mozafari H, Kharrazi H, Rezaei M, Nagel RL (2008) Prevalence of factor V Leiden (G1691A) and prothrombin (G20210A) among Kurdish population from Western Iran. J Thromb Thrombolysis 25(3):280–283
26. Rosen SB, Sturk A (1997) Activated protein C resistance—a major risk factor for thrombosis. Eur J Clin Chem Clin Biochem 35(7):501–516

Short communication

Sanjad Sakati syndrome: a case series from Jordan

J. Albaramki,[1] K. Akl,[1] A. Al- Muhtaseb,[1] M. Al-Shboul,[2] T. Mahmoud,[2] M. El-Khateeb[2] and H. Hamamy[3]

متلازمة سانجاد ساكاتي: سلسلة حالات من الأردن

جمانة البرامكي، كمال عقل، علياء المحتسب، محمد الشبول، تمارا محمود، محمد الخطيب، حنان حمامي

الخلاصة: متلازمة سانجاد ساكاتي هي اضطراب نادر مرتبط بالصبغي الجسدي المتنحي سبق وصفه بين العرب. وقد أبلغ الباحثون عن 8 مرضى من 7 أسر أردنية، أجري لـ 6 منها اختبار الجينات، ووجد خَبن في الموضع 12 bp (166-155 del) ضمن الجين النوعي المسؤول عن التيوبولين إي (TBCE) في الإيكسون 3 في الموضع 1q42-43. وكان لدى جميع المرضى تأخر شديد في النمو، مع ملامح مميزة في النمط الظاهري، وقصور في الغدد المجاورة للدرقية (الدريقات). وسُجِّل وجود قرابة بين الأبوين في جميع الأسر. وهذه هي أول سلسلة للحالات الوراثية التي تم إثباتها لمتلازمة سانجاد ساكاتي في الأردن.

ABSTRACT Sanjad Sakati syndrome is a rare autosomal recessive disorder that has been described in Arabs. We report 8 patients from 7 Jordanian families, 6 of whom underwent genetic testing and were found to have a 12 bp (155-166 del) deletion within the tubulin-specific chaperone E (*TBCE* gene) in exon 3 at 1q42-43. All patients had severe growth retardation, distinct phenotypic features and hypoparathyroidism. Parental consanguinity was recorded in all families. This is the first genetically proven case series of Sanjad Sakati syndrome in Jordan.

Le syndrome de Sanjad-Sakati : une série de cas en Jordanie

RÉSUMÉ Le syndrome de Sanjad-Sakati est un trouble autosomique récessif rare qui a été décrit dans la population arabe. Nous avons étudié les dossiers de huit patients faisant partie de sept familles jordaniennes ; les analyses génétiques réalisées sur six d'entre eux ont révélé une délétion de 12 bp (155-166 del) dans l'exon 3 localisé en 1q42-43 dans le gène TBCE codant la protéine chaperon E spécifique de la tubuline. Tous les patients présentaient un grave retard de croissance, des caractéristiques phénotypiques singulières et une hypoparathyroïdie. Une consanguinité des parents a été observée dans toutes les familles. Il s'agit de la première série de cas du syndrome de Sanjad-Sakati confirmés génétiquement en Jordanie.

[1]*Department of Pediatrics, Jordan University Hospital, Amman, Jordan (Correspondence to J. Albaramki: jumanabaramki@hotmail.com).*
[2]*National Center for Diabetes Endocrinology & Genetics, Amman, Jordan.*
[3]*Department of Genetic Medicine and Development, Geneva University Hospital, Geneva, Switzerland.*

Introduction

Sanjad Sakati syndrome or hypoparathyroidism-retardation-dysmorphism (HRD) is an autosomal recessive disorder that was first described in 1988 [1]. It is characterized by congenital hypoparathyroidism, growth and mental retardation with distinct phenotypic features. It is linked to the *TBCE* gene on chromosome 1q42-43 which encodes for the tubulin-specific chaperone E protein [2–4].

Sanjad Sakati syndrome has been reported in areas of the Middle East and has a high prevalence among Arabs. Since it may be confused with other syndromes that can present with hypocalcaemia and dysmorphic features, genetic testing allows Sanjad Sakati to be excluded in any child presenting with hypocalcaemia and deep-set eyes. The availability of genetic testing enables accurate diagnosis of affected children, discovery of carriers and prospective counselling as well as prenatal diagnosis of Sanjad Sakati syndrome in high-risk families.

This case series reports 8 patients with Sanjad Sakati syndrome from 7 families in Jordan, 6 of whom had genetic testing. There have been no previous reports with genetic testing from Jordan.

Case series

Hospital records were reviewed for the period 2001–2009 only these 8 cases were found. Information was extracted from the medical records and personal interview.

All the patients first presented during the neonatal period, at around 2–3 weeks of age, with hypocalcaemic seizures. Two of the patients were first seen in 2007, 2 in 2004 and 1 each in 2001, 2002, 2006, 2009. Their current mean age is 5 years (range 11 months–10 years). There were 3 females and 5 males and 6 of them had low birth weight.

All 8 patients had measurements taken of their calcium, phosphorus and parathyroid hormone (PTH) levels; 7 had brain imaging and skeletal survey, and 3 patients had an ophthalmological assessment. All of the patients were diagnosed biochemically to have hypoparathyroidism by the low levels of PTH, hypocalcaemia and elevated phosphorus levels (Table 1). All of the patients were put on vitamin D and calcium supplements. One patient developed generalized non-uraemic calcification and another had mild bilateral medullary renal nephrocalcinosis as a complication of the treatment. One patient had refractory hyperphosphataemia.

Three patients had recurrent hospital admissions for various infections, such as pneumonia and meningitis, and 2 patients died at home in 2009 from unknown causes.

Phenotypic features

All the patients had severe failure to thrive, microcephaly, delayed motor milestones, mental retardation and learning difficulties. All of them had teeth abnormalities such as delayed teething, dental caries or abnormal teeth. They had distinct dysmorphic features including deep-set eyes, micrognathia, depressed nasal bridge, microphthalmia, prominent forehead and small hands and feet (Figure 1, Table 2).One patient had large ears and a high-arched palate.

Family history

Parental consanguinity was reported in all 7 families. The parents of 3 cases were first cousins. Three patients had a positive family history of the same condition, 2 of them were siblings. One of the patients had a sibling who had been diagnosed prenatally by genetic testing at 11 weeks of pregnancy and the mother had undergone a selective abortion of the affected fetus.

Imaging results

Seven patients underwent brain imaging: 2 cases showed bilateral symmetrical calcifications in the basal ganglia, 1 had thinning of the corpus callosum and 1 patient had craniosynostosis; the rest had normal brain imaging. Skeletal survey was normal in all patients. Bone age was assessed for 2 patients and was delayed in both.

Table 1 Characteristic of cases

Case	Sex	Date first seen	Calcium (mg/dL)	Phosphorus (mg/dL)	PTH	Brain CT	Consanguinity	Genetic testing	Died
1	Male	Apr-2004	7.9	8.6	Low	Not done	Second degree	Yes	–
2	Male	Nov-2001	6.3	10.0	Low	Calcification, thin corpus callosum	Second degree	No	–
3	Male	Jun-2006	4.80	13.7	Low	Normal	Second degree	No	–
4.	Male	Oct-2007	7.79	8.44	Low	Normal	First degree	Yes	Yes
5	Male	Aug-2007	8.69	8.58	Low	Normal	First degree	Yes	–
5	Female	Aug-2002	6.32	9.68	Low	Normal	First degree	Yes	Yes
7	Female	Aug-2009	4.95	11.95	Low	Craniosynostosis	Second degree	Yes	–
8	Female	Feb-2004	7.90	7.3	Low	Calcification	Second degree	Yes	–

PTH = parathyroid hormone; CT = computed tomography.

Figure 1 One of our patients with low-set ears, deep-set eyes and micrognathia: permission was granted by the family to show the photograph

Ophthalmological assessment

Ophthalmological assessment was done for 3 patients and it showed abnormal retinal vessels dilatation and tortuosity in 1, bilateral dense central corneal opacity suggestive of congenital cataract in another who needed lensectomy, and papilloedema in the third patient.

Genetic testing

EDTA-blood samples were collected from each patient at the time of presentation, and DNA was extracted using the conventional phenol–chloroform proteinase K method [5]. The isolated DNA was dissolved in water and diluted to a concentration of 200 ng/µL.

Polymerase chain reaction (PCR) was performed to identify 12 bp (155–166 del) deletion in exon 3 of the *TBCE* gene since this mutation has been commonly described in of Sanjad Sakati syndrome in nearby Middle Eastern countries. Samples were amplified in duplicate along with positive and negative controls. The sequence of forward and reverse PCR primer was designed by *Primer 3* software. PCR reactions were carried out in 25 µL reaction mixture containing 10 mmol/L Tris hydrochloride pH 8.3, 50 mmol/L potassium chloride, 1.5 mmol/L magnesium chloride, 0.2 mmol/L dNTPs, 10 mmol/L primers and 1 U of hot star *Taq* polymerase (Qiagen, USA). The amplification conditions used were: 95 °C for 4 minutes, followed by 30 cycles at 94 °C for 45 seconds, annealing at 62 °C for 45 seconds and extension at 72 °C for 1 minute. PCR products were directly run over 3% (3:1) low electro-endosmosis (LE) and low molecular mass polypeptide (LMP) agarose gel (Promega, USA) for 120 minutes at 80 V in 1 × Tris boric EDTA buffer. The gel was then stained with ethidium bromide (Promega, USA), visualized by illumination with ultraviolet light, and documented by photography (Gel Doc, Bio-Rad, USA). The size of the product was about 138 bp for the normal allele and 126 bp for the mutant allele (Figure 2).

Six patients underwent genetic testing. All of them had 12 bp (155–166 del) deletion within the *TBCE* gene in exon 3.

For prenatal diagnosis, around 30 mg of chorionic villi were obtained at 11 weeks of gestation using the transcervical approach. Chorionic villi were rinsed in hypotonic solution (37% sodium chloride) and the whitish, branched tissue which represent the fetal tissue were used for DNA extraction by the phenol–chloroform–proteinase K method [5].

Prenatal diagnosis was carried out for 1 case for a consanguineous couple with 2 affected children (boy and girl). The fetal sample showed homozygous deletion of the 12 bp (155–166 del) within the *TBCE* gene in the fetus. Both parents were heterozygous for the deletion mutation.

Discussion

This is the first genetically proven case series of Sanjad Sakati syndrome from Jordan. A recent review from Kuwait revealed a high incidence of the condition of 7–8 per 100 000 live births [3].

Sanjad Sakati syndrome is a rare autosomal recessive disorder and was first described in Arabs by Sanjad et al. in Saudi Arabia in 1988 [1] and in 1991 [6], followed by reports from other countries [7–9]. In 1998, Parvari et al. used homozygosity and linkage disequilibrium to map the gene on chromosome 1q42-43 [2] and in 2002 demonstrated that mutation of the *TBCE* gene caused Sanjad Sakati and autosomal recessive Kenny–Caffey syndrome [3].

Table 2 Clinical picture of Sanjad Sakati syndrome in 8 Jordanian patients

Feature	No. of patients
IUGR	6
Short stature	8
Microcephaly	8
Deep-set eyes	8
Small hands and feet	8
Hypoparathyroidism	8
Mental retardation and learning difficulties	8
Affected sibling	3
Consanguinity	8
First cousin parents	3/7[a]
Second cousin parents	4/7[a]
Positive genetic testing	6
Normal skeletal survey	8
Brain calcification	2/7[b]
Thin corpus callosum	1/7[b]

[a]No. of families assessd = 7.
[b]One patient did not have brain imaging.
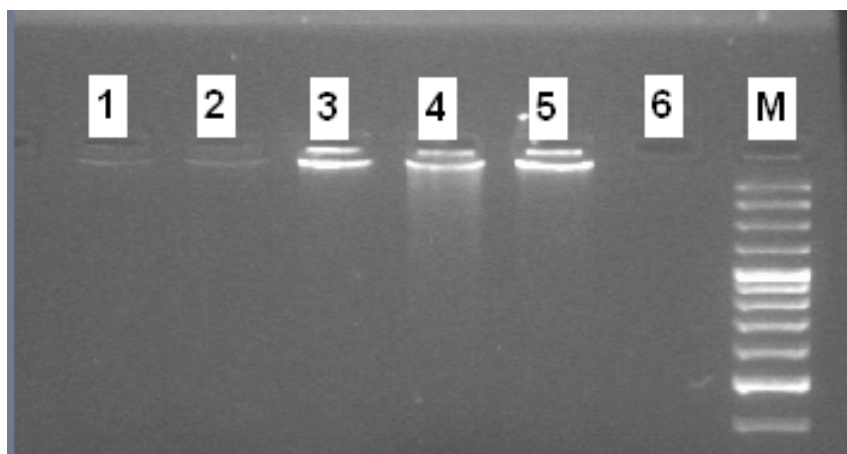IUGR = intrauterine growth retardation.

Figure 2 Lanes 1, 2, 4: homozygous for 12 bp (155–166 del) deletion; Lane 3: heterozygous for 12 bp (155–166 del) deletion; Lanes 5: negative controls; Lane 6: blank and M: 50 bp DNA ladder

The *TBCE* gene encodes for a protein that participates in beta tubulin folding. Homozygous deletion of 12 bp in exon 3 of the *TBCE* gene was confirmed to be the cause of this syndrome (OMIM 241410) [4]. This mutation has been described in Arabs with Sanjad Sakati syndrome, but in 2006 Courten et al. described a 4.5-year-old girl with the syndrome who did not have a mutation in the *TBCE* gene and found another possible gene locus [10].

The syndrome can be confused with autosomal recessive Kenny–Caffey syndrome, caused by mutation in the *TBCE* gene, that shares similar phenotypic features but in addition has osteosclerosis, medullary stenosis of long bones, and normal intelligence. Sanjad Sakati syndrome is characterized by congenital hypoparathyroidism, prenatal and postnatal growth retardation, developmental delay as well as mental retardation. The common dysmorphic features are microcephaly, prominent forehead, deep-set eyes, micrognathia, depressed nasal bridge, small hands and feet, dental anomalies and microphthalmia. Ophthalmic manifestations include errors of refraction, retinal

vascular tortuosity, strabismus [11], and corneal opacities [12]. Thin corpus callosum has been described in patients with this syndrome [13]. Patients with Sanjad Sakati syndrome have increased susceptibility to recurrent infections but have normal immunological profile. Di George syndrome should also be considered in patients with hypoparathyroidism but these patients usually have cardiac defects and impaired immune functions and special facial features different from those found in Sanjad Sakati syndrome. Genetic testing is used to differentiate between these syndromes.

Our patients had a high rate of parental consanguinity reaching 100%, much higher than the 12.5% reported in Kuwait indicating a high rate of heterozygous carriers in Kuwait [7].

The treatment of patients with Sanjad Sakati syndrome is a challenge for most physicians especially in controlling their high phosphate levels, and the adverse effects of therapy include generalized calcifications, as seen in one of our patients.

Nowadays, genetic testing for Sanjad Sakati syndrome can confirm the diagnosis and provide the option of prenatal testing in families with an affected child, or for parents with genetically proven carrier state.

References

1. Sanjad S, Sakati N, Abu-Osba Y. Congenital hypoparathyroidism with dysmorphic features: a new syndrome. *Pediatric Research*, 1988, 23:71A.

2. Parvari R et al. Homozygosity and linkage-disequilibrium mapping of the syndrome of congenital hypoparathyroidism, growth and mental retardation, and dysmorphism to a 1-cM interval on chromosome 1q42-43. *American Journal of Human Genetics*, 1998, 63:163–169.

3. Parvari R et al. Mutation of TBCE causes hypoparathyroidism-retardation-dysmorphism and autosomal recessive Kenny-Caffey syndrome. *Nature Genetics*, 2002, 32:448–452.

4. Kelly TE et al.Confirmation of the assignment of the Sanjad-Sakati (congenital hypoparathyroidism) syndrome (OMIM 241410) locus to chromosome 1q42-43. *Journal of Medical Genetics*, 2000, 37 (1):63–64.

5. Sambrook J, Fritsch EF, Maniatis T. *Molecular cloning: A laboratory manual*, 2nd edition. Cold Spring Harbor, New York, Cold Spring Harbor Laboratory Press, 1989.

6. Sanjad SA et al. A new syndrome of congenital hypoparathyroidism, severe growth failure, and dysmorphic features. *Archives of Disease in Childhood*, 1991, 66(11):193–196.

7. Naguib KK et al. Sanjad–Sakati syndrome/Kenny–Caffey syndrome type 1: a study of 21 cases in Kuwait. *Eastern Mediterranean Health Journal*, 2009, 15(2):345–352.

8. Hershkovitz E et al.Hypoparathyroidism-retardation-Dysmorphism (HRD) syndrome—a review. *Journal of Pediatric Endocrinology and Metabolism*, 2004, 17 (12):1583–1590.

9. Hershkovitz E et al. The new syndrome of congenital hypoparathyroidism associated with dysmorphism, growth retardation, and developmental delay—a report of six patients. *Isreal Journal of Medical Sciences*, 1995, 31(5):326–327.

10. Courtens WF et al. Hypoparathyroidism-retardation-dysmorphism syndrome in a girl: A new variant not caused by a TBCE mutation--clinical report and review. *American Journal of Medical Genetics*, 2006, 140(6):611–617.

11. Al Dhoyan N, Al Hemidan AI, Ozand PT. Ophthalmic manifestations of Sanjad-Sakati syndrome. *Ophthalmic Genetics*, 2006, 27(3):83–87.

12. Khan AO, Al-Assiri A, Al-Mesfer S. Ophthalmic features of hypoparathyroidism-retardation-dysmorphism. *Journal of the American Association for Pediatric Ophthalmology and Strabismus*, 2007,11(3): 288–290.

13. Padidela RF et al. Mutation in the TBCE gene is associated with hypoparathyroidism-retardation-dysmorphism syndrome featuring pituitary hormone deficiencies and hypoplasia of the anterior pituitary and the corpus callosum. *Journal of Clinical Endocrinology and Metabolism*, 2009, 94 (8):2686–2691.

Community genetics services. Report of a WHO Consultation on community genetics in low- and middle-income countries. Geneva, Switzerland, 13–14 September 2010

The above-mentioned document presents the findings and recommendations of WHO Consultation on community genetics in low- and middle-income countries. The objective of the Consultation was to develop an evidence-based report on community genetics services to provide guidance to low- and middle-income countries (LMIC) in accordance with the 2008–2013 Action Plan for the Global Strategy for the Prevention and Control of Noncommunicable Diseases. The goal of community genetics in LMIC is to prevent congenital disorders and genetic diseases at population level and, at the same time, to provide genetics services (diagnosis and counselling) in the community for individuals and families.

Congenital disorders (birth defects) constitute a major health problem worldwide especially in LMIC. Factors that may contribute to the high rates of congenital disorders in LMIC include the general low availability of public health measures directed at the care and prevention of these disorders, the high frequency of haemoglobinopathies in Africa, Middle-East and South-East Asia, the high consanguinity rates in the Eastern Mediterranean and South-East Asia regions that can increase the occurrence of recessively inherited diseases, advanced maternal age at conception in many low- and middle-income countries, which increases the predisposition to chromosomal trisomies such as Down syndrome, and large family size that may increase the number of affected children in families with autosomal recessive conditions. Prevention programmes have been successfully implemented in some LMIC, thus reducing the burden of congenital disorders or genetic diseases. Examples of countries adopting such programmes are, among others, Bahrain Cyprus and the Islamic Republic of Iran.

Further information about this and other WHO publications on genetics is available at: http://www.who.int/genomics/publications/en/index.html

Definition of the phenotypic spectrum of Temtamy preaxial brachydactyly syndrome associated with autosomal recessive *CHYS1* mutations

Samia Temtamy[a*], Mona Aglan[a*], A. Kemal Topaloglu[e], Bernd Wollnik[g], Khalda Amr[a], Tarek H. El-Badry[b], Gamal A. Hosny[c], Nermine Salah Eldin[d], Mohammad Shboul[h], Mustafa Herdem[f], Junxian Ong[h], Bruno Reversade[h*] and Jing Tian[h*]

[a]Department of Clinical Genetics, Division of Human Genetics and Genome Research, [b]Department of Clinical Genetics, Medical Research Division, National Research Centre, [c]Department of Pediatrics, Children Hospital, Cairo University, Cairo, [d]Department of Orthopedic Surgery, Benha University, Benha, Egypt, Departments of [e]Pediatric Endocrinology, [f]Orthopedics and Traumatology, Faculty of Medicine, Cukurova University, Adana, Turkey, [g]Institute of Human Genetics, University of Cologne, Cologne, Germany and [h]Laboratory of Human Embryology, Institute of Medical Biology, A* STAR, Singapore

Correspondence to Samia Temtamy, Division of Human Genetics and Genome Research, National Research, Centre, El-Buhouth St Dokki, Cairo 12111, Egypt
Tel: + 20 122 341 0603; fax: + 20 233 370 931; e-mail: samiatemtamy@yahoo
and
Correspondence to Jing Tian, Human Embryology & Genetics lab., Institute of Medical Biology, A*Star 8A Biomedical Grove 05-40 Immunos Singapore 138648
Tel: +65-64070241; fax: +65-64642006;
e-mail: tian.jing@imb.a-star.edu.sg, jing.tian@reversade.com

*Samia Temtamy, Mona Aglan, Bruno Reversade, and Jing Tian contributed equally to the writing of this article

Background

Temtamy preaxial brachydactyly syndrome (OMIM: 605282) is a rare autosomal recessive disorder first described in 1998. In 2010, *CHYS1* was identified as the causative gene. So far, the syndrome has been reported and homozygous *CHYS1* mutations have been confirmed in 11 patients from consanguineous families originating from Turkey (*n*=3), Egypt (*n*=2), Pakistan (*n*=3), Jordan (*n*=2), and Sri Lanka (*n*=1).

Patients and methods

Here, we report on five new Egyptian patients with Temtamy preaxial brachydactyly syndrome from three consanguineous families. Phenotype analysis of all reported positive cases in the literature, including our patients (*n*=16), is carried out to define the characteristic clinical features of this syndrome.

Results

All five patients were found to have recessive mutations in *CHYS1*. One family was compound heterozygous and all the other families carried homozygous missense mutations. Phenotype analysis of all reported positive cases in the literature defined and confirmed the characteristic clinical features, mainly the facial dysmorphism, typical digital malformations, and associated anomalies.

Conclusion and recommendations

We conclude that Temtamy preaxial brachydactyly syndromeTPBS is an easily identifiable dysmorphic syndrome. The rarity of worldwide reports could be because of underdiagnosis. Because of some phenotypic overlap with other preaxial brachydactyly syndromes, further clinical and molecular research is required to define possible genetic heterogeneity, genotype–phenotype correlations, and the functional role of encoded proteins in digital differentiation and development.

Introduction

Temtamy preaxial brachydactyly syndrome (TPBS; MIM 605282) was first reported in 1998 in an Egyptian patient as a new autosomal recessive multiple congenital anomaly syndrome characterized by bilateral, symmetric preaxial brachydactyly and hyperphalangism of the digits, facial dysmorphism, dental anomalies, sensorineural hearing loss, and delayed motor and mental development (Temtamy *et al.*, 1998). An additional Egyptian patient with similar manifestations apart from hearing loss was further described by Temtamy and Aglan (2008).

The TPBS causative gene studied in the two previously reported Egyptian patients and in an additional three sibs from a consanguineous Turkish family was first reported at the European Society of Human Genetics (ESHG) annual meeting in Vienna, 2009 (Li *et al.*, 2009). Molecular studies were carried out on an additional patient from Sri Lanka and on three Pakistani sibs with TPBS (Race *et al.*, 2010), in addition to those presented at the ESHG meeting (2009) by Li *et al.* (2010). The researchers showed that loss of chondroitin synthase 1 (*CHSY1*) function underlies the pathogenesis of autosomal recessive TPBS. *CHSY1* encodes an evolutionarily conserved type II transmembrane protein comprising a Fringe motif and a glycosyltransferase domain, whose combined enzymatic activity is crucial for the biosynthesis of chondroitin sulfates. The researchers also obtained similar zebrafish phenotypes after *CHSY1* knockdown as well as overexpression, which might explain why in

humans, brachydactyly can be caused by mutations leading either to loss or to gain of bone morphogenetic protein/growth and differentiation factor signaling. This was further supported by a back-to-back manuscript by Tian *et al.* (2010) reporting on two affected siblings with TPBS, offspring of consanguineous Jordanian parents. The researchers detected a truncating frameshift mutation in the same gene *CHSY1* and concluded that *CHSY1* is a secreted FRINGE enzyme required for the adjustment of NOTCH signaling throughout human and fish embryogenesis and particularly during limb patterning (Tian *et al.*, 2010).

In this study, we contribute to the literature five additional Egyptian TPBS patients with *CHYS1* mutations aiming to identify the clinical manifestations in all reported cases in order to define the phenotypic spectrum of this syndrome.

Patients and methods

Five Egyptian patients (four boys, one girl) from three unrelated families were diagnosed at the Limb Malformations and Skeletal Dysplasia Clinic, National Research Centre (NRC), with TPBS. Two families had two similarly affected sibs each. All patients were offspring of consanguineous parents. Their age at presentation ranged from 1 year and 10 months to 7 years and 5 months. Pedigree analysis, clinical and orodental examination, anthropometric measurements, radiological studies of limb anomalies, and bone densitometry (DEXA) were carried out for all cases. Intelligence quotient assessment, hearing test by audiometry, eye examination, abdominal ultrasound, and brain imaging were carried out for selected cases.

Molecular studies

Genomic DNA was isolated from whole-blood samples using the standard phenol/chloroform extraction method. To check for *CHSY1* mutations, the following PCR primers were used: E1F (5'-GAGCTAAGCCGGAGGATGTG-3') and E1R (5'-ATCCCGCCTCTGATCTTTTC-3') for exon 1; E2F (5'-GAACCAAGCAGGCCAAGTAG-3') and E2R (5'-CCAACTTCAACCCTCAAAGA-3') for exon 2; E3F1 (5'-TTTGTGTGCTGTGGTCCATT-3') and E3R1 (5'-GTAAATACGCGTGCCTCCTC-3'), E3F2 (5'-TGGAGATGATCAATGCCAAC-3') and E3R2 (5'-TGGGTCATACTGGCTGAAGA-3'), and E3F3 (5'-TGCCTGTGTCTGGAGAGTTTT-3') and E3R3 (5'-AGGCAAACACTGATCACCTTC-3') for exon 3.

PCR reactions were carried out at a final volume of 50 μl containing 100 ng template DNA using HotStarTaq DNA polymerase (Qiagen, New York, USA). The PCR thermal cycling program was set as follows: 95°C for 15 min, followed by 35 cycles of 45 s denaturation at 95°C, 50 s annealing at 56°C, and 50 s of extension at 72°C, with a final extension at 72°C for 10 min. PCR products were gel recovered using the QIAquick Gel Extraction Kit (Qiagen). Sequence analysis was carried out using the BigDye Terminator cycle sequencing kit (Applied Biosystems, California, USA), and products were run on a 3730 DNA Analyzer (Applied Biosystems).

Results
Family 1
Patient 1
A 7.5-year-old boy, the first child of apparently healthy parents who are first cousins, was referred to us because of short stature and hand anomalies. He has a normal female sib and a similarly affected younger brother (Fig. 1a). Pregnancy and delivery histories were unremarkable. He had a normal history of motor development. On examination, frontal bossing, a round flat face, wide palpebral fissures, and microstomia and micrognathia were noted (Fig. 1b). Orodental manifestations included a high arched palate and a deep overbite. Skeletal examination indicated brachydactyly with radial deviation of the first to third fingers, clinodactyly of the third and fourth fingers, and camptodactyly of the fourth and fifth fingers, with skin webbing between the fingers (Fig. 1c). Both feet had low inserted broad and short big toes, with clinodactyly of the second to fifth toes and a wide gap between the big toes and the second toes (Fig. 1d). Mild pectus excavatum was noted. Muscle tone and reflexes were normal. No abnormalities in the external genitalia were noted. Radiographs of both the hands showed preaxial brachydactyly with hyperphalangism of the index fingers and flexion deformity in the left second proximal and distal phalanges (Fig. 1e). His bone age was severely delayed. Short toes with hypoplastic medially deviated middle and terminal phalanges were detected on radiographs of both feet. An extra phalanx was seen at the right toes (Fig. 1f). His height was 103.3 cm (−3.9 SD); the weight and head circumference measurements were consistent with his age. A learning disability was reported. Stimulation tests indicated a normal growth hormone level. The thyroid profile was normal. Serum calcium, phosphorus, and alkaline phosphatase were normal. No abnormalities were detected by computed tomographic scan of the brain. Fundus examination was normal. DEXA indicated osteopenia at the femur and the spine (Z-scores: −1.34 and −1.21, respectively). Abdominal ultrasound indicated mild hepatosplenomegaly.

Patient 2
A 4-year-old boy, younger brother of patient 1, was studied. On examination, he was found to be similarly affected as his older brother (patient 1). Facial features and digital anomalies are shown in Fig. 1g–k.

Molecular studies on both the patients indicated a (TGT > CGT; c.2251T > C) homozygous mutation in exon 3 of *CHSY1*, causing a missense mutation (p.C751R) in the extracellular type-A glycosyltransferase domain of *CHSY1* (Figs 4a and 5a, d). Each parent was heterozygous for the same single nucleotide polymorphism.

Family 2
Patient 3
A 6.5-year-old boy, offspring of parents who are first cousins, was studied. He has a normal older brother
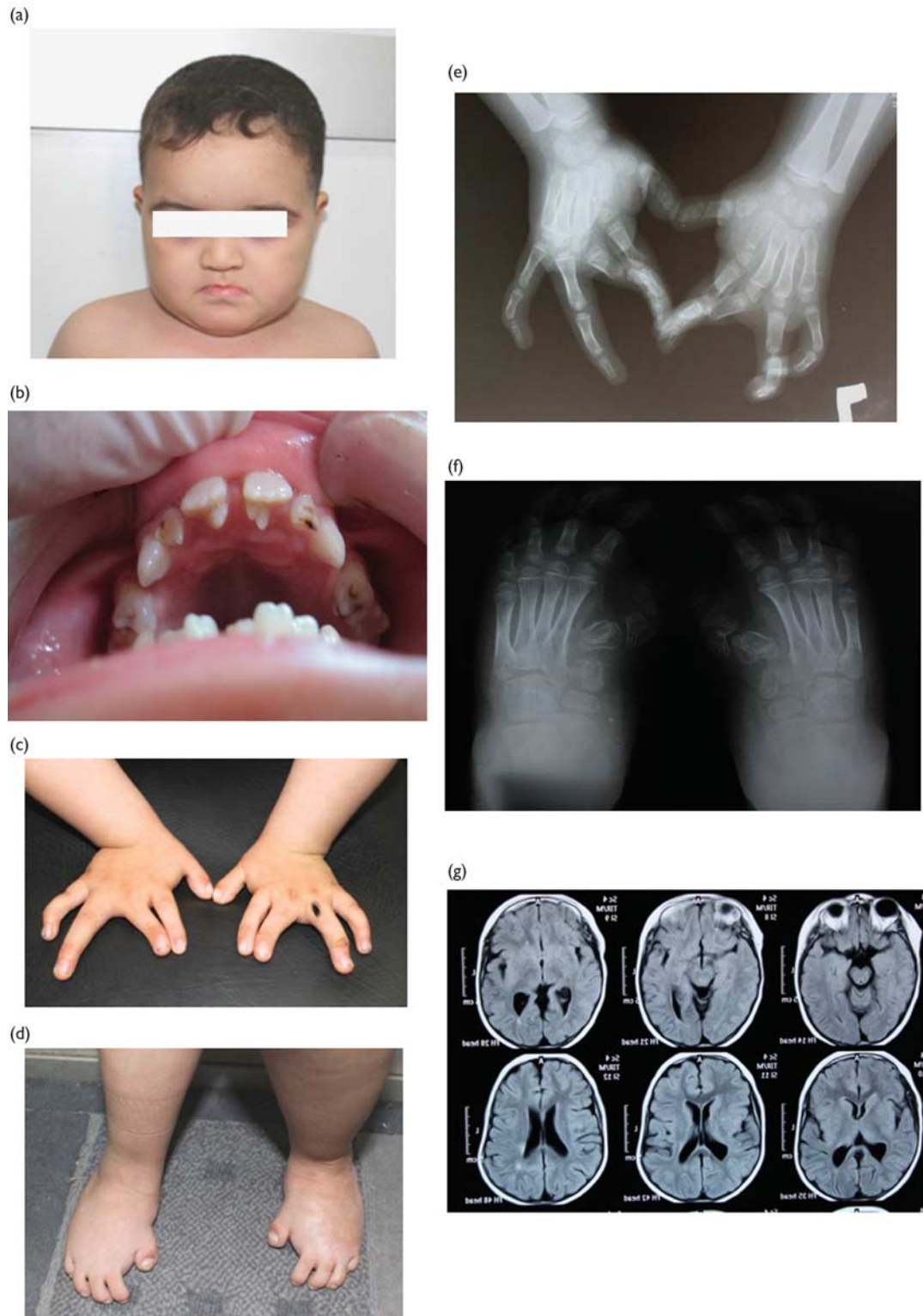
Figure 1
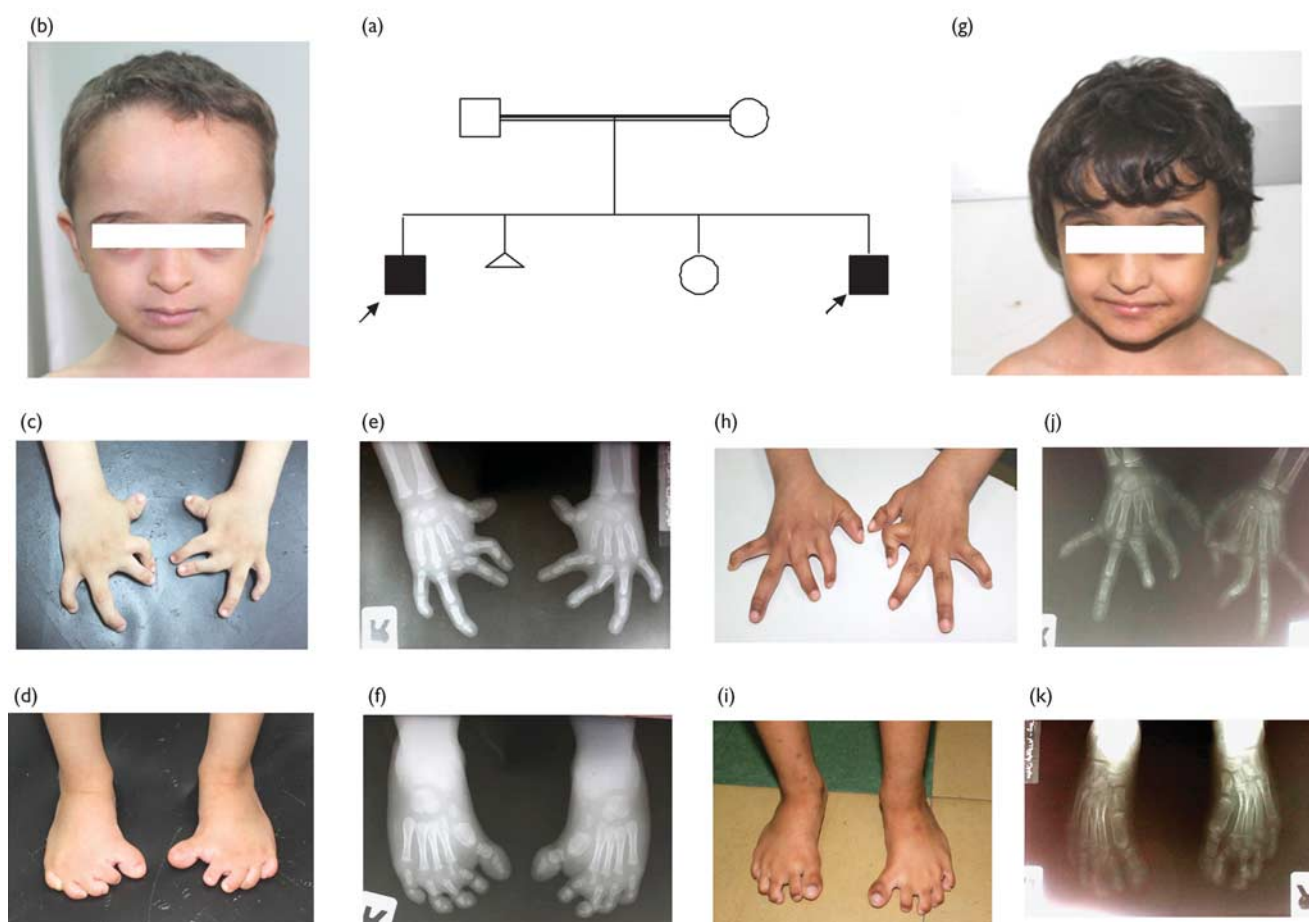
(a) Pedigree of family 1. (b) Facial features of patient 1. (c, d) Hands and feet of patient 1. (e, f) Radiographic films of the hands and feet of patient 1. (g) Facial features of patient 2. (h, i) Hands and feet of patient 2 (j, k). Radiographic films of the hands and feet of patient 2. Note the characteristic facial features with a wide-eye look, relative macrophthalmos, and malar hypoplasia. Preaxial brachydactyly, abducted thumbs and big toes, hyperphalangism, and camptodactyly are evident in the hands and feet.

and had a twin sib who died at birth. There was a mild delay in motor development. On examination, double hair whorl, frontal bossing, a round flat face, wide palpebral fissures, malar hypoplasia, microstomia, micrognathia, a short neck, and low-set nipples with redundant skin at the abdomen were observed (Fig. 2a). Orodental manifestations included a highly attached thick upper labial frenum, enamel hypoplasia, and hypocalcification in addition to microdontia and a talon cusp in the upper central incisors (Fig. 2b). A panoramic view indicated absent lower permanent first incisors and confirmed talon cusps. Hand examination indicated preaxial brachydactyly with short, low inserted thumbs; a wide space between the first and the second fingers, clinodactyly of the fifth fingers, and abnormal dermatoglyphics (Fig. 2c). The patient had limited supination of both elbows. Knock knees, brachydactyly with bilateral low inserted broad big toes, a wide gap between the first and the second toes, and bilateral medial deviation of all toes more on the left side were observed (Fig. 2d). Exaggerated hyperlordosis with mild scoliosis were additional skeletal features. He had hypotonia, normal reflexes, and normal external genitalia. A radiograph of both the

hands showed short first and second metacarpals, an extra phalanx at the index fingers, flexion deformity of the third metacarpophalangeal joints, and hypoplastic pointed distal phalanx of fifth fingers (Fig. 2e). Short broad delta epiphyses of the first metatarsals, short quadrangular proximal phalanx, and hyperphalangism of the first toes were detected on a radiograph of both feet (Fig. 2f). His height at 7.5 years of age was 107 cm (−3.0 SD) and his head circumference was 49.5 cm (−2.0 SD); his weight was the mean weight for his age. Psychological assessment indicated a cooperative child with delayed language, and his intelligence quotient was within the category of mild mental subnormality. The thyroid profile was normal. MRI of the brain indicated a hypovoluminous peritrigonal white matter with an abnormal white matter signal suggestive of postischemic brain insult (Fig. 2g). Fundus examination was normal. Hearing assessment showed bilateral otitis media. DEXA indicated borderline osteoporosis at the femur (Z-score: −2.09) and osteopenia at the spine (Z-score: −1.36). Abdominal ultrasound indicated mild hepatosplenomegaly.

Molecular studies showed a homozygous single nucleotide polymorphism (GGG > TGG; c.664G > T) in exon 2

Figure 2

(a) Facial features of patient 3. Note the round face, wide-eye look, malar hypoplasia, and short neck. (b) Dental anomalies of patient 3 showing talon cusps. (c, d) Hands and feet of patient 3. (e, f) Radiographic films of the hands and feet of patient 3. Note the preaxial brachydactyly, abducted thumbs and big toes, hyperphalangism, and camptodactyly. (g) MRI scan of the brain of patient 3 showing an abnormal white matter signal.
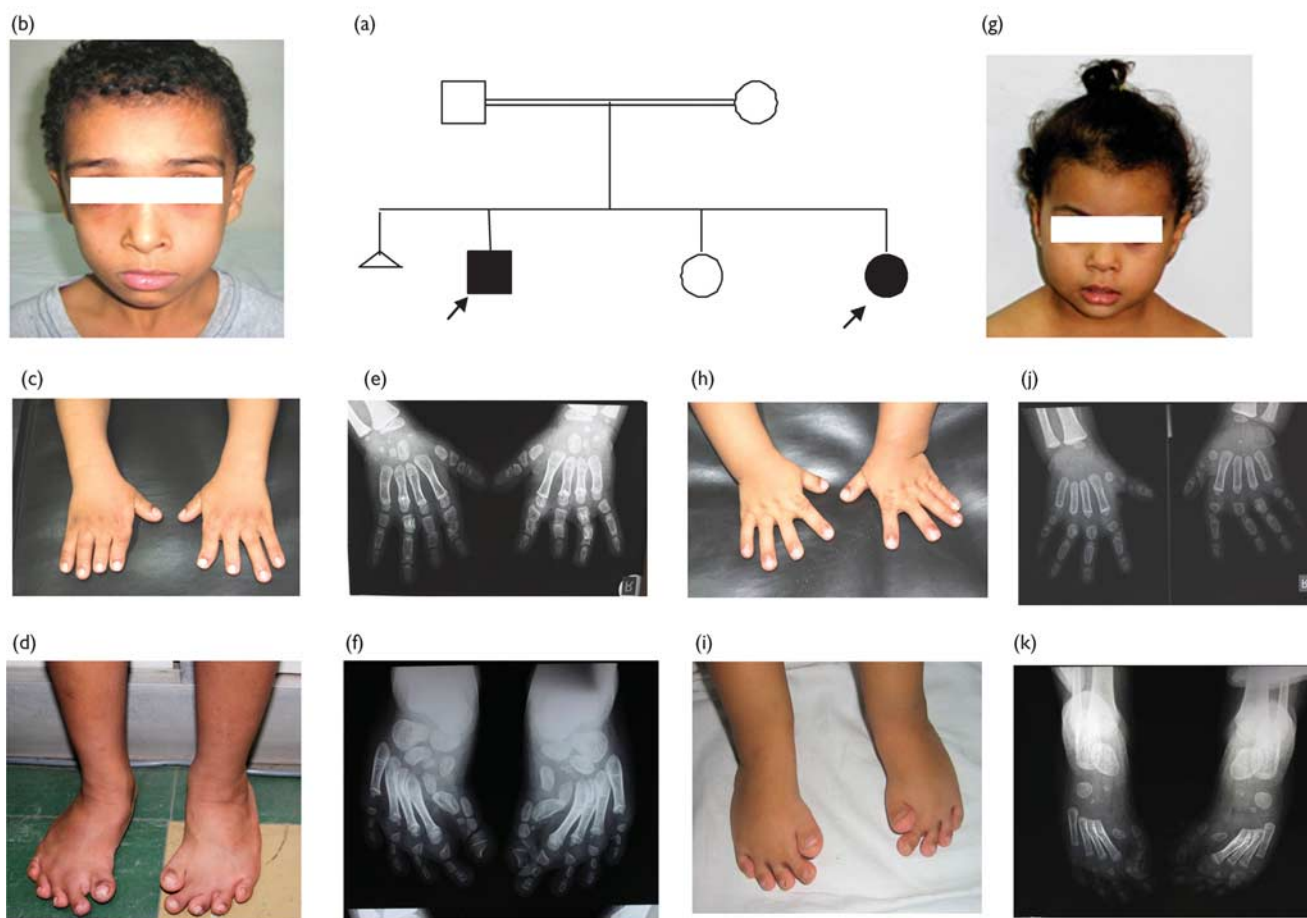
of *CHSY1*, leading to a missense mutation, p.G222W, in the FRINGE domain of the CHSY1 enzyme (Figs 4b and 5b, d). Both parents were heterozygous for the same mutation.
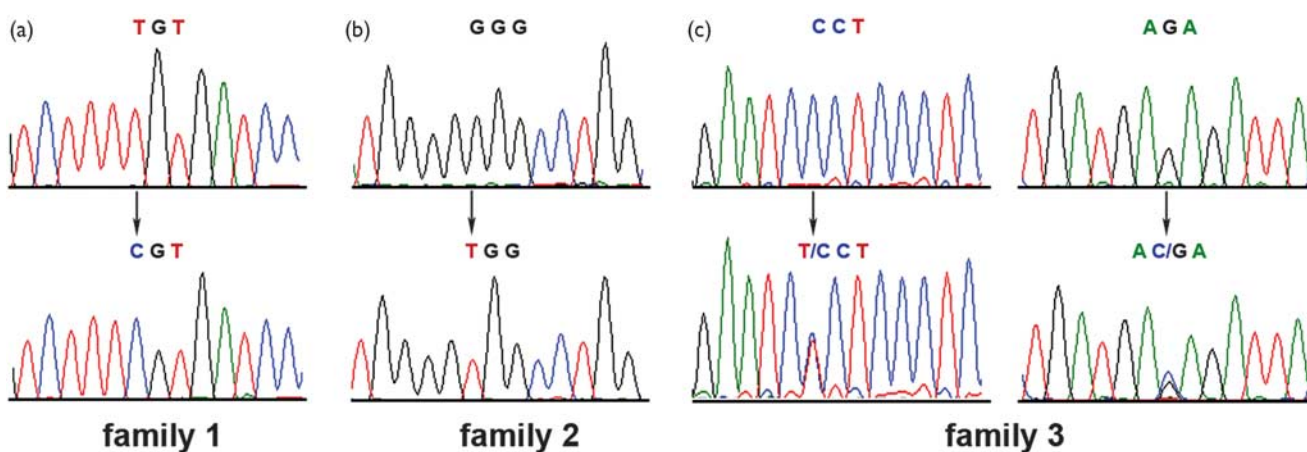
Family 3

Patient 4

A 6.5-year-old boy, offspring of apparently normal parents who are first cousins, was studied. He has a normal female

Figure 3

(a) Pedigree of family 3. (b) Facial features of patient 4. (c, d) Hands and feet of patient 4. (e, f) Radiographic films of hands and feet of patient 4. (g) Facial features of patient 5. (h, i) Hands and feet of patient 5. (j, k) Radiographic films of the hands and feet of patient 5. Note the milder affection compared with that in patients 1–3.

Figure 4

Chromatogram sequencing results showing the mutated codon in each family, all arising from single nucleotide polymorphisms in the homozygous state (families 1 and 2) or a compound heterozygous state in family 3.

sib and a younger similarly affected sister (Fig. 3a). Pregnancy and delivery histories were unremarkable. He had a normal history of motor development. On examina-

tion, frontal bossing, a flat face with malar hypoplasia, wide palpebral fissures, and microstomia and micrognathia were noted (Fig. 3b). Orodental manifestations included a

Figure 5
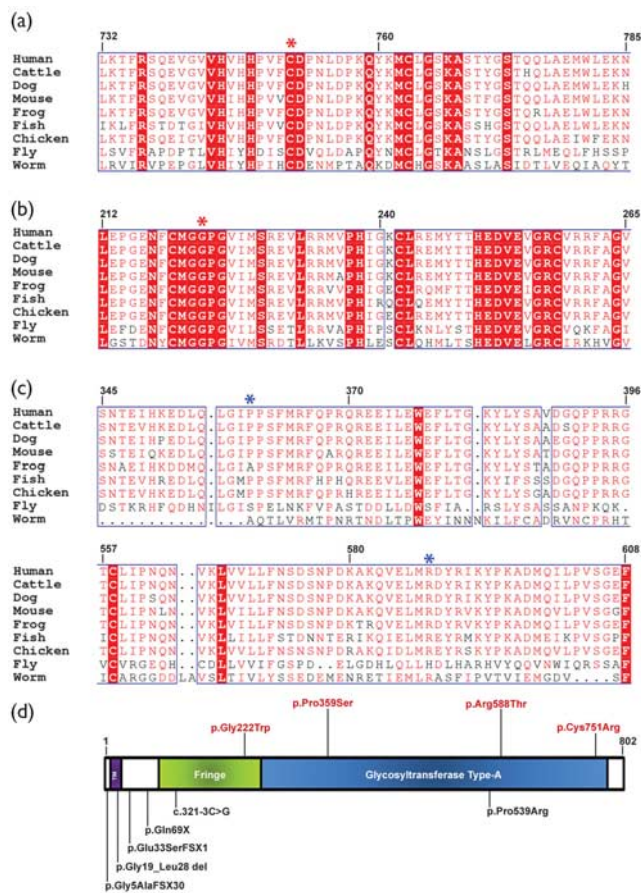
Chondroitin synthase 1 (CHSY1) proteins from human, cattle, dog, mouse, frog, fish, chicken, fly, and worm were aligned for the phylogenetic conservation of the affected amino acid C751 in family 1 (a) and G222 in family 2 (b; red asterisks). The compound heterozygous mutation affecting residues P359 and R588 in family 3 are conserved in vertebrate species, but not in invertebrate species (c; blue asterisks). (d) Summary of reported mutations in *CHSY1* in probands with Temtamy preaxial brachydactyly syndrome. The novel mutations found in this study are shown in red (top), whereas mutations described in previous studies are shown in black (bottom).

pseudo lower labial cleft, a thick upper labial frenum, a high arched palate, and enamel hypocalcification. Hand examination indicated brachydactyly, low inserted broad thumbs, short second and third fingers with a medial deviation of the left index finger, and broad metaphyses at the wrists (Fig. 3c). Both feet had low inserted broad and short big toes with a wide gap between the big toes and the second toes and a medial deviation of the second to fifth toes (Fig. 3d). Muscle tone and reflexes were normal. No abnormalities in the external genitalia were noted. A radiograph of both the hands showed short first metacarpals with hyperphalangism of the first and second fingers, short proximal phalanges of all fingers, and short middle and terminal phalanges of first to third fingers (Fig. 3e). A radiograph of both feet indicated a bilateral adducted forefoot with replacement of the first metatarsal by short deformed bones, short toes with hypoplastic medially deviated phalanges, and hyperphalangism of the big toes (Fig. 3f). His anthropometric measurements were consistent with his age, although relatively short limbs were noted. Serum calcium, phosphorus, and alkaline phospha-

tase were normal. No abnormalities were detected by computed tomography scan of the brain. Hearing assessment was normal.

Patient 5

A 2-year-old girl, the younger sister of patient 4, was studied. On examination, she was found to be similarly affected as her older brother. The facial features and digital anomalies are shown in Fig. 3g–k.

Molecular studies on both the patients indicated compound heterozygosity in exon 3, CCT > TCA (c.1075C > T) and AGA > ACA (c.1763G > A), causing, respectively, the heterozygous missense changes p.P359S and p.R588T (Figs 4c and 5c, d).

Table 1 presents the phenotype analysis of our five new reported cases with TPBS and the 11 previously reported cases (all associated with autosomal recessive *CHSY1* mutations) in order to define the phenotypic spectrum of the syndrome.

Discussion

The present study reports on five additional Egyptian patients, offspring of consanguineous parents with the

Table 1 Phenotype analysis of reported Temtamy preaxial brachydactyly syndrome patients with autosomal recessive *CHSY1* mutations

Phenotype	Proportion	%
Digits		
Preaxial brachydactyly, hyperphalangism, camptodactyly, clinodactyly	16/16	100
Symphalangism	9/16	56
Carpal–tarsal fusion	5/16	31
Development		
Learning disability, mental subnormality	10/16	63
Delayed motor development	6/16	38
Short stature	9/16	56
Craniofacial anomalies		
Wide-eye look and malar hypoplasia	15/16	94
Round face	12/16	75
Microstomia and micrognathia	9/12	56
Dental anomalies	12/16	75
Talon cusps	2/16	12.5
Other skeletal manifestations		
Osteopenia/osteoporosis	5/NA	
Pectus deformity	4/16	25
Coxa valga/genu recurvatum, talipes deformity	2/16	12.5
Proximal radioulnar synostosis	1/16	6.25
Ocular anomalies		
Blue sclera	4/NA	
Squint	1/16	6.25
Macrophthalmos	5/NA	
Remnants of pupillary membrane, tilted optic disk, optic atrophy	2/NA	
ENT		
Sensorineural hearing affection	4/16	25
Laryngomalacia	1/NA	
Brain neuroimaging changes		
Cerebellar vermis anomalies	2/NA	
Cortical atrophy	3/NA	
Degenerative cortical and cerebellar changes	1/NA	
Other affected systems		
Mild hepatosplenomegaly	2/NA	
Recurrent severe respiratory tract infections	2/NA	
Renal anomalies	1/NA	
Hypocellular bone marrow	1/NA	
Severe progressive course	2/16	12.5

ENT, ears, nose, throat; NA, not applicable.

TPBD phenotype, including the characteristic facial features and digital anomalies reported previously by Temtamy *et al.* (1998). The five patients from three families were found to have *CHYS1* missense mutations.

Three of the described TPBS cases in this report had a novel homozygous mutation in either exon 2 or 3 of the *CHYS1* gene, leading to missense mutations in residues that are highly conserved across vertebrate and invertebrate species (Fig. 5). Two sibs were compound heterozygous and had a milder phenotype. The occurrence of compound heterozygous Egyptian sibs, offspring of consanguineous parents, suggests a high mutation rate in the community, which warrants further investigations. The mutation rate for *CHSY1* should be determined in various populations.

Phenotype analysis of the 16 reported cases indicates that preaxial brachydactyly, hyperphalangism, camptodactyly, and clinodactyly are universal findings in the syndrome. Mental subnormality, short stature, a round face, relative microcephaly, a wide-eye look, malar hypoplasia, dental anomalies, microstomia, micrognathia, and osteopenia or osteoporosis were common findings. Follow-up of the first reported case in the literature by the first two authors of this manuscript indicated the progressive course of the syndrome with the development of kyphoscoliosis, pectus excavatum, osteoporosis, and degenerative cortical and cerebellar developments (Temtamy *et al.*, 2010). This emphasizes that follow-up of affected patients is necessary to detect the progressive nature of the syndrome, the appearance of brain changes using MRI, and the deafness apparent with age in some cases.

Of importance to the role of functional polymorphisms of *CHSY1* in the general populations is a recent genome-wide association meta-analysis that reported that allelic variants near *CHSY1* were significantly associated with central corneal thickness in mixed Asians (Cornes *et al.*, 2012). This finding lends further support to *CHSY1*'s role during zebrafish and human eye morphogenesis as reported by Tian *et al.* (2010).

Awareness of the characteristic findings in the syndrome is important for a proper diagnosis and further molecular studies. TPBS is an easily recognizable dysmorphic syndrome. The rarity of worldwide reports could be because of underdiagnosis. Clarkson *et al.* (2004) described a case as the Catel–Manzke syndrome and questioned the possibility of an extended phenotype or a probable new syndrome. After reviewing the manuscript, the possibility of TPBS in this patient was considered by Temtamy (2005).

Because of some phenotypic overlap with other preaxial brachydactyly syndromes, further clinical and molecular research is required to define a possible genetic heterogeneity, genotype–phenotype correlations, milder expressivity in compound heterozygotes, and the roles of other genes and their encoded proteins in digital differentiation and growth. It is important to integrate *CHSY1* function in the cascade of signaling events controlled by the bone morphogenetic protein/growth and differentiation factor pathway, which is most often deregulated in human brachydactylies. In particular, it will be pivotal for understanding the role of *CHSY1* in characterizing its proteoglycan targets. These targets should be post-translationally modified by the covalent addition of chondroitin sulfate moieties, and they serve as essential glycosminoglycans during limb patterning and outgrowth.

References

Clarkson JHW, Homfray T, Heron CW, Moss AL (2004). Catel–Manzke syndrome: a case report of a female with severely malformed hands and feet. An extension of the phenotype or a new syndrome? Clin Dysmorphol 13:237–240.

Cornes BK, Khor CC, Nongpiur ME, Xu L, Tay WT, Zheng Y, *et al.* (2012). Identification of four novel variants that influence central corneal thickness in multi-ethnic Asian populations. Hum Mol Genet 21:437–445.

Li Y, Laue K, Temtamy S, Aglan M, Kotan LD, Yigit G, *et al.* (2010). Temtamy preaxial brachydactyly syndrome is caused by loss-of-function mutations in chondroitin synthase 1, a potential target of BMP signaling. Am J Hum Genet 87:757–767.

Li Y, Temtamy SA, Laue K, Aglan MS, Pawlik B, Numberg G, *et al.* (2009). Homozygous disruption of an extracellular matrix component cause Temtamy preaxial brachydactyly syndrome. The European Conference of Human Genetics; May 23-26, 2009, Vienna, Austria.

Race H, Hall CM, Harrison MG, Quarrell OW, Wakeling EL (2010). A distinct autosomal recessive disorder of limb development with preaxial brachydactyly, phalangeal duplication, symphalangism and hyperphalangism. Clin Dysmorphol 19:23–27.

Temtamy SA (2005). Catel–Manzke digitopalatal syndrome or Temtamy preaxial brachydactyly hyperphalangism syndrome? Clin Dysmorphol 14:211.

Temtamy SA, Aglan MS (2008). Brachydactyly. Orphanet J Rare Dis 3: Art. No. 15.

Temtamy SA, Meguid NA, Ismail SI, Ramzy MI (1998). A new multiple congenital anomaly, mental retardation syndrome with preaxial brachydactyly, hyperphalangism, deafness and orodental anomalies. Clin Dysmorphol 7: 249–255.

Temtamy SA, Aglan MS, Meguid NA (2010). Genetic disorders in the Egyptians. In: Teebi AS, editor. *Genetic disorders among Arab population.* 2nd ed. Berlin Heidelberg, Germany: Springer-Verlag; 2010.

Tian J, Ling L, Shboul M, Lee H, O'Connor B, Merriman B, *et al.* (2010). Loss of CHSY1, a secreted FRINGE enzyme, causes syndromic brachydactyly in humans via increased NOTCH signaling. Am J Hum Genet 87:768–778.

ARTICLE

TMEM237 Is Mutated in Individuals with a Joubert Syndrome Related Disorder and Expands the Role of the TMEM Family at the Ciliary Transition Zone

Lijia Huang,[1,21] Katarzyna Szymanska,[2,21] Victor L. Jensen,[3,21] Andreas R. Janecke,[4,5] A. Micheil Innes,[6] Erica E. Davis,[7] Patrick Frosk,[8] Chunmei Li,[3] Jason R. Willer,[7] Bernard N. Chodirker,[8] Cheryl R. Greenberg,[8] D. Ross McLeod,[6] Francois P. Bernier,[6] Albert E. Chudley,[8] Thomas Müller,[4] Mohammad Shboul,[9] Clare V. Logan,[2] Catrina M. Loucks,[6] Chandree L. Beaulieu,[1] Rachel V. Bowie,[10] Sandra M. Bell,[2] Jonathan Adkins,[11] Freddi I. Zuniga,[12] Kevin D. Ross,[13] Jian Wang,[14] Matthew R. Ban,[14] Christian Becker,[15] Peter Nürnberg,[15,16] Stuart Douglas,[1] Cheryl M. Craft,[12] Marie-Andree Akimenko,[17] Robert A. Hegele,[14] Carole Ober,[13] Gerd Utermann,[5] Hanno J. Bolz,[18,19] Dennis E. Bulman,[20] Nicholas Katsanis,[7] Oliver E. Blacque,[10] Dan Doherty,[11] Jillian S. Parboosingh,[6] Michel R. Leroux,[3,22,*] Colin A. Johnson,[2,22] and Kym M. Boycott[1,22,*]

Joubert syndrome related disorders (JSRDs) have broad but variable phenotypic overlap with other ciliopathies. The molecular etiology of this overlap is unclear but probably arises from disrupting common functional module components within primary cilia. To identify additional module elements associated with JSRDs, we performed homozygosity mapping followed by next-generation sequencing (NGS) and uncovered mutations in *TMEM237* (previously known as *ALS2CR4*). We show that loss of the mammalian TMEM237, which localizes to the ciliary transition zone (TZ), results in defective ciliogenesis and deregulation of Wnt signaling. Furthermore, disruption of *Danio rerio* (zebrafish) *tmem237* expression produces gastrulation defects consistent with ciliary dysfunction, and *Caenorhabditis elegans jbts-14* genetically interacts with *nphp-4*, encoding another TZ protein, to control basal body-TZ anchoring to the membrane and ciliogenesis. Both mammalian and *C. elegans* TMEM237/JBTS-14 require RPGRIP1L/MKS5 for proper TZ localization, and we demonstrate additional functional interactions between *C. elegans* JBTS-14 and MKS-2/TMEM216, MKSR-1/B9D1, and MKSR-2/B9D2. Collectively, our findings integrate TMEM237/JBTS-14 in a complex interaction network of TZ-associated proteins and reveal a growing contribution of a TZ functional module to the spectrum of ciliopathy phenotypes.

Introduction

Ciliopathies, including the Joubert syndrome related disorders (JSRDs [MIM 213300]), represent an expanding group of physiological and developmental disorders caused by dysfunction of primary cilia.[1–4] These microtubule-based structures are present on nearly every cell type in mammals and perform critical functions associated with sensory perception (e.g., vision, hearing, smell, and mechanosensation) and developmental signaling (including Hedgehog, Wnt, and cyclic nucleotide sig-

naling).[5–7] JSRDs are predominantly autosomal-recessive developmental syndromes that are characterized by a specific midhindbrain malformation (hypoplasia of the cerebellar vermis; abnormally deep interpeduncular fossa at the level of the isthmus and upper pons; and horizontalized, thickened and elongated superior cerebellar peduncles), visualized as the molar tooth sign (MTS) on brain imaging. Additional findings can include polydactyly, ocular coloboma, retinal dystrophy, renal disease, and hepatic fibrosis.[8] The JSRDs are genetically heterogeneous with mutations in 14 genes identified to date,[9–24] although

[1]Children's Hospital of Eastern Ontario Research Institute, University of Ottawa, Ottawa, ON K1H 8L1, Canada; [2]Section of Ophthalmology and Neurosciences, Leeds Institute of Molecular Medicine, St. James's University Hospital, Leeds LS9 7TF, UK; [3]Department of Molecular Biology and Biochemistry, Simon Fraser University, Burnaby, BC V5A 1S6, Canada; [4]Department of Pediatrics II, Innsbruck Medical University, Innsbruck 6020, Austria; [5]Division of Human Genetics, Innsbruck Medical University, Innsbruck 6020, Austria; [6]Department of Medical Genetics, University of Calgary, Calgary, AB T3B 6A8, Canada; [7]Center for Human Disease Modeling, Department of Cell Biology, Duke University Medical Center, Durham, NC 27710, USA; [8]Department of Biochemistry and Medical Genetics, University of Manitoba, Winnipeg, MB R3R 0J9, Canada; [9]Institute of Medical Biology: Human Embryology, 8A Biomedical Grove, #05-40 Immunos, Singapore 138648, Singapore; [10]School of Biomolecular and Biomedical Science, UCD Conway Institute, University College Dublin, Belfield, Dublin 4, Ireland; [11]Division of Genetic Medicine, Department of Pediatrics, University of Washington, Seattle, WA 98195, USA; [12]Mary D. Allen Laboratory in Vision Research, Doheny Eye Institute, Departments of Ophthalmology and Cell and Neurobiology, Los Angeles, CA 90033-9224, USA; [13]Department of Human Genetics, University of Chicago, Chicago, IL 60637, USA; [14]Robarts Research Institute and University of Western Ontario, London, ON, N6A 5C1, Canada; [15]Cologne Center for Genomics, University of Cologne, 50931 Cologne, Germany; [16]Center for Molecular Medicine Cologne (CMMC), University of Cologne, 50931 Cologne, Germany; [17]Department of Biology, University of Ottawa, Ottawa, ON K1N 6N5, Canada; [18]Center for Human Genetics, Bioscientia, 55218 Ingelheim, Germany; [19]Institute of Human Genetics, University Hospital of Cologne, 50931 Cologne, Germany; [20]Ottawa Hospital Research Institute and University of Ottawa, Ottawa, ON K1H 8L6, Canada
[21]These authors contributed equally to the work
[22]These authors contributed equally to the work
*Correspondence: leroux@sfu.ca (M.R.L.), kboycott@cheo.on.ca (K.M.B.)

these only account for approximately 50% of mutations in affected individuals.[8] The typically autosomal-recessive and genetically heterogeneous ciliopathies Meckel-Gruber syndrome (MKS [MIM 249000]), nephronophthisis (NPHP [MIM 256100]), and Bardet-Biedl syndrome (BBS [MIM 209900]) phenotypically overlap with the JSRDs. MKS is a more severe group of disorders characterized by posterior fossa defects including occipital encephalocele as well as cystic dysplastic kidneys, hepatic bile duct proliferation, and polydactyly.[25] NPHP is characterized primarily by renal cysts and is the most frequent cause of end-stage kidney disease in the first three decades of life.[26] Primary features of BBS include rod-cone dystrophy, polydactyly, truncal obesity, learning disabilities, hypogonadism and/or genital anomalies, and renal manifestations including NPHP.[2,3]

The ciliary basal body is a modified centriolar structure that is anchored to the plasma membrane and is responsible for nucleating the ciliary axoneme, whose formation depends on intraflagellar transport (IFT). The transition zone (TZ), termed connecting cilium in photoreceptor cells, is the most proximal region of the axoneme and is characterized by Y-shaped structures of unknown composition that join the axonemal doublet microtubules to the ciliary membrane. Recently, many JSRDs/MKS/NPHP proteins have been found to localize either at the basal body, or more specifically, at the ciliary TZ just distal to the basal body.[24,27] These include the evolutionarily conserved B9 domain-containing proteins (MKS1 [MIM 609883], MKSR1/B9D1 [MIM 614144], and MKSR2/B9D2 [MIM 611951]) as well as MKS3/Meckelin/TMEM67 [MIM 609884], MKS5/RPGRIP1L [MIM 610937], MKS6/CC2D2A [MIM 612013], NPHP1 [MIM 607100], and NPHP4 [MIM 607215]. Studies in *Caenorhabditis elegans* have provided evidence that TZ-associated proteins collectively participate in basal body-TZ anchoring to the membrane and establishing a functional ciliary gate during ciliogenesis.[27–30] Several related roles for many of the above-mentioned proteins in mammalian cells have been ascribed, including basal body migration, docking, ciliogenesis, ciliary gate function, and cellular signaling.[24–26,31,32] Whether there are additional TZ components relevant to these cellular processes, some of which could be implicated in human diseases, remains unclear.

Here, we identified mutations in *TMEM237* in individuals affected with a JSRD and studied this largely uncharacterized gene, which encodes a predicted tetraspan transmembrane protein (TMEM) TMEM237/JBTS-14. Our findings reveal that TMEM237 is important for ciliogenesis in mammalian cells, *Danio rerio* (zebrafish), and *C. elegans*. Importantly, we show that TMEM237 interacts functionally with NPHP4, MKS2, MKSR1/B9D1, MKSR2/B9D2, and MKS5/RPGRIP1L at the transition zone. Together, our studies expand the interaction network of TZ proteins and reveal a growing contribution of the TZ in ciliogenesis, signaling, and the JBTS-MKS-NPHP ciliopathy spectrum.

Material and Methods

Research Subjects
We used standard methods to isolate genomic DNA from peripheral blood of the affected persons and family members or from frozen fetal tissue or amniocytes. Informed consent was obtained from all participating individuals, and the studies were approved by the Ethics Boards of the Children's Hospital of Eastern Ontario, Leeds (East) Local Research Ethics Committee, University of Calgary, University of Washington, the University Hospital of Cologne, Duke University, and according to Austrian legislation.

Homozygosity Mapping and Haplotype Analysis
Hutterite Families
A genome scan was initiated with DNA samples from four affected individuals. The samples were amplified individually with a set of 400 polymorphic microsatellite markers (ABI PrismTM Linkage Mapping Set Version 2) with an average spacing of 10 cM and heterozygosity of 0.79. Criteria for regions of interest included homozygosity in at least two out of the four affected individuals and allele sharing in the remaining affected individual(s). For candidate regions, DNA from nine affected individuals and their family members were analyzed with the markers of interest as well as additional microsatellite markers from the 5 cM Linkage Mapping Set (Applied Biosystems) and/or from the Généthon, deCode, or Marshfield maps. Haplotypes were constructed manually, and phase was assigned on the basis of the minimum number of recombinants. LOD scores were not calculated because they were estimated to be below significance for each nuclear family.
Tyrol Families
The 10K Affymetrix SNP array was used to perform genetic mapping with DNA sample from one affected individual. For candidate regions, DNA from all three affected individuals and their family members were analyzed with additional dense microsatellite markers. Haplotypes were constructed manually, and phase was assigned on the basis of the minimum number of recombinants.

Next-Generation Sequencing and Analysis
We used an array capture approach followed by high-throughput Roche 454 sequencing in one affected Hutterite child and his carrier mother. A custom array (NimbleGen) was designed with oligonucleotide probes targeting the minimal region of overlap between the Hutterite and Austrian families. The results from 454 sequencing were analyzed with NextGENe software (SoftGenetics). Sequence reads that passed the quality filtering were aligned to the reference sequences of the human genome with the Sequence Alignment function. Homozygous single nucleotide variants, microinsertions, and microdeletions were called, and variants were filtered out when they were present in dbSNP132.

Cells
Mouse inner medullary collecting duct (IMCD3) cells were grown in Dulbecco's modified Eagle's medium (DMEM)/Ham's F12 supplemented with 10% fetal calf serum at 37°C/5% CO2. Fibroblasts from a normal control were maintained in Fibroblast Growth Medium (Genlantis) supplemented with 0.2 mg/ml geneticin. Fibroblast lines derived from the affected individuals were grown in DMEM/F12 medium.

Antibodies

The following primary antibodies were used: rabbit anti-Tmem237, FLJ-FM, and FLJ-LG, have been described previously;[33] mouse anti-polyglutamylated tubulin clone GT-335 (Enzo Life Sciences); rabbit anti-GFP (Living Colors A.v. Peptide Antibody, Clontech); rabbit-anti-γ-tubulin, mouse anti-β-actin clone AC-15 (Abcam Ltd.); and mouse anti-RhoA (Cytoskeleton). Rabbit anti-meckelin C terminus, raised against amino acids 982-995, has been described previously.[34] Rabbit anti-TMEM216 has also been described.[19] Secondary antibodies were Alexa-Fluor 488-, Alexa-Fluor 568-conjugated goat anti-mouse IgG, and goat anti-rabbit IgG (Molecular Probes). Alexa-Fluor 488 phalloidin conjugate (Molecular Probes) was used to visualize F-actin and 4′,6-diamidino-2-phenylindole (DAPI) to visualize nuclei.

Whole-Cell Extract Preparation and Immunoblotting

Whole-cell extracts (WCE) containing total soluble proteins were prepared from confluent IMCD3 cells that had been transiently transfected with 1.0 μg plasmid constructs in 90 mm tissue culture dishes, or scaled down as appropriate. Proteins were analyzed by SDS-PAGE (with 4%–12% acrylamide gradient gels) and immunoblot analysis according to standard protocols with either rabbit polyclonal antisera (final dilutions of ×200–1,000) or mouse monoclonal antibodies (MAbs) (×1,000–5,000). Appropriate HRP-conjugated secondary antibodies (Dako) were used (final dilutions of ×10,000–25,000) for detection by the enhanced chemiluminescence Femto West immunoblot detection system (Pierce). Full scans of immunoblots are shown in Figure S10 (available online).

RhoA Activation Assays

The activated GTP-bound isoform of RhoA was specifically assayed in pull-down assays with a GST fusion protein of the Rho effector rhotekin (Cytoskeleton) with conditions recommended by the manufacturers. WCEs were processed as rapidly as possible at 4°C and snap-frozen in liquid nitrogen. Total RhoA (in WCEs) and pull-down protein was immunodetected on immunoblot with a proprietary RhoA monoclonal antibody (Cytoskeleton). Immunoblot analysis for total RhoA and β-actin were used as loading controls.

Canonical Wnt Activity (Topflash) Luciferase Assays

For luciferase assays of canonical Wnt activity, fibroblasts were grown in 48-well plates and cotransfected with 0.25 μg Topflash firefly luciferase construct (or Fopflash as a negative control); 0.25 μg of expression constructs (pCMV HA-meckelin, pCMV GFP-TMEM216, pEGFPN1-TMEM237, or empty pCMV-HA/pEGFPN1 vector); and 0.05 μg of pRL-TK (Promega; Renilla luciferase construct used as an internal control reporter). Cells were treated with Wnt3A- [MIM 606359] or Wnt5A- [MIM 164975] conditioned media to stimulate or inhibit the canonical Wnt pathway. We obtained Wnt3A- or Wnt5A-conditioned media from stably-transfected L cells with Wnt3A or Wnt5A expression vectors.[35] Control media were obtained from untransfected L cells. Activities from firefly and Renilla luciferases were assayed with the Dual-Luciferase Reporter Assay system (Promega) on a Mithras LB940 (Berthold Technologies) luminometer. Minimal responses were noted with coexpression of the Fopflash negative control reporter construct (data not shown). Raw readings were normalized with Renilla luciferase values. Results reported are from at least three independent biological replicates.

Transfection and siRNA

For transfection with plasmids, cells at 80% confluency were transfected with TransIT-LK (Mirus) according to the manufacturer's instructions and as described previously.[34] For RNAi knockdown, siRNA duplexes were designed against mouse *Tmem237* sequence (NC_000067.5) with Ambion's custom Silencer Select siRNA service. Antisense sequences were as follows: *Tmem237*: duplex 1 5′-GGAUCUUAGUGAAGAGUUATT and duplex 2 5′-GAACGAAA ACGGCAUUGAUT. The medium or low GC nontargeting scrambled siRNA duplexes (Invitrogen) were used as negative controls. IMCD3 cells were transfected with 100 pmol of each siRNA at 60%–80% confluency with Lipofectamine RNAiMax (Invitrogen) and as described previously.[19]

Immunofluorescence and Confocal Microscopy

Cells were seeded at 2×10^4 cells/well on glass coverslips in six-well plates and fixed in ice-cold methanol (5 min at −20°C) or 2% paraformaldehyde (20 min at room temperature). Permeabilization, blocking methods and immunofluorescence staining were essentially as described previously.[34] Primary antibodies were used at final dilutions of ×200–1,000. Secondary antibodies and phalloidin conjugate were diluted ×200. Confocal images were obtained with a Nikon Eclipse TE2000-E system controlled and processed by EZ-C1 3.50 (Nikon) software. Images were assembled with Adobe Illustrator CS2.

Whole-Mount In Situ Hybridization on Zebrafish Embryos

Whole-mount in situ hybridization was performed as described previously.[36] Briefly, full-length cDNAs of zebrafish *tmem237a* (XM_680251.3), *tmem237b* (NM_001004636.1), *krox20* (NM_130997.2), and *myoD* (NM_131262.2) were obtained by RT-PCR amplification from total RNA extracted from 24 hpf embryos. The cDNAs were cloned into pGEM-T vector (Promega) and used as templates for in vitro synthesis of antisense RNA probes. Embryos were fixed in 4% paraformaldehyde in PBS, hybridized with DIG-labeled riboprobes at 65°C, and followed by incubation with anti-DIG antibody conjugated with alkaline phosphatase (AP) (Roche). NBT and BICP were used as the substrates of AP to generate the purple coloration.

Morpholino Knockdown and Rescue

Two splice-blocking morpholino antisense oligonucleotides (MO) (zf.*tmem237a* MO: 5′-TTGTCTGTGTGTGAAAGGCAGAAATCA-3′ and zf.*tmem237b* MO: 5′- TGGAAACCTACACTTAACAATATGT-3′) (Gene Tools) were used to knockdown *tmem237a* (NC_007120.5) and *tmem237b* (NC_007117.5), respectively, in zebrafish. Gene-specific MOs or control MO (2 ng for rescue and 1 ng for interaction studies) were microinjected into one-two cell stage embryos. Full-length cDNA of human *TMEM237* (NM_001044385.1) was obtained by RT-PCR amplification of total RNA extracted from a human fibroblast cell line, which was then subcloned into pCS2+ vector. The human *TMEM216* and human *MKS3* cDNAs subcloned into pCS2+ vector were described previously.[37,38] In vitro mRNA synthesis was carried out with the mMessagemMachine kit (Ambion). The synthetic mRNA was coinjected with MOs where indicated. For gastrulation phenotypes, embryos were scored according to previously established objective criteria[37–39] at 8–10 somites with masked scoring, n = 76–112 embryos/injection batch. The efficacy of the morpholinos is shown in Figure S11.

C. elegans Strain Construction and Imaging

All strains were maintained and cultured at 20°C. Those carrying mutations in *C. elegans mksr-1*(ok2092), *mksr-2*(tm2452), *mks-5* (tm3100), *mks-3*(tm2547), *mks-6*(gk674), and *nphp-4*(tm925), were obtained from the *C. elegans* Gene Knockout Consortium and the National Bioresource Project and outcrossed to wild-type (N2) at least four times. Standard mating procedures were used to introduce GFP-tagged protein constructs for JBTS-14 and MKS-2 into different genetic backgrounds. Single-worm PCR reactions were used to genotype the various mutants. GFP-tagged variants of *C. elegans* JBTS-14 and MKS-2 were generated by producing translational constructs containing each native promoter and all the exons and introns fused in-frame to EGFP; transgenic lines for these constructs were generated as reported previously.[40] Subcellular localization was assessed by fluorescence microscopy for both the wild-type (N2) or the indicated TZ mutant backgrounds. Mislocalization phenotypes were confirmed by analyzing at least 50 individuals for each strain.

C. elegans Phenotypic Assays for Ciliary Structure and Chemosensation

Assays for defective osmotic avoidance were performed as described with a ring of 8 M glycerol and five individuals per ring for 10 min.[41] The filling of environmentally exposed ciliated sensory neurons with DiI was completed as previously described.[40] Dye-stained worms were imaged with fluorescence microscopy and intensities were quantitated with ImageJ.

Transmission Electron Microscopy

Transmission Electron Microscopy (TEM) was performed on staged young adult worms exactly as described previously.[42]

Identification of *jbts-14* Mutant Strain

A nonsense allele (gk287997) of *jbts-14* (F53A9.4) was identified by genome sequencing of an EMS-mutagenized *C. elegans* strain.

Generation of *mks-2* Mutant Strain

The mutagenesis protocol for generating an *mks-2* (C30B5.9) allele was modified from the protocol described previously.[43] Strain EG1642 (genotype *lin-15B (n765X); oxEx166[HSP:: MosTransposase + cc::gfp]*) carrying the extrachromosomal Mos transposase under a heat-shock promoter was crossed into strain *ttTi38815*, which contains a Mos1 insertion in an intergenic region ~2.4 kb away from C30B5.9 (*mks-2*). Two hundred and fifty young adult (*ttTi38815;nxEx166[HSP::MosTransposase + cc::gfp]*) worms (P0) were placed on one plate and heat shocked (33°C in a water bath for 1 hr; 1 hr in a 20°C room; 33°C in the water bath for 1 hr again). After 2 hr recovery at 20°C, the P0 worms were placed onto individual plates and allowed to lay eggs (F1) for 40 hr at 20°C. The P0 worms were removed and the plates were placed at 20°C until the worms were grown to the F2 generation. Then, ~50% of worms (a population of F1 and F2) from each plate were recovered, and crude DNA lysates (200 μl) were prepared as described at Protocol Online. To identify lysates containing an *mks-2* deletion, we performed PCR by using a primer set (GTACTATAGCGGTGCATTCCAAC and AAAAAACCAACAG AACCAGGCTGC) flanking the gene and Mos1 transposon. One lysate containing an ~3.5 kb deletion was identified. We cloned 400 worms from this plate and screened them by using the same PCR strategy. Using this scheme, we isolated one allele, *mks-*2(*nx111*), containing a 3573 bp deletion that removes the entire *mks-2* coding region.

Results

Mutations in *TMEM237* Cause a JSRD

To uncover additional genes mutated in ciliopathies, we investigated a group of ten related Canadian Hutterite individuals with a severe JSRD[44] that was previously reported as MKS[45] (Table 1). The known loci for JSRDs and MKS were excluded by homozygosity mapping, which suggested that this condition represented a distinct JSRD locus.[44] Genome-wide homozygosity mapping with microsatellite markers with the DNA from four affected individuals localized the gene to the JBTS-14 locus on 2q33. Genotyping additional affected and healthy family members refined the region to a 7.5 Mb interval between D2S2327 and D2S1384 (Figure 1A and Figure S1A). A JSRD in a consanguineous family from Tyrol, Austria[46] (Table 1), was mapped to an overlapping 9.3 Mb region between D2S115 and D2S325 (Figure 1A and Figure S1B). The minimal gene-rich region (D2S115-D2S1384) contains more than 70 genes; we excluded over 30 of these by using Sanger sequencing.

We next employed an array capture approach followed by high-throughput Roche 454 sequencing in one affected Hutterite child and his carrier mother and identified a homozygous C to T transition in *TMEM237* ([NM_001044385.1] c.52C>T) leading to a premature stop codon ([NP_001037850.1] p.Arg18*) (Figures 1B–1E). Screening of normal Hutterite controls (N = 1758) revealed a carrier frequency of 6% for this mutation, but none of the Hutterite controls carried the mutation in the homozygous state. Furthermore, the mutation was not identified in over 105 normal Northern European controls. We next sequenced all the coding and exon/intron boundaries of *TMEM237* in the Austrian JSRD family and identified a homozygous change (c.677+1G>T) at the splice donor site of intron 9 (Figures 1C and 1E, and Table S1), which was not present in the Northern European controls. Subsequently, we performed RT-PCR on RNA from a fibroblast cell line derived from an affected individual; two abnormal transcripts were obtained with primers bordering exons 8 and 11. Sequencing of the products revealed: (1) the usage of a cryptic splice donor site at the beginning of exon 9 and a cryptic splice acceptor site in exon 10, leading to a deletion of 65 amino acids and an insertion of a Serine residue (p.Phe187_Ala251delinsSer) and (2) the skipping of exon 9, resulting in a premature stop codon (p.Arg186*) (Figure 1D and Figure S2).

We screened an additional 201 individuals with JSRD and 90 individuals with MKS/JSRD and identified two additional families with mutations in *TMEM237*. In a Jordanian child born to consanguineous parents (Table 1), a homozygous *TMEM237* frameshift mutation in exon 13 (c.1066dupC) was identified (Figures 1C and 1E). The

Table 1. Clinical and Molecular Data from Families with *TMEM237* Mutations

Individual	Age at Last Assessment	Sex	Living or Deceased	Current Age or Age at Death	Origin	CNS	Kidney	Eye	Other	Nucleotide Changes	Protein Alterations
Family A											
1	3.5 years	M	L	8 years	Hutterite	MTS, PF, H	CK	Nys, Str, OA	–	c.52C>T	p.Arg18*
2	2.5 years	F	D	7 years	Hutterite	MTS, PF, H, En	CK	Nys, Str	–	c.52C>T	p.Arg18*
Family B											
3	27 years	F	D	28 years	Hutterite	CVH	–	Nys, Str	–	c.52C>T	p.Arg18*
4	6 years	F	D	12 years	Hutterite	CVH	–	Nys, Str	–	c.52C>T	p.Arg18*
Family C											
5	10 years	M	D	12 years	Hutterite	MTS	–	Nys, Str, C	IB	c.52C>T	p.Arg18*
Family D											
6	0 days	F	D	SB	Hutterite	En, H	CK	ND	CP	c.52C>T	p.Arg18*
7	2 days	F	D	2 days	Hutterite	H	CK	ND	P	c.52C>T	p.Arg18*
Family E											
8	5 years	F	L	9 years	Hutterite	MTS, En	CK	Nys, Str, C	VSD	c.52C>T	p.Arg18*
Family F											
9	4 months	F	D	13 months	Hutterite	En, H, DWV	CK	Nys, Str	–	c.52C>T	p.Arg18*
Family G											
10	4 years	M	L	8 years	Hutterite	MTS, PF	CK	Nys, Str	–	c.52C>T	p.Arg18*
Family H											
11	3 weeks	F	D	3 weeks	Hutterite	MTS, DWV, H, En	CK	ND	–	c.52C>T	p.Arg18*
12	3 months	F	D	3 months	Hutterite	MTS, DWV, H, En	CK	Nys	–	c.52C>T	p.Arg18*
Family I											
13	3 years	M	L	3 years	Hutterite	MTS, DWV, H	CK	Nys	–	c.52C>T	p.Arg18*
Family J											
14	1 days	F	D	2 days	Hutterite	En	CK	ND	–	c.52C>T	p.Arg18*
Family K											
VIII-2	3 years	F	D	4 years	Austrian	CVA	CK	MGDA	–	c.677+1G>T	p.Phe187_Ala251 delinsSer; p.Arg186*
VIII-4	Fetus, 22 weeks	ND	D	fetus, 22 weeks	Austrian	H, CVA, CCH, MC	CK	MGDA	no LF	c.677+1G>T	p.Phe187_Ala251 delinsSer; p.Arg186*
VIII-5	2 years	F	L	11 years	Austrian	CVA, BH	CK	Nys, MGDA	–	c.677+1G>T	p.Phe187_Ala251 delinsSer; p.Arg186*
Family L											
1	1.5 years	M	ND	ND	Jordanian	MYC, CVI	ND	ND	–	c.1066dupC	p.Gln356Profs*23
Family M											
1	4 years	F	L	4 years	Hispanic, European	MTS, H, PF, CVI	CK	Nys, Str	–	c.[943+1G>T]+ [76C>T]	p.[IIe291_ Trp346 del]+[Gln26*]

The following abbreviations are used: –, not affected; BH, brain stem hypoplasia; C, coloboma; CCH, corpus callosum hypoplasia; CK,cystic kidney; CP, cleft palate; CVA, cerebellar vermis aplasia; CVH, cerebellar vermis hypoplasia; CVI, cortical visual impairment; D, deceased; DWV, Dandy–Walker variant; En, encephalocele; H, hydrocephalus; IB, intracranial bleed; L, living; LF, liver fibrosis; MGDA, morning glory disc anomaly; MC, meningocele; MYC, meningomyelocele; MTS, molar tooth sign; ND, no data; Nys, nystagmus; OA, optic atrophy; P, postaxial polydactyly; PF, posterior fossa abnormality; SB, stillborn; Str, strabismus; VSD, ventricular septal defect.
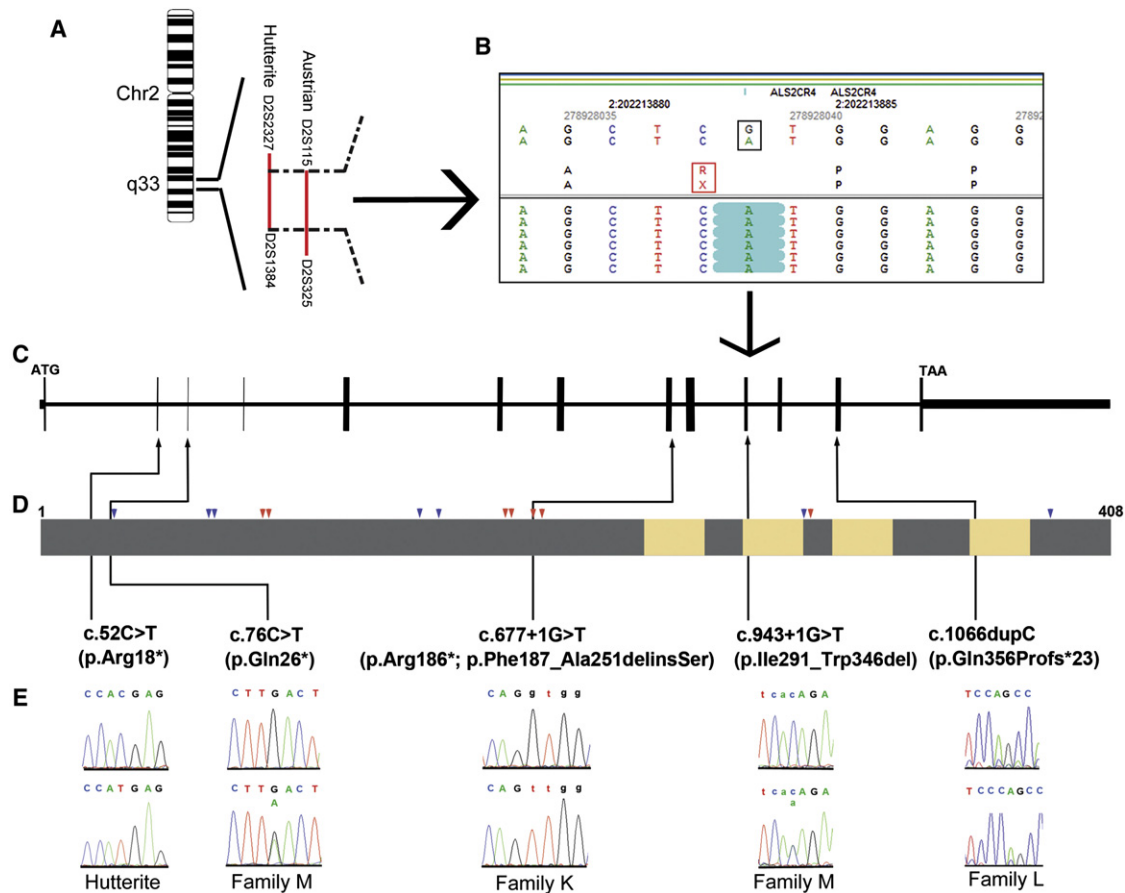
Figure 1. Mutations in *TMEM237* Cause a Joubert Syndrome Related Disorder

(A) Chromosomal location of the overlapping JSRD loci of the Hutterite families and the Austrian family.

(B) Targeted sequence capture followed by massively parallel sequencing and data analysis identified a homozygous mutation in *TMEM237* (*ALS2CR4*) in an affected Hutterite individual. The black box shows the G>A change at the genomic level. The red box shows the resultant amino acid change (R>X). The green highlights show that all the sequence reads from the affected child contain an A.

(C) *TMEM237* genomic organization.

(D) Domain structure of TMEM237 protein. Yellow indicates the transmembrane domains. Grey indicates the extramembrane region. Red arrows and blue arrows indicate the highly conserved short motifs of basic and acidic amino acids, respectively. Black arrows indicate the positions of identified mutations.

(E) Sequence traces of normal controls (top) and affected individuals (bottom) are shown.

frameshift mutation is predicted to result in a truncated protein (p.Gln356Profs*23) (Figure 1D) and was absent in over 105 normal Jordanian controls. Compound heterozygous mutations c.[943+1G>T]+[76C>T] were identified (Figures 1C and 1E) in an affected child from a nonconsanguineous JSRD family of European and Spanish descent (Table 1); her mother carries the c.76C>T mutation, and the father carries the c.943+1G>T mutation. c.76C>T is a nonsense mutation resulting in a premature stop codon (p.Gln26*). We performed RT-PCR on RNA from a lymphoblast cell line derived from the affected individual; one abnormal transcript was obtained with primers bordering exons 8 and 13 (Figure S3). Sequencing of the product revealed deletion of exons 11 and 12, leading to a deletion of 56 amino acids (p.IIe291_Trp346del) (Figure 1D). These mutations were absent in over 105 normal controls. Together, these data demonstrate that mutations in *TMEM237* are causative for JSRD and implicate a largely

uncharacterized member of the tetraspan transmembrane protein family, TMEM237, in normal functions of the primary cilium.

TMEM237 spans 23 kb on 2q33 and contains 14 exons. Two alternative *TMEM237* transcripts (1 [NM_001044385.1] and 2 [NM_152388.2]), translating into two protein isoforms, a (NP_001037850.1) and b (NP_689601.2), have been proposed in humans. Each transcript utilizes one of the two alternative exons, 1 and 2, which are spliced in a mutually exclusive manner. All positional information in this paper refers to transcript 1 and isoform a. In two mouse proteomic studies, Tmem237 was found in the photoreceptor connecting cilium complex and outer segments.[47,48] TMEM237 is a predicted tetraspan transmembrane protein with both amino and carboxyl termini directed to the cytoplasmic side.[33] Alignment of metazoan orthologs with the human protein revealed strong conservation of repetitive short motifs of both basic (R and/or K) and acidic (D and/or E)
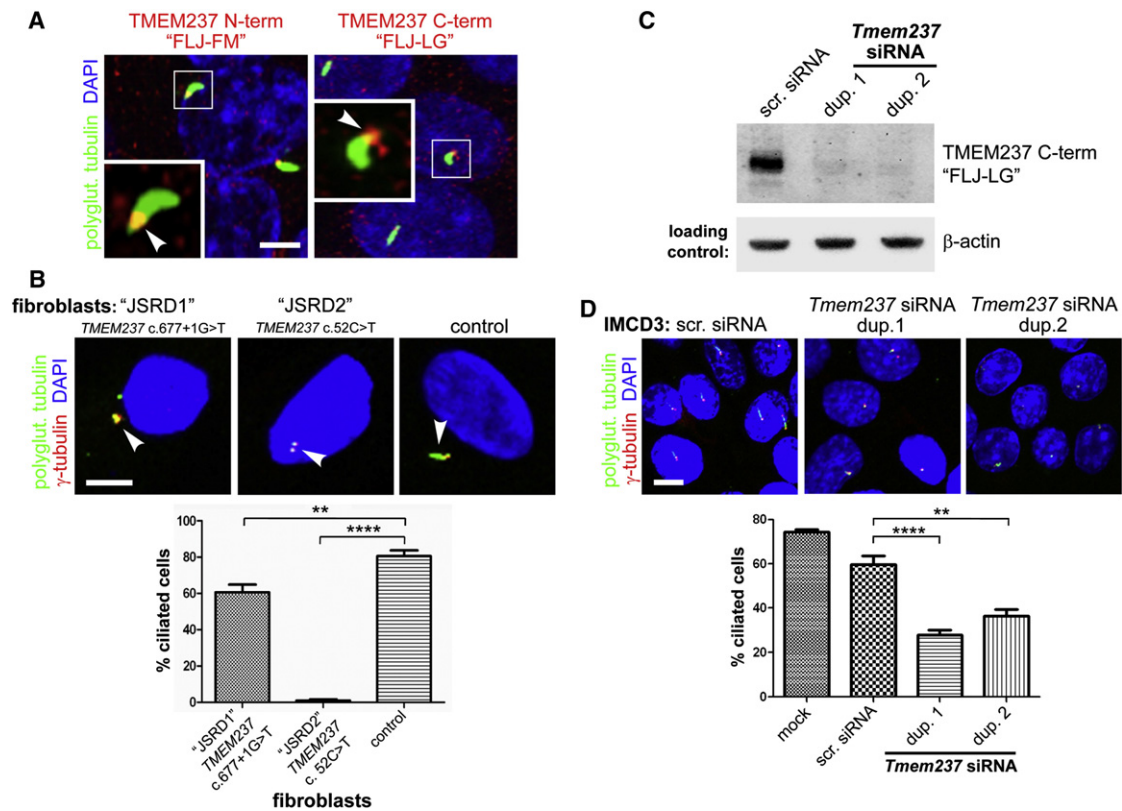
Figure 2. TMEM237 Is Localized to the Ciliary Transition Zone Region and Mutation or Knockdown Results in Defective Ciliogenesis

(A) Overlapping localization of endogenous N-terminal (N-term) or C-terminal (C-term) mouse Tmem237 (red) and polyglutamylated (polyglut.) tubulin (green) at the base of primary cilia and/or mother centriole (arrowheads in magnified insets) of IMCD-3 cells. The scale bar represents 5 μm.

(B) Two different *TMEM237*-mutated fibroblasts lines (JSRD1 with homozygous splice-site mutation c.677+1G>T and JSRD2 with homozygous nonsense mutation c.52C>T as indicated) show defective ciliogenesis and pairing of centrioles (marked by γ-tubulin, red) compared to a normal control line. The scale bar represents 5 μm. Ciliogenesis is quantitated in the lower panel (n = 500 to 600 for each line; statistical significance of comparisons are shown (**p < 0.01, ****p < 0.0001 Student t test); error bars indicate standard error of the mean (SEM).

(C) Tmem237 antisera against the C-terminal mouse protein detects a specific 45 kD band[33] in immunoblot of control cells transfected with scrambled (scr.) siRNA that is lost after transfection with *Tmem237* siRNA duplexes (dup.) 1 or 2. Equal loading is indicated by immunoblot analysis for β-actin.

(D) Defective ciliogenesis in IMCD-3 cells after *Tmem237* siRNA knockdown with duplexes (dup.) 1 or 2. Cells stained and ciliogenesis quantified as in (B); the scale bar represents 10 μm.

amino acid residues throughout the intracellular N-terminal region and predicted intracellular loops between transmembrane helices (Figure 1D and Figure S4). Members of the TMEM family, TMEM216/MKS2 [MIM 613277] and meckelin/MKS3/TMEM67, have both been implicated in JSRDs and MKS[14,19,20,49] and both localize to the ciliary basal body or TZ region. Because other tetraspan transmembrane proteins function through the formation of complexes with each other and other membrane proteins such as Frizzled receptors,[50] it suggests that TMEM237, TMEM216, and MKS3 might cooperate in maintaining normal ciliary functions.

Loss of TMEM237 Causes Ciliogenesis Defects in Mammalian Cells

To elucidate potential roles for TMEM237, we first determined the subcellular localization of the encoded protein. We used two affinity-purified polyclonal antibodies raised against mouse Tmem237 amino acids 76-88 (FLJ-FM) and 390-403 (FLJ-LG) in the amino- and carboxy-terminal domains, respectively.[33] These antibodies were used for immunocytochemical staining of a polarized monolayer of ciliated mouse inner medullary collecting duct (IMCD3) cells. Discrete signals at the proximal region of primary cilia were observed, consistent with localization to the TZ (Figure 2A).

We next explored the role of TMEM237 function in ciliogenesis. Quantitative real-time (qRT) PCR was used to measure *TMEM237* transcript expression in fibroblasts derived from the affected individual with the splice-site mutation (c.677+1G>T, line JSRD1), and the nonsense mutation (c.52C>T, p.Arg18*, line JSRD2), because existing antibodies were not specific for human TMEM237. Total *TMEM237* transcript levels in the JSRD1 and JSRD2 lines were reduced by 99.6% and 98.4%, respectively (Figure S5), although low levels of an exon-skipped mutant

transcript were detectable by RT-PCR in JSRD1 with the c.677+1G>T splice-site mutation (Figure S2A). A failure in ciliogenesis was observed in these fibroblasts, after 48 hr of serum starvation (Figure 2B) but not in controls; similar results were seen previously in cells deficient for MKS3 and TMEM216.[19,31] These data were quantified by analyzing the percentage of cells with evident cilia (defined as >1 μm in length) versus those without cilia (defined as <1 μm in length) (Figure 2B). It is possible that the low levels of the exon-skipped mutant transcript in JSRD1 (c.677+1G>T) were sufficient to maintain some ciliogenesis in those fibroblasts. For independent confirmation of these results, we also tested for ciliogenesis defects in IMCD3 cells disrupted for TMEM237 by transient siRNA knockdown. We first confirmed that the expected 45 kDa protein recognized by immunoblotting with the FLJ-LG antibody[33] in immunoblotting experiments was lost after transient siRNA knockdown (Figure 2C and Figure S6). Consistent with the results obtained from fibroblasts from affected individuals, transfection with two separate Tmem237 siRNA duplexes impaired ciliogenesis in polarized cells (Figure 2D and Figure S7).

TMEM237 Disruption Results in Deregulation of Wnt Signaling

Many aspects of actin-dependent polarized cell behavior, including morphogenetic cell movements[51] and ciliogenesis,[52] are mediated by the planar cell polarity (PCP) pathway of noncanonical Wnt signaling.[53] Perturbation of noncanonical Wnt signaling is implicated in the pathogenesis of MKS[19,34,37] and deregulation of the canonical β-catenin pathway is implicated in the ciliopathy disease state.[54,55] To assess whether these pathways were perturbed after TMEM237 mutation or loss, we first determined levels of key mediators in fibroblasts from affected and control individuals. Immunoblot analysis of protein extract from affected individuals demonstrated constitutive phosphorylation and hyperactivation of Disheveled-1 (Dvl1 [MIM 601365]), a core Wnt signaling protein,[56] and an increase in both soluble and total levels of β-catenin [MIM 116806] (Figure 3A). Levels of downstream effectors for both canonical and noncanonical Wnt signaling, cyclin-D1 [MIM 168461] and phosphorylated myosinIIB [MIM 160776] were also assessed with immunoblot analysis. We observed a slight increase in phosphorylated myosinIIB levels and a striking decrease in the amount of cyclin-D1 in JSRD2 cells (Figure 3A). We next assayed RhoA [MIM 165390] activation because the Rho family of small GTPases are key PCP mediators.[57] Consistent with previous results after MKS3 or TMEM216 mutation or knockdown,[19,34] we found that RhoA signaling was hyperactivated in TMEM237-mutated fibroblasts (Figure 3A) or after Tmem237 knockdown (Figure 3B) despite normal total amounts of RhoA in these cells. RhoA localized to the basal body in confluent IMCD3 cells (Figure 3C), supporting a role in mediating centrosome docking at the apical cell surface prior to ciliogenesis.[19,56] However, after

Tmem237 knockdown, RhoA was mislocalized to peripheral regions of the basal body and to basolateral cell-cell contacts (Figure 3C), consistent with translocation of ectopically-activated RhoA to the cytosol.[58] Because RhoA modulates the actin cytoskeleton in the PCP pathway, we evaluated the cytoskeletal phenotype of TMEM237 fibroblast lines from affected individuals; strikingly, we uncovered prominent actin stress fibers in these but not in control cells (Figure 3C).

TMEM237-mutated fibroblasts carrying the putative null mutation c.52C>T (line JSRD2) also demonstrated dysregulated canonical Wnt signaling (over 5-fold basal levels) compared to control fibroblasts upon stimulation with Wnt3A-conditioned media (Figure 3D). Treatment with Wnt5A had no effect on activation; however, as expected, Wnt5A suppressed the activation by Wnt3A (Figure 3D). Deregulated Wnt signaling activation by Wnt3A was also apparent in mouse embryonic fibroblasts (MEFs) derived from wild-type $Mks3^{+/+}$ and knockout mutant $Mks3^{-/-}$ E18 embryos (Figure 3E). Interestingly, responses were attenuated by expression of TMEM237, MKS3, and TMEM216, indicating either partial complementation of MKS3 loss by other TZ-localized members of the TMEM family or Wnt signal compensation from another cellular site (or process).

Knockdown of tmem237 Causes Developmental Defects in Zebrafish

To provide complementary evidence of a role for TMEM237 in ciliary function, signaling, and development, we turned to zebrafish, an established vertebrate model system for ciliopathies.[37–39,59] Two zebrafish paralogs of TMEM237, tmem237a and tmem237b, have been annotated. They share over 50% protein sequence identity with human TMEM237 (Figure S4) and demonstrate a significant overlap in expression pattern in the developing central nervous system, the eyes, pharyngeal arch cartilage, and the pectoral fin buds (Figure S8). The PCP pathway is known to play an essential role in polarized convergent extension (CE) movements during gastrulation and neurulation.[60] To investigate the possible role of TMEM237 in the PCP pathway and embryonic development, we examined morphant phenotypes after knockdown of tmem237. When disrupting both tmem237a and tmem237b simultaneously, we observed defects in midsomitic embryos that are consistent with other ciliary morphants,[19,37–39,59] including shortening of the anterior-posterior axis and small anterior structures, kinking of the notochord, and broadening and thinning of the somites (Figure 4A). To quantify these defects, we measured the widening of the 5th rhombomere and the shortening of the notochord as labeled by krox20 and myoD riboprobes, respectively, on whole-embryo flatmounts; results suggest altered convergence to the midline and extension along the anterior-posterior axis (Figures 4B and C). These defects could be rescued significantly by coinjection of human TMEM237 mRNA (Figure 4D). Notably, coinjection with either human MKS3 or TMEM216 mRNA
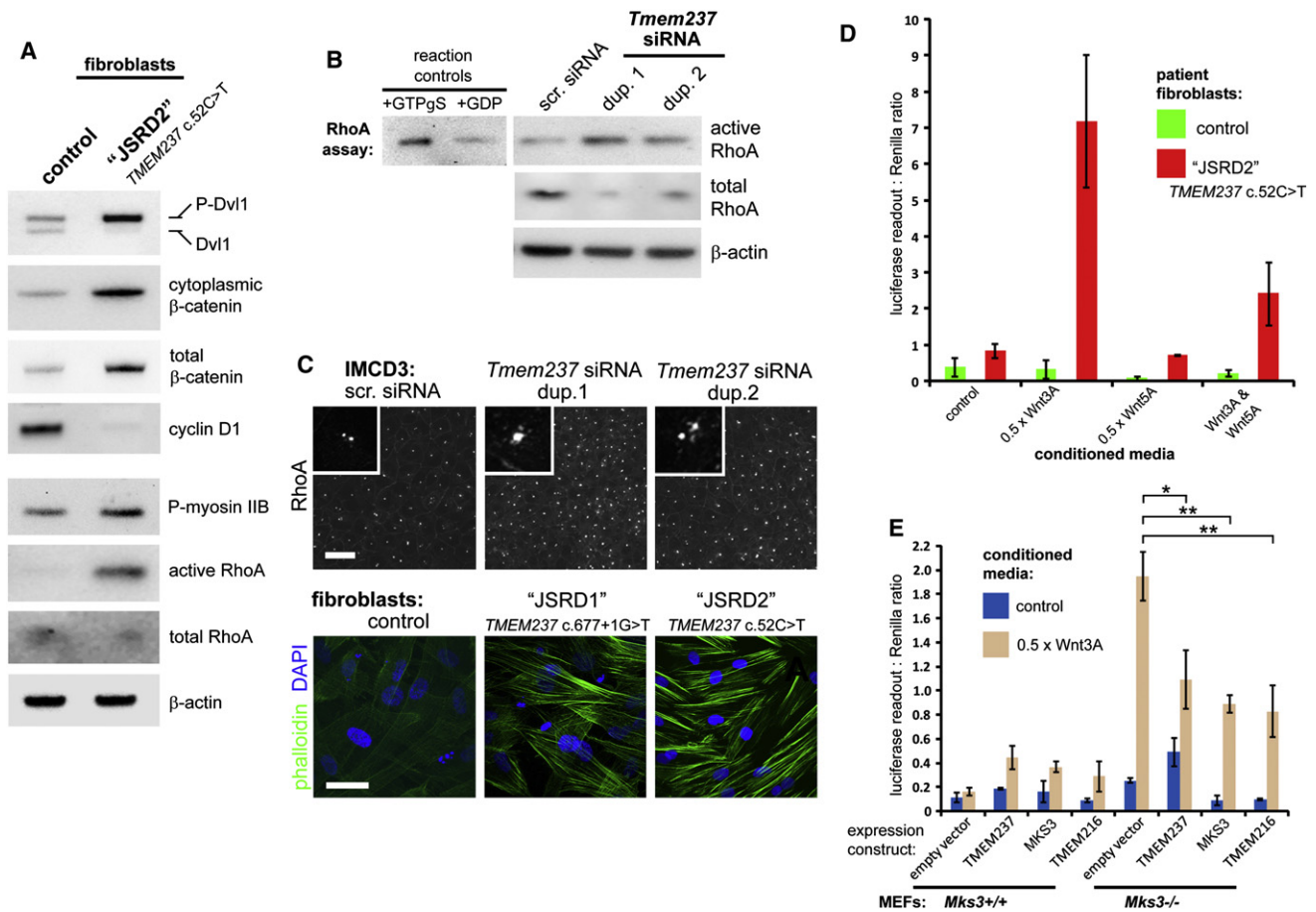
Figure 3. Deregulation of Wnt Signaling Following Mutation or Loss of TMEM237

(A) Immunoblots showing the relative levels of the indicated endogenous mediators of both canonical and noncanonical-PCP Wnt signaling in normal control fibroblasts compared to the *TMEM237*-mutated fibroblast line (JSRD2 c.52C>T line). Identical results were seen for the JSRD1 c.677+1G>T line (data not shown).

(B) Increase in levels of activated RhoA-GTP after *Tmem237* siRNA knockdown with duplexes (dup.) 1 or 2, compared to scrambled (scr.) siRNA. Levels of β-actin are shown as loading controls. Positive control for the assay (loading with nonhydrolyzable GTPγS) and a negative control (loading with GDP) are shown on the left.

(C) Pericentriolar and basolateral subcellular localization of RhoA (top panels) and increase of actin stress fibers (bottom panels; visualized by phalloidin staining, green) in *TMEM237*-mutated fibroblast lines; the scale bars represent 10 μm.

(D) TOP Flash assays of canonical Wnt signaling, showing deregulation in affected fibroblasts (JSRD2 c.52C>T, red) compared to normal control cells (green) after treatment with 0.5 × L cell control-conditioned media (control), and conditioned media containing expressed Wnt3A and/or Wnt5A, as indicated. Activity is expressed as ratios of luciferase reporter construct expression, normalized for loading by measurement of a Renilla construct expression. Values shown are means of three independent replicates; error bars indicate SEM.

(E) TOP Flash assays of canonical Wnt signaling after cotransfection of *Mks3*^{+/+} and *Mks3*^{−/−} MEFs with reporter constructs and empty vector control, wild-type GFP-TMEM237, HA-MKS3, or GFP-TMEM216 as indicated. The empty vector results combine the data from cotransfections with pCMV-HA and pGFPN1. Responses are shown to L cell control-conditioned media (control, blue bars, values are means of three independent replicates) and conditioned media containing expressed Wnt3A (0.5 × Wnt3A, brown bars, values are means of four independent replicates). Error bars indicate SEM. Statistical significance of comparisons are shown (*p < 0.05, **p < 0.01, Student t test).

also led to significant improvement of *tmem237* morphant phenotypes that were indistinguishable from rescue with human *TMEM237* transcript (Figure 4D). Furthermore, reciprocal injections (*TMEM237* mRNA coinjected with either *mks3* or *tmem216* MOs) also resulted in significant improvement (Figures 4E and 4F). Together, these data suggest a functional complementation of TMEM237, TMEM216, and MKS3, consistent with the in vitro functional attenuation of canonical Wnt signaling in mammalian cells (Figure 3E).

TMEM237 Functionally Interacts with Other Transition Zone Proteins to Control Basal Body-Transition Zone Anchoring to the Membrane

To ascertain whether TMEM237 functions together with other ciliopathy proteins localized at the ciliary transition zone, we turned to the model organism *C. elegans*, where a functional network of TZ-associated proteins (MKS-1, MKSR-1/B9D1, MKSR-2/B9D2, MKS-3, MKS-5, MKS-6, NPHP-1, and NPHP-4) has been established and shown to be important for cilium formation and function.[27–30,61–64]
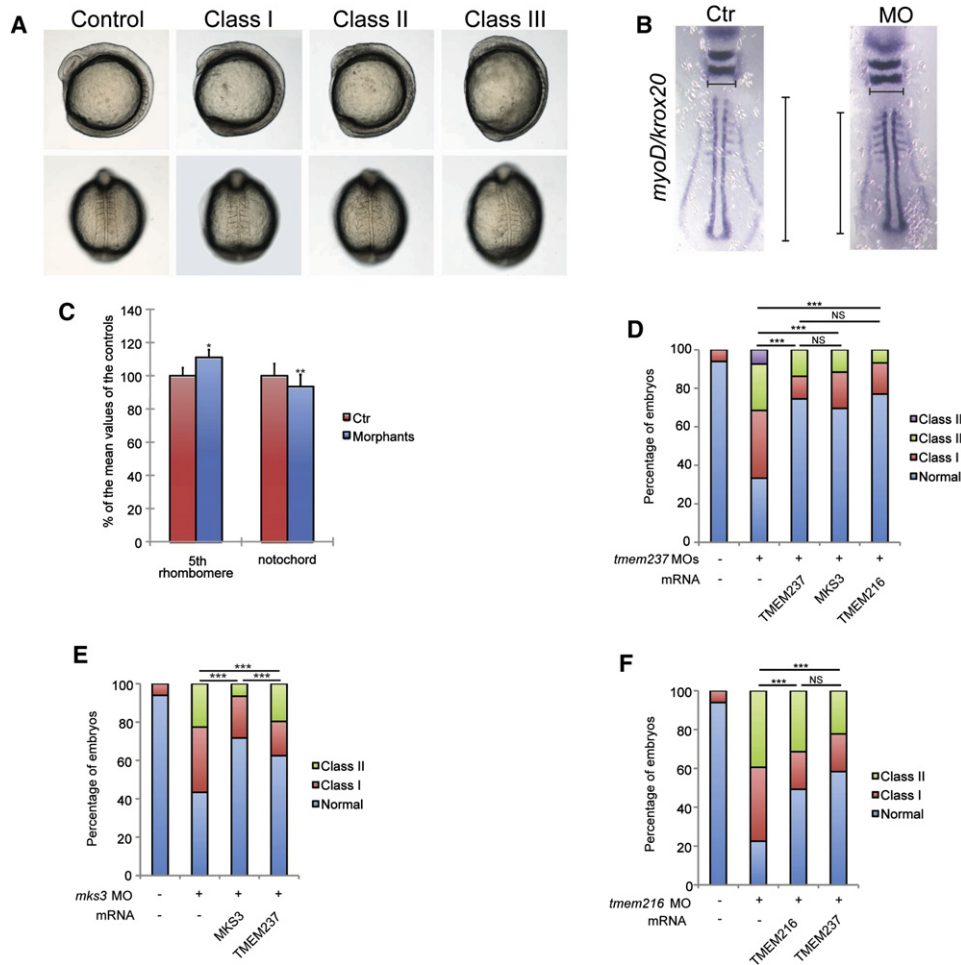
Figure 4. Zebrafish Morphant Phenotypes and Functional Complementation of TMEM Proteins

(A) Representative live embryo images of *tmem237* morphants at 8–10 somites (top, lateral view; bottom, dorsal view). Class I and II embryos were scored on the basis of previously established objective criteria.[37,38,59] Class I, short anterior-posterior axis, small anterior structures, and mild somitic defects; Class II, severe defects in head and eye development, shortening of the body axis, kinked notochords, and broadening of the somites; Class III, severe thinning and shortening of the body axis, curved notochord, broadened and thin somites, and an ovoid embryonic shape suggestive of dorsalization—embryos were severely delayed in development and typically did not survive past the ten somite stage.

(B) Zebrafish embryo flatmounts at the six somite stage hybridized with *krox20* and *myoD* riboprobe cocktails. Representative embryos are shown: control MO (Ctr) injected (left); *tmem237* MOs (MO) injected (right). Gastrulation defects were measured in two dimensions (medial-lateral and anterior-posterior) by the length of the 5th rhombomere (horizontal lines) and notochord (vertical lines), respectively.

(C) Quantification of the mean length of the 5th rhombomere or notochord of morphants (n = 29) are shown as the percentage of the mean length of the controls (n = 22). t test, *p < 0.01; **p < 0.001; error bars indicate SEM.

(D) Coinjection of *tmem237* MOs with human *TMEM237* mRNA, *MKS3* mRNA, or *TMEM216* mRNA significantly rescued morphant phenotypes at eight to ten somites.

(E) *TMEM237* can partially ameliorate *mks3* suppression defects of midsomitic embryos. Comparison of rescue efficiency of human *MKS3* versus *TMEM237* mRNA is shown.

(F) *TMEM237* mRNA rescues *tmem216* suppression phenotypes in a manner indistinguishable from *TMEM216* mRNA coinjection in midsomitic embryos (***p < 0.0001; NS, not significant for D and F).

We first confirmed that, as with mammalian TMEM237 (Figures 2A and 5A), the *C. elegans* ortholog, which we name JBTS-14, localizes to the ciliary TZ. In IMCD3 cells, Tmem237 localized to proximal regions of the cilium (Figure 2A) but just distal to the basal body (Figures 5A and 5B, marked with γ-tubulin and Dvl-1, respectively). In *C. elegans*, GFP-tagged JBTS-14 also concentrated to this ciliary region (marked by the tdTomato-tagged IFT dynein subunit XBX-1) within the cilia of head (amphid) and tail

(phasmid) sensory neurons (Figure 6A). This localization is identical to that of other established *C. elegans* TZ proteins.[27] Next, we identified a likely null mutant in the *C. elegans jbts-14* from a deep-sequenced EMS-mutagenized animal. Similar to other *C. elegans* single TZ gene mutants,[27] the *jbts-14* mutant displayed no gross structural or functional ciliary defects, as judged by its ability to take up fluorescent dye through environmentally-exposed ciliary endings (Figure 6B), and its ability to sense its chemical
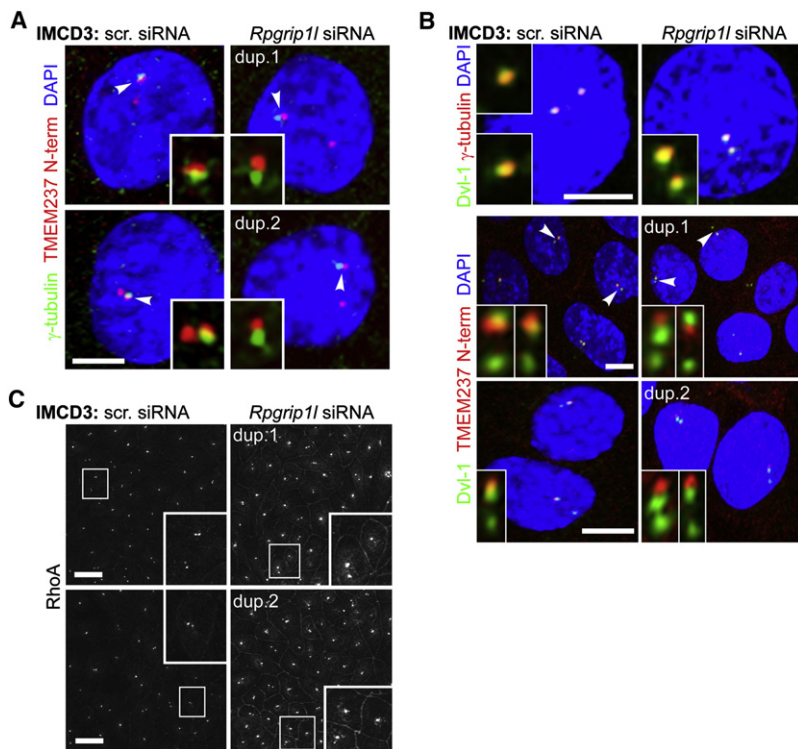
A IMCD3: scr. siRNA / Rpgrip1l siRNA

B IMCD3: scr. siRNA / Rpgrip1l siRNA

C IMCD3: scr. siRNA / Rpgrip1l siRNA

Figure 5. Ciliopathy TMEM Proteins Are Anchored at the Transition Zone by MKS5/RPGRIP1L

(A) In scrambled (scr.) siRNA-treated IMCD-3 cells, Tmem237 (red channel) is at proximal regions of the cilium and partially colocalizes with γ-tubulin (green channel) at the basal body, consistent with Tmem237 localization to the TZ. Colocalization with γ-tubulin is disrupted after *Rpgrip1l* siRNA knockdown with duplexes (dup.) 1 or 2. Insets show magnified regions (indicated by arrowheads on the main image) for the red and green channels only; the scale bars represent 5 μm.

(B) Top panels: Dvl-1 (green channel) is at the basal body that colocalizes with γ-tubulin (red channel) in IMCD-3 cells, as described previously.[19] *Rpgrip1l* siRNA knockdown does not disrupt overall basal body architecture. Bottom panels: in scrambled (scr.) siRNA-treated IMCD-3 cells, Tmem237 partially colocalizes with Dvl-1, but this is disrupted after *Rpgrip1l* siRNA knockdown.

(C) As above, but with RhoA staining; magnified insets are indicated by white frames.

environment (an avoidance of a high osmolarity solution; Figure 6C). Importantly, we identified a functional (genetic) interaction between *jbts-14* and another ciliopathy-associated gene, *nphp-4*. Compared to the single *jbts-14* or *nphp-4* single mutants, the *jbts-14;nphp-4* double mutant displays prominent dye-filling (dyf) and osmolarity avoidance (osm) phenotypes (Figures 6B and C). Such dyf and osm phenotypes occur with essentially all known ciliary mutants in the worm.[65]

To provide a more detailed look at the ciliary anomalies in the *jbts-14;nphp-4* double mutant, we performed TEM on this strain. In wild-type amphid channel neurons, ciliary axonemes extend from a basal body region that contains transition fibers and is found at the distal dendrite tip; the axonemes are defined at their proximal ends by the TZ compartment that makes axoneme-to-membrane connections via Y-links and are followed by microtubule doublets in the middle segment compartment and singlets in the distal segment compartment (wild-type TEMs and corresponding schematics shown in Figure 7). As expected, the single *jbts-14* mutant displayed an essentially wild-type ciliary ultrastructure (data not shown). In contrast, the *jbts-14;nphp-4* double mutant displays distinct cilium formation anomalies, such as axonemes that are either truncated or absent (Figure 7A). Strikingly, improper associations between the basal body-TZ region and the ciliary membrane are almost always observed, coincident with the loss or reduction of Y-link connectors (Figure 7B). In extreme cases, the TZ is fully disconnected (unanchored) from the ciliary membrane, existing instead as an ectopic structure within the distal dendrite region

(Figure 7B; +10 image). In addition, many vesicle or membrane accumulations are found in proximity to the TZ, something never observed in wild-type animals. Overall, these ciliary phenotypes are very similar to those observed in other TZ gene mutant combinations with *nphp-4*.[27] This strongly suggests that JBTS-14 (TMEM237) has a ciliogenesis function that overlaps with that of at least five other TZ proteins: namely, MKS-1, MKSR-1/B9D1, MKS-3/Meckelin/TMEM67, MKS-5/RPGRIP1L, and MKS-6/CC2D2A. Such a shared function is consistent with our finding that the localization of *C. elegans* JBTS-14 to the TZ depends on multiple other TZ proteins (see below), all of which are implicated in JSRDs, MKS, and NPHP ciliopathies.

To determine whether these ciliary phenotypes are specific for JBTS-14 or are general to other ciliopathy-associated TMEMs, we studied MKS-2/TMEM216. The mammalian TMEM216 is another tetraspan transmembrane protein localizing to the base of cilia,[19] and it can partially complement TMEM237 loss in vitro and in vivo (Figures 3E and 4D). As expected, the *C. elegans* MKS-2/TMEM216 ortholog specifically localizes to the TZ (Figure 6A) and functions in a manner similar to JBTS-14. We used transposon-mediated mutagenesis to obtain a likely null allele of *mks-2* and found, as with *jbts-14*, that the single mutant displays no ciliary or chemotaxis defects but functionally interacts with *nphp-4* (Figures 6B and 6C). To further delineate the functional and modular or hierarchical relationships between ciliopathy-associated TMEMs and other established TZ proteins, we determined whether GFP-tagged JBTS-14 or MKS-2 proteins localized correctly in different TZ gene mutant backgrounds. In *mks-5* mutants, both JBTS-14 and MKS-2 failed to localize to the TZ and displayed a diffuse staining pattern within the
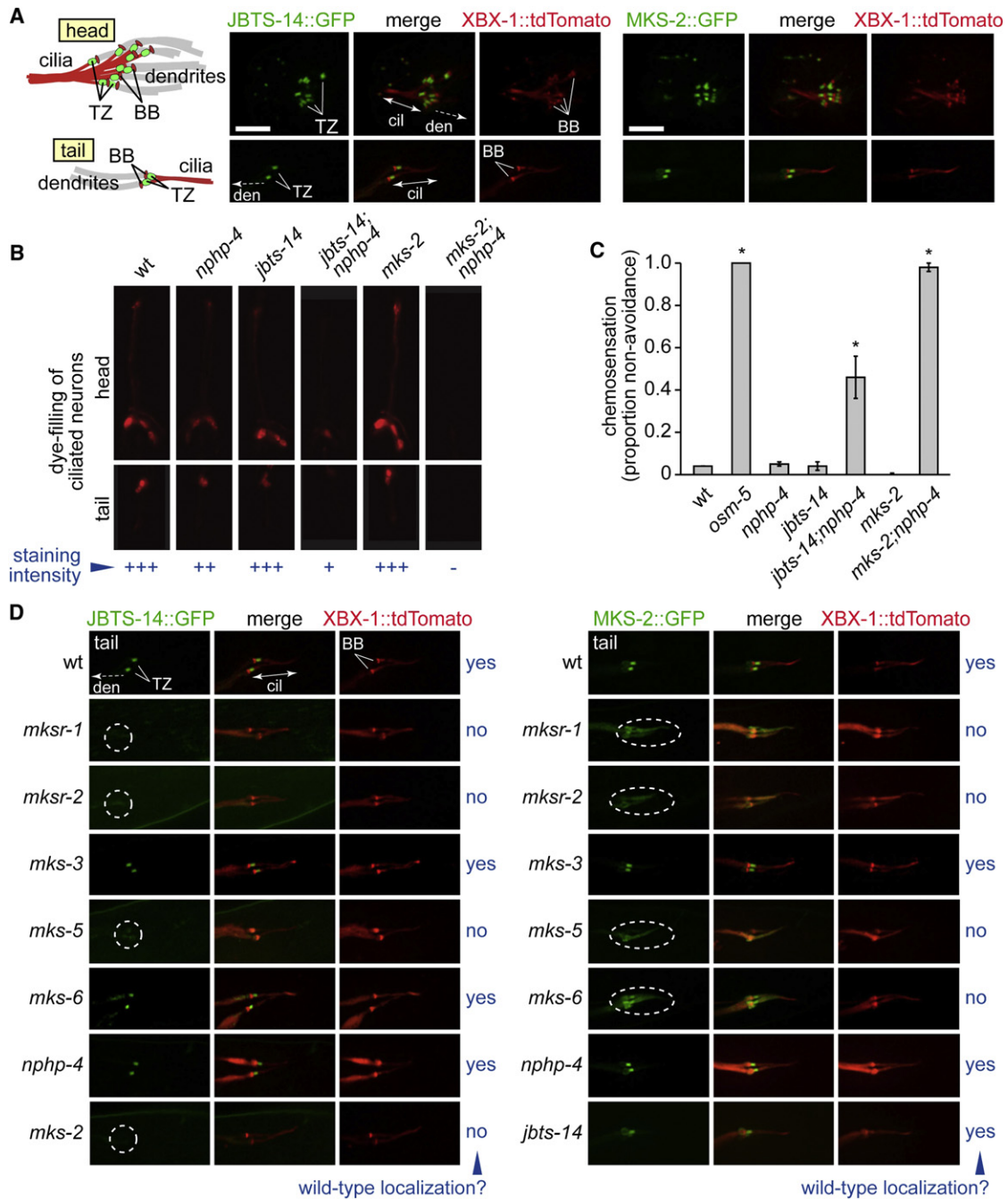
Figure 6. *C. elegans* JBTS-14 Functionally Interacts with NPHP-4 to Promote Ciliogenesis and Forms Part of a Functional Assembly of Proteins at the Transition Zone that Includes MKSR-1/B9D1, MKSR-2/B9D2, MKS-2, and MKS-5/RPGRIP1L

(A) *C. elegans* JBTS-14 and MKS-2 (GFP-tagged) localize specifically to the transition zone (TZ) in amphid (head) and phasmid (tail) cilia. The TZ is immediately distal to the basal body (BB) on the ciliary axoneme, both of which are marked by the tdTomato-tagged XBX-1 intraflagellar transport protein.

(B) Disruption of *jbts-14* or *mks-2* alone does not cause overt ciliogenesis defects, as judged by the ability of worms to take up fluorescent dye through environmentally-exposed cilia. In contrast, the *jbts-14;nphp-4*, or *mks-2;nphp-4* double-mutant animals are dye-filling defective, indicative of cilia structure defects. The *osm-5* ciliary mutant, which lacks cilia altogether, is included as a control.

(C) *jbts-14* or *mks-2* single mutants can avoid a high osmolarity solution, which depends on functional cilia, whereas the *jbts-14;nphp-4* or *mks-2;nphp-4* double mutants are defective in this chemosensory behavior. Chi-square test, *p<0.0001; error bars indicate SEM.

(D) The localization of JBTS-14 (left panels) and MKS-2 (right panels) depends on the presence of several other TZ proteins but not others, as indicated by yes (properly localized) or no and a dotted ellipse for a mislocalized protein. The following abbreviations are used: BB, basal body; cil, cilium; TZ, transition zone; den, dendrite. The scale bar represents 5 μm.
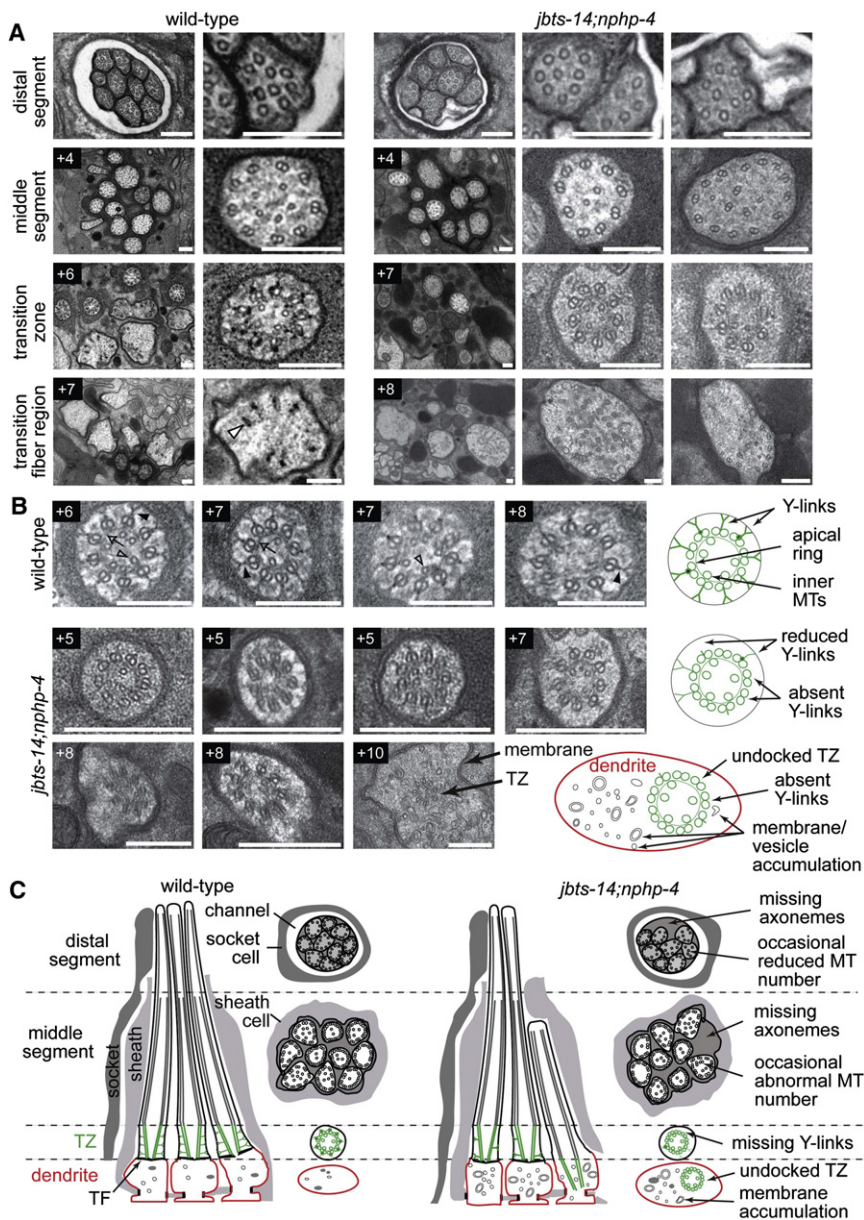
Figure 7. Basal Body-Transition Zone Attachment to the Ciliary Membrane Is Disrupted in Mutant Strain Lacking JBTS-14 and NPHP-4

(A) Low and high-magnification images of *C. elegans* amphid channel sensory cilia from TEM serial cross sections of the amphidal pore. Top row: images from the distal pore region. Boxed numbers denote proximal positioning of sections relative to the top row sections. In wild-type (N2) worms, the amphid pore contains ten axonemes, each consisting of a distal segment (top row: nine singlet microtubules), a middle segment (second row: doublet microtubules) and a transition zone (TZ) (third row: ring of doublet microtubules drawn together by the apical ring and connected to the ciliary membrane via Y-links). At the base of the cilia, within the far distal dendrite region, are transition fibers and occasional vesicles. In *jbts-14;nphp-4* mutants, two to three axonemes are typically missing from the distal pore (top row, left image) and occasionally from more proximal regions (+4; left image), microtubule number is sometimes elevated (+4; right image), and Y-links are consistently missing or reduced from the transition zone compartment (+7; middle and right images). In distal dendrite regions, vesicles and membranes are often abnormally accumulated (+8; middle image) and incomplete, ectopically positioned, ciliary axonemes are occasionally observed (+8; right image). The open arrowhead indicates a transition fiber. The scale bars represent 200 nm.

(B) High-magnification images of transition zone phenotypes in the *jbts-14; nphp-4* double mutant presenting multiple examples of the phenotypes described above, as well as an image showing an undocked TZ in the distal dendrite region (+10). The arrow indicates an apical ring; the closed arrowhead, Y-links; and the open arrowhead, inner microtubules. Images taken from three independently sectioned worms. Boxed numbers denote proximal positioning of sections relative to the distal end of the amphidal pore. Schematics to the right of each row depict normal and abrogated ciliary structures in wild-type and *jbts-14;nphp-4* mutant worms, respectively. The scale bars represent 200 nm.

(C) Schematics of amphid channel cilia (longitudinal and transverse views) showing the major ultrastructural defects observed, including the loss of TZ connections to the ciliary membrane via Y-links. TZ subcompartment (microtubules and Y-links) is highlighted in green, dendritic membrane is highlighted in red.

dendrite and cilium (Figure 6D), indicating that MKS-5/RPGRIP1L is required for proper TZ localization of these two TMEM proteins, similar to that reported for *C. elegans* MKS-3 as well.[27] To confirm this result in mammalian cells, we performed knockdowns of *Mks5/Rpgrip1l* in IMCD3 cells and stained for Tmem237 and the basal body markers γ-tubulin (Figure 5A) or Dvl1 (Figure 5B), and RhoA (Figure 5C). We observed that after scrambled siRNA transfection, basal body architecture was intact (Figure 5B) and that Tmem237 was just distal to the basal body (Figures 5A and 5B; marked by either γ-tubulin or Dvl-1, respectively). This localization to the TZ was disrupted after knockdown of *Mks5/Rpgrip1l*. RhoA was also mislocalized to peripheral regions of the basal body and to basolateral cell-cell contacts (Figure 5C), a pattern identical to that in the cellular phenotype after *Tmem237* knockdown (Figure 3C) as well as *Tmem216/Mks2* knockdown.[19]

We then further assessed the functional requirements for *C. elegans* JBTS-14 and MKS-2 localization to the TZ. We uncovered two additional TZ components, the B9 domain proteins MKSR-1/B9D1 and MKSR-2/B9D2, whose functions are required for the proper TZ localization of JBTS-14 and MKS-2 (Figure 6D). Furthermore, *C. elegans* MKS-2

is at least partially delocalized in the *mks-6* mutant. In contrast, both JBTS-14 and MKS-2 localized normally in two other mutants, *mks-3* and *nphp-4* (Figure 6D). Interestingly, although *C. elegans* MKS-2 localizes properly in the *jbts-14* mutant, the reciprocal experiment shows that JBTS-14 is mislocalized in the *mks-2* mutant. Thus, in a hierarchical or modular interaction network, JBTS-14 could potentially be considered peripheral with respect to MKS-2, whereas MKS-2 connects JBTS-14 to other TZ proteins. Together, these data demonstrate that both JBTS-14 and MKS-2 are likely to be part of a hierarchical or modular assembly that includes other established TZ proteins. Because MKS5/RPGRIP1L is required for the correct localization of JBTS-14/TMEM237 at the TZ in both *C. elegans* and mammalian cells, such functional modules are likely to be evolutionarily conserved.

Assessing the Possible Contribution of *TMEM237* to BBS

The potential functional overlap of TMEM237 with other bona fide ciliopathy causal loci (both in vitro and in vivo), as well as the documented genetic overlap across ciliopathies, raised the question of whether loss of function in this gene transcript could contribute to other overlapping clinical phenotypes. To begin to address this question, we sequenced *TMEM237* in 90 individuals of Northern European origin who had been diagnosed with BBS but were unselected for known mutations. We found one heterozygous change (p.Asp155Ala) in a BBS family with a heterozygous, functionally null *BBS6* [MIM 604896] Thr57Ala mutation,[38,66] which was not present in HapMap, the 1000 Genomes Project, or an additional 200 controls. When tested by our established in vivo zebrafish-based complementation assay,[37–39,59] this allele was shown to be hypomorphic, because it could only partially rescue *tmem237* MO phenotypes (Figure S9A). Digenic inheritance is unlikely because of segregation of the alleles in the family and the fact that we observed no synergistic effect when subeffective doses of *tmem237* and *bbs6* MOs were coinjected in zebrafish embryos (Figure S9B).

Discussion

Ciliopathies are a unique group of genetically heterogeneous human developmental disorders that collectively affect nearly every tissue and organ in the body, presenting with a wide array of physiological and developmental phenotypes.[1–6,67] Remarkably, although discrete clinical entities such as Joubert syndrome, Meckel-Gruber syndrome, Bardet-Biedl syndrome, and nephronophthisis are apparent, there is considerable phenotypic overlap between these conditions and even allelism at a number of loci.[6,8] A key question is therefore whether the phenotypic overlap—and variability—of these cilium-associated disorders can be explained by a common molecular and cellular etiology.

Many of the known JBTS/MKS/BBS/NPHP proteins from vertebrates or other species such as *C. elegans* have now been ascribed roles in cilium biogenesis and signaling at the ciliary transition zone.[27–30] To gain further insight into the genetic causes of the MKS/JBTS group of ciliopathies, we first mapped a locus for JSRD type 14 (JBTS-14) in the Canadian Hutterites, leading to the identification of mutations in *TMEM237*. The mutations identified in this study are all predicted to be null, suggesting that complete loss or near-absence of TMEM237 causes the JSRD type 14 phenotype. Despite this common mechanism, it is interesting to note that the large subgroup of the affected individuals with cystic kidneys also have posterior fossa findings in addition to a MTS, suggesting that these developmental pathways are affected by additional, probably genetic, modifying factors. Although mutations in *TMEM237* only account for <1% cases in our JSRDs-MKS cohort, the high carrier frequency of the c.52C>T mutation in the Hutterite population (approximately 1:15) means that carrier testing, cascade testing in families, and prenatal diagnosis will be of high clinical utility. Families with JSRDs will also benefit from improved diagnosis and accurate genetic counseling.

To further elucidate the molecular etiology of *TMEM237*-associated JSRD, we characterized the function of the TZ-localized TMEM237 protein. Loss of human *TMEM237* results in failure of ciliogenesis and deregulation of both canonical and noncanonical/PCP Wnt signaling pathways. These findings are strikingly similar to previous studies of both TMEM216 and MKS3,[19,34] two additional transmembrane proteins associated with JSRDs and MKS. MKS3 and TMEM216 have been suggested to be noncanonical Wnt receptors that regulate the RhoA pathway and thus mediate the cytoskeleton rearrangements required for basal body docking at the apical region of the cells prior to ciliogenesis.[34] Importantly, we demonstrate that in a complementary zebrafish model system, disruption of TMEM237 causes developmental (convergent extension) phenotypes comparable to those obtained upon abrogation of TZ-localized proteins, including TMEM216 and MKS3.[19] Furthermore, we now show by both an in vitro (Figure 3E) and an in vivo (Figures 4D–4F) assay that there is the probable functional complementation of TMEM237, TMEM216, and MKS3. This finding, and the similarities between the three TMEMs in cellular localization, protein structure, role in cilium formation and function, and clinical phenotypes caused by mutations indicate that TMEM237, TMEM216, and MKS3 probably function in the same pathway or module to regulate ciliogenesis and signaling. This conclusion is supported by the functional interaction of *C. elegans* TZ-localized proteins belonging to the MKS module in mediating basal body-TZ attachment to the membrane and cilium formation.[27] We speculate that TMEM237, TMEM216, MKS3, and perhaps other TMEMs form a receptor-coreceptor complex at the ciliary TZ to mediate and integrate signaling pathways impacting the primary cilium.

One of the central questions remaining concerning the molecular etiology and underlying phenotypic variability of the JBTS-MKS-NPHP ciliopathy spectrum is whether the ciliary defects arise from disruption in one or more macromolecular assemblies, or modules, comparable to that of the BBSome, an oligomeric protein complex containing proteins associated with BBS.[68,69] Support for this model comes from the study of *C. elegans*, which has suggested the existence of two genetically defined modules: one, being an MKS module (consisting of MKS-1, MKSR-1/B9D1, MKSR-2/B9D2, MKS-3, and MKS-6), and the other, an NPHP module, consisting of NPHP-1 and NPHP-4.[27] Specifically, disruption of any single mutant, or combination of mutants, in gene(s) within either module abrogates a ciliary gate function but does not significantly impair the structure of most cilia; in contrast, disrupting any combination of two genes, one from each module, causes transition zone structure anomalies that are concomitant with loss of basal body-TZ anchoring to the membrane and ciliary axoneme structure defects. Importantly, these modules are largely consistent with a physical interaction network recently uncovered in mammalian cells.[22] For example, NPHP1 and NPHP4 are ascribed to a distinct protein interaction module, coincident with the genetically-defined *C. elegans* NPHP module, and MKS1 and MKS6 are part of a physical interaction network that is consistent with the two respective genes being components of the *C. elegans* MKS genetic module. Additionally, disruption of individual mammalian TZ proteins (such as MKS1 and MKS3) in mouse models is on the whole phenotypically less severe than that observed for disruption of IFT, which causes global defects in ciliogenesis;[27] this suggests a functional redundancy in mammals that might be similar to that observed in *C. elegans* and could be exposed by analysis of mouse double knockouts. In this study, we show that *C. elegans* JBTS-14 (TMEM237) functionally interacts with NPHP-4 to promote basal body-TZ attachment to the membrane and cilium formation. Such functions parallel those reported for the other *C. elegans* TZ-localized proteins belonging to the MKS module and thus implicate JBTS-14 in the same molecular pathway.

Overall, our analyses of TMEM237 in mammalian cells, zebrafish, and *C. elegans* strongly support a role for this tetraspan transmembrane protein within an expansive genetic and physical interaction network of proteins localized to the TZ, where it participates in a functional module that regulates cilium biogenesis and signaling. Our findings therefore extend the interaction network of ciliopathy proteins at the TZ, revealing additional complexity at this ciliary region, and underline the importance of an evolutionary conserved JSRD-MKS-NPHP functional module for cilium biogenesis and signaling.

Supplemental Data

Supplemental Data include 11 figures and 1 table and can be found with this article online at http://www.cell.com/AJHG/.

Web Resources

The URLs for data presented herein are as follows:

1000 Genomes Project, http://browser.1000genomes.org/index.html
C. elegans Gene Knockout Consortium, http://celeganskoconsortium.omrf.org/
Entrez Gene, http://www.ncbi.nlm.nih.gov/gene
National Bioresource Project, http://shigen.lab.nig.ac.jp/c.elegans/index.jsp
National Center for Biotechnology Information (NCBI) dbSNP, http://www.ncbi.nlm.nih.gov/projects/SNP/
NCBI Nucleotide database, http://www.ncbi.nlm.nih.gov/nuccore
NCBI protein database, http://www.ncbi.nlm.nih.gov/protein
Online Mendelian Inheritance in Man (OMIM), http://www.omim.org
Protocol Online, http://www.protocol-online.org/
SYSCILIA, http://syscilia.org/
Zebrafish Model Organism Database, http://zfin.org

References

1. Brancati, F., Dallapiccola, B., and Valente, E.M. (2010). Joubert Syndrome and related disorders. Orphanet J. Rare Dis. *5*, 20.

2. Baker, K., and Beales, P.L. (2009). Making sense of cilia in disease: The human ciliopathies. Am. J. Med. Genet. C. Semin. Med. Genet. *151C*, 281–295.

3. Sharma, N., Berbari, N.F., and Yoder, B.K. (2008). Ciliary dysfunction in developmental abnormalities and diseases. Curr. Top. Dev. Biol. *85*, 371–427.

4. Lee, J.E., and Gleeson, J.G. (2011). Cilia in the nervous system: Linking cilia function and neurodevelopmental disorders. Curr. Opin. Neurol. *24*, 98–105.

5. Cardenas-Rodriguez, M., and Badano, J.L. (2009). Ciliary biology: Understanding the cellular and genetic basis of human ciliopathies. Am. J. Med. Genet. C. Semin. Med. Genet. *151C*, 263–280.

6. Hildebrandt, F., Benzing, T., and Katsanis, N. (2011). Ciliopathies. N. Engl. J. Med. *364*, 1533–1543.

7. Johnson, J.L., and Leroux, M.R. (2010). cAMP and cGMP signaling: Sensory systems with prokaryotic roots adopted by eukaryotic cilia. Trends Cell Biol. *20*, 435–444.

8. Parisi, M.A. (2009). Clinical and molecular features of Joubert syndrome and related disorders. Am. J. Med. Genet. C. Semin. Med. Genet. *151C*, 326–340.

9. Bielas, S.L., Silhavy, J.L., Brancati, F., Kisseleva, M.V., Al-Gazali, L., Sztriha, L., Bayoumi, R.A., Zaki, M.S., Abdel-Aleem, A., Rosti, R.O., et al. (2009). Mutations in *INPP5E*, encoding inositol polyphosphate-5-phosphatase E, link phosphatidyl inositol signaling to the ciliopathies. Nat. Genet. *41*, 1032–1036.

10. Valente, E.M., Brancati, F., Silhavy, J.L., Castori, M., Marsh, S.E., Barrano, G., Bertini, E., Boltshauser, E., Zaki, M.S., Abdel-Aleem, A., et al; International JSRD Study Group. (2006). *AHI1* gene mutations cause specific forms of Joubert syndrome-related disorders. Ann. Neurol. *59*, 527–534.

11. Parisi, M.A., Bennett, C.L., Eckert, M.L., Dobyns, W.B., Gleeson, J.G., Shaw, D.W., McDonald, R., Eddy, A., Chance, P.F., and Glass, I.A. (2004). The *NPHP1* gene deletion associated with juvenile nephronophthisis is present in a subset of individuals with Joubert syndrome. Am. J. Hum. Genet. *75*, 82–91.

12. Valente, E.M., Silhavy, J.L., Brancati, F., Barrano, G., Krishnaswami, S.R., Castori, M., Lancaster, M.A., Boltshauser, E., Boccone, L., Al-Gazali, L., et al; International Joubert Syndrome Related Disorders Study Group. (2006). Mutations in *CEP290*, which encodes a centrosomal protein, cause pleiotropic forms of Joubert syndrome. Nat. Genet. *38*, 623–625.

13. Sayer, J.A., Otto, E.A., O'Toole, J.F., Nurnberg, G., Kennedy, M.A., Becker, C., Hennies, H.C., Helou, J., Attanasio, M., Fausett, B.V., et al. (2006). The centrosomal protein nephrocystin-6 is mutated in Joubert syndrome and activates transcription factor ATF4. Nat. Genet. *38*, 674–681.

14. Baala, L., Romano, S., Khaddour, R., Saunier, S., Smith, U.M., Audollent, S., Ozilou, C., Faivre, L., Laurent, N., Foliguet, B., et al. (2007). The Meckel-Gruber syndrome gene, *MKS3*, is mutated in Joubert syndrome. Am. J. Hum. Genet. *80*, 186–194.

15. Delous, M., Baala, L., Salomon, R., Laclef, C., Vierkotten, J., Tory, K., Golzio, C., Lacoste, T., Besse, L., Ozilou, C., et al. (2007). The ciliary gene *RPGRIP1L* is mutated in cerebello-oculo-renal syndrome (Joubert syndrome type B) and Meckel syndrome. Nat. Genet. *39*, 875–881.

16. Arts, H.H., Doherty, D., van Beersum, S.E., Parisi, M.A., Letteboer, S.J., Gorden, N.T., Peters, T.A., Märker, T., Voesenek, K., Kartono, A., et al. (2007). Mutations in the gene encoding the basal body protein *RPGRIP1L*, a nephrocystin-4 interactor, cause Joubert syndrome. Nat. Genet. *39*, 882–888.

17. Cantagrel, V., Silhavy, J.L., Bielas, S.L., Swistun, D., Marsh, S.E., Bertrand, J.Y., Audollent, S., Attié-Bitach, T., Holden, K.R., Dobyns, W.B., et al; International Joubert Syndrome Related Disorders Study Group. (2008). Mutations in the cilia gene *ARL13B* lead to the classical form of Joubert syndrome. Am. J. Hum. Genet. *83*, 170–179.

18. Gorden, N.T., Arts, H.H., Parisi, M.A., Coene, K.L., Letteboer, S.J., van Beersum, S.E., Mans, D.A., Hikida, A., Eckert, M., Knutzen, D., et al. (2008). *CC2D2A* is mutated in Joubert syndrome and interacts with the ciliopathy-associated basal body protein CEP290. Am. J. Hum. Genet. *83*, 559–571.

19. Valente, E.M., Logan, C.V., Mougou-Zerelli, S., Lee, J.H., Silhavy, J.L., Brancati, F., Iannicelli, M., Travaglini, L., Romani, S., Illi, B., et al. (2010). Mutations in *TMEM216* perturb ciliogenesis and cause Joubert, Meckel and related syndromes. Nat. Genet. *42*, 619–625.

20. Edvardson, S., Shaag, A., Zenvirt, S., Erlich, Y., Hannon, G.J., Shanske, A.L., Gomori, J.M., Ekstein, J., and Elpeleg, O. (2010). Joubert syndrome 2 (JBTS2) in Ashkenazi Jews is associated with a *TMEM216* mutation. Am. J. Hum. Genet. *86*, 93–97.

21. Coene, K.L., Roepman, R., Doherty, D., Afroze, B., Kroes, H.Y., Letteboer, S.J., Ngu, L.H., Budny, B., van Wijk, E., Gorden, N.T., et al. (2009). *OFD1* is mutated in X-linked Joubert syndrome and interacts with LCA5-encoded lebercilin. Am. J. Hum. Genet. *85*, 465–481.

22. Sang, L., Miller, J.J., Corbit, K.C., Giles, R.H., Brauer, M.J., Otto, E.A., Baye, L.M., Wen, X., Scales, S.J., Kwong, M., et al. (2011). Mapping the NPHP-JBTS-MKS protein network reveals ciliopathy disease genes and pathways. Cell *145*, 513–528.

23. Dafinger, C., Liebau, M.C., Elsayed, S.M., Hellenbroich, Y., Boltshauser, E., Korenke, G.C., Fabretti, F., Janecke, A.R., Ebermann, I., Nürnberg, G., et al. (2011). Mutations in *KIF7* link Joubert syndrome with Sonic Hedgehog signaling and microtubule dynamics. J. Clin. Invest. *121*, 2662–2667.

24. Garcia-Gonzalo, F.R., Corbit, K.C., Sirerol-Piquer, M.S., Ramaswami, G., Otto, E.A., Noriega, T.R., Seol, A.D., Robinson, J.F., Bennett, C.L., Josifova, D.J., et al. (2011). A transition zone complex regulates mammalian ciliogenesis and ciliary membrane composition. Nat. Genet. *43*, 776–784.

25. Logan, C.V., Abdel-Hamed, Z., and Johnson, C.A. (2011). Molecular genetics and pathogenic mechanisms for the severe ciliopathies: Insights into neurodevelopment and pathogenesis of neural tube defects. Mol. Neurobiol. *43*, 12–26.

26. Hildebrandt, F., Attanasio, M., and Otto, E. (2009). Nephronophthisis: Disease mechanisms of a ciliopathy. J. Am. Soc. Nephrol. *20*, 23–35.

27. Williams, C.L., Li, C., Kida, K., Inglis, P.N., Mohan, S., Semenec, L., Bialas, N.J., Stupay, R.M., Chen, N., Blacque, O.E., et al. (2011). MKS and NPHP modules cooperate to establish basal body/transition zone membrane associations and ciliary gate function during ciliogenesis. J. Cell Biol. *192*, 1023–1041.

28. Bialas, N.J., Inglis, P.N., Li, C., Robinson, J.F., Parker, J.D., Healey, M.P., Davis, E.E., Inglis, C.D., Toivonen, T., Cottell, D.C., et al. (2009). Functional interactions between the ciliopathy-associated Meckel syndrome 1 (MKS1) protein and two novel MKS1-related (MKSR) proteins. J. Cell Sci. 122, 611–624.

29. Williams, C.L., Masyukova, S.V., and Yoder, B.K. (2010). Normal ciliogenesis requires synergy between the cystic kidney disease genes MKS-3 and NPHP-4. J. Am. Soc. Nephrol. 21, 782–793.

30. Williams, C.L., Winkelbauer, M.E., Schafer, J.C., Michaud, E.J., and Yoder, B.K. (2008). Functional redundancy of the B9 proteins and nephrocystins in Caenorhabditis elegans ciliogenesis. Mol. Biol. Cell 19, 2154–2168.

31. Dawe, H.R., Smith, U.M., Cullinane, A.R., Gerrelli, D., Cox, P., Badano, J.L., Blair-Reid, S., Sriram, N., Katsanis, N., Attie-Bitach, T., et al. (2007). The Meckel-Gruber Syndrome proteins MKS1 and meckelin interact and are required for primary cilium formation. Hum. Mol. Genet. 16, 173–186.

32. Vierkotten, J., Dildrop, R., Peters, T., Wang, B., and Rüther, U. (2007). Ftm is a novel basal body protein of cilia involved in Shh signalling. Development 134, 2569–2577.

33. Zuniga, F.I., and Craft, C.M. (2010). Deciphering the structure and function of Als2cr4 in the mouse retina. Invest. Ophthalmol. Vis. Sci. 51, 4407–4415.

34. Dawe, H.R., Adams, M., Wheway, G., Szymanska, K., Logan, C.V., Noegel, A.A., Gull, K., and Johnson, C.A. (2009). Nesprin-2 interacts with meckelin and mediates ciliogenesis via remodelling of the actin cytoskeleton. J. Cell Sci. 122, 2716–2726.

35. Willert, J., Epping, M., Pollack, J.R., Brown, P.O., and Nusse, R. (2002). A transcriptional response to Wnt protein in human embryonic carcinoma cells. BMC Dev. Biol. 2, 8.

36. Thisse, C., and Thisse, B. (2008). High-resolution in situ hybridization to whole-mount zebrafish embryos. Nat. Protoc. 3, 59–69.

37. Leitch, C.C., Zaghloul, N.A., Davis, E.E., Stoetzel, C., Diaz-Font, A., Rix, S., Alfadhel, M., Lewis, R.A., Eyaid, W., Banin, E., et al. (2008). Hypomorphic mutations in syndromic encephalocele genes are associated with Bardet-Biedl syndrome. Nat. Genet. 40, 443–448.

38. Zaghloul, N.A., Liu, Y., Gerdes, J.M., Gascue, C., Oh, E.C., Leitch, C.C., Bromberg, Y., Binkley, J., Leibel, R.L., Sidow, A., et al. (2010). Functional analyses of variants reveal a significant role for dominant negative and common alleles in oligogenic Bardet-Biedl syndrome. Proc. Natl. Acad. Sci. USA 107, 10602–10607.

39. Khanna, H., Davis, E.E., Murga-Zamalloa, C.A., Estrada-Cuzcano, A., Lopez, I., den Hollander, A.I., Zonneveld, M.N., Othman, M.I., Waseem, N., Chakarova, C.F., et al. (2009). A common allele in RPGRIP1L is a modifier of retinal degeneration in ciliopathies. Nat. Genet. 41, 739–745.

40. Blacque, O.E., Reardon, M.J., Li, C., McCarthy, J., Mahjoub, M.R., Ansley, S.J., Badano, J.L., Mah, A.K., Beales, P.L., Davidson, W.S., et al. (2004). Loss of C. elegans BBS-7 and BBS-8 protein function results in cilia defects and compromised intraflagellar transport. Genes Dev. 18, 1630–1642.

41. Culotti, J.G., and Russell, R.L. (1978). Osmotic avoidance defective mutants of the nematode Caenorhabditis elegans. Genetics 90, 243–256.

42. Cevik, S., Hori, Y., Kaplan, O.I., Kida, K., Toivenon, T., Foley-Fisher, C., Cottell, D., Katada, T., Kontani, K., and Blacque, O.E. (2010). Joubert syndrome Arl13b functions at ciliary membranes and stabilizes protein transport in Caenorhabditis elegans. J. Cell Biol. 188, 953–969.

43. Boulin, T., and Bessereau, J.L. (2007). Mos1-mediated insertional mutagenesis in Caenorhabditis elegans. Nat. Protoc. 2, 1276–1287.

44. Boycott, K.M., Parboosingh, J.S., Scott, J.N., McLeod, D.R., Greenberg, C.R., Fujiwara, T.M., Mah, J.K., Midgley, J., Wade, A., Bernier, F.P., et al. (2007). Meckel syndrome in the Hutterite population is actually a Joubert-related cerebello-oculo-renal syndrome. Am. J. Med. Genet. A. 143A, 1715–1725.

45. Schurig, V., Bowen, P., Harley, F., and Schiff, D. (1980). The Meckel syndrome in the Hutterites. Am. J. Med. Genet. 5, 373–381.

46. Janecke, A.R., Müller, T., Gassner, I., Kreczy, A., Schmid, E., Kronenberg, F., Utermann, B., and Utermann, G. (2004). Joubert-like syndrome unlinked to known candidate loci. J. Pediatr. 144, 264–269.

47. Liu, Q., Tan, G., Levenkova, N., Li, T., Pugh, E.N., Jr., Rux, J.J., Speicher, D.W., and Pierce, E.A. (2007). The proteome of the mouse photoreceptor sensory cilium complex. Mol. Cell. Proteomics 6, 1299–1317.

48. Kwok, M.C., Holopainen, J.M., Molday, L.L., Foster, L.J., and Molday, R.S. (2008). Proteomics of photoreceptor outer segments identifies a subset of SNARE and Rab proteins implicated in membrane vesicle trafficking and fusion. Mol. Cell. Proteomics 7, 1053–1066.

49. Smith, U.M., Consugar, M., Tee, L.J., McKee, B.M., Maina, E.N., Whelan, S., Morgan, N.V., Goranson, E., Gissen, P., Lilliquist, S., et al. (2006). The transmembrane protein meckelin (MKS3) is mutated in Meckel-Gruber syndrome and the wpk rat. Nat. Genet. 38, 191–196.

50. Junge, H.J., Yang, S., Burton, J.B., Paes, K., Shu, X., French, D.M., Costa, M., Rice, D.S., and Ye, W. (2009). TSPAN12 regulates retinal vascular development by promoting Norrin- but not Wnt-induced FZD4/beta-catenin signaling. Cell 139, 299–311.

51. Wallingford, J.B., Rowning, B.A., Vogeli, K.M., Rothbächer, U., Fraser, S.E., and Harland, R.M. (2000). Dishevelled controls cell polarity during Xenopus gastrulation. Nature 405, 81–85.

52. Park, T.J., Haigo, S.L., and Wallingford, J.B. (2006). Ciliogenesis defects in embryos lacking inturned or fuzzy function are associated with failure of planar cell polarity and Hedgehog signaling. Nat. Genet. 38, 303–311.

53. Veeman, M.T., Axelrod, J.D., and Moon, R.T. (2003). A second canon. Functions and mechanisms of beta-catenin-independent Wnt signaling. Dev. Cell 5, 367–377.

54. Gerdes, J.M., Liu, Y., Zaghloul, N.A., Leitch, C.C., Lawson, S.S., Kato, M., Beachy, P.A., Beales, P.L., DeMartino, G.N., Fisher, S., et al. (2007). Disruption of the basal body compromises proteasomal function and perturbs intracellular Wnt response. Nat. Genet. 39, 1350–1360.

55. Lancaster, M.A., Louie, C.M., Silhavy, J.L., Sintasath, L., Decambre, M., Nigam, S.K., Willert, K., and Gleeson, J.G. (2009). Impaired Wnt-beta-catenin signaling disrupts adult renal homeostasis and leads to cystic kidney ciliopathy. Nat. Med. 15, 1046–1054.

56. Park, T.J., Mitchell, B.J., Abitua, P.B., Kintner, C., and Wallingford, J.B. (2008). Dishevelled controls apical docking and planar polarization of basal bodies in ciliated epithelial cells. Nat. Genet. 40, 871–879.

57. Winter, C.G., Wang, B., Ballew, A., Royou, A., Karess, R., Axelrod, J.D., and Luo, L. (2001). Drosophila Rho-associated kinase (Drok) links Frizzled-mediated planar cell polarity signaling to the actin cytoskeleton. Cell *105*, 81–91.

58. Lang, P., Gesbert, F., Delespine-Carmagnat, M., Stancou, R., Pouchelet, M., and Bertoglio, J. (1996). Protein kinase A phosphorylation of RhoA mediates the morphological and functional effects of cyclic AMP in cytotoxic lymphocytes. EMBO J. *15*, 510–519.

59. Merveille, A.C., Davis, E.E., Becker-Heck, A., Legendre, M., Amirav, I., Bataille, G., Belmont, J., Beydon, N., Billen, F., Clément, A., et al. (2011). CCDC39 is required for assembly of inner dynein arms and the dynein regulatory complex and for normal ciliary motility in humans and dogs. Nat. Genet. *43*, 72–78.

60. Keller, R. (2002). Shaping the vertebrate body plan by polarized embryonic cell movements. Science *298*, 1950–1954.

61. Jauregui, A.R., and Barr, M.M. (2005). Functional characterization of the C. elegans nephrocystins NPHP-1 and NPHP-4 and their role in cilia and male sensory behaviors. Exp. Cell Res. *305*, 333–342.

62. Winkelbauer, M.E., Schafer, J.C., Haycraft, C.J., Swoboda, P., and Yoder, B.K. (2005). The C. elegans homologs of nephrocystin-1 and nephrocystin-4 are cilia transition zone proteins involved in chemosensory perception. J. Cell Sci. *118*, 5575–5587.

63. Hopp, K., Heyer, C.M., Hommerding, C.J., Henke, S.A., Sundsbak, J.L., Patel, S., Patel, P., Consugar, M.B., Czarnecki, P.G., Gliem, T.J., et al. (2011). *B9D1* is revealed as a novel Meckel syndrome (MKS) gene by targeted exon-enriched next-generation sequencing and deletion analysis. Hum. Mol. Genet. *20*, 2524–2534.

64. Dowdle, W.E., Robinson, J.F., Kneist, A., Sirerol-Piquer, M.S., Frints, S.G., Corbit, K.C., Zaghloul, N.A., van Lijnschoten, G., Mulders, L., Verver, D.E., et al. (2011). Disruption of a ciliary B9 protein complex causes Meckel syndrome. Am. J. Hum. Genet. *89*, 94–110.

65. Inglis, P.N., Ou, G., Leroux, M.R., and Scholey, J.M. (2007). The sensory cilia of Caenorhabditis. In WormBook, The C. elegans Research Community, ed. 10.1895/wormbook.1.126.2, http://www.wormbook.org.

66. Katsanis, N., Beales, P.L., Woods, M.O., Lewis, R.A., Green, J.S., Parfrey, P.S., Ansley, S.J., Davidson, W.S., and Lupski, J.R. (2000). Mutations in *MKKS* cause obesity, retinal dystrophy and renal malformations associated with Bardet-Biedl syndrome. Nat. Genet. *26*, 67–70.

67. Wolf, M.T., and Hildebrandt, F. (2011). Nephronophthisis. Pediatr. Nephrol. *26*, 181–194.

68. Nachury, M.V., Loktev, A.V., Zhang, Q., Westlake, C.J., Peränen, J., Merdes, A., Slusarski, D.C., Scheller, R.H., Bazan, J.F., Sheffield, V.C., and Jackson, P.K. (2007). A core complex of BBS proteins cooperates with the GTPase Rab8 to promote ciliary membrane biogenesis. Cell *129*, 1201–1213.

69. Jin, H., White, S.R., Shida, T., Schulz, S., Aguiar, M., Gygi, S.P., Bazan, J.F., and Nachury, M.V. (2010). The conserved Bardet-Biedl syndrome proteins assemble a coat that traffics membrane proteins to cilia. Cell *141*, 1208–1219.

ARTICLE

Loss of CHSY1, a Secreted FRINGE Enzyme, Causes Syndromic Brachydactyly in Humans via Increased NOTCH Signaling

Jing Tian,[1] Ling Ling,[1] Mohammad Shboul,[1] Hane Lee,[2] Brian O'Connor,[2] Barry Merriman,[2] Stanley F. Nelson,[2] Simon Cool,[1] Osama H. Ababneh,[3] Azmy Al-Hadidy,[3] Amira Masri,[3] Hanan Hamamy,[4] and Bruno Reversade[1,5,*]

We delineated a syndromic recessive preaxial brachydactyly with partial duplication of proximal phalanges to 16.8 Mb over 4 chromosomes. High-throughput sequencing of all 177 candidate genes detected a truncating frameshift mutation in the gene CHSY1 encoding a chondroitin synthase with a Fringe domain. CHSY1 was secreted from patients' fibroblasts and was required for synthesis of chondroitin sulfate moieties. Noticeably, its absence triggered massive production of JAG1 and subsequent NOTCH activation, which could only be reversed with a wild-type but not a Fringe catalytically dead CHSY1 construct. In vitro, depletion of CHSY1 by RNAi knockdown resulted in enhanced osteogenesis in fetal osteoblasts and remarkable upregulation of JAG2 in glioblastoma cells. In vivo, chsy1 knockdown in zebrafish embryos partially phenocopied the human disorder; it increased NOTCH output and impaired skeletal, pectoral-fin, and retinal development. We conclude that CHSY1 is a secreted FRINGE enzyme required for adjustment of NOTCH signaling throughout human and fish embryogenesis and particularly during limb patterning.

Introduction

Precise diagnosis of brachydactylies, defined by the shortening of fingers and/or toes, is often difficult because of their vast diversity and partial clinical overlap. Five main types of brachydactylies, termed brachydactyly (BD) types A– E (MIM 112500, MIM 112600, MIM 112700, MIM 112800, MIM 112900, MIM 112910, MIM 113000, MIM 113100, MIM 113200, MIM 113300, MIM 112440, and MIM 607004), are classified according to which metacarpals and/or metatarsals, phalanges, and digits are affected.[1] At the molecular level, extracellular components of two signaling pathways, BMP/GDF and Hedgehog, have been shown to cause shortening of digits in humans. Defective BMP/GDF signaling accounts for BDA2, BDB, and BDC and can be caused by mutations in the genes encoding the extracellular BMP antagonist NOGGIN (MIM 602991), the BMP ligand GDF5 (MIM 601146), BMP2 (MIM 112261), and the BMP receptors BMPR1B (MIM 603248) and ROR2 (MIM 602337).[2–6] The Hedgehog pathway accounts for BDA1, which is caused by mutations in the ligand IHH (MIM 600726), and mutations in SHH (MIM 600725) cause triphalangeal thumb–polysyndactyly syndrome (MIM 174500).[7,8] Recently, mutations in the extracellular ligand PTHLH (MIM 168470) were found to be responsible for BDE, which can also be caused by HOXD13 (MIM 142989) mutations.[9,10]

Here we report on the genetic etiology of a syndromic recessive preaxial brachydactyly caused by a loss-of-function mutation in the evolutionarily conserved gene CHSY1 (MIM 608183). CHSY1 encodes a type II transmembrane protein comprising a Fringe motif and a glycosyl-transferase domain. CHSY1 was found to be secreted, and functional experiments carried out in patients' cells, human fetal osteoblasts cells, and gliobastoma cells revealed remarkable NOTCH upregulation in the absence of CHSY1 activity. Knockdown of chsy1 in developing zebrafish embryos was able to partially phenocopy the human disorder: it enhanced Notch signaling and impaired skeletal and pectoral-fin development while triggering dramatic retinal overgrowth. Taken together, our results identify an additional layer of control in the genetic pathway that operates in the vertebrate developing limb. Our data also suggest that CHSY1, because of its FRINGE activity, might represent another class of extracellular modulators of NOTCH signaling.

Material and Methods

Patients and Clinical Assessment

The affected children were initially diagnosed at the National Center for Diabetes, Endocrinology & Genetics in Jordan by Prof. Hanan Hamamy. Genomic DNA from saliva samples (Oragene, Canada) from the five members of this kindred and skin biopsies from one affected sibling (II:2) and his unaffected sister (II:1) were obtained after parents gave their informed consent and the local ethics commission gave its approval.

Genotyping and Homozygosity Mapping

To perform homozygosity and identity-by-descent (IBD) mapping, we analyzed the SNP chip data of the affected and unaffected siblings by using custom programs (B. Merriman) written in the Mathematica (Wofram Research) data-analysis software. In brief, we determined candidate IBD homozygous blocks in an individual

[1]Institute of Medical Biology, A*STAR, Singapore; [2]Department of Human Genetics, David Geffen School of Medicine, University of California, Los Angeles, Los Angeles, CA 90095, USA; [3]Departments of Ophthalmology, Radiology and Pediatrics, Faculty of Medicine, University of Jordan, Jordan; [4]Department of Genetic Medicine and Development, Geneva University Hospital, Geneva, Switzerland; [5]Department of Pediatrics, National University of Singapore, Singapore
*Correspondence: bruno@reversade.com

as follows: using the Illumina 610k SNP Chip (Human610-Quadv1_B) genotype data, we used AB genotypes to define boundaries of homozygous blocks. Blocks that were larger than 2 cM in size were classified as candidate IBD homozygous blocks. Centi-Morgan distances between SNPs were determined from the HapMap Phase II recombination rate map. Regions of identity (both alleles inherited IBD) between pairs of siblings were determined in a similar pedigree-free fashion. The final exclusion mapping that allowed us to obtain candidate disease loci was performed by mathematical manipulation of the various intervals defined by homozygosity and identity mapping. Specifically, we defined candidate disease loci as those that were homozygous identical by descent in affected siblings, identical by descent between affected siblings, and not identical by descent for unaffected siblings. We obtained candidate disease loci by taking the mathematical intersection of the intervals of homozygosity and identity, respectively, and then the mathematical complement of these by the intervals of identity between affected-unaffected sibling pairs.

Capture of Genomic Loci

In brief, custom arrays (Agilent 244K) were designed to target every exonic sequence of the genes present in the four homozygous indentical-by-descent regions (chr3: 147266776–155630168; chr5: 168552990–174355393; chr12: 18663–545927; and chr15: 99141618–100314150), excluding the highly repeated regions. In total, 1009 contigs encompassing 320,677 bp were targeted. DNA library for one affected subject was prepared according to the Illumina library generation protocol version 2.3 and was hybridized to the custom arrays according to the Agilent CGH 244K array protocol, then washed, eluted, and amplified. The sample was submitted to one channel of Illumina flowcell and sequenced by Illumina Genome Analyzer (GAII) according to the standard manufacturer's protocol. The image data were processed by the provided GA Pipeline (Firecrest version 1.3.4 and Bustard version 1.3.4), and all sequences were aligned to the human reference genome (UCSC build 18) by Blat-like Fast Accurate Search Tool (BFAST). We filtered mismatches to identify variants that were seen ten or more times and that did not overlap with a known dbSNP129 entry polymorphism. Non-synonymous mutations were identified with additional SeqWare tools and the "knownGene" gene model from the UCSC hg18. The open-source SeqWare project that provides a LIMS tool for tracking samples (SeqWare LIMS) and a pipeline for sequence analysis (SeqWare Pipeline) was used throughout this work.

Mutation Analysis

Positional candidate genes were obtained from the GenBank and Ensembl databases. Genes were analyzed by direct sequencing of DNA with primers flanking each exon. Primer sequences were based on the reference sequences of each gene. The primer sequences for CHSY1 (NM_014918.4) and HTLF (NM_002158.3) mutation screening are given in Table S4. Sequence analysis was done with the BigDye Terminator cycle sequencing kit (Applied Biosystems, Foster City, CA), and products were run on a 3730 DNA Analyzer (Applied Biosystems, Foster City, CA).

Cell Culture

Primary human skin fibroblasts were cultivated in DMEM (Lonza) supplemented with 10% fetal calf serum (FCS) (Lonza). Human fetal osteoblast (hFOB) cells were obtained from ATCC (USA) and maintained in Ham's F12 DMEM supplemented with 10%

FCS and 0.3 mg/ml G418 (Invitrogen, USA) at 33.5°C. Human gliobastoma (T98G) cells were obtained from ATCC (USA) and maintained in EMEM (ATCC) supplemented with 10% FCS. Inhibition of γ-secretase activity was carried out by incubation of cells with 2 or 5 μM of γ–secretase inhibitor X (Calbiochem, 565771) added fresh daily for 72 hr.

RNA Interference

hFOB and gliobastoma cells were seeded at 20,000 cells/cm^2 in 6-well plates and transfected via Lipofectamine 2000 (Invitrogen, USA) with two siRNAs specific for human CHSY1 (25 pmol of each) or scrambled siRNA as a negative control. The siRNAs were purchased from QIAGEN (Germany), and their sequence is given in Table S4. For Taqman realtime PCR, cells were assayed 48 or 72 hr after transfection.

Quantitative PCR

RNA was isolated from patients' fibroblasts, T98G cells, and hFOB cells by the Trizol (Invitrogen) method. RNA (1 μg) was reverse transcribed with the Revert Aid kit (Fermentas) and random hexamers. Quantitative PCR was performed with Taqman probes (Applied Biosystems). Primers, ABI probes, assay IDs, and sequences are given in Table S4.

Statistical Analysis

Each experiment was repeated at least three times, and data were expressed as means ± SE. Differences among treatments were analyzed by a Student's t test. Significant differences were considered to be those with a p value of < 0.05.

Immunoblot Analysis

Supernatant fractions were obtained after incubation of primary skin fibroblasts in Pro293a-CDM conditioning serum-free media (BioWhittaker) for 72 hr. Cells were lysed in RIPA extraction buffer. Electrophoresis of samples in SDS polyacrylamide gels with or without DTT was followed by transfer on PVDF membranes. The following antibodies were used for probing immunoblots: mouse anti-ACTIN (Chemicon; Mab1501R), rat anti-NOTCH2 (Developmental Studies Hybridoma Bank; C651.6DbHN), goat anti-JAG1 (Santa Cruz Biotechnology; sc-6011), goat anti-HES1 (R&DSystems; AF3317), and rabbit anti-CHSY1 (Proteintech; 14420-1-AP).

Immunohistochemistry Analysis

For immunostaining, skin biopsies were fixed in 4% (weight/volume) paraformaldehyde in 1× PBS and embedded in wax, and sections of 5 μm were placed on coverslips. A mouse monoclonal antibody against Chondroitin Sulfate (Sigma; CS-56) was incubated for 1 hr in 10% normal goat serum at room temperature at a 1: 200 dilution. For visualization, an anti-mouse IgG-HRP (Dako) conjugate was applied. Images were collected with a stereomicroscope M205 FA equipped with an ICD camera from Leica.

Morpholino Oligos, RNA Injections, and Embryological Methods

Two 25 bp Morpholino (MO) antisense oligomers, CS1 and CS2, for zebrafish chsy1 were obtained from Gene Tools; their sequences are given in Table S4. MOs were resuspended in sterile water to a concentration of 3 mM according to the manufacturer's instructions. Embryos were injected at the 1 cell stage with 1 nl consisting

of 0.2 nM CS1 and 1 nM CS2. Protocols for injections, whole-mount in situ hybridization, and alcian blue staining can be found at our laboratory's website. A ZeissAxioplan microscope equipped with a Zeiss AxioCam HRc was used for capturing images of embryos. Pictures were assembled with Photoshop CS5.

Results

A Frameshift Mutation in *CHSY1* Is Identified by Homozygosity Mapping and High-Throughput Sequencing

Homozygosity mapping was performed on a Jordanian consanguineous family consisting of two unaffected parents (I:1 and I:2, Figure 1A), two affected children (II:2 and II:3, Figure 1A), and one unaffected sibling (II:1, Figure 1A). The clinical synopsis included congenital skeletal anomalies most evident on the hands and feet, symmetrical and bilateral preaxial brachydactyly, micrognathia, short stature, and variable degrees of learning disability (Figures 1B–1D; see also Figure S1). X-ray examinations revealed unified capitate and hamate bones and partial duplication of proximal phalanges of digits 1 to 3, suggestive of hyperphalangism (Figures 1C and 1D). The clinical features of the two index cases in this study match those described earlier by Dr. Samia Temtamy in another inbred family from Egypt.[11] On the basis of their comparison (Figure S1), we reason that this Jordanian family might represent another case of Temtamy Preaxial Brachydactyly Syndrome (MIM 605282).

Genotyping of the five individuals on 610k Illumina SNP arrays and subsequent identical-by-descent mapping revealed four candidate regions totaling 16.8 Mb on chromosomes 3, 5, 12, and 15 (Figure 1E). To screen the 177 candidate genes in these regions for mutations, we employed a targeted genomic loci capture[12] followed by high throughput resequencing (Figure 1F). In one affected proband, 224 genomic mismatches were identified; of these, two were homozygous and located in the coding region of *HTLF* (MIM 143089) and *CHSY1* (Table S1). The *HLTF* mutation did not cosegregate with the disease in the family. The nonsense mutation in *CHSY1*, caused by a 1 bp deletion (Figure 1F), was inherited according to the autosomal-recessive pattern inferred by this pedigree. Because *CHSY1* lies at the telomeric end of chromosome 15q, hemizygous deletions of *CHSY1* occur in patients with chromosome 15q26-qter Deletion Syndrome (MIM 612626);[13] these distinct genetic diseases share some common phenotypes, which are compared in Figure S1.

CHSY1 encodes chondroitin synthase 1, an evolutionarily conserved sugar-synthesizing enzyme present both in invertebrates and vertebrates (Figure 1G). Human CHSY1, and its paralogous protein CHSY3 (MIM 609963), consists of a carboxy-terminal type-A glycosyltransferase catalytic site and an N-terminal Fringe domain.[14,15] When aligned to the three canonical FRINGE proteins, i.e., LUNATIC (MIM 602576), MANIC (MIM 602577), and RADICAL (MIM 602578) FRINGE, the CHSY1 and CHSY3 proteins show conservation of the DXD motif, which is required for the glycosyltransferase activity of FRINGE enzymes (Figure 1H).[16,17]

The *CHSY1* Frameshift Mutation Abolishes CHSY1 Protein Synthesis and Depletes Chondroitin Sulfates in Patients

The biallelic one-base cytosine deletion in codon 32 of the ORF of *CHSY1* (c.96 del) introduces a frameshift leading to a premature stop codon 2 amino acids downstream at position 34 (p.Glu33SerFSX1). This nonsense mutation is predicted to yield a severely truncated CHSY1 protein missing both its catalytic domains (Figure 2A). To confirm the absence of CHSY1 in affected individuals, we isolated and cultured dermal fibroblasts from the male proband (II:2) and his noncarrier unaffected sibling (II:1). CHSY1, of the expected molecular weight, i.e, 88 kDa, was detected by immunoblotting in nonreducing conditions in the supernatant of primary fibroblasts but was undetectable in that of mutant fibroblasts (Figure 2B). In reducing conditions, CHSY1 migrated at 60 kDa, suggesting that the mature secreted protein might comprise two or more peptides linked by disulfide bridges. It is noteworthy that soluble CHSY1 was found to accumulate in the supernatant of primary human fibroblast cultures, whereas its primary amino acid sequence does not target it a priori for secretion. In support of our finding, CHSY1 was previously reported to be the most prominent extracellular protein in the conditioned medium of co-cultures involving myeloma cells and osteoclasts;[18] hence, CHSY1 might be processed for secretion in the Golgi via shedding of its N-terminal transmembrane domain (Figure 2A). This is in contrast to canonical FRINGE enzymes, which are known to reside in the *cis*-Golgi and not in the extracellular milieu unless overexpressed.[16]

CHSY1 is pivotal to the biosynthesis of chondroitin sulfates (CSs), which belong to the glycosaminoglycans (GAGs), consisting of alternating glucuronic acid (GlcUA) and N-acetyl galactosamine (GalNAc) residues. Once synthesized, CSs are covalently bound to side chains of extracellular proteoglycans. CHSY1 possesses both the glucuronyltransferase II and N-acetylgalactosaminyl-transferase II enzymatic activities necessary for the synthesis of the repeating disaccharide unit of CS.[14] To determine the impact of the loss of CHSY1 activity on the deposition and distribution of CSs, immunohistochemistry on patients' skin sections was performed with a monoclonal antibody directed at CS groups. Lower levels of CS in the stratum corneum, stratum germinativum, and dermal layers of the affected patient (II:2) relative to the control (II:1) were seen (Figures 2C and 2D). CS levels were also reduced in cultures of CHSY1-deficient primary fibroblasts (data not shown), which had a slower growth rate and different cell morphology than control fibroblasts (Figures 2C and 2D, insets). Taken together, our data suggest the CHSY1 is a secreted enzyme involved in the synthesis of
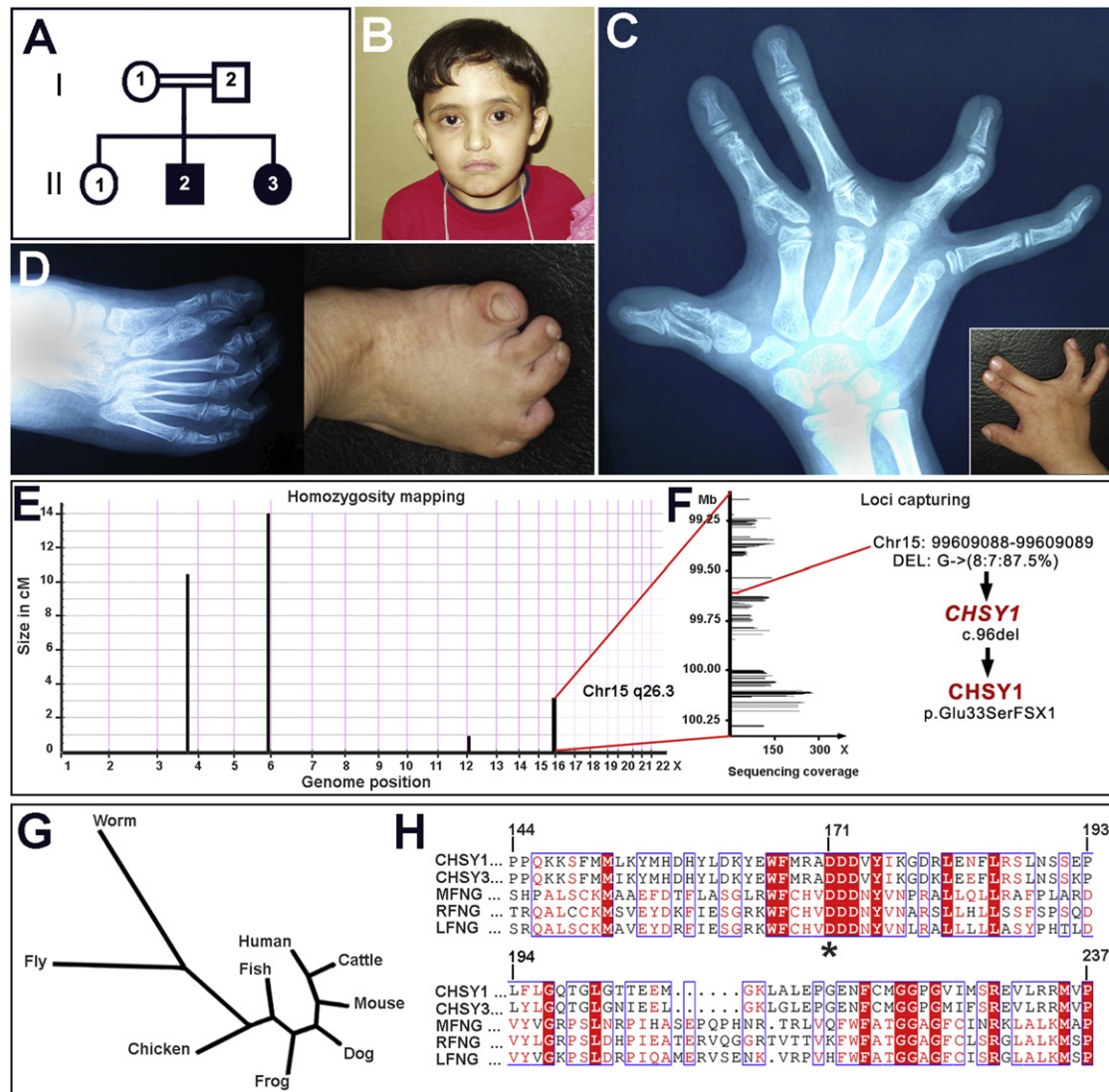
Figure 1. Phenotypic Characteristics of Investigated Patients with Syndromic Recessive Brachydactyly Caused by a Frameshift Mutation in *CHSY1*

(A) Affected children, male (II:2) and female (II:3), were born to first-cousin parents (I:1 and I:2) with one unaffected child (II:1).

(B) Head shot of affected boy (II:2) with protruding eyes, downward turn of mouth, and micrognathia.

(C) X-ray radiograph of male proband's right hand when he was 8 years of age, showing partial duplications of proximal phalanges in digits 1, 2, and 3 (inset: hand photograph).

(D) X-ray radiograph and picture of male proband's right foot showing severe skeletal anomalies. The big toe exhibits short and duplicated metatarsals and proximal phalanges. The second and fourth proximal phalanges are duplicated as well.

(E) Homozygosity mapping delineated four candidate loci totaling 19 cM on chromosomes 3, 5, 12, and 15.

(F) Genomic capturing and resequencing of candidate loci revealed a 1 bp deletion in *CHSY1* on chromosome 15; this deletion caused an early-termination stop codon at amino acid 34 of the CHSY1 enzyme.

(G) Phylogenetic tree showing conservation of CHSY1 across invertebrate and vertebrate species.

(H) The CHSY1 enzyme and its paralogous protein CHSY3 bear a Fringe domain that aligns to that of canonical MANICAL (MFNG), RADICAL (RFNG), and LUNATIC (LFNG) FRINGE. A conserved DDD motif is highlighted with a star.

CS moieties and that the reported nonsense mutation leads to a loss of function in humans.

Loss of CHSY1 Activity Triggers Massive NOTCH Activation in Patients' Cells

To gain insights into the pathogenesis of the disease, we sought to determine how secreted CHSY1 activity was coupled to known extracellular proteins causing brachydactyly in mice and humans.[1,19] Out of 16 genes whose mutations result in brachydactyly,[1,19] *CHSY1* transcripts were most correlated with those of the *NOTCH2* (MIM 600275) and *NOTCH1* (MIM 190198) receptors (Table S2). Because CHSY1 bears a Fringe domain, which modulates ligand interaction with NOTCH receptors,[20] and because NOTCH2 activation was shown to be regulated by CHSY1 levels in co-cultures of myeloma cells and osteoclasts,[18] we assessed components of the NOTCH signaling pathway in patients' primary fibroblast cell
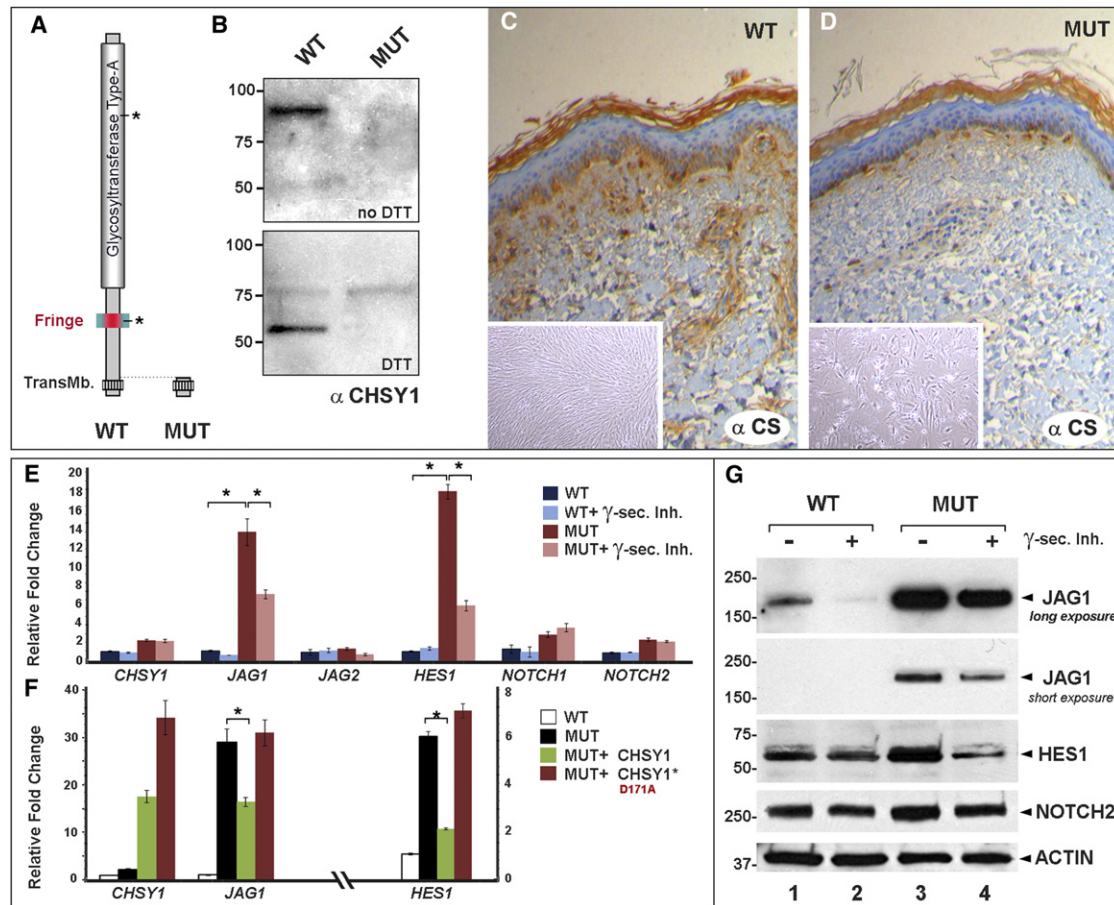
Figure 2. Loss of CHSY1 Results in Depletion of Chondroitin Sulfates and Activation of NOTCH Signaling

(A) The full-length CHSY1 (WT) consists of a type II transmembrane domain, a Fringe motif, and a type A glycosyltransferase domain. The frameshift mutation (MUT) deletes more than 95% of CHSY1, including both of its putative catalytic sites, marked with an asterisk.

(B) CHSY1 is found in the supernatant of primary fibroblast cultures from unaffected sibling II:1 (WT) but not from that of the affected proband II:2 (MUT).

(C and D) Depletion of CS, a product of the CHSY1 enzyme, is observed by immunohistochemistry in the skin of affected II:2 (D) versus unaffected sibling II:1 (C). CHSY1-deficient primary fibroblasts (D, inset) have aberrant morphologies and slower growth rates than control fibroblasts (C, inset).

(E) Massive upregulation of *JAG1* and *HES1* in affected primary fibroblasts, indicative of abnormally high NOTCH signaling, is observed by q-PCR analysis. Mutant *CHSY1* transcripts were not subjected to nonsense-mediated decay. Upregulation of NOTCH signaling was reversed by the addition of a γ-secretase inhibitor.

(F) Overexpression of intact *CHSY1*, but not of a Fringe-dead *CHSY1* D171A mutant, can reverse NOTCH activation in CHSY1-deficient fibroblasts.

(G) Abnormally high JAG1 protein production is seen in CHSY1-deficient fibroblasts (lanes 3 and 4) compared to control fibroblasts (lanes 1 and 2). Addition of a γ-secretase inhibitor rescues NOTCH activation measured by HES1 levels in CHSY1-deficient cells (compare lanes 3 and 4).

Values in (E) and (F) represent means ± SE of data from three independent experiments, *$p < 0.05$.

cultures. By quantitative PCR, relative transcript abundance of *JAG1* (MIM 601920), a NOTCH ligand, and *HES1* (MIM 139605), an immediate target of NOTCH, were found to be significantly upregulated—14-fold and 18-fold, respectively—in comparison to unaffected cells (Figure 2E). Levels of *NOTCH1* and *NOTCH2* were moderately increased. Endogenous *CHSY1* transcripts were found to be higher in *CHSY1* null cells, suggesting that the reported frameshift does not trigger the surveillance nonsense-mediated-decay pathway. Addition of a γ-secretase inhibitor, blocking NOTCH signaling at the receptor level,[21] partially rescued NOTCH over-activation in CHSY1-deficient patient cells (Figure 2E). The remarkable transcriptional upregulation of *JAG1* and *HES1* was confirmed at the protein level by immunoblotting (Figure 2G); an average 10-fold increase in JAG1 protein synthesis was seen in primary CHSY1-deficient fibroblasts at various passages (compare lanes 1 and 3, Figure 2G). Likewise, inhibiting γ-secretase activity partially rescued HES1 levels in CHSY1-deficient cells. JAG1 levels were also reduced, albeit to a lesser extent (compare lanes 3 and 4, Figure 2G).

Next, to determine whether CHSY1-mediated NOTCH inhibition required the Fringe domain, we carried out
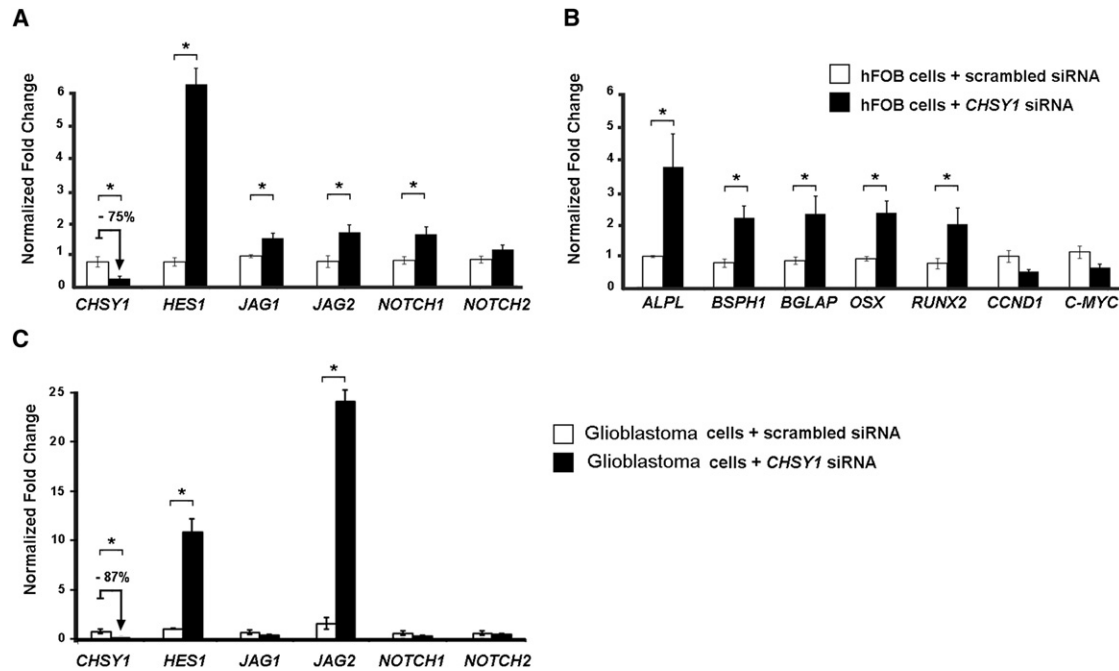
Figure 3. CHSY1 Knockdown Promotes NOTCH Signaling and Enhances Osteogenesis In Vitro
(A) CHSY1 siRNA in human fetal osteoblasts (hFOB) cells achieved 75% knockdown with concurrent 6-fold upregulation of HES1, an immediate NOTCH target. Other genes belonging to the NOTCH pathway were moderately but significantly upregulated.
(B) CHSY1 siRNA triggered upregulation of osteogenic markers, indicative of premature differentiation, whereas proliferation markers were downregulated.
(C) CHSY1 siRNA in human glioblastoma cells (T98G) achieved 87% knockdown and a paralleled 10-fold upregulation of HES1 and 24-fold increase in JAG2 transcription.
Values in (A)–(C) represent means ± SE of data from three independent experiments, *p < 0.05.

rescue experiments in patients' primary cells. NOTCH up-regulation in CHSY1-deficient cells could only be reversed by transfection of wild-type human CHSY1 but not of a D171A Fringe catalytically dead mutant construct[17] (Figure 2F), indicating that CHSY1 requires an intact Fringe domain to execute its function. Together, these results argue that secreted CHSY1, via its Fringe domain, exerts NOTCH inhibitory activity in human primary skin fibroblasts and that its absence triggers massive JAG1 protein synthesis.

CHSY1 Knockdown by siRNA in Human Osteoblast Progenitor Cells Triggers NOTCH Activation and Premature Osteogenic Differentiation

To address the ossification anomalies, we then modeled loss of CHSY1 by siRNA in a human fetal osteoblast (hFOB) progenitor cell line (Figures 3A and 3B). CHSY1 siRNA, which achieved more than 75% knockdown efficiency, resulted in markedly increased NOTCH signaling, as indicated by the 6-fold increase in the abundance of HES1 transcripts (Figure 3A); levels of JAG1, JAG2 (MIM 602570), and NOTCH1 were moderately but significantly increased. Concurrent with NOTCH upregulation, markers of osteogenic differentiation such as ALPL (MIM 171760), BSPH1 (MIM 147563), BGLAP (MIM 112260), OSX (MIM 606633), and RUNX2 (MIM 600211) were significantly augmented, whereas markers of proliferation such as

CCND1 (MIM 168461) and C-MYC (MIM 190080) were reduced (Figure 3B). Alkaline phosphatase activity was increased by 40% (data not shown). Taken together, these results suggest that CHSY1 knockdown, which leads to NOTCH activation, suffices to bring about premature, or enhanced, osteogenic differentiation in a hFOB progenitor cell line. These in vitro data provide a possible patho-mechanism for the observed accessory bones and hyper-phalangism seen in the two affected children.

To substantiate CHSY1's specificity on NOTCH signaling, we repeated RNAi knockdown in a human neural glioblastoma cell line (Figure 3C). Unexpectedly, JAG2, but not JAG1 as in primary patient fibroblasts, was greatly increased (24-fold). As in hFOB and patient primary cells, HES1 levels were also upregulated, indicative of robust NOTCH activation. Together, these in vitro experiments argue that CHSY1 bears widespread repressive activity on NOTCH signaling and that this inhibition is likely to be gene and tissue specific.

Loss of Function of chsy1 in Zebrafish Embryos Impairs Skeletogenesis and Leads to Increased Notch Signaling

To model, in vivo, the birth defects observed in CHSY1 mutant individuals, we next performed chsy1 morpholino (MO) injections in developing zebrafish embryos (Figure 4). To block translation of maternal and zygotic chsy1
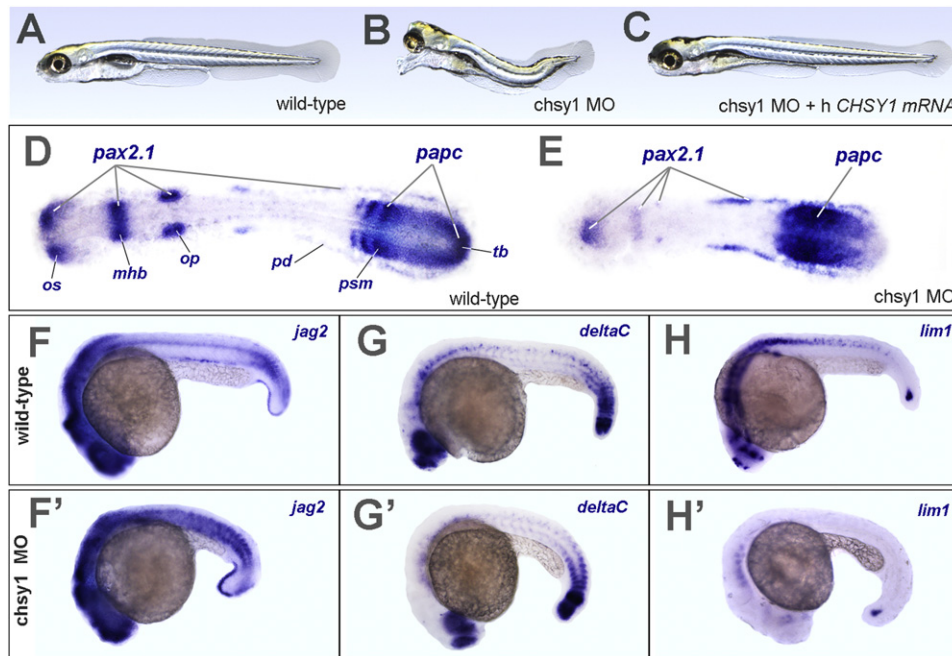
Figure 4. *chsy1* Knockdown in Zebrafish Embryos Affects Segmentation and Increases Notch Signaling

(A) Six-day-old wild-type embryo.

(B) Six-day-old *chsy1* MO-injected embryo with a protruding mouth-piece, eyes joined at the midline, and arched trunk.

(C) Six-day-old *chsy1* MO-injected embryo rescued with 200 pg of human *CHSY1* mRNA.

(D) Ten-somite-stage wild-type embryo stained with *pax2.1* marking the optic stalk (os), midbrain-hindbrain boundary (mhb), otic placodes (op), and pronephric duct (pd) and with *papc* marking the pre-somitic mesoderm (psm) and the tailbud (tb).

(E) Ten-somite stage *chsy1* morphant embryo displays a fused anterior eyefield, near-absent isthmic organizer, and otic placodes marked by *pax2.1*. Aberrant segmentation of the pre-somitic mesoderm and lack of *papc* staining in the tailbud indicate anomalies in somitogenesis.

(F and F′) Wild-type (F) and *chsy1* morphant (F′) 24 hpf embryos stained for the Notch ligand *jag2*. Note ectopic or delayed clearance of *jag2* expression in trunk somites.

(G and G′) Wild-type (G) and *chsy1* morphant (G′) 24 hpf embryos stained for the Notch ligand *deltaC*. Note the enhanced expression in presomitic mesoderm at the tailbud level.

(H and H′) Wild-type (H) and *chsy1* morphant (H′) 24 hpf embryos that were stained with *lim1* and whose expression is downregulated by Notch signaling. The loss of *lim1* expression in head and trunk structures indicates greater-than-normal Notch signaling in *chsy1* morphants relative to controls.

transcripts, we used two MOs against *chsy1*, as previously described.[22] *chsy1* was ubiquitously present from the unfertilized oocyte to the end of somitogenesis (Figure S2). By day two, its expression was limited to head structures; there was prominent expression in the inner ear and diffuse expression in developing chondrocytes of the pectoral-fin bud (Figure S2J). Compared to wild-type siblings at 6 days (Figure 4A), morphant *chsy1* embryos developed into stunted larvae with severe eye anomalies and cartilage and pectoral-fin defects (Figure 4B). The specificity of the MOs was addressed by rescue experiments; *chsy1* MOs were coinjected with human *CHSY1* mRNA at the one-cell stage. In 87% (n = 149/171) of the coinjected embryos, *chsy1* morphant phenotypes were rescued (Figure 4C; see also Table S3). At the ten-somite stage, *chsy1* morphants exhibited obvious segmentation anomalies marked by poorly segmented presomitic mesoderm and absence of *papc* expression in the tailbud (Figures 4D and 4E). Anterior defects in *chsy1* morphants comprised a single anterior eyefield, as opposed to split eyefields in control embryos, and reduced *pax2.1* expression in otic

placodes and in the midbrain-hindbrain boundary (Figures 4D and 4E). By 24 hpf, expression of the two notch ligands *jag2* and *deltaC* was increased in *chsy1* morphants as compared to wild-type embryos (Figures 4 F–4G′), *jag2* was found to be ectopically expressed in trunk paraxial mesoderm, indicative of impaired segmentation, whereas *deltaC* levels in tailbud and presomitic mesoderm were enhanced (Figures 4F–4G′). We next assessed *lim1*, a target of Notch signaling whose expression is repressed by the Notch pathway.[23] Reflecting greater-than-normal Notch activity in *chsy1* morphants, *lim1* expression was visibly dampened in head and trunk structures relative to those of control embryos (Figures 4H and 4H′). Collectively, these results indicate that *chsy1* activity is essential for toning down Notch signaling across various embryonic structures during zebrafish development.

Zebrafish *chsy1* Morphant Embryos Partially Phenocopy Human Disorder

By day 5, zebrafish *chsy1* morphant embryos exhibited major skeletal anomalies encompassing severe jaw
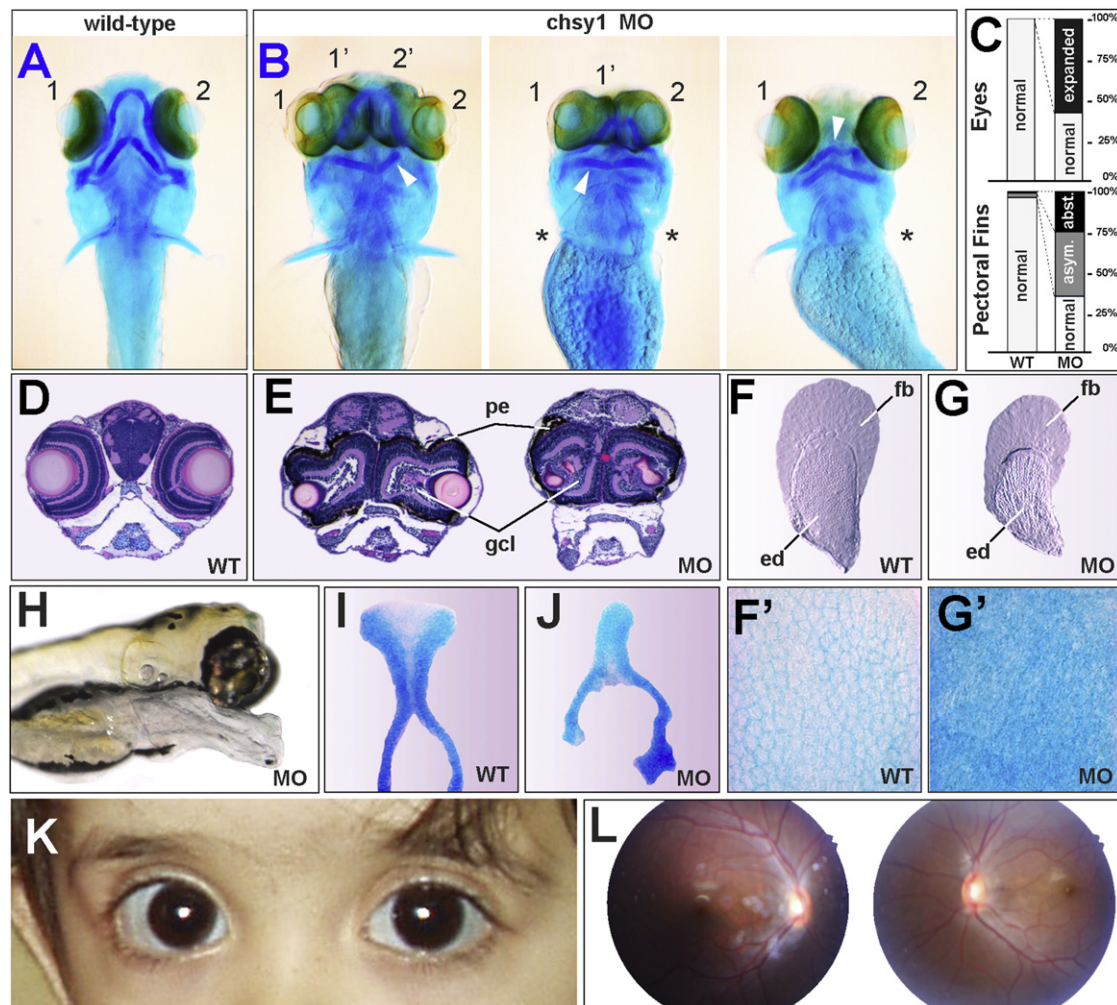
Figure 5. Phenotypes of *chsy1* Zebrafish Morphant Embryos Partially Phenocopy Human Disorder
(A) Ventral view of alcian-blue-stained 5-day-old wild-type embryo.
(B) Three representative *chsy1* MO-injected embryos exhibiting variable phenotypic penetrance, including skeletal anomalies (arrowheads), massive overgrowth of retinas, and pectoral-fin defects ranging from asymmetric development to unilateral or bilateral aplasia (asterisks).
(C) Percentage of eyes and pectoral-fin defects scored in *chsy1* MO compared to wild-type embryos. (Asym., asymmetric; Abst., absent).
(D) Hematoxylin and Eosin (H&E) head sections of 5-day-old wild-type embryo.
(E) H&E sections through midline-joining retinas of *chsy1* morphant embryos at 5 days of development. Note hyperplasia of pigmented epithelium (pe) and increased cell numbers in the ganglion cell layer (gcl).
(F and F') Pectoral fin of a 6-day-old wild-type embryo. (F') High-magnification view of the endoskeletal disc showing cartilage tissue with monolayered chondrocytes stained with alcian blue.
(G and G') Pectoral fin of a mildly affected 6-day-old *chsy1* MO-injected embryo exhibiting hypoplasia of the endoskeletal disc (ed) relative to the fin blade (fb). (G') High-magnification view of cartilage tissue with multilayered disorganized chondrocytes in the endoskeletal disc of *chsy1* morphant embryo stained with alcian blue.
(H) Lateral view of 5-day-old *chsy1* morphant embryos with severe jaw hypoplasia and eye defects.
(I) Ethmoid plate of a 5-day-old wild-type embryo stained with alcian blue.
(J) Irregularly shaped ethmoid plate of a 5-day-old *chsy1* morphant embryo.
(K) Affected girl (II:3), showing bilateral macrophthalmia and blue sclera.
(L) Color fundus photographs of affected girl (II:3) at 6 years of age. The girl had bilateral tilted eye discs and normal visual acuity in each eye.

hypoplasia, impaired pectoral-fin development, and prominent eyes (Figures 5A–5G'). The anterior paired pectoral fins, which are analogous to the mammalian forelimbs, were affected in 65% (n = 94/144) of MO-injected embryos (Figure 5C). Anomalies in the development of the pectoral fins ranged from pronounced asymmetries to unilateral or bilateral aplasia (Figures 5A and 5B). Bright-field images of dissected pectoral fins from mildly affected *chsy1*-morphant embryos revealed structural anomalies of the endoskeletal disc, a structure analogous to the bones found in higher pentadactyl vertebrates. In contrast, fin blades, of which no equivalent tissue exists in mammals, were relatively normal in morphants (Figures 5F and 5G). Higher magnification of alcian-blue-stained chondrocytes

in the *chsy1*-morphant limb buds revealed a disorganized, multilayered tissue (Figure 5G′) as opposed to the mono-layer tissue organization in wild-type limb buds (Figure 5F′). Other remarkable cartilage defects, including disgenesis of the ethmoid plate (Figures 5I and 5J), in the neurocranium resulted in a protruding-snout, "seahorse" phenotype (Figure 5H).

Unexpectedly, eye anomalies were also present in more than 50% (n = 84/144) of morphant embryos (Figures 5A–5E). In extreme cases, *chsy1* morphants developed four eyes resembling complete bilateral retinal duplications (Figure 5B). Histological examination showed instead one pair of overgrown retinas, which joined at the midline. No lens duplication was recorded. *chsy1* morphant eyes presented with the expected retinal cell layers but had augmented cell numbers in the ganglion cell layer and the pigmented epithelium (Figures 5D and 5E). This prominent eye phenotype found in *chsy1* morphant fish prompted us to re-examine our two human index cases for possible ocular anomalies. Fundoscopic evaluations did not reveal altered retinal thickness, but we noted that both probands exhibited macrophthalmia accompanied by bilateral blue sclera, remnants of pupillary membrane over the crystalline lens, and tilted optic discs in both eyes (Figures 5K and 5L). This suggests that *CHSY1* may play a role in eye morphogenesis in humans as well. Thus, knockdown of *chsy1* in zebra-fish embryos revealed a conserved role for CHSY1 during embryogenesis in vertebrates. The phenotypes observed upon knockdown of *chsy1* in fish partially phenocopy the human disorder, revealing a conserved role for CHSY1 in skeletal development and limb morphogenesis during vertebrate embryogenesis.

Discussion

In summary, loss of CHSY1 is a cause of recessive syndromic brachydactyly and evokes phenotypes that overlap with mutations in the BMP, GDF, and Hedgehog pathways.[1] The pathophysiological basis of this syndrome appears to be enhanced, or premature, ossification—possibly driven by greater-than-normal NOTCH signaling—leading to congenital skeletal anomalies most obvious in digits. This is consistent with studies performed in mice, where appropriate Notch signaling was found to be essential for the normal progression of chondrocyte differentiation into bone in the developing appendicular and axial skeletal elements.[24] The particular splitting of proximal phalanges in digits 1, 2, and 3 in this syndrome might be explained by double epiphyses growing along the longitudinal, rather than horizontal, axis. An analogous situation has been reported in Brachydactyly type A2, caused by mutations in *GDF5*, where a single epiphysis, albeit turned, results in a triangular bone.[3]

At the molecular level, we propose that CHSY1 inhibits the NOTCH pathway in the extracellular space via its Fringe domain. The aberrant production of JAG1 protein in human CHSY1-deficient fibroblasts raises the possibility that ectopic NOTCH signaling mediated by JAG1 during embryogenesis could in part be responsible for the birth defects specific to this syndrome. Control of CHSY1 activity in a tissue-specific manner may therefore constitute a therapeutic target for patients with Alagille syndrome (MIM 118450) caused by JAG1 haploinsufficiency.[25,26]

We speculate that CHSY1, which needs an intact Fringe domain to exert its NOTCH inhibitory activity, might post-translationally modify NOTCH-related proteins. However, substantiating that NOTCH receptors, or their ligands, are actual substrates of CHSY1 will require biochemical evidence. If so, CSs, of which two paralogs exist in the human genome, might function as a new class of FRINGE enzymes controlling NOTCH output during developmental, physiological, or pathological processes. Concurrently and alternatively, CHSY1 loss, which leads to reduced CS moieties and therefore altered proteoglycan synthesis, might affect other signaling pathways associated with brachydactylies. When one considers that sulfated glycans can modulate FGF/FGFR interactions, that CS affect IHH signaling,[27,28] and that both FGF and IHH can in turn regulate BMP/GDF,[29] it is conceivable that reduced CS might impede digit development by altering these pathways, instead of or in addition to NOTCH signaling.

The in vivo knock-down experiments carried out in zebrafish embryos confirmed *chsy1*'s role during skeletogenesis and unmasked its importance during eye development. Emulating the results obtained in cell culture, Notch over-activation, marked by *jag2* upregulation and silencing of *lim1*, in *chsy1* morphant embryos argues that *chsy1* is also necessary for driving repression of Notch signaling during development. It is noteworthy that *chsy1* morphant embryos bear striking resemblance to the maternal zebra-fish mutant *pug* described by the group of Mary Mullins.[30] *Pug* mutants lack pectoral fins, have eyes joined at the midline, and present with segmentation anomalies similar to what is described here. It is therefore tempting to speculate that *pug* might be a *chsy1* maternal mutant. Although *chsy1* and *pug* might not be allelic, these two genes might instead delineate a common pathway controlling limb patterning in addition to the oocyte-to-embryo transition. In support of CHSY1's putative role in the earliest stages of development, RNA-interference-mediated depletion of *ChSy* (paralogous to human *CHSY1*) in *C. elegans* triggers cytokenesis reversal, and blocks cell divisions at the 2- to 4-cell stage.[31] Should CHSY1's role during oogenesis be conserved in humans, we are aware that the reported loss-of-function mutation in this study would only unmask the zygotic function of *CHSY1*. In contrast, a biallelic maternal mutation might lead to early embryonic lethality, and signs of sterility in homozygous *CHSY1* mutant women should hereafter be anticipated.

Supporting Data
In the same issue, Li et al. report on the characterization of five loss-of-function alleles of *CHSY1* as being responsible

for Temtamy Preaxial Brachydactyly Syndrome. With the exception of hearing loss, clinical manifestations in their affected cases match those described in the two proband herein. Their work indicates that transcriptional regulation of *chsy1* expression in zebrafish is regulated by the BMP pathway, which is a prominent cause of brachydactylies in humans. Taken together, our findings outline a possible means, through CHSY1 regulation, by which BMP signals are coupled to NOTCH signaling, a scenario often reiterated during the course of discreet developmental programs.

Supplemental Data

Supplemental Data include two figures and four tables and can be found with this article at http://www.cell.com/AJHG/.

Acknowledgments

Web Resources

The URLs for data presented herein are as follows:

Blat-like Fast Accurate Search Tool (BFAST)[32], http://sourceforge.net/apps/mediawiki/bfast/index.php?title=Main_Page
Ensembl, http://www.ensembl.org
HapMap Phase II recombination rate map, http://www.hapmap.org/downloads/recombination/latest/
Human reference genome (UCSC build 18), http://genome.ucsc.edu
GenBank, http://www.ncbi.nlm.nih.gov/mapview
Gene-gene correlation tool[33], http://genome.ucla.edu/~jdong/GeneCorr.html
Online Mendelian Inheritance in Man (OMIM), http://www.ncbi.nlm.nih.gov/omim
Pipeline for sequence analysis (SeqWare Pipeline), http://seqware.sourceforge.net
Reversade laboratory's website, http://www.reversade.com

References

1. Temtamy, S.A., and Aglan, M.S. (2008). Brachydactyly. Orphanet J. Rare Dis. *3*, 15.
2. Lehmann, K., Seemann, P., Silan, F., Goecke, T.O., Irgang, S., Kjaer, K.W., Kjaergaard, S., Mahoney, M.J., Morlot, S., Reissner, C., et al. (2007). A new subtype of brachydactyly type B caused by point mutations in the bone morphogenetic protein antagonist NOGGIN. Am. J. Hum. Genet. *81*, 388–396.
3. Seemann, P., Schwappacher, R., Kjaer, K.W., Krakow, D., Lehmann, K., Dawson, K., Stricker, S., Pohl, J., Plöger, F., Staub, E., et al. (2005). Activating and deactivating mutations in the receptor interaction site of GDF5 cause symphalangism or brachydactyly type A2. J. Clin. Invest. *115*, 2373–2381.
4. Dathe, K., Kjaer, K.W., Brehm, A., Meinecke, P., Nürnberg, P., Neto, J.C., Brunoni, D., Tommerup, N., Ott, C.E., Klopocki, E., et al. (2009). Duplications involving a conserved regulatory element downstream of BMP2 are associated with brachydactyly type A2. Am. J. Hum. Genet. *84*, 483–492.
5. Lehmann, K., Seemann, P., Stricker, S., Sammar, M., Meyer, B., Süring, K., Majewski, F., Tinschert, S., Grzeschik, K.H., Müller, D., et al. (2003). Mutations in bone morphogenetic protein receptor 1B cause brachydactyly type A2. Proc. Natl. Acad. Sci. USA *100*, 12277–12282.
6. Schwabe, G.C., Tinschert, S., Buschow, C., Meinecke, P., Wolff, G., Gillessen-Kaesbach, G., Oldridge, M., Wilkie, A.O., Kömec, R., and Mundlos, S. (2000). Distinct mutations in the receptor tyrosine kinase gene ROR2 cause brachydactyly type B. Am. J. Hum. Genet. *67*, 822–831.
7. Gao, B., Guo, J., She, C., Shu, A., Yang, M., Tan, Z., Yang, X., Guo, S., Feng, G., and He, L. (2001). Mutations in IHH, encoding Indian hedgehog, cause brachydactyly type A-1. Nat. Genet. *28*, 386–388.
8. Sun, M., Ma, F., Zeng, X., Liu, Q., Zhao, X.L., Wu, F.X., Wu, G.P., Zhang, Z.F., Gu, B., Zhao, Y.F., et al. (2008). Triphalangeal thumb-polysyndactyly syndrome and syndactyly type IV are caused by genomic duplications involving the long range, limb-specific SHH enhancer. J. Med. Genet. *45*, 589–595.
9. Klopocki, E., Hennig, B.P., Dathe, K., Koll, R., de Ravel, T., Baten, E., Blom, E., Gillerot, Y., Weigel, J.F., Krüger, G., et al. (2010). Deletion and point mutations of PTHLH cause brachydactyly type E. Am. J. Hum. Genet. *86*, 434–439.
10. Johnson, D., Kan, S.H., Oldridge, M., Trembath, R.C., Roche, P., Esnouf, R.M., Giele, H., and Wilkie, A.O. (2003). Missense mutations in the homeodomain of HOXD13 are associated with brachydactyly types D and E. Am. J. Hum. Genet. *72*, 984–997.
11. Temtamy, S.A., Meguid, N.A., Ismail, S.I., and Ramzy, M.I. (1998). A new multiple congenital anomaly, mental retardation syndrome with preaxial brachydactyly, hyperphalangism, deafness and orodental anomalies. Clin. Dysmorphol. *7*, 249–255.
12. Lee, H., O'Connor, B.D., Merriman, B., Funari, V.A., Homer, N., Chen, Z., Cohn, D.H., and Nelson, S.F. (2009). Improving the efficiency of genomic loci capture using oligonucleotide arrays for high throughput resequencing. BMC Genomics *10*, 646.
13. Rump, P., Dijkhuizen, T., Sikkema-Raddatz, B., Lemmink, H.H., Vos, Y.J., Verheij, J.B., and van Ravenswaaij, C.M. (2008). Drayer's syndrome of mental retardation, microcephaly, short stature and absent phalanges is caused by a recurrent deletion of chromosome 15(q26.2—>qter). Clin. Genet. *74*, 455–462.
14. Kitagawa, H., Uyama, T., and Sugahara, K. (2001). Molecular cloning and expression of a human chondroitin synthase. J. Biol. Chem. *276*, 38721–38726.
15. Yada, T., Sato, T., Kaseyama, H., Gotoh, M., Iwasaki, H., Kikuchi, N., Kwon, Y.D., Togayachi, A., Kudo, T., Watanabe, H., et al. (2003). Chondroitin sulfate synthase-3. Molecular cloning and characterization. J. Biol. Chem. *278*, 39711–39725.

16. Johnston, S.H., Rauskolb, C., Wilson, R., Prabhakaran, B., Irvine, K.D., and Vogt, T.F. (1997). A family of mammalian Fringe genes implicated in boundary determination and the Notch pathway. Development *124*, 2245–2254.

17. Munro, S., and Freeman, M. (2000). The notch signalling regulator fringe acts in the Golgi apparatus and requires the glycosyltransferase signature motif DXD. Curr. Biol. *10*, 813–820.

18. Yin, L. (2005). Chondroitin synthase 1 is a key molecule in myeloma cell-osteoclast interactions. J. Biol. Chem. *280*, 15666–15672.

19. Pan, Y., Liu, Z., Shen, J., and Kopan, R. (2005). Notch1 and 2 cooperate in limb ectoderm to receive an early Jagged2 signal regulating interdigital apoptosis. Dev. Biol. *286*, 472–482.

20. Hicks, C., Johnston, S.H., diSibio, G., Collazo, A., Vogt, T.F., and Weinmaster, G. (2000). Fringe differentially modulates Jagged1 and Delta1 signalling through Notch1 and Notch2. Nat. Cell Biol. *2*, 515–520.

21. Milano, J., McKay, J., Dagenais, C., Foster-Brown, L., Pognan, F., Gadient, R., Jacobs, R.T., Zacco, A., Greenberg, B., and Ciaccio, P.J. (2004). Modulation of notch processing by gamma-secretase inhibitors causes intestinal goblet cell metaplasia and induction of genes known to specify gut secretory lineage differentiation. Toxicol. Sci. *82*, 341–358.

22. Zhang, J., Lefebvre, J.L., Zhao, S., and Granato, M. (2004). Zebrafish unplugged reveals a role for muscle-specific kinase homologs in axonal pathway choice. Nat. Neurosci. *7*, 1303–1309.

23. Appel, B., Givan, L.A., and Eisen, J.S. (2001). Delta-Notch signaling and lateral inhibition in zebrafish spinal cord development. BMC Dev. Biol. *1*, 13.

24. Mead, T.J., and Yutzey, K.E. (2009). Notch pathway regulation of chondrocyte differentiation and proliferation during appendicular and axial skeleton development. Proc. Natl. Acad. Sci. USA *106*, 14420–14425.

25. Li, L., Krantz, I.D., Deng, Y., Genin, A., Banta, A.B., Collins, C.C., Qi, M., Trask, B.J., Kuo, W.L., Cochran, J., et al. (1997). Alagille syndrome is caused by mutations in human Jagged1, which encodes a ligand for Notch1. Nat. Genet. *16*, 243–251.

26. Boyer-Di Ponio, J., Wright-Crosnier, C., Groyer-Picard, M.T., Driancourt, C., Beau, I., Hadchouel, M., and Meunier-Rotival, M. (2007). Biological function of mutant forms of JAGGED1 proteins in Alagille syndrome: inhibitory effect on Notch signaling. Hum. Mol. Genet. *16*, 2683–2692.

27. Cortes, M., Baria, A.T., and Schwartz, N.B. (2009). Sulfation of chondroitin sulfate proteoglycans is necessary for proper Indian hedgehog signaling in the developing growth plate. Development *136*, 1697–1706.

28. Häcker, U., Nybakken, K., and Perrimon, N. (2005). Heparan sulphate proteoglycans: The sweet side of development. Nat. Rev. Mol. Cell Biol. *6*, 530–541.

29. Minina, E., Kreschel, C., Naski, M.C., Ornitz, D.M., and Vortkamp, A. (2002). Interaction of FGF, Ihh/Pthlh, and BMP signaling integrates chondrocyte proliferation and hypertrophic differentiation. Dev. Cell *3*, 439–449.

30. Wagner, D.S., Dosch, R., Mintzer, K.A., Wiemelt, A.P., and Mullins, M.C. (2004). Maternal control of development at the midblastula transition and beyond: Mutants from the zebrafish II. Dev. Cell *6*, 781–790.

31. Mizuguchi, S., Uyama, T., Kitagawa, H., Nomura, K.H., Dejima, K., Gengyo-Ando, K., Mitani, S., Sugahara, K., and Nomura, K. (2003). Chondroitin proteoglycans are involved in cell division of Caenorhabditis elegans. Nature *423*, 443–448.

32. Homer, N., Merriman, B., and Nelson, S.F. (2009). BFAST: An Alignment Tool for Large Scale Genome Resequencing. PLoS ONE *4*, e7767.

33. Day, A., Dong, J., Funari, V.A., Harry, B., Strom, S.P., et al. (2009). Disease gene characterization through large-scale co-expression analysis. PLoS ONE *4*, e8491.

Supplemental Data

Loss of CHSY1, a Secreted FRINGE Enzyme, Causes Syndromic Brachydactyly in Humans via Increased NOTCH Signaling

Jing Tian, Ling Ling, Mohammad Shboul, Hane Lee, Brian O'Connor, Barry Merriman, Stanley F. Nelson, Simon Cool, Osama H. Ababneh, Azmy Al-Hadidy, Amira Masri, Hanan Hamamy, and Bruno Reversade

Figure S1. Phenotypic characteristics of investigated patients

(A) Hands and feet photographs of affected brother (II:4) and sister (II:5) showing marked brachydactyly and abnormally positioned fingers. Right hand showing brachydactyly in digits 1-4, with a wide space between digits 3 and 4, and clinodactyly of digits 4 and 5. Left hand showing brachydactyly in digits 1-4, with camptodactyly of digit 5. Both feet showing brachydactyly with medial deviation of digits 2-5 on the right and digits 4 and 5 on the left, and with plantar deviation of digits 4 and 5 bilaterally.

(B) Hands and feet radiographs of affected brother (II:4) and sister (II:5) showing bilateral involvement. Carpal bones show fusion of capitate and hamate with short first and third metacarpals. First and second proximal phalanges are duplicated bilaterally. Short proximal and middle phalanges in digits 2-4 with fusion. Digits 5 revealed clinodactyly due to deformed middle phalanges. Feet radiographs show unified calcaneum, cuboid, lateral and middle cuneiform bones. The great toes reveal short and duplicated metatarsals and proximal phalanges. The second and fourth proximal phalanges are duplicated and there is evident clinodactyly at right 2nd, 3rd, 4th and 5th toes and left 3rd, 4th and 5th toes.

(C) Clinical synopsis of investigated patients compared with Temtamy Preaxial Brachydactyly Syndrome and Chr.15q26.1-qter Deletion Syndrome.

C	Current family	Temtamy Preaxial Brachydactyly Syndrome (MIM 605282)	Chr.15q26.1-qter Deletion Syndrome (MIM 612626)
Consanguinity	+	+	-
Number of affected siblings and origin	**2** Jordan	**2** Egypt	**-**
Delayed milestones	+/-	+	+
Short stature	+	+	+
Microcephaly	+/-	+	+
Mild facial dysmorphism	+	+	+
Learning disability	+/-	+	+
Hearing impairment	-	+	-
Renal anomaly	+/-	-	+/-
External male genitalia	-	+	+
Blepharophimosis	-	-	+
Primary optic atrophy	-	+	-
Tilted optic disc	+/-	-	-
Talon cusps	-	+	-
Brachydactyly	+	+	+
Congenital cardiac anomalies	-	-	+
Partial camptodactyly	+	+	
Duplicated phalanges/metatarsals	+	+	-
Absent phalanges	-	-	+
Symphalangism	+	+	-
Capitate hamate fusion	+	+	-
11 ribs	+	n.d.	-
kyphoscoliosis and pectus excavatum	-	+	-
Coaxa valga	+	-	-
Genu recurvatum	+/-	-	-

n.d., not determined; +/-, variable; +, affirmative; -, negative.

Figure S2. Developmental expression pattern of *chsy1* during zebrafish embryogenesis

(A) H&E section of growing oocytes.

(B) *chsy1* transcripts are abundant in growing oocytes. Scale bar: 100 μm.

(C) Maternally-supplied *chsy1* transcripts are localized to the animal pole in the zygote.

(D) At the 8-cell stage, *chsy1* mRNA is present in all cells.

(E) By the dome stage, *chsy1* transcripts are ubiquitous.

(F) After the mid-blastula transition, in the gastrulating embryo at 50% epiboly, zygotic expression of *chsy1* is ubiquitous.

(G) At the onset of neurulation (90% epiboly), *chsy1* transcripts are present in all cells.

(H) Unrestricted transcription of *chsy1* is observed in all tissues by the 8-10-somite stage.

(I) Expression of *chsy1* is seen in the tailbud and head structures of one-day old embryos while no expression is visible in the trunk.

(J) Persistent and restricted expression of *chsy1* in the head structures of 3-day old embryos.

Top inset: Prominent *chsy1* staining is seen in the epithelial protrusions of the inner ears at 72 hpf. Bottom inset: 72 hpf pectoral fin bud showing *chsy1* expression in growing chondrocytes of the endoskeletal disc, but not in developing fin blades.

4

A H&E

oocytes

B

oocytes

C 1-cell

D 8-cell

E dome

F 50%-epiboly

G 90%-epiboly

H 8-10-somite

I 24hpf

J 72hpf
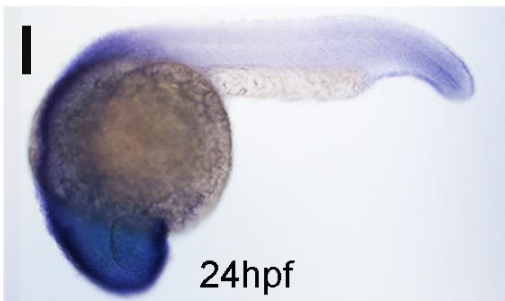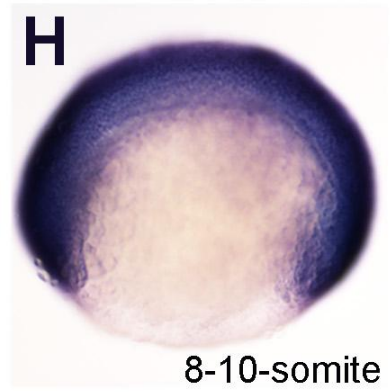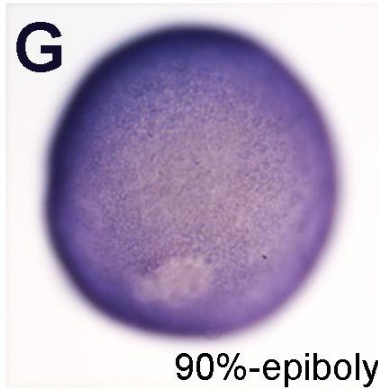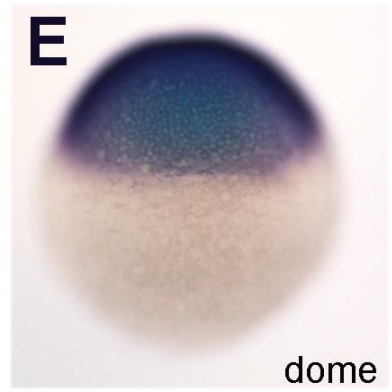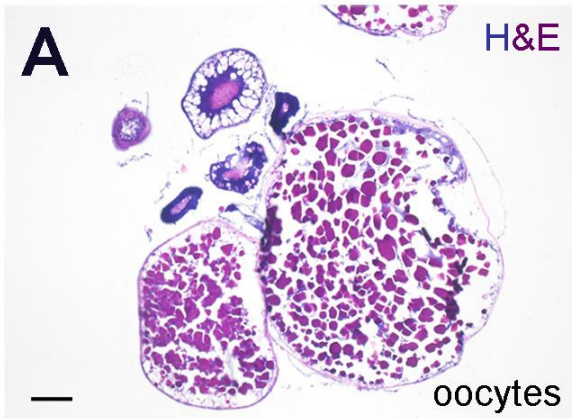
Table S1. List of mismatches and mutations following loci-capturing and re-sequencing of the 4 genomic candidate regions identified by homozygosity mapping

Please refer to accompanying Excel document Table S1.
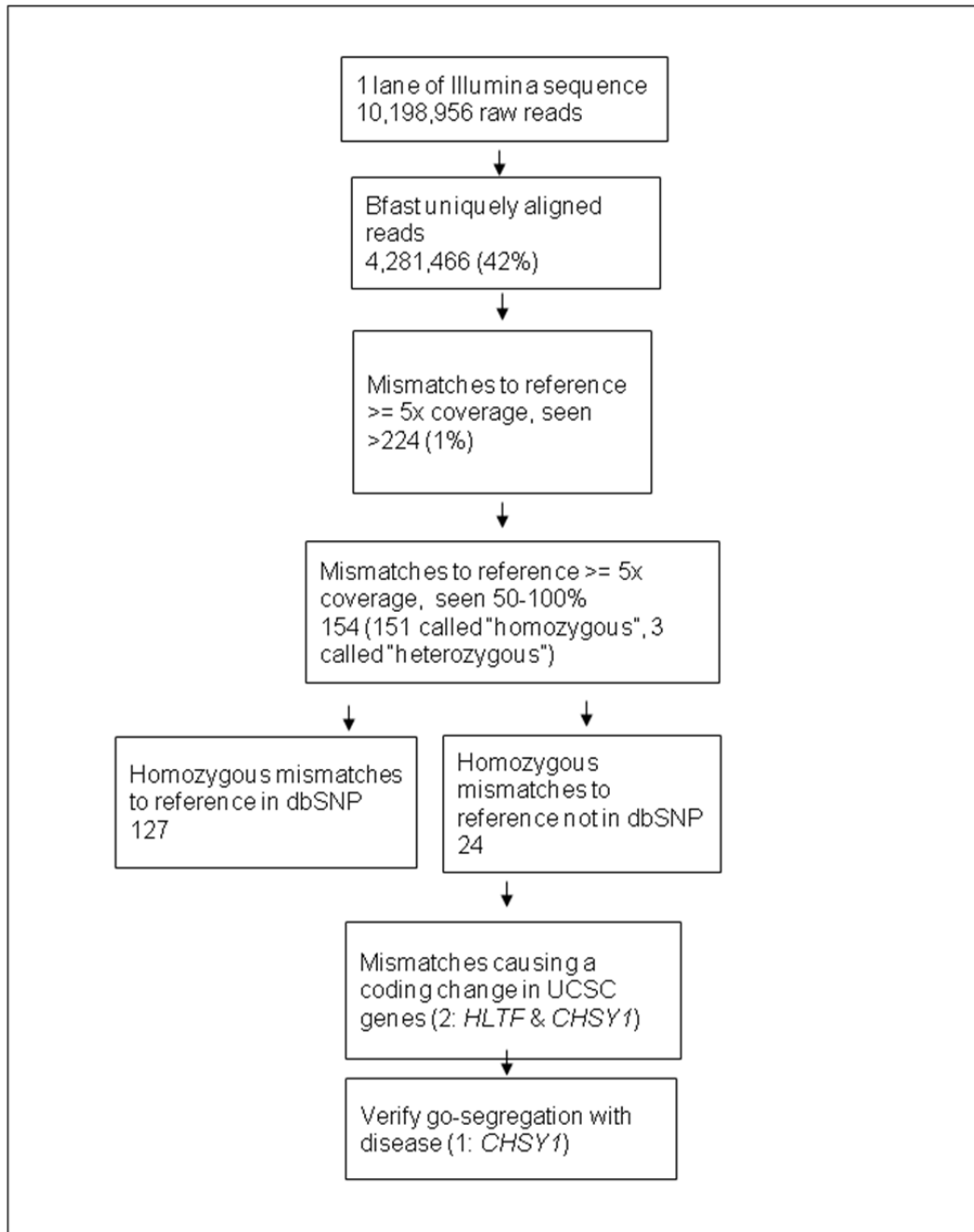
Table S2. Computed *CHSY1* transcript correlations with genes coding for extracellular proteins known to cause brachydactyly in mice or humans.

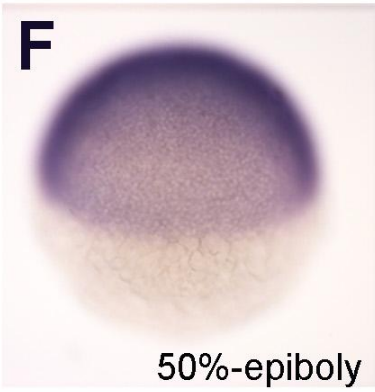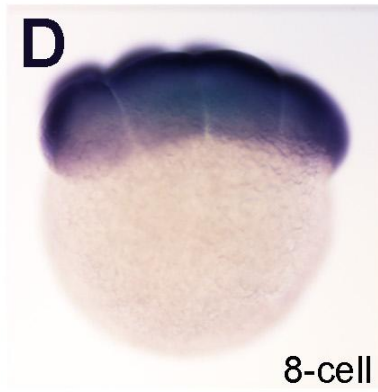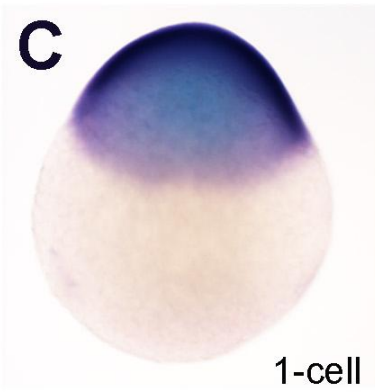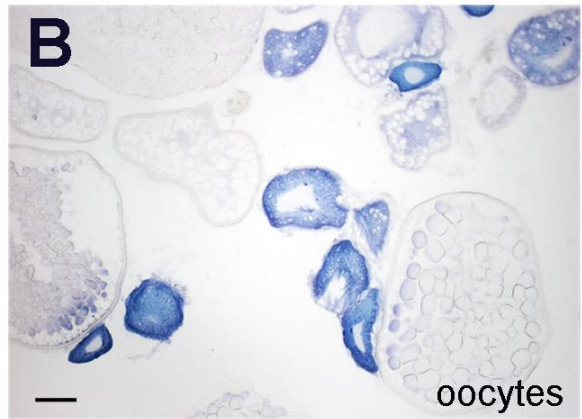| No.	Genomic location	Gene symbol	ProbeSet ID	correlation to *CHSY1*
1	chr15:99533455-99609660	*CHSY1*	203044_at	1.00
2	chr1:120255700-120262661	*NOTCH2*	212377_s_at	0.51
3	chr9:138508717-138510187	*NOTCH1*	218902_at	0.30
4	chr17:52026583-52027915	*NOG*	231798_at	0.23
5	chr9:93524709-93752265	*ROR2*	205578_at	0.10
6	chr8:38387809-38388908	*FGFR1*	226705_at	0.09
7	chr20:6696310-6708923	*BMP2*	205289_at	0.06
8	chr12:28006529-28014268	*PTHLH*	206300_s_at	0.03
9	chr10:103520074-103525647	*FGF8*	208449_s_at	0.02
10	chr4:96244580-96294895	*BMPR1B*	229975_at	0.02
11	chr11:69294966-69299352	*FGF4*	206783_at	-0.01
12	chr14:53486409-53488674	*BMP*	211518_s_at	-0.03
13	chr20:33484562-33489441	*GDF5*	206614_at	-0.08
14	chr7:155285438-155286036	*SHH*	236263_at	-0.11
15	chr14:104679120-104706206	*JAG2*	32137_at	-0.11
16	chr2:219627691-219630665	*IHH*	215420_at	-0.14

1: correlated, indicative of co-expression
0: not correlated
-1: anti-correlated

Table S3. Phenotypic analysis of *chsy1* loss-of-function and rescue experiments

Injection	Concentration	Total number (n)	Chsy1-specific Phenotype (%)	Normal (%)
ATG MO (CS1)	0.2 mM	102	64	36
Splice donor MO (CS2)	1 mM	110	15	85
CS1+ CS2	0.2 mM + 1 mM	157	92	8
h CHSY1 mRNA	200 ng/µl	86	0	96
CS1+*h CHSY1* mRNA	0.2 mM+ 200 ng/µl	107	9	91
CS2+ *h CHSY1* mRNA	1 mM + 200 ng/µl	96	2	98
CS1+CS2+ *h CHSY1* mRNA	0.2 mM + 1 mM + 200 ng/µl	171	13	87

Table S4. List of PCR primers, Q-PCR primers, siRNAs and Morpholinos

Genomic DNA primer sequences

Gene	Exon	primer	sequence	Product size [bp]
CHSY1	E1	forward reverse	GGCATGGTCCCCTCTTAAA CCCGAGTCTGCAGGTATTTC	547
HLTF	E10	forward reverse	GATGGGCTGGATGAGTACAAA TGCAGTGGTGCGATCTTAAC	650

Human and Zebrafish cDNA primer sequences used for cloning

Gene	primer	sequence	Product size [bp]
Human *CHSY1*	forward reverse	GCATGGTCCCCTCTTAAA CAAAGCTGGACATTAGGCTG	2682
Zebrafish *chsy1*	forward reverse	AGCGTTGTGGACGGGACTG GGTCTATTCTGTCCTCATTG	2494

Morpholino sequences

Morpholino name	description	sequence
CS1	ATG morpholino	AAGATCTGCGACTCCTTCCTGCCAT
CS2	Splice donor morpholino	TGTGCATTTATTTACCTATATGCTG

9

Human cDNA primer sequences used for Quantitative PCR

Gene	ABI assay ID	Primer & probe	sequence
CHSY1	Hs00208704_m1		
HES1	Hs00172878_m1		
JAG1	Hs01070036_m1		
JAG2	Hs00171432_m1		
NOTCH1	Hs01062014_m1		
NOTCH2	Hs01050719_m1		
ALPL	Hs01029144_m1		
ACTIN	4352935E		
RUNX2	Hs00231692_m1		
CCND1	Hs00277039_m1		
C-MYC	Hs00153408_m1		
BSPH1		probe	ct g+Ct +T+Ta a+Tt +Ttg +Ct+C agc
		Left primer	AGAGGAAGCAATCACCAAAATGA
		Right priner	TTGAGAAAGCACAGGCCATTC
BGLAP		probe	TTG T+GT C+CA AG+C AG+G A+GG +GC
		Left primer	GGTGCAGAGTCCAGCAAAGG
		Right priner	CGCCTGGGTCTCTTCACTACC
OSX		probe	CTT +TC+C A+CA +AA+C T+CT +CAT +CTC
		Left primer	CATGCCTCCTCAGCTCACCTT
		Right priner	AAGCCGGAGTGCAGGTATCA

ThalassoChip, an array mutation and single nucleotide polymorphism detection tool for the diagnosis of β-thalassaemia

Christos Shammas[1], Thessalia Papasavva[1], Xenia Felekis[1], Christos Christophorou[1], Hanno Roomere[2], Jan Traeger Synodinos[3], Emmanuel Kanavakis[3], Mohammed El-Khateeb[4], Hanan Hamamy[4], Tamara Mahmoud[4], Mohammad Shboul[4], Amal El Beshlawy[5], Dvora Filon[6], Ibtessam R. Hussein[7], Renzo Galanello[8], Giovanni Romeo[9] and Marina Kleanthous[1,]*

[1] Department of Molecular Genetics Thalassaemia, The Cyprus Institute of Neurology and Genetics, Nicosia, Cyprus

[2] Asper Biotech Ltd., Tartu, Estonia

[3] Department of Medical Genetics, Athens University Medical School, Athens, Greece

[4] National Center for Diabetes, Endocrinology and Genetics, University of Jordan, Amman, Jordan

[5] Hematology Department of the Pediatric Hospital, Cairo University, Cairo, Egypt

[6] Department of Hematology, Hadassah-Hebrew University Medical Center, Jerusalem, Israel

[7] Center of Excellence for Genome Research in Medicine, King AbdulAziz University, Jeddah, Saudi Arabia

[8] Department of Science, Biomedicine and Biotechnology, University of Cagliari, Cagliari, Italy

[9] European Genetic Foundation, Bologna, Italy

Abstract

Background: The detection and diagnosis of β-thalassaemia for populations with molecular heterogeneity, or diverse ethnic groups, has increased the need for the development of an array high-throughput diagnostic tool that can deliver large scale genetic detection. We report on the update and validation of the ThalassoChip, a β-thalassaemia genetic diagnostic tool which is based on arrayed primer extension (APEX) technology.

Methods: ThalassoChip slides with new and redesigned probes were prepared for testing the microarray. Six hundred and sixty DNA samples collected from eight Mediterranean countries were used for standardisation, optimisation and validation of the ThalassoChip. The β-globin gene region was amplified by PCR, the products were hybridised to the probes after fragmentation and the APEX reaction followed.

Results: The ThalassoChip was updated with new probes and now has the ability to detect 57 β-globin gene mutations and three single nucleotide polymorphisms (SNPs) in a single test. The ThalassoChip as well as the PCR and APEX reactions were standardised and optimised using 500 DNA samples that were previously genotyped using conventional diagnostic techniques. Some probes were redesigned in order to improve the specificity and sensitivity of the test. Validation of the ThalassoChip performed using 160 samples analysed in blinded fashion showed no error.

Conclusions: The updated version of the ThalassoChip is versatile, robust, cost-effective and easily adaptable, but most notably can provide comprehensive genetic diagnosis for β-thalassaemia and other haemoglobinopathies.

Clin Chem Lab Med 2010;48:1713–8.

*Corresponding author: Marina Kleanthous, PhD, Head, Department of Molecular Genetics Thalassaemia, The Cyprus Institute of Neurology and Genetics, 6 International Airport Ave., Ag. Dhometios, P.O. Box 23462, Nicosia, Cyprus
Phone: +357 22392652, Fax: +357 22392615,
E-mail: marinakl@cing.ac.cy

Introduction

β-Thalassaemia is an autosomal recessive disorder caused by a reduction or lack of production of β-globin chains. β-Thalassaemia still remains one of the most significant single gene disorders as most thalassaemia patients require regular lifelong blood transfusions to survive, and early detection is essential to support the care of patients. In addition, molecular characterisation of carriers plays a central role in disease prevention, and is an absolute requirement when offering prenatal diagnosis to carrier couples (1). However, the current increase in migration patterns have complicated the identification of mutations due to the presence of a wider spectrum of mutations in most countries worldwide (2–4).

Current molecular diagnostic approaches for thalassaemia include PCR-based techniques capable of detecting the wide spectrum of α- and β-globin gene mutations. The methods include allele-specific oligonucleotide (ASO) probes, amplification refractory mutation system (ARMS) and sequencing for point mutations and gap-PCR for specific deletions. Other indirect methods include denaturing gradient gel electrophoresis (DGGE), as well as denaturing high performance liquid chromatography (dHPLC). More recently, several emerging techniques including multiplex ligation-dependent probe amplification (MLPA) and quantitative multiplex PCR short fluorescent fragments (QMPSF) for the detection of deletions, and real-time PCR and high-resolution melting

curve analysis for the detection of point mutation have been used (5, 6).

Microarray technology is able to explore genetic abnormalities of polygenic disorders, such as heart disease, mental illness, and infectious diseases, and to distinguish pathological entities, such as acute myeloid leukaemia and acute lymphoblastic leukaemia (7, 8). Microarrays are used to study the therapeutic response to drugs and establish genetic profiles of treated and untreated patients. Microarrays can revolutionise the diagnosis of β-thalassaemia and Hb variants (9). Chan et al. in 2004 (10) developed a thalassaemia array covering the commonest mutations of α- and β-thalassaemias in Southeast Asia. Nanogen Microelectronic technology was used for the detection of β-thalassaemia mutations (11, 12). We developed and validated a microarray chip, called ThalassoChip, to serve as a high throughput, large scale β-globin mutation and polymorphism detection system (13, 14). The ThalassoChip is able to detect mutations and SNPs at low concentrations of genetic samples, and can show detectable signal with just 0.15 ng of human genomic DNA (15).

The ThalassoChip is based on arrayed primer extension (APEX) technology. It involves extension of oligonucleotides probes that are designed to stop a single nucleotide short relative to the position of the allelic variant (16). The probes are immobilised via the 5′ end on a glass surface, while their 3′ end is free for enzymatic extension. An amplicon containing the region which harbours the mutation(s) or single nucleotide polymorphisms (SNPs) under investigation is hybridised to the complementary probe sequence that is immobilised on the microarray chip. A single base extension of the probe is performed by incorporation of the appropriate dye-labelled dideoxynucleotide complementary to the variant base, followed by termination of the reaction. An automatic laser imaging system, Genorama QuattroImager, is used to read the APEX slide. Fluorescent labels (Fluorescein, Cy3, Cy5 and Texas Red) for the four dideoxynucleotides are read at four different emission wavelengths (17–20).

In this study, we report on the update and validation of the ThalassoChip, a β-thalassaemia genetic diagnostic tool which is based on APEX technology. This system has the ability to detect over 60 β-globin gene mutations and polymorphisms in a single step.

Materials and methods

Spotting

Probes (oligonucleotides) of 20–25 nucleotide bases in length were designed to be complementary to known SNPs and mutation regions, but terminating one base before the variant nucleotide position, were used for spotting. The microarray slides have a double-sided amino-silane coating onto which the oligos are electrostatically attached by their 5′ termini (21). The slide coating has the ability to preserve the probes anchored to the slide. Each spot has a diameter of 90–100 μm, with a minimum distance of 150 μm (optimal 250–375 μm) between spots.

New probes have been designed to update the ThalassoChip. The oligonucleotide probes were synthesised according to the wild type sequence, with an amino-linking group at the 5′ end attached to the glass slide. The 3′ end of the probe is free for enzymatic extension by DNA polymerase during the APEX reaction step. For each nucleotide variation, probes were designed to target both sense and antisense strands, and each probe was spotted in duplicate in order to increase the reliability of diagnosis. The β-globin gene sequence was derived from the NCBI database with accession number NG_000007.

The ThalassoChip routine screening process involved the following steps: a) DNA extraction and amplification of the appropriate region by PCR, b) purification of the amplified region followed by fragmentation, c) hybridisation of amplicons followed by APEX reaction, oligonucleotide probe extension by a single fluorescently labeled ddNTP, d) genotype determination using a four-channel imager.

DNA samples

During the standardisation and validation process of the ThalassoChip, 660 human genomic DNA samples with various genotypes were tested. Five hundred DNA samples were extracted from whole blood using either the Puregene Blood Core Kit C (Qiagen, Hilden, Germany) or the QIAmp DNA Blood Mini kit (Qiagen, GmBh, Hilden, Germany). One hundred and sixty DNA samples were provided by the collaborating partners, from countries, such as Cyprus, Egypt, Morocco, Jordan, Saudi Arabia, Israel, Greece and Italy. The DNA sample concentration was adjusted to 50–100 ng/μL using pure sterile water. All samples used in this study were obtained with informed consent from the patients, and all work was performed in accordance to the declaration of Helsinki ethical guidelines as reflected in a priori approval by the Cyprus national Ethics Committee.

Polymerase chain reaction

Four sets of primers were designed to amplify the β-globin regions that contain the majority of mutations and polymorphisms (Figure 1). Each set of primers covered an area approximately 200 bases long. The primers were designed taking into consideration their melting temperature (T_m), their propensity to form dimers with themselves or with other primers, and care was taken to avoid annealing of the primers to SNPs or mutations. Optimal PCR conditions were selected for each set of primers. Primer sequences were designed as follows: Primer set 1: Forward: 5′-CTAAGCCAGTGC-CAGAAGAGCCAAG-3′; Reverse: 5′-TCAGTGCCTATCAGAAA-CCCAAGAG-3′. Primer set 2: Forward: 5′-GGGTTTCTGATAGG-CACTGACTCTCTC-3′; Reverse: 5′-ACTGTACCCTGTTACTTC-TCCCCTT-3′. Primer set 3: Forward: 5′-TTCAGGGCAATA-
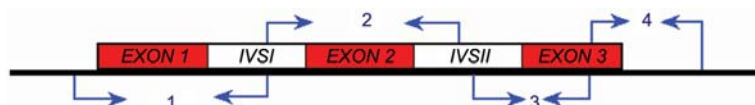

Figure 1   β-Globin gene including positions of the four sets of primers used for PCR amplification.

ATGATACAATG-3′; Reverse: 5′-AAGTGATGGGCCAGCACA-CAG-3′. Primer set 4: Forward: 5′-GTGTGCTGGCCCAT-CATCTTG-3′; Reverse: 5′-CCTCCCACATTCCCTTTTTAG-3′.

The PCR reaction (25 μL) contained the following reagents: 10×PCR buffer (500 mM KCl, 15 mM MgCl$_2$ and 100 mM Tris-HCl, Amersham Pharmacia Biotech, Uppsala Sweden), 2 μL of deoxynucleoside triphosphate mix (2 mM dATP, 2 mM dCTP, 2 mM dGTP, 1.6 mM dTTP, and 0.04 mM dUTP), 10 pmol/μL of primers, 2.5 U of Taq Polymerase (5 U/μL; Amersham Pharmacia Biotech, Uppsala, Sweden) and 100 ng of human genomic DNA. The PCR programme that produced the greatest yield followed the touch-down PCR protocol which also avoids amplification of non-specific sequences (22). The initial incubation was performed at 95°C for 5 min followed by 5 cycles of denaturation at 95°C for 30 s and primer annealing at 60°C and extension at 72°C for 20 s. The programme continued with another 30 cycles of annealing at 58°C for 30 s and then changed to 20 s for the final 8 cycles. The final extension was performed at 72°C for 5 min. PCR products were purified and concentrated (to 15 μL in volume) using the *Qiagen* QIAquick *PCR Purification Kit* (Hilden, Germany) as per the manufacturer's protocol. Each PCR product was tested by gel electrophoresis to ensure that each set of PCR reactions produced a single product of the expected size.

Fragmentation

All PCR products amplified included 20% substitution of dTTPs with dUTPs. This enabled subsequent fragmentation with thermo-labile uracil-N-glycosylase (by HK™, Madison, WI, USA) which hydrolyses the N-glycosidic bond between the deoxyribose sugar and uracil in DNA that contains deoxyuridine when it is heated to 38°C. During the fragmentation process shrimp alkaline phosphatase (SAP) was also added which catalyses the release of the 5′ phosphate group from the DNA. Dephosphorylation of the excess dNTPs that remain after PCR can interfere with the APEX reaction. The fragmentation mixture (30 μL) consisted of: 10×UNG buffer [500 mM Tris-HCl, pH 9.0; 200 mM (NH$_4$)$_2$SO$_4$], 0.03 U/μL of SAP (1 U/μL) (Amersham Bioscience Inc., Milwaukee, WI, USA), 0.03 U/μL of UNG (1 U/μL) (Epicentre Technologies, Madison, WI, USA) and approximately 75 ng/μL of purified PCR product.

The fragmented PCR product was heated to 95°C for 10 min which enabled the deactivation of the SAP enzyme as well as denaturation of the double stranded DNA duplexes. Fragmentation efficiency was confirmed by electrophoresis.

Amplicon hybridisation and the APEX reaction

During the APEX reaction, the microarray oligonucleotide probes were extended by a single fluorescently-labeled dideoxynucleoside triphosphate which was complementary to the DNA template. The DNA polymerase reaction was run at high temperature (58°C) to avoid or minimize undesirable secondary structure oligos, while permitting efficient hybridisation to the target site. Each slide was incubated for 15 min and any excess reagents were removed by washing the slides with boiling water, allowing annealed DNA to denature and wash away. This process can avoid background fluorescence and rehybridisation of unbound oligonucleotides.

The buffer reaction mixture (40 μL) that was used consisted of Tris-HCl/MgCl$_2$ buffer (260 nM, pH 9.5 and 65 mM, respectively; Amersham Pharmacia Biotech, Uppsala, Sweden), four different terminator nucleotides, each tagged with individual fluorophores: 12 μM of Fluorescein ddUTP, 19 μM of Cy3 ddCTP, 12 μM of Texas Red ddATP, 12 μM of Cy5 ddGTP (NEN, Boston, MA, USA, and Amersham Pharmacia Biotech, Uppsala, Sweden), 12 μM Thermosequenase DNA polymerase (Amersham Pharmacia Biotech, Uppsala, Sweden) and 70 ng/μL of denatured DNA.

Workstation

The device used for the detection of mutations and polymorphisms during the validation of the chip was the Genorama QuattroImager detector 003 (Genorama Ltd., Tartu, Estonia). The detector is a four-channel imaging system composed of laser light sources and an integrated camera. The signal detection process is based on the recording of fluorescence emitted at the surface of the ThalassoChip that permits homologous exposure. The appropriate frequency of light source stimulates the labelled nucleotides to emit light that is captured by a charged coupled devised digital camera with 20 μm resolution (23).
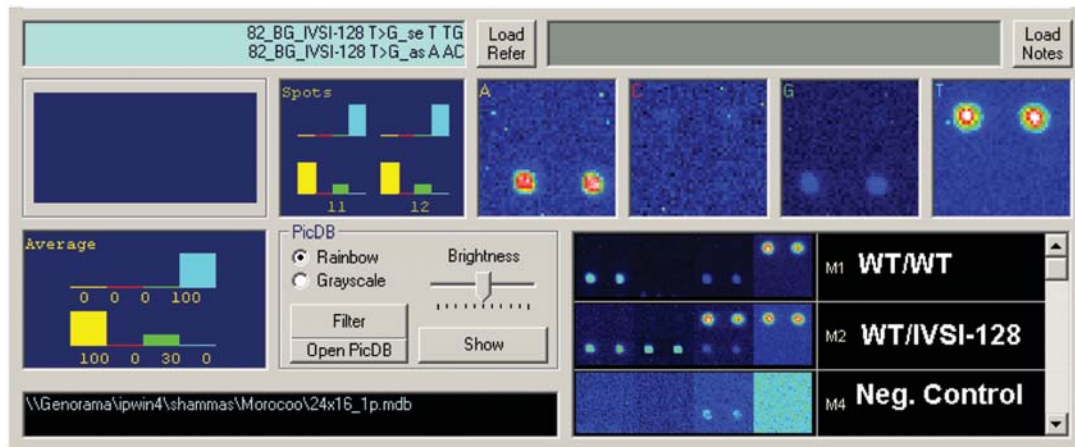
Figure 2 Image from the BaseCaller 4.5 software used for the APEX analysis of sequence IVSI-128 (T→G).
The four-channel fluorescent images from each type of flurophore dNTP are shown in the top right boxes marked A, C, G and T, respectively. The sense strand (top) and anti-sense strand (bottom) are each determined twice to minimize errors. PicDB image from previous samples can be seen on the lower right hand corner. Sample observed in the PicDM images labeled M1 is WT, M2 is heterozygous for IVSI-128 and M4 is the negative control.

Table 1   List of the β-globin mutations and polymorphisms that have been spotted on the ThalassoChip and validation results.

	Common name	HGVS nomenclature	N/M	M/M
1	–101 (C→T)	HBB:c.–151C>T	1	
2	–92 (C→T)	HBB:c.–142C>T		1
3	–88 (C→T)	HBB:c.–138C>T	1	
4	–87 (C→G)	HBB:c.–137C>G	1	
5	–30 (T→A/C)	HBB:c.–80T>A/HBB:c.–80T>C	1	
6	–28 (A→C)	HBB:c.–78A>C	1	
7	+20 (C→G/T) (SNP)	HBB:c.–31C>T	17	2
8	+22 (G→A)	HBB:c.–29G>A	1	
9	+30 (T→C)	HBB:c.–21C>G	2	
10	+33 (C→G)	HBB:c.–18C>G	1	
11	Cd 1 delG	HBB:c.4delG	1	
12	Cd 2 (CAC→CAT) (SNP)	HBB:c.9C>T	6	
13	Cd 5 (CCT→del-CT)	HBB:c.17_18delCT	9	
14	Cd 6 (GAG → AAG) HbC	HBB:c.19G>A	1	
15	Cd 6 (GAG →del-A)	HBB:c.20delA	1	
16	Cd 6 (GAG →GTG) HbS	HBB:c.20A>T	1	
17	Cd 8 (AAG→del-AA)	HBB:c.25_26delAA	5	
18	Cd 8/9 insG	HBB:c.27_28insG	4	
19	Cd 9/10 insT	HBB:c.30_31insT	1	
20	Cd 15 (G→A)	HBB:c.48G>A	3	
21	Cd 22–24 delAAGTTGG	HBB:c.68_74delAAGTTGG	1	
22	Cd 24 (T→A)	HBB:c.75T>A	1	
23	Cd 24 delG/insCAC	HBB:c.74delinsCAC	1	
24	Cd 25/26 insT	HBB:c.78_79insT	1	
25	Cd 26 (GAG→AAG) HbE	HBB:c.79G>A	1	
26	Cd 27 (GCC→TCC) Hb Knossos	HBB:c.82G>T	1	
27	Cd 28 delC	HBB:c.85delC	1	
28	Cd 30 (A→G)	HBB:c.91A>G	5	
29	IVSI-1 (G→A/T)	HBB:c.92+1G>A / HBB:c.92+1G>T	9	1
30	IVS-2 (T→G)	HBB:c.92+2T>G	1	
31	IVSI (-3)/Cd 29 (C→T)	HBB:c.90C>T	1	
32	IVSI-5 (G→A/T/C)	HBB:c.92+5G>A/HBB:c.92+5G>T/HBB:c.92+5G>C	8	
33	IVSI-6 (T→C)	HBB:c.92+6T>C	12	
34	IVSI del17bp	HBB:c.93–17_93–1delTATTTTCCCACCCTTAG	1	
35	IVSI del25bp	HBB:c.93–21_96del	3	
36	IVSI del44bp	HBB:c.76_92+27del	1	
37	IVSI-110 (G→A)	HBB:c.93–21G>A	14	1
38	IVSI-116 (T→G)	HBB:c.93–15T>G	1	
39	IVSI-128 (T→G)	HBB:c.93–3T>G	1	
40	IVSI-130 (G→C/A)	HBB:c.93–1G>C/HBB:c.93–1G>A	3	
41	Cd 30 (G→C)	HBB:c.93G>C	3	
42	Cd 36/37 delT	HBB:c.112delT	2	
43	Cd 37 (G→A)	HBB:c.113G>A	9	2
44	Cd 39 (CAG→TAG)	HBB:c.118C>T	16	2
45	Cd 44 (TCC→del-C)	HBB:c.135delC	1	
46	Cd 76 (GCT→del-C)	HBB:c.230delC	0	
47	Cd 90 (G→T)	HBB:c.271G>T	1	
48	IVSII-1 (G→A)	HBB:c.315+1G>A	2	1
49	IVSII-74 (G→T) (SNP)	HBB: c.315+74G>T	2	
50	IVSII-654 (C→T)	HBB:c.316–197C>T	1	
51	IVSII-666 (T→C)	HBB:c.316–185T>C	1	
52	IVSII-705 (T→G)	HBB:c.316–146T>G	1	
53	IVSII-745 (C→G)	HBB:c.316–106C>G	17	2
54	IVSII-844 (C→G)	HBB:c.316–7C>G	0	
55	IVSII-848 (C→A)	HBB:c.316–3C>A	1	
56	IVSII-849 (A→C)	HBB:c.316–2A>C	1	
57	Cd106/107 insG	HBB:c.321_322insG	1	
58	Cd 121 (GAA→CAA) Hb D	HBB:c.364G>C	1	
59	Cd 121 (GAA→AAA) Hb O	HBB:c.364G>A	1	
60	+1570 (T→C)	HBB:c.*+96T>C	1	

Data processing

Image analysis software was used to determine the genotype extension that has been produced during the APEX reaction, and each image was merged producing a single output file. Two types of software were used for the analysis, both of which are included in the Genorama™ Genotyping software. The BaseCaller software is used for data processing and single sample analysis (Figure 2) while the PicDB software was used for simultaneous analysis and comparison of multiple images.

Results

ThalassoChip update

New probes have been designed to update the ThalassoChip which can now detect 54 β-thalassaemia mutations that are common in Mediterranean countries, three haemoglobin variants (*HbS*, *HbE* and *HbC*) and three SNPs located in the β-globin gene (Table 1). The three SNPs that were included in the ThalassoChip are *Cd 2 (CAC→CAT)*, *IVSII-74 (G→T)* and *+20 (C→G/T)* polymorphism that is 100% associated with the *IVSII-745 (C→G)* β⁰-thalassaemia mutation.

Chip standardisation

Five hundred human genomic DNA samples were used for standardisation and optimisation of the ThalassoChip. All samples were previously genetically tested using conventional methods. The samples were used for the comprehensive determination and assessment of each probe, as well as for standardisation of the PCR reaction mixes, PCR programmes and optimisation of APEX conditions. Probes that showed low signal intensity were improved by changes made to the probe length or sequence that improved melting temperature. Changes in binding affinity had to be assured that did not induce changes in binding specificity.

Chip validation

After the standardisation process, 160 human genomic DNA samples were run in blinded fashion. All samples were subsequently shown to be concordant with the conventional diagnosis that was made previously. All samples were screened against the 60 mutations and polymorphisms. As shown in Table 1, at least one sample from the pool was heterozygous (N/M) or homozygous (M/M) for each mutation and polymorphism with the exception of *IVSII-844 (C→G)* and *Cd 76 (GCT→del-C)*; due to their rarity in the Mediterranean region, only wild type alleles were tested. The normal allele for each probe was validated more than 140 times.

A general limiting factor in this study was the inadequate signal detection levels emitted from the Texas Red labelled ddATP. No changes were observed when the dye concentration was increased. Replacing the adenosine fluorophore with a higher intensity fluorescent dye could have improved the APEX analysis.

The relative fluorescent light intensity emitted when a sample is homozygous for an allele is usually twice as intense compared to a heterozygous sample, since the heterozygous sample has half of its probes extended with wild type nucleotide and the other half with the mutant nucleotide. This phenomenon can make peak assignment difficult when dealing with heterozygous samples.

Discussion

The ThalassoChip potentially offers an alternative approach for the diagnosis of β-thalassaemia mutations and haemoglobin variants. The microarray is a diagnostic tool with low operating costs. It is estimated that each test costs 40 €, and can determine a wide spectrum of mutations and polymorphisms in a single experiment. This tool can provide diagnosis for populations with molecular heterogeneity. The current version of the ThalassoChip contains probes that can detect mutations common in the Mediterranean region, but it is being continuously updated to include more mutations that can cover more diverse ethnic groups. The APEX reactions are entirely reproducible under standardised conditions. These conditions include 1) the use of good quality human genomic DNA at the appropriate concentration, 2) optimised PCR amplification conditions, 3) successful DNA fragmentation 4) use of the optimised APEX reaction conditions.

The ThalassoChip can now serve as a diagnostic tool for β-thalassaemia and other haemoglobinopathies, but can also progress to an automated system that includes a greater number of mutations, even those underlying α- and δ-thalassaemia. The only disadvantage of this approach when compared to DNA sequencing is that the microarray chip is limited to detecting only known nucleotide changes for which the APEX probes have been designed, whereas previously undetected polymorphisms and new mutations will be missed.

Conflict of interest statement

References

1. Old JM, Varawalla NY, Weatherall DJ. Rapid detection and prenatal diagnosis of beta-thalassaemia: studies in Indian and Cypriot populations in the UK. Lancet 1990;336:834–7.
2. van Baal S, Kaimakis P, Phommarinh M, Koumbi D, Cuppens H, Riccardino F, et al. FINDbase: a relational database recording frequencies of genetic defects leading to inherited disorders worldwide. Nucleic Acids Res 2007;35:D690–5.

3. Patrinos GP, Giardine B, Riemer C, Miller W, Chui DH, Anagnou NP, et al. Improvements in the HbVar human hemoglobin variants and thalassemia mutations for population and sequence variation studies. Nucleic Acids Res 2004;32:D537–41.

4. Giardine B, van Baal S, Kaimakis P, Riemer C, Miller W, Samara M, et al. HbVar database of human hemoglobin variants and thalassemia mutations 2007, update. Hum Mut 2007;28:206.

5. Kanavakis E, Traeger-Synodinos J, Vrettou C, Maragoudaki E, Tzetis M, Kattamis C. Prenatal diagnosis of the thalassaemia syndromes by rapid DNA analytical methods. Mol Hum Reprod 1999;3:523–8.

6. Hartveld CL, Kleanthous M, Traeger-Synodynos J. Prenatal diagnosis of hemoglobin disorders. Present and future strategies. Clin Biochem 2009;42:1767–79.

7. Tham CK, Heng CK, Chin WC. Predicting risk of coronary artery disease from DNA microarray-based genotyping using neural networks and other statistical analysis tool. J Bioinform Comput Biol 2003;1:521–39.

8. Diehn M, Alizadeh AA, Brown PO. Examining the living genome in health and disease with DNA microarrays. J Am Med Assoc 2000;283:2298–9.

9. Cremonesi L, Ferrari M, Giordano PC, Harteveld CL, Kleanthous M, Papasavva T, et al. An overview of current microarray-based human globin gene mutation detection methods. Hemoglobin 2007;31:289–311.

10. Chan K, Man Wong S, Chan TK, Chan V. A thalassaemia array for Southeast Asia. Br J Haematol 2004;124:232–9.

11. Ferrari M, Stenirri S, Bonini P, Cremonesi L. Molecular diagnostics by microelectronic microchips. Clin Chem Lab Med 2003;41:462–7.

12. Ferrari M, Cremonesi L, Bonini P, Foglieni B, Stenirri S. Single-nucleotide polymorphism and mutation identification by the nanogen microelectronic chip technology. Methods Mol Med 2005;114:93–106.

13. Gemignani F, Perra C, Landi S, Canzian F, Kurg A, Tönisson N, et al. Reliable detection of β-thalassemia and G6PD mutations by a DNA microarray. Clin Chem 2002;48:2051–4.

14. Kurg A, Tönisson N, Georgiou I, Shumaker J, Tollett J, Metspalu A. Arrayed primer extension: solid-phase four-color DNA resequencing and mutation detection technology. Genet Test 2000;4:1–7.

15. Papasavva TH, Kalikas I, Kyrri A, Kleanthous M. Arrayed primer extension for the noninvasive prenatal diagnosis of beta-thalassemia based on detection of single nucleotide polymorphisms. Ann N Y Acad Sci 2008;1137:302–8.

16. Heller MJ. DNA microarray technology: devices, systems, and applications. Annu Rev Biomed Eng 2002;4:129–53.

17. Moutereau S, Narwa R, Matheron C, Vongmany N, Simon E, Goossens M. An improved electronic microarray-based diagnostic assay for identification of MEFV mutations. Hum Mutat 2004;23:621–8.

18. Tõnisson N, Kurg A, Lõhmussaar E, Metspalu A. Arrayed primer extension on the DNA chip – method and applications. In: Schena M, editor. DNA Microarrayes. Biology and Technology. BioTechniques Books, 2000.

19. Tõnisson N, Kurg A, Kaasik K, Lohmussaar E, Metspalu A. Unravelling genetic data by arrayed primer extension. Clin Chem Lab Med 2000;38:165–70.

20. Pullat J, Metspalu A. Arrayed primer extension reaction for genotyping on oligonucleotide microarray. Methods Mol Biol 2008;444:161–7.

21. Tillib SV, Mirzabekov AD. Advances in the analysis of DNA sequence variations using oligonucleotide microchip technology. Curr Opin Biotechnol 2001;12:53–8.

22. Don RH, Cox PT, Wainwright BJ, Baker K, Mattick JS. Touchdown' PCR to circumvent spurious priming during gene amplification. Nucleic Acids Res 1991;19:4008.

23. Guo Z, Guilfoyle RA, Thiel AJ, Wang R, Smith LM. Direct fluorescence analysis of genetic polymorphisms by hybridization with oligonucleotide arrays on glass supports. Nucleic Acids Res 1994;22:5456–65.

nature
genetics

Mutations in *PYCR1* cause cutis laxa with progeroid features

Bruno Reversade[1,33], Nathalie Escande-Beillard[1,33], Aikaterini Dimopoulou[2], Björn Fischer[2], Serene C Chng[1], Yun Li[3], Mohammad Shboul[1], Puay-Yoke Tham[1], Hülya Kayserili[4], Lihadh Al-Gazali[5], Monzer Shahwan[6], Francesco Brancati[7,8], Hane Lee[9], Brian D O'Connor[9], Mareen Schmidt-von Kegler[2,10], Barry Merriman[9], Stanley F Nelson[9], Amira Masri[11], Fawaz Alkazaleh[11], Deanna Guerra[12], Paola Ferrari[13], Arti Nanda[14], Anna Rajab[15], David Markie[16], Mary Gray[16], John Nelson[17], Arthur Grix[18], Annemarie Sommer[19], Ravi Savarirayan[20], Andreas R Janecke[21], Elisabeth Steichen[22], David Sillence[23], Ingrid Haußer[24], Birgit Budde[25], Gudrun Nürnberg[25], Peter Nürnberg[25], Petra Seemann[10,26], Désirée Kunkel[26], Giovanna Zambruno[27], Bruno Dallapiccola[7], Markus Schuelke[28], Stephen Robertson[29], Hanan Hamamy[6], Bernd Wollnik[3,30,31], Lionel Van Maldergem[32], Stefan Mundlos[2,10,26] & Uwe Kornak[2,10]

Autosomal recessive cutis laxa (ARCL) describes a group of syndromal disorders that are often associated with a progeroid appearance, lax and wrinkled skin, osteopenia and mental retardation[1–3]. Homozygosity mapping in several kindreds with ARCL identified a candidate region on chromosome 17q25. By high-throughput sequencing of the entire candidate region, we detected disease-causing mutations in the gene *PYCR1*. We found that the gene product, an enzyme involved in proline metabolism, localizes to mitochondria. Altered mitochondrial morphology, membrane potential and increased apoptosis rate upon oxidative stress were evident in fibroblasts from affected individuals. Knockdown of the orthologous genes in *Xenopus* and zebrafish led to epidermal hypoplasia and blistering that was accompanied by a massive increase of apoptosis. Our findings link mutations in *PYCR1* to altered mitochondrial function and progeroid changes in connective tissues.

Wrinkly skin and bone loss are typical features associated with aging. In some monogenetic diseases these changes occur prematurely, resulting in a progeroid appearance of affected individuals. As a clinical feature, wrinkly skin or cutis laxa is used as a common denominator of several overlapping syndromal disorders including autosomal dominant cutis laxa (MIM123700), autosomal recessive cutis laxa type I (MIM219100), autosomal recessive cutis laxa type II (ARCL2; MIM219200, also called wrinkly skin syndrome (WSS; MIM278250)), de Barsy syndrome (DBS; MIM219150), and gerodermia osteodysplastica (MIM231070)[1–4]. Diagnosis is often difficult in these conditions owing to a broad clinical overlap[5,6].

[1]Institute of Medical Biology, A*STAR, Singapore, Singapore. [2]Institute of Medical Genetics, Charité Universitaetsmedizin Berlin, Germany. [3]Center for Molecular Medicine Cologne, University of Cologne, Cologne, Germany. [4]Medical Genetics Department, Istanbul Medical Faculty, University of Istanbul, Turkey. [5]Department of Paediatrics, Faculty of Medicine and Health Sciences, United Arab Emirates University, Al Ain, United Arab Emirates. [6]National Center for Diabetes, Endocrinology and Genetics, Amman, Jordan. [7]Ospedale Casa Sollievo della Sofferenza (CSS), San Giovanni Rotondo and Istituto CSS-Mendel, Rome, Italy. [8]Centro Studi Invecchiamento (Ce.S.I.), Department of Biomedical Sciences, Gabriele d'Annunzio University, Chieti, Italy. [9]Department of Human Genetics, David Geffen School of Medicine, University of California, Los Angeles, Los Angeles, California, USA. [10]Max Planck Institute for Molecular Genetics, Berlin, Germany. [11]Departments of Pediatrics, Obstetrics and Gynecology, Faculty of Medicine, The University of Jordan, Amman, Jordan. [12]Department of Biomedical Sciences, University of Modena and Reggio Emilia, Modena, Italy. [13]Department of Pediatrics, University of Modena and Reggio Emilia, Modena, Italy. [14]As'ad Al-Hamad Dermatology Center, Al-Sabah Hospital, Kuwait City, Kuwait. [15]Genetic Unit, Directorate General of Health Affairs, Ministry of Health, Muscat, Sultanate of Oman. [16]Department of Pathology, University of Otago, Dunedin, New Zealand. [17]Genetic Services of Western Australia, King Edward Memorial Hospital for Women, Perth, Australia. [18]The Permanente Medical Group, Sacramento, California, USA. [19]The Ohio State University College of Medicine and Nationwide Children's Hospital, Molecular and Human Genetics, Columbus, Ohio, USA. [20]University of Melbourne, Murdoch Childrens Research Institute, Royal Children's Hospital, and Genetic Health Services Victoria, Parkville, Victoria, Australia. [21]Division of Clinical Genetics, Innsbruck Medical University, Innsbruck, Austria. [22]Klinik fuer Kinder- und Jugendheilkunde, Universitaet Innsbruck, Innsbruck, Austria. [23]Department of Clinical Genetics, The Children's Hospital at Westmead, Sydney, New South Wales, Australia. [24]Universitaets-Hautklinik Heidelberg, Heidelberg, Germany. [25]Cologne Center for Genomics, Universität zu Köln, Germany. [26]Berlin-Brandenburg Center for Regenerative Therapies, Charité Universitaetsmedizin Berlin, Germany. [27]Laboratory of Molecular and Cell Biology, Istituto Dermopatico dell'Immacolata - Istituto di Ricovero e Cura a Carattere Scientifico, Rome, Italy. [28]Department of Neuropediatrics and NeuroCure Clinical Research Center, Charité Universitaetsmedizin Berlin, Germany. [29]Department of Paediatrics and Child Health, University of Otago, Dunedin, New Zealand. [30]Cologne Excellence Cluster on Cellular Stress Responses in Aging-Associated Diseases (CECAD), University of Cologne, Cologne, Germany. [31]Institute of Human Genetics, University of Cologne, Cologne, Germany. [32]Centre de génétique humaine, Centre Hospitalier Universitaire du Sart-Tilman, Liège, Belgium. [33]These authors contributed equally to this work. Correspondence should be addressed to B.R. (bruno@reversade.com) or S.M. (stefan.mundlos@charite.de).

Table 1 Phenotypic characteristics of investigated subjects with ARCL

Family	Origin	No. aff. ind.	IUGR	Lax, wrinkly skin	Hip dislocation	Hernias	Osteopenia	Abnormal corpus callosum	Mental retardation	Athetoid movements	Cataract	Initial diagnosis	Status	cDNA	Consequence	Exon	Literature ref. on phenotype
J.I.	Iraq	1	+	++	+	−	+	−	−	−	−	WSS	Hom	138+1G>A	ND	2	
T.P.	Palestine	1	+	+	−	−	ND	+	+	+	−	WSS	Hom	616G>T	G206W	5	7
S.P.	Palestine	3	+	++	+	−	+	+/−	+/−	−	−	GO or WSS	Hom	617_633+6del	ND	5	5
I.K.	Kuwait	2	+	++	++	++	++	−	+	−	−	GO or WSS	Hom	797G>A	R266Q + splicing	6	6
F.S.	Kuwait	1	+	+	++	++	++	−	+	−	−	GO or WSS	Hom	797G>A	R266Q + splicing	6	6
S.J.	Jordan	5	+	++	−	+	ND	+	+	−	−	WSS	Hom	797+2_797+5del	K215_D319del	6	
D.I.	Italy	1	+	++	−	++	++	ND	+	−	−	GO	Het	11delG	G4fsX50	1	
													Het	355C>G	R119G	4	
S.O.	Oman	1	−	++	+	−	+	−	+	−	−	GO	Het	356G>A	R119H	4	
													Het	566C>T	A189V	5	
G.O.	Oman	3	ND	++	−	−	+	ND	+	−	−	GO	Hom	356G>A	R119H	4	1
H.B.	Bahrain	2	+	++	++	+	−	ND	+	−	−	GO	Hom	535G>A	A179T	4	
M.A.	Austria	1	+	+	++	+	++	ND	+	−	−	GO	Hom	540+1G>A	ND	4	
M.Q.	Qatar	1	ND	++	++	+	++	ND	+	−	−	GO	Hom	616G>A	G206R	5	
H.U.	United States	1	+	+	−	−	−	+	+	−	−	GO	Hom	633+1G>C	ND	5	8
N.A.	Australia	1	+	++	+	−	ND	ND	+	−	−	GO	Het	633+1G>C	ND	5	
													Het	797+1G>T	ND	6	
A.S.	Syria	1	+	+	−	+	+	+	+	−	−	GO	Hom	797+2_797+5del	K215_D319del	6	5
D.T.	Turkey	1	+	++	+	−	ND	ND	+/−	−	−	DBS	Hom	355C>G	R119G	4	
M.F.	Italy	1	+	++	ND	++	ND	ND	+	+	−	DBS	Het	355C>G	R119G	4	3
													Het	356G>A	R119H	4	
S.T.	Turkey	2	+	+	+	−	ND	+	+	+	−	DBS	Hom	540+1G>A	ND	6	
E.U.	United States	1	+	++	+	++	ND	+	+	−	+	DBS	Hom	752G>A	R251H	6	
J.A.	Australia	3	+	++	−	−	ND	ND	++	+	+	DBS	Hom	769G>A	A257T	6	9
K.T.	Turkey	1	−	+	+	−	ND	+	+	−	−	DBS	Hom	797G>A	R266Q + splicing	6	
I.T.	Turkey	1	+	+	+	−	ND	−	+	−	−	DBS	Hom	797+2_797+5del	K215_D319del	6	

GO, geroderma osteodysplastica; WSS, wrinkly skin syndrome; DBS, de Barsy syndrome. No. aff. ind., number of affected individuals in family; IUGR, intrauterine growth retardation; Hom, homozygous; Het, heterozygous. ND, not determined; +/−, mild; +, average; ++, strong. For hernias: +, unilateral; ++, bilateral.

Here we describe mutations in *PYCR1* associated with a spectrum of disorders characterized by wrinkly skin, osteopenia and progeroid appearance. The clinical features of the 35 affected individuals from 22 families included in our study are summarized in **Table 1**. They include congenital skin wrinkling, most pronounced on the dorsum of hands and feet; generalized connective tissue weakness; finger contractures; hernias; osteopenia; and a triangular face with a progeroid appearance that is due to lax skin and hypoplasia of the jaw often resulting in prognathism (**Fig. 1a–d**). Ultrastructural investigation of the skin showed rarefaction and fragmentation of elastic fibers similar to changes described in ARCL[2] (**Fig. 1e–h**). No glycosylation abnormalities were detected by standard diagnostics (data not shown). A variable degree of mental retardation was observed in all cases but one. In many subjects, agenesis of the corpus callosum was evident. Although most affected individuals were classified as having geroderma osteodysplastica or WSS, more severely affected individuals also showed childhood cataracts or dystonic movements and were therefore diagnosed as having DBS[1,3,5–9].

Homozygosity mapping in five consanguineous families revealed a minimal candidate region of 2.8 Mb on chromosome 17q25 between markers rs8065431 and rs1046896 (**Fig. 1i**). To screen the 59 candidate genes in this region for disease-causing mutations we combined conventional sequencing and genomic locus capture followed by high-throughput sequencing (H. Lee, B. O'Connor, B. Merriman, N. Homer, Z. Chen *et al.*, unpublished data) (**Fig. 1j**). The latter identified 552 genomic mismatches, of which 7 were newly identified SNPs that cause non-synonymous changes (**Supplementary Table 1**). We next cross-examined genes with mutations in four other sequenced samples to evaluate the causality of the observed changes.

Both methods identified mutations in *PYCR1*, the gene encoding the enzyme Δ^1-pyrroline-5-carboxylate reductase 1 (PYCR1).

In total, we identified eight missense mutations, one frameshift mutation, five splice-site mutations and one 22-bp deletion encompassing the exon-intron boundary of exon 5 (**Table 1** and **Supplementary Fig. 1a**). Six of these mutations were recurrent, even though the affected individuals did not have a common ethnic background. Bioinformatic analysis predicted deleterious effects for all changes with the exception of the heterozygous A189V, for which we cannot rule out the possibility that it is a rare variant (**Supplementary Fig. 1b**).

As skin was the most severely affected organ, we isolated skin fibroblasts from probands and their unaffected siblings to examine PYCR1 protein expression (**Fig. 2**). Strongly reduced PYCR1 protein levels were detected in a subject (S.J.) with a homozygous splice site mutation and in a compound heterozygous subject (D.I.) with a missense and a frameshift mutation (**Fig. 2a**). The missense mutations G206W (T.P.) and R251H (E.U.) resulted in a reduction in protein abundance relative to control cells (**Fig. 2b–f**). The PYCR1 protein, which has been often described as cytosolic, colocalized with various mitochondrial markers (data not shown), among them Δ^1-pyrroline-5-carboxylate synthase (P5CS), which also belongs to the proline metabolic pathway (**Fig. 2b**)[10,11]. We therefore conclude that PYCR1 is a mitochondrial protein and that the reported mutations lead to a loss of function.

Pycr1 was most highly expressed in bone and skin, the two tissues most severely affected in human subjects (**Supplementary Fig. 2a**). Two paralogs of *PYCR1* exist in human, the highly similar *PYCR2* and the more distantly related *PYCRL*. No significant expression
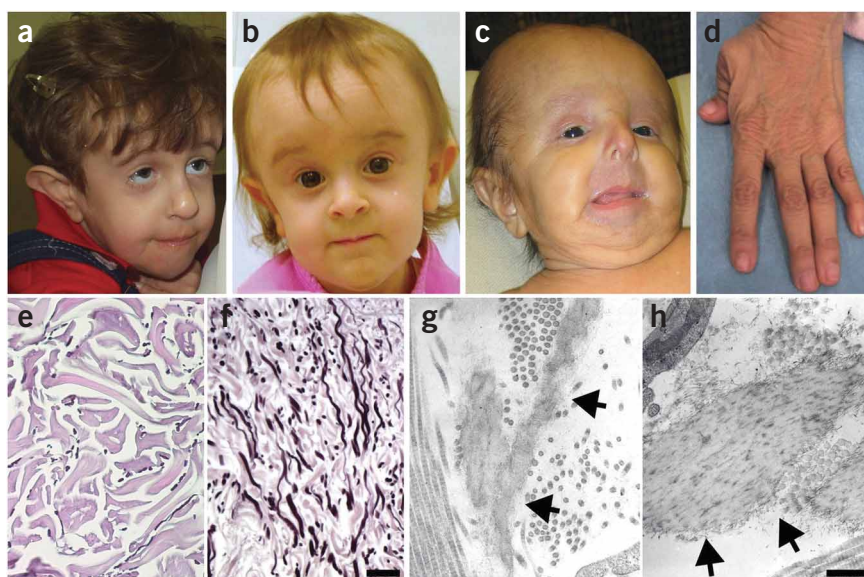
Figure 1 Phenotypic characteristics and genetic findings of subjects with *PYCR1*-related autosomal recessive cutis laxa with progeroid appearance. (**a**) Affected 2-year-old girl from family T.P., initially diagnosed with wrinkly skin syndrome. (**b**) Affected 18-month-old girl from family D.I. clinically categorized as having gerodermia osteodysplastica. (**c**) Newborn boy from family E.U. diagnosed with de Barsy syndrome. Typical facial gestalt including triangular face, malar hypoplasia and dysplastic, large ears. (**d**) Skin wrinkling at the dorsum of the hand and typical adducted thumb in an affected individual from family H.B. Participants gave consent for publication of all photos. (**e**–**h**) Findings in skin biopsy from affected individual from family D.I. (**e**,**f**) Weigert staining reveals sparse, thinned and fragmented elastic fibers in the reticular dermis compared to control (**f**); scale bar, 100 μm. (**g**,**h**) Ultrastructural analyses corroborate the markedly reduced elastic fiber (arrows) size with a reduction in both the fibrillar and amorphous components in an affected individual from family D.I. compared to control (**h**); scale bar, 500 nm. (**i**) Homozygosity mapping resulted in a minimal candidate region of 2.8 Mb on chromosome (chr.) 17q25 between markers rs8065431 and rs1046896. Only the four most informative pedigrees are shown. (**j**) Genomic capture followed by next-generation sequencing of the maximal candidate region extending from 72.05–78.77 Mb. A sequence change of C > T was sequenced seven times in a subject from family G.O. This base change resulted in a single R119H substitution in PYCR1.
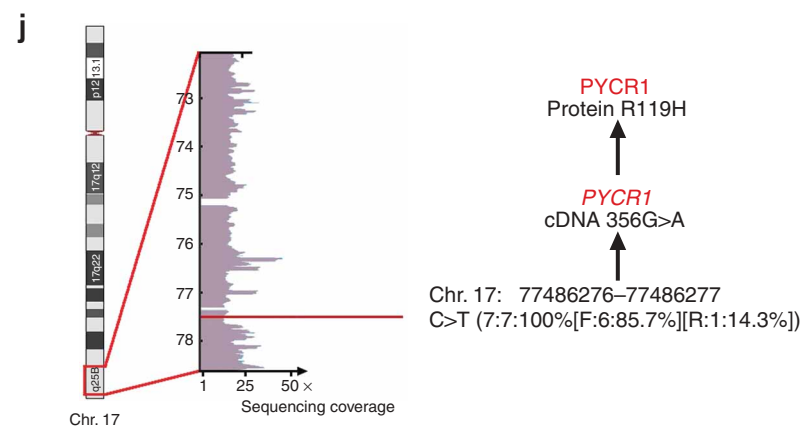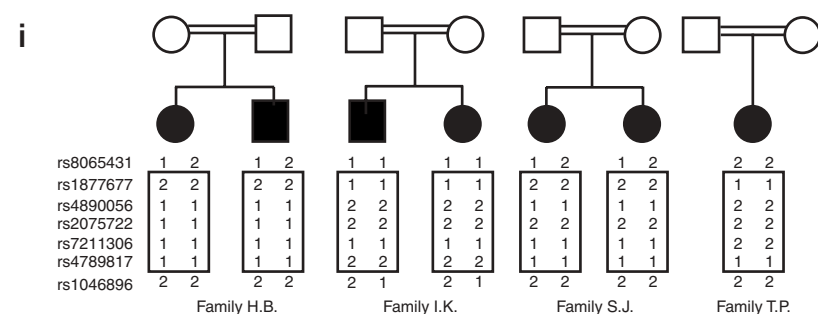
stress (**Fig. 3c–e**). Addition of H_2O_2 to the cell culture medium induced the collapse of the filamentous mitochondrial network in cells from affected individuals, whereas almost no changes were observed in mitochondria of control cells (**Fig. 3e**). Under normal culture conditions, affected and control fibroblasts showed no differences in their levels of apoptosis or mitochondrial membrane potential. However, after a short exposure to H_2O_2 a decreased mitochondrial membrane potential and a fivefold increase in cell death in affected fibroblasts compared to controls was observed (**Fig. 3f,g**). This suggests that PYCR1 is involved in the cell's response to oxidative stress. In contrast, we detected no significant differences in the respiration rates or reactive oxygen species (ROS) production between affected and control cells (**Supplementary Fig. 4**).

We next addressed PYCR1's function during embryogenesis, as patients show ARCL phenotypes at birth. As *PYCR1* is conserved throughout evolution (**Fig. 4a**)[12], we used a morpholino-based knockdown strategy (**Fig. 4b**) to model the disease in *Xenopus* embryos. By stage 30, Pycr1 morphant embryos showed obvious skin defects and failed, in a cell-autonomous fashion, to develop eyes and a tail bud (**Fig. 4c–f**). By the swimming tadpole stage, skin hypoplasia led to regions of ectodermal edema (**Fig. 4g,h**). Histological sections revealed disorganization of the skin epithelium, with enlarged cells and nuclei (**Fig. 4i,j**). We observed a similar phenotype upon morpholino knockdown of the *Pycr1* and *Pycr2* genes in zebrafish (**Supplementary**

changes in fibroblasts from individuals with *PYCR1* mutations were observed for *PYCR2* or for *ALDH18A1*, encoding P5CS (**Supplementary Fig. 2b**). As PYCR1 catalyzes the obligatory and final step in *de novo* proline synthesis, we first investigated whether affected individuals showed hypoprolinemia. Serum proline levels in affected individuals were slightly low, but within normal range (**Supplementary Fig. 3a**). Likewise, cultured skin fibroblasts did not show evidence of low proline (**Supplementary Fig. 3b**) or of reduced proliferation rates in medium without proline (**Supplementary Fig. 3c**), arguing against a proline auxotrophy.

On the basis of the mitochondrial localization of PYCR1, we examined the mitochondrial network in more detail. Ultrastructural analysis revealed abnormal morphology of mitochondria and their cristae (**Fig. 3a,b**). These differences were exacerbated upon oxidative
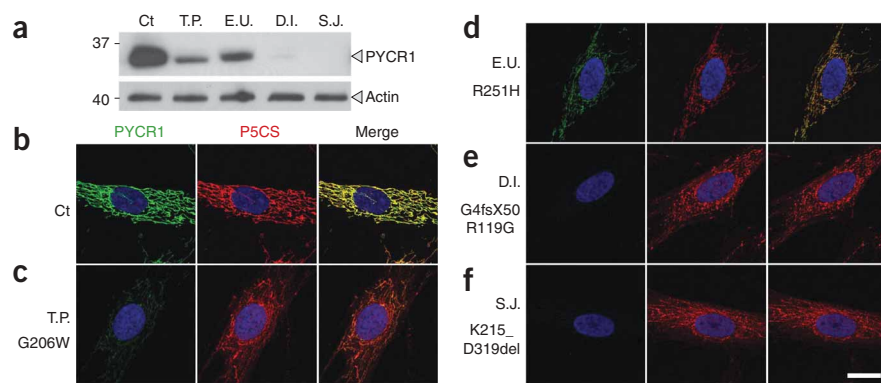
Figure 2 Effect of *PYCR1* mutations. (**a**) Immunoblot analysis of PYCR1 protein expression in primary skin fibroblasts from controls and patients. Actin served as a loading control. PYCR1 expression is absent in affected individuals D.I. and S.J., whereas E.U. and T.P. show a substantial reduction. (**b–f**) Immunofluorescent detection of PYCR1 and P5CS in mitochondria from skin fibroblasts. (**b**) In control (Ct) fibroblasts, PYCR1 and the mitochondrial matrix protein P5CS colocalize. In fibroblasts from subjects D.I. (**e**) and S.J. (**f**), immunostaining for PYCR1 is undetectable. In contrast, in fibroblasts from T.P. (**c**) and E.U. (**d**), PYCR1 staining in mitochondria is lower in intensity relative to control. Mitochondrial network is abnormal in D.I., S.J. and T.P. Scale bar, 20 μm.

morphant embryos. Despite shared blood circulation (**Supplementary Video 3**), skin hypoplasia and stunted growth were not rescued in parabiotic Pycr1 morphants even though fewer regions of edema were observed (**Fig. 5c–e**). We conclude that the ancestral *Pycr1* gene in *Xenopus* plays dual but independent roles during blood and skin development that may be attributed to the paralogous *PYCR1* and *PYCR2* genes in human. Indeed, a role for PYCR2 in human erythrocytes has been well documented[10,11].

The marked increased cell death in the developing skin of frogs and fish, as revealed by acridine orange and TUNEL staining (**Fig. 5f–i** and **Supplementary Fig. 5i,j**), underscores the specific requirement for *Pycr1* in this particular tissue. This parallels the data obtained with cells from affected individuals. Together these lines of evidence suggest that *PYCR1* m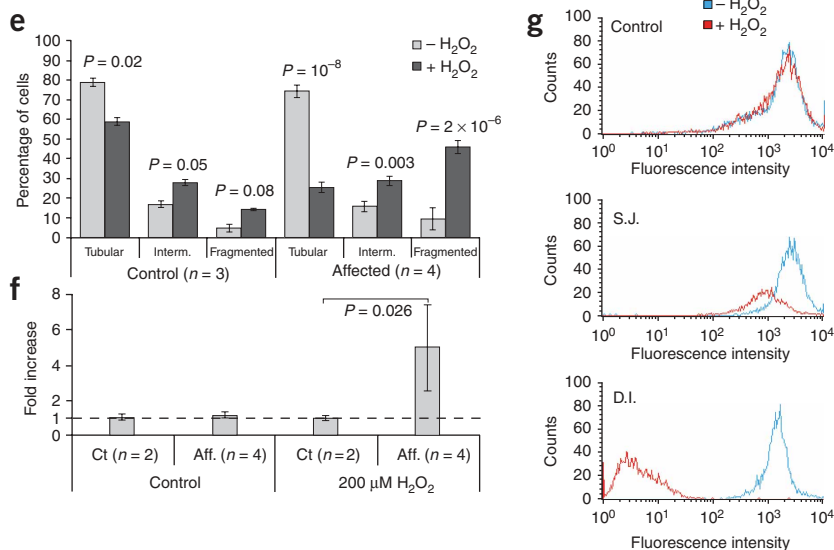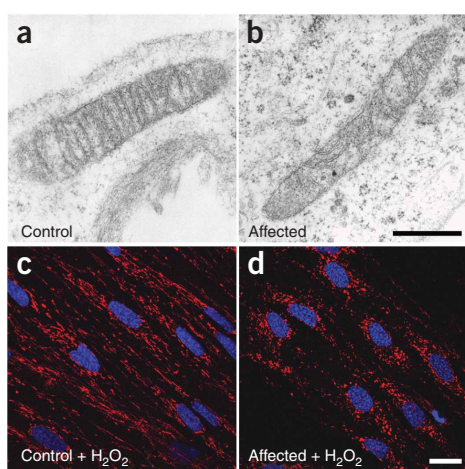utants have compromised mitochondrial function that leads to apoptosis during embryogenesis and a general inability to thrive during adult life.

Fig. 5a–j). Microinjection of human *PYCR1* mRNA partially rescued the phenotype observed in frogs and fish (**Supplementary Figs. 5 and 6**). Pycr1 morphant frogs had no circulating red blood cells (**Supplementary Videos 1** and **2**), as validated by the loss of *Scl* expression, a marker of primitive hematopoiesis (**Fig. 5a,b**). To rule out the possibility that the skin atrophy was caused by anemia, we performed a parabiosis experiment joining control and Pycr1

PYCR1 belongs to the NAD(P)H-binding Rossmann-fold domain superfamily and catalyzes the conversion of Δ^1-pyrroline-5-carboxylate to L-proline. Determination of the crystal structure revealed that the mature enzyme consists of five homodimer subunits around a peripheral circular groove[12]. Several heritable disorders have been

Figure 3 Loss of PYCR1 causes increased sensitivity to oxidative stress. (**a,b**) Ultrastructural analysis of mitochondrial morphology. Whereas mitochondria in control fibroblasts (**a**) have regularly arranged cristae, fibroblasts from affected individual D.I. (**b**) show strongly altered cristae and a smaller diameter. Scale bar, 1 μm. (**c,d**) Changes in mitochondrial morphology upon oxidative stress. Addition of 500 μM H_2O_2 to cell culture medium for 10 min leads to mitochondrial network collapse in fibroblasts from affected individual from family S.J. (**d**); tubular mitochondrial network remains largely intact in control cells (**c**). Scale bar, 20 μm. (**e**) Quantification of mitochondrial morphology changes upon oxidative stress. Without oxidative stress (gray), most control ($n = 3$) and affected ($n = 4$) cells showed tubular mitochondria. Only a few cells with fragmented or intermediate (interm.) morphologies were seen. In contrast, under oxidative stress (black) the number of cells with fragmented mitochondria increased much more in affected cells than in control. (**f**) Quantification of apoptotic cell death by TUNEL 24 h after oxidative stress. Fibroblasts from control (Ct; $n = 2$) and affected individuals (Aff; $n = 4$) showed no differences in apoptosis under normal culture conditions (control). Fivefold more ($P = 0.026$) apoptosis was observed in cells from affected individuals 24 h after a 10 min incubation with 200 μM H_2O_2. Normalized to Ct cells in control experiment. Data in **e,f** averaged from three independent experiments; error bars, s.d. (**g**) Mitochondrial membrane potential is reduced in fibroblasts from affected individuals S.J. and D.I. after 2 h incubation with 200 μM H_2O_2 but unchanged in control cells. Representative results.
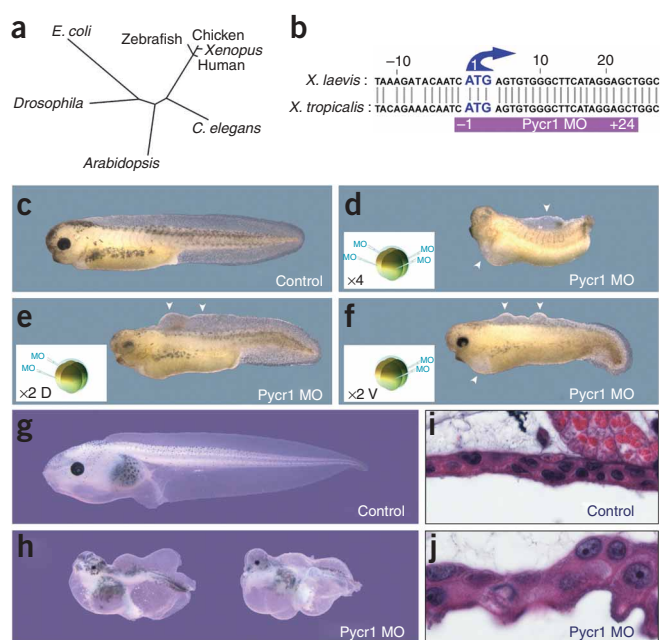
Figure 4 Phenotype of Pycr1 *Xenopus* morphants. (**a**) *Pycr1* is evolutionary conserved among bacteria, plants, insects and vertebrates. (**b**) Design of a translation-blocking morpholino (MO) oligonucleotide for *Xenopus Pycr1*. (**c**) Control embryo at stage 30. (**d**) Pycr1 morphants injected in each blastomere at the four-cell stage failed to grow a tail and had underdeveloped eyes. (**e**) Dorsal (D) MO injections impaired eye but not tail development. (**f**) Ventral (V) MO injections impaired tail but not eye development. Arrowheads, skin wrinkles. (**g**) Control embryo at the swimming tadpole stage. (**h**) Pycr1 morpholino-injected embryos showing severe growth retardation and large regions of ectodermal edema over the entire body, which develop from wrinkles seen earlier (**e,f**). (**i**) Histological section of skin from control embryo at stage 45 showing bilayered epidermis consisting of outer periderm and inner sensorial layer. (**j**) Disorganized architecture of epidermis with enlarged cells, enlarged nuclei and cellular protrusions in Pycr1 morphant.

ATP6V0A2, encoding subunit a2 of the V-ATPase complex that localizes to endosomes and the Golgi apparatus, have been identified in ARCL2 (ref. 19). The *GORAB* gene also encodes a Golgi-localized protein[18]. The phenotypic similarities suggest a common, yet to be determined, pathogenetic mechanism in these conditions. Notably, increased apoptosis is also seen in fibroblasts from individuals with ARCL2 having *ATP6V0A2* defects[20].

Besides energy production, mitochondria serve many different functions, among them the generation of potentially harmful ROS[21]. ROS are involved in the regulation of apoptosis and as such have become a central focus of aging research[22]. ROS were initially regarded as toxic side products of oxidative phosphorylation, and their importance for redox-dependent signaling processes has emerged only recently[22,23]. Indeed, proline has been implicated in the regulation of ROS abundance, and PYCR1 and PYCR2 have been implicated in the regulation of the $NAD(P)H/NAD(P)^+$ ratio in the cytoplasm and in the mitochondrion[10,11,24]. Mitochondrial fragmentation is a known phenomenon that has been described as impairing cellular function in neurodegenerative disorders[25]. Notably, changes in mitochondrial

linked to the proline metabolic pathway[13]. Most notably, P5CS deficiency causes a condition of mental retardation, joint hypermobility and skin laxity (MIM612652)[14–16]. As in the subjects described herein, P5CS deficiencies are not consistently characterized by low serum proline[14,15]. Furthermore, fibroblasts from the subjects described here did not show the proliferation defect described upon P5CS deficiency[16]. The phenotype of *PYCR1*-related disease overlaps with other forms of cutis laxa, mirrored by the fact that affected individuals from this cohort have been previously described under the diagnoses WSS, gerodermia osteodysplastica or DBS[1,3,5–9]. Whereas gerodermia osteodysplastica caused by mutations in *GORAB* (formerly known as *SCYL1BP1*) does not lead to intellectual impairment, ARCL2 often includes mild or moderate mental retardation and brain anomalies[2,17,18]. The mutations we detected cluster in exons 4, 5 and 6, which encode the catalytic sites of PYCR1 and are predominantly missense and splice-site mutations. Although a wide range of phenotypes was observed (see **Table 1**), no clear genotype-phenotype correlation could be discerned. Mutations in

Figure 5 Skin hypoplasia in Pycr1 morphants is accompanied by spontaneous apoptosis and is independent of anemia. (**a**) *Scl* expression at stage 25 marks site of primitive hematopoiesis in ventral ectoderm of control embryo. (**b**) *Scl* expression was abrogated in Pycr1 morphants suffering anemia (**Supplementary Videos 1** and **2**). (**c**) Parabiosis performed at stage 22 between a Pycr1-depleted (MO) tadpole (top) and control (bottom) did not rescue from apoptosis (inset, stage 33), stunted growth and skin defects despite shared blood circulation (**Supplementary Video 3**). (**d**) Histological staining. Epidermis of Pycr1 parabiotic morphant embryo remained disorganized relative to control. (**e**) Histological section through epidermis of parabiotic control tadpole at stage 45 showing normal skin architecture. (**f**) Acridine-orange background staining of control embryo (inset, bright-field image). (**g**) Acridine-orange labeling of dying cells (intense green) in Pycr1 morphant embryos injected only in the ventral (V) half (inset, bright-field image). Only the ventro-posterior half of the embryo, derived from the injected ventral blastomeres, is undergoing apoptosis. (**h**) TUNEL staining in stage 33 tadpole showing few apoptotic cells (inset, control at stage 25). (**i**) Pycr1 morphants, with a markedly increased number of dying cells at stage 33 relative to control (inset, stage 25).
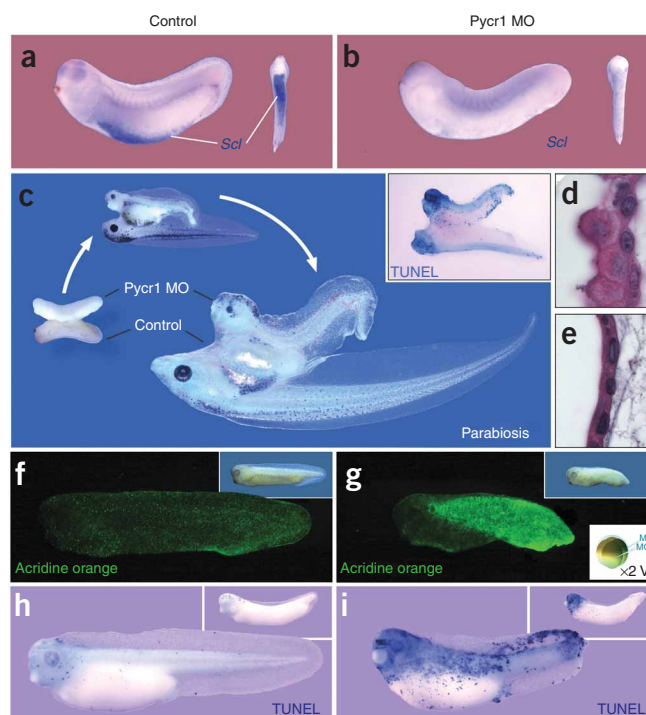
fusion have also been shown to trigger cellular senescence[26]. Although the exact role of PYCR1 in mitochondrial function and integrity remains to be determined, its orthologs in other species, such as *Saccharomyces*, *Arabidopsis* and *Drosophila*, have been linked to stress resistance, which suggests that human *PYCR1* as well may provide adaptive protection against stress by maintaining a reservoir of rapidly mobilizable proline and reducing equivalents in mitochondria[10,12].

In summary, mutations in *PYCR1* leading to a loss of PYCR1 function are a major cause of autosomal recessive cutis laxa, evoking a phenotype that overlaps with gerodermia osteodysplastica, ARCL2 and DBS. The pathophysiological basis appears to be an impaired mitochondrial function leading to developmental defects through increased apoptosis. Our finding highlights the importance of mitochondrial function in the process of aging and might help to develop new treatment strategies for common age-related disorders[22].

METHODS
Methods and any associated references are available in the online version of the paper at http://www.nature.com/naturegenetics/.

Accession codes. GenBank RefSeq DNA: *Homo sapiens PYCR1* isoform A, NM_006907.2; *H. sapiens PYCR1* isoform B, NM_153824.1; *Xenopus laevis Pycr1*, NM_001091619; *Danio rerio pycr1*, BC095354; *D. rerio pycr2*, BC060905.

Note: Supplementary information is available on the Nature Genetics website.

AUTHOR CONTRIBUTIONS
B.R., N.E.-B., S.M. and U.K. designed the study. H.K., L.A.-G., M. Shahwan, B.R., F.B., S.F.N., A.M., F.A., D.G., P.F., A.N., A.R., D.M., M.G., J.N., A.G., A.S., R.S., A.R.J., E.S., D.S., B.D., S.R., H.H., B.W. and L.v.M. made clinical diagnoses and collected clinical data and samples. B.R., B.M., A.D., G.N., B.F., Y.L., B.B., P.N. and B.W. conducted genotyping and linkage analysis. H.L., B.O., B.M. and S.N. performed genomic loci capture. B.R., N.E.-B., A.D., B.F., D.K., S.C., M.S., P.-Y.T. performed immunoblotting, immunostaining, TUNEL, and proline level and FACS analysis. B.R., N.E.-B. and S.C. performed Xenopus work, ISH and Pycr1 constructs. U.K., B.F., M.S.-v.K. and P.S. performed zebrafish work. B.F., U.K. and M. Schuelke performed respiratory chain measurements. I.H. and G.Z. were responsible for ultrastructural and histological analysis of skin biopsies. B.R., N.E.-B., S.M. and U.K. wrote the manuscript.

Published online at http://www.nature.com/naturegenetics/.
Reprints and permissions information is available online at http://npg.nature.com/reprintsandpermissions/.

1. Rajab, A. *et al.* Geroderma osteodysplasticum hereditaria and wrinkly skin syndrome in 22 patients from Oman. *Am. J. Med. Genet. A* **146A**, 965–976 (2008).
2. Morava, E. *et al.* Defining the phenotype in an autosomal recessive cutis laxa syndrome with a combined congenital defect of glycosylation. *Eur. J. Hum. Genet.* **16**, 28–35 (2008).
3. Guerra, D. *et al.* The De Barsy syndrome. *J. Cutan. Pathol.* **31**, 616–624 (2004).
4. Zhang, M.C. *et al.* Cutis laxa arising from frameshift mutations in exon 30 of the elastin gene (ELN). *J. Biol. Chem.* **274**, 981–986 (1999).
5. Al-Gazali, L.I., Sztriha, L., Skaff, F. & Haas, D. Gerodermia osteodysplastica and wrinkly skin syndrome: are they the same? *Am. J. Med. Genet.* **101**, 213–220 (2001).
6. Nanda, A. *et al.* Gerodermia osteodysplastica/wrinkly skin syndrome: report of three patients and brief review of the literature. *Pediatr. Dermatol.* **25**, 66–71 (2008).
7. Hamamy, H., Masri, A. & Ajlouni, K. Wrinkly skin syndrome. *Clin. Exp. Dermatol.* **30**, 590–592 (2005).
8. Sommer, A. Photo essay–geroderma osteodysplastica. *Am. J. Med. Genet. C. Semin. Med. Genet.* **145C**, 291–292 (2007).
9. Kunze, J. *et al.* De Barsy syndrome–an autosomal recessive, progeroid syndrome. *Eur. J. Pediatr.* **144**, 348–354 (1985).
10. Phang, J.M., Pandhare, J. & Liu, Y. The metabolism of proline as microenvironmental stress substrate. *J. Nutr.* **138**, 2008S–2015S (2008).
11. Hagedorn, C.H. & Phang, J.M. Transfer of reducing equivalents into mitochondria by the interconversions of proline and delta 1-pyrroline-5-carboxylate. *Arch. Biochem. Biophys.* **225**, 95–101 (1983).
12. Meng, Z. *et al.* Crystal structure of human pyrroline-5-carboxylate reductase. *J. Mol. Biol.* **359**, 1364–1377 (2006).
13. Mitsubuchi, H., Nakamura, K., Matsumoto, S. & Endo, F. Inborn errors of proline metabolism. *J. Nutr.* **138**, 2016S–2020S (2008).
14. Baumgartner, M.R. *et al.* Delta1-pyrroline-5-carboxylate synthase deficiency: neuro-degeneration, cataracts and connective tissue manifestations combined with hyper-ammonaemia and reduced ornithine, citrulline, arginine and proline. *Eur. J. Pediatr.* **164**, 31–36 (2005).
15. Bicknell, L.S. *et al.* A missense mutation in ALDH18A1, encoding Delta1-pyrroline-5-carboxylate synthase (P5CS), causes an autosomal recessive neurocutaneous syndrome. *Eur. J. Hum. Genet.* **16**, 1176–1186 (2008).
16. Baumgartner, M.R. *et al.* Hyperammonemia with reduced ornithine, citrulline, arginine and proline: a new inborn error caused by a mutation in the gene encoding delta(1)-pyrroline-5-carboxylate synthase. *Hum. Mol. Genet.* **9**, 2853–2858 (2000).
17. Van Maldergem, L. *et al.* Cobblestone-like brain dysgenesis and altered glycosylation in congenital cutis laxa, Debre type. *Neurology* **71**, 1602–1608 (2008).
18. Hennies, H.C. *et al.* Gerodermia osteodysplastica is caused by mutations in *SCYL1BP1*, a Rab-6 interacting golgin. *Nat. Genet.* **40**, 1410–1412 (2008).
19. Kornak, U. *et al.* Impaired glycosylation and cutis laxa caused by mutations in the vesicular H$^+$-ATPase subunit ATP6V0A2. *Nat. Genet.* **40**, 32–34 (2008).
20. Hucthagowder, V. *et al.* Loss-of-function mutations in ATP6V0A2 impair vesicular trafficking, tropoelastin secretion, and cell survival. *Hum. Mol. Genet.* **18**, 2149–2165 (2009).
21. Wallace, D.C. A mitochondrial paradigm of metabolic and degenerative diseases, aging, and cancer: a dawn for evolutionary medicine. *Annu. Rev. Genet.* **39**, 359–407 (2005).
22. Balaban, R.S., Nemoto, S. & Finkel, T. Mitochondria, oxidants, and aging. *Cell* **120**, 483–495 (2005).
23. D'Autreaux, B. & Toledano, M.B. ROS as signalling molecules: mechanisms that generate specificity in ROS homeostasis. *Nat. Rev. Mol. Cell Biol.* **8**, 813–824 (2007).
24. Krishnan, N., Dickman, M.B. & Becker, D.F. Proline modulates the intracellular redox environment and protects mammalian cells against oxidative stress. *Free Radic. Biol. Med.* **44**, 671–681 (2008).
25. Knott, A.B., Perkins, G., Schwarzenbacher, R. & Bossy-Wetzel, E. Mitochondrial fragmentation in neurodegeneration. *Nat. Rev. Neurosci.* **9**, 505–518 (2008).
26. Lee, S. *et al.* Mitochondrial fission and fusion mediators, hFis1 and OPA1, modulate cellular senescence. *J. Biol. Chem.* **282**, 22977–22983 (2007).

ONLINE METHODS

Subjects. Several of the subjects presented here have already been described in the literature. All other individuals were recruited based on a clinical diagnosis of either gerodermia osteodysplastica, autosomal recessive cutis laxa (also called wrinkly skin syndrome) or de Barsy syndrome. Inclusion criteria were a progeroid appearance; lax, wrinkly skin at early age; hernias; hip dislocation; and osteopenia. In some individuals, mental retardation, brain malformations (abnormality of the corpus callosum), athetoid movements and/or cataracts were present; these individuals were considered to have de Barsy syndrome. DNA samples were obtained from 22 families after participants gave their informed consent and after approval by the local ethics commission (Ethikkommission der Charité).

Genotyping and linkage analysis. We performed genome-wide linkage analysis in eight families using the GeneChip Human Mapping 250K Arrays (Affymetrix). Genotypes were called by the GeneChip DNA Analysis Software (v2.0, Affymetrix). We verified sex by counting heterozygous SNPs on the X chromosome. Relationship errors were evaluated with the help of the program Graphical Relationship Representation. The program PedCheck[27] was applied to detect mendelian errors and data for SNPs with such errors were removed from the data set. Nonmendelian errors were identified by using the program MERLIN[28] and genotypes unlikely for related samples were deleted. Nonparametric linkage analysis using all genotypes of a chromosome simultaneously was carried out with MERLIN. Parametric linkage analysis was performed by a modified version of the program GENEHUNTER 2.1 through stepwise use of a sliding window with sets of 110 or 200 SNPs[29]. Haplotypes were reconstructed with GENEHUNTER 2.1 and presented graphically with HaploPainter[30].

Mutation analysis. Positional candidate genes were obtained from the GenBank and Ensembl databases. Genes were analyzed by direct sequencing of DNA with primers flanking each exon. Primer sequences were based on the reference sequences of each gene. The primer sequences for *PYCR1* mutation screening are given in **Supplementary Table 2**. Sequence analysis was done with the BigDye Terminator cycle sequencing kit (Applied Biosystems), and products were run on a 3730 DNA Analyzer (Applied Biosystems).

Genomic locus capture. Briefly, custom arrays (Agilent 244K) were designed to target every exonic sequence of the genes present in the locus 17q25 between 72048357 and 78774742, excluding the highly repeated regions. DNA libraries were prepared following the Illumina library generation protocol version 2.3 and were hybridized to the custom arrays according to the Agilent CGH 244K array protocol, then washed, eluted and amplified. Each sample was submitted to one channel of an Illumina flow cell and sequenced by Illumina Genome Analyzer using standard manufacturer's protocol. We sequenced a total of five samples from four different families. The image data was processed by the provided Genome Analyzer Pipeline version 1.0 and all sequences were aligned to the human reference genome (University of California Santa Cruz, build 18) by Blat-like Fast Accurate Search Tool (BFAST (see URLs); N. Homer, B. Merriman and S.F. Nelson, unpublished data). Mismatches were filtered for those seen two or more times, where the mutation was seen 100% of the time (homozygous), and did not overlap with a known dbSNP129 entry mismatch. The open-source SeqWare project, which provides a laboratory information management system tool for tracking samples (SeqWare laboratory information management system) and a pipeline for sequence analysis (SeqWare Pipeline) was used throughout this work.

Cell culture. Human skin fibroblasts were cultivated in DMEM (Lonza) supplemented with 10% FCS (Lonza), 1% Ultraglutamine (Lonza) and 1% penicillin/streptomycin (Lonza) at 5% CO_2 and 37 °C.

Quantitative PCR. RNA was isolated from organs of postnatal day 4 mice using the Trizol (Invitrogen) method. One microgram of RNA was reverse-transcribed using the Revert Aid kit (Fermentas) and random hexamers. Quantitative PCR was performed with SYBR green (Applied Biosystems). Primers are given in **Supplementary Table 2**.

Immunoblot analysis. Mitochondrial and cytosolic fractions of whole cell lysates of primary skin fibroblasts were obtained with a mitochondrial isolation kit for mammalian cells (Thermo Scientific) and resolved by electrophoresis in SDS polyacrylamide gels. For immunoblot analysis, PVDF membranes were probed with anti-actin A5060 (Sigma) 1:1,000 and rabbit anti-PYCR1 (Proteintech) 1:500.

Immunofluorescence analysis. For immunofluorescence, cells were washed in phosphate-buffered saline (PBS) three times. Cells were fixed in 4% (wt/vol) paraformaldehyde in PBS for 10 min and permeabilized with 0.4% (vol/vol) Triton-X100 in 3% BSA in PBS for 10 min at 4 °C. Specific antibodies to PYCR1 (rabbit anti-PYCR1, Proteintech 1:500) and P5CS (mouse anti-P5CS, Abnova, 1:300) were incubated overnight in 3% BSA at 4 °C. For visualization an antibody to mouse immunoglobulin G (anti–mouse IgG) Alexa Fluor 555 conjugate (Invitrogen, Molecular Probes) and an anti-rabbit IgG Alexa Fluor 488 (Invitrogen, Molecular Probes) conjugate was applied. DNA was stained by DAPI and cells were mounted in Fluoromount (Scientific Services). Images were collected by using an LSM 510 Meta (Carl Zeiss) with a ×63 Plan Apochromat oil immersion objective.

Ultrastructural analysis. All specimens were fixed for at least 2 h at 19–22 °C in 3% glutaraldehyde solution in 0.1 M cacodylate buffer, pH 7.4, cut into pieces of ∼1 mm³, washed in buffer, postfixed for 1 h at 4 °C in 1% osmium tetroxide, rinsed in water, dehydrated through graded ethanol solutions, transferred into propylene oxide, and embedded in epoxy resin (glycidether 100). Semithin and ultrathin sections were cut with an ultramicrotome (Reichert Ultracut E). Ultrathin sections were treated with uranyl acetate and lead citrate, and examined with an electron microscope (Philips EM 400).

Mitochondrial morphology. Morphology of the mitochondrial network was investigated as previously described[31]. Fifty-percent-confluent fibroblasts were loaded with 100 nM Mito Tracker Red CM-H2XRos (Invitrogen). Cells were incubated with 500 µM H_2O_2 for 5 min and then fixed in 4% (wt/vol) paraformaldehyde in PBS for 10 min at 4 °C. DNA was stained by DAPI and cells were mounted in Fluoromount (Scientific Services). Pictures of every sample were collected randomly using a BX60 Olympus microscope.

Apoptosis assay. For apoptosis measurement after hydrogen peroxide (neoLab) treatment, cells were incubated with 200 µM H_2O_2 for one hour without FCS as described[32]. Subsequently medium with 0.4% FCS was added and cells were incubated at normal conditions for additional 24 h. Cells were fixed in 4% (wt/vol) paraformaldehyde in PBS for 10 min and permeabilized with 0.1% (vol/vol) Triton-X100 in 3% BSA in PBS for 2 min on ice. For apoptosis determination the TUNEL assay (Roche) was performed according to manufacturer specifications. Cells were fixed in 4% (wt/vol) paraformaldehyde in PBS for 10 min at 4 °C. DNA was stained by DAPI and cells were mounted in Fluoromount (Scientific Services). Pictures were collected randomly. Each experiment was performed three times. More than 2,000 cells were analyzed per assay.

Mitochondrial transmembrane potential measurements. To evaluate mitochondrial transmembrane potential, primary fibroblasts were treated with 200 µM H_2O_2 for 2 h without FCS. After two washes in PBS, 5×10^5 cells per milliliter were incubated with 40 nM of the fluorescent dye 3,3′-dihexyloxacarbocyanine iodide (DiOC$_6$(3); Molecular Probes) for 15 min at 37 °C in PBS, followed by analysis on a FACSCalibur cytofluorometer (BD Biosciences).

Polarography. Cultured skin fibroblasts of affected ($n = 3$) and unaffected ($n = 3$) subjects were trypsinized and washed in PBS twice. Permeabilization was done immediately in 50 µg/ml digitonin for 30 s before measurement and verified by the Trypan blue exclusion test (>99% permeabilization was required). Fibroblasts (7×10^6) were resuspended in reaction buffer and injected into the reaction chamber with a Clark-type electrode (Hansatech), and oxygen concentrations were measured in 0.7-ml reaction volume at 37 °C with substrates and inhibitors according to standard protocols[33]. The oxygen consumption is given as fmol O_2 per minute per cell. All measurements were reproduced two to four times. Epstein-Barr virus–immortalized lymphoblastoid cell lines from affected subjects ($n = 4$), heterozygous parents ($n = 2$) and

unaffected controls ($n = 2$) were grown in RPMI (Lonza) suspension culture, pelleted by centrifugation and washed twice with PBS. Digitonin permeabilization was done for 60 s, and 2×10^7 cells in 0.7 ml were used for one experiment as described above.

Reactive oxygen species measurement. Skin fibroblasts were trypsinized, washed in medium and resuspended in PBS containing 0.2% BSA. The cell suspension was incubated for 15 min with 20 μM 2,7-dichlorodihydrofluorescein diacetate (Molecular Probes) at 19–22 °C with and without 1 mM H_2O_2. Fluorescence intensity was determined by FACS using a Canto II (Becton Dickinson) cell sorter and the analysis software Flowjo (Tree Star). Cell viability was controlled by DAPI (Molecular Probes) incubation.

Proliferation assay. For the assessment of the proliferation rate, 2.5×10^4 cells were seeded on glass coverslips. The cells were incubated for 8 h in medium containing 10 μM bromodeoxyuridine (BrdU) (Roche). Cells were fixed in 4% (wt/vol) paraformaldehyde in PBS for 10 min after 24, 48 and 72 h and then incubated in 3 M HCl for 10 min at 19–22 °C. After permeabilization with 0.1% (vol/vol) Triton-X100 in 3% BSA in PBS for 30 min at 4 °C, cells were incubated with an antibody to BrdU (G3G4, Developmental Studies Hybridoma Bank) 1:500 for 1 h at 19-22 °C. For visualization, an anti–mouse IgG Alexa Fluor 488 conjugate (Invitrogen, Molecular Probes) was applied. DNA was stained by DAPI and cells were mounted in Fluoromount (Scientific Services). The experiment was also performed in medium with 10% dialyzed FCS and in medium supplemented with 5 mM L-proline (Sigma-Aldrich).

Morpholino oligonucleotides and RNA injections. Morpholino 25-bp antisense oligomers for *X. laevis Pycr1*, *D. rerio pycr1* and *D. rerio pycr2* were obtained from Gene Tools and are described in **Supplementary Table 2**. The morpholinos were resuspended in sterile water to a concentration of 1 mM according to manufacturer's instructions. *Xenopus* embryos were injected four times radially at the two- to four-cell stage with 4 nl (33 ng morpholino per injection). For zebrafish experiments, morpholinos were injected at the one-cell stage with 4 nl (33 ng morpholino per injection), or with 2 nl of each morpholino when co-injected. Synthetic capped mRNAs of human *PYCR1* cDNA transcribed *in vitro* with an SP6 kit (Ambion) was used for rescue experiments at 200 pg in each blastomere at the four-cell stage for *Xenopus* embryos or at 20 pg to 200 pg for zebrafish embryos at the one-cell stage.

Embryological methods. Protocols for fertilization, injections, whole-mount *in situ* hybridization and TUNEL[34] can be found at our protocols website (see

URLs). Analysis of cell death on live embryos was performed by incubating tadpoles in the dark for 30 min with acridine orange (2 μg/ml) in Barth solution[35] 0.1×. After extensive washes in Barth 0.1×, images of embryos were captured under fluorescence (excitation/emission, 500/530 nm) with a Leica DFC 300 FX camera. Parabiosis was performed at stage 22, on dechorionated embryos joined by ventral ectoderm after small incisions. Parabiotic embryos were cultured in Barth 1× until healed and transferred into Steinberg solution[35]. A stereomicroscope M205 FA equipped with an ICD camera (Leica) was used to capture images of embryos in successive focal planes. Images were then merged into one picture with Photoshop CS3 (Adobe).

Statistical analysis. All error bars represent s.d. The significance of pairwise comparisons was determined by Student's *t*-test. Correction for multiple testing were done according by the Bonferroni method.

URLs. GenBank, http://www.ncbi.nlm.nih.gov/mapview/. Ensembl, http://www.ensembl.org/. University of California Santa Cruz human reference genome (build 18, http://genome.ucsc.edu/). Blat-like Fast Accurate Search Tool (BFAST, http://genome.ucla.edu/bfast/. SeqWare, http://seqware.sourceforge.net/. Unabridged protocols, http://www.reversade.com-a.googlepages.com/protocols.

27. O'Connel, J.R. & Weeks, D.E. PedCheck: a program for identification of genotype incompatibilities in linkage analysis. *Am. J. Hum. Genet.* **63**, 259–266 (1998).
28. Abecasis, G.R., Cherny, S.S., Cookson, W.O. & Cardon, L.R. Merlin—rapid analysis of dense genetic maps using sparse gene flow trees. *Nat. Genet.* **30**, 97–101 (2002).
29. Thiele, H. & Nurnberg, P. HaploPainter: a tool for drawing pedigrees with complex haplotypes. *Bioinformatics* **21**, 1730–1732 (2005).
30. Kruglyak, L., Daly, M.J., Reeve-Daly, M.P. & Lander, E.S. Parametric and nonparametric linkage analysis: a unified multipoint approach. *Am. J. Hum. Genet.* **58**, 1347–1363 (1996).
31. Duvezin-Caubet, S. *et al.* Proteolytic processing of OPA1 links mitochondrial dysfunction to alterations in mitochondrial morphology. *J. Biol. Chem.* **281**, 37972–37979 (2006).
32. Teramoto, S. *et al.* Hydrogen peroxide-induced apoptosis and necrosis in human lung fibroblasts: protective roles of glutathione. *Jpn. J. Pharmacol.* **79**, 33–40 (1999).
33. Hofhaus, G., Shakeley, R.M. & Attardi, G. Use of polarography to detect respiration defects in cell cultures. *Methods Enzymol.* **264**, 476–483 (1996).
34. Hensey, C. & Gautier, J. Programmed cell death during *Xenopus* development: a spatiotemporal analysis. *Dev. Biol.* **203**, 36–48 (1998).
35. Sive, H., Grainger, R.M. & Harland, R.M. *Early Development of Xenopus Laevis: A Laboratory Manual* (Cold Spring Harbor Press, New York, 2000).